Visualizing, Approximating, and Understanding Black-Hole Binaries

Thesis by

David A. Nichols

In Partial Fulfillment of the Requirements

for the Degree of

Doctor of Philosophy

California Institute of Technology

Pasadena, California

2012

(Defended April 30, 2012)

To my parents and sister

Acknowledgments

It is often said that it takes a village to raise a child, and it seems to take no fewer number of people to take an undergraduate and make him a postdoctoral researcher. For the many people who have helped me as I worked toward my Ph.D., I would like to acknowledge them individually and in (mostly) chronological order from when they first contributed (knowingly or not) to my completing this thesis.

I must, therefore, begin by thanking my parents. They brought me into this world and instilled in me a value for education, integrity, and the pursuit of the truth; they supported my interests, were encouraging, and always willing to listen; they even attempted to keep up on my latest aspect of black-hole research—I do not think there is much else I could ask from them.

I am also indebted to my sister, Rebecca. She has been a friend, an inspiration, and a role model. I do not think I would have attempted as much, or worked as hard, had it not been for her example leading the way since I was young.

I would like to acknowledge Kip Thorne. It was his teaching that drew me to relativity, and his challenging homework assignments that brought me into the theoretical astrophysics group, and started me on research that would become the first chapters of this thesis. He introduced me to Yanbei Chen, who would become my thesis adviser. He has an incredible understanding of general relativity, and I have learned and benefitted much from my interactions with him.

I would like to express my gratitude to my adviser Yanbei Chen. He has been a wealth of ideas, and was always happy to discuss a wide range of topics across many branches of physics with me. He provided me with invaluable guidance on choosing research problems and presenting my results in writing and in speech. He encouraged me to deepen my understanding of relativity and helped me to develop as a scientist.

I also benefitted from working with many collaborators during this thesis: Jeff Kaplan and Kip Thorne for Chapter 2; Yanbei Chen, Drew Keppel, and Kip Thorne for Chapter 3; Yanbei Chen, Michael Cohen, Drew Keppel, Geoffrey Lovelace, Keith Matthews, Mark Scheel, and Ulrich Sperhake for Chapter 4; Yanbei Chen for Chapters 5 and 6; Yanbei Chen, Huan Yang, Fan Zhang, and Aaron Zimmerman for Chapter 7; and Jeandrew Brink, Yanbei Chen, Jeff Kaplan, Geoffrey Lovelace, Keith Matthews, Robert Owen, Mark Scheel, Kip Thorne, Fan Zhang, and Aaron Zimmerman for

Chapters 8–11.

My collaborators and I had many fruitful discussions with several people while writing and doing research for the papers that became the chapters of this thesis. They include Luc Blanchet, Yanbei Chen, and Drew Keppel for Chapter 2; Jeff Kaplan and Geoffrey Lovelace for Chapter 3; Michael Boyle, Jeandrew Brink, Lawrence Kidder, Robert Owen, Harald Pfeiffer, Saul Teukolsky, and Kip Thorne for Chapter 4; Lee Lindblom, Geoffrey Lovelace, Yasushi Mino, Ulrich Sperhake, Mark Scheel and Béla Szilágyi, Kip Thorne, and Huan Yang for Chapter 5; Jeandrew Brink, Tanja Hinderer, Lee Lindblom, Yasushi Mino, Mark Scheel, Belá Szilágyi, Kip Thorne, Huan Yang, and Aaron Zimmerman for Chapter 6; Emanuele Berti, Jeandrew Brink, and Zhongyang Zhang for Chapter 7; Larry Kidder and Saul Teukolsky for Chapter 8; Yanbei Chen, Tanja Hinderer, Jeffrey D. Kaplan, Geoffrey Lovelace, Charles Misner, Ezra Newman, Robert Owen, and Kip Thorne for Chapter 9; John Belcher, Larry Kidder, Richard Price, and Saul Teukolsky for Chapter 10; and Larry Kidder and Saul Teukolsky for Chapter 11.

In working on the chapters of this thesis, I was supported by several public and private sources of funding: the public grants were NSF Grants PHY-0601459, PHY-0653653, and PHY-1068881, and NSF CAREER Grant PHY-0956189; the private grants came from the Brinson Foundation and the David and Barbara Groce Fund at the California Institute of Technology. My collaborators were funded by these grants and several others, including: NSF Grants DMS-0553302, DMS-0553677, PHY-0652929, PHY-0652952, PHY-0652995, PHY-0960291, PHY-0969111, PHY-1005426, PHY-1005655, and PHY-1068881; NASA Grants NNX09AF96G and NNX09AF97G; and the Sherman Fairchild Foundation. Some calculations were done using the `SpEC` code, and others were performed on the Ranger cluster under NSF TeraGrid Grant PHY-090003.

I am particularly grateful to Barbara and David Groce, who started a graduate fellowship for my adviser's students (of which I was the first recipient). I enjoyed our interactions over these past years, and I was humbled by the interest they took in my work and my progress in my Ph.D.

I am also lucky to have had many interesting and informative discussions with members of the theoretical astrophysics group, which, although they did not directly contribute to the chapters of this thesis, were just as important to the Ph.D. process. In particular, I would like to bring to attention the graduate-student-lunch and theoretical-astrophysics-meeting attendees (who are too many to mention). I would also like to mention my office companions over the years, Kristen Boydstun, Tony Chu, Drew Keppel, Keith Matthews, and Elena Murchikova, who helped to make working in the office as pleasant as possible.

I am also pleased to acknowledge the members of my thesis committee, Mark Scheel, Christopher Hirata, and Alan Weinstein, who were all obliging and good-natured about serving on my committee.

I am also thankful for JoAnn Boyd and Shirley Hampton, who made the administrative aspects of being a graduate student a breeze, and Chris Mach, who kept the computers, on which so many

of the calculations in this thesis were performed, running smoothly.

There are certainly others whom I am forgetting to mention, and to those people I apologize; my memory may be short, but their contributions to this thesis are not.

Abstract

Numerical-relativity simulations of black-hole binaries and advancements in gravitational-wave detectors now make it possible to learn more about the collisions of compact astrophysical bodies. To be able to infer more about the dynamical behavior of these objects requires a fuller analysis of the connection between the dynamics of pairs of black holes and their emitted gravitational waves. The chapters of this thesis describe three approaches to learn more about the relationship between the dynamics of black-hole binaries and their gravitational waves: modeling momentum flow in binaries with the Landau-Lifshitz formalism, approximating binary dynamics near the time of merger with post-Newtonian and black-hole-perturbation theories, and visualizing spacetime curvature with tidal tendexes and frame-drag vortexes.

In Chapters 2–4, my collaborators and I present a method to quantify the flow of momentum in black-hole binaries using the Landau-Lifshitz formalism. Chapter 2 reviews an intuitive version of the formalism in the first-post-Newtonian approximation that bears a strong resemblance to Maxwell's theory of electromagnetism. Chapter 3 applies this approximation to relate the simultaneous bobbing motion of rotating black holes in the superkick configuration—equal mass black holes with their spins anti-aligned and in the orbital plane—to the flow of momentum in the spacetime, prior to the black-holes' merger. Chapter 4 then uses the Landau-Lifshitz formalism to explain the dynamics of a head-on merger of spinning black holes, whose spins are anti-aligned and transverse to the infalling motion. Before they merge, the black holes move with a large, transverse, velocity, which we can explain using the post-Newtonian approximation; as the holes merge and form a single black hole, we can use the Landau-Lifshitz formalism without any approximations to connect the slowing of the final black hole to its absorbing momentum density during the merger.

In Chapters 5–7, we discuss using analytical approximations, such as post-Newtonian and black-hole-perturbation theories, to gain further understanding into how gravitational waves are generated by black-hole binaries. Chapter 5 presents a way of combining post-Newtonian and black-hole-perturbation theories—which we call the hybrid method—for head-on mergers of black holes. It was able to produce gravitational waveforms and gravitational recoils that agreed well with comparable results from numerical-relativity simulations. Chapter 6 discusses a development of the hybrid model to include a radiation-reaction force, which is better suited for studying inspiralling black-

hole binaries. The gravitational waveform from the hybrid method for inspiralling mergers agreed qualitatively with that from numerical-relativity simulations; when applied to the superkick configuration, it gave a simplified picture of the formation of the large black-hole kick. Chapter 7 describes an approximate method of calculating the frequencies of the ringdown gravitational waveforms of rotating black holes (quasinormal modes). The method generalizes a geometric interpretation of black-hole quasinormal modes and explains a degeneracy in the spectrum of these modes.

In Chapters 8–11, we describe a new way of visualizing spacetime curvature using tools called tidal tendexes and frame-drag vortexes. This relies upon a time-space split of spacetime, which allows one to break the vacuum Riemann curvature tensor into electric and magnetic parts (symmetric, trace-free tensors that have simple physical interpretations). The regions where the eigenvalues of these tensors are large form the tendexes and vortexes of a spacetime, and the integral curves of their eigenvectors are its tendex and vortex lines, for the electric and magnetic parts, respectively. Chapter 8 provides an overview of these visualization tools and presents initial results from numerical-relativity simulations. Chapter 9 uses topological properties of vortex and tendex lines to classify properties of gravitational waves far from a source. Chapter 10 describes the formalism in more detail, and discusses the vortexes and tendexes of multipolar spacetimes in linearized gravity about flat space. The chapter helps to explain how near-zone vortexes and tendexes become gravitational waves far from a weakly gravitating, time-varying source. Chapter 11 is a detailed investigation of the vortexes and tendexes of stationary and perturbed black holes. It develops insight into how perturbations of (strongly gravitating) black holes extend from near the horizon to become gravitational waves.

Contents

List of Tables

List of Figures

Chapter 1

Introduction

To place the chapters of this thesis into context, I will briefly review the history, and the contributions to the understanding, of the two-body problem in Einstein's theory of general relativity in Section 1.1. I also discuss using gravitational-wave observations to learn more about space and time around two nearby, strongly gravitating bodies in that section as well. The next part, Section 1.2, is a more detailed overview of how the individual chapters of this thesis provide greater intuitive understanding of the dynamics and the gravitational waves from binaries made of black holes with similar masses.

1.1 The Two-Body Problem in General Relativity and Its Importance for Gravitational-Wave Measurements

1.1.1 A Brief Overview of the Two-Body Problem

While the two-body problem in Newtonian mechanics—computing the evolution of the centers of mass of two gravitating objects—can be solved exactly and analytically, the equivalent problem in Einstein's theory of general relativity is much more complicated, and it is only within the past decade that this problem has been solved numerically for strongly gravitating objects like black holes and neutron stars (see, e.g., [1] for a review of black-hole binary mergers and [2] for a review of neutron-star binaries and black-hole–neutron-star binaries). A brief comparison of the two theories can help one argue why the Newtonian problem was considerably simpler than the Einsteinian one. Newton's theory relates the acceleration of the center of mass of the two bodies to the central gravitational force; this relation is a differential equation for the center of mass, and its solutions are conic sections (see, e.g., [3]). Einstein's theory, however, replaces the idea of a gravitational force in favor of treating space and time as a unified manifold called curved spacetime, and test particles undergo nonuniform motion, because they follow geodesics (paths of minimal distance) in spacetime (see, e.g., [4]). Moreover, bodies (or more generally, any distribution of stress-energy)

curve spacetime via Einstein's field equations,

$$G_{\mu\nu} = 8\pi T_{\mu\nu} \,, \tag{1.1}$$

the statement that the Einstein curvature tensor $G_{\mu\nu}$ is proportional to the stress-energy tensor, $T_{\mu\nu}$.[1] Although Einstein's equations are written in a compact form, the simplicity of which is comparable to Newton's third law, they are a shorthand for a system of second-order nonlinear partial differential equations for the metric tensor, $g_{\mu\nu}$, which encodes the proper distance between two spacetime events, by

$$ds^2 = g_{\mu\nu} dx^\mu dx^\nu \,. \tag{1.2}$$

In a self-consistent evolution, one would also need to evolve the fields that comprise the bodies in the curved spacetime simultaneously with Einstein's equations. Because of the complexity of these evolution equations, it will not come as a surprise that the initial insights into the two-body problem came from approximate solutions to these equations (as we describe below).

An important step in the history of the two-body problem in general relativity was made by Einstein, Infeld, and Hoffman [5], who found equations of motion describing the evolution of any finite number of point masses in what is now called the post-Newtonian (PN) expansion. After the early work of Einstein, Infeld, and Hoffman, Chandrasekhar [6] formulated the complete first post-Newtonian (1PN) expansion of Einstein's equations for fluid sources, as an expansion in inverse powers of the speed of light. Chandrasekhar's work proved to be an important contribution for developing an astrophysical understanding of the two-body problem. For many astrophysical objects, this approximation describes the spacetime around these objects very well (although visualizing the spacetime curvature remains a challenge). There are compact astrophysical bodies, in particular for black holes (the subject of this thesis), that have sufficiently large spacetime curvature that this approximation is poor close to the centers of these bodies. Interestingly, the principle of effacement (see, e.g., [7]) argues that as long as the bodies are sufficiently far apart, their internal structure does not effect their equations of motion or their spacetime metric far from the bodies; therefore, the PN approximation holds away from the centers of any types of bodies (compact or not, though it is only valid close to the bodies for non-compact objects). The post-Newtonian expansion has been subsequently generalized to higher orders (see, e.g., [8]), and, with these developments, one could understand strongly gravitating bodies with even smaller separations, and one could delve even closer to the strongly gravitating bodies.

The post-Newtonian approximation, while useful in a large volume of the spacetime, is not the optimal expansion when examining the spacetime close to the members of the binary (particularly

[1] We follow the conventions of [4] for the metric and curvature quantities in this thesis, and we use geometrized units in which $G = c = 1$. We will also use Greek indices to denote spacetime indices, Latin indices to denote spatial indices, and 0 to denote the time-like index.

when the masses of the two bodies are comparable) or when the ratio of masses of the smaller and larger compact bodies is small. For this extreme-mass-ratio binary, in particular, it is more accurate to start with the spacetime of the larger compact object. Astrophysical observations (see, e.g., [9] for a review of the observational evidence) suggest that the larger object will be a supermassive non-rotating Schwarzschild black hole [10] or a rotating Kerr black hole [11]. The spacetime of the binary can be approximated by perturbations of the larger object by the smaller (see, e.g., [12, 13, 14, 15] for a Schwarzschild black hole and [16] for a Kerr black hole). One can even calculate the back reaction of the particle on itself—a problem often referred to as the gravitational self force—which is well understood theoretically and is beginning to be used in practical calculations (see, e.g., [17] for a review of the self-force problem). Because this problem is quite well understood, in this thesis we will focus on binaries with compact objects of comparable masses. One can again use perturbation theory of the compact objects (Schwarzschild and Kerr black holes in this thesis) to describe the tidal effects of one object on the other (see, e.g., [18]). As with the PN expansion, this approximation becomes inaccurate when the compact bodies are separated by too small a distance.

Unlike the instantaneous force of Newtonian gravity, changes in the curvature of spacetime occur at the speed of light. An interesting phenomenological consequence of this fact is that is that the curvature of spacetime itself can propagate like a wave and, like all other waves, can carry energy, momentum, and angular momentum (see, e.g., [4]). Any accelerating massive body will generate gravitational radiation, and, in a binary, the two bodies will gravitationally attract one another implying (in the absence of other overwhelming forces) that the two bodies must accelerate, and, therefore, radiate. Unlike in Newtonian gravity, which allows two bodies to stay on eternal elliptical orbits or perfect hyperbolae, even in an equivalently idealized two-body problem in general relativity, the orbits of these bodies must change. Furthermore, for gravitationally bound bodies, emitted radiation tends to drive the binary into circular orbits (originally shown by Peters and Matthews [19, 20]), and the separation of the circular orbits will decrease at an ever increasing rate as the members of the binary draw closer. The emitted gravitational radiation is important for inferring information about astrophysical compact binaries, as I will discuss later.

For bound, compact objects, there are no physical processes expected to oppose this dissipation from emitted gravitational waves, and eventually the members of a compact binary will reach a separation where no approximation that has been developed to date describes the spacetime very precisely. Not long after, the binary's bodies will themselves collide at some point, often called the merger. For black holes, Hawking [21] showed that their areas must always increase; therefore, the product of a merger of black holes must itself be a black hole. Furthermore, the no-hair theorem [22, 23, 24, 25, 26, 27] suggests that the product of this merger must itself settle into, generically, a Kerr-Newman black hole. Recently, numerical solutions of Einstein's equations by several independent computer codes (see, e.g., [1] for a review) confirmed this intuitive argument when they discovered

that there is a brief stage during which the compact objects orbit close to one another, followed by the two black holes relaxing to a Kerr black hole [28, 29].

Again, unlike in Newtonian mechanics, the two-body problem for gravitationally bound bodies in general relativity will ultimately result in a one-body problem after the two objects merge (though for non-compact objects, this may be an exceedingly slow process). Focusing again on black-hole binaries, after the short phase around the merger of the holes, one can then use perturbation theory of Kerr black holes to describe the spacetime after merger quite accurately. A summary of the different approximations one can use at different times in the evolution of a comparable-mass, black-hole binary is shown as a schematic in Fig. 1.1.

The comparable-mass binary in Fig. 1.1 highlights the fact that much of the spacetime can be reasonably approximated by some combination of series expansions, though there is a spacetime region around the black holes near the time of merger that is only accessible to numerical solutions of Einstein's equations (called numerical relativity). At the same time, however, it is often difficult to connect the different analytical approximations in the different spacetime regions, so as to make a cohesive picture of the two-body problem for compact objects. Numerical-relativity simulations, however, give this coherent description of the spacetime, but they are still computationally expensive, and they can be challenging to interpret. Thus, one can envision (at least) two ways to gain insight into numerical-relativity simulations of compact binaries: (i) one can find or invent simpler quantities that capture the essential elements of the dynamics of the simulation; these quantities can be compared to similar ones from (approximate) analytical spacetimes to aid their interpretation, or (ii) one can make simplified analytical models with fewer features and regions than those shown in Fig. 1.1, but whose dynamics can be checked against those of numerical-relativity simulations; in turn, if the simplified analytical model works sufficiently well, then the analytical model can serve as an effective description for the exact numerical-relativity dynamics (to the accuracy to which the comparison holds). Ideally, the two approaches would influence one another (e.g., the simplified quantities used to explore numerical simulations could inspire simpler analytical models directly).

There have been several other methods proposed of both the former and the latter types that aim to understand properties of numerical-relativity simulations. A few methods that follow the former principle are the correlated screens of Rezzolla et al. [30, 31, 32], the theory of dynamical horizons (see, e.g., [33] for a review) and other quasilocal spacetime objects (see, e.g., [34] for a review); methods that follow the latter idea include the close-limit approximation (see, e.g., [35, 36]) and the effective-one-body method (see [37, 38] for its initial formulation). Nevertheless, there is no definitive way to perform one or the other ways of interpreting the simulations. Chapters 2–4 and 8–11, therefore, present new proposals for understanding collisions of compact binaries that follow the first approach, labeled (i) above, and Chapters 5–6 describe a new method to approach (ii). Before discussing the details of these chapters in Section 1.2, I will briefly describe why the merger

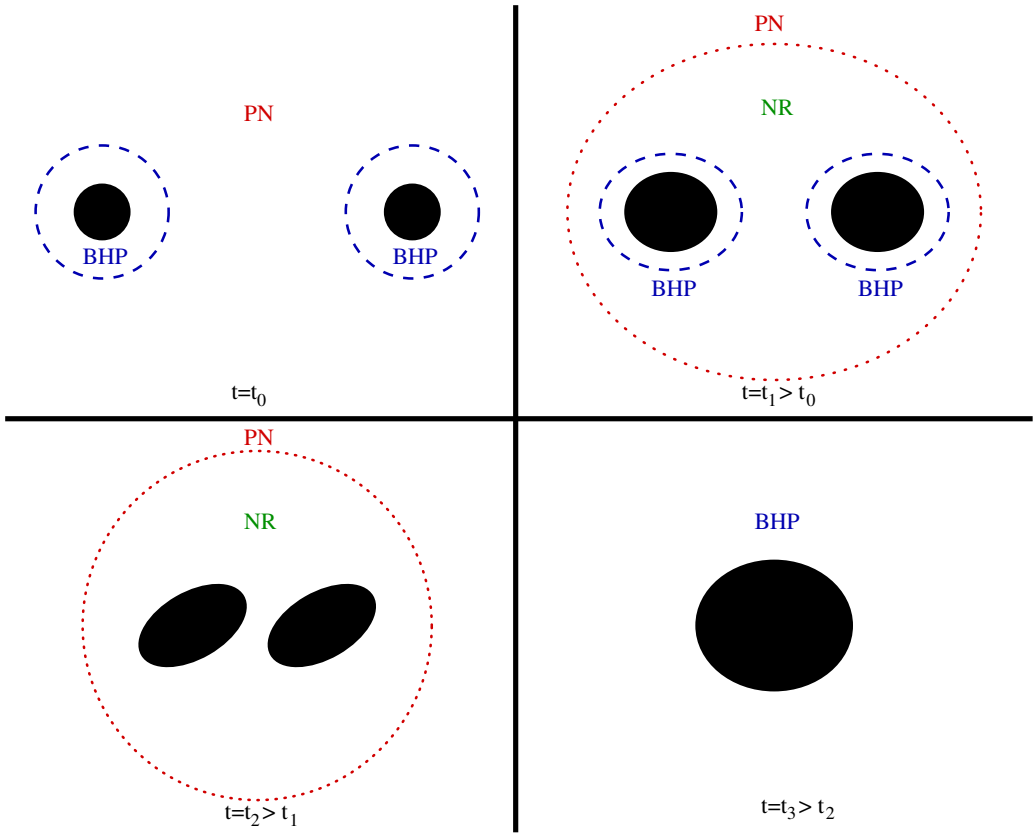

Figure 1.1: A schematic of when and where one can use different approximation techniques to describe the spacetime of a comparable-mass, black-hole binary (not drawn to scale). *Top-left panel*: A widely-separated binary, early in its evolution. Post-Newtonian (PN) theory is a good approximation for most of the spacetime, except near the black holes, where the spacetime is approximated better by black-hole-perturbation (BHP) theory of a tidally perturbed black hole. The two approximations are both valid in the vicinity of the dashed, blue circles surrounding the black holes. *Top-right panel*: The members of the binary move closer at later times, and there begins to be a region where neither PN nor BHP theories work well (between the larger oval and the circles around the black holes) that only numerical-relativity (NR) simulations can accurately describe. Post-Newtonian theory remains valid outside the red, dotted oval, and black-hole-perturbation theory is a good approximation within the circles. *Bottom-left panel*: The two black holes are now so close to merging that there no longer is a region where black-hole-perturbation theory is valid close to the holes. Far enough away (outside the oval) spacetime can again be approximated by post-Newtonian theory or, arguably, black-hole-perturbation theory (see Chapters 5 and 6). *Bottom-right panel*: The black-hole-binary problem ends in a state that can be described by black-hole-perturbation theory everywhere and, ultimately, a stationary black hole.

of two compact objects is an important source of gravitational waves, and what one might learn from this signal.

1.1.2 Gravitational-Wave Measurements from Compact Binary Sources

Because a binary made of compact objects will radiate gravitational waves, there is the possibility to detect these waves, and thereby learn information about the binary and its spacetime dynamics. The detectors leading the search are the ground-based, gravitational-wave observatories, LIGO and VIRGO, whose basic principle of operation is detecting tiny (as small as 10^{-18} m) differences in the arm lengths of the two orthogonal arms of the kilometer-scale Michelson interferometers (see, e.g., the review [39]). Their peak sensitivity is at several-hundred Hertz, which is ideal for measuring the gravitational waves from the late stages of two neutron stars inspiraling prior to their merger, or for finding the waves from the last orbits, the merger, and the ringdown of two black holes with masses approximately ten to one-hundred times the mass of the sun (see, e.g., the review [40] for a more complete description of sources of gravitational waves). Because the displacements are so small, one must use careful data-analysis techniques to extract the signal from the noise—specifically, one can use matched filtering, which requires a precise knowledge of the gravitational waveform (the review [41], e.g., contains a more complete description of data analysis techniques). The number of waveforms needed to search through the data to find gravitational waves is quite large; it is greater than the number of numerical-relativity simulations that can run in time for the advanced LIGO experiment. At the same time, however, the gravitational waves come from a time in the binary's evolution that only numerical-relativity can accurately study.

Putting the several premises above together, one can now see why developing a simplified, but accurate, analytical understanding of the two-body problem is a pressing issue: to be able to generate a sufficient number of gravitational waveforms to use to detect gravitational waves in current experiments, one will need to use simplified analytical models that capture the necessary nonlinear aspects of general relativity that are carried in the gravitational waveform. Deeper analytical understanding of the two-body problem (for compact binaries) is an important aspect of the search for gravitational waves. As a result, there has been some important work in this direction, including, for example, the analytical methods discussed in Section 1.1, the effective-one-body method fit to numerical-relativity simulation (see, e.g., [42, 43, 44, 45]), and the phenomenological frequency-based methods [46, 47]. Nevertheless, there is plenty of room to continue to develop new and simpler models that help one understand the two-body problem in general relativity.

It is also of interest to see the degree to which gravitational-wave observations can reveal properties of the spacetime. For compact binaries where one object is significantly more massive than the other, Ryan [48] showed that one can, in principle, extract the spacetime geometry of the larger object from measurements of the gravitational waves (this result was also generalized by Li and

Lovelace [49]). There is no equivalent procedure for comparable-mass, black-hole binaries, but it is possible to infer the masses, spins, distance, and location in the sky from gravitational-wave measurements for these binaries. Thus, one will need to use a combination of numerical and analytical methods to understand the dynamics of the binary corresponding to objects of those masses and spins. As I describe in the next section, this thesis presents three ways that one might realize this idea.

1.2 Methods to Understand the Dynamics of Compact Binaries in This Thesis

The next ten chapters of this thesis describe three approaches to understanding the dynamics and spacetime of black-hole binaries. The first method uses the Landau-Lifshitz formalism to explain the gravitational-wave recoil of certain black-hole binaries. The next set of approaches are analytical: the one aims to show that much of the dynamics and waveform of black-hole binaries can be understood using only post-Newtonian and black-hole-perturbation theories; the other shows that the oscillations of a black-hole spacetime after merger has a simple description in terms of motion around the unperturbed black hole. The third method describes a way to visualize the spacetime curvature with constructions that are analogous to the field lines of electromagnetism, though they have a very different, yet simple, physical interpretation.

1.2.1 Understanding Momentum Flow in Black-Hole Binaries

This section introduces a formalism for quantifying the flow of momentum in black-hole binaries. The four parts of this section describe the inspiration for investigating this problem, a description of the challenges with using such a method, and the results of applying this method in the post-Newtonian approximation and in numerical-relativity simulations.

1.2.1.1 Black-Hole Kicks as the Motivating Factor for Studying Momentum Flow

The method for understanding black-hole dynamics described in Part I (Chapters 2–4) of this thesis had, as its origin, the goal of explaining the large gravitational-wave recoils that arise during the merger and ringdown of black-hole binaries. The idea of a gravitational-wave recoil was first discussed in general terms by Peres [50], and was later considered in gravitational collapse by Bekenstein [51] and in binaries by Fitchett [52]. The recoil (often called the kick) occurs when a binary asymmetrically emits gravitational waves at the time of merger. The gravitational waves carry energy, momentum, and angular momentum away from the final merged black hole, and, consequently, when the emission is asymmetric, the final black hole will move with a velocity equal to the negative of the gravitational wave's momentum divided by the black hole's mass. In numerical-relativity simulations, black-hole kicks were first explored from the collision of unequal-mass black holes, and

the largest kicks were found to be only at most a thousandth of the speed of light (first explored in detail by [53, 54, 55] for non-spinning black holes). Interestingly, much larger kicks—approximately one hundredth of the speed of light—were found for rotating black holes, whose axes of rotation were anti-aligned, and which pointed in the plane of orbit [56, 57]. The configuration of the binary that led to this large recoil was often called the superkick merger (see Figs. 3.1 and 3.2). Subsequently, even larger kicks were found if the black holes' spins were somewhat aligned with the orbital angular momentum [58]; these large kicks could have testable astrophysical consequences [59].

In Part I, my collaborators and I were interested in understanding the dynamics of the superkick configuration and similar black-hole mergers. Specifically, there were two features of the merger that we aimed to understand: (i) prior to the collision of the black holes, the two holes (and hence the orbital plane) bobbed along and opposite the direction of the angular momentum sinusoidally and simultaneously during each orbit, and (ii) during merger, the two black holes combine to form a single black hole, and this hole gets kicked along the axis of angular momentum, and the magnitude (and direction) depends sinusoidally on the angle between the separation of the black holes and their spin axes near the time of merger. We were interested, in particular, in understanding how the bobbing motion related to the kick of the merged black hole. Although Pretorius [60] offered an explanation for how the kick is produced, his proposal did not describe the nature of the transition from the bobbing to the kick at the level of detail that we were hoping to find. We were more interested in how the momentum contained in the gravitational field extended from near the black holes to near infinity (where it is carried by the gravitational waves). As a result, we proposed a way to connect the momentum of the gravitational field to those of the holes. There is a subtlety in doing this, however, that we discuss in the next part.

1.2.1.2 The Challenge of Studying Momentum Flow

While there is a well-defined notion that the gravitational field contributes to the momentum density of a system, as was famously noted in the textbook on relativity, *Gravitation*, "Anybody who looks for a magic formula for 'local gravitational energy-momentum' is looking for the right answer to the wrong question" [4]. The intuitive reason that gravitational momentum density cannot be localized is that, by the equivalence principle (see, e.g., [61]), one can find a reference frame in which locally, there is no gravitational field and no gravitational momentum density. As a result, any way of describing a local energy-momentum of the gravitational field must rely upon some auxiliary structure with respect to which the energy-momentum must be measured. A common way to do this is to introduce an auxiliary flat metric, and to define a stress-energy pseudotensor from the full spacetime metric with respect to the flat metric. This does not uniquely define a pseudotensor, but there is a common choice, called the Landau-Lifshitz pseudotensor [62, 4], that is quadratic in the Christoffel symbols, and that produces a well-defined energy and momentum in the asymptotically

flat part of any spacetime [4].

The Landau-Lifshitz pseudotensor, $t^{\mu\nu}_{\rm LL}$ is defined from the superpotential,

$$H^{\mu\alpha\nu\beta}{}_{,\alpha\beta} \equiv (\mathfrak{g}^{\mu\nu}\mathfrak{g}^{\alpha\beta} - \mathfrak{g}^{\mu\alpha}\mathfrak{g}^{\nu\beta})_{,\alpha\beta} = 16\pi(-g)(T^{\mu\nu} + t^{\mu\nu}_{\rm LL})\,, \tag{1.3}$$

where $(-g)$ is the determinant of the covariant components of the metric, $\mathfrak{g}^{\mu\nu} \equiv \sqrt{-g}g^{\mu\nu}$ is the metric density, a comma denotes a derivative with respect to the Cartesian coordinates of the auxiliary flat metric, and $T^{\mu\nu}$ is the stress-energy tensor of the matter sources in the spacetime (which vanishes for a black-hole binary). In an asymptotically flat spacetime, the surface integral of the divergence of the superpotential defines a momentum in the asymptotically flat region of the spacetime through the expression

$$p^{\mu}_{\rm tot} = \frac{1}{16\pi}\oint_{\mathcal{S}} H^{\mu\alpha 0 j}{}_{,\alpha} d\Sigma_j\,, \tag{1.4}$$

where $\mathcal{S}$ is a sphere of a very large radius in a slice of constant time. For a spacetime without black holes, one can use Gauss's law to show that the above expression is equivalent to a volume integral of the momentum density throughout the spatial slice. To define a black-hole momentum, we will promote the equation above to a quasilocal quantity (see, e.g., [34]) by defining a black-hole momentum to be an equivalent surface integral on the event horizon (or the apparent horizon) at a given time,

$$p^{\mu}_{\rm BH} = \frac{1}{16\pi}\oint_{\mathcal{H}} H^{\mu\alpha 0 j}{}_{,\alpha} d\Sigma_j\,, \tag{1.5}$$

where $\mathcal{H}$ is the event horizon surface at a fixed time. If we define the field momentum as an integral over the region outside the horizons and within the large sphere $\mathcal{S}$ (denoted by $\mathcal{V}$) by

$$p^{\mu}_{\rm field} = \int_{\mathcal{V}} (-g) t^{\mu 0}_{\rm LL}\,, \tag{1.6}$$

then by Gauss's law one has momentum conservation,

$$p^{\mu}_{\rm tot} = p^{\mu}_{\rm BH} + p^{\mu}_{\rm field}\,. \tag{1.7}$$

As a result, the Landau-Lifshitz pseudotensor does have some desirable features: it defines the momentum of the system in the asymptotically flat portion of the spacetime, and it allows one to define quasilocal black-hole momenta and field momenta that satisfy a conservation law. The possible flaw of this approach is that the Landau-Lifshitz formalism relies upon an arbitrary mapping between the physical metric and the auxiliary flat metric, which could introduce a great amount of arbitrariness to the results. To explore the degree of this ambiguity, we compute the pseudotensor in the first post-Newtonian approximation, and we found that it has useful intuitive power there, because it resembles the Poynting vector of electromagnetism. When applied to the early stages of the

superkick configuration, the Landau-Lifshitz formalism could explain the bobbing. We then turned to numerical-relativity simulations using different coordinate conditions, and we found qualitatively similar behavior in the different cases. We will describe these results in greater detail in the next two parts of this section.

1.2.1.3 Momentum Flow in the Post-Newtonian Approximation

It has been known for many years that the post-Newtonian approximation to Einstein's field equations of general relativity could be written in a way that closely resembles Maxwell's equations of electromagnetism. This was done first by Forward [63] in the linearized, slow-motion approximation, and by Damour, Soffel, and Xu (DSX) [64, 65, 66, 67] for the complete 1PN approximation for arbitrary bodies). Less well known, however, was the fact that the Landau-Lifshitz pseudotensor can be written in a way that closely resembles the stress-energy tensor for the electromagnetic field (though, it can, in principle, be extracted from the results of DSX or Pati and Will [68]).

One purpose of Chapter 2 of this thesis (work performed in collaboration with Jeffrey D. Kaplan and Kip S. Thorne and published in *Physical Review D* [69]) is to review and specialize the results of DSX, so as to make their complex formalism more accessible. In particular, we restricted our results to perfect-fluid sources and to compact bodies characterized by only their masses and spins. The other is to compute the Landau-Lifshitz pseudotensor in the first post-Newtonian approximation. We found that the momentum density and the stress tensor can be written as

$$(-g)t^{0j}_{\rm LL}\boldsymbol{e}_j = -\frac{1}{4\pi}\boldsymbol{g}\times\boldsymbol{H} + \frac{3}{4\pi}\dot{U}_N\boldsymbol{g}\ , \tag{1.8}$$

$$(-g)t^{ij}_{\rm LL} = \frac{1}{4\pi}(g_ig_j - \frac{1}{2}\delta_{ij}g_kg_k) + \frac{1}{16\pi}(H_iH_j - \frac{1}{2}\delta_{ij}H_kH_k) - \frac{3}{8\pi}\dot{U}_N^2\delta_{ij}\ , \tag{1.9}$$

(Eqs. (2.16a) and (2.16b) of Chapter 2), where $\boldsymbol{g}$ is the gravitoelectric field (gradient of the 1PN generalization of the Newtonian potential), $\boldsymbol{H}$ is the gravitomagnetic field (curl of the gravitomagnetic potential), and U_N is the Newtonian potential. Aside from two terms involving the time derivative of the Newtonian potential, and the coefficients of proportionality, the momentum density is identical to the Poynting vector, and the stress tensor is analogous to Maxwell's stress tensor in electromagnetism. Thus, although there still exists some arbitrariness in the map between the coordinates of the first-post-Newtonian approximation and those of the auxiliary flat space, the Landau-Lifshitz tensor, nevertheless, takes a form that has great intuitive power, because of its strong similarity to the stress-energy tensor in electromagnetism. We were encouraged, therefore, to use the Landau-Lifshitz formalism to study the superkick merger.

Before discussing this, however, I will briefly comment on my specific contributions to that chapter. I checked many of the 1PN calculations, and ensured that the results were written in a consistent notation throughout the paper. I also derived the Landau-Lifshitz tensor, checked

the statement of energy conservation in the approximation, and computed the geodesic equation. I contributed to the writing, editing, and the review of the paper when it was accepted for publication.

In Chapter 3 of this thesis (research done in collaboration with Yanbei Chen, Drew G. Keppel, and Kip S. Thorne and published in *Physical Review D* [70]) we applied the Landau-Lifshitz formalism of Chapter 2 to study the superkick configuration. We showed that when the holes are far apart, as they orbit each other their Landau-Lifshitz momenta will simultaneously bob perpendicularly to the orbital plane. During each cycle the Landau-Lifshitz momentum density redistributes itself in such a way that the total Landau-Lifshitz field momentum is exactly balanced the black-holes' momenta. Interestingly, we also found that the definitions of the momentum in the harmonic-gauge post-Newtonian equations and of the Landau-Lifshitz momentum differ, but the difference amounts to only an overall factor of two-thirds.

Because we used the post-Newtonian approximation, we could not understand the dynamics of the binary around the time of merger; consequently, we could not compute how the momentum near the black holes related to the momentum carried by the gravitational waves. At the same time, however, we saw that the Landau-Lifshitz formalism was quite useful for gaining intuitive understanding of the dynamics of the superkick configuration prior to merger, and we noted that it gave semi-quantitative agreement in terms of the amplitude and velocity of the bobbing motion. We, therefore, decided to apply the technique to numerical-relativity simulations of colliding black holes, which would allow us to make a connection between the momentum near the black holes and the gravitational-wave kick. These numerical-relativity simulations are the subject of Chapter 4.

Before discussing them, however, I will again note my specific contributions to Chapter 3. My most direct contribution was that I performed the calculations in the three appendices and I wrote those three sections. I also computed the Landau-Lifshitz momenta in the text, made the figure of the Landau-Lifshitz momentum density, and checked over the more formal calculations in the latter half of the paper. I did some writing and editing throughout the paper, and I again reviewed the paper before it was published.

1.2.1.4 Momentum Flow in Numerical-Relativity Simulations

The culmination of our work involving the Landau-Lifshitz formalism is in Chapter 4 of this thesis, which describes research completed in collaboration with Yanbei Chen, Michael I. Cohen, Jeffrey D. Kaplan, Drew G. Keppel, Geoffrey Lovelace, Keith D. Matthews, Mark A. Scheel, and Ulrich Sperhake (and which was published in *Physical Review D* [71]). In this chapter, we performed a numerical-relativity simulation, not of the superkick merger, but of a simpler, though similar, configuration of black holes: an equal-mass, head-on collision of two black holes with spins that are transverse to the head-on motion but anti-aligned (see Fig. 4.1). This configuration of black holes gets a kick that is significantly smaller than the superkick, but is dynamically similar to the

superkick (i.e., it comes from an asymmetry in the gravitational waves that is induced by the spin of the black holes, and it is in a direction that is perpendicular to the separation and the spins of the holes). Consequently, this head-on collision is a simpler test-bed to explore the mechanisms that generate these non-planar kicks than the longer and more complex superkick configuration.

The dynamics of the Landau-Lifshitz momenta of the black holes were quite rich. As the two holes fell toward each other, they also dragged each other in the direction perpendicular to the plane defined by their spins and separation. The post-Newtonian approximation predicted this behavior, and for the simulations that started at large separations, the agreement of the numerical-relativity and post-Newtonian momenta were quite good. Only around the time of the merger, when the transverse speed of the black holes neared one-hundredth of the speed of light, did they begin to disagree. At merger and during the subsequent ringing of the black hole as it settled down, the numerical-relativity simulations showed that the (now merged) black hole reversed its direction and settled to a small speed in the opposite direction of its motion during infall; moreover, the hole's final velocity agreed with the kick that one computes from the emitted gravitational waves. We interpreted the change in direction of the black hole to be a result of the hole engulfing momentum density in the surrounding region space as its horizon expanded and oscillated during and after merger. We performed simulations using the two major classes of coordinate conditions commonly used by numerical-relativity codes, and the results agreed quite well; we therefore argued that the formalism should be useful for building qualitative understanding of the dynamics of binaries.

My contribution to Chapter 4 came primarily in comparing the post-Newtonian trajectories and momentum density to the equivalent quantities from the numerical-relativity simulations, and in writing in that section. I also wrote the review of the Landau-Lifshitz formalism in that chapter. While I did not run the simulations that are published in the paper, I did run some additional simulations that were not included. As with the other papers, I contributed to the writing and editing in various other parts, and I helped to review the paper during the proofing stage.

1.2.2 Approximating the Inspiral, Merger, and Ringdown in Black-Hole Binaries

This part describes the chapters in this thesis that use analytical methods to make simplified and more intuitive descriptions of more complicated phenomena in general relativity. It begins with a review of the standard approximation techniques used in general relativity and of several variations on these well-known techniques. Then, the next part (a summary of Chapter 5) describes a method that uses just post-Newtonian and black-hole-perturbation theories to capture much of the dynamics and the waveform of head-on collisions of black-hole binaries. The portion afterward, summarizing Chapter 6, describes a generalization of this method to treat inspiralling black-hole binaries. Finally, the last part, relating to Chapter 7, sets forth a geometric description of high-frequency black-hole

quasinormal modes in terms of geodesic motion near the region of unstable spherical null geodesics.

1.2.2.1 Approximation Methods in General Relativity

Although Section 1.1 introduced the approximation techniques commonly used to describe the spacetime of a black-hole binary, it will be useful to discuss these methods—post-Newtonian and black-hole-perturbation theories, in particular—in more detail. This will help to explain how these approximations are typically used, and how they have been generalized and modified to better approximate the waveform and dynamics of binaries; in turn, this will help to put the methods of this thesis in the context of other analytical approaches. Most importantly, it will point out that with a few exceptions (see, e.g., [72, 73, 74]) each approximation is typically used individually at a given time, because it can be difficult to match the spacetime description of different approximation methods. This gives a compelling reason to develop simplified analytical models of the dynamics and waveforms of binaries.

The Post-Newtonian Approximation The post-Newtonian approximation is a series expansion for the metric (about flat space) for bodies that move with small velocities. The series has currently been computed to include seventh-order powers of the velocity, usually denoted by 3.5PN order (see, e.g., the review by Blanchet [8]). Computing the metric for a given distribution of stress energy can be difficult in practice, but the outline of the procedure (usually called the nonlinear, or post-Minkowskian expansion) can be summarized in a few steps: (i) choose harmonic coordinates

$$h^{\mu\nu}{}_{,\nu} = (\mathfrak{g}^{\mu\nu} - \eta^{\mu\nu})_{,\nu} = 0\,, \tag{1.10}$$

where $\eta^{\mu\nu}$ is a flat, Lorentz metric, (ii) write the Einstein field equations as

$$\Box h^{\mu\nu} = -16\pi(-g)(T^{\mu\nu} + t^{\mu\nu}_{\rm LL}) + (h^{\mu\alpha}{}_{,\beta} h^{\nu\beta}{}_{,\alpha}\,, -h^{\mu\nu}{}_{,\alpha\beta} h^{\alpha\beta}) \tag{1.11}$$

where $\Box$ is the flat-space D'Alembertian (wave) operator, (iii) solve the equation iteratively by inverting the wave operator for the next-order piece in terms of the lower-order nonlinear terms on the right-hand side. Even for the simplest sources (point particles) solving for the metric in this expansion is computationally quite difficult (see the review [8] for the details about inverting these operators). Because the metric has been computed to 3.5PN order for point particles, the explicit expressions for the spacetime metric can be used for a variety of calculations (e.g., computing the waveform for LIGO data analysis [41]). When applied to binary systems, the post-Newtonian metric perturbation is usually used both to compute the trajectories of the bodies and the gravitational waves that they produce. The post-Newtonian approximation is used throughout the entire space up until a time when bodies are sufficiently close and moving sufficiently rapidly that the series becomes inaccurate; at this point, other approximation methods are used instead.

Black-Hole-Perturbation Theory One can, in principle, solve for the metric of a perturbed black hole using a procedure analogous to that of post-Newtonian theory (i.e., by solving a wave equation for the metric perturbations in a harmonic gauge); in practice, this can be a challenging computational task, and it is often simpler to use other methods. There are two methods to compute perturbations of Schwarzschild black holes: the first involves solving for the metric perturbations directly through a procedure developed by Regge and Wheeler [12] and Zerilli [13], and the second calculates curvature perturbations using the Newman-Penrose formalism [75] (based on work by Bardeen and Press [14]). The Newman-Penrose formalism is the simplest way to study perturbations of a Kerr black hole (originally studied by Teukolsky [16]); from these curvature perturbations, one can then construct metric perturbations based on the research of Chrzanowski [76], Kegeles and Cohen [77], Wald [78], and Stewart [79]). An important class of solutions in black-hole perturbation theory are the quasinormal modes of a black hole (see the reviews [80, 81, 82, 83]). These modes appear after the merger of a black-hole binary, when the final black hole settles into a quiescent state [84, 85]. Consequently, black-hole-perturbation theory is usually used to describe the entire spatial region after the nonlinear dynamics during merger give way to small oscillations of the final black hole.

Regge-Wheeler-Zerilli Metric Perturbations Regge and Wheeler [12] and Zerilli [13] found a way to compute two scalar functions from the metric perturbations of a Schwarzschild black hole that have definite parities and that satisfy the two simple wave equations. It is common to decompose the solutions to the wave equation into spherical harmonics, so that the radial- and time-dependent parts of the solutions satisfy the two simple one-dimensional wave equations below:

$$[\partial_t^2 - \partial_{r_*}^2 + V^l_{(\mathrm{e,o})}(r)]\Psi^{l,m}_{(\mathrm{e,o})} = 0\,. \tag{1.12}$$

The radial coordinate is defined by $r_* = r + 2M\log[r/(2M) - 1]$, and the potentials $V^l_{(\mathrm{e,o})}(r)$ are

$$V^l_{(\mathrm{e,o})}(r) = \left(1 - \frac{2M}{r}\right)\left(\frac{\lambda}{r^2} - \frac{6M}{r^3}U^l_{(\mathrm{e,o})}(r)\right)\,, \tag{1.13}$$

where we defined $\lambda = l(l+1)$ and $\Lambda = (l-1)(l+2)/2 = \lambda/2 - 1$ and where

$$U^l_{(\mathrm{o})}(r) = 1, \quad U^l_{(\mathrm{e})}(r) = \frac{\Lambda(\Lambda+2)r^2 + 3M(r-M)}{(\Lambda r + 3M)^2}\,. \tag{1.14}$$

Their procedure was generalized by Moncrief [15], who showed that there are modified versions of their quantities (which are labeled in the same way by $\Psi^{l,m}_{(\mathrm{e,o})}$) that are invariant under small changes of coordinates. Moreover, these quantities are physically interesting, because they are proportional to the two polarizations of a gravitational wave, at large radii. It was shown by Price [86] for the odd-parity and Aksteiner and Andersson [87] for both parities that the Regge-Wheeler and Zerilli

equations are actually proportional to perturbations of the Newman-Penrose curvature scalar Ψ_2 [75]; it happens that Ψ_2 has a simple relationship with the metric perturbations. Although this was not known when the curvature perturbations described next were found, it lends credence to the idea that curvature perturbations could satisfy simpler wave equations than metric perturbations do.

Curvature-Scalar Perturbations and Their Metric Perturbations Bardeen and Press [14] showed that one could also write a separable wave equation for the perturbations of the Newman-Penrose scalars Ψ_0 and Ψ_4 in the Schwarzschild spacetime. These perturbations are gauge invariant, and easy to understand physically: Ψ_0 is related to the ingoing gravitational waves at the horizon, and Ψ_4 corresponds to the outgoing gravitational waves at infinity [75]. Their work was also important, because Teukolsky generalized their result to find separable wave equations for the same Newman-Penrose scalars in the Kerr spacetime (the explicit expression for the partial differential equation is somewhat lengthy, and it will not be shown here). With Teukolsky's equation, one could now easily compute perturbations of any astrophysically relevant black hole. For some computations, it is convenient to have a metric perturbation, and Chrzanowski [76] (whose work was clarified and generalized by Kegeles and Cohen [77], Wald [78], and Stewart [79] and revisited more recently by Lousto and Whiting [88], Ori [89], and Keidl et al. [90, 91, 92]) was able to find two gauges in which to construct metric perturbations (ingoing- and outgoing-radiation gauges). As a result, there are several relatively convenient ways in which to compute metric and curvature perturbations of astrophysical black holes.

Black-Hole Quasinormal Modes An important tool for understanding black-hole perturbations are their quasinormal modes (see the reviews [80, 81, 82, 83]). These are the characteristic modes of black holes subject to an ingoing boundary condition at the horizon, and an outgoing condition at infinity. The frequencies of these modes can be found by solving the boundary-value problem for the, as yet, undetermined frequency. While there are a wide range of methods to do this, the most commonly used is due to Leaver [93]. Leaver found that there are a large number (possibly infinite) of modes for each multipolar index (called the overtone number of the mode); the frequency of this mode is a complex number (i.e., it oscillates at a frequency given by its real part and decays at a rate proportional to its imaginary part). For high-frequency modes of Schwarzschild and slowly rotating Kerr black holes, their frequencies are simply related to the frequency of unstable spherical geodesic orbits of massless particles (see, e.g., the paper by Ferrari and Mashhoon [94]). These modes have also been found to be excited significantly during the merger of a black-hole binary (see, e.g., [84, 85]). When applying black-hole perturbation theory to study the dynamics of a binary, therefore, we reiterate that it is only after the time of merger that black-hole-perturbation theory is used to approximate the spacetime geometry for the entire spatial volume of that spacetime region.

Combinations and Extensions of the Approximation Techniques There is a gap around the time of merger of a black-hole binary during which neither the post-Newtonian approximation nor black-hole-perturbation theory accurately describes the entirety of the spatial region of a comparable-mass binary. To develop an analytical approximations of the spacetime during the merger, three types of approaches have been taken: (i) extending post-Newtonian theory to hold later into the merger, (ii) pushing black-hole-perturbation theory back to earlier times in the merger, and (iii) replacing the black-hole binary merger with an simpler problem that has analogous dynamics. The effective-one-body approach [37, 38] follows method (i), because it maps the dynamics of the binary's reduced mass in the post-Newtonian approximation to the dynamics of a point particle around an effective, deformed black hole. The effective-one-body method agrees with the post-Newtonian expansion during the inspiral and produces accurate dynamics during the merger, but it cannot be extended past the merger of the black holes; as a result, when computing the waveform from this method, one must directly add quasinormal modes to the end of the waveform (see, e.g., [45]). The close-limit approximation (see, e.g., [35, 36]) and the Lazarus project [95, 96] use approach (ii) to describe binary dynamics. They extend the validity of black-hole-perturbation theory to earlier times by using initial data that approximates a binary near merger and evolving it as a perturbation to the single, merged black hole. To connect the waveform and the dynamics to those prior to the merger, they must match to post-Newtonian quantities at earlier times. Thus, neither methods (i) nor (ii) provide a full description of the spacetime at all times, but they require meshing two descriptions at some point (which they can do reasonably well). Finally, method (iii) uses analytical spacetimes to approximate binary dynamics (for example, with Robinson-Trautman spacetimes by Rezzolla et al. [30, 31]). These have intuitive appeal, but it is not always clear how closely the model problem relates to an actual merger of black holes. From the discussion of the different methods above, one can see that while these approaches have achieved some success, there is still room to make improved analytical models of the merger.

1.2.2.2 The Hybrid Method for Head-on Black-Hole Mergers

Chapter 5 of this thesis (in collaboration with Yanbei Chen and published in *Physical Review D* [97]) presents a new way of combining post-Newtonian and black-hole-perturbation theories to make an approximate model of head-on, black-hole-binary mergers, which we call the hybrid method. Instead of matching the two approximation methods at a single fixed time, we assume that post-Newtonian theory holds within a time-like world tube defined by the centers of the black holes, and that black-hole-perturbation theory (of a Schwarzschild black hole) is valid on the exterior. Furthermore, we suppose that the dynamics of the binary follow a radially plunging geodesic in the background Schwarzschild spacetime, so that the range where post-Newtonian theory is valid falls inside the horizon around the time of the merger and ringdown of the black holes. We then match

the metrics of the two approximation techniques on the world tube. From the perspective of the black-hole-perturbation theory on the exterior, this prescription defines a boundary-value problem for the Regge-Wheeler and Zerilli functions based on a post-Newtonian estimate for their values.

To test this method, we compared our leading-order model of the black-hole-binary merger described in Chapter 4 with the actual numerical-relativity simulation of that chapter. The quantities that were most amenable to comparison were different multipolar components of the gravitational waveform at infinity, and the gravitational-wave kick predicted by the two methods. We found remarkably good agreement between the $l = 2$, $m = 1$ components of the waveform and strong agreement between the $l = 2$, $m = 2$ parts. Because the gravitational-wave kick arises from the interaction of these two multipoles in the waveform, the gravitational-wave kick agreed quite well. In addition to its accuracy, the hybrid method allowed us to interpret parts of the waveform in terms of where the position of the world tube was at the corresponding retarded time. When it was far outside the black-hole effective potential, this was the infall phase; when it entered the potential, this corresponded to the merger phase; and when the world tube was well within the potential, this was the ringdown.

The material in this chapter is mostly my own work, though I greatly benefitted from Yanbei Chen's checks of my calculations and suggestions about the presentation of the ideas in the text. More specifically, I wrote the code to numerically evolve the boundary-value problem for the Zerilli function, and I generated all the figures in the text except the first. I did nearly all the writing in the paper, and I was responsible for editing and reviewing the paper when it was under review at the journal.

1.2.2.3 The Hybrid Method for Inspiralling Black-Hole Mergers

In Chapter 6 of this thesis (again research done in collaboration with Yanbei Chen and published in *Physical Review D* [98]) we generalized the hybrid method for head-on mergers of black holes to treat inspiralling black-hole binaries. The main obstacle preventing us from directly applying the hybrid method above to a quasicircular binary is the absence of a good way to prescribe a trajectory that the black holes should follow (i.e., to determine the location at which we should place the boundary data for the evolution of the Zerilli function in the exterior perturbed Schwarzschild spacetime). Our solution was instead to choose that the world tube, where we match the two metrics, should evolve via the equations of point-particle motion in the background Schwarzschild spacetime. We would then modify the conservative dynamics of this point particle by subjecting it to a radiation-reaction force determined from the outgoing radiation in the exterior, black-hole spacetime. When we made this assumption, and matched the two metrics as we had done for the hybrid approach for head-on

mergers, we arrived at the following set of evolution equations:

$$\dot{A}(t) = \frac{\partial H}{\partial p_A(t)}\,, \quad \dot{\alpha}(t) = \frac{\partial H}{\partial p_\alpha(t)}\,, \quad \dot{p}_A(t) = -\frac{\partial H}{\partial A(t)}\,, \tag{1.15}$$

$$\dot{p}_\alpha(t) = -\mu\sqrt{\frac{15}{2\pi}}\frac{24}{A(t)}\Im[\Psi_{(\mathrm{e})}(t)e^{2i\alpha(t)}]\,, \tag{1.16}$$

$$\begin{aligned}\dot{\Psi}_{(\mathrm{e})}(t) &= -\frac{1}{2}\int_0^{u_s(t)} V_{(\mathrm{e})}^{(l=2)}(r)\Psi_{(\mathrm{e})}(u',v)du' \\ &\quad - \left[\left(\frac{A(t)-2M}{A(t)+2M}\right) - \frac{\dot{A}}{2}\right]\left(\frac{6\Psi_{(\mathrm{e})}(t)}{A(t)} - \frac{80Q(t)}{A(t)^3}\right)\,,\end{aligned} \tag{1.17}$$

$$\frac{\partial^2\Psi_{(\mathrm{e})}}{\partial u\partial v} = -\frac{V_{(\mathrm{e})}^{(l=2)}(r)\Psi_{(\mathrm{e})}(u,v)}{4}\,. \tag{1.18}$$

The last equation is the Zerilli equation written in terms of the light-cone coordinates $u = t - r_*$ and $v = t + r_*$, the first lines are three of the Hamiltonian equations for the reduced-mass motion of the binary (H is the point-particle Hamiltonian of the background Schwarzschild black hole), the second line is the last of Hamilton's equations (with the radiation-reaction force producing dissipation in the system), and the third line is an evolution equation for the post-Newtonian-inspired perturbation on the boundary ($Q(t)$ is the quadrupole moment). From a mathematical perspective, the system of equations above defines a boundary-value problem for a partial differential equation with a time-like boundary, where the boundary value, and the location of the boundary itself, is determined at each time by a system of Hamiltonian equations with dissipation coming from the field satisfying the partial differential equation. This somewhat complicated problem, nevertheless, gives physically reasonable results.

We checked the hybrid method against numerical-relativity simulations in two cases: an equal-mass, non-spinning, quasicircular, black-hole merger, and the superkick merger. For the first merger, we compared the $l = 2$, $m = 2$ multipolar mode of the gravitational waveform produced by the two methods, and we found that the phase of the waveforms agreed well during the inspiral, but the amplitude agreed less well. During the merger and ringdown, the two began to differ, because we continued to model the post-merger black hole as non-spinning, although, in fact, the numerical-relativity simulation predicts that the black hole is rotating rapidly. We next investigated the superkick merger with the hybrid method, paying particular attention to the momentum flux. We found that when we allowed the spins to precess geodetically around the final black hole, this increased the momentum flux and gave it a time-dependence qualitatively like that seen in numerical-relativity simulations. The kick also depended sinusoidally upon the angle between the black hole's separations and spins, but the magnitude was somewhat larger than that of numerical-relativity simulations. Modeling the final black hole as non-spinning was largely responsible for this difference, because it led to more energy being radiated during the merger and ringdown phases.

As with the head-on hybrid paper, the majority of the work in this paper was my own. Again, Yanbei Chen developed an independent code to check my results, and he provided invaluable advice about the organization and presentation of the manuscript. Nevertheless, the code used to generate all the figures and the results in this chapter was my own, as was most of the writing throughout the chapter. Again, I was involved in the editing and review of the paper when the manuscript was under the peer-review process.

1.2.2.4 A Geometric Approximation for the Ringdown of Black Holes

Chapter 7 (in collaboration with Yanbei Chen, Huan Yang, Fan Zhang, and Aaron Zimmerman and based on a paper in preparation) describes a method of approximating the quasinormal-mode frequencies of Kerr black holes, in the eikonal limit (when the frequency is large and the wavelength is short). Because there is already an efficient and precise method of finding the modes' frequencies based on a continued-fraction method by Leaver [93], the main power of this approximation is the intuitive description it gives of a mode's frequency. Our work is inspired by an insight originally by Ferrari and Mashhoon [94], who found that for a quasinormal mode with multipolar indices l and m (with $l \gtrsim m \gg 1$) of a slowly rotating Kerr black hole, the real part of the mode's frequency is given by

$$\omega_{\rm R} = l\omega_{\rm orb} + m\omega_{\rm prec}\,, \tag{1.19}$$

where $\omega_{\rm orb}$ is the Keplerian frequency of the unstable null geodesic at the velocity-of-light circle (often called a spherical photon orbit) and $\omega_{\rm prec}$ is the Lense-Thirring precession frequency (see, e.g., [4]) at the radius of this orbit.

In this chapter, we showed that there exists a formula of the same form as the equation above, for the quasinormal modes of Kerr black holes of any astrophysical spins. We were able to show this through a geometric-optics argument (see, e.g., [4]) and a WKB analysis (see, e.g., [99, 100] for a WKB analysis relating to quasinormal modes of black holes). The interesting geometric difference between the slowly rotating and rapidly rotating Kerr results is the location of the corresponding spherical photon orbit. For slowly rotating Kerr black holes, all the orbits still reside on the same spherical photon orbit of a Schwarzschild black hole, and the dependence of the frequencies on m comes only from the precessional frequency. For rapidly rotating Kerr black holes, on the other hand, the spherical photon orbits for a given l and m occur at different radii and have different orbital and precessional frequencies; this makes the frequency of the mode quite different, and gives good agreement (less than a percent) with exact calculations of the mode's frequency. The equation above also can be used to show that there is a degeneracy in the quasinormal-mode spectrum of Kerr black holes, when the orbital and precessional frequencies are rationally related. Interestingly, but not surprisingly, at these values, the corresponding spherical photon orbits are closed.

Most of my work on this chapter was on the final part, regarding the connection between the

degeneracy in the quasinormal-mode spectrum, and the corresponding closed, spherical photon orbits. I reviewed and checked the calculations in the other parts of the paper, and I assisted in the writing and editing throughout the paper.

1.2.3 Visualizing Spacetime Curvature with Vortex and Tendex Lines

The final four chapters of this thesis, Chapters 8–11 introduce a method to visualize all aspects of the spacetime curvature in vacuum, and present visualizations of several analytical spacetimes that are often used to describe gravitational-wave generation. The first part of this section describes the motivation for and an overview of our method; the next part discusses the results in more detail.

1.2.3.1 The Challenges of Spacetime Visualization and the Method of This Thesis

Most methods to visualize spacetime curvature use isometric embedding diagrams of certain interesting two-dimensional spacetime surfaces into three-dimensional flat Euclidean space (see, e.g., [101, 102, 103, 104]). These diagrams usually introduce a fictitious height so that the Euclidean arclength between two points on the diagram better represents the proper distance between two points on the surface in the curved spacetime. Embedding diagrams are somewhat limited in scope, because (i) they can only represent two-dimensional surfaces, which may not capture much of the spacetime structure in the absence of spacetime symmetries, and (ii) it is not always possible to make an embedding diagram (e.g., the horizon of Kerr black holes of high spins cannot be embedded into a Euclidean flat space [101]). Note that it is always possible to locally embed a surface, but when one tries to form a global embedding one can run into problems [101, 102]. Visualizing certain components of the metric tensor (the lapse and shift [4], for example) is a different method, but it is also highly coordinate dependent.

Another obstacle in building intuition about the dynamics of black-hole binaries is the fact that the most interesting physical quantity, the Weyl curvature tensor (identical to the Riemann curvature tensor in vacuum) is a rank-four tensor, commonly denoted by $C_{\mu\nu\alpha\beta}$ (see, e.g., [4]). One might worry that the Weyl tensor has an intractable number of components (because each index runs over the four spacetime indices), but the symmetries of the tensor require that it only has ten independent components (see, e.g., [4]). Nevertheless, without a way of reducing the four-dimensional, spacetime quantities to three-dimensional objects that are easier to understand physically, it will be difficult to visualize or gain intuition from the Weyl tensor.

Our idea is to make use of a well-known time-space split of the Weyl curvature tensor into two symmetric and trace-free tensors, which are called its electric and magnetic parts (because of an analogy to the time-space split of the field strength tensor of electromagnetism into electric and magnetic fields; see, e.g., [105] and references therein). Specifically, for a set of observers with four-velocities u^μ that are hypersurface forming (and where $\gamma^{\mu\nu} = g^{\mu\nu} + u^\mu u^\nu$ is the spatial metric in

the spatial hypersurface), these tensors are defined by

$$\mathcal{E}_{\alpha\beta} = \gamma_\alpha{}^\rho \gamma_\beta{}^\sigma C_{\rho\mu\sigma\nu} u^\mu u^\nu \,, \qquad \text{i.e.,} \quad \mathcal{E}_{ij} = C_{i\hat{0}j\hat{0}} \,, \tag{1.20}$$

$$\mathcal{B}_{\alpha\beta} = -\gamma_\alpha{}^\rho \gamma_\beta{}^\sigma {}^*C_{\rho\mu\sigma\nu} u^\mu u^\nu \,, \quad \text{i.e.,} \quad \mathcal{B}_{ij} = \frac{1}{2} \epsilon_{ipq} C^{pq}{}_{j\hat{0}} \,, \tag{1.21}$$

where ${}^*C_{\rho\mu\sigma\nu}$ is the dual of the Weyl tensor. These tensors together contain the full ten degrees of freedom of the Weyl tensor, and they have been known for quite some time to encode information about the effects of the curvature on nearby inertial frames. Specifically, two nearby events separated by a spatial vector ξ^j will feel a differential acceleration Δa^i and, if there are inertial guidance gyroscopes at these events, they will differentially precess at a rate $\Delta\Omega^i$, which is given by

$$\Delta a^i = -\mathcal{E}^i{}_j \xi^j \quad \text{and} \quad \Delta\Omega^i = \mathcal{B}^i{}_j \xi^j \,, \tag{1.22}$$

respectively (see [106]). We will describe the electric part as the tidal field and the magnetic part as the frame-drag field, to emphasize the physical effects of these fields on inertial observers.

Even though the tidal and frame-drag fields are rank-two spatial tensors, it is still somewhat inconvenient to visualize them directly. Because these tensors are symmetric (and trace-free), they always have three orthogonal eigenvectors (and their eigenvalues sum to zero); therefore, we found it more convenient to compute their generalized eigenvalues, λ, and eigenvectors, v^j, by solving the following equation:

$$\mathcal{E}_{ij} v^j = \lambda \gamma_{ij} v^j \,. \tag{1.23}$$

We could then plot the streamlines of the eigenvectors and the eigenvalues themselves as a way to conveniently visualize the complete information about the Weyl curvature tensor. To emphasize the physical meanings of these lines and scalar functions, we gave them names that reflect these facts: for the tidal field, we call the eigenvalues the *tendicities*, the streamlines the *tendex lines*, and the regions of large eigenvalue *tendexes* (all based on the Latin verb *tendere*, meaning to stretch); for the frame-drag field, the equivalent quantities are *vorticities*, *vortex lines*, and *vortexes* (from the Latin *vertere*, meaning to turn).

1.2.3.2 Overview of Spacetimes Visualized with this Method

Our chief interest is to visualize numerical-relativity simulations of merging black holes and to use these tools as a way of understanding the features of the spacetime curvature involved in generating gravitational waves. Because these tools are a new way of describing the spacetime curvature, we found it useful to visualize well-known analytical spacetimes with the vortex and tendex quantities, to build intuition in these simpler spacetimes, before using the same tools to understand gravitational-wave generation in numerical-relativity simulations. Chapters 8–11 of this thesis review the results

we have found thus far. More specifically, Chapter 8 is an introduction to the topic with a few results from numerical-relativity simulations, Chapter 9 focuses on the gravitational waves at infinity, Chapter 10 describes the generation of waves by systems that are linear perturbations of flat space, and Chapter 11 focuses on wave generation from perturbations of rotating and non-rotating black holes.

An Overview of Applications of Tendexes and Vortexes Chapter 8 (in collaboration with Jeandrew Brink, Yanbei Chen, Jeffrey D. Kaplan, Geoffrey Lovelace, Keith D. Matthews, Robert Owen, Mark A. Scheel, Kip S. Thorne, Fan Zhang, and Aaron Zimmerman and published in *Physical Review Letters* [107]) introduces vortexes and tendexes. It touches upon horizon vortexes and tendexes—the components of the frame-drag and tidal fields, respectively, with both indices normal to the horizon—which relate simply to other geometric quantities on the horizon. It briefly describes the vortexes of stationary Kerr black holes, the tendex lines of a static Schwarzschild black hole, and the vortexes of an odd-parity, quadrupolar perturbation of a Schwarzschild black hole in the plane of reflection symmetry of the perturbation. It concludes by investigating the dynamics of several black-hole binary mergers. For the same head-on merger of black holes in Chapter 4, we found that the gravitational waves were generated during the ringdown by vortexes (which were originally pinned to two regions of horizon vorticity from the spins of the black hole prior to merger) detaching from the horizon and becoming deformed tori of large vorticity that become one part of the gravitational waves at infinity. This chapter also describes a simulation of a superkick merger and a merger of black holes with spins anti-aligned with the orbital angular momentum. For these last two simulations, we only looked at the dynamics of the horizon vorticity, which, after merger, contains contributions from the orbital angular momentum and the spins of the black holes. As the black holes settle down, the different regions of horizon vorticity appear to diffuse into one another as the black hole relaxes to a stationary Kerr hole.

I contributed to this paper in several ways. I worked mostly on explaining the connection between the horizon quantities and other geometrical variables on the horizon. I did most of the writing in that section, I helped with the editing in other sections, and I contributed to the review of the paper when it was in its editorial review with the journal.

Tendexes and Vortexes of Gravitational Waves In Chapter 9 (work in collaboration with Fan Zhang and Aaron Zimmerman that was published in *Physical Review D* [108]) we explored the vortex and tendex lines of gravitational waves near future null infinity. Because vortex and tendex lines near infinity form a non-directional field of lines on a surface of spherical topology, one can apply a version of the Poincaré-Hopf theorem [109] to show that there must be at least one critical point in the field of lines. Interestingly, for eigenvector fields of a symmetric tensor (and the corresponding field of their streamlines), one can show that there are critical points only where

the eigenvalues are equal [109]. For gravitational radiation at infinity, we demonstrated that this only occurs when the tendicity and vorticity vanish; hence there must be isolated points at infinity where the gravitational radiation vanishes. We then illustrated this fact with several examples of multipolar radiation in linearized theory: quadrupolar radiation, beamed quadrupolar radiation in a model of the superkick merger, and higher multipoles and their superposition. For quadrupolar radiation, there are four zeros, and for higher multipoles, the number increased. We also argued that when the radiation is most strongly beamed, this corresponds to when the critical points all collect in a single point at one of the poles.

My main contribution was to the last part of this paper: the visualization of multipolar radiation at infinity. I produced the seven figures in this section, did the calculation necessary to make them, and did the majority of the writing. I assisted with the writing and editing of the other parts of this paper, and I checked the calculations elsewhere. Finally, I helped with the review of this paper when it was being published in the journal.

Tendexes and Vortexes of Linearized Perturbations about Flat Space Chapter 10 (work done with Jeandrew Brink, Yanbei Chen, Jeffrey D. Kaplan, Geoffrey Lovelace, Keith D. Matthews, Robert Owen, Mark A. Scheel, Kip S. Thorne, Fan Zhang, and Aaron Zimmerman and published in *Physical Review D* [110]) serves two main purposes. On the one hand, it is a more systematic overview of the properties of the vortex and tendex quantities, and on the other, it is an exploration of the vortexes and tendexes of static and dynamic sources in linearized theory about flat space. We pay particular attention to how the dynamical sources generate gravitational waves in this chapter. We show that, like a Kerr black hole, a spinning particle in linearized theory has a positive and negative vortex sticking out of each pole, and the vortex lines head out from one vortex, loop around, and return to it. When two spinning particles have their spins anti-aligned and are placed side-by-side, most of the vortex lines connect from one particle to the other, which is very similar to the tendex lines of a static current quadrupole. We then look at the vortex lines from a rotating and an oscillating current quadrupole in linearized theory. A rotating current quadrupole has two positive and two negative vortexes that spiral out from the equator and become the two polar vortexes of gravitational waves; an oscillating current quadrupole emits two positive and negative equatorial vortex bulges that, at large radii, collect into the two alternating polar vortexes of gravitational waves. The tendexes of a mass quadrupole can be shown to be identical to the vortexes of a current quadrupole; hence one can apply the results for current quadrupoles to mass quadrupoles when the vortexes and tendexes are switched. We conclude by looking at the tendex lines of a linearized-theory model of a binary, and we find that near the binary, the tendexes look like those of two static particles, and far from the source, they look like those of quadrupolar gravitational waves.

Most of my work was in the final section of the paper on gravitational waves and their generation. I performed many of the calculations there (and checked those that I did not originally do) and made

seven of the figures. I did a significant fraction of the writing in that section as well. In the rest of the paper, I checked over the calculations, and did some editing and writing. I was also in charge of reviewing the paper when it was in press at the journal.

Tendexes and Vortexes of Stationary and Perturbed Black Holes The last chapter in this part (Chapter 11, based on research performed with Jeandrew Brink, Yanbei Chen, Jeffrey D. Kaplan, Geoffrey Lovelace, Keith D. Matthews, Robert Owen, Mark A. Scheel, Kip S. Thorne, Fan Zhang, and Aaron Zimmerman, a draft of which is in preparation) investigates the vortexes and tendexes of static and perturbed black holes. In particular, it is aimed at addressing how perturbations near the black holes extend out towards infinity and become gravitational waves. Even for static black holes, there were several interesting results. As long as the observers had a four-velocity that passed smoothly through the horizon, the vortexes and tendexes were qualitatively similar for these different observers. For perturbed black holes, the tendexes and vortexes of the perturbations were not very different from those of linear perturbations of flat space; however, in the near zone, the black hole horizon and its tendicity and vorticity replaced the near-zone multipoles of the linearized-theory perturbations. As a result, we found that an electric-parity perturbation had two positive and two negative perturbative tendexes that spiraled out from the horizon tendexes; only at larger radii did these tendexes collect into the polar tendexes of gravitational waves. Accompanying these tendexes were four positive and four negative equatorial vortexes in the near zone, which at larger radii collected into the polar vortexes of gravitational waves. Thus, we described the near-zone tendexes as inducing near-zone vortexes that together become the gravitational waves, asymptotically. The qualitative details of the perturbative vortexes and tendexes did not depend strongly upon the spin of the black hole (although they had the appearance of being dragged by the spin of the background black hole for rapidly rotating Kerr black holes). We also looked at the vortexes and tendexes of magnetic-parity perturbations of these black holes, and their description of gravitational waves was nearly dual to that of electric-parity perturbations (dual in the sense that vortexes and tendexes played the opposite role). Unlike in linearized theory, the duality is no longer exact.

I made several contributions to this chapter, mostly dealing with the tendexes and vortexes of perturbed Schwarzschild and Kerr black holes in an ingoing-radiation gauge. I performed the calculations in this section and in seven of the accompanying appendices that were needed to generate the fourteen figures relating to these perturbations. I did most of the writing in that section and those appendices. In doing this, I checked over many of the calculations for static black holes earlier in the paper. I also contributed significantly to the section on the horizon tendicity and vorticity, including the writing. I have checked many of the calculations in the Regge-Wheeler section and appendices. Where I did not significantly write, I also contributed to the editing.

1.3 Summarizing the Introductory Remarks

The two-body problem in general relativity is still an active area of research for binaries made of compact objects like black holes and neutron stars. Gravitational-wave observations from mergers of compact binaries provide a unique way to study these highly relativistic systems and further understand the two-body problem in relativity. The ability to directly learn about the strong and dynamical spacetime curvature around these objects from gravitational-wave observations is not yet possible; instead we must use numerical-relativity simulations and analytical approximations to infer the spacetime dynamics from information about the masses and spins of the objects. Analytical approximations are simple and easy to understand, but they cannot accurately describe the complete dynamics of a black-hole binary. Numerical-relativity simulations can model binary dynamics well, but they are difficult to interpret and still take a long time to run; therefore, analytical and numerical methods are well suited to work together to better understand binary dynamics.

The chapters of this thesis explore three different methods that use both analytical and numerical techniques to understand black-hole binaries. The next three chapters introduce a way to quantify the momentum carried by the gravitational field, and they use it to connect the momentum of black holes in a binary to the momentum carried away by gravitational waves. The three following chapters describe ways to use approximate methods in different ways to reduce binary dynamics to simpler analytical descriptions. The four chapters afterward introduce a method of visualizing the spacetime curvature, and they apply the method to help understand the generation of gravitational waves by binary systems.

Bibliography

[1] J. Centrella, J. G. Baker, B. J. Kelly, and J. R. van Meter, Rev. Mod. Phys. **82**, 3069 (2010).

[2] M. D. Duez, Classical Quantum Gravity **27**, 114002 (2010).

[3] L. N. Hand and J. D. Finch, *Analytical Mechanics* (Cambridge University Press, Cambridge, UK, 1998).

[4] C. W. Misner, K. S. Thorne, and J. A. Wheeler, *Gravitation* (W. H. Freeman, New York, 1973).

[5] A. Einstein, L. Infeld, and B. Hoffmann, Ann. Math. **39**, 65 (1938).

[6] S. Chandrasekhar, Astrophys. J. **142**, 1488 (1965).

[7] T. Damour, in *300 Years of Gravitation*, edited by S. W. Hawking and W. Israel (Cambridge University Press, Cambridge, UK, 1987).

[8] L. Blanchet, Living Rev. Relativity **9**, 4 (2006).

[9] A. Celotti, J. C. Miller, and D. W. Sciama, Classical Quantum Gravity **16**, A3 (1999).

[10] K. Schwarzschild, Sitzungsber. Preuss. Akad. Wiss. Berlin (Math. Phys.) **1916**, 189 (1916).

[11] R. P. Kerr, Phys. Rev. Lett. **11**, 237 (1963).

[12] T. Regge and J. A. Wheeler, Phys. Rev. **108**, 1063 (1957).

[13] F. J. Zerilli, Phys. Rev. Lett. **24**, 737 (1970).

[14] J. M. Bardeen and W. H. Press, J. Math. Phys. **14**, 7 (1973).

[15] V. Moncrief, Ann. Phys. (N.Y.) **88**, 323 (1974).

[16] S. A. Teukolsky, Phys. Rev. Lett. **29**, 1114 (1972).

[17] E. Poisson, A. Pound, and I. Vega, Living Rev. Relativity **14**, 7 (2011).

[18] E. Poisson and I. Vlasov, Phys. Rev. D **81**, 024029 (2010).

[19] P. C. Peters and J. Mathews, Phys. Rev. **131**, 435 (1963).

[20] P. C. Peters, Phys. Rev. **136**, B1224 (1964).

[21] S. W. Hawking, Phys. Rev. Lett. **26**, 1344 (1971).

[22] W. Israel, Phys. Rev. **164**, 1776 (1967).

[23] W. Israel, Commun. Math. Phys. **8**, 245 (1968).

[24] B. Carter, Phys. Rev. Lett. **26**, 331 (1971).

[25] S. W. Hawking, Commun. Math. Phys. **25**, 152 (1972).

[26] D. C. Robinson, Phys. Rev. D **10**, 458 (1974).

[27] D. C. Robinson, Phys. Rev. Lett. **34**, 905 (1975).

[28] M. Campanelli, C. O. Lousto, and Y. Zlochower, Phys. Rev. D **79**, 084012 (2009).

[29] R. Owen, Phys. Rev. D **81**, 124042 (2010).

[30] L. Rezzolla, R. P. Macedo, and J. L. Jaramillo, Phys. Rev. Lett. **104**, 221101 (2010).

[31] J. L. Jaramillo, R. P. Macedo, P. Moesta, and L. Rezzolla, Phys. Rev. D **85**, 084030 (2012).

[32] J. L. Jaramillo, R. P. Macedo, P. Moesta, and L. Rezzolla, Phys. Rev. D **85**, 084031 (2012).

[33] A. Ashtekar and B. Krishnan, Living Rev. Relativity **7**, 10 (2004).

[34] L. B. Szabados, Living Rev. Relativity **12**, 4 (2009).

[35] R. H. Price and J. Pullin, Phys. Rev. Lett. **72**, 3297 (1994).

[36] G. Khanna, J. Baker, R. J. Gleiser, P. Laguna, C. O. Nicasio, H.-P. Nollert, R. Price, and J. Pullin, Phys. Rev. Lett. **83**, 3581 (1999).

[37] A. Buonanno and T. Damour, Phys. Rev. D **59**, 084006 (1999).

[38] A. Buonanno and T. Damour, Phys. Rev. D **62**, 064015 (2000).

[39] M. Pitkin, S. Reid, S. Rowan, and J. Hough, Living Rev. Relativity **14**, 5 (2011).

[40] B. Sathyaprakash and B. F. Schutz, Living Rev. Relativity **12**, 2 (2009).

[41] P. Jaranowski and A. Krlak, Living Rev. Relativity **15**, 4 (2012).

[42] T. Damour and A. Nagar, Phys. Rev. D **79**, 081503 (2009).

[43] A. Buonanno, Y. Pan, H. P. Pfeiffer, M. A. Scheel, L. T. Buchman, and L. E. Kidder, Phys. Rev. D **79**, 124028 (2009).

[44] Y. Pan, A. Buonanno, L. T. Buchman, T. Chu, L. E. Kidder, H. P. Pfeiffer, and M. A. Scheel, Phys. Rev. D **81**, 084041 (2010).

[45] Y. Pan, A. Buonanno, M. Boyle, L. T. Buchman, L. E. Kidder, H. P. Pfeiffer, and M. A. Scheel, Phys. Rev. D **84**, 124052 (2011).

[46] P. Ajith, S. Babak, Y. Chen, M. Hewitson, B. Krishnan, A. M. Sintes, J. T. Whelan, B. Brügmann, P. Diener, N. Dorband, et al., Phys. Rev. D **77**, 104017 (2008).

[47] P. Ajith, M. Hannam, S. Husa, Y. Chen, B. Brügmann, N. Dorband, D. Müller, F. Ohme, D. Pollney, C. Reisswig, et al., Phys. Rev. Lett. **106**, 241101 (2011).

[48] F. D. Ryan, Phys. Rev. D **52**, 5707 (1995).

[49] C. Li and G. Lovelace, Phys. Rev. D **77**, 064022 (2008).

[50] A. Peres, Phys. Rev. **128**, 2471 (1962).

[51] J. D. Bekenstein, Astrophys. J. **183**, 657 (1973).

[52] M. J. Fitchett, Mon. Not. R. Astron. Soc. **203**, 1049 (1983).

[53] J. G. Baker, J. Centrella, D.-I. Choi, M. Koppitz, J. R. van Meter, and M. C. Miller, Astrophys. J. Lett. **653**, L93 (2006).

[54] F. Herrmann, I. Hinder, D. Shoemaker, and P. Laguna, Classical Quantum Gravity **24**, S33 (2007).

[55] J. A. González, U. Sperhake, B. Brügmann, M. Hannam, and S. Husa, Phys. Rev. Lett. **98**, 091101 (2007).

[56] M. Campanelli, C. O. Lousto, Y. Zlochower, and D. Merritt, Phys. Rev. Lett. **98**, 231102 (2007).

[57] J. A. González, M. Hannam, U. Sperhake, B. Brügmann, and S. Husa, Phys. Rev. Lett. **98**, 231101 (2007).

[58] C. O. Lousto and Y. Zlochower, Phys. Rev. Lett. **107**, 231102 (2011).

[59] C. O. Lousto, Y. Zlochower, M. Dotti, and M. Volonteri, Phys. Rev. D **85**, 084015 (2012).

[60] F. Pretorius, in *Relativistic Objects in Compact Binaries: From Birth to Coalescences*, edited by M. Colpi (Springer Verlag, 2009).

[61] C. M. Will, Living Rev. Relativity **9**, 3 (2006).

[62] L. D. Landau and E. M. Lifshitz, *Classical Theory of Fields* (Addison Wesley, Reading, MA, 1962).

[63] R. L. Forward, Proc. IRE **49**, 892 (1961).

[64] T. Damour, M. Soffel, and C. Xu, Phys. Rev. D **43**, 3273 (1991).

[65] T. Damour, M. Soffel, and C. Xu, Phys. Rev. D **45**, 1017 (1992).

[66] T. Damour, M. Soffel, and C. Xu, Phys. Rev. D **47**, 3124 (1993).

[67] T. Damour, M. Soffel, and C. Xu, Phys. Rev. D **49**, 618 (1994).

[68] M. E. Pati and C. M. Will, Phys. Rev. D **62**, 124015 (2000).

[69] J. D. Kaplan, D. A. Nichols, and K. S. Thorne, Phys. Rev. D **80**, 124014 (2009).

[70] D. Keppel, D. A. Nichols, Y. Chen, and K. S. Thorne, Phys. Rev. D **80**, 124015 (2009).

[71] G. Lovelace, Y. Chen, M. Cohen, J. D. Kaplan, D. Keppel, K. D. Matthews, D. A. Nichols, M. A. Scheel, and U. Sperhake, Phys. Rev. D **82**, 064031 (2010).

[72] N. Yunes and W. Tichy, Phys. Rev. D **74**, 064013 (2006).

[73] N. Yunes, W. Tichy, B. J. Owen, and B. Brügmann, Phys. Rev. D **74**, 104011 (2006).

[74] N. K. Johnson-McDaniel, N. Yunes, W. Tichy, and B. J. Owen, Phys. Rev. D **80**, 124039 (2009).

[75] E. Newman and R. Penrose, J. Math. Phys. **3**, 566 (1962).

[76] P. L. Chrzanowski, Phys. Rev. D **11**, 2042 (1975).

[77] L. S. Kegeles and J. M. Cohen, Phys. Rev. D **19**, 1641 (1979).

[78] R. M. Wald, Phys. Rev. Lett. **41**, 203 (1978).

[79] J. M. Stewart, Proc. R. Soc. Lond. A **367**, 527 (1979).

[80] K. D. Kokkotas and B. Schmidt, Living Rev. Relativity **2**, 2 (1999).

[81] H.-P. Nollert, Classical Quantum Gravity **16**, R159 (1999).

[82] E. Berti, V. Cardoso, and A. O. Starinets, Classical Quantum Gravity **26**, 163001 (2009).

[83] R. A. Konoplya and A. Zhidenko, Rev. Mod. Phys. **83**, 793 (2011).

[84] A. Buonanno, G. B. Cook, and F. Pretorius, Phys. Rev. D **75**, 124018 (2007).

[85] E. Berti, V. Cardoso, J. A. Gonzalez, U. Sperhake, M. Hannam, S. Husa, and B. Brügmann, Phys. Rev. D **76**, 064034 (2007).

[86] R. H. Price, Phys. Rev. D **5**, 2439 (1972).

[87] S. Aksteiner and L. Andersson, Classical Quantum Gravity **28**, 065001 (2011).

[88] C. O. Lousto and B. F. Whiting, Phys. Rev. D **66**, 024026 (2002).

[89] A. Ori, Phys. Rev. D **67**, 124010 (2003).

[90] T. S. Keidl, J. L. Friedman, and A. G. Wiseman, Phys. Rev. D **75**, 124009 (2007).

[91] T. S. Keidl, A. G. Shah, J. L. Friedman, D.-H. Kim, and L. R. Price, Phys. Rev. D **82**, 124012 (2010).

[92] A. G. Shah, T. S. Keidl, J. L. Friedman, D.-H. Kim, and L. R. Price, Phys. Rev. D **83**, 064018 (2011).

[93] E. W. Leaver, Proc. R. Soc. Lond. A **402**, 285 (1985).

[94] V. Ferrari and B. Mashhoon, Phys. Rev. D **30**, 295 (1984).

[95] J. Baker, M. Campanelli, and C. O. Lousto, Phys. Rev. D **65**, 044001 (2002).

[96] M. Campanelli, B. Kelly, and C. O. Lousto, Phys. Rev. D **73**, 064005 (2006).

[97] D. A. Nichols and Y. Chen, Phys. Rev. D **82**, 104020 (2010).

[98] D. A. Nichols and Y. Chen, Phys. Rev. D **85**, 044035 (2012).

[99] B. F. Schutz and C. M. Will, Astrophys. J. Lett. **291**, L33 (1985).

[100] S. Iyer and C. M. Will, Phys. Rev. D **35**, 3621 (1987).

[101] L. Smarr, Phys. Rev. D **7**, 289 (1973).

[102] J. D. Romano and R. H. Price, Classical Quantum Gravity **12**, 875 (1995).

[103] D. Marolf, Gen. Relativ. Gravit. **31**, 919 (1999).

[104] M. Bondarescu, M. Alcubierre, and E. Seidel, Classical Quantum Gravity **19**, 375 (2002).

[105] R. Maartens and B. A. Bassett, Classical Quantum Gravity **15**, 705 (1998).

[106] F. B. Estabrook and H. D. Wahlquist, J. Math. Phys. **5**, 1629 (1964).

[107] R. Owen, J. Brink, Y. Chen, J. D. Kaplan, G. Lovelace, K. D. Matthews, D. A. Nichols, M. A. Scheel, F. Zhang, A. Zimmerman, et al., Phys. Rev. Lett. **106**, 151101 (2011).

[108] A. Zimmerman, D. A. Nichols, and F. Zhang, Phys. Rev. D **84**, 044037 (2011).

[109] T. Delmarcelle and L. Hesselink, in *Proceedings of the Conference on Visualization 1994* (IEEE Computer Society Press, Los Alamitos, CA, 1994), pp. 140–147.

[110] D. A. Nichols, R. Owen, F. Zhang, A. Zimmerman, J. Brink, Y. Chen, J. D. Kaplan, G. Lovelace, K. D. Matthews, M. A. Scheel, et al., Phys. Rev. D **84**, 124014 (2011).

Part I

Understanding Momentum Flow in Black-Hole Binaries

Chapter 2

Post-Newtonian Approximation in Maxwell-Like Form

The equations of the linearized first post-Newtonian approximation to general relativity are often written in a "gravitoelectromagnetic" Maxwell-like form, because it facilitates physical intuition. Relying heavily on work of Damour, Soffel, and Xu, this paper expresses the first post-Newtonian approximation, including all nonlinearities, in a Maxwell-like form, focusing especially on the gravitational momentum and its conservation as expressed in terms of the Landau-Lifshitz pseudotensor. The authors and their colleagues are finding this formalism useful in developing physical intuition into numerical-relativity simulations of compact binaries with spin.

Originally published as J. D. Kaplan, D. A. Nichols, and K. S. Thorne, Phys. Rev. D **80** 124014 (2009).

2.1 Introduction

In 1961, Robert L. Forward [1] (building on earlier work of Einstein [2, 3] and especially Thirring [4, 5, 6]; see [7] for an English translation of the last two papers) wrote the linearized, slow-motion approximation to general relativity in a form that closely resembles Maxwell's equations; and he displayed this formulation's great intuitive and computational power. In the half century since then, this Maxwell-like formulation and variants of it have been widely explored and used; see, e.g., [8, 9, 10, 11, 12, 13, 14, 15] and references therein.

In 1965–1969 S. Chandrasekhar [16, 17] formulated the first post-Newtonian (weak-gravity, slow-motion) approximation to general relativity in a manner that has been widely used for astrophysical calculations during the subsequent 40 years. When linearized, this first post-Newtonian (1PN) approximation can be (and often is) recast in Maxwell-like form.

In 1991, T. Damour, M. Soffel, and C. Xu (DSX) [18] extended this Maxwell-like 1PN formalism to include all 1PN nonlinearities. They did so as a tool in developing a general formalism for the celestial mechanics of bodies, each of which has an arbitrary internal structure and an external gravitational field characterized by an infinite number of multipole moments. (For more recent work in this direction, see [19].)

In recent months, we and our colleagues have been exploring the gravitational field momentum and momentum flow in numerical-relativity simulations of compact, spinning binaries [20]. During its inspiral phase, a binary's motion and precession can be described by the 1PN approximation; and we have found a variant of the DSX Maxwell-like formalism to be useful in understanding the binary's dynamics.

In this paper, we present our variant of the DSX, Maxwell-like formalism.[1] It is simultaneously a specialization of DSX and an extension. The specialization arises (i) from our choice to fix the coordinates (gauge) as fully harmonic instead of maintaining partial gauge invariance, and (ii) from the fact that for compact bodies (black holes and neutron stars), the only multipole moments that influence the binary's dynamics at first post-Newtonian order are each body's mass and its spin angular momentum; thus, we ignore all other moments. The generalization arises from our desire to understand, in depth, the distribution and flow of linear momentum inside the binary. For this purpose we use the Landau-Lifshitz energy-momentum pseudotensor, expressed in a DSX, Maxwell-like form—a tool that we have added to the DSX formalism.

The DSX papers [18, 21, 22, 23] are so long and complex that it is not easy to extract the bare essentials that go into simpler 1PN analyses. For researchers who want those bare essentials and want to see how they are related to more conventional approaches to 1PN theory, our paper may prove useful. To serve that purpose (and in order to make clear contact with DSX), we present our variant of the DSX formalism for the case of a perfect fluid as well as for a system of compact bodies described by their masses and spins.

This paper is organized as follows: In Section 2.2 we present the basic DSX equations for 1PN theory in a Maxwell-like form. In Section 2.3 we specialize the DSX formalism to a perfect fluid and make contact with the conventional 1PN notation. In Section 2.4 we derive the density and flux of gravitational momentum in terms of the DSX gravitoelectric and gravitomagnetic fields and we write down the laws of momentum conservation and the Maxwell-like gravitational force density acting on the fluid. In Section 2.5 we discuss energy conservation. In Section 2.6 we specialize to the vacuum in the near zone of a system made from compact bodies. Finally, in Section 2.7, we summarize our formalism both for a self-gravitating fluid and for a system of compact bodies.

[1] When we carried out our analysis and wrote it up in the original version of this paper, we were unaware of the Maxwell-like formalism in DSX [18]; see our preprint at http://arxiv.org/abs/0808.2510v1. When we learned of DSX from Luc Blanchet, we used it to improve our own formalism (by replacing our definition for the gravitoelectric field with that of DSX) and we rewrote this paper to highlight the connection to DSX.

Throughout this paper we set $G = c = 1$, Greek letters run from 0 to 3 (spacetime) and Latin from 1 to 3 (space), and we use the notation of field theory in flat space in a 3+1 split, so spatial indices are placed up or down equivalently and repeated spatial indices are summed whether up or down or mixed. We use boldface characters to represent spatial vectors, i.e., $\boldsymbol{w}$ is the boldface version of w_j.

2.2 The DSX Maxwell-Like Formulation of 1PN Theory

Damour, Soffel, and Xu (DSX) [18] express the 1PN metric in terms of two gravitational potentials, a scalar w and a vector w_j:

$$\begin{aligned} g_{00} &= -e^{-2w} = -1 + 2w - 2w^2 + O(U_N^3) \,, \\ g_{0i} &= -4w_i + O(U_N^{5/2}) \,, \\ g_{ij} &= \delta_{ij} e^{2w} = \delta_{ij}(1 + 2w) + O(U_N^2) \end{aligned} \tag{2.1}$$

(Eqs. (3.3) of DSX). The Newtonian limit of w is $U_N =$ (Newtonian gravitational potential), and w_i is of order $U_N^{3/2}$:

$$w = U_N + O(U_N^2) \,, \quad w_i = O(U_N^{3/2}) \,. \tag{2.2}$$

The harmonic gauge condition implies that

$$w_{,t} + w_{j,j} = 0 \tag{2.3}$$

(Eq. (3.17a) of DSX); here and throughout commas denote partial derivatives. Using this gauge condition (which DSX do not impose), the 1PN Einstein field equations take the following remarkably simple form:

$$\nabla^2 w - \ddot{w} = -4\pi(T^{00} + T^{jj}) + O(U_N^3/\mathcal{L}^2) \,, \tag{2.4a}$$

$$\nabla^2 w_i = -4\pi T^{0i} + O(U_N^{5/2}/\mathcal{L}^2) \tag{2.4b}$$

(Eqs. (3.11) of DSX). Here $T^{\alpha\beta}$ is the stress-energy tensor of the source (which we presume, below, to be a perfect fluid), ∇^2 is the flat-space Laplacian (i.e., $\nabla^2 w = w_{,jj}$), repeated indices are summed, dots denote time derivatives (i.e., $\ddot{w} = w_{,tt}$), and $\mathcal{L}$ is the length scale on which w varies.

Following DSX, we introduce the 1PN *gravitoelectric field* $\boldsymbol{g}$ (denoted $\boldsymbol{e}$ or $\boldsymbol{E}$ by DSX , depending on the context) and *gravitomagnetic field* $\boldsymbol{H}$ (denoted $\boldsymbol{b}$ or $\boldsymbol{B}$ by DSX):

$$\boldsymbol{g} = \boldsymbol{\nabla} w + 4\dot{\boldsymbol{w}} + O(U_N^3/\mathcal{L}) \,, \tag{2.5a}$$

$$\boldsymbol{H} = -4\boldsymbol{\nabla} \times \boldsymbol{w} + O(U_N^{5/2}/\mathcal{L}) \,. \tag{2.5b}$$

(Eqs. (3.21) of DSX). The Einstein equations (2.4) and these definitions imply the following 1PN Maxwell-like equations for $\boldsymbol{g}$ and $\boldsymbol{H}$:

$$\boldsymbol{\nabla}\cdot\boldsymbol{g} = -4\pi(T^{00}+T^{jj}) - 3\ddot{w} + O(gU_N^2/\mathcal{L}) \;, \tag{2.6a}$$

$$\boldsymbol{\nabla}\times\boldsymbol{g} = -\dot{\boldsymbol{H}} + O(gU_N^2/\mathcal{L}) \;, \tag{2.6b}$$

$$\boldsymbol{\nabla}\cdot\boldsymbol{H} = 0 + O(HU_N/\mathcal{L}) \;, \tag{2.6c}$$

$$\boldsymbol{\nabla}\times\boldsymbol{H} = -16\pi T^{0i}\boldsymbol{e}_i + 4\dot{\boldsymbol{g}} + O(HU_N/\mathcal{L}) \tag{2.6d}$$

(Eqs. (3.22) in Damour, Soffel, and Xu [18]). Here $\boldsymbol{e}_i$ is the unit vector in the i direction.

In terms of $\boldsymbol{g}$ and $\boldsymbol{H}$, the geodesic equation for a particle with ordinary velocity $\boldsymbol{v} = d\boldsymbol{x}/dt$ takes the following form:

$$\frac{d}{dt}\left[\left(1+3U_N+\frac{1}{2}\boldsymbol{v}^2\right)\boldsymbol{v}\right] = \left(1-U_N+\frac{3}{2}\boldsymbol{v}^2\right)\boldsymbol{g} + \boldsymbol{v}\times\boldsymbol{H} + O(gU_N^2) \;. \tag{2.7}$$

Note that the spatial part of the particle's 4-momentum is $m\boldsymbol{u} = m(1+U_N+\frac{1}{2}\boldsymbol{v}^2)\boldsymbol{v}$ at 1PN order. This accounts for the coefficient $1+U_N+\frac{1}{2}\boldsymbol{v}^2$ on the left-hand side of Eq. (2.7). The remaining factor $2U_N$ is related to the difference between physical lengths and times, and proper lengths and times. In the linearized, very low velocity approximation, this geodesic equation takes the "Lorentz-force" form $d\boldsymbol{v}/dt = \boldsymbol{g} + \boldsymbol{v}\times\boldsymbol{H}$, first deduced (so far as we know) in 1918 by Thirring [4], motivated by Einstein's 1913 [2] insights about similarities between electromagnetic theory and his not-yet-perfected general relativity theory. The 1PN deviations of the geodesic equation, Eq. (2.7), from the usual Lorentz-force form might make one wonder about the efficacy of the DSX definition of $\boldsymbol{g}$. That efficacy will show up most strongly when we explore the gravitational momentum density in Section 2.4 below.

2.3 Specialization to a Perfect Fluid

We now specialize our source to a perfect fluid and make contact with a set of 1PN gravitational potentials that are widely used. We pay special attention to connections with a paper by Pati and Will [24], because that paper will be our foundation, in Section 2.4, for computing the density and flux of gravitational field momentum. We describe our perfect fluid in the following standard notation: ρ_o = (density of rest mass), Π = (internal energy per unit rest mass, i.e., specific internal energy), P = (pressure), all as measured in the fluid's local rest frame; $v_j \equiv dx^j/dt$ = (fluid's coordinate velocity).

Following Blanchet and Damour [25], and subsequently Pati and Will (Eqs. (4.3) and (4.13) of [24]), we introduce a post-Newtonian variant U of the Newtonian potential, which is sourced by

$T^{00} + T^{jj}$:

$$\nabla^2 U = -4\pi(T^{00} + T^{jj}) \ . \tag{2.8}$$

Accurate to 1PN order, the source is, Eq. (2.19d)

$$T^{00} + T^{jj} = \rho_o(1 + \Pi + 2\boldsymbol{v}^2 + 2U_N + 3P/\rho_o) \ , \tag{2.9}$$

where U_N is the Newtonian limit of U

$$U_N(\boldsymbol{x}, t) = \int \frac{\rho_o(\boldsymbol{x}', t)}{|\boldsymbol{x} - \boldsymbol{x}'|} d^3x' \ . \tag{2.10a}$$

Correspondingly, U can be written as

$$U = \int \frac{\rho_o(1 + \Pi + 2\boldsymbol{v}^2 + 2U_N + 3P/\rho_0)}{|\boldsymbol{x} - \boldsymbol{x}'|} d^3x' \ . \tag{2.10b}$$

Here and below the fluid variables and gravitational potentials in the integrand are functions of $(\boldsymbol{x}', t)$ as in Eq. (2.10a). In Eq. (2.10a) for U_N, ρ_o can be replaced by any quantity that agrees with ρ_o in the Newtonian limit, e.g., by the post-Newtonian "conserved mass density" ρ_* of Eq. (2.14b) below. We also introduce Chandrasekhar's Post-Newtonian scalar gravitational potential χ (Eq. (44) of [16]), which is sourced by $2U_N$, $\nabla^2\chi = -2U_N$ or equivalently

$$\chi = -\int \rho_o |\boldsymbol{x} - \boldsymbol{x}'| d^3x' \ . \tag{2.11}$$

Pati and Will use the notation $-X$ for χ (Eqs. (4.14), (4.12a), and (4.3) of [24]).

It is straightforward to show that the 1PN solution to the wave equation, Eq. (2.4a), for the DSX scalar potential w is

$$w = U - \frac{1}{2}\ddot{\chi} \ ; \tag{2.12}$$

and the 1PN solution to the Laplace equation, Eq. (2.4b), for the DSX vector potential w_j is

$$w_j = \int \frac{\rho_o v_j}{|\boldsymbol{x} - \boldsymbol{x}'|} d^3x' \ . \tag{2.13}$$

The fluid's evolution is governed by rest-mass conservation, momentum conservation, and energy conservation. The 1PN version of rest-mass conservation takes the following form:

$$\rho_{*,t} + \boldsymbol{\nabla} \cdot (\rho_* \boldsymbol{v}) = 0 \ , \tag{2.14a}$$

where

$$\rho_* = \rho_o u^0 \sqrt{-g} = \rho_o \left(1 + \frac{1}{2}\boldsymbol{v}^2 + 3U\right) \tag{2.14b}$$

(Eqs. (117) and (118) of Chandrasekhar [16]). Here u^0 is the time component of the fluid's 4-velocity and g is the determinant of the covariant components of the metric. We shall discuss momentum conservation and energy conservation in the next two sections.

We note in passing that Chandrasekhar and many other researchers write their 1PN spacetime metric in a different gauge from our harmonic one. The two gauges are related by a change of time coordinate

$$t_{\rm C} = t_{\rm H} - \frac{1}{2}\dot{\chi} \; , \tag{2.15a}$$

and correspondingly the metric components in the two gauges are related by

$$g^{\rm C}_{00} = g^{\rm H}_{00} + \ddot{\chi} \; , \quad g^{\rm C}_{0j} = g^{\rm H}_{0j} + \frac{1}{2}\dot{\chi}_{,j} \; . \tag{2.15b}$$

Here C refers to the Chandrasekhar gauge and H to our harmonic gauge.

2.4 Momentum Density, Flux, and Conservation

Chandrasekhar [17], Pati and Will [24], and others have found the Landau-Lifshitz pseudotensor to be a convenient tool for formulating the conservation of momentum in post-Newtonian approximations. We shall adopt it as well.

From Pati and Will's 2PN harmonic-gauge Eqs. (2.6), (4.4b), and (4.4c) for the pseudotensor, we have deduced the following 1PN expressions for the relevant components of the Landau-Lifshitz pseudotensor (the gravitational momentum density and momentum flux) in terms of the DSX gravitoelectric and gravitomagnetic fields $\boldsymbol{g}$ and $\boldsymbol{H}$:

$$(-g)t^{0j}_{\rm LL}\boldsymbol{e}_j = -\frac{1}{4\pi}\boldsymbol{g}\times\boldsymbol{H} + \frac{3}{4\pi}\dot{U}_N\boldsymbol{g} \; , \tag{2.16a}$$

$$(-g)t^{ij}_{\rm LL} = \frac{1}{4\pi}(g_ig_j - \frac{1}{2}\delta_{ij}g_kg_k) + \frac{1}{16\pi}(H_iH_j - \frac{1}{2}\delta_{ij}H_kH_k) - \frac{3}{8\pi}\dot{U}_N^2\delta_{ij} \; . \tag{2.16b}$$

Each equation is accurate up to corrections of order U_N times the smallest term on the right side (2PN corrections). For comparison, in flat spacetime the electromagnetic momentum density is $\frac{1}{4\pi}\boldsymbol{E}\times\boldsymbol{B}$ and the momentum flux is $\frac{1}{4\pi}(E_iE_j - \frac{1}{2}\delta_{ij}E_kE_k) + \frac{1}{4\pi}(B_iB_j - \frac{1}{2}\delta_{ij}B_kB_k)$. Aside from a sign in Eq. (2.16a) and the two terms involving $\dot{U}_N$, the gravitational momentum flux and density, Eqs. (2.16), are identical to the electromagnetic ones with $\boldsymbol{E}\to\boldsymbol{g}$ and $\boldsymbol{B}\to\boldsymbol{H}$. This makes the gravitoelectric and gravitomagnetic fields $\boldsymbol{g}$ and $\boldsymbol{H}$ powerful tools for building up physical intuition about the distribution and flow of momentum in our studies of compact binaries [20].

Here we describe how we found Eqs. (2.16) from those of Pati and Will [24] (henceforth PW): (i) Show that the last two terms in Eq. (2.6) of PW are of 2PN order for $\{\alpha,\beta\} = \{0j\}$ or $\{ij\}$, so that at 1PN order $16\pi(-g)t^{\alpha\beta}_{\rm LL} = \Lambda^{\alpha\beta}$. (ii) Show that our notation is related to that of PW by $\chi = -X$, U the same, $w = U - \frac{1}{2}\ddot{\chi} = \frac{1}{4}(N+B) - \frac{1}{8}(N+B)^2$ (for the last of these, see Eqs. (5.2),

(5.4a), and (5.4c) of PW), and at Newtonian order $U_N = \frac{1}{4}N$. (iii) In PW Eqs. (4.4b) and (4.4c) for $\Lambda^{\alpha\beta}$, keep only the Newtonian and 1PN terms: the first curly bracket in Eq. (4.4b) and first and second curly brackets in Eq. (4.4c). Rearrange those terms so they involve only $\boldsymbol{K}$, $N + B$ and the Newtonian-order N, use the above translation of notation, and use the definitions (2.5) of $\boldsymbol{g}$ and $\boldsymbol{H}$. Thereby, bring PW Eqs. (4.4b) and (4.4c) into the form of Eq. (2.16).

In the Landau-Lifshitz formalism, the local law of 4-momentum conservation $T^{j\mu}{}_{;\mu} = 0$ takes the form

$$[(-g)(T^{j\mu} + t^{j\mu}_{\rm LL})]_{,\mu} = 0 \tag{2.17}$$

(Eqs. (20.23a) and (20.19) of [26], or (100.8) of [27]). Here (as usual), commas denote partial derivatives, and semicolons denote covariant derivatives. Using Eqs. (2.16) and $(-g) = 1 + 4U_N$ at leading order (from Eq. (2.2) with $w = U_N$ at leading order), and using the field equations, Eqs. (2.6), for $\boldsymbol{g}$ and $\boldsymbol{H}$, this takes the simple Lorentz-force-like form

$$[(1 + 4U_N)T^{i0}]_{,t} + [(1 + 4U_N)T^{ij}]_{,j} = (T^{00} + T^{jj})g_i + \epsilon_{ijk}T^{0j}H_k \ . \tag{2.18}$$

Here, the Levi-Civita tensor ϵ_{ijk} produces a cross product of the momentum density with the gravitomagnetic field. For comparison, in flat spacetime, the momentum conservation law for a charged medium interacting with electric and magnetic fields E_i and B_i has the form $T^{i0}{}_{,t} + T^{ij}{}_{,j} = \rho_e E_i + \epsilon_{ijk}J_j B_k$, where ρ_e is the charge density and J_j the charge flux (current density). The right-hand side of Eq. (2.18) (the gravitational force density) is identical to that in the electromagnetic case, with $\rho_e \to (T^{00} + T^{jj})$, $J_j \to T^{0j}$, $\boldsymbol{E} \to \boldsymbol{g}$, and $\boldsymbol{B} \to \boldsymbol{H}$. Again, this makes $\boldsymbol{g}$ and $\boldsymbol{H}$ powerful foundations for gravitational intuition.

For our perfect fluid, the components of the 1PN stress-energy tensor, which appear in the momentum conservation law, Eq. (2.18), are (Eqs. (20) of Chandrasekhar [16])

$$T^{00} = \rho_o(1 + \Pi + \boldsymbol{v}^2 + 2U_N) \ , \tag{2.19a}$$

$$T^{i0} = \rho_o(1 + \Pi + v^2 + 2U_N + P/\rho_o)v_j \ , \tag{2.19b}$$

$$T^{ij} = \rho_o(1 + \Pi + \boldsymbol{v}^2 + 2U_N + P/\rho_o)v_i v_j + P(1 - 2U_N)\delta_{ij} \ , \tag{2.19c}$$

$$T^{00} + T^{jj} = \rho(1 + \Pi + 2\boldsymbol{v}^2 + 2U_N + 3P/\rho_o) \ . \tag{2.19d}$$

2.5 Energy Conservation

For a perfect fluid, the exact (not just 1PN) law of energy conservation, when combined with mass conservation and momentum conservation, reduces to the first law of thermodynamics $d\Pi/dt = -Pd(1/\rho_o)/dt$; whenever one needs to invoke energy conservation, therefore, the first law is the

simplest way to do so. For this reason, and because deriving the explicit form of 1PN energy conservation $[(-g)(T^{0\mu}+t^{0\mu}_{\rm LL})]_{,\mu}=0$ is a very complex and delicate task (see Section VI of [28]), we shall not write it down here.

However, we do write down the Newtonian law of energy conservation in harmonic gauge, because we will occasionally need it in our future papers. Chandrasekhar calculated $(-g)(T^{0\mu}+t^{0\mu}_{\rm LL})$ in [17]; his Eqs. (48) and (57) are the time-time and time-space components, respectively. When one writes the expressions in terms of the "conserved rest-mass density" ρ_*, Eq. (2.14b), and in our Maxwell-like form, Newtonian conservation of energy states that

$$\left[\rho_*(1+\Pi+\frac{1}{2}v^2+3U_N)-\frac{7}{8\pi}\boldsymbol{g}\cdot\boldsymbol{g}\right]_{,t}$$
$$+\boldsymbol{\nabla}\cdot\left[\rho_*\boldsymbol{v}(1+\Pi+\frac{P}{\rho}+\frac{1}{2}v^2+3U_N)+\frac{3}{4\pi}\dot{U}_N\boldsymbol{g}-\frac{1}{4\pi}\boldsymbol{g}\times\boldsymbol{H}\right]=0\ . \tag{2.20}$$

While this equation is perfectly correct, it expresses Newtonian energy conservation in terms of the post-Newtonian gravitomagnetic field $\boldsymbol{H}$. It is possible to rewrite the $\boldsymbol{H}$-dependent term using the relationship,

$$\nabla\cdot[-1/(4\pi)(\boldsymbol{g}\times\boldsymbol{H})]=\nabla\cdot[-4U_NT^{0j}\boldsymbol{e}_j+(1/\pi)U_N\dot{\boldsymbol{g}}]\ , \tag{2.21}$$

which is accurate to terms of order $\boldsymbol{g}\cdot\dot{\boldsymbol{H}}$. This relationship can be found by applying Eq. (2.6b) once and (2.6d) twice, in combination with elementary vector-calculus identities. The statement of Newtonian energy conservation then depends only upon the Newtonian potential and its gradient and time derivative:

$$\left[\rho_*(1+\Pi+\frac{1}{2}v^2+3U_N)-\frac{7}{8\pi}\boldsymbol{g}\cdot\boldsymbol{g}\right]_{,t}+\boldsymbol{\nabla}\cdot\left[\rho_*\boldsymbol{v}(1+\Pi+\frac{P}{\rho}+\frac{1}{2}v^2-U_N)+\frac{3}{4\pi}\dot{U}_N\boldsymbol{g}+\frac{1}{\pi}U_N\dot{\boldsymbol{g}}\right]=0\ . \tag{2.22}$$

Notice that moving from Eq. (2.20) to Eq. (2.22) involves adding a divergence-free piece to the energy flux; it, therefore, entails changing how the energy flux is localized—a change that, strictly speaking, takes the energy flux out of harmonic gauge.

If the coefficients of the gravitational terms in Eq. (2.22) look unfamiliar, it is because even at Newtonian order, the density and flux of gravitational energy are gauge-dependent. In some other gauge, they will be different; see Box 12.3 of [29].

2.6 Gravitational Potentials in the Vacuum of a System of Compact, Spinning Bodies

For a system of compact, spinning bodies (neutron stars or black holes[2]), the gravitational potentials U_N, U, w_i, and χ in the vacuum between the bodies take the following forms:

$$U_N = \sum_A \frac{M_A}{r_A} , \tag{2.23a}$$

$$U = \sum_A \frac{M_A}{r_A}\left(1 + \frac{3}{2}\boldsymbol{v}_A^2 - \sum_{B\neq A}\frac{M_B}{r_{AB}}\right) + 2\sum_A \frac{\epsilon_{ijk}v_A^i S_A^j n_A^k}{{r_A}^2} , \tag{2.23b}$$

$$\chi = -\sum_A M_A r_A , \tag{2.23c}$$

$$w = U - \frac{1}{2}\ddot{\chi} , \tag{2.23d}$$

$$w_i = \sum_A \frac{M_A v_A^i}{r_A} + \frac{1}{2}\sum_A \frac{\epsilon_{ijk}S_A^j n_A^k}{{r_A}^2} . \tag{2.23e}$$

Here the notation is that of Section IV of Thorne and Hartle [31]: the sum is over the compact bodies labeled by capital Latin letters A, B; M_A, S_A^j and v_A^j are the mass, spin angular momentum, and coordinate velocity of body A; r_A is the coordinate distance from the field point to the center of mass of body A; r_{AB} is the coordinate distance between the centers of mass of bodies A and B; n_A^j is the unit vector pointing from the center of mass of body A to the field point; and ϵ_{ijk} is the Levi-Civita tensor.

Equations (2.23) for the potentials can be deduced by comparing our 1PN spacetime metric coefficients, Eqs. (2.2) and (2.12), with those in Eqs. (4.4) of [31]. An alternative derivation is given in the appendix.

2.7 Conclusion

In our Maxwell-like formulation of the 1PN approximation to general relativity, the evolution of the fluid and gravitational fields is governed by: (i) the law of momentum conservation, Eqs. (2.18) and (2.19) (which can be thought of as evolving the fluid velocity v_j); (ii) the law of mass conservation, Eq. (2.14) (which can be thought of as evolving the mass density ρ_o); (iii) the equation of state $P(\rho_o)$ and first law of thermodynamics $d\Pi = -Pd(1/\rho_o)$ (which determine P and Π once ρ_o is known); Eqs. (2.10), (2.13), and (2.11) for the gravitational potentials U, χ, and w_j; and Eqs. (2.5) or (2.6) for the gravitoelectric and gravitomagnetic fields $\boldsymbol{g}$, $\boldsymbol{H}$.

When specialized to a system of compact bodies, e.g., a binary made of black holes or neutron

[2]These expressions, though usually derived for fluid bodies such as neutron stars (see Appendix 2.A), are also valid for black holes by virtue of "effacement"; see Section 6.4 of [30].

stars, the system is governed by: (i) 1PN equations of motion and precession for the binary (not given in this paper; see, e.g., Eqs. (4.10), (4.11), and (4.14) of [31]); (ii) momentum flow within the binary as described by the Landau-Lifshitz pseudotensor, Eqs. (2.16), and its conservation law, Eq. (2.17), in which the gravitoelectric and gravitomagnetic fields are expressed as sums over the bodies via Eqs. (2.23) and (2.5); and (iii) other tools developed by Landau and Lifshitz (Section 100 of [27]). We are finding this formalism powerful in gaining insight about compact binaries [20].

2.A Appendix: Derivation of the 1PN Gravitational Potentials

For completeness, we sketch here a derivation of the 1PN gravitational potentials, Eqs. (2.23), in the vacuum of a system made of several compact bodies. Our derivation is based on Eqs. (2.10)–(2.11) for the potentials in the perfect-fluid 1PN formalism and on a fluid model for the systems' bodies. In this derivation, one must split the fluid velocity $\boldsymbol{v}$ inside body A into the sum of the body's center of mass velocity $\boldsymbol{v}_A$ and its internal fluid velocity $\boldsymbol{v}'$ relative to its center of mass, $\boldsymbol{v} = \boldsymbol{v}_A + \boldsymbol{v}'$. The two terms in w_i, Eq. (2.23e), arise from $\boldsymbol{v}_A$ and $\boldsymbol{v}'$, respectively. In U, Eq. (2.23b), the angular momentum term arises from the cross term $4\boldsymbol{v}_A \cdot \boldsymbol{v}'$ in the $\boldsymbol{v}^2$ of Eq. (2.10b); and the terms proportional to M_A can be deduced from Eq. (2.10b) and Eq. (2.25), below, for M_A, which we derive as follows: (i) Split the total Newtonian gravitational potential U_N into an external piece $U_{Ne} = \sum_{B\neq A} M_B/r_{AB}$ due to all the other bodies, and a piece U'_N due to the fluid of body A itself. (ii) Then M_A is the integral, over the body's rest-frame proper volume, of the body's own rest-mass density plus densities of internal kinetic energy, internal compressional and thermal energy and self gravitational energy[3]:

$$M_A = \int_A \rho_o \left(1 + \frac{1}{2}\boldsymbol{v}'^2 + \Pi - \frac{1}{2}U'_N\right)\left[1 + 3\left(U_{Ne} + U'_N\right)\right]\left[1 + \frac{1}{2}\left(\boldsymbol{v}_A + \boldsymbol{v}'\right)^2\right] d^3x \; . \tag{2.24}$$

Here the $1 + 3(U_{Ne} + U'_N)$ converts from coordinate volume d^3x to proper volume in the coordinate frame, and $1 + \frac{1}{2}(\boldsymbol{v}_A + \boldsymbol{v}')^2$ converts from coordinate-frame proper volume to fluid-frame proper volume (Lorentz contraction effect). (iii) Expand the product of the square-bracketed expressions and ignore terms of order $U^2 \sim (\boldsymbol{v}^2)^2$, which are negligible; drop the $\boldsymbol{v}_A \cdot \boldsymbol{v}'$ term which gives zero contribution because the body's linear momentum in its own rest frame $\left(\int_A \rho_o \boldsymbol{v}' d^3x\right)$ vanishes; and add on the expression $\int_A \left(\rho_o \boldsymbol{v}'^2 - \frac{1}{2}\rho_o U'_N + 3P\right) d^3x$, which vanishes by the virial theorem (e.g., Eq. (39.21b) of MTW [26]). The result is

$$M_A = \int_A \rho_o \left(1 + \Pi + 3P/\rho_o + 2\boldsymbol{v}'^2 + \frac{1}{2}v_A^2 + 2U'_N + 3U_{Ne}\right) d^3x \; . \tag{2.25}$$

[3]One can deduce this from the role of the gravitationally measured mass, M_A, in the global conservation law for the body's mass-energy (Box 19.1 of MTW [26]).

Bibliography

[1] R. L. Forward, Proc. IRE **49**, 892 (1961).

[2] A. Einstein, Phys. Z. **14**, 1261 (1913).

[3] A. Einstein, *Four Lectures on the Theory of Relativity* (Princeton University Press, Princeton, NJ, 1922).

[4] H. Thirring, Phys. Z. **19**, 204 (1918).

[5] H. Thirring, Phys. Z. **19**, 33 (1918).

[6] H. Thirring, Phys. Z. **19**, 156 (1918).

[7] B. Mashhoon, F. W. Hehl, and T. D. H, Gen. Relativ. Gravit. **16**, 711 (1984).

[8] V. B. Braginsky, C. M. Caves, and K. S. Thorne, Phys. Rev. D **15**, 2047 (1977).

[9] R. M. Wald, *General Relativity* (University of Chicago Press, Chicago, 1984).

[10] B. Mashhoon, Phys. Lett. A **173**, 347 (1993).

[11] B. Mashhoon, F. Gonwald, and H. I. M. Lichtenegger, Lect. Notes Phys. **562**, 83 (2001).

[12] S. J. Clark and R. W. Tucker, Classical Quantum Gravity **17**, 4125 (2000).

[13] B. Mashhoon, Classical Quantum Gravity **25**, 085014 (2008).

[14] E. Goulart and F. T. Falciano, arXiv:0807.2777.

[15] L. F. O. Costa and C. A. R. Herdeiro, Phys. Rev. D **78**, 024021 (2008).

[16] S. Chandrasekhar, Astrophys. J. **142**, 1488 (1965).

[17] S. Chandrasekhar, Astrophys. J. **158**, 45 (1969).

[18] T. Damour, M. Soffel, and C. Xu, Phys. Rev. D **43**, 3273 (1991).

[19] S. Kopeikin and I. Vlasov, Phys. Rep. **400**, 209 (2004).

[20] D. Keppel, D. A. Nichols, Y. Chen, and K. S. Thorne, Phys. Rev. D **80**, 124015 (2009).

[21] T. Damour, M. Soffel, and C. Xu, Phys. Rev. D **45**, 1017 (1992).

[22] T. Damour, M. Soffel, and C. Xu, Phys. Rev. D **47**, 3124 (1993).

[23] T. Damour, M. Soffel, and C. Xu, Phys. Rev. D **49**, 618 (1994).

[24] M. E. Pati and C. M. Will, Phys. Rev. D **62**, 124015 (2000).

[25] L. Blanchet and T. Damour, Ann. Inst. Henri Poincaré **50**, 337 (1989).

[26] C. W. Misner, K. S. Thorne, and J. A. Wheeler, *Gravitation* (W. H. Freeman, New York, 1973).

[27] L. D. Landau and E. M. Lifshitz, *Classical Theory of Fields* (Addison Wesley, Reading, MA, 1962).

[28] S. Chandrasekhar and Y. Nutku, Astrophys. J. **158**, 55 (1969).

[29] R. D. Blandford and K. S. Thorne, *Applications of Classical Mechanics* (`http://www.pma.caltech.edu/Courses/ph136/yr2008/`, California Institute of Technology, 2009).

[30] T. Damour, in *300 Years of Gravitation*, edited by S. W. Hawking and W. Israel (Cambridge University Press, Cambridge, UK, 1987).

[31] K. S. Thorne and J. B. Hartle, Phys. Rev. D **31**, 1815 (1985).

Chapter 3

Momentum Flow in Black Hole Binaries: I. Post-Newtonian Analysis of the Inspiral and Spin-Induced Bobbing

A brief overview is presented of a new Caltech-Cornell research program that is exploring the nonlinear dynamics of curved spacetime in binary-black-hole collisions and mergers, and of an initial project in this program aimed at elucidating the flow of linear momentum in black-hole binaries (BBHs). The "gauge-dependence" (arbitrariness) in the localization of linear momentum in BBHs is discussed, along with the hope that the qualitative behavior of linear momentum will be gauge-independent. Harmonic coordinates are suggested as a possibly preferred foundation for fixing the gauge associated with linear momentum. For a BBH or other compact binary, the Landau-Lifshitz formalism is used to define the momenta of the binary's individual bodies in terms of integrals over the bodies' surfaces or interiors, and define the momentum of the gravitational field (spacetime curvature) outside the bodies as a volume integral over the field's momentum density. These definitions will be used in subsequent papers that explore the internal nonlinear dynamics of BBHs via numerical relativity. This formalism is then used, in the 1.5PN approximation, to explore momentum flow between a binary's bodies and its gravitational field during the binary's orbital inspiral. Special attention is paid to momentum flow and conservation associated with synchronous spin-induced bobbing of the black holes, in the so-called "extreme-kick configuration" (where two identical black holes have their spins lying in their orbital plane and antialigned).

Originally published as D. G. Keppel, D. A. Nichols, Y. Chen, and K. S. Thorne, Phys. Rev. D **80** 124015 (2009).

3.1 Introduction: Motivation and Overview

3.1.1 Motivation

Since the spectacular breakthrough by Pretorius [1] in the spring of 2005, numerical relativists have been successfully simulating the inspiral, merger, and ringdown of binary black holes (BBHs). Much effort is now going into extracting physical and astrophysical information from these simulations. Almost all of this effort takes an "S-matrix" viewpoint: for chosen initial conditions (the two holes' initial masses, vectorial spins, and orbital elements), what is the final emitted gravitational waveform and what is the final hole's mass, vectorial spin, and kick velocity? Equally interesting, it seems to us, are the things these simulations can teach us about the nonlinear dynamics of curved spacetime. This paper is the first in a new research program by the Caltech-Cornell relativity and numerical-relativity research groups, aimed at exploring nonlinear spacetime dynamics in BBHs.

3.1.2 Momentum Flow in Black-Hole Binaries

Several sets of analytical tools already exist for exploring fully nonlinear space-time dynamics, for example dynamical horizons [2] and quasilocal energy-momentum and angular momentum [3]. One of our goals is to develop additional analytical and quasi-analytical tools and use them to extract physical insights from numerical simulations. Our initial focus in this direction is on the distribution and flow of linear momentum in strongly nonlinearly curved spacetimes—with linear momentum defined via pseudotensors that arise from viewing general relativity as a nonlinear field theory in a flat auxiliary spacetime.[1] This paper is the first in a series that will deal with this subject.

An instructive example is the extreme-kick configuration, in which two identical, spinning black holes are initially in a quasi-circular orbit, with oppositely directed spins lying in the orbital plane (Fig. 3.1). As Campanelli, Lousto, Zlochower, and Merritt [5, 6] (henceforth CLZM) discovered and Gonzalez et al. [7] helped flesh out, of all initial configurations, this one may have the largest kick speed for the final black hole[2], and it also exhibits intriguing orbital motions: During the pre-merger inspiral, as the holes circle each other, they bob up and down (in the z direction of Fig. 3.1), sinusoidally and synchronously. After merger the combined hole gets kicked up or down with a final speed that depends on the orbital phase at merger (relative to the spin directions). This bobbing and then the kick, as deduced by CLZM from numerical simulations, is graphed quantitatively in Fig. 3.2.

Momentum conservation dictates that, when the holes are moving upward together with momentum $p_A^z + p_B^z$, there must be some equal and opposite downward momentum in their gravitational field (in the curved spacetime surrounding them), and when the holes are moving downward, there

[1] Chen, Nester, and Tung have shown that various formulations of pseudotensors can also be motivated by quasi-local points of view [4].

[2] For binaries in non-circular orbits, larger kick velocities have been observed by Healy et al. [8].

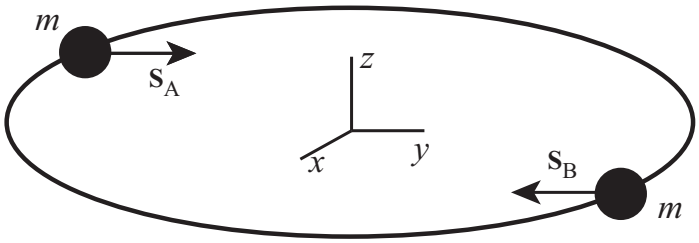

Figure 3.1: Extreme-kick configuration for a black-hole binary. Two identical holes A and B, with masses $m = M/2$, move in a circular orbit with their spin angular momenta $\boldsymbol{S}_A$ and $\boldsymbol{S}_B$ antialigned and lying in the orbital plane.

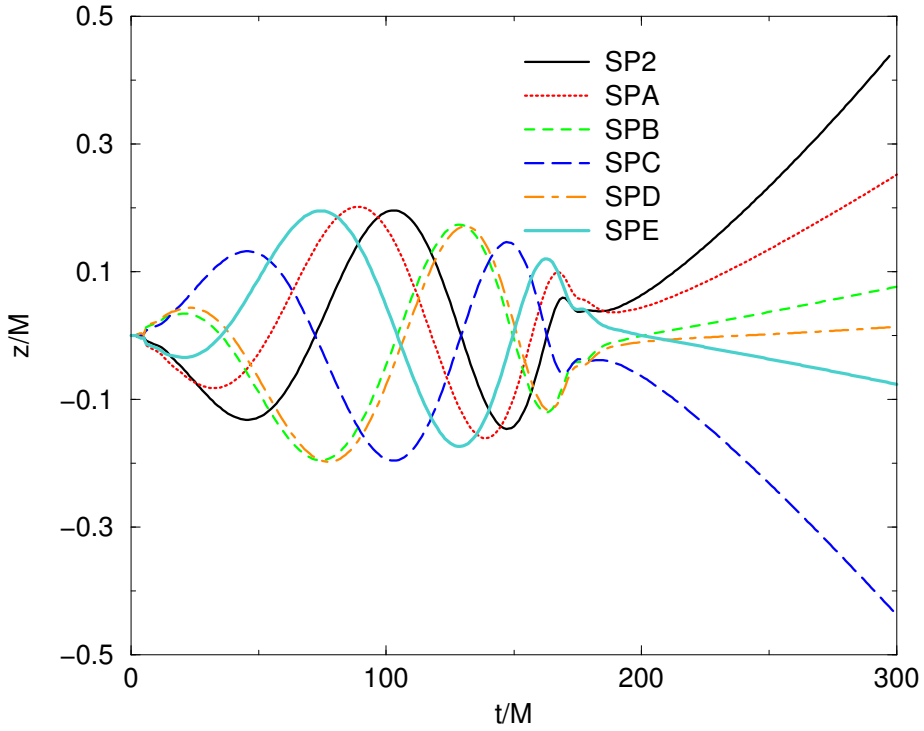

Figure 3.2: Bobbing and kick of binary black holes in the extreme-kick configuration of Fig. 3.1, as simulated by Campanelli, Lousto, Zlochower, and Merritt (CLZM) [5]. Plotted vertically (as a function of time horizontally) is the identical height, z, of the two black holes; then, transitioning through merger (presumably at $t/M \sim 170$), the height of the merged hole, above the initial orbital plane. This height versus time is shown for six different initial configurations, each leading to a different orbital phase at merger. In all six configurations, the initial holes' spins are half the maximum allowed, $a/m = 0.5$. The height z and time t are those of the "punctures" that represent the holes' centers in the CLZM computations, as defined in their computational coordinate system, which becomes Lorentzian at large radii. These z and t are measured in units of the system's total (ADM) mass $M \simeq 2m$.

must be an equal and opposite upward field momentum. How is this field momentum distributed, and what are the details of the momentum flow between the field and holes? To what extent is the final kick of the merged hole (e.g., in configuration SP2 of Fig. 3.2) an inertial continuation of the holes' immediate pre-merger bobbing? Correspondingly, to what extent is the burst of downward gravitational-wave momentum that accompanies the kick caused by near-zone, bobbing field momentum continuing "inertially" downward after merger? And, to what extent are other momentum-flow processes responsible for the motion shown in Fig. 3.2? These are the kinds of questions we would like to answer by an in-depth study of momentum flow in BBHs.

3.1.3 Gauge-Dependence of Momentum Flow and the Landau-Lifshitz Formalism

The momentum distribution and flow in a relativistic binary are delicate concepts, because momentum conservation arises from, and requires, translation invariance of a spacetime. Spacetime is translation invariant when flat, but not, in general, when curved. Two key exceptions are: (i) Spacetime is locally translation invariant in the vicinity of any event, and this leads to the local law of 4-momentum conservation $T^{\alpha\beta}{}_{;\beta} = 0$ (where $T^{\alpha\beta}$ is the total stress-energy tensor of all non-gravitational particles and fields). (ii) Around any isolated system (e.g., a BBH) spacetime can be idealized as asymptotically translation invariant, and this leads to the definition and conservation law for the system's total momentum (e.g., the binary's final kick momentum is equal and opposite to the momentum carried off by gravitational waves). However, inside the binary the curvature of spacetime prevents one from defining a globally conserved momentum density and flux in any generally covariant way.

Nevertheless, we are quite hopeful that momentum flow can be developed into a powerful tool for building physical intuition into BBHs and into the nonlinear dynamical behavior of curved spacetime that is generated by collisions of spinning black holes. To do so, however, will require living with the fact that the momentum distribution and momentum flux inside a binary cannot be generally covariant—i.e., they must be, in some sense, gauge-dependent.

There, in fact, is a long and successful history of physicists building up physical intuition with the aid of gauge-dependent concepts; it is that history that gives us hope. For example, in Maxwell's flat-spacetime electrodynamics, the vector potential satisfies the wave equation only if one first imposes Lorenz gauge. Our physical intuition about electromagnetic waves relies, to a considerable extent, on Lorenz-gauge considerations. Similarly, in developing post-Newtonian ephemerides for the solar system, celestial mechanicians have chosen a specific gauge in which to work, and their intuition about relativistic effects in the solar system relies to a great extent on that gauge's gauge-dependent constructs. The choice of gauge was, to some extent, arbitrary; but, once the choice was made, intuition could start being built. As a third example, in black-hole perturbation theory relativists

have built up physical intuition based on the Regge-Wheeler gauge, and based on the Teukolsky equation, each of which are gauge-dependent constructs.

The density, flux, and conservation of linear momentum, in the curved spacetime of a black-hole binary, must rely explicitly or implicitly on a mapping of the binary's curved spacetime onto an auxiliary, translation-invariant flat spacetime. This reliance is spelled out explicitly in a reformulation of general relativity as a nonlinear field theory in flat spacetime presented in Landau and Lifshitz's *Classical Theory of Fields* [9]. (See also Chapter 20 of MTW [10] and a more elegant, covariant formulation of the formalism developed by Babak and Grishchuk [11].) In the original Landau-Lifshitz formulation, one chooses any asymptotically Lorentzian coordinates that one wishes, one maps onto an auxiliary flat spacetime by asserting that these chosen ("preferred") coordinates are globally Lorentzian in the auxiliary spacetime (so in them the auxiliary metric has components $\mathrm{diag}[-1,1,1,1]$), and one then reformulates the Einstein equations as a nonlinear field theory in the space of that flat, auxiliary metric. The result is a total stress-energy tensor

$$\tau^{\alpha\beta} = (-g)(T^{\alpha\beta} + t^{\alpha\beta}_{\rm LL}) \; , \tag{3.1}$$

where g is the determinant of the covariant components of the physical metric, $T^{\alpha\beta}$ is the non-gravitational stress-energy tensor, and $t^{\alpha\beta}_{\rm LL}$ is the Landau-Lifshitz pseudotensor. By virtue of the translation invariance of the auxiliary spacetime, this $\tau^{\alpha\beta}$ has vanishing coordinate divergence $\tau^{\alpha\beta}{}_{,\beta} = 0$ in the chosen "preferred" coordinates. Equivalently, this $\tau^{\alpha\beta}$ has vanishing covariant divergence $\tau^{\alpha\beta}{}_{|\beta} = 0$ with respect to the auxiliary flat metric. The components τ^{j0} and τ^{jk} then represent the density and the flux of a conserved linear momentum, respectively.

We envision each numerical relativity group choosing the coordinates used in its simulations to be the preferred coordinates of this mapping to flat spacetime, resulting in each group's adopting a different gauge. If we are lucky, this will lead to momentum distributions and flows in different groups' simulations that are qualitatively and semi-quantitatively similar. If that is not the case, then we advocate that the community adopt, as a communally agreed-upon preferred coordinate system (and thence gauge), harmonic coordinates—though even then it might be necessary to face up to the fact that harmonic coordinates are not uniquely defined until one gives appropriate initial conditions. We envision joint numerical and quasi-analytical explorations, over the coming months, that lead simultaneously to a choice or choices of preferred coordinates for the mapping to flat spacetime and to physical insights into the flow of momentum in BBHs.

This paper represents a first small step in this direction. To ensure that we understand quite clearly what is going on, we shall focus in this paper on a binary's pre-merger bobbing, and we shall study it and its momentum flow using the post-Newtonian approximation to general relativity in harmonic coordinates. Subsequent papers in this series will use the Landau-Lifshitz formalism to

explore momentum flow in black-hole mergers.

3.1.4 Overview of This Paper

We begin our post-Newtonian analysis in Section 3.2 by presenting our main ideas and results in the simplest interesting context: the extreme-kick configuration. We then, in the remainder of the paper, present a detailed post-Newtonian analysis of spin-induced momentum flow in the inspiral phase of generic compact binaries (BBHs, neutron-star binaries, or neutron-star–black-hole binaries). This detailed analysis begins in Section 3.3 with a very brief summary of the Landau-Lifshitz formalism, followed in Section 3.4 by a use of the formalism to give a general treatment of 4-momentum conservation for a fully relativistic system of compact bodies. We express the binary's total 4-momentum (as measured gravitationally by distant observers) as the sum of the 4-momenta of its two bodies (expressed as integrals over their surfaces or, for stars, volume integrals over their interiors) and the 4-momentum of their external gravitational field (expressed as a volume integral over the exterior). We also derive expressions for the rate of change of the 4-momentum of each body as a surface integral of the flux of 4-momentum being exchanged between the body and the external field.

In Section 3.5, we specialize to the inspiral of a generic compact binary, as analyzed in harmonic coordinates, at leading nontrivial post-Newtonian order (1.5PN for the effects of spin); and we focus on the distribution and flow of linear momentum (the spatial part of 4-momentum) induced by the bodies' spins. We begin in Section 3.5.1 by computing the spin-induced perturbation of the field momentum $\delta\tau^{0j}$ in terms of the binary's masses, vectorial spins, and geometry; and we then integrate this density over the exterior of the bodies to obtain the total field-momentum perturbation $\delta\boldsymbol{p}_{\rm field}$ in terms of the bodies' masses, spins, and vectorial separation. In Section 3.5.2, we discuss the definition of a body's center of mass $\boldsymbol{x}_{\rm cm}$ and corresponding velocity $\boldsymbol{v} = d\boldsymbol{x}_{\rm cm}/dt$, and we write down the influence of the bodies' spins $Md\delta\boldsymbol{v}/dt$ on their equations of motion. In Section 3.5.3 and Appendix 3.B, we use our definition of center of mass to deduce an expression for the spin-induced perturbation of a body's momentum $\delta\boldsymbol{p}$ in terms of its mass times velocity perturbation $M\delta\boldsymbol{v}$, and cross products of the bodies' spins with their separation vector. Finally, in Section 3.5.4, we verify momentum conservation; i.e., we verify that, as the binary evolves and momentum is fed back and forth between the bodies and the field, the bodies' equations of motion ensure that the spin-induced perturbation of the total momentum (bodies plus field) is conserved.

3.2 Bobbing and Momentum Flow in the Extreme-Kick Configuration

In this section, we shall present an overview of our momentum-flow ideas and results in the context of the extreme-kick configuration (Figs. 3.1 and 3.2).

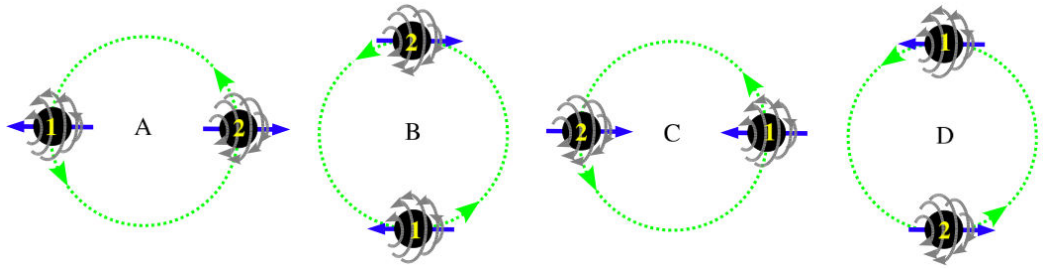

Figure 3.3: Pretorius' physical explanation for the holes' bobbing in the extreme-kick configuration

Pretorius [12] has offered a lovely physical explanation for the holes' bobbing (Fig. 3.2) in this configuration. In Fig. 3.3, taken from his paper, we see snapshots of the holes at four phases in their orbital motion. In each snapshot, each hole's spin drags space into motion (drags inertial frames) in the direction depicted by gray, semi-circular arrows. In phase B, hole 1 drags space and thence hole 2 into the sheet of paper (or computer screen); and hole 2 drags space and thence hole 1 also inward.[3] In phase D each hole drags the other outward. This picture agrees in phasing and semi-quantitatively in amplitude with the bobbing observed in the simulations (Fig. 3.2).

The agreement is semi-quantitative but not quantitative. In addition to frame dragging, there is a second influence of the holes' spins on their motions, at the same 1.5 post-Newtonian (1.5PN) order: a force on each body due to the coupling of its own spin to the Riemann curvature tensor produced by the other body. For the extreme-kick configuration (Fig. 3.1), in harmonic coordinates, the mass times the coordinate acceleration produced by frame dragging (expressed as a weak perturbation, "δ", to the motion of a nonspinning binary) is $(d^2\delta\boldsymbol{x}_A/dt^2)_{\rm FD} = (4/r_{AB}^3)\boldsymbol{S}_B \times \boldsymbol{v}_{AB}$, and that produced by spin-curvature coupling is $(d^2\delta\boldsymbol{x}_A/dt^2)_{\rm SC} = (3/r_{AB}^3)\boldsymbol{S}_A \times \boldsymbol{v}_{AB}$ (first and second lines of Eq. (4.11c) of [14]). Here r_{AB} is the separation between the two holes, $\boldsymbol{v}_{AB} = \boldsymbol{v}_A - \boldsymbol{v}_B = 2\boldsymbol{v}_A$ is the coordinate velocity of hole A relative to hole B, and $\boldsymbol{S}_A$ and $\boldsymbol{S}_B$ are the spin angular momenta of holes A and B as defined in post-Newtonian theory (e.g., in the binary's PN metric, Eq. (4.2) of [14]). Since $\boldsymbol{S}_B = -\boldsymbol{S}_A$, the sum of the frame-dragging acceleration and spin-curvature-coupling acceleration is

$$\left(\frac{d^2\delta\boldsymbol{x}_A}{dt^2}\right)_{\text{spin effects}} = \frac{2}{r_{AB}^3}\boldsymbol{S}_A \times \boldsymbol{v}_A \ . \tag{3.2}$$

We get the acceleration of hole B by replacing all subscript Bs by subscript As. The two holes' accelerations are identical (synchronous bobbing) because $\boldsymbol{S}_B = -\boldsymbol{S}_A$, $\boldsymbol{v}_B = -\boldsymbol{v}_A$.

We can easily integrate this equation in time by noting that the spin precesses much more slowly than the orbital motion (so that $\boldsymbol{S}_A$ can be approximated as constant) and by noting that $\boldsymbol{v}_A$ rotates with angular velocity $\Omega = \sqrt{M/r_{AB}^3} = \sqrt{2m/r_{AB}^3}$, where M is the total mass and m is the mass of

[3] This is very similar to the way that two fluid vortices (e.g., an aerofoil's starting and stopping vortex pair) drive each other into motion; see, e.g., [13].

each hole as defined in post-Newtonian theory. The result, after one integration, can be written as

$$m\delta\boldsymbol{v}_A = m\delta\boldsymbol{v}_B = -\frac{m}{r_{AB}^2}\boldsymbol{S}_A \times \boldsymbol{n}_{AB} \ . \tag{3.3}$$

Here $\delta\boldsymbol{v}_A$ and $\delta\boldsymbol{v}_B$ are the holes' velocity perturbations (bobbing) produced by their spins, and $\boldsymbol{n}_{AB} = (\boldsymbol{x}_A - \boldsymbol{x}_B)/r_{AB}$ is the unit vector that points from hole B toward hole A. (As with the convention for propagators, we regard things as "moving" from right to left; the vector n_{AB} points from B to A.) One might think that Eq. (3.3) represents the holes' bobbing momentum, but as we shall see in Section 3.2.2 it does not—for subtle but physically understandable reasons. The bobbing momentum of each hole is actually 2/3 times Eq. (3.3); see Eq. (3.19) below.

We can integrate Eq. (3.3) once more to obtain each hole's bobbing displacement (change of location) in harmonic coordinates. We write the result in a form that is easily compared with Fig. 3.2:

$$\frac{\delta\boldsymbol{x}_A}{m} = -\boldsymbol{v}_A \times \frac{\boldsymbol{S}_A}{m^2} \ . \tag{3.4}$$

Because $\boldsymbol{S}_A$ remains approximately constant while $\boldsymbol{v}_A$ rotates uniformly in time (if we ignore radiation-reaction-induced inspiral), and because $\boldsymbol{S}_A$ and $\boldsymbol{v}_A$ both lie in the orbital plane, Eq. (3.4) represents an approximately sinusoidal bobbing orthogonal to the orbital plane (z direction), with (peak-to-peak) amplitude $\delta z/M = v_A S_A/m^2 = \frac{1}{2}v_A$, where we have used the spin magnitude $S_A/m^2 = a/m = 0.5$ of the CLZM simulations. (The 1.5PN bobbing acceleration, velocity, and momentum, Eqs. (3.2)–(3.4), depend only on the Newtonian limits of the PN masses m and spins $\boldsymbol{S}_A = -\boldsymbol{S}_B$, and the CLZM simulations use a puncture mass and a spin that have this same Newtonian limit. Therefore, when comparing the simulations with our PN analysis, we can identify the simulations' masses and spins with PN-theory's masses and spins.)

The CLZM simulations cover only the last two orbits before inspiral, when the post-Newtonian approximation is failing badly and the inspiral is rapid. Nevertheless, we can hope for rough quantitative agreement. The simulation shows a maximum bobbing amplitude $\delta z/M \simeq 0.4$, which agrees with our 1.5PN amplitude $\delta z/M = \frac{1}{2}v_A$ if v_A is near the speed of light, as it should be just before merger. Half an orbit earlier the simulation's bobbing amplitude is smaller by about a factor $1/1.7 \simeq 1/\sqrt{2.5}$, which is what our 1.5PN formula predicts if the orbital radius is 2.5 times larger than at maximum amplitude—and this agrees fairly well with Fig. 2 of CLZM [5].

3.2.1 Field Momentum in the Extreme-Kick Configuration

In harmonic gauge at leading post-Newtonian order, the Landau-Lifshitz formalism gives for the density of field momentum

$$\tau^{0j}\boldsymbol{e}_j = -\frac{\boldsymbol{g} \times \boldsymbol{H}}{4\pi} \tag{3.5}$$

(Eq. (4.1a) of [15]). Here, to the accuracy we need, $\boldsymbol{g}$ is the Newtonian gravitational acceleration field (the *gravitoelectric field*), $\boldsymbol{H}$ is the gravitational analog of the magnetic field (the *gravitomagnetic field*), and $\boldsymbol{e}_j$ is the basis vector in the j direction of the flat-spacetime field theory that we are using. (As we shall see, and as is discussed in Ref. [15] and references cited therein, the analogy with electrodynamics can be very powerful in building up insight into gravitational momentum density and flux.)

Before applying Eq. (3.5) to the extreme-kick configuration, let us build up a bit of physical insight into it. Just as the ratio of the momentum and the mass-energy defines a velocity for a particle, we can also regard the ratio of the momentum density to the mass-energy density in the relativistic gravitational field, τ^{0j}/τ^{00}, as a field velocity

$$v^j_{\rm field} \equiv \frac{\tau^{0j}}{\tau^{00}} \ . \tag{3.6}$$

One can show that in harmonic coordinates the vacuum field momentum density τ^{00} is negative; in fact, it is

$$\tau^{00} = -\frac{7}{8\pi}\boldsymbol{g}\cdot\boldsymbol{g} \tag{3.7}$$

at leading PN order.[4] Correspondingly, the gravitational field's velocity (as "seen" in our auxiliary flat spacetime) points in the direction of $+\boldsymbol{g}\times\boldsymbol{H}$ and has a magnitude of order $|\boldsymbol{H}|/|\boldsymbol{g}|$. The direction of this field velocity is the same as the direction of motion of an inertial point mass (relative to our harmonic coordinates) that is induced by a brief joint action of $\boldsymbol{g}$ followed by $\boldsymbol{H}$. The geodesic equation, in harmonic coordinates, and for low particle velocities $\boldsymbol{v}$, takes the Lorentz-force form

$$\frac{d\boldsymbol{v}}{dt} = \boldsymbol{g} + \boldsymbol{v}\times\boldsymbol{H} \tag{3.8}$$

(Eq. (2.7) of [15]) at leading order. In a very short time interval t, the field $\boldsymbol{g}$ acting on a particle initially at rest produces a velocity $\boldsymbol{v} = \boldsymbol{g}t$, and then $\boldsymbol{H}$ acts on this velocity to produce $\delta\boldsymbol{v} = \frac{1}{2}(\boldsymbol{g}\times\boldsymbol{H})t^2$—which points in the direction of the field velocity.

Now, let us study the field momentum for the extreme-kick black-hole binary. For the moment we are only interested in that portion of the field momentum which is induced by the holes' spins, since this is the portion that must flow back and forth between the field and the bobbing holes in order to conserve total momentum. This portion arises from one hole's gravitoelectric field $\boldsymbol{g}$ coupling to the spin-induced part of the the other hole's gravitomagnetic field

$$\delta\tau^{0j}\boldsymbol{e}_j = -\frac{\boldsymbol{g}_A\times\boldsymbol{H}^{\rm spin}_B}{4\pi} - \frac{\boldsymbol{g}_B\times\boldsymbol{H}^{\rm spin}_A}{4\pi} \ . \tag{3.9}$$

[4] This is τ^{00} in harmonic coordinates (gauge) in vacuum, at leading (Newtonian) order; see, e.g., the first term in Eq. (4.4a) of [16]. This Newtonian gravitational energy density is gauge dependent; see, e.g., the discussion in Box 12.3 of [17].

The leading-order expressions for $\boldsymbol{g}_A$ and $\boldsymbol{H}_A$ are

$$\boldsymbol{g}_A = -\frac{m}{r_A^2}\boldsymbol{n}_A \,, \tag{3.10a}$$

$$\boldsymbol{H}_A = -2\frac{(3\boldsymbol{n}_A\cdot\boldsymbol{S}_A)\boldsymbol{n}_A - \boldsymbol{S}_A}{r_A^3} \tag{3.10b}$$

(Eqs. (2.5) and (6.1) of [15]), where $\boldsymbol{n}_A$ is the unit radial vector pointing from the center of hole A to the field point, and r_A is the distance from the center of hole A to the field point. The gravitoelectric field (actually the Newtonian gravitational acceleration), Eq. (3.10a), has identically the same form as the Coulomb electric field of a point charge, with the charge replaced by the hole's mass m_A and the sign reversed. Similarly, the gravitomagnetic field, Eq. (3.10b), is identical to the dipolar magnetic field of a point magnetic dipole, with the magnetic moment replaced by the opposite of twice the hole's spin, i.e., $-2\boldsymbol{S}_A$. The fields for hole B are the same as Eqs. (3.10), but with each subscript A replaced by a B.

Combining Eqs. (3.9) and (3.10) we obtain for the binary's density of field momentum (that portion which must flow during bobbing[5])

$$\delta\tau^{0j}\boldsymbol{e}_j = \frac{m}{2\pi r_A^3 r_B^2}\left[3(\boldsymbol{S}_A\cdot\boldsymbol{n}_A)(\boldsymbol{n}_A\times\boldsymbol{n}_B) - (\boldsymbol{S}_A\times\boldsymbol{n}_B)\right] + (A\leftrightarrow B)\,, \tag{3.11}$$

and integrating this over the space outside the holes, we obtain for the total field momentum that flows during bobbing (the part of the field momentum that depends on the holes' spins)[6]

$$\delta\boldsymbol{p}_{\rm field} = \frac{4}{3}\frac{m}{r_{AB}^2}\boldsymbol{S}_A\times\boldsymbol{n}_{AB}\,. \tag{3.12}$$

This is equal and opposite to the sum of the holes' bobbing momenta $\delta p_A + \delta p_B$, as we shall see in Section 3.2.3 below.

Figure 3.4 shows the z component (perpendicular to the orbital plane) of the field-momentum density $\delta\tau^{0z}$, as measured in the orbital plane at four different moments in the binary's orbital evolution. Only that part of the momentum which flows during bobbing, Eq. (3.11), is pictured. Red depicts momentum density flowing out of the paper ($+z$ direction), and blue, into the paper. The yellow arrows show the holes' vectorial spins $\boldsymbol{S}$, and the circle with two arrows is the binary's orbital trajectory. In the top-left and bottom-right frames, the black holes are momentarily stationary at the top and bottom of their bobbing; see Eqs. (3.3) and (3.4). Nevertheless, the momentum density has a non-trivial distribution. In the top-right and bottom-left frames, the black holes are moving downward and upward, respectively, with maximum speed. In both cases, the field-momentum

[5]There are portions of the momentum density that do not flow during bobbing, which will be important for our comparisons with numerical relativity. The full expression, therefore, is listed in Appendix 3.A.

[6]Equations (3.11) and (3.12) are special cases of Eqs. (3.35) and (3.38) below, where the details of the integration are carried out.

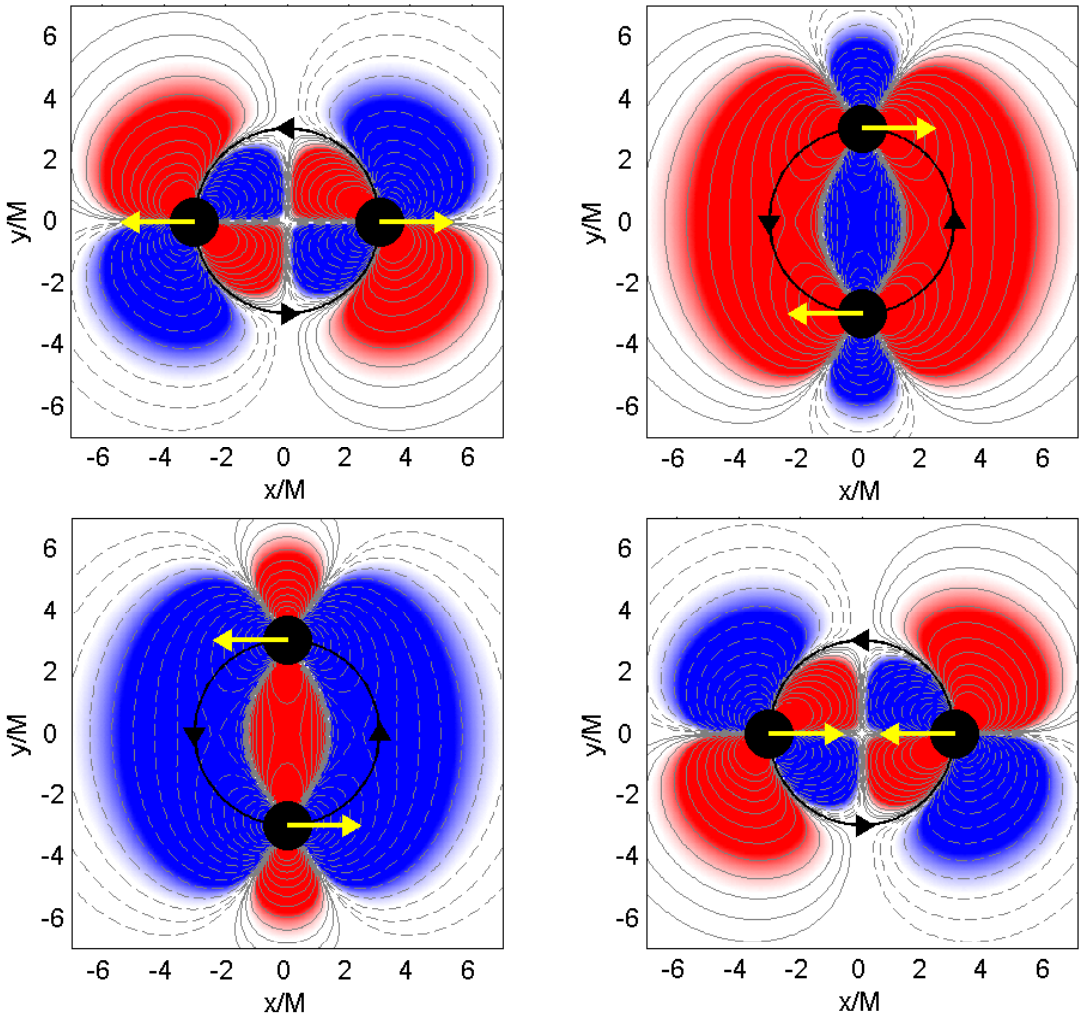

Figure 3.4: The four pictures show the z component of field-momentum density $\delta\tau^{0z}$ in the orbital plane at four different times, a quarter orbit apart. Red represents positive momentum density (coming out of the paper), and blue, negative (going into the paper). Only the piece of momentum density $\delta\tau^{0z}$ that flows during bobbing, Eq. (3.11), is depicted. The yellow arrows are the black holes' vectorial spins; the large, black circle with arrows shows the orbital path of the two holes. In the top-left picture, one sees the density of momentum when the black holes are at the top of their bob (maximum z) and momentarily stationary; see Eqs. (3.3) and (3.4). The gravitational-field momentum is zero, but the momentum density itself shows rich structure. A quarter orbit later, in the top right, the holes are moving downward (into the paper) at top speed. The momentum between the black holes (blue region) flows into the paper with them, while the surrounding momentum (red region) flows out of the paper ($+z$ direction). A half orbit after the first picture, in the lower left, the holes are momentarily at rest at the bottom of their bob (minimum z), the net field momentum is zero, and the momentum distribution is opposite that in the first picture (as one would expect during sinusoidal bobbing). Similarly, three quarters of the way through the orbit, in the lower right, the holes have reached their maximum upward speed, and the momentum distribution is identical to the second figure, but with the opposite sign.

density between the two holes flows in the same direction as the bobbing, whereas the momentum surrounding the binary is in the opposite direction and larger. This leads to a net momentum conservation for the binary, as discussed in Section 3.5.4.

It is worth noting that the four figures, going counterclockwise from the top-left, are taken a quarter period apart in orbital phase. The first and third differ by half an orbital period (as do the second and fourth); consequently, the momentum patterns of each pair are identical, but signs are reversed (red exchanged with blue, as dictated by the symmetry of the configuration). This feature is responsible for the sinusoidal bobbing.

It is instructive, in building up physical intuition, to draw pictures of hole A's gravitoelectric field lines (radial field lines parallel to $\boldsymbol{g}_A$), hole B's gravitomagnetic field lines (dipolar field lines parallel to $\boldsymbol{H}_B$), and, with them, the direction of $-\boldsymbol{g}_A \times \boldsymbol{H}_B$ at various points in Fig. 3.4 (and similarly for $\boldsymbol{g}_B$, $\boldsymbol{H}_A$ and $-\boldsymbol{g}_B \times \boldsymbol{H}_A$). This and Eq. (3.9) help one understand the momentum distribution (red and blue coloring) in Fig. 3.4.

3.2.2 The Holes' Momenta

In this section, we shall use a roundabout route to explain, physically, why the momentum $\boldsymbol{p}_A$ of black hole A is not $m\boldsymbol{v}_A$ and to derive an expression for it.

Begin by considering, for pedagogical purposes, a rigidly and slowly rotating body in flat spacetime with rotational velocity $\boldsymbol{v}_{\rm rot}(\boldsymbol{x})$. Let ρ be the mass-energy density of the body's material in the local rest frame of a bit of material. Then in an inertial frame where the body is at rest except for its rotation (the body's "momentary inertial frame"), its mass-energy density is $T^{00} = \rho(1 + v_{\rm rot}^2)$, where $\frac{1}{2}v_{\rm rot}^2$ comes from kinetic energy and $\frac{1}{2}v_{\rm rot}^2$ from Lorentz contraction. We define the body's center-of-mass location $\boldsymbol{x}_{\rm cm}$ by

$$M\boldsymbol{x}_{\rm cm} = \int T^{00}\boldsymbol{x} d^3x \quad \text{in body's momentary rest frame,} \tag{3.13}$$

where $M \equiv \int T^{00} d^3x$ is the body's mass. If the body is weakly gravitating, this location will be the center of the monopolar part of its gravitational field.

Now let this rotating body move with a linear velocity $\boldsymbol{v}$ that is small compared to its rotational velocity, so that its mass-energy density is $T^{00} = \rho[1 + (\boldsymbol{v} + \boldsymbol{v}_{\rm rot})^2] \simeq \rho[1 + \boldsymbol{v}_{\rm rot}^2 + 2\boldsymbol{v}_{\rm rot} \cdot \boldsymbol{v}]$. If we use this T^{00} to compute $\int T^{00}\boldsymbol{x} d^3x$, we will not get the $\boldsymbol{x}_{\rm cm}$ of Eq. (3.13) because the term $2\rho\boldsymbol{v}_{\rm rot} \cdot \boldsymbol{v}$ will weight $\boldsymbol{x}$ more heavily on the side of the body where $\boldsymbol{v}_{\rm rot} \cdot \boldsymbol{v} > 0$ and less heavily on the side where $\boldsymbol{v}_{\rm rot} \cdot \boldsymbol{v} < 0$. If we want to compute the correct $\boldsymbol{x}_{\rm cm}$ by an integral performed in a frame where the body is moving, we must correct for this effect. The correction factor is well known ([18] and Section 3.5.2 below):

$$M\boldsymbol{x}_{\rm cm} = \int T^{00}\boldsymbol{x} d^3x - \boldsymbol{v} \times \boldsymbol{S} \,, \tag{3.14}$$

where $\boldsymbol{S}$ is the body's angular momentum. Other definitions of the center of mass are sometimes used, but they all differ from the locations one would identify, in the body's rest frame, as the mass-energy-weighted location, Eq. (3.13), and the center of weak monopolar gravity—i.e., they are physically motivated less well than this one is.

Equation (3.14), when extended into general relativity in the obvious manner,

$$M\boldsymbol{x}_{\rm cm} = \int \tau^{00}\boldsymbol{x}d^3x - \boldsymbol{v}\times\boldsymbol{S} \tag{3.15}$$

(where $\tau^{\alpha\beta}$, Eq. (3.1), is the total stress-energy tensor), is called the *physical spin supplementary condition* (SSC) [18]; see Eq. (3.42) below, where a formal derivation is presented. In general relativity, this condition guarantees that in the body's local rest frame, $\boldsymbol{x}_{\rm cm}$ is at the center of the monopolar part of the body's (possibly strong) gravitational field, or more precisely the center of the monopolar part of the time-time component of the metric density $\mathfrak{g}^{00} \equiv \sqrt{-g}g^{00}$, which plays a major role in the Landau-Lifshitz field-theory-in-flat-spacetime formalism.

The black-hole velocities $\boldsymbol{v}_A$ and $\boldsymbol{v}_B$ used in this paper and in the standard harmonic-coordinate, post-Newtonian equations of motion, are the (coordinate) time derivatives of the holes' centers of mass:

$$\boldsymbol{v}_A = d\boldsymbol{x}_{A\,\rm cm}/dt\ . \tag{3.16}$$

By specializing Eq. (3.15) to body A, differentiating with respect to time, using the conservation law $\tau^{00}{}_{,0} + \tau^{0j}{}_{,j} = 0$, and integrating the volume integral by parts, we obtain (Eq. (3.47) below and its derivation)

$$p^j_A = \underbrace{mv^j_A}_{\rm kinetic} + \underbrace{(\boldsymbol{a}_A\times\boldsymbol{S}_A)^j}_{\rm SSC} + \underbrace{\int_{\partial A}(x^j - x^j_{{\rm cm}\,A})(\tau^{0k} - \tau^{00}v^k_A)d\Sigma_k}_{\rm surface}\ , \tag{3.17}$$

where

$$p^j_A \equiv \int_A \tau^{0j}d^3x \tag{3.18}$$

is the total 4-momentum of body A. Here $\boldsymbol{a}_A$ is the acceleration of body A produced by the gravity of body B and m is the mass of body A. For a black hole, the linear momentum must be defined via a surface integral rather than the volume integral $\int_A \tau^{0j}d^3x$ (Eq. (3.30b) below), but Eq. (3.17) still turns out to be true; see the paragraph following Eq. (3.47) below.

Equation (3.17) has a physical interpretation that is closely related to the one for the center-of-mass equation, Eq. (3.15), that underlies it. Rearranged, this equation says $m\boldsymbol{v}^j_A = p^j_A - (\boldsymbol{a}_A\times\boldsymbol{S}_A)^j - \int_{\partial A}(x^j - x^j_{{\rm cm}\,A})(\tau^{0k} - \tau^{00}v^k_A)d\Sigma_k$. The left side is the time derivative of the center-of-mass location, weighted by the body's mass (or the kinetic momentum). The first term on the right side is the body's total momentum, i.e., the volume integral of τ^{0j}. The second (SSC) term corrects

Body	Kinetic: Frame-Dragging	Kinetic: Spin-Curvature	SSC	Surface	Total
$\boldsymbol{p}_A$	$-4\boldsymbol{a}_B \times \boldsymbol{S}_B$	$3\boldsymbol{a}_A \times \boldsymbol{S}_A$	$\boldsymbol{a}_A \times \boldsymbol{S}_A$	$-\frac{2}{3}\boldsymbol{a}_A \times \boldsymbol{S}_A$	$-\frac{2}{3}\boldsymbol{a}_A \times \boldsymbol{S}_A$
$\boldsymbol{p}_B$	$-4\boldsymbol{a}_A \times \boldsymbol{S}_A$	$3\boldsymbol{a}_B \times \boldsymbol{S}_B$	$\boldsymbol{a}_B \times \boldsymbol{S}_B$	$-\frac{2}{3}\boldsymbol{a}_B \times \boldsymbol{S}_B$	$-\frac{2}{3}\boldsymbol{a}_B \times \boldsymbol{S}_B$
$\boldsymbol{p}_{\rm field}$					$\frac{2}{3}(\boldsymbol{a}_A \times \boldsymbol{S}_A + \boldsymbol{a}_B \times \boldsymbol{S}_B)$

Table 3.1: Spin-dependent, time-varying pieces of the bodies' and field's momenta at 1.5PN order, for the extreme-kick binary (circular orbit with spins antialigned and in the orbital plane). The bodies' momenta are broken down into kinetic, SSC, and surface terms and are expressed in terms of the bodies' spins $\boldsymbol{S}_{A,B}$ and Newtonian-order gravitational accelerations $\boldsymbol{a}_{A,B} = -m\boldsymbol{n}_{A,B}/r_{AB}^2$. See Eqs. (3.43) and (3.49) for a similar decomposition in a generic binary.

for the fact that for a spinning body τ^{0j} weights the center of mass too heavily on the side of the body where the rotational velocity and linear velocity are coaligned ($\boldsymbol{v}_{\rm A\ rot} \cdot \boldsymbol{v}_{\rm A} > 0$) and too lightly on the side where they are antialigned. The third (surface) term corrects for a contribution to the momentum arising from mass flowing into and out of the body (mass flux $\tau^{0i} - \tau^{00}v^i$) at different locations on the body's face.

3.2.3 Momentum Conservation for the Extreme-Kick Configuration

We now specialize Eq. (3.17) for the momentum of a body in a generic binary to the extreme-kick configuration and focus on the spin-dependent piece of the momentum that is exchanged between the bodies and the field. By inserting the expressions $\delta\tau^{0j}\boldsymbol{e}_j = -\boldsymbol{g}_B \times \boldsymbol{H}_A/4\pi$ and $\boldsymbol{a}_A = \boldsymbol{g}_B(\boldsymbol{x} = \boldsymbol{x}_{A\,\rm cm})$ into Eq. (3.17), with $\boldsymbol{g}$ and $\boldsymbol{H}$ given by Eqs. (3.10), and performing the integrals, we obtain

$$\delta\boldsymbol{p}_A = -\frac{2}{3}\frac{m}{r_{AB}^2}\boldsymbol{S}_A \times \boldsymbol{n}_{AB}\ . \tag{3.19}$$

This spin-induced perturbation of the linear momentum of body A, when added to an equal amount for body B gives $-\frac{4}{3}(m/r_{AB}^2)\boldsymbol{S}_A \times \boldsymbol{n}_{AB}$, which is equal and opposite to the spin-induced perturbation of the field momentum, Eq. (3.12). Therefore, as the holes circle each other, momentum flows sinusoidally back and forth between the holes and the field, with no change in the total momentum; the total momentum is conserved during the bobbing.

Let us examine in detail how momentum conservation is achieved for the bodies' bobbing. Our detailed analysis (above) breaks each object's momentum perturbation $\delta\boldsymbol{p}_{A,B}$ into three terms, the kinetic momentum $m\delta\boldsymbol{v}_{A,B}$, a term due to the SSC, and a surface-integral term (see Table 3.2.3). The total kinetic momentum

$$m\delta\boldsymbol{v}_A + m\delta\boldsymbol{v}_B = -(\boldsymbol{a}_A \times \boldsymbol{S}_A + \boldsymbol{a}_B \times \boldsymbol{S}_B) \neq 0 \tag{3.20}$$

is not conserved because the frame-dragging and spin-curvature-coupling terms do not cancel. The total body momentum $\delta\boldsymbol{p}_A + \delta\boldsymbol{p}_B$ is not conserved either; it sums up to 2/3 of the total kinetic

momentum:

$$\delta \boldsymbol{p}_A + \delta \boldsymbol{p}_B = -\frac{2}{3}(\boldsymbol{a}_A \times \boldsymbol{S}_A + \boldsymbol{a}_B \times \boldsymbol{S}_B) \neq 0 \,. \tag{3.21}$$

To achieve momentum conservation, there is a non-zero spin-dependent total field momentum distributed outside of the bodies, given by

$$\delta \boldsymbol{p}_{\text{field}} = \frac{2}{3}(\boldsymbol{a}_A \times \boldsymbol{S}_A + \boldsymbol{a}_B \times \boldsymbol{S}_B) \,. \tag{3.22}$$

Note that this total external field momentum is only $-2/3$ of the spin-dependent total kinetic momentum (instead of the -1 that one might have expected).

It is important to notice that for each body, a canonical momentum can be formed by adding the SSC term to the kinetic momentum

$$\boldsymbol{p}_{A\,\text{canonical}} = m\boldsymbol{v}_A + \boldsymbol{a}_A \times \boldsymbol{S}_A \,. \tag{3.23}$$

The total canonical momentum $\boldsymbol{p}_A + \boldsymbol{p}_B$ is conserved, because the sum of the contribution from the surface terms of the bodies' momenta and the external field momentum are equal and opposite. (This holds for any generic binary, not just the extreme-kick configuration; see Section 3.5 below). This canonical momentum can be motivated simply from special-relativistic kinetics—without the need for any knowledge of field momentum—and it is used in the Hamiltonian approach to post-Newtonian dynamics [19, 18]. Although the canonical momentum explains momentum conservation for the two-body dynamics, it does not provide information about the distribution of field momentum nor the role of field momentum in momentum conservation. Our analysis reveals substantial spin-dependent field momentum outside of the bodies, with the same order of magnitude as the total spin-dependent kinetic momentum.

One might wonder about the usefulness of distinguishing between the bodies' (localized) momenta and the (distributed) field momenta, because a different choice of gauge might move momentum between these two components or move all the field momentum into the interiors of the objects. We argue that our choice of harmonic gauge, the analogue of Lorenz gauge in electrodynamics, is a promising tool for analyzing compact binaries, because its metric perturbations (both physical and gauge) propagate at the speed of light; this will make gauge effects behave causally just as do physical effects. For this reason, and because of the physical intuition that the above analysis brings, we advocate using harmonic gauge and its nonzero field momentum in analyzing compact, inspiraling binaries.

3.3 The Landau-Lifshitz Formalism in Brief

We turn, now, to a detailed analysis of momentum flow in generic compact binary systems. We begin in this section with a very brief review of the Landau-Lifshitz (LL) formulation of general relativity as a nonlinear field theory in flat spacetime [9].

This formulation starts (as discussed in Section 3.2 above) by introducing an (arbitrary) coordinate system in which the auxiliary flat metric takes the Minkowski form $\eta_{\mu\nu} = \mathrm{diag}[-1, 1, 1, 1]$. Gravity is described, in this formulation, by the physical metric density

$$\mathfrak{g}^{\mu\nu} = \sqrt{-g} g^{\mu\nu} \ . \tag{3.24}$$

Here g is the determinant of the covariant components of the physical metric, and $g^{\mu\nu}$ are the contravariant components of the physical metric. In terms of the superpotential

$$H^{\mu\alpha\nu\beta} \equiv \mathfrak{g}^{\mu\nu}\mathfrak{g}^{\alpha\beta} - \mathfrak{g}^{\mu\alpha}\mathfrak{g}^{\nu\beta} \ , \tag{3.25}$$

the Einstein field equations take the field-theory-in-flat-spacetime form

$$H^{\mu\alpha\nu\beta}{}_{,\alpha\beta} = 16\pi\tau^{\mu\nu} \ . \tag{3.26}$$

Here $\tau^{\mu\nu} = (-g)(T^{\mu\nu} + t^{\mu\nu}_{\mathrm{LL}})$ is the total effective stress-energy tensor introduced in Eq. (3.1), indices after the comma denote partial derivatives (covariant derivatives with respect to the flat auxiliary metric), and the Landau-Lifshitz pseudotensor $t^{\mu\nu}_{\mathrm{LL}}$ (actually a real tensor in the auxiliary flat spacetime) is given by Eq. (100.7) of LL [9] or, equivalently, Eq. (20.22) of MTW [10]. By virtue of the symmetries of the superpotential (which are the same as those of the Riemann tensor), the field equations in the form of Eq. (3.26) imply the differential conservation law for 4-momentum

$$\tau^{\mu\nu}{}_{,\nu} = 0 \ , \tag{3.27}$$

which is equivalent to $T^{\mu\nu}{}_{;\nu} = 0$ (where the semicolon denotes a covariant derivative with respect to the physical metric).

It is shown in LL and in MTW that the total 4-momentum of any isolated system (as measured gravitationally in the asymptotically flat region far from the system) is

$$p^{\mu}_{\mathrm{tot}} = \frac{1}{16\pi} \oint_{\mathcal{S}} H^{\mu\alpha 0 j}{}_{,\alpha} d\Sigma_j \ , \tag{3.28}$$

where $d\Sigma_j$ is the surface-area element (defined, of course, using the flat auxiliary metric), and the integral is over an arbitrarily large closed surface, $\mathcal{S}$, surrounding the system. This total 4-momentum

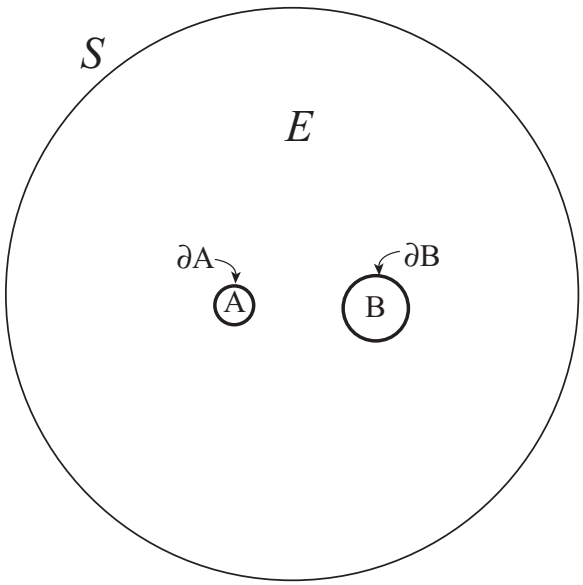

Figure 3.5: The regions of space around and inside a compact binary system

satisfies the standard conservation law

$$\frac{dp^{\mu}_{\rm tot}}{dt} = -\oint_{\mathcal{S}} \tau^{\mu j} d\Sigma_j \ . \tag{3.29}$$

The proof of this given in LL and MTW relies on an assumption that the interior of $\mathcal{S}$ be simply connected, i.e., that it not contain any black holes. As we show here, however, that assumption is not necessary. First, differentiate Eq. (3.28) with respect to t, then use $H^{\mu\alpha 0 j}{}_{,\alpha 0} = H^{\mu\alpha\nu j}{}_{,\alpha\nu} - H^{\mu\alpha k j}{}_{,\alpha k}$. The first term is $-16\pi\tau^{\mu j}$ by virtue of the the field equations (3.26) and the antisymmetry of the superpotential on its last two indices; and its surface integral gives the right side of Eq. (3.29). That same antisymmetry on the second term $-H^{\mu\alpha k j}{}_{,\alpha k}$ permits us to write it as the curl of a 3-vector field, whose surface integral vanishes by virtue of Stokes' theorem. The result is Eq. (3.29).

3.4 Four-Momentum Conservation for Fully Nonlinear Compact Binaries

We now apply this LL formalism to a binary system made of black holes and (or) neutron stars; see Fig. 3.5. We denote the binary's two bodies, and the regions of space inside them, by the letters A and B, and we label their surfaces by ∂A and ∂B. For a black hole, ∂A could be the hole's absolute event horizon or its apparent horizon, whichever one wishes. For a neutron star, ∂A will be the star's physical surface. We denote by $\mathcal{E}$ the region outside both bodies, but inside the arbitrarily large surface $\mathcal{S}$ where the system's total momentum is computed. (In later papers in this series, $\mathcal{S}$ will sometimes be the outer boundary of a numerical-relativity computational grid.)

By applying Gauss's theorem to Eq. (3.28) for the binary's total 4-momentum and using the Einstein field equations in Eq. (3.26), we obtain an expression for the binary's total 4-momentum as a sum over contributions from each of the bodies and from the gravitational field in the region $\mathcal{E}$ outside them:

$$p^\mu_{\rm tot} = p^\mu_A + p^\mu_B + p^\mu_{\rm field} \ . \tag{3.30a}$$

Here

$$p^\mu_A \equiv \frac{1}{16\pi} \oint_{\partial A} H^{\mu\alpha 0 j}{}_{,\alpha} d\Sigma_j \tag{3.30b}$$

is the 4-momentum of body A and similarly for body B, and

$$p^\mu_{\rm field} \equiv \int_{\mathcal{E}} \tau^{0\mu} d^3x \ . \tag{3.30c}$$

is the gravitational field's 4-momentum in the surrounding space. If either of the bodies has a simply connected interior (is a star rather than a black hole), then we can use Gauss's theorem and the Einstein field equations, Eq. (3.26), to convert the surface integral, Eq. (3.30b), for the body's 4-momentum into a volume integral over the body's interior:

$$p^\mu_A = \int_A \tau^{0\mu} d^3x \ . \tag{3.30d}$$

By an obvious extension of the argument we used to derive Eq. (3.29) for the rate of change of the binary's total 4-momentum, we can deduce from Eq. (3.30b) the corresponding equation for the rate of change of the 4-momentum of body A:

$$\frac{dp^\mu_A}{dt} = -\oint_{\partial A} (\tau^{\mu k} - \tau^{\mu 0} v^k_A) d\Sigma_k \ . \tag{3.31}$$

Here the second term arises from the motion of the boundary of body A with coordinate velocity $v^k_A = dx^k_{A\,\rm cm}/dt$. Equation (3.31) describes the flow of the gravitational field's 4-momentum into and out of body A. We shall use Eqs. (3.30), (3.29), and (3.31), specialized to linear momentum (index μ made spatial) as foundations for our study of momentum flow in compact binaries.

The actual values of the body's and the field's 4-momenta, computed in the above ways, will depend on the arbitrary coordinate system that we chose in which to make the auxiliary metric be diag$[-1,1,1,1]$ and in which to perform the above computations. This is the gauge dependence that we discussed above. In the remainder of this paper, we shall choose harmonic coordinates, in which the gravitational field satisfies the harmonic-gauge condition

$$\mathfrak{g}^{\alpha\beta}{}_{,\beta} = 0 \ . \tag{3.32}$$

We shall also specialize the above equations to the 1.5 post-Newtonian approximation and use them to study momentum flow during the inspiral phase of generic compact binaries. In future papers, we shall use the above equations, combined with numerical-relativity simulations, to study momentum flow during the collision, merger, and ringdown phases of compact binaries.

3.5 Post-Newtonian Momentum Flow in Generic Compact Binaries

3.5.1 Field Momentum Outside the Bodies

In general, the portion of the field momentum that is induced by the bodies' spins and that flows back and forth between the field and the bodies, as the bodies move, has the same form as that of the extreme-kick configuration at 1.5PN order,

$$\delta\tau^{0j}\boldsymbol{e}_j = -\frac{\boldsymbol{g}_A \times \boldsymbol{H}_B^{\rm spin}}{4\pi} - \frac{\boldsymbol{g}_B \times \boldsymbol{H}_A^{\rm spin}}{4\pi} \; ; \tag{3.33}$$

see Eq. (3.9). We find it convenient to rewrite the bodies' gravitoelectric and gravitomagnetic fields, Eqs. (3.10), as

$$g_K^j = m_K \left(\frac{1}{r_K}\right)_{,j} \; , \quad H_K^j = -2S_K^i \left(\frac{1}{r_K}\right)_{,ij} \; , \tag{3.34}$$

where K is A or B and where, as before, r_K is the (flat-space) distance of the field point from the center of mass of body K. Inserting Eqs. (3.34) into Eq. (3.33) and manipulating the derivatives, we obtain the following expression for the field momentum density:

$$\delta\tau^{0j} = -\frac{1}{2\pi}\epsilon_{jpl}\left[S_A^q m_B \left(\frac{1}{r_A}\right)_{,q}\left(\frac{1}{r_B}\right)_{,l}\right]_{,p} + (A \leftrightarrow B) \; . \tag{3.35}$$

Here $(A \leftrightarrow B)$ means the same expression with labels A and B interchanged. Notice that this expression for the momentum density is the curl of a vector field, or, equally well, it can be viewed as the divergence of a tensor field.

The total spin-induced, flowing field momentum is the integral of Eq. (3.35) over the exterior region $\mathcal{E}$ (see Fig. 3.5). Using Gauss's law, that volume integral can be converted into the following integral over the boundary of $\mathcal{E}$

$$\delta p^j_{\rm field} = -\frac{1}{2\pi}\epsilon_{jpl} S_A^q m_B \int_{\partial\mathcal{E}} \left(\frac{1}{r_A}\right)_{,q}\left(\frac{1}{r_B}\right)_{,l} d\Sigma_p + (A \leftrightarrow B) \; . \tag{3.36}$$

The boundary of $\mathcal{E}$ has three components: the surface $\mathcal{S}$ far from the binary on which we compute the binary's total momentum, and the surfaces ∂A and ∂B of bodies A and B. The integral over $\mathcal{S}$ vanishes because the integrand is proportional to $1/r^4$ and the surface area is proportional to r^2,

and $\mathcal{S}$ is arbitrarily far from the binary ($r \to \infty$). When integrating over the bodies' surfaces, we shall flip the direction of the vectorial surface element so it points out of the bodies (into $\mathcal{E}$), thereby picking up a minus sign and bringing Eq. (3.36) into the form

$$\delta p^j_{\rm field} = \frac{1}{2\pi}\epsilon_{jpl} S^q_A m_B \left[\int_{\partial\mathcal{A}} \left(\frac{1}{r_A}\right)_{,q} \left(\frac{1}{r_B}\right)_{,l} d\Sigma_p + \int_{\partial\mathcal{B}} \left(\frac{1}{r_A}\right)_{,q} \left(\frac{1}{r_B}\right)_{,l} d\Sigma_p\right] + (A \leftrightarrow B)\,. \quad (3.37)$$

We presume (as is required by the PN approximation) that the bodies' separation is large compared to their radii. Then on ∂A, we can write $(1/r_A)_{,q} = -n^q_A/r^2_A$ and $(1/r_B)_{,l} = n^l_{AB}/r^2_{AB}$, where n_A is the unit vector pointing away from the center of mass of body A, n^l_{AB} is the unit vector pointing from the center of mass of body B toward the center of mass of body A, and r_{AB} is the (flat-spacetime) distance between the two bodies' centers of mass. The first integral in Eq. (3.37) then becomes $n_{AB}/r^2_B \int_{\partial A} n^q_A/r^2_A d\Sigma_p$. For simplicity, we take the surface of integration to be a sphere immediately above the physical surface of body A and ignore the tiny contribution from the region between that sphere and the physical surface. On this sphere, we write $d\Sigma_p = r^2_A n^p_A d\Omega_A$, where $d\Omega_A$ is the solid-angle element, and we then carry out the angular integral using the relation $\int_{\partial A} n^q_A n^p_A d\Omega_A = (4\pi/3)\delta_{qp}$. Thereby, we obtain for the first integral in Eq. (3.37) $(4\pi/3)\delta_{qp} n_{AB}/r^2_B$ independent of the radius, r_A, of the sphere of integration. (If the body is not spherical, the contribution from the tiny volume between our spherical integration surface and the physical surface will be negligible.) Evaluating the second integral in Eq. (3.37) in the same way, and carrying out straightforward manipulations, we obtain for the external field momentum

$$\delta \boldsymbol{p}_{\rm field} = \frac{2}{3r^2_{AB}}(m_B \boldsymbol{S}_A - m_A \boldsymbol{S}_B) \times \boldsymbol{n}_{AB}\,. \quad (3.38)$$

For the extreme-kick configuration, which has $m_A = m_B = m$ and $\boldsymbol{S}_B = -\boldsymbol{S}_A$, this field momentum becomes Eq. (3.12).

3.5.2 Centers of Mass and Equation of Motion for the Binary's Compact Bodies

We restrict our discussion, temporarily, to a body that is a star rather than a black hole, and temporarily omit the subscript K that identifies which body. Then, following the standard procedure in special relativity (e.g., Box 5.6 of MTW [10]), we define the star's center-of-mass world line to be that set of events $x^\mu_{\rm cm}$ satisfying the covariant field-theory-in-flat-spacetime relationship

$$S^{\alpha\beta} p_\beta = 0\,. \quad (3.39)$$

Here $p^\beta = \int \tau^{0\beta} d^3x$ is the body's 4-momentum and

$$S^{\alpha\beta} \equiv \int [(x^\alpha - x^\alpha_{\rm cm})\tau^{\beta 0} - (x^\beta - x^\beta_{\rm cm})\tau^{\alpha 0}] d^3x \tag{3.40}$$

is the body's tensorial angular momentum. Here the integrals extend over the star's interior, and because the star's momentum is changing, we take the time component of $x^\mu_{\rm cm}$ to be the same as the time at which the integral is performed, $x^0_{\rm cm} = x^0$. (If the momentum were not changing, this restriction would be unnecessary; see Box 5.6 of MTW.)

In a reference frame where the body moves with ordinary velocity $v^j = p^j/p^0$, Eq. (3.39) says $S^{i0} = S^{ij} v_j$. We wish to rewrite this in a more illuminating form, accurate to first order in the velocity $\boldsymbol{v}$. At that accuracy, we can evaluate S^{ij} in the body's rest frame, obtaining $S^{ij} = \epsilon^{ijk} S_k$, where S_k is the body's spin angular momentum

$$S_k = \int \epsilon_{klm} (x^l - x^l_{\rm cm}) \tau^{m0} d^3x \ . \tag{3.41}$$

Using definition of S^{i0} in Eq. (3.40), with $x^0_{\rm cm} = x^0$, our definition of the center of mass in Eq. (3.39) then takes the concrete form

$$m\boldsymbol{x}_{\rm cm} = \int \boldsymbol{x} \tau^{00} d^3x - \boldsymbol{v} \times \boldsymbol{S} \ . \tag{3.42}$$

Here on the left side we have replaced $p^0 = \int \tau^{00} d^3x$ by its value in the body's rest frame, which is the mass m (the two differ by amounts quadratic in $\boldsymbol{v}$).

Notice that, when computed in the body's rest frame in which $\boldsymbol{v} = 0$, the center of mass is $m\boldsymbol{x}_{\rm cm} = \int \boldsymbol{x} \tau^{00} d^3x$, but when computed in any frame moving slowly with respect to the rest frame, this expression must be corrected by the term $-\boldsymbol{v} \times \boldsymbol{S}$ that we discussed physically in Section 3.2.2, Eq. (3.14). We asserted and used Eq. (3.42), the physical SSC, in our analysis of the extreme-kick configuration; see Eq. (3.15).

In our harmonic-coordinate system, and at the 1.5PN order of our analysis, the dominant, time–time component of the Einstein field equations, Eq. (3.26), reduces to $\eta^{\mu\nu} \mathfrak{g}^{00}{}_{,\mu\nu} = 16\pi\tau^{00}$. The type of analysis carried out in Section 19.1 of MTW [10] then reveals that in the star's rest frame, the monopolar part of its $\mathfrak{g}^{00}$ is centered on the location $\boldsymbol{x}_{\rm cm}$; or, equivalently, when one expands the star's $\mathfrak{g}^{00}$ around $\boldsymbol{x}_{\rm cm}$ in its own rest frame, there is no dipolar $1/r^2$ term (no mass-dipole moment). This well-known result (see, e.g., [20, 14]) can be used as an alternative definition of $\boldsymbol{x}_{\rm cm}$—a definition that works for black holes as well as for stars.

Using this monopolar-field-centered definition of $\boldsymbol{x}_{\rm cm}$, Thorne and Hartle [14] have employed matched asymptotic expansions (valid for black holes) to derive the equations of motion for a system of compact bodies, e.g., a compact binary; see their Eqs. (4.10) and (4.11). For a compact binary, the spin-induced contributions to these equations of motion at 1.5PN order are (Eq. (4.11c) of Thorne

and Hartle)

$$m_A \frac{d\delta \boldsymbol{v}_A}{dt} = \frac{m_A}{r_{AB}^3}\left\{6\boldsymbol{n}_{AB}\left[(\boldsymbol{S}_B\times\boldsymbol{n}_{AB})\cdot\boldsymbol{v}_{AB}\right]+4\boldsymbol{S}_B\times\boldsymbol{v}_{AB}-6(\boldsymbol{S}_B\times\boldsymbol{n}_{AB})(\boldsymbol{v}_{AB}\cdot\boldsymbol{n}_{AB})\right] + \frac{m_B}{r_{AB}^3}\left\{6\boldsymbol{n}_{AB}\left[(\boldsymbol{S}_A\times\boldsymbol{n}_{AB})\cdot\boldsymbol{v}_{AB}\right]+3\boldsymbol{S}_A\times\boldsymbol{v}_{AB}-3(\boldsymbol{S}_A\times\boldsymbol{n}_{AB})(\boldsymbol{v}_{AB}\cdot\boldsymbol{n}_{AB})\right] . \tag{3.43}$$

Here

$$\boldsymbol{v}_A \equiv \frac{d\boldsymbol{x}_{\mathrm{cm}\,A}}{dt} , \quad \delta\boldsymbol{v}_A = \frac{d\delta\boldsymbol{x}_{\mathrm{cm}\,A}}{dt} , \quad \boldsymbol{v}_{AB} = \boldsymbol{v}_A - \boldsymbol{v}_B \tag{3.44}$$

are the velocity of (the center of mass of) body A, the spin-induced perturbation of that velocity, and the relative velocity of bodies A and B. The first two lines of Eq. (3.43) are due to frame dragging by the other body (body B); the last two lines are a force due to the coupling of body A's spin to B's spacetime curvature.

3.5.3 The Momenta of the Binary's Bodies

As in the previous subsection, we initially restrict ourselves to a body that is a star; then we shall generalize to a black hole. We initially omit the star's label A or B for ease of notation.

For a star, we can derive an expression for the momentum $p^j = \int \tau^{0j} d^3x$ (with the integral over the star's interior) in terms of the star's velocity $v^j = dx^j_{\mathrm{cm}}/dt$ by differentiating the expression for the center of mass, Eq. (3.42), with respect to time. To allow for the possibility that the mass might change with time, we set $m = \int \tau^{00} d^3x$ before doing the differentiation; i.e., we differentiate

$$x^j_{\mathrm{cm}} \int_A \tau^{00} d^3x = \int_A x^j \tau^{00} d^3x - (\boldsymbol{v}\times\boldsymbol{S})^j . \tag{3.45}$$

Using $\tau^{00}{}_{,0} = -\tau^{0k}{}_{,k}$ and Gauss's theorem, we bring the left side into the form $v^j \int_A \tau_{00} d^3x - x^j_{\mathrm{cm}} \int_{\partial A} (\tau^{0j} - \tau^{00} v^j) d\Sigma_j$. The last term arises from the motion of the surface of the star through space with velocity $\boldsymbol{v}$. Manipulating the time derivative of the integral on the right side of Eq. (3.45) in this same way, we bring it into the form

$$\int_A \tau^{0j} d^3x - \int_{\partial A} x^j (\tau^{0k} - \tau^{00} v^k) d\Sigma_k = p^j - \int_{\partial A} x^j (\tau^{0k} - \tau^{00} v^k) d\Sigma_k , \tag{3.46}$$

where p^j is the star's momentum. Inserting these expressions for the left-side and the right-side integral into Eq. (3.45), noting that the star's spin angular momentum evolves (due to precession) far more slowly than its velocity, denoting the time derivative of its velocity by $d\boldsymbol{v}/dt = \boldsymbol{a}$ (acceleration), solving for p^j, and restoring subscript As, we obtain

$$p^j_A = m_A v^j_A + \int_{\partial A} (x^j - x^j_{\mathrm{cm}\,A})(\tau^{0k} - \tau^{00} v^k_A) d\Sigma_k + (\boldsymbol{a}_A \times \boldsymbol{S}_A)^j .$$

Although we have derived this equation for a star, it must be true also for a black hole. The reason is that all the quantities that appear in it are definable without any need for integrating over the body's interior, and all are expressible in terms of the binary's masses and spins and its bodies' vectorial separation, in manners that are insensitive to whether the bodies are stars or holes. To illustrate this statement, in Appendices 3.B and 3.C we deduce Eq. (3.47) for a black hole, restricting ourselves to the spin-induced portion of the momentum that is being exchanged with the field, δp_A^j.

It is this δp_A^j that interests us. Because the spin has no influence on τ^{00} at the relevant order (which is $\delta\tau^{0k} \sim gH$ and $\delta\tau^{00} \sim g^2$, where g and H are the gravitoelectric and gravitomagnetic fields), Eq. (3.47) implies that

$$\delta p_A^j = m_A \delta v_A^j + \int_{\partial A} (x^j - x^j_{\mathrm{cm}\,A}) \delta\tau^{0k} d\Sigma_k + (\boldsymbol{a}_A \times \boldsymbol{S}_A)^j \ . \tag{3.47}$$

The acceleration $\boldsymbol{a}_A$ of body A is, at the order needed, just the gravitoelectric field of body B at the location of A, $a_A = -(m_B/r_{AB}^2)\boldsymbol{n}_{AB}$. Performing the surface integral on a sphere just above the body's physical surface we can write $x^j - x^j_{\mathrm{cm}\,A} = n_A^j r_A$ and $d\Sigma_k = r_A^2 d\Omega_A$. Inserting these into Eq. (3.47), we obtain

$$\delta p_A^j = \underbrace{m_A \delta v_A^j}_{\text{kinetic term}} + \underbrace{\int_{\partial A} r_A^3 \delta\tau^{0k} n_A^j n_A^k d\Omega_A}_{\text{surface term}} + \underbrace{\frac{m_B}{r_{AB}^2}(\boldsymbol{S}_A \times \boldsymbol{n}_{AB})^j}_{\text{SSC term}} \ . \tag{3.48}$$

Here "SSC term" refers to the "spin supplementary condition" required to get the correct, physical center of mass; see text following Eq. (3.15). In the surface term, the field momentum density $\delta\tau^{0k}$ is given by Eq. (3.35). The second term ($A \leftrightarrow B$) is smaller than the first by M/r_{AB} and thus is negligible. Inserting the first term into the integral, using $(1/r_A)_{,qp} = (3n_A^q n_A^p - \delta_{qp})/r_A^3$ and $(1/r_B)_{,l} = -n_B^l/r_B^2$, and $\int n_A^j n_A^l d\Omega_A = \frac{4\pi}{3}\delta_{jl}$, we bring Eq. (3.48) into the form

$$\begin{aligned} \delta \boldsymbol{p}_A &= \underbrace{m_A \delta \boldsymbol{v}_A}_{\text{kinetic term}} \underbrace{- \frac{2}{3}\frac{m_B}{r_{AB}^2}\boldsymbol{S}_A \times \boldsymbol{n}_{AB}}_{\text{surface term}} + \underbrace{\frac{m_B}{r_{AB}^2}\boldsymbol{S}_A \times \boldsymbol{n}_{AB}}_{\text{SSC term}} \\ &= m_A \delta \boldsymbol{v}_A + \frac{1}{3}\frac{m_B}{r_{AB}^2}\boldsymbol{S}_A \times \boldsymbol{n}_{AB} \ . \end{aligned} \tag{3.49}$$

As an illustration of the power of the Maxwell-like formulation of the post-Newtonian approximation, we rederive this equation in Appendix 3.C using a straightforward surface integral of the Maxwell-like expression for the gravitational stress tensor.

3.5.4 Momentum Conservation

The total spin-induced momentum perturbation, $\delta \boldsymbol{p}_{\rm tot} = \delta \boldsymbol{p}_A + \delta \boldsymbol{p}_B + \delta \boldsymbol{p}_{\rm field}$, Eqs. (3.49) and (3.38), is

$$\delta \boldsymbol{p}_{\rm tot} = m_A \delta \boldsymbol{v}_A + m_B \delta \boldsymbol{v}_B + \frac{1}{r_{AB}^2}(m_B \boldsymbol{S}_A - m_A \boldsymbol{S}_B) \times \boldsymbol{n}_{AB} \ . \tag{3.50}$$

Momentum conservation requires that the time derivative of this $\delta \boldsymbol{p}_{\rm tot}$ vanish. The time derivative of the kinetic terms can be read off the equation of motion, Eq. (3.43):

$$m_A \frac{d\delta \boldsymbol{v}_A}{dt} + m_B \frac{d\delta \boldsymbol{v}_B}{dt} = -\frac{1}{r^3}(m_B \boldsymbol{S}_A - m_A \boldsymbol{S}_B) \times [\boldsymbol{v}_{AB} - 3(\boldsymbol{n}_{AB} \cdot \boldsymbol{v}_{AB})\boldsymbol{n}_{AB}] \ . \tag{3.51}$$

By inserting $\boldsymbol{n}_{AB} = (\boldsymbol{x}_{{\rm cm}\,A} - \boldsymbol{x}_{{\rm cm}\,B})/r_{AB}$ into the second term of Eq. (3.50) and differentiating with respect to time, we obtain the negative of Eq. (3.51). Therefore,

$$d\delta \boldsymbol{p}_{\rm tot}/dt = 0 \ ; \tag{3.52}$$

i.e., as the binary's evolution drives spin-induced momentum back and forth between the bodies and the field, the total momentum remains conserved, as it must. Interestingly, during the summation of momentum terms, one finds that the surface terms in $\delta \boldsymbol{p}_A + \delta \boldsymbol{p}_B$ have exactly cancelled the field momentum $\delta \boldsymbol{p}_{\rm field}$, leaving the total momentum as the sum of the bodies' kinetic term and their SSC term—i.e., leaving it equal to the bodies' total *canonical momentum* (see the discussion at the end of Section 3.2.3).

3.6 Conclusion

In this paper, we have explored the flow of momentum between a compact binary's bodies and their external gravitational field (spacetime curvature), at 1.5PN order, during the binary's orbital inspiral. In subsequent papers, we shall explore momentum flow in numerical-relativity simulations of a binary's collision, merger, and ringdown. We expect these studies to give useful intuitive insights into the internal dynamics of binary black holes and the nonlinear dynamics of curved spacetime.

3.A Appendix: The Total PN Momentum Density

In Section 3.2.1, Eqs. (3.9) and (3.11) show the portion of the field momentum that generates bobbing. There are, however, additional pieces of field momentum at the same PN order that do not contribute to the bobbing, and these expressions become important for comparisons of the post-Newtonian analysis with numerical-relativity results (to be presented in future papers). There are three extra sources of terms. First, the gravitomagnetic field has a part $\boldsymbol{H}^{\rm velo}$ that depends upon

the body's velocity. Using Eqs. (2.5) and (6.1) of [15], one can see that

$$\boldsymbol{H}^{\rm velo} = \frac{4m_A(\boldsymbol{n}_A \times \boldsymbol{v}_A)}{r_A^2} + (A \leftrightarrow B) \ . \tag{3.53}$$

Second, there are terms from the coupling of the gravitomagnetic field of body A with its own gravitoelectric field $\tau^{0j}\boldsymbol{e}_j = -(\boldsymbol{g}_A \times \boldsymbol{H}_A)/(4\pi)$, and similarly for body B, for both the spin and velocity pieces of $\boldsymbol{H}$. Finally, there is a part due to $(3\dot{U}_N\boldsymbol{g})/(4\pi)$, where U_N is the Newtonian potential and the dot denotes differentiation with respect to time (see Eq. (4.1) of [15]). When one accounts for these additional expressions, the full field momentum density is written most concisely as

$$\tau^{0j} = \tau^{0j}_{\rm spin} + \tau^{0j}_{\rm velo} \ , \tag{3.54a}$$

where $\tau^{0j}_{\rm spin}$ and $\tau^{0j}_{\rm velo}$ are the terms that depend upon the spins and the velocities, respectively. These terms are given by

$$\tau^{0j}_{\rm spin}\boldsymbol{e}_j = \frac{m_B}{2\pi r_A^3 r_B^2}\left[3(\boldsymbol{S}_A\cdot\boldsymbol{n}_A)(\boldsymbol{n}_A\times\boldsymbol{n}_B) - (\boldsymbol{S}_A\times\boldsymbol{n}_B)\right] - \frac{1}{2\pi}\frac{m_A}{r_A^5}(\boldsymbol{S}_A\times\boldsymbol{n}_A) + (A\leftrightarrow B) \ , \tag{3.54b}$$

and

$$\begin{aligned}\tau^{j0}_{\rm velo}\boldsymbol{e}_j \quad = \quad & \frac{m_A}{4\pi r_A^2}\left\{\frac{m_B[4(\boldsymbol{n}_B\cdot\boldsymbol{v}_A)\boldsymbol{n}_A - 4(\boldsymbol{n}_A\cdot\boldsymbol{n}_B)\boldsymbol{v}_A]}{r_B^2} - \frac{3m_B(\boldsymbol{n}_A\cdot\boldsymbol{v}_A)\boldsymbol{n}_B}{r_B^2}\right. \\ & \left. + \frac{m_A[(\boldsymbol{n}_A\cdot\boldsymbol{v}_A)\boldsymbol{n}_A - 4\boldsymbol{v}_A]}{r_A^2}\right\} + (A\leftrightarrow B) \ .\end{aligned} \tag{3.54c}$$

In the body of this paper, we have confined attention to the first group of terms in Eq. (3.54b) and the terms with $(A \leftrightarrow B)$; they are the part of the field momentum that gets exchanged with the bodies during bobbing.

3.B Appendix: Momentum of a Black Hole Computed via a Surface Integral of Superpotential

In the text, we derived Eq. (3.47) for the momentum of a body in a binary assuming the body was a star, so that we could perform volume integrals. We then asserted that this expression is also valid for black holes. The spin-induced portion of this expression that gets exchanged with the field as the body moves is given by Eq. (3.47), which reduces to Eq. (3.49). In this appendix, we shall sketch a derivation of Eq. (3.49) directly from the surface-integral definition, Eq. (3.30b), of a black hole's momentum,

$$\delta p_A^j = \frac{1}{16\pi}\int_{\partial A} \delta H^{j\alpha 0k}{}_{,\alpha} d\Sigma_k \ . \tag{3.55}$$

Evaluating this surface integral up to the desired 1.5PN-order accuracy turns out to require some 2.5PN-order fields. Qualitatively, this can be anticipated, because the superpotential we use in the surface integral is sourced by the spin-orbit piece of field momentum and, therefore, is necessarily a non-leading PN term. One can see this more clearly by expanding $\delta H^{j\alpha 0k}{}_{,\alpha}$ in terms of the metric density and using the symmetries of the superpotential H (which are the same as the Riemann tensor). In general, the momentum is given by

$$\delta p_A^j = -\frac{1}{16\pi}\int_{\partial A}(\mathfrak{g}^{jk}\mathfrak{g}^{\alpha 0} - \mathfrak{g}^{j\alpha}\mathfrak{g}^{0k})_{,\alpha} d\Sigma_k \ . \tag{3.56}$$

In harmonic gauge, however, $\mathfrak{g}^{\alpha\beta}{}_{,\beta} = 0$, and the spatial metric is flat until 2PN order, while the time-space components are of 1.5PN order. As a result, the terms at lowest and next-to-lowest PN order are contained within two terms,

$$\delta p_A^j = \frac{1}{16\pi}\int_{\partial A}(\mathfrak{g}^{j0}{}_{,k} + \mathfrak{g}^{jk}{}_{,0}) d\Sigma_k \ . \tag{3.57}$$

In this expression, the momentum arises from linear terms involving the metric density, instead of quadratic ones. As a result, one must keep pieces of the metric perturbation that are of higher PN accuracy. (If we evaluate the time derivative of $\delta \boldsymbol{p}_A$ using the surface integral in Eq. (3.31), we do not face such a delicacy; the integrand there is quadratic and requires only 1.5PN fields for its evaluation; see Appendix 3.C.)

To find the momentum in terms of the standard post-Newtonian potentials, we use a standard way that the metric perturbations are written in recent post-Newtonian literature (e.g., by Blanchet, Faye, and Ponsot [21]):

$$g_{00} = -1 + 2V - 2V^2 + 8\hat{X} \ , \tag{3.58a}$$

$$g_{i0} = -4V_i - 8\hat{R}_i \ , \tag{3.58b}$$

$$g_{ij} = \delta_{ij}(1 + 2V + 2V^2) + 4\hat{W}_{ij} \ , \tag{3.58c}$$

$$\sqrt{-g} = 1 + 2V + 4V^2 + 2\hat{W}_{kk} \ . \tag{3.58d}$$

For spinning systems, we adopt the notation of Tagoshi, Ohashi, and Owen [22], where $\mathcal{O}(m,n)$ means to order c^{-m} for non-spinning terms and χc^{-n} for terms involving a single spin χ. (Here $\chi = |\boldsymbol{S}|/m^2$ is the body's dimensionless spin.) In this notation, the terms we need for our calculation are of the order $\mathcal{O}(3,6)$, while the above post-Newtonian potentials have been obtained up to the following orders [22, 23]:

$$V = \mathcal{O}(2,5) \ , \quad V_j = \mathcal{O}(3,4) \ , \quad \hat{W}_{jk} = \mathcal{O}(4,5) \ , \quad \hat{R}_j = \mathcal{O}(5,6) \ . \tag{3.59}$$

In terms of these post-Newtonian potentials, V, V_i, $\hat{R}_i$, $\hat{X}$, and $\hat{W}_{ij}$, the perturbed metric density is

$$\mathfrak{g}^{00} = -1 - 4V - 2\left(\hat{W}_{kk} + 4V^2\right) + \mathcal{O}(6,7)\,, \tag{3.60a}$$

$$\mathfrak{g}^{0i} = -4V_i - 8\left(\hat{R}_i + VV_i\right) + \mathcal{O}(6,7)\,, \tag{3.60b}$$

$$\mathfrak{g}^{ij} = \delta_{ij} - 4\left(\hat{W}_{ij} - \frac{1}{2}\delta_{ij}\hat{W}_{kk}\right) + \mathcal{O}(6,7)\,. \tag{3.60c}$$

As a consequence, Eq. (3.57) is given by

$$\delta p_A^j = \frac{1}{16\pi}\int_{\partial A}\left\{\left[-4V_j - 8\left(\hat{R}_{j(S)} + V_{(M)}V_{j(S)}\right)\right]_{,k} - 4\left[\hat{W}_{jk(S)} - \frac{1}{2}\delta_{jk}\hat{W}_{ii(S)}\right]_{,0}\right\} d\Sigma_k\,, \tag{3.61}$$

where a subscript (S) means keep only the parts of those potentials proportional to the spins of the bodies, and a subscript (M) involves pieces of the potential without spins (proportional to the masses of the bodies). Terms without a subscript have both pieces.

Tagoshi, Ohashi, and Owen express the potentials $V_{(M)}$, V_j, $\hat{R}_{j(S)}$, and $\hat{W}_{jk(S)}$ in terms of the bodies' masses, vectorial velocities, vectorial spins, and vectorial separations, and distance to the field-point location; see their Eqs. (A1a), (A1d), (A1f), and (A1g). While the full equations are quite lengthy, the portions that generate momentum flow—those involving the coupling of the mass of one body to the spin of the other—are somewhat simpler. For convenience, we give these portions of the equations below, rewritten in our notation, with the typos noted by G. Faye et al. [23] corrected.

$$V_{(M)} = \frac{m_A}{r_A} + (A \leftrightarrow B)\,, \tag{3.62a}$$

$$V_j = \frac{m_A v_A^j}{r_A} + \epsilon_{jkl}S_A^k\left\{n_A^l\left[-\frac{3m_B}{2r_A^2 r_{AB}} - \frac{m_B(\boldsymbol{n}_A\cdot\boldsymbol{n}_{AB})}{4r_A r_{AB}^2}\right] + n_{AB}^l\frac{3m_B}{4r_A r_{AB}}\right\} + (A \leftrightarrow B)\,, \tag{3.62b}$$

$$\hat{W}_{jk(S)} = \left[\frac{1}{2}\left(\epsilon_{ijl}S_A^l v_A^k + \epsilon_{ikl}S_A^l v_A^j\right) - \delta_{jk}\epsilon_{ilm}v_A^l S_A^m\right]\frac{n_A^i}{r_A^2} + (A \leftrightarrow B)\,, \tag{3.62c}$$

$$\begin{aligned}\hat{R}_{j(S)} = {} & n_A^j\epsilon_{ikl}S_A^l\left[n_A^i(n_{AB}^k + n_B^k)\left(\frac{m_B}{r_A s^2} + \frac{2m_B}{s^3}\right) - 2n_{AB}^i n_B^k\frac{m_B}{s^3}\right] \\ & + n_{AB}^j\epsilon_{ikl}S_A^l\left[-2n_A^i n_b^k\frac{m_B}{s^3} + (n_A^i + n_B^i)n_{AB}^k\left(-\frac{m_B}{r_{AB}s^2} - \frac{2m_B}{s^3}\right)\right] \\ & + \epsilon_{jkl}S_A^k\left[n_A^l\left(-\frac{m_B}{2r_A^2 r_{AB}} + \frac{m_B}{r_{AB}s^2}\right) + n_{AB}^l\left(-\frac{m_B}{2r_A r_{AB}^2} + \frac{m_B}{2r_{AB}^2 r_B} + \frac{m_B}{r_A s^2}\right)\right. \\ & \left. + n_B^l\left(\frac{m_B}{r_A s^2} + \frac{m_B}{r_{AB}s^2}\right)\right] + (A \leftrightarrow B)\,.\end{aligned} \tag{3.62d}$$

Here, as before, m_A, $\boldsymbol{v}_A$, and $\boldsymbol{S}_A$ are the mass, velocity, and spin angular-momentum of object A; r_A is the separation of body A from a point in space, and r_{AB} is the separation of the two objects; and $\boldsymbol{n}_A$ and $\boldsymbol{n}_{AB}$ are unit vectors pointing along r_A and r_{AB}, respectively. A new quantity, $s = r_A + r_B + r_{AB}$, has been introduced, in addition. Inserting these expressions into Eq. (3.61)

gives us $\delta H^{j\alpha 0k}{}_{,\alpha}$, and the momentum of body A is then found by performing a surface integral over A's surface. The surface integrals are computed under the same assumptions as in Section 3.5.1: namely, the separation of the bodies is much larger than their radii, and each surface of integration is a sphere immediately above a body's surface. When they are computed, one finds the same result as Eq. (3.49),

$$\delta \boldsymbol{p}_A = m_A \delta \boldsymbol{v}_A + \frac{1}{3}\frac{m_B}{r_{AB}^2}\boldsymbol{S}_A \times \boldsymbol{n}_{AB} \ . \tag{3.63}$$

By tracing backward the logic from Eq. (3.49) to Eq. (3.47), we obtain the spin-dependent part of Eq. (3.47), without any recourse anywhere to (invalid) integrals over the hole's interior—as was claimed in the text. One can find the momentum for body B by exchanging A and B in Eq. (3.63).

As a consistency check, we can evaluate the system's total momentum by doing a surface integral at infinity:

$$\delta p^j_{\rm tot} = \frac{1}{16\pi}\oint_{\mathcal{S}} \delta H^{j\alpha 0k}{}_{,\alpha} d\Sigma_k \ . \tag{3.64}$$

The quantity $\delta H^{j\alpha 0k}{}_{,\alpha}$ is exactly the same as above, from which one can find

$$\delta p^j_{\rm tot} = m_A \delta v^j_A + \frac{m_B \left(\boldsymbol{S}_A \times \boldsymbol{n}_{AB}\right)^j}{r_{AB}^2} + (A \leftrightarrow B) \ . \tag{3.65}$$

This, combined with the fact that

$$\delta \boldsymbol{p}_{\rm tot} = \delta \boldsymbol{p}_A + \delta \boldsymbol{p}_B + \delta \boldsymbol{p}_{\rm field} \ , \tag{3.66}$$

as well as Eq. (3.63), gives

$$\delta p^j_{\rm field} = \frac{2m_B \left(\boldsymbol{S}_A \times \boldsymbol{n}_{AB}\right)^j}{3r_{AB}^2} + (A \leftrightarrow B) \ , \tag{3.67}$$

as found in Section 3.5.1.

3.C Appendix: Momentum of a Black Hole Computed via a Surface Integral of the Gravitational Stress Tensor

As an illustration of the power of the Maxwell-like formulation of post-Newtonian theory, in this appendix, we shall compute the spin-induced contribution $\delta \boldsymbol{p}_A$ to the momentum of black hole A using an integral of the Maxwell-like stress tensor. This is a far more straightforward approach than the superpotential surface integral of Appendix 3.B.

Our starting point is Eq. (3.31) specialized to the spin-induced part of the body's linear momentum:

$$\frac{d\delta p^i_A}{dt} = -\oint_{\partial A} (\delta \tau^{ij} - \delta \tau^{0i} v^j_A) d^2 S_j \ . \tag{3.68}$$

Here the gravitational stress tensor τ^{ij} and momentum density τ^{0i} have the standard Maxwell-like forms when expressed in terms of the gravitoelectric field $\boldsymbol{g}$ and gravitomagnetic field $\boldsymbol{H}$

$$\tau^{ij} = \frac{1}{4\pi}\left(g_i g_j - \frac{1}{2}\delta_{ij} g_k g_k\right) + \frac{1}{16\pi}\left(H_i H_j - \tfrac{1}{2}\delta_{ij} H_k H_k\right) , \tag{3.69a}$$

$$\tau^{0j}\boldsymbol{e}_j = -\frac{1}{4\pi}\boldsymbol{g}\times\boldsymbol{H} \tag{3.69b}$$

(Eqs. (4.1) of [15]), and $\delta\tau^{ij}$ and $\delta\tau^{0j}$ are the portions that are linear in the bodies' spins. In Eqs. (3.69) we have dropped two terms that involve the time derivative of the Newtonian gravitational potential because (at the post-Newtonian order to which we are working) they are independent of the bodies' spins.

We shall evaluate the momentum-density integral, the second term of Eq. (3.68), first, and then the stress-tensor integral. For our black-hole binary, the spin-induced part of the momentum density in Eq. (3.69b) is Eq. (3.11), which we rewrite in index notation as

$$\delta\tau^{0j} = \frac{m_A}{2\pi r_A^2 r_B^3}\left[3\epsilon_{jlq} n_B^l n_A^q \left(S_B^k n_B^k\right) - \epsilon_{jlq} S_B^l n_A^q\right] + (A\leftrightarrow B) . \tag{3.70}$$

By (i) inserting this into Eq. (3.68), (ii) taking the holes' separation r_{AB} to be large compared to the radius r_A of the surface ∂A of hole A where the integral is performed, (iii) expanding r_B and $\boldsymbol{n}_B = \boldsymbol{x}_B/r_B$ (evaluated on the surface of hole A) in powers of r_A/r_{AB}, (iv) keeping only the terms in the expansion that give the leading-order nonzero contribution to the integral, and (v) performing the integral, we obtain

$$\begin{aligned}\boldsymbol{e}_i \oint_{\partial A} \delta\tau^{0i} v_A^j d^2 S_j = {} & \frac{2m_B}{15 r_{AB}^3}\left[-5\left(\boldsymbol{S}_A\times\boldsymbol{v}_A\right) + 6\left(\boldsymbol{S}_A\times\boldsymbol{n}_{AB}\right)\left(\boldsymbol{n}_{AB}\cdot\boldsymbol{v}_A\right)\right. \\ & \left. -9\left(\boldsymbol{v}_A\times\boldsymbol{n}_{AB}\right)\left(\boldsymbol{S}_A\cdot\boldsymbol{n}_{AB}\right)\right] \\ & -\frac{2m_A}{3 r_{AB}^3}\left[\left(\boldsymbol{S}_B\times\boldsymbol{v}_A\right) + 3\left(\boldsymbol{v}_A\times\boldsymbol{n}_{AB}\right)\left(\boldsymbol{S}_B\cdot\boldsymbol{n}_{AB}\right)\right] .\end{aligned} \tag{3.71}$$

For the stress-tensor term in Eq. (3.68), the gravitoelectric and gravitomagnetic fields to the accuracies needed are

$$\begin{aligned} g^i = {} & -\frac{m_A n_A^i}{r_A^2} + \frac{2\epsilon_{klq} v_A^k S_A^l \left(\delta^{iq} - 3 n_A^i n_A^q\right)}{r_A^3} + \frac{2\epsilon_{ikl} S_A^k \left[3\left(n_A^q v_A^q\right) n_A^k - v_A^k\right]}{r_A^3} \\ & + (A\leftrightarrow B) , \end{aligned} \tag{3.72a}$$

$$H^i = \frac{4 m_A \epsilon_{ikl} v_A^l n_A^k}{r_A^2} + \frac{2 S_A^i - 6\left(S_A^k n_A^k\right) n_A^i}{r_A^3} + (A\leftrightarrow B) \tag{3.72b}$$

(Eqs. (6.1) and (2.5) of [15]). The first term in Eq. (3.72a) is the Newtonian gravitational acceleration; the other two terms are the spin-induced post-Newtonian contributions. The two terms in Eq. (3.72b) are the gravitomagnetic fields produced by the linear momentum of body A and by

its spin. By inserting these into the Maxwell-like expression, Eq. (3.69a), for the stress tensor and keeping the leading-order terms that are linear in the spins, then inserting into the first term of Eq. (3.68) and performing the surface integral in the same manner, using steps (i) through (v), as for the momentum density term, we obtain (straightforwardly, but tediously)

$$\begin{aligned}
-\boldsymbol{e}_i \oint_{\partial A} \delta\tau^{ij} d^2 S_j \;\; = \;\; & -\frac{2m_A}{3r_{AB}^3}\left\{6\left(\boldsymbol{S}_B\times\boldsymbol{v}_B\right)-9\left(\boldsymbol{S}_B\times\boldsymbol{n}_{AB}\right)\left(\boldsymbol{v}_B\cdot\boldsymbol{n}_{AB}\right)\right. \\
& \left.+9\left[\boldsymbol{v}_B\cdot\left(\boldsymbol{S}_B\times\boldsymbol{n}_{AB}\right)\right]\boldsymbol{n}_{AB}+2\left(\boldsymbol{S}_B\times\boldsymbol{v}_A\right)+6\left(\boldsymbol{v}_A\times\boldsymbol{n}_{AB}\right)\left(\boldsymbol{S}_B\cdot\boldsymbol{n}_{AB}\right)\right\} \\
& +\frac{2m_B}{15r_{AB}^3}\left\{21\left(\boldsymbol{S}_A\times\boldsymbol{v}_A\right)-27\left(\boldsymbol{S}_A\times\boldsymbol{n}_{AB}\right)\left(\boldsymbol{v}_A\cdot\boldsymbol{n}_{AB}\right)\right. \\
& +\left[\left(36\boldsymbol{v}_A-15\boldsymbol{v}_B\right)\cdot\left(\boldsymbol{S}_A\times\boldsymbol{n}_{AB}\right)\right]\boldsymbol{n}_{AB} \\
& \left.+5\left(\boldsymbol{S}_A\times\boldsymbol{v}_B\right)+30\left(\boldsymbol{v}_B\times\boldsymbol{n}_{AB}\right)\left(\boldsymbol{S}_A\cdot\boldsymbol{n}_{AB}\right)\right\} \; . \qquad (3.73)
\end{aligned}$$

By adding Eqs. (3.71) and (3.73) to obtain Eq. (3.68) and then using the vector identity

$$\left(\boldsymbol{v}\times\boldsymbol{n}\right)\left(\boldsymbol{S}\cdot\boldsymbol{n}\right)=-\left[\boldsymbol{v}\cdot\left(\boldsymbol{S}\times\boldsymbol{n}\right)\right]\boldsymbol{n}+\left(\boldsymbol{S}\times\boldsymbol{n}\right)\left(\boldsymbol{v}\cdot\boldsymbol{n}\right)-\boldsymbol{S}\times\boldsymbol{v} \qquad (3.74)$$

to eliminate all terms of the form $\left(\boldsymbol{v}\times\boldsymbol{n}\right)\left(\boldsymbol{S}\cdot\boldsymbol{n}\right)$, and setting $\boldsymbol{v}_A-\boldsymbol{v}_B=\boldsymbol{v}_{AB}$, we obtain the following expression for the rate of change of the momentum of body A:

$$\begin{aligned}
\frac{d\delta\boldsymbol{p}_A}{dt} \;\; = \;\; & \frac{m_B}{r_{AB}^3}\left\{\frac{10}{3}\boldsymbol{S}_A\times\boldsymbol{v}_{AB}-4\left(\boldsymbol{S}_A\times\boldsymbol{n}_{AB}\right)\left(\boldsymbol{v}_{AB}\cdot\boldsymbol{n}_{AB}\right)+6\left[\boldsymbol{v}_{AB}\cdot\left(\boldsymbol{S}_A\times\boldsymbol{n}_{AB}\right)\right]\boldsymbol{n}_{AB}\right\} \\
& +\frac{m_A}{r_{AB}^3}\left\{4\boldsymbol{S}_B\times\boldsymbol{v}_{AB}-6\left(\boldsymbol{S}_B\times\boldsymbol{n}_{AB}\right)\left(\boldsymbol{v}_{AB}\cdot\boldsymbol{n}_{AB}\right)+6\left[\boldsymbol{v}_{AB}\cdot\left(\boldsymbol{S}_B\times\boldsymbol{n}_{AB}\right)\right]\boldsymbol{n}_{AB}\right\} \; . \qquad (3.75)
\end{aligned}$$

By combining with the equation of motion for body A, Eq. (3.43), we obtain

$$\frac{d\delta\boldsymbol{p}_A}{dt}=m_A\frac{d\delta\boldsymbol{v}_A}{dt}+\frac{m_B}{r_{AB}^3}\left\{\frac{1}{3}\boldsymbol{S}_A\times\boldsymbol{v}_{AB}-\left(\boldsymbol{S}_A\times\boldsymbol{n}_{AB}\right)\left(\boldsymbol{v}_{AB}\cdot\boldsymbol{n}_{AB}\right)\right\} \; . \qquad (3.76)$$

By integrating this in time, we obtain the text's final expression for the momentum of black hole A, the second line of Eq. (3.49). And by tracing backward the logic from Eq. (3.49) to Eq. (3.47), we obtain the spin-dependent part of Eq. (3.47), without any recourse anywhere to (invalid) integrals over the hole's interior—as was claimed in the text and shown by a higher-PN argument in Appendix 3.B.

Bibliography

[1] F. Pretorius, Phys. Rev. Lett. **95**, 121101 (2005).

[2] A. Ashtekar and B. Krishnan, Living Rev. Relativity **7**, 10 (2008).

[3] L. B. Szabados, Living Rev. Relativity **7**, 4 (2004).

[4] C. M. Chen, J. M. Nester, and R. S. Tung, Phys. Rev. D **72**, 104020 (2005).

[5] M. Campanelli, C. O. Lousto, Y. Zlochower, and D. Merritt, Astrophys. J. Lett. **659**, L5 (2007).

[6] M. Campanelli, C. O. Lousto, Y. Zlochower, and D. Merritt, Phys. Rev. Lett. **98**, 231102 (2007).

[7] J. A. Gonzalez, U. Sperhake, B. Brügmann, M. Hannam, and S. Husa, Phys. Rev. Lett. **98**, 091101 (2007).

[8] J. Healy et al., Phys. Rev. Lett. **102**, 041101 (2009).

[9] L. D. Landau and E. M. Lifshitz, *Classical Theory of Fields* (Addison Wesley, Redding Mass., 1962), Sec. 100.

[10] C. W. Misner, K. S. Thorne, and J. A. Wheeler, *Gravitation* (W. H. Freeman, New York, 1973).

[11] S. V. Babak and L. P. Grishchuk, Phys. Rev. D **61**, 024038 (1999).

[12] F. Pretorius, in *Physics of Relativistic Objects in Compact Binaries: From Birth to Coalescence*, edited by M. Colpi et al. (Springer, Netherlands, 2009).

[13] A. H. Shapiro, *Vorticity*, a film in a series produced by the National Committee on Fluid Mechanics (1961). Available for streaming at `http://web.mit.edu/hml/ncfmf.html`; segment 4 minutes 26 seconds into Part II.

[14] K. S. Thorne and J. B. Hartle, Phys. Rev. D **31**, 1815 (1985).

[15] J. D. Kaplan, D. A. Nichols, and K. S. Thorne, Phys. Rev. D **82**, 124014 (2009).

[16] M. E. Pati and C. M. Will, Phys. Rev. D **62**, 124015 (2000).

[17] R. D. Blandford and K. S. Thorne, *Applications of Classical Physics* (textbook nearing completion) `http://www.pma.caltech.edu/Courses/ph136/yr2008`.

[18] L. E. Kidder, Phys. Rev. D **52**, 821 (1995).

[19] T. Damour, P. Jaranowski, and G. Schäfer, Phys. Rev. D **77**, 064032 (2008).

[20] K. S. Thorne, Rev. Mod. Phys **52**, 299 (1980).

[21] L. Blanchet, G. Faye, and B. Ponsot, Phys. Rev. D **58**, 124002 (1998).

[22] H. Tagoshi, A. Ohashi, and B. J. Owen, Phys. Rev. D **63**, 044006 (2001).

[23] G. Faye, L. Blanchet, and A. Buonanno, Phys. Rev. D **74**, 104033 (2006).

Chapter 4

Momentum Flow in Black-Hole Binaries: II. Numerical Simulations of Equal-Mass, Head-on Mergers with Antiparallel Spins

Research on extracting science from binary-black-hole (BBH) simulations has often adopted a "scattering matrix" perspective: given the binary's initial parameters, what are the final hole's parameters and the emitted gravitational waveform? In contrast, we are using BBH simulations to explore the nonlinear dynamics of curved spacetime. Focusing on the head-on plunge, merger, and ringdown of a BBH with transverse, antiparallel spins, we explore numerically the momentum flow between the holes and the surrounding spacetime. We use the Landau-Lifshitz field-theory-in-flat-spacetime formulation of general relativity to define and compute the density of field energy and field momentum outside horizons and the energy and momentum contained within horizons, and we define the effective velocity of each apparent and event horizon as the ratio of its enclosed momentum to its enclosed mass-energy. We find surprisingly good agreement between the horizons' effective and coordinate velocities. During the plunge, the holes experience a frame-dragging-induced acceleration orthogonal to the plane of their spins and their infall ("downward"), and they reach downward speeds of order 1000 km/s. When the common apparent horizon forms (and when the event horizons merge and their merged neck expands), the horizon swallows upward field momentum that resided between the holes, causing the merged hole to accelerate in the opposite ("upward") direction. As the merged hole and the field energy and momentum settle down, a pulse of gravitational waves is emitted, and the merged hole has a final effective velocity of about 20 km/s upward, which agrees with the recoil velocity obtained by measuring the linear momentum carried to infinity by the emitted gravitational radiation. To investigate the

gauge dependence of our results, we compare generalized-harmonic and BSSN-moving-puncture evolutions of physically similar initial data; although the generalized-harmonic and BSSN-moving-puncture simulations use different gauge conditions, we find remarkably good agreement between our results in these two cases. We also compare our simulations with the post-Newtonian trajectories and near-field energy-momentum.

Originally published as G. Lovelace, Y. Chen, M. Cohen, J. D. Kaplan, D. Keppel, K. D. Matthews, D. A. Nichols, M. A. Scheel, and U. Sperhake, Phys. Rev. D **82** 064031 (2010).

4.1 Introduction

4.1.1 Motivation

Following Pretorius's 2005 breakthrough [1], several research groups have developed codes to solve Einstein's equations numerically for the inspiral, merger, and ringdown of colliding binary black holes (BBHs). Most simulations of BBH mergers to date use the moving-puncture method [2, 3], but BBH mergers have also been successfully simulated by spectral methods [4].

A major goal of current research is to successfully extract the physical content of these simulations. Typically, efforts toward this goal adopt a "scattering matrix" approach. Information obtained from numerical simulations on a finite set of islands in the seven-dimensional[1] parameter space is being extrapolated, by various research groups, to design complicated functions that give the final parameters of the merged hole and the emitted gravitational waveforms as functions of the binary's initial parameters.

In this paper, however, we take a different perspective: we focus our attention on the nonlinear dynamics of curved spacetime during the holes' merger and ringdown. Following [5] (paper I in this series), our goal is to develop physical insight into the behavior of highly dynamical spacetimes, such as the strong-field region near the black-hole horizons in a merging binary. As in Paper I, we focus this study on the distribution and flow of linear momentum in BBH spacetimes. In contrast to Paper I's description of the pre-merger motion of the holes in the post-Newtonian approximation, in this paper, we study the momentum flow during the plunge, merger, and ringdown of merging black holes in fully relativistic simulations.

4.1.2 Linear Momentum Flow in Binary Black Holes and Gauge Dependence

Typically, numerical simulations calculate only the total linear momentum of a BBH system and ignore the (gauge-dependent) linear momenta of the individual black holes. However, linear mo-

[1] One parameter for the mass ratio and six for the individual spins; additional parameters might arise from eccentric orbits and the apparent dependence, in some configurations, of the recoil on the initial phase of the binary.

mentum has been considered by Krishnan, Lousto, and Zlochower [6]. Inspired by the usefulness of quasilocal angular momentum (see, e.g., [7] for a review) as a tool for measuring the spin of an individual black hole, Krishnan and colleagues proposed an analogous (but gauge-dependent) formula for the quasilocal linear momentum, and they calculate this quasilocal linear momentum for, e.g., the highly-spinning, unequal-mass BBH simulations in [8]. This quasilocal linear momentum is also used to define an orbital angular momentum in [9].

In this paper, we adopt a different, complementary method for measuring the holes' linear momenta: for the first time, we apply the Landau-Lifshitz momentum-flow formalism (described in Paper I and summarized in Section 4.2) to numerical simulations of merging black holes. In this formalism, a mapping between the curved spacetime and an auxiliary flat spacetime (AFS) is chosen, and general relativity is reinterpreted as a field theory defined on this flat spacetime. The AFS has a set of translational Killing vectors, which we use to define a localized, conserved linear momentum. In particular, we calculate (i) a momentum density, (ii) the momentum enclosed by horizons, and (iii) the momentum enclosed by distant coordinate spheres. In the asymptotically flat region around a source, there is a preferred way to choose the mapping between the curved spacetime and the AFS; consequently, in this limit item (iii) is gauge-invariant. In general, though, the choice of mapping is arbitrary, and it follows that items (i) and (ii) are necessarily gauge-dependent.

By examining the linear momentum flow in a dynamical spacetime—and living with the inevitable gauge dependence—we hope to develop strong intuition into the behavior of BBHs. As discussed in Section I C of Paper I, we envision different numerical-relativity groups choosing "preferred" gauges based on the coordinates of their numerical simulations. While there is no reason, *a priori*, why simulations in different gauges should agree, one of our hopes from Paper I is realized for the cases we consider: namely, in this paper, we calculate the horizon-enclosed momentum using generalized-harmonic and BSSN-moving-puncture evolutions of similar initial data, and we do find surprisingly good agreement between the two (see Figs. 4.7 and 4.14), even though the simulations use manifestly different gauge conditions (Eqs. (4.14) for the generalized-harmonic simulations and Eqs. (4.53)–(4.54) for the BSSN-moving-puncture simulations). These are two of the most commonly used gauge conditions in numerical relativity.

Therefore, we continue to hope that in general—for the gauges commonly used in numerical simulations—the momentum distributions for evolutions of physically similar initial data will turn out to be at least qualitatively similar. If further investigation reveals this to be the case, then different research groups can simply use the coordinates used in the their simulations as the "preferred coordinates" for constructing the mapping to the AFS. Otherwise, we would advocate (as in Section I C of Paper I) that different numerical-relativity groups construct the mapping to the AFS by first agreeing on a choice of preferred coordinates (e.g., a particular harmonic gauge) and then transforming the results of their simulations to those coordinates.

4.1.3 Binary-Black-Hole Mergers with Kicks

An important application of this approach is exploring the momentum flow in BBH mergers with gravitational recoil, or black-hole kicks. Kicks arising from a BBH coalescence can have direct observational signatures [10, 11, 12] and can have influence on the structure of galaxies [13, 14, 15], the reionization history of the Universe [16], and the assembly of supermassive black holes [17, 18, 19, 20, 21]. For a long time, estimates of the recoil magnitude were based on approximations [22, 23, 24, 25]; accurate calculations of fully nonlinear general relativity have only become possible after the breakthroughs in the field of numerical relativity [1, 2, 3].

Several groups have used numerical simulations to study the kick resulting from the merger of non-spinning and spinning binaries (see, e.g., [26, 27, 28, 29, 30, 31]). Remarkably, recoil velocities of several thousand km/s have been found for quasicircular binaries with equal and opposite spins in the orbital plane [30, 32, 33] (the extreme-kick, or superkick, configuration), and velocities of order 10^4 km/s have been produced from similar binaries in hyperbolic orbits [34]. Given the potential astrophysical repercussions of such large recoil velocities, the community is now using various approaches to obtain a better understanding of the kick as a function of the initial BBH parameters [35, 36, 37, 38, 39, 40] and making phenomenological fitting formulas; see [41, 9, 38, 42, 43, 8], and references therein.

On the other hand, our understanding of the local dynamics in these extraordinarily violent events is still rather limited. Some insight into the origin of the holes' kick velocity has been obtained by examining the individual multipole moments of the emitted gravitational waves [44, 45] and by approximating the recoil analytically using post-Newtonian [24, 46], effective-one-body [25], and black-hole-perturbation theory [47]. Pretorius presented an intuitive picture which describes aspects of the extreme-kick configuration in terms of the frame-dragging effect (see Fig. 5 of [48]). Recently, Rezzolla, Macedo, and Jaramillo explained the deceleration of the common horizon in a recoiling BBH merger in terms of the anisotropic distribution of the common horizon's curvature [49].

Investigating the momentum distribution and flow in recoiling BBH mergers could help to build further intuition into the nonlinear dynamics of the spacetime and their influence on the formation of kicks. Paper I explored the former issue, but it could not address the latter. Specifically, Paper I examined the distribution and the flow of linear momentum in BBH spacetimes using the Landau-Lifshitz formalism in the post-Newtonian approximation; it then specialized this approach to the extreme-kick configuration. During inspiral, the two black holes bob simultaneously and sinusoidally along the axis defined by the orbital angular momentum. Paper I explained the bobbing as arising from the exchange of momentum between the near-zone gravitational field and the black holes; it also gave a detailed description of the black holes' momenta in terms of frame drag-

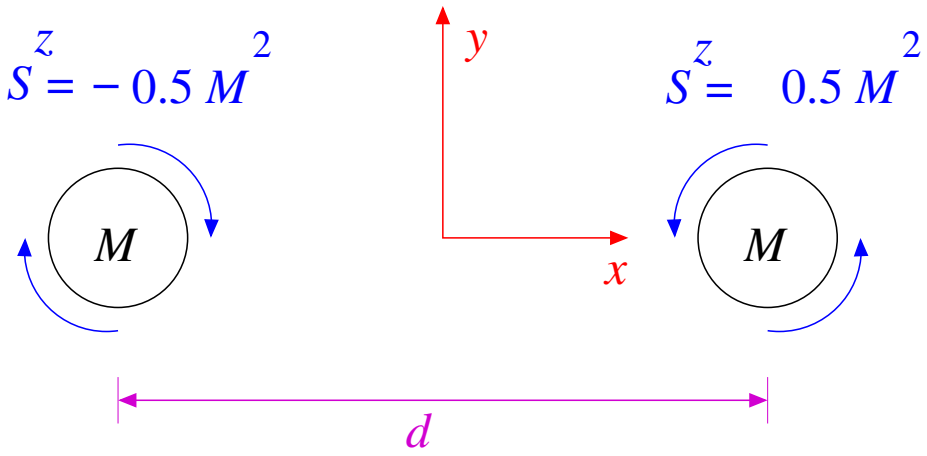

Figure 4.1: Initial configuration of the head-on BBH considered in this chapter. The holes move primarily along the x axis, but they also accelerate in the $-y$ (downward) direction because of frame dragging. See Table 4.1 for the value of $d = 2x_0$.

ging, spin-curvature coupling, asymmetric energy flux through the horizons, and the physical spin supplementary condition.

Because Paper I analyzed the system using the post-Newtonian approximation, its analysis could not be extended to and after merger. Consequently, it was not possible to address how the nonlinear dynamics in the near zone prior to the merger develops into the final behavior of the merged black hole. This paper (Paper II) uses full numerical-relativity simulations of BBHs to understand how the momentum flow behaves during the plunge, merger, and ringdown of BBHs.

4.1.4 Overview and Summary

As a first investigation of the momentum flow in numerical-relativity simulations of BBHs, in this paper, we apply the Landau-Lifshitz momentum-flow formalism to a head-on plunge, merger, and ringdown of an equal-mass binary. The holes initially have antiparallel spins of equal magnitude that are transverse to the holes' head-on motion (Fig. 4.1). They primarily fall toward each other in the $\pm x$ direction, but each hole's spin drags the space around itself, causing the other hole to accelerate in the downward, $-y$ direction. After the holes merge, the final black hole is kicked upward by the emitted gravitational waves, in the $+y$ direction. It is natural to wonder how the initial motion downward from frame dragging relates to the final, upward kick velocity of the merged hole. To address this issue, we compute the 4-momentum p^μ inside each apparent horizon using the Landau-Lifshitz formalism; we then define an effective velocity as

$$v^i_{\rm LL} := \frac{p^i}{p^0} \,. \tag{4.1}$$

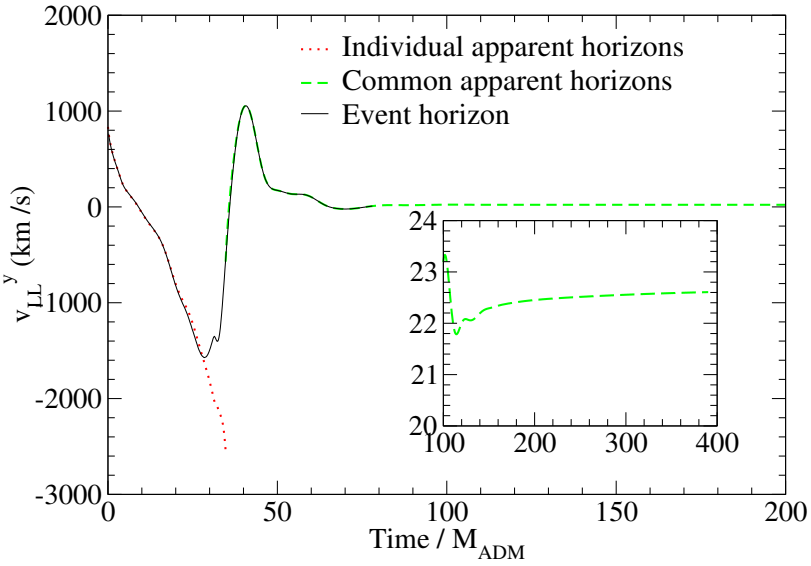

Figure 4.2: The effective velocity $v_{\rm LL}^{y}$ for the individual (red dotted line) and common (green dashed line) apparent horizons and for the event horizon (black solid line). The inset shows the velocity of the common apparent horizon at late times.

In Section 4.4, we find that this effective velocity behaves similarly to the apparent horizons' coordinate velocities.[2]

The effective y velocity for the generalized-harmonic simulation described in Section 4.3.1.2 is shown in Fig. 4.2. Before the merger, the individual apparent horizons accelerate in the $-y$ (downward) direction, eventually reaching velocities of order 10^3 km/s. When the common apparent horizon forms, the horizon pulsates. During the first half-pulsation, the horizon expands and accelerates to $\sim 10^3$ km/s in the $+y$ (upward) direction. This happens because as the common horizon forms and expands, it swallows not only the downward linear momentum inside each individual horizon but also a large amount of upward momentum in the gravitational field between the holes (see Fig. 4.3). During the next half-pulsation, as the horizon shape changes from oblate to prolate (see Fig. 4.10), the horizon swallows more downward momentum, thereby losing most of its upward velocity. Eventually, after strong damping of the pulsations, the common horizon settles to a very small velocity of about 23 km/s in the $+y$ direction (see the inset of Fig. 4.2), which is consistent with the kick velocity inferred from the emitted gravitational radiation (see Section 4.4).

The flow of momentum between field and holes is also described quite simply in terms of the holes' event horizon. Unlike apparent horizons, the event horizon evolves and expands continuously in time, rather than discontinuously. As the event horizon expands, it continuously swallows surrounding field momentum, and that swallowing produces a continuous evolution of the event horizon's velocity, an evolution that is nearly the same as for the apparent-horizon velocity. Figure 4.2 shows how the

[2]By coordinate velocity, we mean the velocity of the center of the apparent horizon, as measured in our asymptotically inertial coordinates.

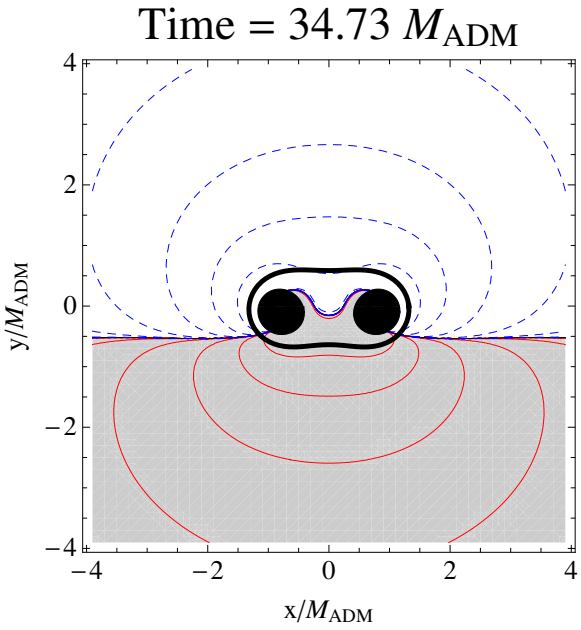

Figure 4.3: A contour plot of the y component of the momentum density at the moment when the common apparent horizon forms. The common horizon encloses the momentum inside the individual horizons and also the momentum in the gravitational field. The grey-shaded region and solid, red contours indicate positive momentum density, while the white-shaded region and blue, dashed contours indicate negative momentum density. The individual apparent horizons are shaded black, and the common apparent horizon is shown as a thick black line.

effective velocity of the event horizon smoothly transitions from matching the individual apparent horizons' velocities to matching the common apparent horizon's velocity. For further details, see Section 4.4.1.2 and especially Figs. 4.12 and 4.13.

In the remainder of this paper, we discuss our results and the simulations that are used to obtain them. In Section 4.2, we briefly review the Landau-Lifshitz formalism and momentum conservation. The simulations themselves are presented in Section 4.3. We analyze the simulations' momentum flow in Section 4.4 and conclude in Section 4.5. In the appendices, we describe in greater depth the numerical methods used for the simulations presented in this paper.

4.2 Four-Momentum Conservation for the Landau-Lifshitz Formalism

In this section, we briefly review the Landau-Lifshitz formulation of general relativity and the statement of 4-momentum conservation within this theory. Landau and Lifshitz, in their *Classical Theory of Fields* (hereafter referred to as LL), formulated general relativity as a nonlinear field theory in flat spacetime [50]. (Chapter 20 of MTW [51] and a paper by Babak and Grishchuk [52] are also helpful sources that describe the formalism.) Landau and Lifshitz develop their formalism by first laying down arbitrary asymptotically Lorentz coordinates on a given curved (but asymptotically-

flat) spacetime. They use these coordinates to map the curved (i.e., physical) spacetime onto an auxiliary flat spacetime (AFS) by enforcing that the coordinates on the AFS are globally Lorentz. The auxiliary flat metric takes the Minkowski form, $\eta_{\mu\nu} = \mathrm{diag}(-1, 1, 1, 1)$.

In this formulation, gravity is described by the metric density

$$\mathfrak{g}^{\mu\nu} := \sqrt{-g} g^{\mu\nu} \ , \tag{4.2}$$

where g is the determinant of the covariant components of the physical metric, and $g^{\mu\nu}$ are the contravariant components of the physical metric. When one defines the superpotential

$$H^{\mu\alpha\nu\beta} := \mathfrak{g}^{\mu\nu}\mathfrak{g}^{\alpha\beta} - \mathfrak{g}^{\mu\alpha}\mathfrak{g}^{\nu\beta} \ , \tag{4.3}$$

the Einstein field equations take the field-theory-in-flat-spacetime form

$$H^{\mu\alpha\nu\beta}{}_{,\alpha\beta} = 16\pi\tau^{\mu\nu} \ . \tag{4.4}$$

Here $\tau^{\mu\nu} := (-g)(T^{\mu\nu} + t^{\mu\nu}_{\mathrm{LL}})$ is the total effective stress-energy tensor, indices after the comma denote partial derivatives (or, equivalently, covariant derivatives with respect to the flat auxiliary metric), and the Landau-Lifshitz pseudotensor $t^{\mu\nu}_{\mathrm{LL}}$ (a real tensor in the auxiliary flat spacetime) is given by Eq. (100.7) of LL [50] (or, equivalently, Eq. (20.22) of MTW [51]):

$$\begin{aligned} 16\pi(-g)t^{\alpha\beta}_{\mathrm{LL}} &= \mathfrak{g}^{\alpha\beta}{}_{,\lambda}\mathfrak{g}^{\lambda\mu}{}_{,\mu} - \mathfrak{g}^{\alpha\lambda}{}_{,\lambda}\mathfrak{g}^{\beta\mu}{}_{,\mu} + \frac{1}{2}g^{\alpha\beta}g_{\lambda\mu}\mathfrak{g}^{\lambda\nu}{}_{,\rho}\mathfrak{g}^{\rho\mu}{}_{,\nu} \\ &- g^{\alpha\lambda}g_{\mu\nu}\mathfrak{g}^{\beta\nu}{}_{,\rho}\mathfrak{g}^{\mu\rho}{}_{,\lambda} - g^{\beta\lambda}g_{\mu\nu}\mathfrak{g}^{\alpha\nu}{}_{,\rho}\mathfrak{g}^{\mu\rho}{}_{,\lambda} + g_{\lambda\mu}g^{\nu\rho}\mathfrak{g}^{\alpha\lambda}{}_{,\nu}\mathfrak{g}^{\beta\mu}{}_{,\rho} \\ &+ \frac{1}{8}\left(2g^{\alpha\lambda}g^{\beta\mu} - g^{\alpha\beta}g^{\lambda\mu}\right)\left(2g_{\nu\rho}g_{\sigma\tau} - g_{\rho\sigma}g_{\nu\tau}\right)\mathfrak{g}^{\nu\tau}{}_{,\lambda}\mathfrak{g}^{\rho\sigma}{}_{,\mu} \ . \end{aligned} \tag{4.5}$$

Because of the symmetries of the superpotential—they are the same as those of the Riemann tensor—the field equations, Eq. (4.4), imply the differential conservation law for 4-momentum

$$\tau^{\mu\nu}{}_{,\nu} = 0 \ . \tag{4.6}$$

Equation (4.6) is equivalent to $T^{\mu\nu}{}_{;\nu} = 0$, where the semicolon denotes a covariant derivative with respect to the physical spacetime metric.

In both LL and MTW, it is shown that the total 4-momentum of any isolated system (measured in the asymptotically flat region far from the system) is

$$p^{\mu}_{\mathrm{tot}} = \frac{1}{16\pi}\oint_{\mathcal{S}} H^{\mu\alpha 0j}{}_{,\alpha} d\Sigma_j \ , \tag{4.7}$$

where $d\Sigma_j$ is the surface-area element of the flat auxiliary metric, and $\mathcal{S}$ is an arbitrarily large surface

surrounding the system. This total 4-momentum satisfies the usual conservation law

$$\frac{dp^{\mu}_{\rm tot}}{dt} = -\oint_{\mathcal{S}} \tau^{\mu j} d\Sigma_j \ . \tag{4.8}$$

See the end of Section III of [5] for a brief proof of why this holds for black holes.

Because this paper focuses on BBHs, we will make a few further definitions that will be used frequently in our study. First, we label the two[3] black holes in the binary (and the regions of space within their horizons) by A and B, and denote their surfaces (sometimes the hole's event horizon and other times the apparent horizon) by ∂A and ∂B, as shown in Fig. 3.5. We let $\mathcal{E}$ stand for the region outside both bodies but inside the arbitrarily large surface $\mathcal{S}$ where the system's total momentum is computed (in our case, this is taken to be a fixed coordinate sphere inside the outer boundary of the numerical-relativity computational grid).

With the aid of Gauss's theorem and the Einstein field equations, Eq. (4.4), one can reexpress Eq. (4.7) for the binary's total 4-momentum as a sum over contributions from each of the bodies and from the gravitational field in the region $\mathcal{E}$ outside them:

$$p^{\mu}_{\rm tot} = p^{\mu}_{A} + p^{\mu}_{B} + p^{\mu}_{\rm field} \ . \tag{4.9a}$$

Here

$$p^{\mu}_{A} := \frac{1}{16\pi} \oint_{\partial A} H^{\mu\alpha 0 j}{}_{,\alpha} d\Sigma_j \tag{4.9b}$$

is the 4-momentum of body A (an equivalent expression holds for body B), and

$$p^{\mu}_{\rm field} := \int_{\mathcal{E}} \tau^{0\mu} d^3x \tag{4.9c}$$

is the gravitational field's 4-momentum in the exterior of the black holes. We define an effective velocity of black hole A (with similar expressions holding for hole B) by

$$v^{j}_{\rm LL} := \frac{p^{j}_{A}}{p^{0}_{A}} \ . \tag{4.10}$$

In analogy to Eq. (4.8) for the rate of change of the binary's total 4-momentum, one can write the corresponding equation for the rate of change of the 4-momentum of body A:

$$\frac{dp^{\mu}_{A}}{dt} = -\oint_{\partial A} (\tau^{\mu k} - \tau^{\mu 0} v^{k}_{A}) d\Sigma_k \ . \tag{4.11}$$

Equation (4.11) describes the flow of field 4-momentum into and out of body A (the second term

[3] After the holes merge, there is only one horizon, which we label ∂C. Equations (4.8)–(4.10) hold after removing terms with subscript B and then substituting $A \to C$.

comes from the motion of the boundary of body A with local coordinate velocity v_A^k).[4]

We will use Eqs. (4.8)–(4.10) as the basis for our study of momentum flow in black-hole binaries. The actual values of the body and field 4-momenta, computed in the above ways, will depend on the arbitrary mapping between the physical spacetime and the AFS; this is the gauge dependence that will be discussed in Section 4.4.2.

4.3 Simulations of Head-on Binary-Black-Hole Collisions with Anti-Aligned Spins

In order to investigate the gauge dependence of our results, we compare simulations of the same physical system using two separate methods that employ different choices of coordinates. One method is a pseudospectral, excision scheme based on generalized-harmonic coordinates; the other is a finite-difference, moving-puncture scheme that uses the Baumgarte-Shapiro-Shibata-Nakamura (BSSN) [53, 54] formulation, 1+log slicing, and a gamma-driver shift condition (henceforth referred to as "BSSN-moving-puncture gauge;" for details, see Appendix 4.B.2). The coordinates used in the two methods differ both for the initial data and during the evolution. In this section, we summarize the construction of the initial data and the evolution systems for both methods, and we present convergence tests and estimate numerical uncertainties. Further details about our numerical methods are given in Appendices 4.A and 4.B.

4.3.1 Generalized-Harmonic Simulations

4.3.1.1 Quasiequilibrium Excision Data

The evolutions described in Section 4.3.1.2 begin with quasiequilibrium excision data constructed using the method in [55]. This procedure requires an arbitrary choice of a conformal three-metric; we choose this metric to be flat almost everywhere, but curved (such that the metric is nearly that of a single Kerr-Schild hole) near the horizons.

Our initial-data method also requires us to choose an outer-boundary condition on a shift vector β^i; for a general binary that is orbiting and inspiraling, we use[5]

$$\beta^i = (\mathbf{\Omega}_0 \times r)^i + \dot{a}_0 r^i + V_0^i, \ r \to \infty \ , \tag{4.12}$$

where Ω_0 is the angular velocity, $\dot{a}_0 r^i$ is the initial radial velocity, and V_0^i is a translational velocity. Note that Eq. (4.12) corresponds to a different choice of the shift than that in [55]. In this paper,

[4]When the body's event horizon is stationary (e.g., sufficiently far from merger), the velocity, $v_A^k = dx^k_{A\,\mathrm{cm}}/dt$, is the center-of-mass velocity of body A. If the body's event horizon is dynamical (e.g., during the merger phase), however, then v_A^k is the local coordinate velocity of the event-horizon surface, $v_A^k = dx^k_{\partial A}/dt$. See Section 4.4.1.2 for a discussion of the dynamics of the event horizon.

[5]The shift vector β^i used here and in Appendix 4.A for the construction of initial data is not the same as the shift vector used during our evolutions. Except for Section 4.3.1.1 and Appendix 4.A, we always use β^i to refer to the shift during the evolution.

Set	$x_o/M_{\rm ADM}$	$M_{\rm irr}/M_{\rm ADM}$	$M_{\rm Chr}/M_{\rm ADM}$	$S_z/M_{\rm Chr}^2$
S1	3.902	0.4986	0.5162	± 0.5000
P1	4.211	0.4970	0.5146	± 0.5000
P2	8.368	0.4802	0.5072	± 0.5091
H1	14.864	0.4870	0.5042	± 0.5000

Table 4.1: Parameters of the initial data configurations studied in this work. Model S1 (see Section 4.3.1.1) gives the parameters used to construct a set of superposed-Kerr-Schild quasiequilibrium, excision initial data. Model H1 (see Appendix 4.A.2) gives the parameters for the larger-separation, superposed-harmonic-Kerr initial-data set. Both S1 and H1 were used in generalized-harmonic, pseudospectral evolutions. P1 and P2 provide the Bowen-York parameters for the two systems evolved with the BSSN-moving-puncture method. The holes are initially separated by a coordinate distance $d = 2x_0$ and are located at coordinates $(x, y, z) = (\pm x_0, 0, 0)$. For clarity, only four significant figures are shown.

we focus on head-on collisions, which have $\Omega_0 = \dot{a}_0 = 0$. However, V_0^i must be nonzero to make the total linear momentum of the initial data vanish.

Table 4.1 summarizes the initial data used in this paper. It contains information about three different measures of the binary's mass, the Arnowitt-Deser-Misner (ADM) mass $M_{\rm ADM}$ (Eq. (11.2.14) in [56]; see also [57, 58]), the irreducible mass $M_{\rm irr}$, and the Christodoulou mass $M_{\rm Chr}$ of one of the holes. The Christodoulou, $M_{\rm Chr}$, is related to $M_{\rm irr}$ and the spin of the hole S_z by

$$M_{\rm Chr}^2 = M_{\rm irr}^2 + \frac{S_z^2}{4M_{\rm irr}^2}. \tag{4.13}$$

Table 4.1 also shows the dimensionless spin $S_z/M_{\rm Chr}^2$; by definition, this measure of the spin lies in the interval $-1 \leq S_z/M_{\rm Chr}^2 \leq 1$.

For set S1 listed in Table 4.1, V_0^i is adjusted so that the initial effective velocity of the entire spacetime $v_{\rm tot}^i := p_{\rm tot}^i/p_{\rm tot}^0$ is smaller than 0.1 km/s, which is approximately the size of our numerical truncation error (see Fig. 4.8): $(|v_{\rm tot}^x|, |v_{\rm tot}^y|, |v_{\rm tot}^z|) = (4\times10^{-4}, 5\times10^{-2}, 2\times10^{-3})$ km/s at the time $t = 0$. The construction of initial data is described in more detail in Appendix 4.A.

4.3.1.2 Generalized-Harmonic Evolutions

We evolve the quasiequilibrium excision data described in Section 4.3.1.1 pseudospectrally, using a generalized-harmonic gauge [59, 60, 61, 62], in which the coordinates x^μ satisfy the gauge condition

$$g_{\mu\nu}\nabla^\rho\nabla_\rho x^\mu = H_\nu\left(x^\rho, g_{\sigma\tau}\right) \ , \tag{4.14}$$

where H_ν is a function of the coordinates and the spacetime metric. In this subsection, we summarize the computational grid used for our generalized-harmonic evolutions, and we briefly discuss our numerical accuracy. Details of our pseudospectral evolution methods are given in Appendix 4.B.1.

Our computational grid covers only the exterior regions of the black holes (black-hole excision);

there is an artificial inner boundary just inside each apparent horizon. No boundary conditions are needed at these boundaries because the formulation of Einstein's equations we use [62] admits only causal characteristic speeds, even for gauge modes and constraint-violating modes. The grid extends to a large radius $r_{\rm max}/M_{\rm ADM} \sim 400$. A set of overlapping subdomains of different shapes (spherical shells near each hole and far away, cylinders elsewhere) covers the entire space between the excision boundaries and $r = r_{\rm max}$.

Because different subdomains have different shapes and the grid points are not distributed uniformly, we describe the resolution of our grid in terms of the total number of grid points summed over all subdomains. We label our resolutions N0, N1, and N2, corresponding to approximately 55^3, 67^3, and 79^3 grid points, respectively. After merger, we regrid onto a new computational domain that has only a single excised region (just inside the newly-formed apparent horizon that encompasses both holes). This new grid has a different resolution (and a different decomposition into subdomains) from the old grid. We label the resolution of the post-merger grid by A, B, and C, corresponding to approximately 63^3, 75^3, and 87^3 grid points, respectively. We label the entire run using the notation "N$x.y$", where the characters before and after the decimal point denote the pre-merger and post-merger resolution for that run. For example, "N2.B" denotes a run with approximately 67^3 grid points before merger, and 75^3 grid points afterward. On the outermost portion of the grid ($r/M_{\rm ADM} \gtrsim 200$), we use a coarser numerical resolution than we do elsewhere. (We only measure the gravitational-wave flux and linear momentum at radii of $r/M_{\rm ADM} \leq 160$.)

To demonstrate the convergence of our evolutions, we plot the constraint violation in Fig. 4.4 for several resolutions. The quantity plotted is the L^2 norm of all the constraints of the generalized-harmonic system, normalized by the L^2 norm of the spatial gradients of all the dynamical fields, as defined by Eq. (71) of [62]. The left portion of the plot depicts the constraint violation during the plunge, the right third of the plot shows the constraint violation during the ringdown, and the middle panel shows the constraints shortly before and after the common apparent horizon forms. Throughout the evolution, we generally observe exponential convergence, although the convergence rate is smaller near merger. After merger, there are two sources of constraint violations: those generated by numerical truncation error after merger (these depend on the resolution of the post-merger grid) and those generated by numerical-truncation error before merger and are still present in the solution (these depend on the resolution of the pre-merger grid). We see from Fig. 4.4 that the constraint violations after merger are dominated by the former source. Also, at about $t/M_{\rm ADM} = 200$, the constraint violation increases noticeably (but is still convergent); at this time, the outgoing gravitational waves have reached the coarser, outermost region of the grid.

Finally, in Fig. 4.5, we demonstrate the accuracy of the recoil velocity $v_{\rm kick} = 22$ km/s, inferred from the gravitational-wave signal Ψ_4. The Weyl scalar Ψ_4, is asymptotically related to the

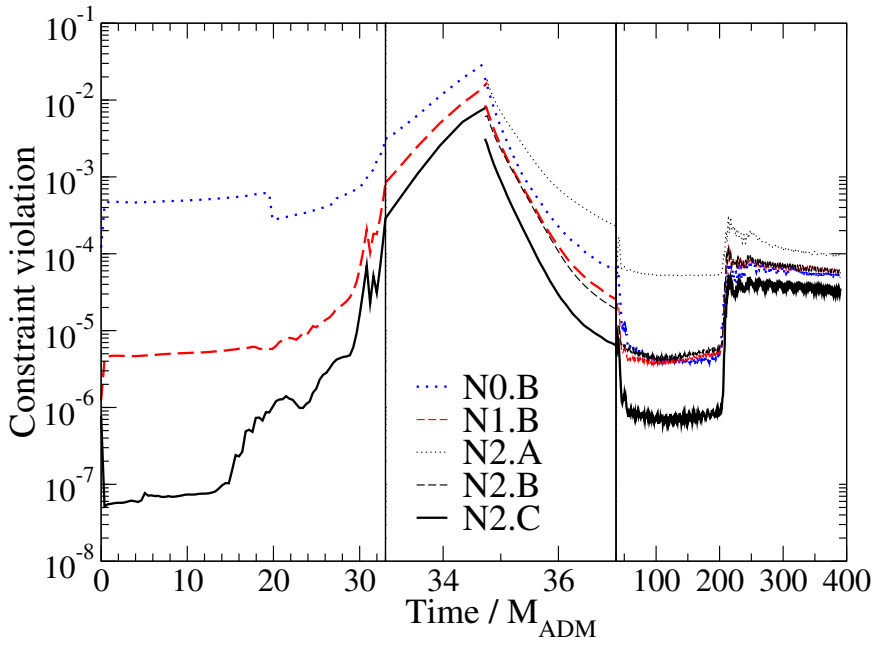

Figure 4.4: Constraint violation at different numerical resolutions for the generalized-harmonic evolutions S1. The common apparent horizon forms at time $t/M_{\rm ADM} = 34.73$. Labels of the form N$x.y$ indicate the grid resolution, where the pre-merger resolution is labeled (from coarse to fine) by $x = 0, 1, 2$ and the post-merger resolution is labeled (similarly) by $y = A, B, C$. The constraints decrease exponentially with higher resolution; the convergence rate is smaller near merger.

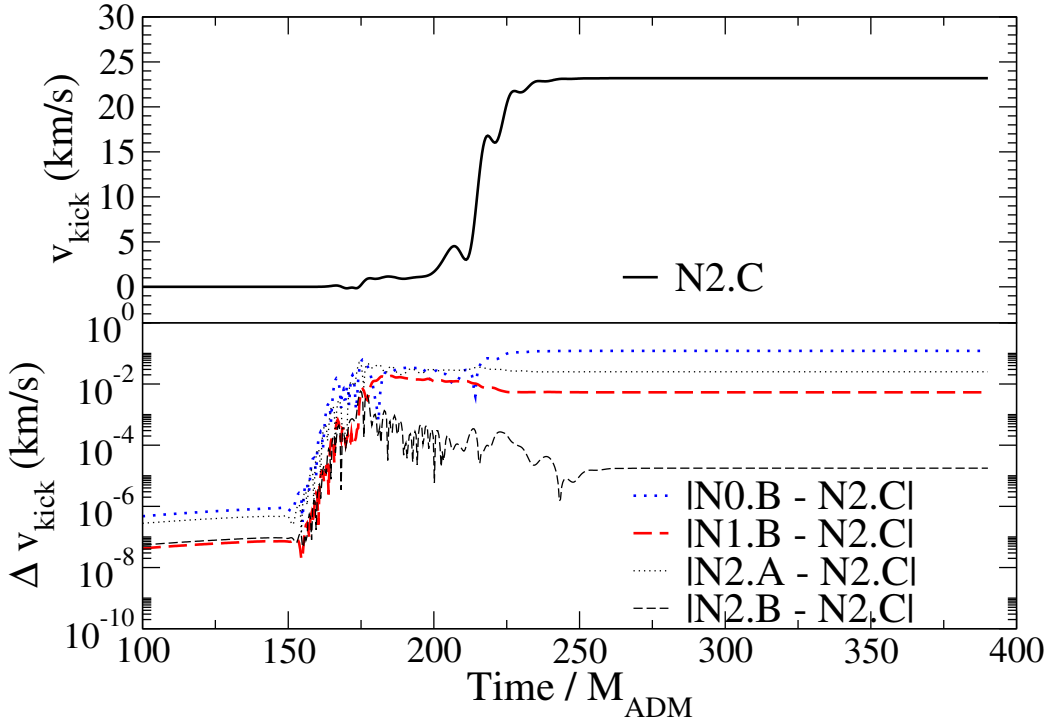

Figure 4.5: Recoil velocity for the initial-data set S1, inferred from the gravitational-wave signal Ψ_4 extracted at $r_{\rm extr}/M_{\rm ADM} = 160$ at the highest resolution (upper panel). Differences between several coarser resolutions and the highest resolution are plotted in the lower panel.

gravitational-wave amplitudes h_+ and $h_\times$ by

$$\Psi_4 = \frac{d^2}{dt^2} h_+ - i \frac{d^2}{dt^2} h_\times . \tag{4.15}$$

We extract the spin-weighted spherical-harmonic coefficients of $\Psi_4(t)$ from the simulation as described in [4], and we integrate these coefficients over time to obtain $\dot{h}^{\ell m}(t)$, which are the spin-weighted spherical-harmonic coefficients of $\dot{h} = \dot{h}_+ - i\dot{h}_\times$. For each (ℓ, m), the integration constant is chosen so that the average value of $\dot{h}^{\ell m}(t)$ is zero. The $\dot{h}^{\ell m}(t)$ are then used to compute the 4-momentum flux of the gravitational waves from Eqs. (3.14)–(3.19) of [63]. Integrating this flux over time yields the total radiated energy-momentum, $p^\mu_{\rm rad}$. The recoil velocity can then be computed from energy-momentum conservation: $v^i_{\rm kick} = -p^i_{\rm rad}/M_{\rm final}$, where $M_{\rm final} := M_{\rm ADM} - E_{\rm rad}$ and $E_{\rm rad}$ is the energy radiated to infinity. For set S1, we obtain a radiated energy of $E_{\rm rad}/M_{\rm ADM} = (5.6840 \pm 0.0008) \times 10^{-4}$, where the quoted error includes truncation error and uncertainty from extrapolation to infinite radius (as discussed below). The top panel of Fig. 4.5 shows the recoil velocity as a function of time for our highest-resolution simulation, while the lower panel shows differences between the highest resolution (N2.C) and lower resolutions. From these differences, we estimate a numerical uncertainty for the final recoil velocity of 5×10^{-3} km/s for N1.B and 2×10^{-5} km/s for N2.B.

This numerical uncertainty includes only the effects of numerical-truncation error; there are, however, other potential sources of uncertainty in the simulations that must also be considered. The first is the spurious "junk" gravitational radiation that arises because the initial data do not describe a binary in perfect equilibrium. This radiation is not astrophysically realistic, but by carrying a small amount of energy-momentum that contributes to the measured $p^\mu_{\rm rad}$ at large distances, the spurious radiation does affect how accurately we can determine the final recoil velocity. In our investigation of momentum flow (Section 4.4), we do not correct for the initial data's failure to be in equilibrium; here, we estimate the contribution of the junk radiation to the final recoil velocity. First, we note that for head-on collisions, the physical gravitational waves are emitted predominantly after merger. Therefore, we estimate the influence of the spurious radiation by examining the accumulated recoil velocity at time $t = \Delta t + r$, where r is the radius of the extraction surface and Δt is a cutoff time. Because the holes merge so quickly (because they begin at a small initial separation), the spurious and physical contributions to the recoil are not clearly distinguishable in Fig. 4.5. Varying $\Delta t/M_{\rm ADM}$ between 31.1 and 38.3 (the event and common apparent horizons form at $t/M_{\rm ADM} = 31.1$ and $t/M_{\rm ADM} = 34.7$, respectively), we estimate that the spurious radiation contributes approximately 1 km/s (about 5%) to the recoil velocity—a much larger uncertainty than the truncation error. The same variation of Δt implies that the spurious radiation contributes about 10% of the total radiated energy $E_{\rm rad}$.)

Another potential source of uncertainty in $v^i_{\rm kick}$ arises from location on the computation grid at which we measure the gravitational radiation. In particular, the quantity Ψ_4 in Eq. (4.15) should ideally be measured at future null infinity. Instead, we measure Ψ_4 on a set of coordinate spheres at fixed radii, compute $v^i_{\rm kick}$ on each of these spheres, and extrapolate the final equilibrium value of $v^i_{\rm kick}$ to infinite radius (see Fig. 4.11). We estimate our uncertainty in the extrapolated value by comparing polynomial extrapolation of linear, quadratic, and cubic orders in $1/r$; we find an uncertainty of 3×10^{-3} km/s for the quadratic fit. Note that if we had not extrapolated to infinity, but had instead simply used the value of $v^y_{\rm kick}$ at our largest extraction sphere ($r/M_{\rm ADM} = 160$), we would have made an error of 0.85 km/s, which is much larger than the uncertainty from numerical truncation error. Finally, we mention that our computation of Ψ_4 is not strictly gauge-invariant unless Ψ_4 is evaluated at future null infinity. As long as gauge effects in Ψ_4 fall off faster than $1/r$ as expected, extrapolation of $v^y_{\rm kick}$ to infinity should eliminate this source of uncertainty.

4.3.2 BSSN-Moving-Puncture Simulations

4.3.2.1 Bowen-York Puncture Initial Data

In order to address the degree of gauge dependence in our calculations using the Landau-Lifshitz formalism, we also simulate BBH mergers using the so-called moving-puncture method, which employs the covariant form of "1+log" slicing [2, 64] for the lapse function, α, and a "Gamma-driver" condition (based on the original "Gamma-freezing" condition introduced in [65]) for the shift vector. The precise evolution equations for the gauge variables as well as further technical details of our puncture simulations are given in Appendix 4.B.2.

Our simulations start with puncture initial data [66] provided, in our case, by the spectral solver of [67]. The initial data are fully specified in terms of the initial spin $\vec{S}_{1,2}$, linear momentum $\vec{P}_{1,2}$, and initial coordinate position $\vec{x}_{1,2}$, as well as the bare mass parameters $m_{1,2}$ of either hole [68]. In order to assess the impact of the initial binary separation, we evolve the two models labeled by P1 and P2 in Table 4.1. There we also list the individual black-hole masses, $M_{\rm Chr}$, and normalize all quantities using the total ADM mass $M_{\rm ADM}$. The main difference between the two configurations is the initial separation of the holes. The lapse and shift are initially set to $\alpha = \gamma^{-1/6}$ and $\beta^i = 0$, respectively, where γ is the determinant of the physical three-metric.

4.3.2.2 BSSN-Moving-Puncture Evolutions

The evolution of the puncture initial data is performed using sixth-order spatial discretization of the BSSN equations and a fourth-order Runge-Kutta time-integration method. We use Berger-Oliger [69] mesh refinement, which is implemented as part of Schnetter's CARPET package [70, 71]. The prolongation operator is of fifth order in space and quadratic in time. Outgoing-radiation boundary conditions are implemented using second-order accurate advection derivatives (see, for example,

Section VI in [72]).

Using the notation of Section II E of [73], the grid setup, in units of $M_{\rm ADM}$, for these evolutions is given by (rounded to three significant digits)

$$\{(202, 101, 58.8, 25.2, 12.6) \times (3.15, 1.58, 0.788),\ h\},$$
$$\{(201, 100, 58.5, 25.1) \times (6.27, 3.13, 1.57, 0.784),\ h\},$$

for the P1 and P2 evolutions, respectively. Here, h denotes the resolution on the innermost refinement level. For model P1, we perform a convergence analysis by setting h to $h_{\rm c} = M_{\rm ADM}/49.5$, $h_{\rm m} = M_{\rm ADM}/57.1$, and $h_{\rm f} = M_{\rm ADM}/64.7$, for the coarse, medium, and fine resolutions, respectively. Model P2 is evolved using $h = M_{\rm ADM}/49.8$. Before we discuss the physical results from the BSSN-moving-puncture simulations, we estimate the numerical errors from discretization, a finite extraction radius, and the presence of unphysical gravitational radiation in the initial data.

In order to study the dependence of the results on resolution, we evolved model P1 of Table 4.1 using different resolutions $h_{\rm c}$, $h_{\rm m}$, and $h_{\rm f}$ on the finest level and correspondingly larger grid spacings by a factor of two on each consecutive level. Numerical simulations based on finite-difference techniques have numerical errors that depend polynomially on the grid resolution h (because derivatives in the differential equations are approximated by solving a Taylor expansion to a fixed polynomial order). A numerical result, f_h, will, therefore, differ from the continuum limit f by a discretization error $e(h) := f_h - f = \text{const} \times h^n + \ldots$, where n is the order of convergence and the dots denote higher-order terms. In our case, the lowest-order ingredient in the code comes from the temporal prolongation operator, which is only second-order accurate. The consistency of the code can then be tested by calculating the order of convergence of a quantity

$$Q_n := \frac{f_{h_c} - f_{h_m}}{f_{h_m} - f_{h_f}}\ , \tag{4.16}$$

where $f(h_c)$, $f(h_m)$, and $f(h_f)$ denote the numerical solution at coarse, medium, and fine resolution, respectively. Inserting the above-mentioned error function $e(h)$, and ignoring higher-order terms, the expected convergence factor for a scheme of $n^{\rm th}$-order accuracy is

$$Q_n = \frac{h_c^n - h_m^n}{h_m^n - h_f^n}. \tag{4.17}$$

The kick velocity from the high-resolution simulation, as inferred from the gravitational-radiation flux at $r_{\rm ex}/M_{\rm ADM} = 73.5$, is shown in the upper panel of Fig. 4.6. The bottom panel shows the differences between the velocities obtained at the different resolutions, scaled for second-order convergence using a factor $Q_2 = 1.49$. By using Richardson extrapolation, we estimate the error in the final kick for the fine-resolution run to be 1 km/s or 5%. We similarly find overall second-

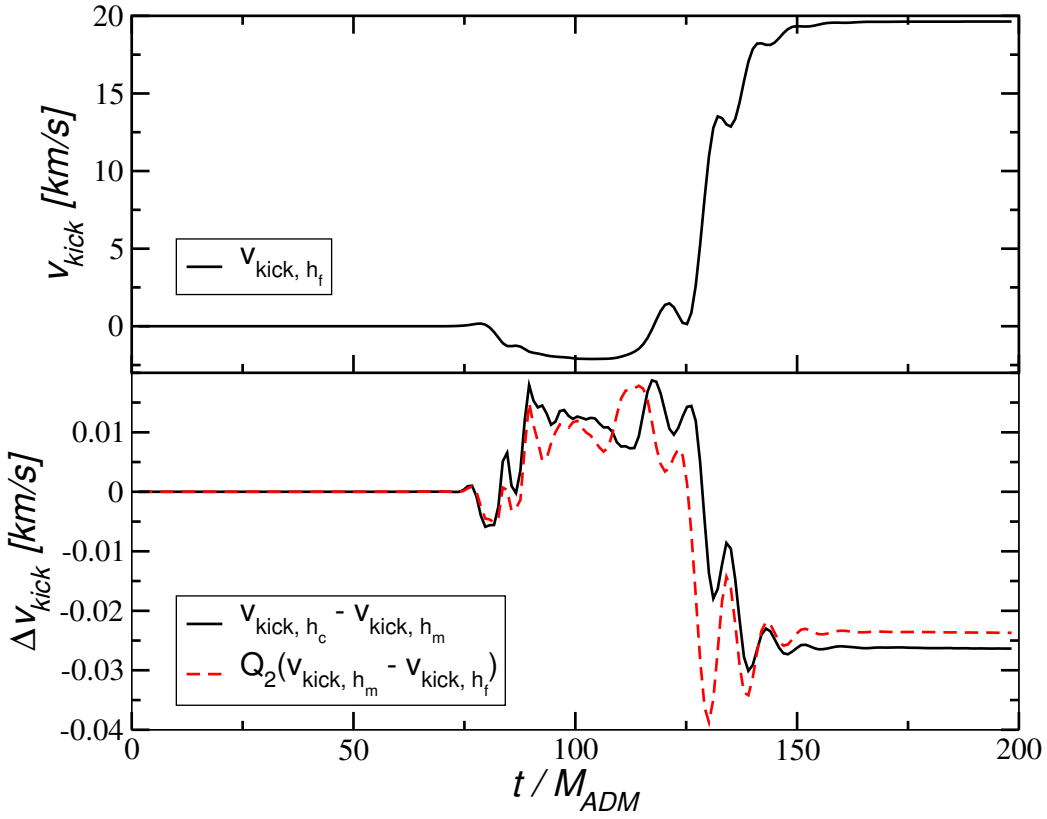

Figure 4.6: Gravitational recoil for model P1, as estimated from the gravitational-wave signal, Ψ_4, and extracted at $r_{\rm ex}/M_{\rm ADM} = 73.5$ using the highest resolution (upper panel). Differences in the recoil obtained at coarse, medium, and fine resolution rescaled for second-order convergence are shown in the lower panel.

order convergence for the velocity derived from the components of the Landau-Lifshitz tensor, as integrated over the apparent horizon. The error in that quantity barely varies throughout the entire simulation and stays at a level just below $\Delta v_{\rm LL} \approx 50$ km/s and 60 km/s for the fine and coarse resolutions, respectively.

The gravitational-wave signal is also affected by the finite extraction radius at which it is measure and by the linear momentum contained in the spurious initial radiation. We estimate the uncertainty from the use of a finite extraction radius by fitting the final kick velocity obtained for the medium-resolution simulation of model P1 at radii $r_{\rm ex}/M_{\rm ADM} = 31.5, \ldots, 94.5$ in steps of 10.5. The resulting final-kick velocities are well approximated by a polynomial of the form $a_0 + a_1/r_{\rm ex} + a_2/r_{\rm ex}^2$. For $r_{\rm ex}/M_{\rm ADM} = 73.5$ we obtain an uncertainty of 0.4 km/s, corresponding to a relative error of 2.2%.

Finally, we take into account contributions from the spurious initial radiation by discarding the wave signal up to $t - r_{\rm ex} = \Delta t$. For model P1, it is not entirely clear where exactly the spurious wave signal stops and the physical signal starts. By varying Δt from 30 to 45 $M_{\rm ADM}$ we obtain an additional error of about ± 1 km/s. For model P2, no such problem arises, because of the smaller amplitude of the spurious radiation, and because the longer time prior to the merger allows the junk radiation to escape the computational grid before the merger happens. We estimate the resulting total uncertainty by summing the squares of the individual errors and obtain 7.5% and 5.5% for models P1 and P2, respectively.

Using these uncertainties, the gravitational-waves in the simulation P1 carry away a total radiated energy, $E_{\rm rad}/M_{\rm ADM} = (0.042 \pm 0.008)\%$, and they generate a recoil velocity $v_{\rm kick} = (20.3 \pm 1.5)$ km/s. For model P2, the analogous results are $E_{\rm rad}/M_{\rm ADM} = (0.0555 \pm 0.0023)\%$ and $v_{\rm kick} = (19.7 \pm 1.1)$ km/s.

4.4 Momentum Flow

In this section, we turn to the momentum flow during the evolutions described in Section 4.3. First, in Section 4.4.1, we measure the momentum of the holes during plunge, merger, and ringdown, during a generalized-harmonic evolution of the initial-data set S1 (see Table 4.1), focusing on the momentum density and the inferred Landau-Lifshitz velocity $v^y_{\rm LL}$ along and opposite to the frame-dragging direction (which in this paper are chosen to be the $\mp y$ direction, respectively). In Section 4.4.2, we look at the momentum flow in a BSSN-moving-puncture simulation with similar initial data, and, by comparing the BSSN-moving-puncture and generalized-harmonic simulations, we investigate the influence of the choice of gauge on our results. Then, in Section 4.4.3, we compare the momentum density and velocity of the holes with post-Newtonian calculations of the same quantities.

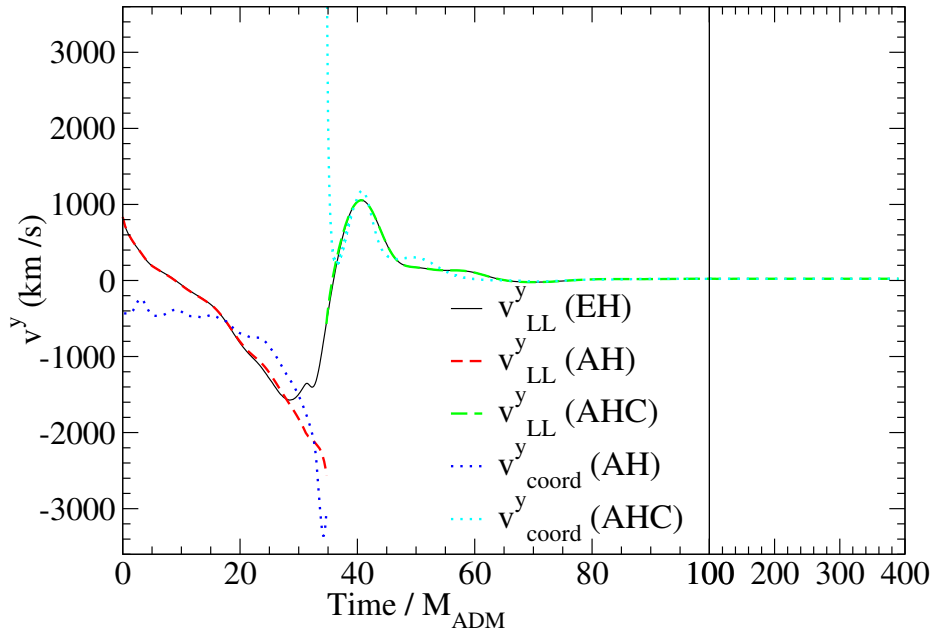

Figure 4.7: The velocity of the individual and merged black holes. The Landau-Lifshitz velocity $v^y_{\rm LL} := p^y_{\rm LL}/p^t_{\rm LL}$, where $p^\mu_{\rm LL}$ is the Landau-Lifshitz 4-momentum, is computed on the individual and common apparent horizons (labeled AH and AHC, respectively) and also on the event horizon (labeled EH). For comparison, the coordinate velocities $v^y_{\rm coord}$ of the apparent horizons are also shown. The data shown are from the high-resolution evolution N2.*C*.

4.4.1 Generalized-Harmonic Results

Throughout the generalized-harmonic evolutions summarized in Section 4.3.1.2, we measure the 4-momentum density by explicitly computing the Landau-Lifshitz pseudotensor, Eq. (4.5). Because our evolution variables are, in essence, the spacetime metric $g_{\mu\nu}$ and its first derivative $g_{\mu\nu,\rho}$, we are able to compute the momentum density without taking any additional numerical derivatives. In addition to calculating the momentum density, we also compute the 4-momentum p^μ_A of Eq. (4.9b) enclosed by (i) the apparent horizons, (ii) the event horizon, and (iii) several spheres of large radius. From the enclosed momentum, we evaluate the effective velocity $v^j_{\rm LL}$, Eq. (4.10).

4.4.1.1 Apparent Horizons

The effective velocities of the apparent horizons are shown in Fig. 4.7 (dashed curves). To demonstrate convergence, Fig. 4.8 shows the differences between apparent-horizon effective velocities computed at different resolutions. During the plunge, the difference between the medium and fine resolutions is less than 0.1 km/s until shortly before merger, when it reaches a few tenths of a km/s. Shortly after merger, the difference between the highest and medium continuation resolutions between N2.B and N2.C falls from about 1 km/s to about 0.1 km/s.

For comparison, Fig. 4.7 also shows the apparent horizons' coordinate velocities (dotted curves); the coordinate and effective velocities agree qualitatively during the plunge and quantitatively during

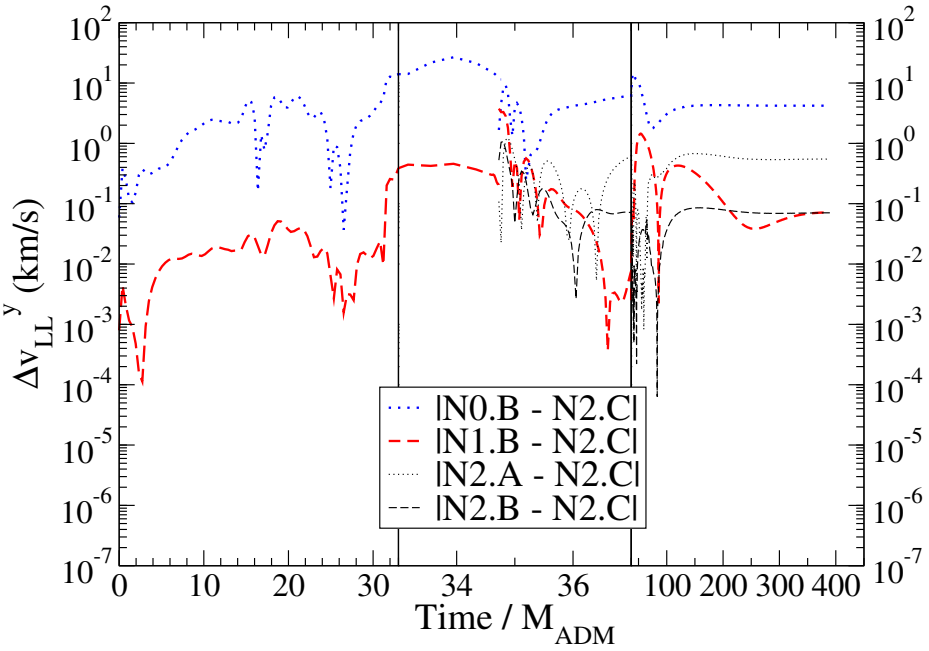

Figure 4.8: Convergence of $v^y_{\rm LL}$ with resolution. Specifically, differences between $v^y_{\rm LL}$ at the highest resolution N2.C and at various lower resolutions are shown. Labels of the form Nx.y indicate the grid resolution, where the pre-merger resolution is labeled (from coarse to fine) by $x = 0, 1, 2$ and the post-merger resolution is labeled by $y = A, B, C$. The difference between the second-highest and highest resolution is below 0.1km/s except near the time of the merger, when it grows as large as 1 km/s.

the merger. There is no reason to expect this observed agreement *a priori*; this is one sense in which our gauge choice appears to be reasonable. Also, Fig. 4.7 shows that the effective velocities of the individual apparent horizons and the event horizon agree well until shortly before merger, when the event horizon's velocity smoothly transitions to agree with the common apparent horizon's velocity (see Section 4.4.1.2 below).

Because of frame dragging during the plunge, the individual apparent horizons accelerate in the downward ($-y$) direction, eventually reaching velocities of thousands of km/s. When the common apparent horizon appears, however, its velocity is much closer to zero, and it quickly changes sign, eventually reaching speeds of about 1000 km/s in the $+y$ direction (i.e., in the direction opposite the frame-dragging direction). Then, as the common horizon rings down, the velocity relaxes to the final kick velocity of about 20 km/s in the $+y$ direction.

It is of considerable interest to understand why the horizon velocities suddenly reversed directions around the time of merger, going from thousands of km/s in the frame-dragging direction to over a thousand km/s in the opposite direction. Figure 4.9 helps to address this issue by showing contours of constant values of the y component of the momentum density, at several times. At $t = 0$, the momentum density has an irregular shape, because the initial data are initially not in equilibrium; by the time $t/M_{\rm ADM} = 26.92$, the momentum density has relaxed. When the common apparent horizon forms (at time $t/M_{\rm ADM} = 34.73$), it encloses not only the momentum of the individual apparent horizons but also the momentum in the gravitational field between the holes.

It turns out that the net momentum outside the individual horizons but inside the common horizon points in the $+y$ direction; as the common horizon expands, it absorbs more and more of this upward momentum. Figure 4.10 compares the common apparent horizon's effective velocity to its area and shape; the latter is indicated by the pointwise maximum and minimum of the horizon's intrinsic scalar curvature. During the first half-period of oscillation (to the left of the left-most dashed vertical line), the common horizon expands (as seen by its increasing area). As it expands, the upward-pointing linear momentum it encloses causes $v^y_{\rm LL}$ to increase. After the first half-period, the horizon shape is maximally oblate (see panel B on the right side of Fig. 4.10), and $v^y_{\rm LL}$ is at its maximum value of about 1000 km/s.

After another half-period of oscillation, the apparent horizon becomes prolate and encloses enough downward-pointing momentum that $v^y_{\rm LL}$ has decreased to only about +200 km/s. After one additional full period, the effective velocity has fallen to nearly zero. As the horizon is ringing down, the momentum density in the surrounding gravitational field also oscillates: the final four panels in Fig. 4.9 show how the momentum density relaxes to a final state as the horizon relaxes to that of a boosted Schwarzschild black hole.

Also as the horizon rings down, gravitational waves are emitted, and these waves carry away a small amount of linear momentum. The net radiated momentum is only a small fraction of the

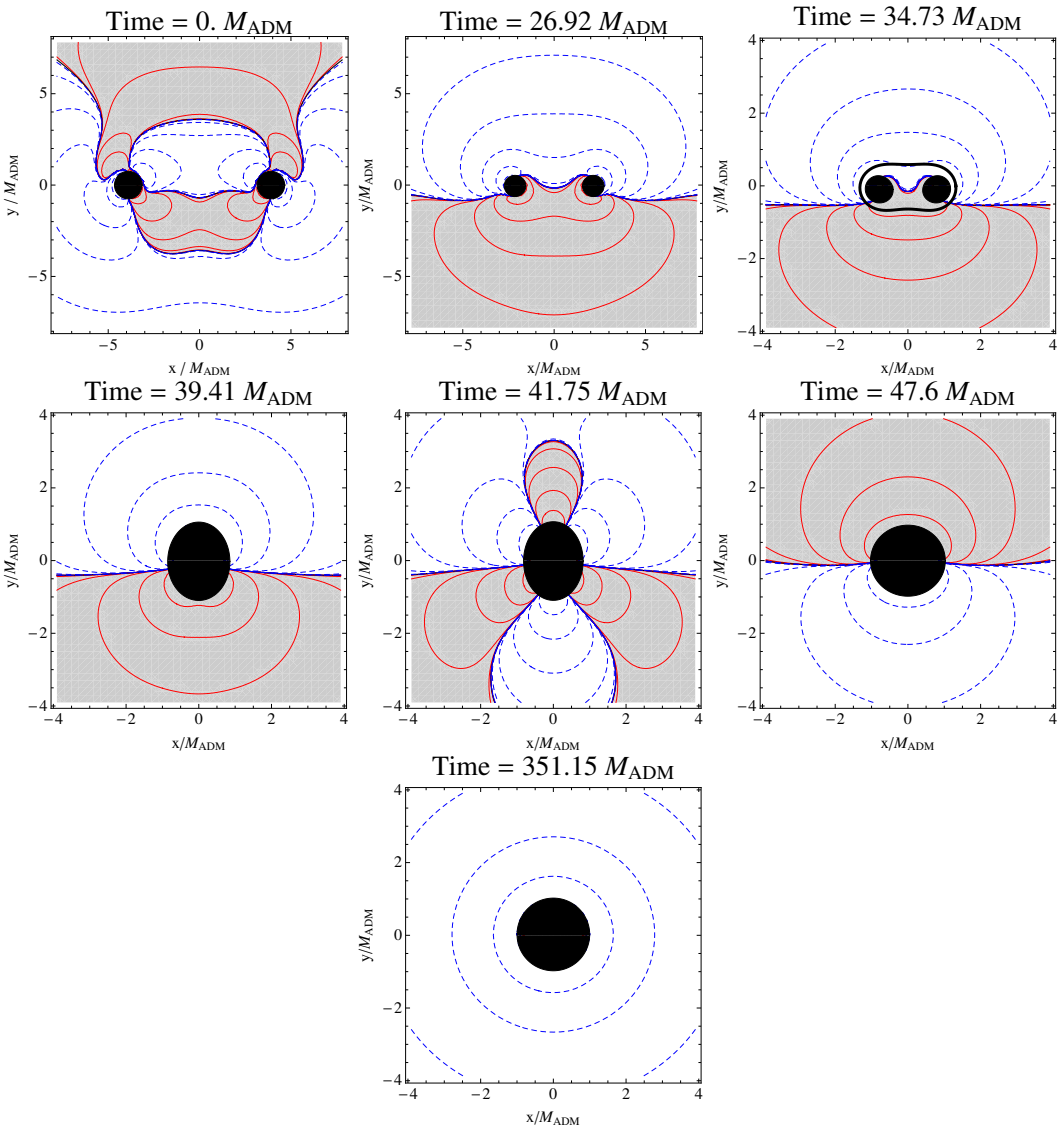

Figure 4.9: Contour plots of the y (up-down) component of the momentum density (the y direction points along or opposite to the holes' motion from frame dragging). Adjacent contours correspond to a factor of 10 difference in the magnitude of the momentum density. Contours of positive y-momentum density are shown as solid red lines, while contours of negative y-momentum density are shown as dashed blue lines. The region containing positive y-momentum density is shaded grey. The regions inside the apparent horizons are shaded black, except for the upper-right panel, where the region inside the *individual* horizons is shaded black, while the common apparent horizon is indicated by a thick black line. The data shown are from the high-resolution evolution N2.C.

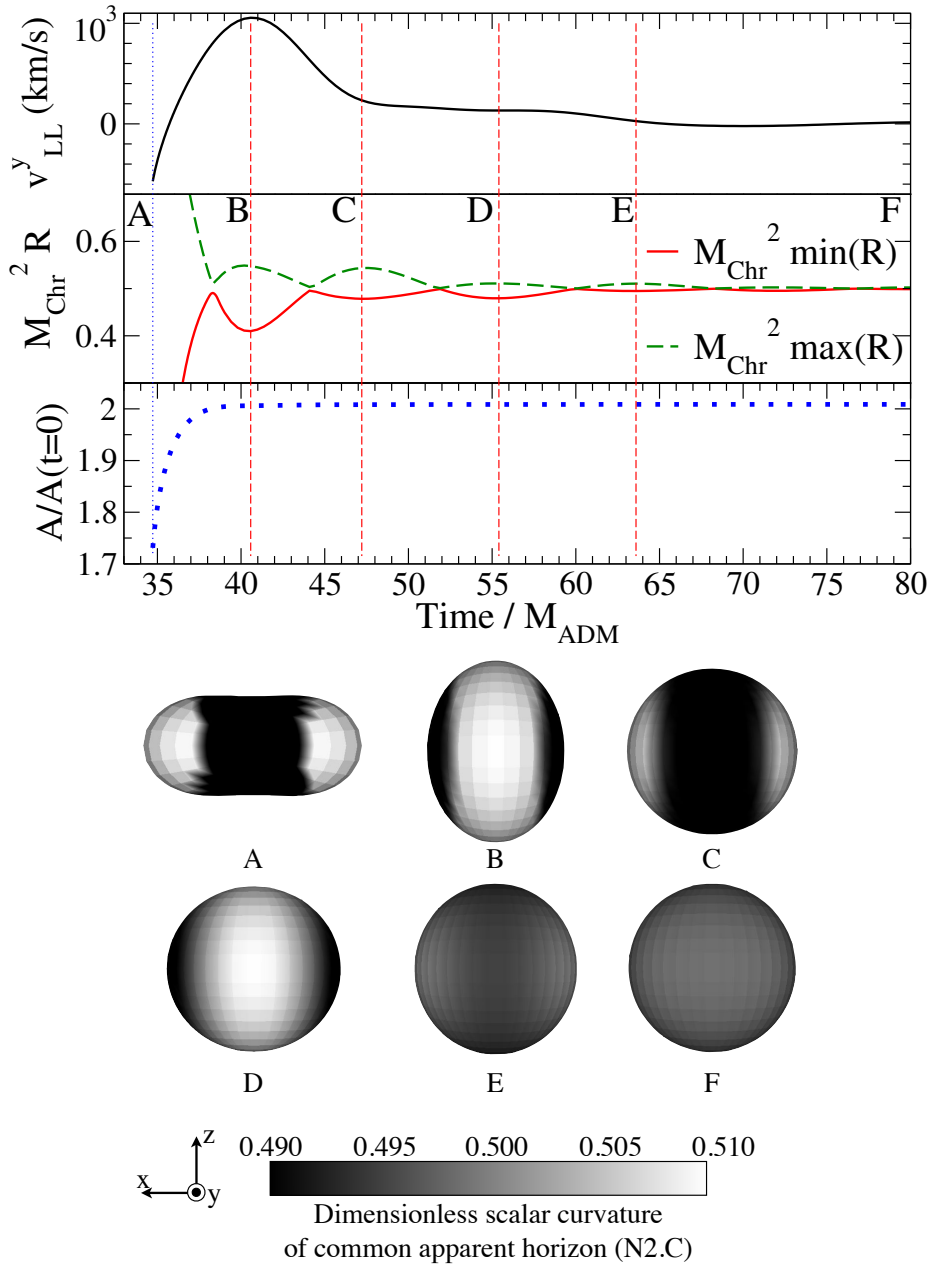

Figure 4.10: *Top:* A comparison of the common apparent horizon's effective velocity and the horizon's shape and area. The top panel shows the horizon's effective velocity $v^y_{\rm LL}$. The middle panel shows the pointwise minimum and maximum of the horizon's dimensionless intrinsic scalar curvature; both $M^2_{\rm Chr}\min(R)$ and $M^2_{\rm Chr}\max(R)$ relax to the Schwarzschild value of 1/2 as the horizon rings down. (The first four local minima of $M^2_{\rm Chr}\min(R)$ are indicated by vertical dashed lines.) The bottom panel shows the area A of the common apparent horizon normalized by the total area of the individual horizons at $t = 0$. The data shown are from the high-resolution evolution N2.C. *Bottom:* The dimensionless intrinsic scalar curvature $M^2_{\rm Chr}R$ of the common apparent horizon at the times labeled A–F in the left panel. The horizon begins peanut-shaped, then rings down, eventually settling down to a sphere with a constant curvature $M^2_{\rm chr}R = 0.5$.

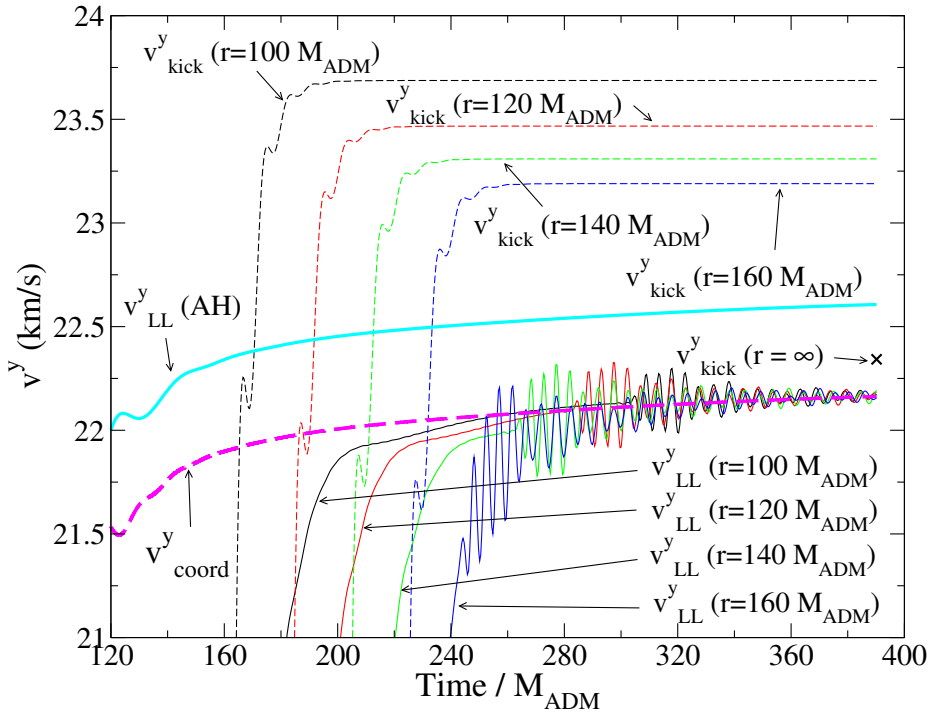

Figure 4.11: A comparison of various measures of the final velocity of the merged black hole in simulation S1. The measures shown are the following: the kick velocity inferred from the gravitational-wave flux (thin dashed lines) and the Landau-Lifshitz effective velocities $v^y_{\rm LL}$ (thin solid lines), measured on spheres of radius $r/M_{\rm ADM} = 100$, 120, 140, and 160; the value of the kick velocity at the final time extrapolated to $r = \infty$ (black x); the effective velocity measured on the common apparent horizon (thick solid line); and the coordinate velocity (thick dashed line). All data shown are taken from the high-resolution evolution N2.C.

momenta of the individual holes at the time of merger: the final effective velocity of the merged hole is about 20 km/s in the upward-pointing direction, or about 1% of the individual holes' downward velocity just before merger.

Several measures of the final velocity of the merged hole are shown in Fig. 4.11. The kick velocity $v^y_{\rm kick}$, which is inferred from the outgoing gravitational waves, is measured on four coordinate spheres (with radii $r/M_{\rm ADM} = 100$, 120, 140, and 160); the effective velocity is measured on the same coordinate spheres. At late times, we find that the effective velocity $v^y_{\rm LL}$ has no significant dependence on the radius of the extraction surface; it simply approaches the coordinate velocity $v^y_{\rm coord}$ of the common apparent horizon. The dependence of $v^y_{\rm kick}$ on the extraction radius is expected, because our method of extracting Ψ_4 at finite radius has gauge-dependent contributions that vanish as $r \to \infty$. When $v^y_{\rm kick}$ is extrapolated to infinite radius[6], however, it does agree well (within 0.2 km/s) with $v^y_{\rm LL}$. Also, the effective velocity $v^y_{\rm LL}$ calculated on the horizon also agrees fairly well (within about 0.5 km/s) with $v^y_{\rm LL}$ measured on distant spheres.

[6]To extrapolate, we fit the velocities $v^y_{\rm kick}$ at the final time to a function of radius r of the form $a_0 + a_1/r + a_2/r^2$.

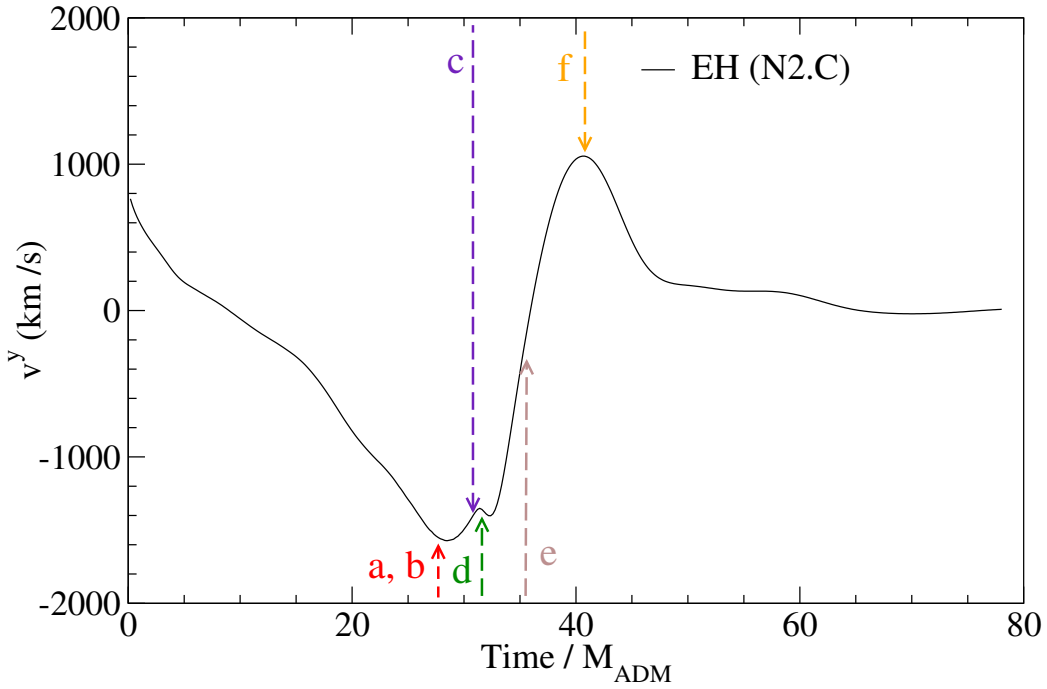

Figure 4.12: The effective velocity $v^y_{\rm LL}$ calculated on the event horizon surface, with the specified snapshots in Fig. 4.13 of the event horizon surface marked. The points a and b occur at $t/M_{\rm ADM} = 27.7$, c at $t/M_{\rm ADM} = 30.8$, d at $t/M_{\rm ADM} = 31.6$ e at $t/M_{\rm ADM} = 35.5$, and f at $t/M_{\rm ADM} = 40.8$.

4.4.1.2 Event Horizon

We would like to compare our quantitative results of the effective velocity $v^y_{\rm LL}$ calculated using the event horizon surface (Fig. 4.12) with qualitative observations of the event horizon's dynamics (Fig. 4.13). We find that the greatest variation in both the event horizon geometry and the value of $v^y_{\rm LL}$ occurs over a period of about $\Delta t/M_{\rm ADM} = 13$ from $t/M_{\rm ADM} = 28$ to $t/M_{\rm ADM} = 41$. At time $t/M_{\rm ADM} = 27.7$, the cusps of the event horizon just begin to become noticeable (Figs. 4.13a and b). One can see in Fig. 4.12 that this is the time at which $v^y_{\rm LL}$ changes from decreasing to increasing. Shortly after[7], at $t/M_{\rm ADM} = 31.1$, the two separate event horizons coalesce into a common event horizon, and the common event horizon rapidly expands to form a convex shape by $t/M_{\rm ADM} = 35.5$ (Figs. 4.13d and e). At this time, we note that $v^y_{\rm LL}$ is rapidly increasing (Fig. 4.12, arrow e); this rapid increase corresponds to the quickly expanding event horizon surface.

We interpret this process as the merging black holes swallowing the gravitational field momentum between the holes. The resulting change in $v^y_{\rm LL}$ can be divided into two distinct portions: (i) one that comes from the changing event horizon surface in space, i.e., the field momentum swallowed by the black holes (in Eq. (4.11), the second term) and (ii) a second that comes from the change of field momentum at the black holes' surface, i.e., the field momentum flowing into the black holes

[7]Note that at $t/M_{\rm ADM} = 31.1$, we (smoothly) modify our gauge condition (Eq. (4.45) and the surrounding discussion). The separate event horizons coalesce at time $t/M_{\rm ADM} = 31.1$ as well; this is a coincidence.

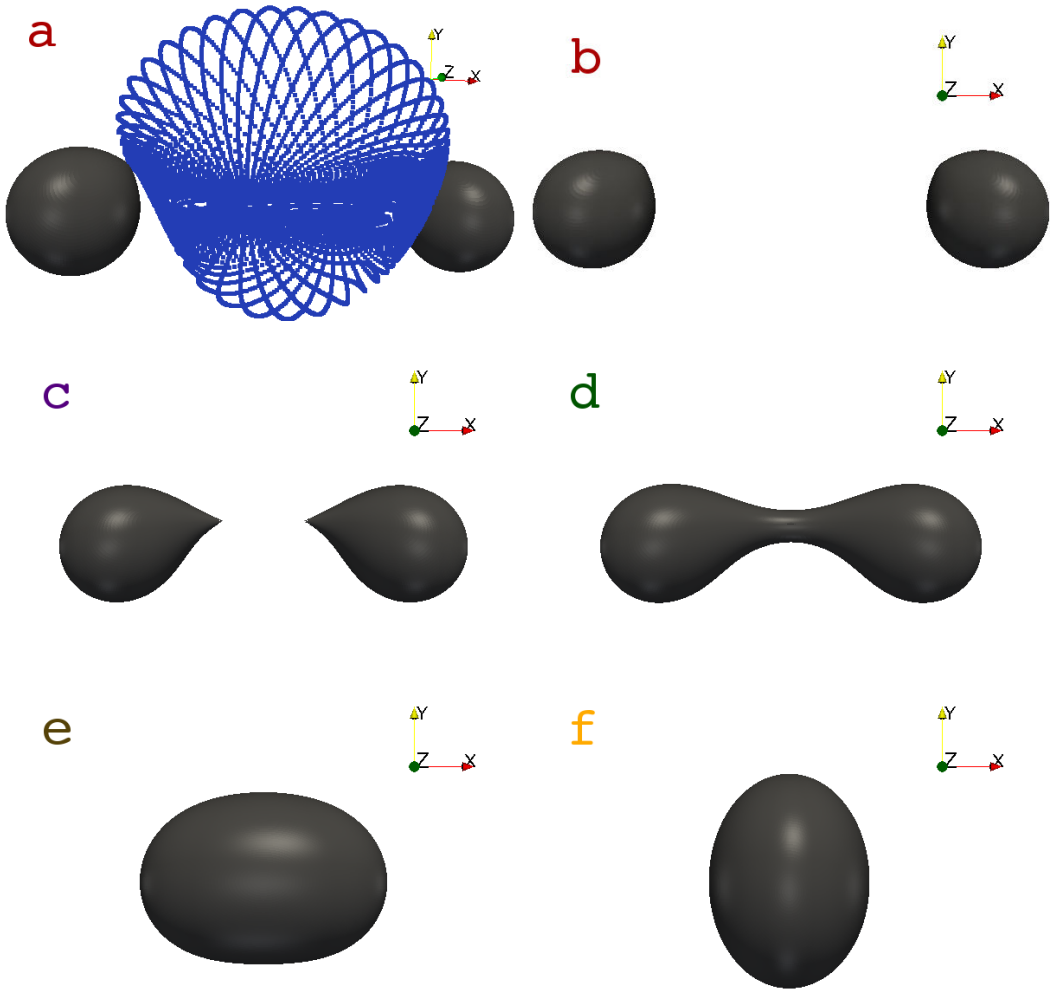

Figure 4.13: Snapshots of the event horizons at the times indicated in Fig. 4.12: a,b, $t/M_{\rm ADM} = 27.7$; c, $t/M_{\rm ADM} = 30.8$; d, $t/M_{\rm ADM} = 31.6$; e, $t/M_{\rm ADM} = 35.5$; f, $t/M_{\rm ADM} = 40.8$. All snapshots are looking down the z axis to the x-y plane, except for shot a, which is slightly skewed (slightly rotated about the y axis) to better see the geodesic structure. In shot a, the future generators of the horizon are visible as small blue dots. Note how the future generators map out a surface that meets the event horizon at the event horizon's cusps; this is where the future generators join the horizon. The data shown are from the high-resolution evolution N2.C.

(in Eq. (4.11), the first term). While this distinction is clearly coordinate dependent, it could, after further investigation, provide an intriguing and intuitive picture of the near-zone dynamics of merging black-hole binaries.

4.4.2 BSSN-Moving-Puncture Results and Gauge Dependence

As described in Section 4.2, the Landau-Lifshitz formalism that we applied to our numerical simulations relies upon a mapping between the curved spacetime of the simulation and an auxiliary flat spacetime. In the asymptotically flat region far from the holes, there is a preferred way to construct this mapping. Consequently, when the surface of integration is a sphere approaching infinite radius, Eq. (4.9b) gives a gauge-invariant measure of the system's total 4-momentum (see, e.g., Section 20.3 of [51]). However, when the surface of integration is in the strong-field region of the spacetime (e.g., when the surface is a horizon), the 4-momentum enclosed is gauge-dependent. The momentum density, a pseudotensor, is always gauge-dependent.

The gauge dependence of the effective velocity can be investigated at late times—when the spacetime has relaxed to its final, stationary configuration—by comparing the velocity obtained on the horizon with gauge-invariant measures of the kick velocity (Fig. 4.11). At the final time in our generalized-harmonic simulation, the effective velocities of the apparent and event horizons agree within tenths of a km/s with the (extrapolated) kick velocity inferred from the gravitational-wave flux; at late times, the horizon effective velocities also agree with the effective velocity measured on coordinate spheres of large radius. At least at late times, then, the effective velocity $v^y_{\rm LL}$ is not significantly affected by our choice of gauge.

To investigate how strongly the influence of the choice of gauge affects our results in the highly dynamical portion of the evolution—when we have no gauge-invariant measure of momentum or velocity—we have evolved initial data that are physically similar using two manifestly different gauge conditions: (i) the generalized-harmonic condition used in our spectral evolutions, and (ii) the 1+log slicing and Gamma-driver shift conditions used in our BSSN-moving-puncture evolutions. Figures 4.14 and 4.15 display the velocity obtained from the horizon integral of the components of the Landau-Lifshitz tensor in the BSSN-moving-puncture evolutions described in Section 4.3.2.2. For comparison, we also plot the velocity obtained for model S1 in the left panel (dashed curve). The most remarkable feature in these plots is a large temporary acceleration of the black holes in the frame-dragging direction. The magnitude of the velocity reaches about 4500 km/s, which is of the order of the superkicks first reported in [32, 30]. In contrast to those inspiraling configurations, however, the black-hole motion reverses during the merger and settles down to a small value of -30 ± 50 km/s.

In order to understand to what extent this behavior is dependent on specific properties of the puncture evolution (such as the particular form of the spurious radiation, which differs in our

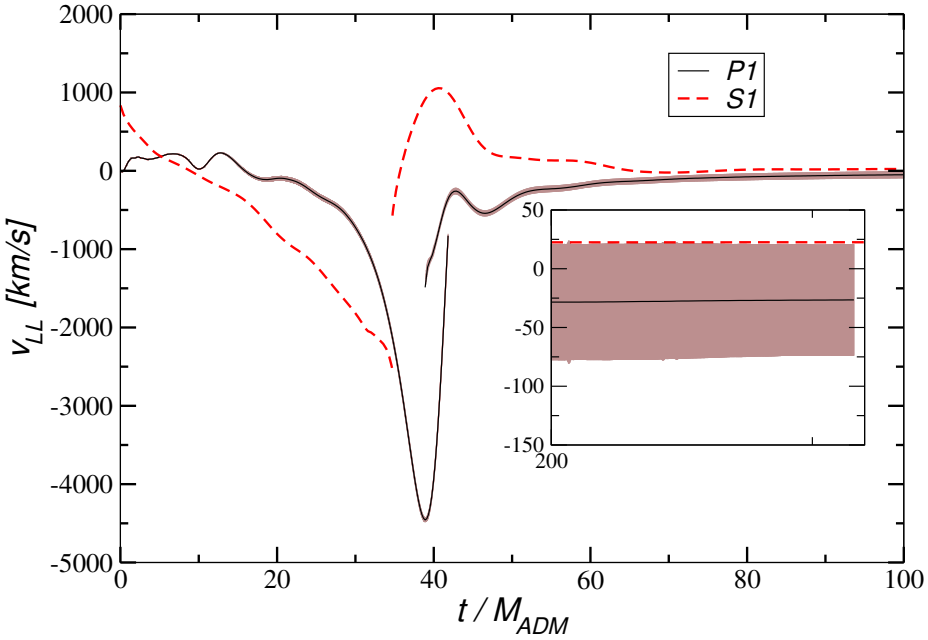

Figure 4.14: The y component of the effective velocity for models P1 (the solid curves) and S1 (the dashed curves). The shaded area represents the numerical uncertainty for the P1 evolution. Prior to merger, the velocities of the individual horizons are identical, for the P1 and S1 simulations, respectively.

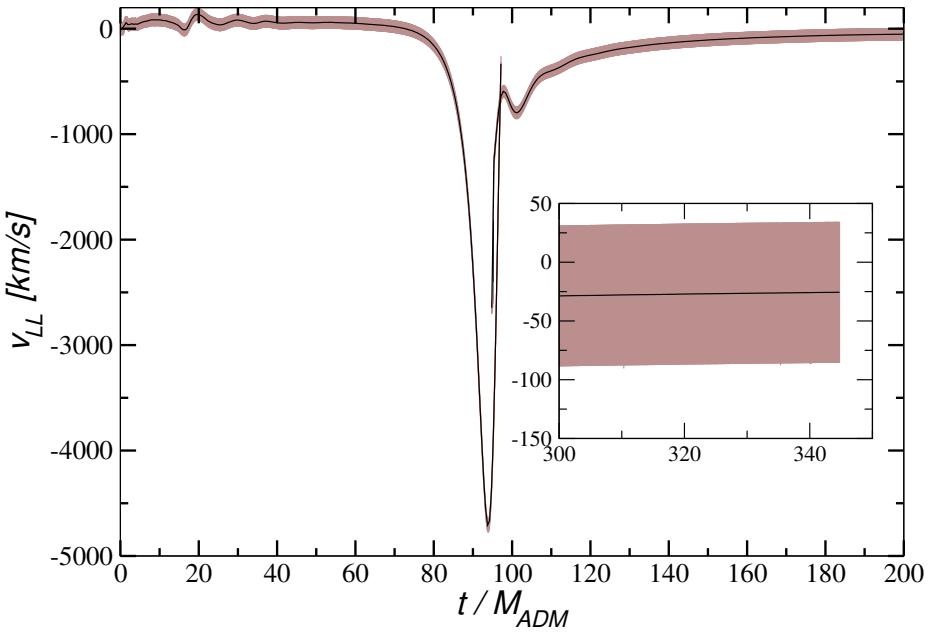

Figure 4.15: The same component of the effective velocity as that in Fig. 4.14, with the error represented identically. This figure shows the effective velocity for the evolution P2 of Table 4.1, however.

generalized-harmonic and BSSN-moving-puncture evolutions), we have performed the following additional simulations: First, we have changed the gauge parameter η in Eq. (4.54) to 0.75 and 1.25. We do not observe a significant change in the behavior of the effective velocity for this modification. Second, in order to gain further insight into the dependence of the effective velocity on the initial separation of the black holes, we have increased the initial separation of the holes to allow for a longer pre-merger interaction phase.

The parameters summarizing the second model are those labeled by P2 in Table 4.1. This simulation was performed with the LEAN code as summarized in Section 4.3.2.1, using a resolution $h_c = M_{ADM}/49.8$. The resulting velocity is shown in Fig. 4.15, and it represents numerical uncertainties as the gray shading around the solid line. The remarkable similarity between this figure and its counterpart Fig. 4.14 for model P1 demonstrates that the numerical results are largely independent of the initial separation.

Comparing the effective velocities for simulations S1 and P1 in Fig. 4.14, the qualitative behavior of the apparent horizons' effective velocities agrees across the two gauges. In both the generalized-harmonic and BSSN-moving-puncture simulations we see the following similarities: (i) during the plunge, the individual apparent horizons accelerate to speeds larger than 1000 km/s in the frame-dragging direction; (ii) when the common horizon forms, its velocity is much smaller in magnitude, because the common horizon has enclosed momentum pointing opposite the frame-dragging direction; and (iii) the velocity relaxes to a value of only tens of km/s that (within numerical uncertainty) agrees with the kick velocity measured using the gravitational-wave flux. The generalized-harmonic and BSSN-moving-puncture effective velocities do exhibit significant quantitative differences, however; e.g., the slopes of the initial acceleration in the frame-dragging direction are quite different in the two cases. These differences are expected given the different choices of gauge and the gauge-dependent nature of the effective velocity in the strong-field region.

Still, we find these results encouraging; two popular gauge choices used in the numerical-relativity community do give remarkable qualitative agreement. This qualitative agreement certainly does not constitute a proof of a gauge independence of our findings; however, we feel encouraged in our hope that the gauge dependence in practice is not too severe, at least for the set of gauges actually used in numerical simulations. Most importantly from a practical point of view, these results suggest that it is possible that such local descriptions can be derived from the current generation of BBH codes without the different numerical-relativity groups having to agree upon one and the same gauge choice for (at least qualitative) comparisons of their momentum densities and effective velocities. Future investigations using a wider class of coordinate conditions should further clarify the significance of gauge choices in this context.

4.4.3 Comparison with Post-Newtonian Predictions

In this section, we compare our results to post-Newtonian predictions. For each comparison, first the S1 data set (Table 4.1) is presented along with post-Newtonian predictions of a corresponding initial configuration, then the H1 data set (Table 4.1) is presented along with its post-Newtonian predictions. The post-Newtonian trajectories for spinning point particles were generated by evolving the post-Newtonian equations of motion [74, 75]. The difference between the two data sets are (i) set H1 begins with a larger initial separation than set S1, and (ii) set H1 is evolved in a nearly harmonic gauge.[8] Comparing evolutions of data sets S1 and H1 illustrates how these two effects improve the comparisons one can make with post-Newtonian predictions. The top panels of Figs. 4.16–4.18 are a comparison between the highest-resolution evolution (N2.C) of the initial data set S1 and several orders of post-Newtonian predictions; the right panels of Figs. 4.16–4.18 are analogous comparisons between post-Newtonian results and those from a numerical-relativity evolution beginning from the initial data set H1.

Figure 4.16 shows that the bulk, longitudinal motions (i.e., motion in the x direction) agree both qualitatively and quantitatively with post-Newtonian predictions through most of the plunge (i.e., up until a few $M_{\rm ADM}$ before the formation of the common apparent horizon) for both data sets. In the top panel of Fig. 4.16, we have added another 2.5 PN curve that is offset vertically such that the 2.5 PN coordinate velocity agrees exactly with the numerical effective velocity at $t/M_{\rm ADM} \approx 18.34$; this is done in order to account for the period of initial relaxation in the S1 data set. Quantitative agreement is then found between 2.5 PN predictions and both the effective and coordinate velocities from $t/M_{\rm ADM} \approx 5$ through $t/M_{\rm ADM} \approx 20$. The bottom panel of Fig. 4.16, which has less of an initial relaxation because of the increased separation, shows excellent agreement between both the effective and coordinate velocities and the 2.0 PN and 2.5 PN predictions.

For the smaller (though more interesting) transverse motion (i.e., the motion along the y direction), we find only qualitative agreement between the numerical data and post-Newtonian predictions. Spin-orbit coupling (more specifically, frame-dragging plus spin-curvature coupling, see Eq. (5.11) of paper I and the discussion thereafter) causes the holes to move in the $-y$ direction during the plunge, reaching speeds of order 1000 km/s before the holes merge. The post-Newtonian expansion in our calculations (see paper I and [74, 75]) uses a harmonic gauge and a physical spin supplementary condition (SSC), $S^{\alpha\beta}u_\beta = 0$, where $S^{\alpha\beta}$ is the spin angular momentum tensor of the black hole and u^β its four-velocity (see e.g., Section II B of Paper I).

Specifically, in Paper I, the authors found that for an equal-mass binary with anti-aligned spins at leading 1.5 PN order, the black holes' effective velocity $v^y_{\rm LL}$ is not equal to the post-Newtonian

[8] Note that even if simulation H1 were exactly (instead of only approximately) harmonic, there would be no guarantee that H1 would evolve in the same harmonic gauge as that gauge in which we compute the PN trajectories. This is because of the residual gauge freedom within the set of harmonic coordinates (see, e.g., [76]).

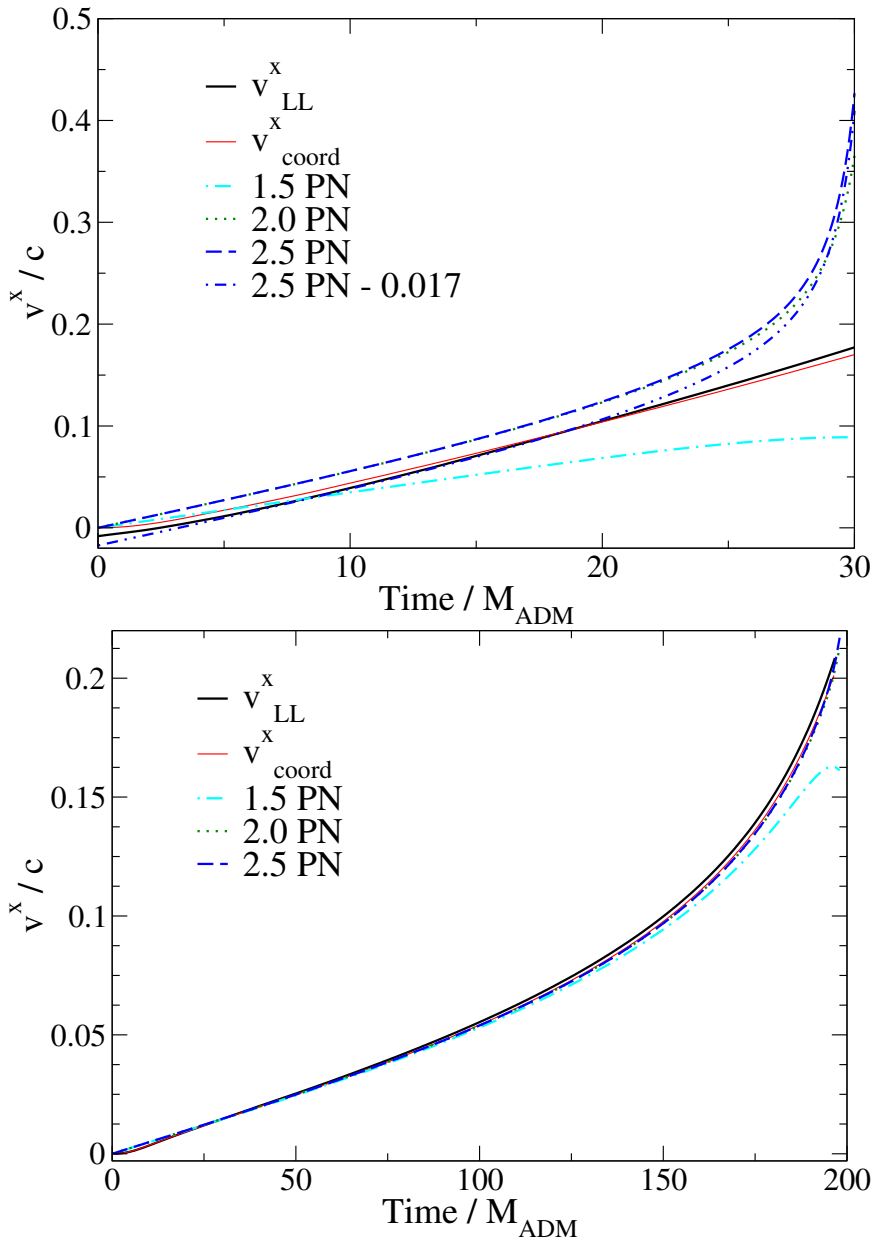

Figure 4.16: A comparison of numerical and post-Newtonian longitudinal velocities (i.e., v^x/c) versus time. The predicted coordinate velocities at several post-Newtonian orders are shown as broken curves. *Top:* A comparison of S1 numerical data and post-Newtonian predictions. The numerical and post-Newtonian curves agree qualitatively. When the 2.5 PN curve is offset by a certain amount, it agrees quantitatively with the coordinate velocity $v^x_{\rm coord}$ and the effective velocity $v^x_{\rm LL}$. *Bottom:* A comparison of H1 numerical data and PN predictions. The effective velocity $v^x_{\rm LL}$ (thick black line) closely tracks the coordinate velocity $v^x_{\rm coord}$; both numerical curves also agree well with the 2.0 PN and 2.5 PN curves.

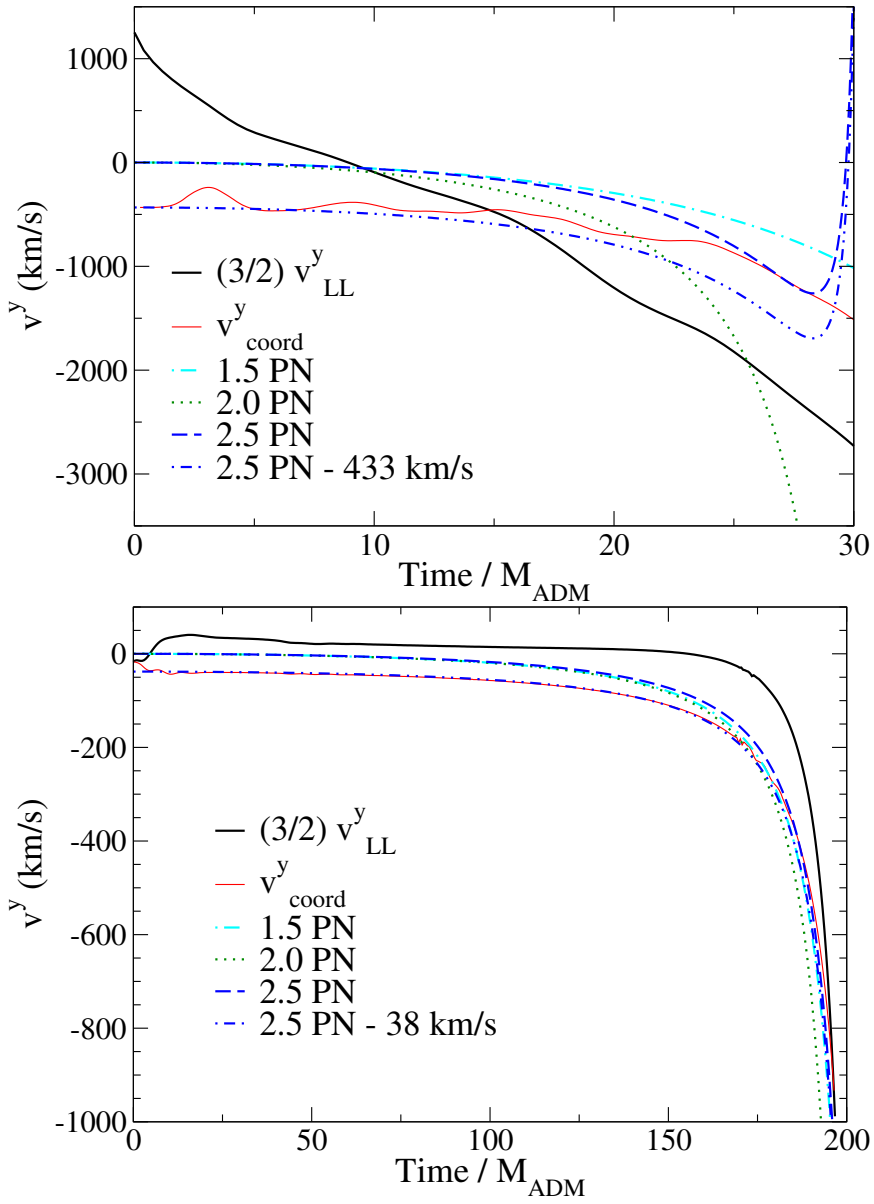

Figure 4.17: A comparison of numerical and post-Newtonian transverse velocities (i.e., v^y in km/s) versus time. The top panel shows numerical results from simulation S1, while the bottom panel shows numerical results from simulation H1. The predicted coordinate velocity at several post-Newtonian orders are shown as broken curves. The effective velocity is shown in black; it has been rescaled by a factor of 3/2 in order to aid comparison with the post-Newtonian point-particle velocities, as discussed in Section 4.4.3. The turn in the 2.5 PN curves is due to a 2.5 PN-order, spin-orbit term becoming quite large at a separation of roughly $r/M_{\rm ADM} \approx 2$. This is related to the post-Newtonian approximation breaking down at this small separation.

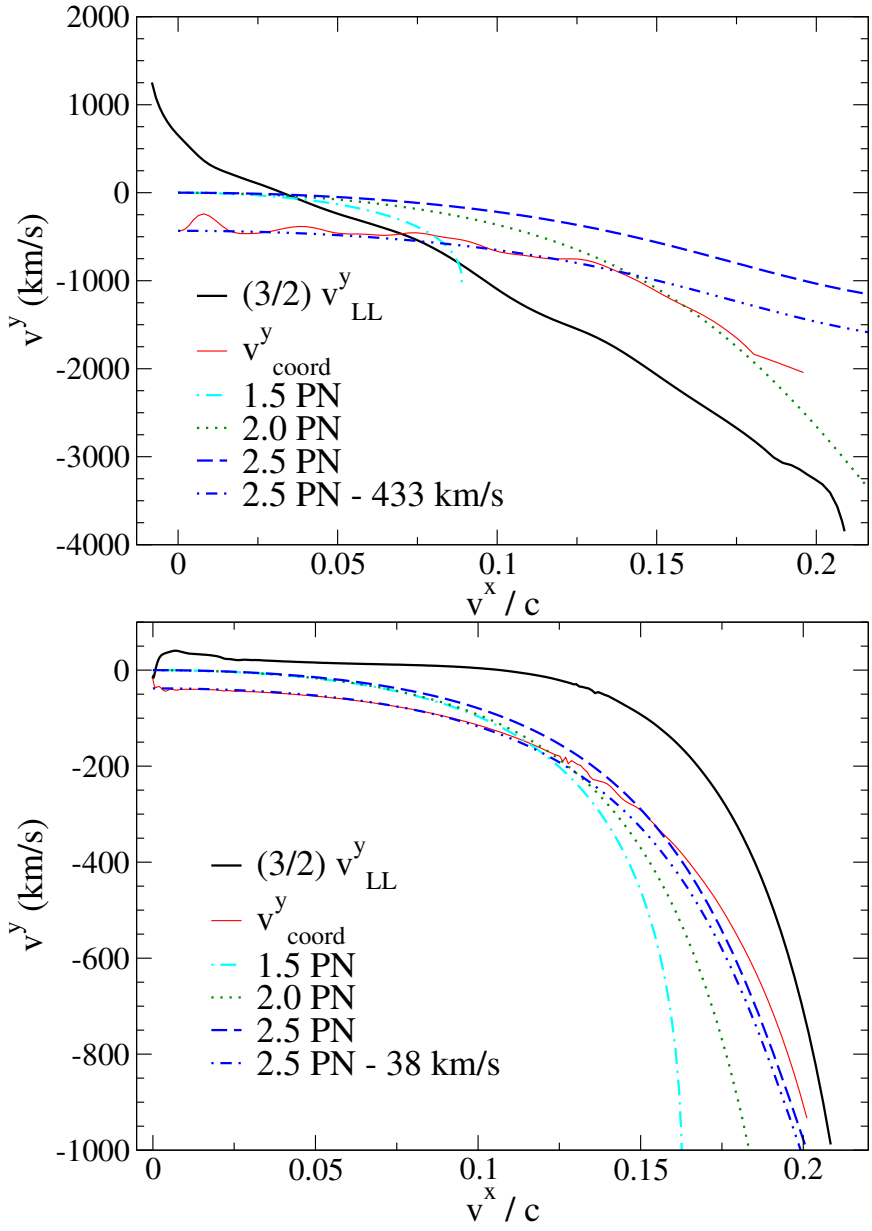

Figure 4.18: A comparison of numerical and post-Newtonian velocities. In the figure, v^y in km/s is plotted against v^x/c. The effective velocity $v^y_{\rm LL}$ of the highest-resolution (N2.C) evolution of initial data S1 (Table 4.1), on the top, and of the evolution of initial data H1 (Table 4.1), on the bottom, are shown as a thick black line. The predicted coordinate velocity at several post-Newtonian orders are shown as broken curves. The transverse effective velocities only agree qualitatively with post-Newtonian predictions; however, the coordinate velocity agrees very well with post-Newtonian predictions. In the top panel, the coordinate velocity has been artificially truncated shortly before merger, because at that point we do not have a good measure of the coordinate velocity. The effective velocity has been rescaled by a factor of 3/2 to aid comparison with the post-Newtonian point-particle velocities, as discussed in Section 4.4.3.

coordinate velocity of a point particle; rather, the coordinate velocity is 3/2 times the effective velocity. Roughly speaking, this difference arises from the fact that in the Landau-Lifshitz description one defines the velocity in terms of a surface integral over a body of finite size divided by its mass-energy, which is different from the velocity defined by the derivative of the center-of-mass world line of the particle. This introduces effects due to the field momentum within the body that are not present in the strictly center-of-mass description. Paper I's Sections II B, II C, and V C, as well as its Table I explain this fact in greater detail. Because the majority of the comparison between post-Newtonian and numerical-relativity results takes place at separations and speeds during which the leading, 1.5 PN-order terms contribute most strongly, we continue to use the factor of 3/2 to convert between coordinate and effective velocities for higher post-Newtonian terms.

In Figs. 4.17 and 4.18, we compare the post-Newtonian, point-particle y velocity with the numerical y-coordinate velocity and 3/2 of the numerical effective y velocity, $v^y_{\rm LL}$. For the comparison to the S1 data set, we find qualitative agreement with both the effective and coordinate velocities and the post-Newtonian predictions. We think this agreement is not better because of the large initial relaxations present in the S1 data set related to small initial separation. The small separation of the black holes also poses problems for the post-Newtonian approximation. As one can see, in Fig. 4.17 the 2.5 PN curve decelerates and the velocity changes sign. This happens because a next-to-leading-order, spin-orbit term becomes significantly larger at this point (a post-Newtonian separation of roughly $r/M_{\rm ADM} \approx 2$). This suggests that the post-Newtonian approximation is moving out of its domain of convergence. However, in the H1 comparison, we find excellent agreement between the coordinate velocity and the 2.5 PN prediction, but only qualitative agreement between the effective velocity and post-Newtonian predictions. In these figures, offsets of -433 km/s (for S1 data) and -38 km/s (for H1 data) have been used to make 2.5 PN coordinate velocity agree better with numerical results. These offsets are well motivated, because the numerical initial data were chosen so that the initial total momentum of the entire spacetime vanishes. In the post-Newtonian approximation, one would expect that there would be and initial nonvanishing initial y velocity of (see Table I of Paper I)

$$v^y_{\rm coord} = \frac{\chi}{4(r_0/M_{\rm ADM})^2}\,, \tag{4.18}$$

where χ is the spin parameter of each black hole, and r_0 is the hole's initial separation. This corresponds to -616 km/s for the S1 data, and -42 km/s for H1 data. Again, the agreement is qualitative for S1 data, and quantitative for H1 data.

One final comparison we make between the H1 data set and post-Newtonian predictions is the near-field momentum density, shown in Fig. 4.19. The numerical data (left column) come from the harmonic evolution H1, while the 1.5 PN momentum density (right column) is computed from Eqs. (A2a)–(A2c) in Paper I using the numerical-relativity, black-hole trajectories. The top panels,

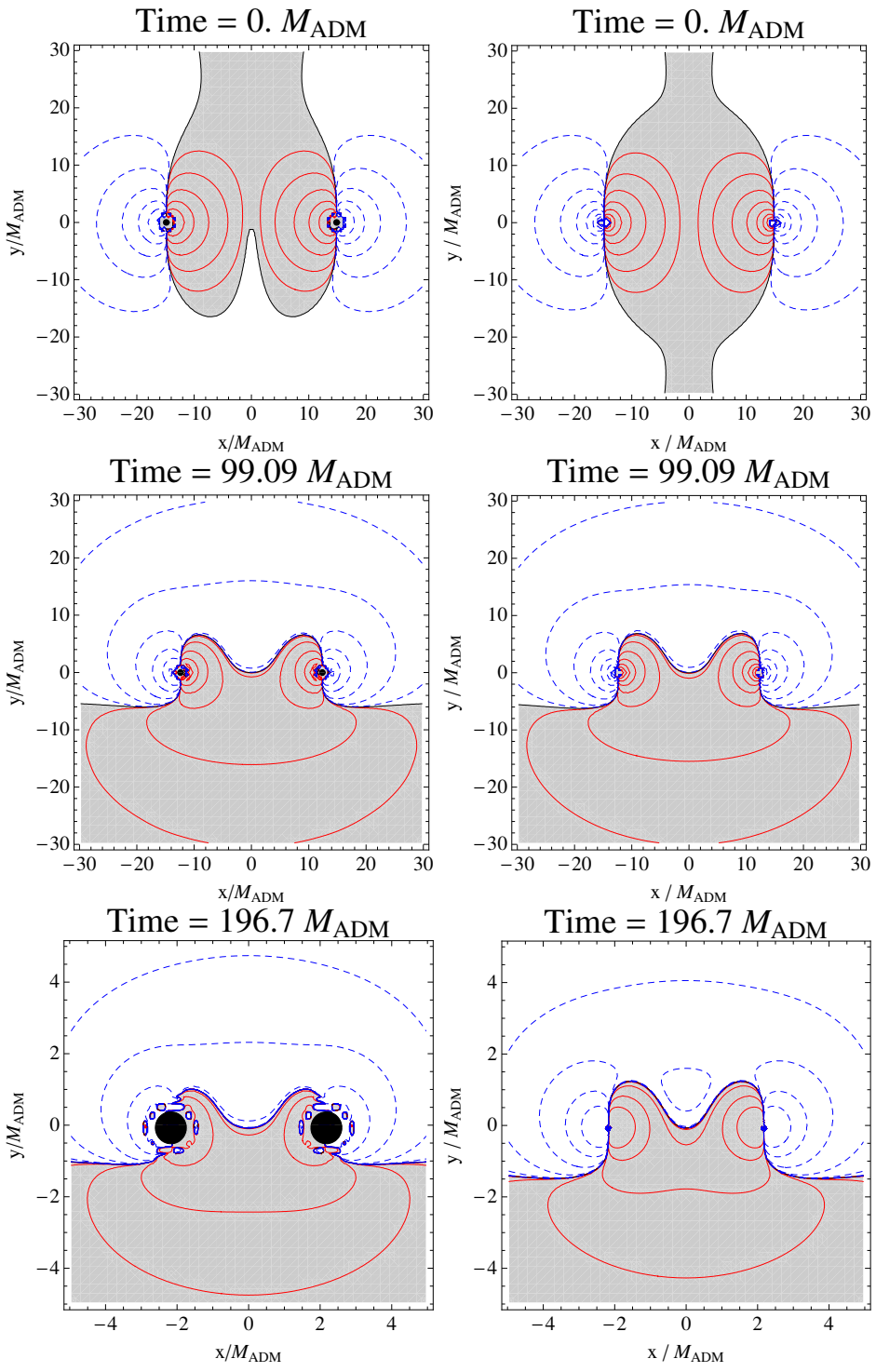

Figure 4.19: Comparison of numerical (left column) and post-Newtonian (right column) y-momentum density. The numerical data comes from the harmonic evolution, H1, described in Appendix 4.A.2. The 1.5 PN momentum density is computed from Eqs. (A2a)–(A2c) in Paper I, using the numerical-relativity, black-hole trajectories. As in Fig. 4.9, contours represent powers of 10 in y-momentum density. The positive y-momentum-density contours are shown in red, and the negative ones are shown in blue. The region of positive y-momentum density is shaded grey. In the numerical plots, the apparent horizons are shown in black.

comparing the momentum densities of the H1 initial-data set to the post-Newtonian results, show differences that presumably come from the fact that the numerical-relativity initial data is out of equilibrium at the start of the evolution. The center panels show the momentum densities agree very well once enough time has elapsed for the spacetime to relax and for the spurious radiation to be emitted (but before the holes have fallen too close together). The bottom panels make a final comparison just before the holes get close enough to merge, and it shows differences appearing between the numerical data and the post-Newtonian predictions very near the holes—which could be an indication of the breakdown of the post-Newtonian approximation.

These comparisons with post-Newtonian predictions have yielded several interesting results. The primary result of these comparisons is the surprisingly good agreement found between post-Newtonian predictions and the coordinate velocities, especially from the harmonic-gauge evolution. Also, the longitudinal effective and coordinate velocities track each other closely; consequently, the longitudinal effective velocity agrees with post-Newtonian predictions. The transverse effective velocities agree qualitatively with the post-Newtonian predictions, in the sense that they both indicate that the holes accelerate in the expected frame-dragging direction to speeds of order 1000 km/s. Finally, we have also found the qualitative agreement between the harmonic-gauge numerical data and the post-Newtonian approximation also holds for the near-zone momentum density after the initial data relaxes but before the proper separation of the holes is too small.

4.5 Conclusion

With the goal of building up greater physical intuition, we have used the Landau-Lifshitz formalism to explore the nonlinear dynamics of fully relativistic simulations of a head-on BBH plunge, merger, and ringdown. We have defined and computed an effective velocity of the black holes in terms of the momentum and mass-energy enclosed by their horizons, and we have interpreted the holes' transverse motion—which reaches speeds of order 1000 km/s—as a result of momentum flow between the holes and the gravitational field of the surrounding spacetime. We have found that the merged hole's final effective velocity—about 20 km/s—agrees with the recoil velocity implied by the momentum carried off by the emitted gravitational waves.

Our measures of linear momentum and effective velocity are gauge-dependent. Nevertheless, after comparing simulations of comparable initial data in generalized-harmonic and BSSN-moving-puncture gauges, we observed weak gauge dependence for the generalized-harmonic and BSSN-moving-puncture evolutions of this paper. Additionally, we have found surprisingly good agreement between the holes' effective and coordinate velocities, and, at late times, the holes' final effective velocities and gauge-invariant measures of the kick velocity agree.

These results bode well for future explorations of momentum flow in fully relativistic, numerical simulations of more astrophysically realistic binaries. We are particularly eager to investigate sim-

ulations of superkick BBH mergers (the inspiral of a superkick configuration was considered using the post-Newtonian approximation in Paper I). Other future work includes studies of the linear and angular momentum flow in inspiraling (rather than head-on) mergers, as well as mergers with larger spins.

4.A Appendix: Excision Initial Data

4.A.1 Superposed-Kerr-Schild (SKS) Initial Data

The initial data for the generalized-harmonic simulations presented in this paper were constructed using the methods described in [55]. In this appendix, we describe in more detail these initial data (which we summarized in Section 4.3.1.1).

A 3+1 (space-time) decomposition splits the spacetime metric $g_{\mu\nu}$ into a spatial metric γ_{ij}, lapse α, and shift β^i, i.e.,

$$ds^2 = g_{\mu\nu}dx^\mu dx^\nu = -\alpha^2 dt^2 + \gamma_{ij}(dx^i + \beta^i dt)(dx^j + \beta^j dt) \ . \tag{4.19}$$

On the initial spatial slice (at time $t = 0$), the initial data must specify the spatial metric γ_{ij} and the extrinsic curvature K_{ij}, which is related to the time derivative of the spatial metric by

$$\partial_t \gamma_{ij} = -2\alpha K_{ij} + 2\nabla_{(i}\beta_{j)} \ . \tag{4.20}$$

We use the quasiequilibrium formalism [77, 78, 79, 80, 81], in which γ_{ij} and K_{ij} are expanded as

$$\gamma_{ij} = \psi^4 \tilde{\gamma}_{ij} \ , \tag{4.21}$$

$$K_{ij} = A_{ij} + \frac{1}{3}\gamma_{ij} K \ . \tag{4.22}$$

The conformal metric $\tilde{\gamma}_{ij}$, the trace of the extrinsic curvature K, and their time derivatives can be chosen freely. We adopt the quasiequilibrium choices

$$\tilde{u}_{ij} := \partial_t \tilde{\gamma}_{ij} = 0 \ , \tag{4.23}$$

$$\partial_t K = 0 \ . \tag{4.24}$$

The remaining free data are based on a weighted superposition of two boosted, spinning Kerr-Schild

black holes (Eqs. (45)–(46) of [55]):

$$\tilde{\gamma}_{ij} := f_{ij} + \sum_{a=1}^{2} e^{-r_a^2/w_a^2} \left(\gamma_{ij}^a - f_{ij}\right) , \tag{4.25}$$

$$K := \sum_{a=1}^{2} e^{-r_a^2/w_a^2} K_a . \tag{4.26}$$

Here f_{ij} is the metric of flat space, r_a is the Euclidean distance from the center of the apparent horizon of hole a, and γ_{ij}^a and K_a are the spatial metric and mean curvature of a boosted (with velocity $\tilde{v}^i$), spinning (with spin $\tilde{S}/\tilde{M}^2$) Kerr-Schild black hole centered at the initial position of hole a. In this paper, we choose $\tilde{v}^i = 0$ (since we seek data describing holes falling head-on from rest), $\tilde{M}/M_{\rm ADM} = 0.39$, and $\tilde{S}/\tilde{M}^2 = 0.5$. The Gaussian weighting parameter is chosen to be $w_a = d/3$, where d is the initial coordinate separation between the two holes; note that this choice causes the conformal metric to be flat everywhere except near each hole. The holes are located at coordinates $(x, y, z) = (x_0 \equiv \pm d/2, 0, 0)$.

These free data are then inserted into the extended conformal thin sandwich (XCTS) equations (e.g., Eqs. (13)–(15) of [78])[9], which are then solved for the conformal factor ψ, the lapse α, and the shift β^i. The XCTS equations are solved using a spectral elliptic solver [82] on a computational domain with (i) a very large outer boundary (which is chosen to be a coordinate sphere with radius $r/\tilde{M} = 10^9$), and (ii) with the region inside the holes' apparent horizons excised. The excision surfaces $\mathcal{S}$ are surfaces of constant Kerr radius $r_{\rm Kerr}$, where

$$\frac{x^2 + y^2}{r_{\rm Kerr}^2 + \tilde{S_a}^2/\tilde{M_a}^2} + \frac{z^2}{r_{\rm Kerr}^2} = 1 . \tag{4.27}$$

The excision surfaces are the apparent horizons of the holes; this is enforced by the boundary condition given by Eq. (48) of [78]. On the apparent horizon, the lapse satisfies the boundary condition

$$\alpha\psi = 1 + \sum_{a=1}^{2} e^{-r_a^2/w_a^2} (\alpha_a - 1) \text{ on } \mathcal{S} , \tag{4.28}$$

where α_a is the lapse of the Kerr-Schild metric corresponding to hole a. The shift satisfies

$$\beta^i = \alpha s^i - \Omega_r \xi^i \text{ on } \mathcal{S} . \tag{4.29}$$

The first term in Eq. (4.29) implies that the holes are initially at rest, and the second term determines the spin of the hole. To make the spin point in the $\pm z$ direction with magnitude $S/M_{\rm Chr}^2 = 0.5$ (measured using the method described in Appendix A of [55]), we choose $M_{\rm ADM}\Omega_r = \mp 0.244146$

[9] The XCTS equations are also given by Eqs. (37a)–(37d) of [55], aside from the following typographical error: the second term in square brackets on the right-hand side of Eq. (37c) should read $(5/12)K^2\psi^4$ (not $(5/12)K^4\psi^4$).

and $\xi^i = \partial_\phi$, where ∂_ϕ is the rotation vector on the apparent horizon corresponding to rotation about the $+z$ axis. On the outer boundary $\mathcal{B}$, the spacetime metric is flat:

$$\psi = 1 \text{ on } \mathcal{B} , \tag{4.30}$$

$$\alpha\psi = 1 \text{ on } \mathcal{B} . \tag{4.31}$$

Our initial data, Eq. (4.29), are constructed in a frame comoving with the black holes. Thus, an asymptotic rotation, expansion, and translation in the comoving shift β^i cause the holes to initially have radial, angular, or translational velocity in the inertial frame. This corresponds to the boundary condition

$$\beta^i = \left(\mathbf{\Omega}_0 \times \mathbf{r}\right)^i + \dot{a}_0 r^i + V_0^i \text{ on } \mathcal{B} . \tag{4.32}$$

We choose $\dot{a}_0 = 0$ and $\mathbf{\Omega}_0 = 0$. To make the total momentum of the initial data vanish, we choose $V^y = -0.001444$ and $V^x = V^z = 0$. This choice gives the holes an initial coordinate velocity of 0.001444 (433 km/s in physical units) in the $-y$ direction (see Fig. 4.7). Note that the initial data are evolved in inertial, not comoving, coordinates, so that the shift during the evolution is different from the comoving shift, β^i, obtained from the XCTS equations. The former asymptotically approaches zero, not a constant vector V_0^i.

4.A.2 Superposed-Harmonic-Kerr (SHK) Initial Data

We also present a simulation, H1 in Table 4.1, that is similar to S1, but which starts at a larger initial separation between the holes and which evolves in a gauge that is nearly harmonic. The construction of this superposed-harmonic-Kerr initial data for this run follows that of the superposed-Kerr-Schild (S1) initial data described in Appendix 4.A.1. The differences are as follows:

The first difference is our choice of coordinates. In Appendix 4.A, the quantities γ^a_{ij}, K_a, and α_a that appear in Eqs. (4.25), (4.26), and (4.28) refer to the three-metric, the trace of the extrinsic curvature, and the lapse function of the Kerr metric in Kerr-Schild coordinates. Here we still use Eqs. (4.25), (4.26), and (4.28), but γ^a_{ij}, K_a, and α_a now refer to the three-metric, the trace of the extrinsic curvature, and the lapse function of the Kerr metric in fully harmonic coordinates, Eqs. (22)–(31), (41), and (43) of [83]. Furthermore, the computational domain is excised on surfaces of constant Boyer-Lindquist radius, $r_{\rm BL}$, where

$$\frac{x^2 + y^2}{\left(r_{\rm BL} - \tilde{M}_a\right)^2 + \tilde{S}_a{}^2/\tilde{M}_a{}^2} + \frac{z^2}{\left(r_{\rm BL} - \tilde{M}_a\right)^2} = 1 . \tag{4.33}$$

The initial coordinate separation was chosen to be $d/M_{\rm ADM} = 29.73$ and the Gaussian weighting parameter that appears in Eqs. (4.25), (4.26), and (4.28) is $w_a = d/9$. To obtain $S/M^2_{\rm Chr} = \{0, 0, \pm 0.5\}$ we choose $M_{\rm ADM}\Omega_r = \mp 0.261332$ in Eq. (4.29), and to make the total momentum

vanish we choose $V_0^y = -0.0000582185$ in Eq. (4.32).

Solving the XCTS equations results in initial data that is approximately harmonic. Harmonic coordinates satisfy $\nabla^c \nabla_c x^a = 0$, or equivalently, $\Gamma_a := \Gamma_{ab}{}^b = 0$. We can evaluate the degree to which the harmonic-gauge condition is satisfied in our initial data by examining the normalized magnitude of Γ_a:

$$f := \left(\frac{\sum_a |\Gamma_a|^2}{\frac{1}{4}\sum_a \sum_b |\Gamma_{ab}{}^b|^2} \right)^{1/2} . \tag{4.34}$$

The denominator consists of the sum of squares of terms that must cancel to produce $\Gamma_a = 0$, so that $f = 1$ corresponds to complete violation of the harmonic coordinate condition. On the apparent horizons $f < 0.049$, while in the asymptotically flat region far from the holes $f < 0.0083$. In the regions where the Gaussians in Eqs. (4.25), (4.26), and (4.28) transition the XCTS free data from harmonic Kerr to conformally flat we cannot expect the data to be strongly harmonic, and we find that $f < 0.12$.

The techniques employed in the spectral evolution from this SHK initial data follow those used for the SKS initial data as described in Appendix 4.B.1. In particular, the generalized-harmonic-gauge source function, H_a, Eq. (4.14), is constructed by demanding that $\tilde{H}_{a'}$ remains frozen to its value in the initial data. The evolution proceeds in nearly harmonic gauge because of the way the initial data are constructed.

Three of these H1 evolutions were performed at resolutions of approximately 61^3, 67^3, and 72^3 grid points. The constraints were found to be convergent. The data presented in this paper is taken from the highest-resolution run. These simulations are specifically constructed to provide data for comparison with PN approximations, which restricts our choice of gauge to remain approximately harmonic. Currently this gauge choice prevents us from continuing our H1 evolutions beyond the plunge phase, and we have not observed the formation of a common horizon.

4.B Appendix: Numerical Methods for Evolutions

4.B.1 Generalized-Harmonic Evolutions

We evolve the initial data summarized in Section 4.3.1.1 using the Caltech-Cornell pseudospectral code SpEC. This code and the methods it employs are described in detail in [84, 85, 4]. Some of these methods have been simplified for the head-on problem discussed here, and others have been modified to account for a nonzero center-of-mass velocity; consequently, we will describe the important differences here.

We evolve a first-order representation [62] of the generalized-harmonic system [59, 60, 61]. We handle the singularities by excising the black-hole interiors from the computational domain. Our

outer boundary conditions [62, 86, 87] are designed to prevent the influx of unphysical constraint violations [88, 89, 90, 91, 92, 93, 94] and undesired incoming gravitational radiation [95, 96], while allowing outgoing gravitational radiation to pass freely through the boundary. We find the event horizon using the techniques of [97], except that for calculating derivatives of quantities on the event horizon surface, we use a sixth-order, finite-differencing stencil, which is an improvement on the second-order stencil used in [97]. (The formation of cusps on the event horizon prevents us from taking spectral derivatives there.)

We employ the dual-frame method described in [84]: we solve the equations in an "inertial frame" that is asymptotically Minkowski, but our domain decomposition is fixed in a "comoving frame" that is allowed to shrink, translate, and distort relative to the inertial frame. The positions of the centers of the black holes are fixed in the comoving frame; we account for the motion of the holes by dynamically adjusting the coordinate mapping between the two frames. Note that the comoving frame is referenced only internally in the code as a means of treating moving holes with a fixed domain. Therefore, all coordinate quantities (e.g., black-hole trajectories) mentioned in this paper are inertial-frame values unless explicitly stated otherwise.

The mapping from comoving to inertial coordinates is changed several times during the run. During the plunge phase, we denote the mapping by $\mathcal{M}_{\rm p}(x^i, x'^i)$, where primed coordinates denote the comoving frame and unprimed coordinates denote the inertial frame. Explicitly, $\mathcal{M}_{\rm p}(x^i, x'^i)$ is the mapping

$$x = F(r', t) \sin\theta' \cos\phi' \,, \tag{4.35}$$

$$y = F(r', t) \sin\theta' \sin\phi' + e^{-r'^2/r_{\rm T}'^2} Y(t) \,, \tag{4.36}$$

$$z = F(r', t) \cos\theta' \cos\phi' \,, \tag{4.37}$$

where

$$F(r', t) := r' \left\{ a(t) + [1 - a(t)] \frac{r'^2}{R_0'^2} \right\} \,. \tag{4.38}$$

Here $a(t)$ and $Y(t)$ are functions of time, (r', θ', ϕ') are spherical polar coordinates in the comoving frame centered at the origin, and R_0' and $r_{\rm T}'$ are constants. For the choice $R_0' = \infty$ and $r_{\rm T}' = \infty$, the mapping is simply an overall contraction by $a(t) \leq 1$ plus a translation $Y(t)$ in the y direction. Choosing R_0' equal to the outer-boundary radius, $R_{\rm max}'$, and choosing $r_{\rm T}' \sim R_{\rm max}'/6$ causes the map to approach the identity near the outer boundary; this prevents the outer boundary from falling close to the strong-field region during merger, and makes it easier to keep the outer-boundary motion smooth through the merger/ringdown transition. The functions $a(t)$ and $Y(t)$ are determined by dynamical control systems as described in [84]. These control systems adjust $a(t)$ and $Y(t)$ so that

the centers of the apparent horizons remain stationary in the comoving frame. For the evolutions presented here, we use $R'_0/M_{\rm ADM} = 532.2 = 1.1 R'_{\rm max}/M_{\rm ADM}$ and $r'_{\rm T}/M_{\rm ADM} = 31.21 = 4d_0/M_{\rm ADM}$, where d_0 is the initial separation of the holes.

The gauge freedom in the generalized-harmonic system is fixed via a freely specifiable, gauge source function, H_a, that satisfies the constraint

$$0 = \mathcal{C}_a := \Gamma_{ab}{}^{b} + H_a \ , \tag{4.39}$$

where $\Gamma^{a}{}_{bc}$ are the spacetime Christoffel symbols. To choose this gauge source function, we define a new quantity $\tilde{H}_a$ that transforms like a tensor and agrees with H_a in inertial coordinates (i.e., $\tilde{H}_a = H_a$). Then, we choose $\tilde{H}_a$ so that the constraint, Eq. (4.39) is satisfied initially, and we demand that $\tilde{H}_{a'}$ is constant in the moving frame.

Shortly before merger (at time $t_1/M_{\rm ADM} = 31.1$), we make two modifications to our algorithm to reduce numerical errors and gauge dynamics during merger. First, we begin controlling the size of the individual apparent horizons so that they remain constant in the comoving frame, and, therefore, they remain close to their respective excision boundaries. This is accomplished by changing the map between comoving and inertial coordinates as follows. We define the map $\mathcal{M}_{\rm AH_1}(\tilde{x}^i, x'^i)$ for black hole 1 as

$$\begin{aligned}
\tilde{x} &= x'_{\rm AH_1} + \bar{r}\sin\theta'\cos\phi', && (4.40)\\
\tilde{y} &= y'_{\rm AH_1} + \bar{r}\sin\theta'\sin\phi', && (4.41)\\
\tilde{z} &= z'_{\rm AH_1} + \bar{r}\cos\theta', && (4.42)\\
\bar{r} &:= r' - e^{-(r'-r'_0)^3/\sigma_1^3}\lambda_1(t), && (4.43)
\end{aligned}$$

where (r', θ', ϕ') are spherical polar coordinates centered at the (fixed) comoving-coordinate location of black hole 1, which we denote as $(x'_{\rm AH_1}, y'_{\rm AH_1}, z'_{\rm AH_1})$. The constant $R'_{\rm AH_1}$ is the desired average radius (in comoving coordinates) of black hole 1. Similarly, we define the map $\mathcal{M}_{\rm AH_2}(\tilde{x}^i, x'^i)$ for black hole 2. Then, the full map from the comoving coordinates x'^i to the inertial coordinates x^i is given by

$$\mathcal{M}_{\rm m}(x^i, x'^i) := \mathcal{M}_{\rm p}(x^i, \bar{x}^i)\mathcal{M}_{\rm AH_2}(\bar{x}^i, \tilde{x}^i)\mathcal{M}_{\rm AH_1}(\tilde{x}^i, x'^i) \ . \tag{4.44}$$

The constants are chosen to be $\sigma_1/M_{\rm ADM} = 0.780$, $\sigma_2/M_{\rm ADM} = 0.780$, and $r'_0/M_{\rm ADM} = 1.01$. The functions $\lambda_1(t)$ and $\lambda_2(t)$ are determined by dynamical control systems that drive the comoving-coordinate radius of the apparent horizons towards their desired values $R'_{\rm AH_1}/M_{\rm ADM} = R'_{\rm AH_2}/M_{\rm ADM} = 1.56$. Note that in comoving coordinates, the shape of the horizons is not necessarily spherical; only the average radius of the horizons is controlled.

The second change we make at time $t_1/M_{\rm ADM} = 31.1$ is to smoothly roll the gauge source

function H_a to zero by adjusting $\tilde{H}_{a'}(t)$ according to

$$\tilde{H}_{a'}(t) = \tilde{H}_{a'}(t_1) e^{-(t-t_1)^2/\tau^2} \ , \tag{4.45}$$

where $\tau/M_{\rm ADM} = 0.5853$. This choice makes it easier for us to continue the evolution after the common horizon has formed, and it also reduces gauge dynamics that otherwise cause oscillations in the observed Landau-Lifshitz velocity, $v^y_{\rm LL}$, during the ringdown.

When the two black holes are sufficiently close to each other, a new apparent horizon suddenly appears, encompassing both black holes. At time $t_m/M_{\rm ADM} = 34.73$ (which is shortly after the common horizon forms), we interpolate all variables onto a new computational domain that contains only a single excised region, and we choose a new comoving coordinate system so that the merged (distorted, pulsating) apparent horizon remains spherical in the new comoving frame. This is accomplished in the same way as described in Section II D of [4], except that here the map from the new comoving coordinates to the inertial coordinates contains an additional translation in the y direction that handles the nonzero velocity of the merged black hole. In [4] a third change, namely, a change of gauge, was necessary to continue the simulation after merger. In the simulations discussed here, however, Eq. (4.45) has caused H_a to fall to zero by the time of merger, and we find it suffices to simply allow H_a to remain zero after merger.

For completeness, we now explicitly describe the map from the new comoving coordinates x''^i to the inertial coordinates x^i. This map is given by

$$\begin{aligned}
x &= r \sin\theta'' \cos\phi'' \ , && (4.46)\\
y &= r \sin\theta'' \sin\phi'' + e^{-r''^2/r''^2_{\rm T}} Y(t) \ , && (4.47)\\
z &= r \cos\theta'' \ , && (4.48)\\
r &= \tilde{r} \left[1 + \sin^2(\pi\tilde{r}/2R''_{\rm max}) \left(A(t) \frac{R'_{\rm max}}{R''_{\rm max}} + [1 - A(t)] \frac{R'^3_{\rm max}}{R''_{\rm max} R'^2_0} - 1 \right) \right] \ , && (4.49)\\
\tilde{r} &= r'' - q(r'') \sum_{\ell=0}^{\ell_{\rm max}} \sum_{m=-\ell}^{\ell} \lambda_{\ell m}(t) Y_{\ell m}(\theta'', \phi'') \ , && (4.50)
\end{aligned}$$

(r'', θ'', ϕ'') are spherical polar coordinates in the new comoving coordinate system, $R''_{\rm max}$ is the value of r'' at the outer boundary, and $r''_{\rm T}/M_{\rm ADM}$ is a constant chosen to be 31.21. The function $q(r'')$ is given by

$$q(r'') = e^{-(r''-R''_{\rm AH})^3/\sigma_q^3} \ , \tag{4.51}$$

where $R''_{\rm AH}$ is the desired radius of the common apparent horizon in comoving coordinates. The function $A(t)$ is

$$A(t) = A_0 + [A_1 + A_2(t - t_m)] e^{-(t-t_m)/\tau_A} \ , \tag{4.52}$$

where the constants A_0, A_1, and A_2 are chosen so that $A(t)$ matches smoothly onto $a(t)$ from Eq. (4.38): $A(t_m) = a(t_m)$, $\dot{A}(t_m) = \dot{a}(t_m)$, and $\ddot{A}(t_m) = \ddot{a}(t_m)$. The constant $\tau_A/M_{\rm ADM}$ is chosen to be on the order of 5. The functions $Y(t)$ and $\lambda_{\ell m}(t)$ are determined by dynamical control systems that keep the apparent horizon spherical and centered at the origin in comoving coordinates; see [4] for details.

4.B.2 BSSN-Moving-Puncture Evolutions

In addition to the generalized-harmonic evolutions, we performed a second set of simulations using the so-called moving-puncture technique [3, 2] using the Lean code [73, 98]. This code is based on the Cactus computational toolkit [99] and uses mesh refinement provided by the Carpet package [70, 71]. Initial data are provided in the form of the TwoPunctures thorn by Ansorg's spectral solver [67] and apparent horizons are calculated with Thornburg's AHFinderDirect [100, 101].

The most important ingredient in this method for the present discussion is the choice of coordinate conditions. A detailed study of alternative gauge conditions for moving-puncture-type, black-hole evolutions is given in [102]. In particular, they demonstrate how the common choice of a second-order, time-evolution equation for the shift vector, β^i, can be integrated in time analytically and, thus, reduced to a first-order equation. Various test simulations performed with the Lean code confirm their Eq. (26) as the most efficient method to evolve the shift vector. In contrast to the shift, moving-puncture codes show little variation in the evolution of the lapse function. Here, we follow the most common choice, so that our gauge conditions are given by

$$\partial_t \alpha = \beta^i \partial_i \alpha - 2\alpha K \,, \tag{4.53}$$

$$\partial_t \beta^i = \beta^m \partial_m \beta^i + \frac{3}{4}\tilde{\Gamma}^i - \eta \beta^i \,. \tag{4.54}$$

Above, $\tilde{\Gamma}^i$ is the contracted Christoffel symbol of the conformal 3-metric, K the trace of the extrinsic curvature (see, for example, Eq. (1) of [73]) and η is a free parameter set to 1, unless otherwise specified. For further details about the moving-puncture method and the specific implementation in the Lean code, we refer to Section II of [73]. Except for the use of sixth- instead of fourth-order spatial discretization [103], we did not find it necessary to apply any modifications relative to the simulations presented in that work.

We calculate the 4-momentum in the Lean code in the same way as it is described in Section 4.2. The only difference is that in a BSSN code the four metric and its derivatives are not directly available but need to be expressed in terms of the 3-metric γ_{ij}, the extrinsic curvature K_{ij}, as well as the lapse α and shift β^i. The key quantity for the calculation of the 4-momentum is the integrand

in Eq. (4.7). A straightforward calculation gives it in terms of the canonical ADM variables

$$\partial_\alpha H^{0\alpha 0j} = \frac{1}{\chi^3}\left[\frac{3}{\chi}\gamma^{jm}\partial_m\chi + \gamma^{km}\gamma^{jn}\partial_k\gamma_{mn}\right] , \tag{4.55}$$

$$\partial_\alpha H^{i\alpha 0j} = \frac{1}{\chi^3}\left[2\alpha(K^{ij} - \gamma^{ij}K) + \gamma^{ij}\partial_m\beta^m - \gamma^{im}\gamma_m\beta^j\right] - \beta^i\partial_\alpha H^{0\alpha 0j} , \tag{4.56}$$

where $K := K^i{}_i$ and $\chi := \det\gamma^{-1/3}$ have been used for convenience because they are fundamental variables in our BSSN implementation.

Bibliography

[1] F. Pretorius, Phys. Rev. Lett. **95**, 121101 (2005).

[2] M. Campanelli, C. Lousto, P. Marronetti, and Y. Zlochower, Phys. Rev. Lett. **96**, 111101 (2006).

[3] J. G. Baker, J. Centrella, D.-I. Choi, M. Koppitz, and J. van Meter, Phys. Rev. Lett. **96**, 111102 (2006).

[4] M. A. Scheel, M. Boyle, T. Chu, L. E. Kidder, K. D. Matthews, and H. P. Pfeiffer, Phys. Rev. D **79**, 024003 (2009).

[5] D. Keppel, D. A. Nichols, Y. Chen, and K. S. Thorne, Phys. Rev. D **80**, 124015 (2009).

[6] B. Krishnan, C. O. Lousto, and Y. Zlochower, Phys. Rev. **D76**, 081501(R) (2007).

[7] L. B. Szabados, Living Rev. Relativity **12** (2009).

[8] C. O. Lousto and Y. Zlochower, Phys. Rev. D **79**, 064018 (2009).

[9] C. O. Lousto and Y. Zlochower, Phys. Rev. D **77**, 044028 (2008).

[10] A. Loeb, Phys. Rev. Lett. **99**, 041103 (2007).

[11] S. Komossa, H. Zhou, and H. Lu, Astrophys. J. **678**, L81 (2008).

[12] K. Menou, Z. Haiman, and B. Kocsis, New Astron. Rev. **51**, 884 (2008).

[13] M. Boylan-Kolchin, C.-P. Ma, and E. Quataert, Astrophys. J **613**, L37 (2004).

[14] A. Gualandris and D. Merritt, Astrophys. J **678**, 780 (2008).

[15] S. Komossa and D. Merritt, Astrophys. J. Lett. **689**, l89 (2008).

[16] P. Madau, M. J. Rees, M. Volonteri, F. Haardt, and S. P. Oh, Astrophys. J. **604**, 484 (2004).

[17] Z. Haiman, Astrophys. J **613**, 36 (2004).

[18] P. Madau and E. Quataert, Astrophys. J. **606**, L17 (2004).

[19] D. Merritt, M. Milosavljevic, M. Favata, S. A. Hughes, and D. E. Holz, Astrophys. J. **607**, L9 (2004).

[20] M. Volonteri, Astrophys. J **663**, L5 (2007).

[21] L. Blecha and A. Loeb, Mon. Not. R. Astron. Soc. **390**, 1311 (2008).

[22] M. J. Fitchett, Mon. Not. Roy. Astr. Soc. **203**, 1049 (1983).

[23] M. Favata, S. A. Hughes, and D. E. Holz, Astrophys. J. **607**, L5 (2004).

[24] L. Blanchet, M. S. S. Qusailah, and C. M. Will, Astrophys. J. **635**, 508 (2005).

[25] T. Damour and A. Gopakumar, Phys. Rev. D **73**, 124006 (2006).

[26] J. G. Baker, J. Centrella, D.-I. Choi, M. Koppitz, J. R. van Meter, and M. C. Miller, Astrophys. J. **653**, L93 (2006).

[27] J. A. González, U. Sperhake, B. Brügmann, M. Hannam, and S. Husa, Phys. Rev. Lett. **98**, 091101 (2007).

[28] F. Herrmann, I. Hinder, D. Shoemaker, P. Laguna, and R. A. Matzner, Astrophys. J. **661**, 430 (2007).

[29] M. Koppitz, D. Pollney, C. Reisswig, L. Rezzolla, J. Thornburg, P. Diener, and E. Schnetter, Phys. Rev. Lett. **99**, 041102 (2007).

[30] M. Campanelli, C. O. Lousto, Y. Zlochower, and D. Merritt, Astrophys. J. Lett. **659**, L5 (2007).

[31] W. Tichy and P. Marronetti, Phys. Rev. **D76**, 061502(R) (2007).

[32] J. A. Gonzalez, M. D. Hannam, U. Sperhake, B. Brügmann, and S. Husa, Phys. Rev. Lett. **98**, 231101 (2007).

[33] M. Campanelli, C. O. Lousto, Y. Zlochower, and D. Merritt, Phys. Rev. Lett. **98**, 231102 (2007).

[34] J. Healy, F. Herrmann, I. Hinder, D. M. Shoemaker, P. Laguna, and R. A. Matzner, Phys. Rev. Lett. **102**, 041101 (2009).

[35] L. Boyle, M. Kesden, and S. Nissanke, Phys. Rev. Lett. **100**, 151101 (2008).

[36] L. Boyle and M. Kesden, Phys. Rev. D **78**, 024017 (2008).

[37] J. D. Schnittman and A. Buonanno, Astrophys. J. **662**, L63 (2007).

[38] J. G. Baker, W. D. Boggs, J. Centrella, B. J. Kelly, S. T. McWilliams, M. C. Miller, and J. R. van Meter, Astrophys. J. **682**, L29 (2008).

[39] W. Tichy and P. Marronetti, Phys. Rev. D **78**, 081501 (2008).

[40] C. O. Lousto, M. Campanelli, Y. Zlochower, and H. Nakano, Classical Quantum Gravity **27**, 114006 (2010).

[41] J. G. Baker, W. D. Boggs, J. Centrella, B. J. Kelly, S. T. McWilliams, M. C. Miller, and J. R. van Meter, Astrophys. J. **668**, 1140 (2007).

[42] J. A. Gonzalez, U. Sperhake, and B. Brügmann, Phys. Rev. D **79**, 124006 (2009).

[43] L. Rezzolla, Classical Quantum Gravity **26**, 094023 (2009).

[44] J. D. Schnittman, A. Buonanno, J. R. van Meter, J. G. Baker, W. D. Boggs, J. Centrella, B. J. Kelly, and S. T. McWilliams, Phys. Rev. D **77**, 044031 (2008).

[45] S. H. Miller and R. A. Matzner, Gen. Relativ. Gravit. **41**, 525 (2009).

[46] E. Racine, A. Buonanno, and L. E. Kidder, Phys. Rev. D **80**, 044010 (2009).

[47] Y. Mino and J. Brink, Phys. Rev. D **78**, 124015 (2008).

[48] F. Pretorius, in *Physics of Relativistic Objects in Compact Binaries: From Birth to Coalescence*, edited by M. Colpi et al. (Springer, Netherlands, 2009).

[49] L. Rezzolla, R. P. Macedo, and J. L. Jaramillo, Phys. Rev. Lett. **104**, 221101 (2010).

[50] L. D. Landau and E. M. Lifshitz, *Classical Theory of Fields* (Addison Wesley, Reading, MA, 1962).

[51] C. W. Misner, K. S. Thorne, and J. A. Wheeler, *Gravitation* (W. H. Freeman, New York, 1973).

[52] S. V. Babak and L. P. Grishchuk, Phys. Rev. D **61**, 024038 (1999).

[53] M. Shibata and T. Nakamura, Phys. Rev. D **52**, 5428 (1995).

[54] T. W. Baumgarte and S. L. Shapiro, Phys. Rev. D **59**, 024007 (1998).

[55] G. Lovelace, R. Owen, H. P. Pfeiffer, and T. Chu, Phys. Rev. D **78**, 084017 (2008).

[56] R. M. Wald, *General Relativity* (University of Chicago Press, Chicago and London, 1984).

[57] R. Arnowitt, S. Deser, and C. W. Misner, in *Gravitation: An Introduction to Current Research*, edited by L. Witten (Wiley, New York, 1962).

[58] J. W. York, Jr., in *Sources of Gravitational Radiation*, edited by L. L. Smarr (Cambridge University Press, Cambridge, England, 1979).

[59] H. Friedrich, Commun. Math. Phys. **100**, 525 (1985).

[60] D. Garfinkle, Phys. Rev. D **65**, 044029 (2002).

[61] F. Pretorius, Classical Quantum Gravity **22**, 425 (2005).

[62] L. Lindblom, M. A. Scheel, L. E. Kidder, R. Owen, and O. Rinne, Classical Quantum Gravity **23**, S447 (2006).

[63] M. Ruiz, R. Takahashi, M. Alcubierre, and D. Núñez, Gen. Relativ. Gravit. **40**, 1705 (2008).

[64] C. Bona, J. Massó, E. Seidel, and J. Stela, Phys. Rev. D **56**, 3405 (1997).

[65] M. Alcubierre, B. Brügmann, P. Diener, M. Koppitz, D. Pollney, E. Seidel, and R. Takahashi, Phys. Rev. D **67**, 084023 (2003).

[66] S. Brandt and B. Brügmann, Phys. Rev. Lett. **78**, 3606 (1997).

[67] M. Ansorg, B. Brügmann, and W. Tichy, Phys. Rev. D **70**, 064011 (2004).

[68] J. M. Bowen and J. W. York, Jr., Phys. Rev. D **21**, 2047 (1980).

[69] M. J. Berger and J. Oliger, J. Comput. Phys. **53**, 484 (1984).

[70] E. Schnetter, S. H. Hawley, and I. Hawke, Classical Quantum Gravity **21**, 1465 (2004).

[71] *Carpet: Adaptive mesh refinement for the cactus framework, computer code*, `http://www.carpetcode.org`.

[72] M. Alcubierre, B. Brügmann, P. Diener, M. Koppitz, D. Pollney, E. Seidel, and R. Takahashi, Phys. Rev. D **67**, 084023 (2003).

[73] U. Sperhake, Phys. Rev. D **76**, 104015 (2007).

[74] G. Faye, L. Blanchet, and A. Buonanno, Phys. Rev. D **74**, 104033 (2006).

[75] H. Tagoshi, A. Ohashi, and B. J. Owen, Phys. Rev. D **63**, 044006 (2001).

[76] E. Racine and E. E. Flanagan, Phys. Rev. D **71**, 044010 (2005).

[77] G. B. Cook, Phys. Rev. D **65**, 084003 (2002).

[78] G. B. Cook and H. P. Pfeiffer, Phys. Rev. D **70**, 104016 (2004).

[79] M. Caudill, G. B. Cook, J. D. Grigsby, and H. P. Pfeiffer, Phys. Rev. D **74**, 064011 (2006).

[80] E. Gourgoulhon, P. Grandclément, and S. Bonazzola, Phys. Rev. D **65**, 044020 (2002).

[81] P. Grandclément, E. Gourgoulhon, and S. Bonazzola, Phys. Rev. D **65**, 044021 (2002).

[82] H. P. Pfeiffer, L. E. Kidder, M. A. Scheel, and S. A. Teukolsky, Comput. Phys. Commun. **152**, 253 (2003).

[83] G. B. Cook and M. A. Scheel, Phys. Rev. D **56**, 4775 (1997).

[84] M. A. Scheel, H. P. Pfeiffer, L. Lindblom, L. E. Kidder, O. Rinne, and S. A. Teukolsky, Phys. Rev. D **74**, 104006 (2006).

[85] M. Boyle, D. A. Brown, L. E. Kidder, A. H. Mroué, H. P. Pfeiffer, M. A. Scheel, G. B. Cook, and S. A. Teukolsky, Phys. Rev. D **76**, 124038 (2007).

[86] O. Rinne, Classical Quantum Gravity **23**, 6275 (2006).

[87] O. Rinne, L. Lindblom, and M. A. Scheel, Classical Quantum Gravity **24**, 4053 (2007).

[88] J. M. Stewart, Classical Quantum Gravity **15**, 2865 (1998).

[89] H. Friedrich and G. Nagy, Commun. Math. Phys. **201**, 619 (1999).

[90] J. M. Bardeen and L. T. Buchman, Phys. Rev. D **65**, 064037 (2002).

[91] B. Szilágyi, B. Schmidt, and J. Winicour, Phys. Rev. D **65**, 064015 (2002).

[92] G. Calabrese, J. Pullin, O. Reula, O. Sarbach, and M. Tiglio, Commun. Math. Phys. **240**, 377 (2003).

[93] B. Szilágyi and J. Winicour, Phys. Rev. D **68**, 041501(R) (2003).

[94] L. E. Kidder, L. Lindblom, M. A. Scheel, L. T. Buchman, and H. P. Pfeiffer, Phys. Rev. D **71**, 064020 (2005).

[95] L. T. Buchman and O. C. A. Sarbach, Classical Quantum Gravity **23**, 6709 (2006).

[96] L. T. Buchman and O. C. A. Sarbach, Classical Quantum Gravity **24**, S307 (2007).

[97] M. Cohen, H. P. Pfeiffer, and M. A. Scheel, Classical Quantum Gravity **26**, 035005 (2009).

[98] U. Sperhake, B. Brügmann, J. Gonzalez, M. Hannam, and S. Husa, in *Proceedings of the Eleventh Marcel Grossmann Meeting* (2007).

[99] *The Cactus Computational Toolkit*, http://www.cactuscode.org.

[100] J. Thornburg, Phys. Rev. D **54**, 4899 (1996).

[101] J. Thornburg, Class. Quant. Grav. **21**, 743 (2004).

[102] J. R. van Meter, J. G. Baker, M. Koppitz, and D.-I. Choi, Phys. Rev. D **73**, 124011 (2006).

[103] S. Husa, J. A. González, M. Hannam, B. Brügmann, and U. Sperhake, Classical Quantum Gravity **25**, 105006 (2008).

Part II

Approximating the Inspiral, Merger, and Ringdown in Black-Hole Binaries

Chapter 5

A Hybrid Method for Understanding Black-Hole Mergers: I. Head-on Mergers

Black-hole-binary coalescence is often divided into three stages: inspiral, merger, and ringdown. The post-Newtonian (PN) approximation treats the inspiral phase, black-hole perturbation (BHP) theory describes the ringdown, and the nonlinear dynamics of spacetime characterize the merger. In this paper, we introduce a hybrid method that incorporates elements of PN and BHP theories, and we apply it to the head-on collision of black holes with transverse, anti-parallel spins. We compare our approximation technique with a full numerical-relativity simulation, and we find good agreement between the gravitational waveforms and the radiated energy and momentum. Our results suggest that PN and BHP theories may suffice to explain the main features of outgoing gravitational radiation for head-on mergers. This would further imply that linear perturbations to exact black-hole solutions can capture the nonlinear aspects of head-on binary-black-hole mergers accessible to observers far from the collision.

Originally published as D. A. Nichols and Y. Chen, Phys. Rev. D **82**, 104020 (2010).

5.1 Introduction

Even prior to the complete numerical-relativity simulations of black-hole-binary mergers [1, 2, 3, 4], black-hole collisions were thought to take place in three stages: inspiral (or infall), merger, and ringdown. During inspiral, the speed of the holes is sufficiently low and the separation of the bodies is large enough that the system behaves like two separate particles that follow the post-Newtonian (PN) equations of motion. Eventually, the black holes become sufficiently close that the dynamics given by the PN expansion significantly differ from those of full relativity. This stage is the merger, during which the two black holes become a single, highly distorted, black hole. The merger phase

is brief; the strong deformations lose their energy to gravitational radiation, and the system settles down to a weakly perturbed, single black hole. The ringdown phase describes these last small oscillations of the black hole.

Of the three stages of binary-black-hole coalescence, the merger remains the most inaccessible to analytical tools. Nevertheless, full numerical relativity is not the only technique to have success investigating the merger. Historically, most analytical investigations of the merger phase arise from trying to extend the validity of perturbative techniques, particularly black-hole-perturbation (BHP) and PN theories. Those researchers working from a BHP approach try to push the approximation to hold at earlier times, whereas those employing a PN method attempt to stretch the technique to hold later into merger. Alternatively, one can see if there are exact, nonlinear analytical models whose dynamics can represent various aspects of black-hole-binary mergers. Rezzolla, Macedo, and Jaramillo [5] recently took this latter approach in their study of anti-kicks from black-hole mergers. In their work, they showed that they could relate the curvature anisotropy on the past apparent horizon of a Robinson-Trautman spacetime to the kick velocity (computed from the Bondi momentum). Through appropriate tuning of the initial data, they could recover kick velocities found in numerical-relativity simulations of unequal-mass, inspiraling black holes. While this type of approach is interesting and has proved successful, our work focuses on using perturbative approaches (and we will, therefore, take a more comprehensive look at the prior use of perturbative methods to understand mergers).

From the BHP side, Price and Pullin [6], initially, and many collaborators, subsequently, (see, e.g., [7]) developed the "close-limit approximation" (CLA). This technique begins with initial data containing two black holes that satisfy the vacuum Einstein equations and splits it into a piece representing the final, merged black hole and perturbations upon that black hole. The exact form of the initial data varies in the CLA, but for head-on collisions of black holes, it typically involves some variation of Misner [8], Lindquist [9], or Brill-Lindquist [10] time-symmetric, analytic, wormhole-like solutions. To investigate the late stages of an inspiral, the CLA usually begins from non-time-symmetric, but conformally flat, multiple black-hole initial data set forth by Bowen and York [11]. Independent of the initial data, however, the CLA translates the original problem of the merger into a calculation involving BHP theory. The CLA does not allow for a very large separation of the black holes; as a result, only the very end of the merger is captured in this process. Moreover, "junk radiation" appears in the waveform because the initial data do not describe the binary black-hole-merger spacetime in both the wave zone and the near zone. Unlike in full numerical-relativity simulations where the junk radiation leaves the grid during the well-understood inspiral phase, in the CLA the junk radiation appears during the merger stage. This radiation (both from the absence of waves in the initial data and from errors in the near-zone physics), therefore, is difficult to disentangle from the physical waveform.

The Lazarus Project (see, e.g., [12]) followed roughly the same approach as the CLA, but it used even more realistic black-hole-binary initial data for its CLA calculation; namely, its initial data came from a numerical-relativity simulation just prior to the merger. At the same time, however, because the initial data is now numerical, one loses the analytical understanding of the properties of spacetime near the merger. More recently, Sopuerta, Yunes, and Laguna [13] applied the CLA in combination with PN flux formulas to obtain an estimate of the gravitational recoil from unequal-mass binaries (including binaries with small eccentricity [14]). They proposed using more realistic initial data in the CLA, which Le Tiec and Blanchet [15] ultimately carried out. Le Tiec and Blanchet chose to use the 2PN metric (keeping only the first post-Minkowski terms) as initial data for the CLA, and they applied it with considerable success to inspirals of unequal-mass black-hole binaries in a paper with Will [16]. Despite the improved initial data, this approach does not eliminate the problem of junk radiation discussed above. It would be of interest to see if even more realistic initial data, such as that of Johnson-McDaniel, Yunes, Tichy, and Owen [17] would lead to improved results within the CLA.

From the PN side, Buonanno et al., in [18], as well as Damour and Nagar [19] take a different approach to understanding the physics of the merger. Using the effective-one-body (EOB) method [20], they study the dynamics of the system until roughly the beginning of the merger phase. To obtain a complete waveform, they attach a ringdown waveform by smoothly fitting quasinormal modes to the EOB inspiral and plunge waveform. When they calibrate the two free parameters of this model to numerical-relativity waveforms, the EOB results match numerical-relativity waveforms precisely. In this method, they fit the PN dynamics and the ringdown at the light ring of the EOB particle motion; it is not immediately apparent, however, what this feature tells about the nature of the merger.

As a result, there remains a need to develop simple analytical models that help reveal the behavior of spacetime during the merger. Toward this end, it is helpful to delve deeper into the question of what exactly is the merger. First, the inspiral-merger-ringdown classification is based on the validity of the PN expansion and that of BHP. The inspiral, in other words, is just the set of times for which the PN expansion holds on the whole spatial domain (to a given level of accuracy). Correspondingly, the ringdown is the times for which BHP works everywhere throughout space. The merger, in this picture, is just the gap between those times during which PN and BHP theories give accurate results.

In this paper, we propose that we can push each approximation technique beyond its current range of use, as long as we do not apply it to all of space at a given time. We observe that at any time, there is a region outside a certain radius from the center of mass in which BHP applies. While this seemingly runs contrary to the common notion that PN theory is the natural description of the weak-field region of a black-hole-binary spacetime, a black-hole metric in the limit of radii much larger than the mass and binary separation is identical to that of PN in the same region. If the PN

expansion applies to the remaining portion of the spacetime (within the region where BHP holds), then BHP and PN theories could cover the entire physics of black-hole-binary coalescence. While it is somewhat unreasonable to suppose that PN theory truly applies to the strong-field region of a binary-black-hole spacetime, revisiting Price's treatment of non-spherical stellar collapse suggests that this may not be essential.

In Price's 1972 paper [21], he addresses, among other issues, why aspherical portions of stellar collapse quickly disappear when, in fact, one could plausibly argue the contrary. Namely, if any non-spherical perturbations asymptote to the horizon (from the perspective of an observer far away), they would remain visible to this observer indefinitely. Price realizes, however, that the exterior of a collapsing star is just the Schwarzschild solution (because of Birkhoff's theorem, up to small perturbations), and perturbations on the Schwarzschild spacetime evolve via a radial wave equation in an effective potential. Moreover, he notes that when the surface of the star passes through the curvature effective potential of the Schwarzschild spacetime, the gravitational perturbations induced by the star redshift. Finally, because the effective potential reflects low-frequency perturbations, the spacetime distortions produced by the stellar interior become less important, and observers outside the star ultimately see it settle into a spherical black hole in a finite amount of time. Most importantly, this argument does not depend strongly upon the physics of the stellar interior; as long as there is gravitational collapse to a black hole, this idea holds.

In this paper, we adopt this idea, but we replace the stellar physics of the interior with a PN, black-hole-binary spacetime (see Fig. 5.1). While in Price's case, the division of spacetime into two regions comes naturally from tracking the regions of space containing the star and vacuum, in our case the split is somewhat more arbitrary; one simply needs to find a region in which both PN and BHP theories hold, to some level of accuracy. How we choose the boundary between the two regions and the quantities that we evolve are topics that will be discussed in greater detail in Section 5.2.

To test the above idea in this paper, we study a head-on collision of two black holes with transverse, anti-aligned spins and compare the waveforms and energy-momentum flux obtained from our approximation method with the equivalent quantities from full numerical simulations. Specifically, we organize this paper as follows. In Section 5.2, we give a more detailed motivation for our model, and we then present the mathematical procedure we use in our method, for an equal-mass, head-on collision of black holes. In Section 5.3, we present an explicit calculation for the head-on collision of two black holes with transverse, anti-aligned spins, and we compare waveforms, radiated energy, and radiated linear momentum from our model with the equivalent quantities from a full numerical-relativity simulation. In Section 5.4 we discuss how our method can help interpret the waveform during merger, and finally, in Section 5.5, we conclude. We will use geometrical units ($G = c = 1$) and the Einstein summation convention throughout this paper.

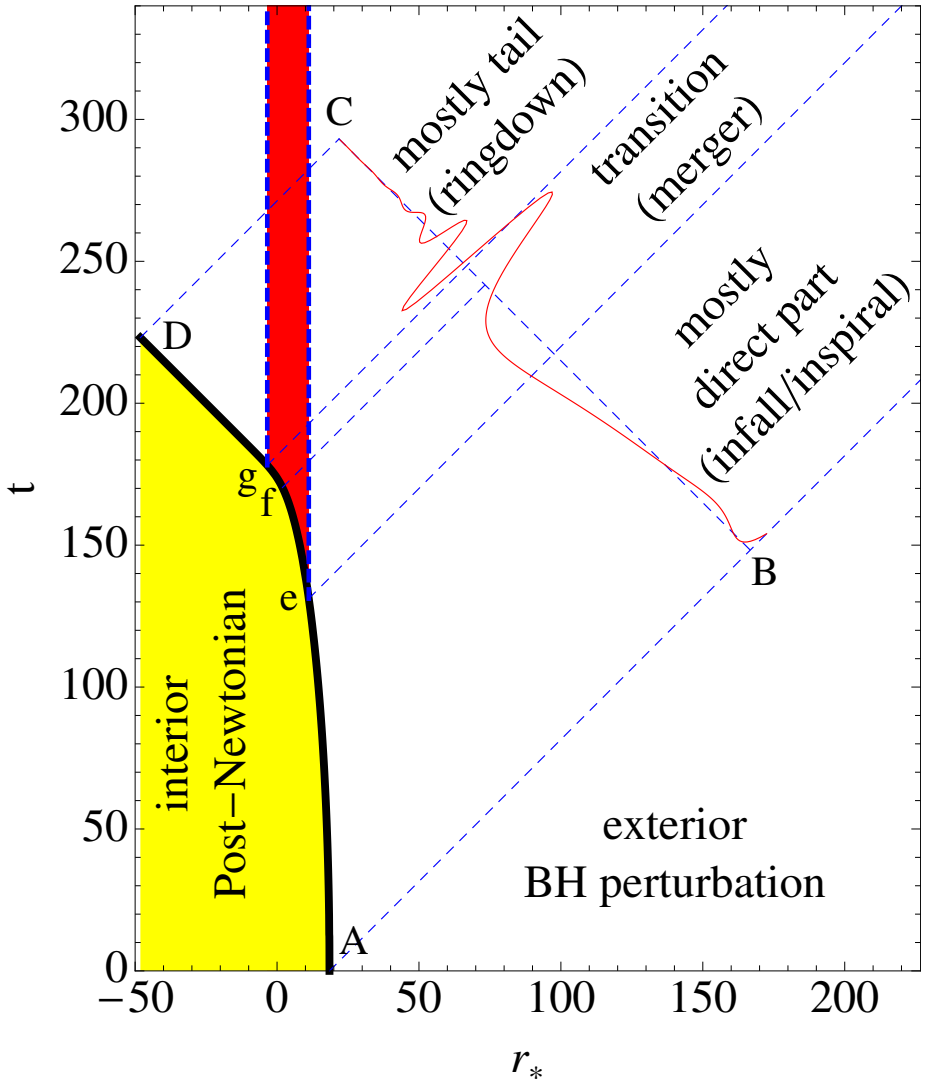

Figure 5.1: A spacetime diagram of a black-hole collision, modeled after Price's description of stellar collapse. We choose the trajectory of the two holes as a way to separate the spacetime into an interior and an exterior region. The exterior region is a perturbed, black-hole spacetime, whereas the interior is that of a post-Newtonian (PN) black-hole-binary system, shaded in yellow (light gray). The red (dark gray) region of the diagram shows the place at which the effective potential of the black hole is significantly greater than zero. This formalism allows us to divide the waveform into three sections: inspiral (or infall), which extends from the beginning of the binary's evolution until the $l = 2$ effective potential of the exterior BHP spacetime starts to be exposed; merger, which extends from the end of inspiral to when the majority of the exterior potential is revealed; and ringdown, which represents the remainder. We overlay the even-parity, ($l = 2$,$m = 0$) mode of the waveform.

5.2 A Detailed Description of the Method

5.2.1 Further Motivation

Before going into the details of our procedure, it is worth spending some time discussing why our specific implementation of PN and BHP theories will help avoid some of the difficulties that arose in other methods in the Introduction and noting the limitations and assumptions that underlie our approach.

It is certainly hard to argue that existing orders of PN (up to v^6 in the metric, for near-zone dynamics [22]) and BHP (up to second order for Schwarzschild, see [23] for a gauge-invariant formulation) theories are accurate in the whole space, simultaneously. Nevertheless, it is plausible to argue that these approximation techniques cover different spatial regions at different times in a way such that each theory is either valid to a reasonable level of accuracy or occupying a portion of spacetime that will not influence physical observables where it fails. Using an approach of this type, we aim to get the most out of the approximation methods.

Specifically, we find that the following procedure gives good agreement with the waveform of a numerical-relativity simulation presented in Section 5.3. First, we have the reduced mass of the binary follow a plunging geodesic in the Schwarzschild spacetime. Then, we divide this trajectory in half to make a coordinate radius (and thus a coordinate sphere) that passes through the centers of the black holes; the set of all the coordinate spheres defines a time-like surface in spacetime. Finally, we apply PN theory within this time-like surface and BHP on the exterior. The two theories must agree on this time-like surface, which we will subsequently call the shell.

Matching PN and BHP theories on this shell has certain advantages. Because BHP theory relies upon a multipole expansion, this makes it necessary to treat the PN interior in terms of multipoles of the potentials. For one, this is useful, because physical observables like the radiated energy and momentum very often do not need many multipoles to find accurate results. (In fact, in our example in Section 5.3, we see that the quadrupole perturbations alone suffice.) Second, a multipole expansion may also be helpful for the convergence of the approach. For two point particles, for example, each multipole component of the Newtonian potential $U_N^{(l)}$ at the location of the particles satisfies $U_N^{(l)} \lesssim M/R$, where M is the mass of the binary and R is the distance from the center of mass. This is small for much of the infall, when $R \gg M$, and even when the binary reaches what will be the peak of the effective potential of the merged black hole, $U_N^{(l)} \sim 1/3$.

Because the effective potential of the final black hole tends to mask perturbations within (as they are redshifted and cannot escape), our hope (supported by the example in Section 5.3) is that PN theory is still reasonably accurate at the peak of the potential. Then, in our approach, the PN error will be hidden by this potential and, along with BHP in the exterior, it will suffice to explain the physics outside the black hole (in particular the gravitational waveform and the energy

and momentum flux). Of course whether such a mechanism exists is not easily deduced analytically from first principles; only by comparing our results with those from full numerical relativity will we test this premise (which we do in Section 5.3.2).

If this holds, our procedure has several advantages. For one, the matching works well at larger separations (which diminishes the influence of junk radiation). More importantly, though, as the matching shell moves from large separations at early times to the vicinity of the horizon at late times, the spacetime smoothly transitions from predominantly PN to essentially BHP. One can see this most clearly in the way that the effective potential is revealed in Fig. 5.1. This leads to a waveform that smoothly transitions between an inspiral at early times to a ringdown at late times. Whether we correctly capture the merger phase is most easily confirmed by comparing with results from numerical relativity. Finally, our method can give a way to interpret the waveform during the different stages of a binary-black-hole coalescence by relating parts of the waveform with the retarded position of the matching shell at that point (for further detail, see Section 5.4).

There is also reason to suspect that the domain of BHP may extend to relatively early times in the merger, outside the binary. A paper by Racine, Buonanno and Kidder [24] gives evidence in favor of this idea. In particular, they find, when studying the "superkick" configuration (an equal-mass, quasicircular binary of black holes with transverse, antiparallel spins), that the higher-order spin-orbit contributions to linear-momentum flux dominate over the leading-order terms. These terms include both direct higher PN terms and tail terms, where the tail refers to gravitational radiation that is scattered off of spacetime curvature and propagates within the light cone (as opposed to the direct piece that propagates on the light cone). This suggests that even early on, the background curvature plays an important role in generating the kick. Whether a Schwarzschild black hole properly represents this curvature is another idea that is difficult to argue for directly, but can be confirmed by comparison with the results of numerical relativity.

In its current implementation, the feature of our approach that is most arbitrary is setting the boundary between the PN interior and the BHP exterior. Nevertheless, our procedure works for head-on collisions, and in future work, we will develop a more systematic way of treating the boundary.

5.2.2 Details of the Implementation

The procedure that we follow can be broken down, more or less, into five steps: (i) we describe relevant physics in the PN interior; (ii) we match the metric of the PN interior to the BHP metric through a boundary; (iii) we explicitly construct the boundary between the PN and BHP spacetimes; (iv) we evolve the metric perturbations in the exterior Schwarzschild spacetime; (v) we extract the waveforms and compute the radiated energy and momentum. We shall devote a subsection to each of these topics below.

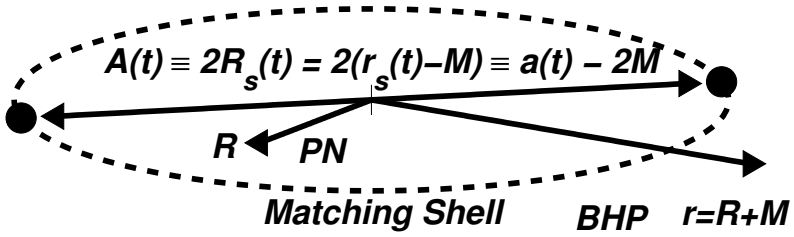

Figure 5.2: At a given moment in time, the Schwarzschild and PN radial coordinates, the binary separation, and the position of the shell where we match the two theories

Before we do so, however, it will be helpful to clarify our notation regarding the different coordinates we use for the two metrics and the matching shell. In the PN coordinate system, we use Minkowski coordinates (T, X, Y, Z) and spherical-polar coordinates (R, Θ, Φ) within spatial slices. We will consider linear perturbations to Minkowski space only in a PN harmonic gauge. For our BHP, we employ Schwarzschild coordinates (t, r, θ, φ), and similarly, we only examine linear perturbations to the Schwarzschild spacetime. As we will show in Section 5.2.2.3, we can match these descriptions when $R, r \gg M$. This procedure is accurate up to terms of order $(M/R)^2$ in the monopole part of the metric and M/R in the higher-multipole portions, assuming that we relate the two coordinate systems by

$$T = t\,,\ \Theta = \theta\,,\ \Phi = \varphi\,, R = r - M\,. \tag{5.1}$$

The identification above allows us to label every point in spacetime by two sets of coordinates, (t, r, θ, φ) and (t, R, θ, φ), where $R = r - M$. Because our program relies upon applying PN theory in an interior region and BHP on the exterior, it is therefore natural to talk about a coordinate shell at which we switch between PN and BHP descriptions of the space-time. On this shell, we can use either the Minkowski or Schwarzschild coordinates.

In keeping with the notation above, we shall denote the separation of the binary by $A(t) = 2R(t)$ in PN coordinates and $a(t) = 2r(t)$ in Schwarzschild coordinates. Finally, we will denote the radial coordinate on the boundary by adding a subscript s to the PN or Schwarzschild coordinate radii (e.g., $R_s(t) = A(t)/2$ or $r_s(t) = a(t)/2$). We summarize the two coordinate systems, and how they match, in Table 5.1 and Fig. 5.2.

	PN Spacetime	Matching Shell	Perturbed Schwarzschild Spacetime
Coordinates	(t, R, θ, φ)	$(t, R_s(t), \theta, \varphi)$ or $(t, r_s(t), \theta, \varphi)$	(t, r, θ, φ), $r = R + M$
Binary Separation	$A(t)$	$A(t)$ or $a(t)$	$a(t)$
Matching Radius	$R(t) = A(t)/2$	$R_s(t) = a(t)/2 - M$ or $r_s(t) = A(t)/2 + M$	$r(t) = a(t)/2$

Table 5.1: This table summarizes our notation for the coordinates, the binary separation, and the matching radius that we use for the PN spacetime, the BHP spacetime, and the matching region between the two.

While we introduce a new method of matching PN and BHP theories, the idea of combining PN and BHP approximations is not new. In fact, it is at the core of the effective-one-body formalism of Buonanno and Damour [20]. In the EOB description, however, they match the point-particle Hamiltonians of PN and BHP theories, rather than joining the spacetime geometry. It would be interesting, as a future study, to see whether one can combine our procedure with that of the EOB to produce a geometrical EOB approach. Le Tiec and Blanchet [15], on the other hand performed a more accurate matching between PN and BHP in their close-limit calculation with 2PN initial data, but their matching only takes place on a single spatial slice of initial data. It would also be interesting to extend their higher-order approach to our procedure as well.

5.2.2.1 The PN Interior Solution

For our method, we will need to describe the metric of the PN spacetime in the interior, which we do at leading Newtonian order:

$$ds^2_{\rm PN} = -(1-2U_N)dt^2 - 8w_i dt dX^i + (1+2U_N)\delta_{ij}dX^i dX^j \,. \tag{5.2}$$

Here U_N is the Newtonian potential and w_i is the gravitomagnetic potential, and the index i runs over X, Y, and Z. Our notation follows [25] (the above takes the results of Eq. (2.1) of that paper). We then expand the Newtonian potential, U_N, into multipoles, keeping only the lowest multipoles necessary to complete the calculation. In this paper the monopole and quadrupole pieces suffice (the dipole piece can always be made to vanish),

$$U_N \approx U_N^{(0)} + U_N^{(2)} \,. \tag{5.3}$$

The quadrupole piece can be expressed as a term without angular dependence times a spherical harmonic, as is done below,

$$U_N^{(2)} = U_N^{2,m} Y_{2,m}(\theta,\varphi) \,. \tag{5.4}$$

We will follow the same procedure with the gravitomagnetic potential, although here we will, temporarily, keep the dipole term,

$$w_i \approx w_i^{(1)} + w_i^{(2)} \,. \tag{5.5}$$

We will be able to remove the dipole term through a gauge transformation, but this discussion is much simpler on a case-by-case basis. When we write the gravitomagnetic potential, $\mathbf{w}$, in spherical-polar coordinates, we will be able to remove the radial component through a gauge transformation. We will, therefore, consider just the θ and φ components of $\mathbf{w}$, and when writing it in index notation, we will denote them with Latin letters from the beginning of the alphabet, (e.g., $a, b = \theta, \varphi$). We can then expand the components $w_a^{(2)}$ in terms of two vector spherical harmonics,

$$w_a^{(2)} = w_{(\mathrm{e})}^{2,m} \nabla_a Y_{2,m}(\theta,\varphi) + w_{(\mathrm{o})}^{2,m} \epsilon_a{}^b \nabla_b Y_{2,m}(\theta,\varphi)\,. \tag{5.6}$$

Here ∇_a is the covariant derivative on a 2-sphere, and $\epsilon_a{}^b$ is the Levi-Civita tensor (with nonzero components $\epsilon_\theta{}^\varphi = 1/\sin\theta$ and $\epsilon_\varphi{}^\theta = -\sin\theta$). A convenient abbreviation for the two spherical harmonics above is

$$w_a^{(2)} = w_{(\mathrm{e})}^{2,m} Y_a^{2,m} + w_{(\mathrm{o})}^{2,m} X_a^{2,m}\,. \tag{5.7}$$

The two terms are denoted by (e) and (o) as a short hand for even and odd, because they transform as $(-1)^l$ and $(-1)^{l+1}$ under parity transformations, respectively. The odd- and even-parity vector spherical harmonics are given explicitly by

$$X_\theta^{l,m} = -\frac{1}{\sin\theta}\frac{\partial Y^{lm}}{\partial\varphi}\,, \quad X_\varphi^{l,m} = \sin\theta\frac{\partial Y^{lm}}{\partial\theta} \tag{5.8}$$

and

$$Y_\theta^{l,m} = \frac{\partial Y^{lm}}{\partial\theta}\,, \quad Y_\varphi^{l,m} = \frac{\partial Y^{lm}}{\partial\varphi}\,, \tag{5.9}$$

respectively. These are the only parts of the PN metric that will be necessary for our approach.

5.2.2.2 Matching to a Perturbed Schwarzschild Black Hole

We then note that the Schwarzschild metric takes the form

$$ds^2 = -\left(1-\frac{2M}{r}\right)dt^2 + \left(1-\frac{2M}{r}\right)^{-1}dr^2 + r^2 d^2\Omega\,, \tag{5.10}$$

where the last piece is the metric of a 2-sphere. We will use r without any subscript to denote the Schwarzschild radial coordinate. When $M \ll r$ the Schwarzschild metric takes the form

$$ds^2 \approx -\left(1-\frac{2M}{r}\right)dt^2 + \left(1+\frac{2M}{r}\right)dr^2 + r^2 d^2\Omega\,. \tag{5.11}$$

By making the coordinate transformation $R = r - M$, and identifying M/R with the monopole piece of the Newtonian potential, $U_N^{(0)}$, then one can find that the Schwarzschild metric takes the form of the Newtonian metric in spherical coordinates,

$$ds^2 \approx -(1-2U_N^{(0)})dt^2 + (1+2U_N^{(0)})(dR^2 + R^2 d^2\Omega)\,. \tag{5.12}$$

This similarity between the PN and Schwarzschild metrics suggests a way to match the two at the boundary. We will assume that the monopole piece of the Newtonian potential becomes the M/r term in the Schwarzschild metric. For the remaining pieces of the Newtonian metric (namely $U_N^{(2)}$ and $w_i^{(2)}$) we will translate them directly into the Schwarzschild metric after performing any

needed gauge transformations to make such a direct match reasonable.

The original works on perturbations of the Schwarzschild spacetime are those of Regge and Wheeler [26] for the odd-parity perturbations and Zerilli [27] for the even-parity perturbations. Moncrief [28] then used a variational principle to show that one can derive quantities from the metric perturbations of Regge, Wheeler, and Zerilli that satisfy a well-posed, initial-value problem in any coordinates that deviate from Schwarzschild at linear order in perturbation theory. These quantities are related to the gravitational waves at infinity, and they satisfy a one-dimensional wave equation in a potential. We follow Moncrief's approach in computing these so-called gauge-invariant, metric-perturbation functions, but for our notation, we use that of a recent review article by Ruiz et al. [29].

Both the even-parity (transform as $(-1)^l$ under parity) and odd-parity (transform as $(-1)^{l+1}$ under parity) perturbations are not very difficult to find. By writing the PN metric in spherical-polar coordinates,

$$ds^2 = -(1 - 2U_N^{(0)} - 2U_N^{(2)})dt^2 + (1 + 2U_N^{(0)} + 2U_N^{(2)})(dR^2 + R^2 d^2\Omega) - 8w_b^{(2)} dt dx^b \,, \tag{5.13}$$

where $dx^b = d\theta, d\varphi$, one can see that the even-parity perturbations are nearly diagonal in the metric. In fact, at leading Newtonian order, it is exactly diagonal, because the non-diagonal term coming from $w_{(\mathrm{e})}^{2,m}$ arises at a higher PN order. We will show this explicitly in Section 5.3. For this reason, we only consider the diagonal metric components in the discussion below.

The even-parity metric perturbations in Schwarzschild are often denoted

$$\begin{aligned} (h_{tt}^{l,m})_{(\mathrm{e})} &= H_{tt}^{l,m} Y^{l,m} \,, \qquad (h_{rr}^{l,m})_{(\mathrm{e})} = H_{rr}^{l,m} Y^{l,m} \,, \\ (h_{\theta\theta}^{l,m})_{(\mathrm{e})} &= r^2 K^{l,m} Y^{l,m} \,, \qquad (h_{\varphi\varphi}^{l,m})_{(\mathrm{e})} = r^2 \sin^2\theta K^{l,m} Y^{l,m} \,, \end{aligned} \tag{5.14}$$

a specialization of Eqs. (57)–(59) of Ruiz et al. Thus, by matching the two metrics, one can see that

$$H_{tt}^{2,m} = H_{rr}^{2,m} = K^{2,m} = 2U_N^{2,m} \,. \tag{5.15}$$

The odd-parity term is somewhat simpler, because the only metric perturbation of the Schwarzschild spacetime to which we must match, at leading order, is

$$(h_{t\theta}^{l,m})_{(\mathrm{o})} = h_t^{l,m} X_\theta^{l,m} \,, \qquad (h_{t\varphi}^{l,m})_{(\mathrm{o})} = h_t^{l,m} X_\varphi^{l,m} \,, \tag{5.16}$$

Eq. (61) of Ruiz et al. From this, one can find that

$$h_t^{2,m} = -4 w_{(\mathrm{o})}^{2,m} \,. \tag{5.17}$$

The matching procedure thus gives a way to produce perturbations in the Schwarzschild spacetime.

5.2.2.3 The Boundary Shell

We now must find a boundary region where one can match a PN metric expanded in multipoles with a perturbed Schwarzschild metric. For head-on collisions, we find that the boundary can be a spherical shell whose radius varies in time as the binary evolves. We can motivate where this boundary should be with a few simple arguments, but the true test of the matching idea will come from comparisons with exact waveforms from numerical relativity.

We know that at early times and for larger separations of the black holes, the PN spacetime is valid around the two holes; thus it is not unreasonable to suppose that the shell should have a radius equal to half the binary separation. Later in the evolution, BHP will be valid everywhere, so the shell should asymptote to the horizon of the merged hole (as seen by outside observers). The trajectory of the shell should be smooth throughout the entire process as well. Finally, the boundary should mimic the reduced-mass motion of the system, which physically generates the gravitational waves.

A simple way to achieve this quantitatively is instead of having the motion of the reduced mass follow the PN equations of motion, we impose that it undergoes plunging geodesic motion in the Schwarzschild spacetime. Given that the exterior spacetime is a perturbed Schwarzschild, and that we are matching the two approximations on a shell that passes through the centers of the two black holes, it is just as reasonable to use a trajectory in the Schwarzschild spacetime. Moreover, at large separations, the motion of the reduced mass of the system in both Schwarzschild and PN are quite similar; we primarily choose the geodesic in Schwarzschild for its behavior at late times. For completeness, we write down the differential equation we use to find the motion of a radial geodesic in Schwarzschild. Because we think of the black holes as point particles residing in the PN coordinate system, we write the evolution of the binary separation $A(t)$, measured in the PN coordinates,

$$\begin{aligned} \frac{dA(t)}{d\tau} &= -\sqrt{B^2 - [1 - 2M/A(t)]}\,, \\ \frac{dt}{d\tau} &= B\left(1 - \frac{2M}{A(t)}\right)^{-1}\,, \end{aligned} \tag{5.18}$$

where B is a positive constant ($B = 1 - 2M/A(0)$ for a head-on plunge from rest). This expression can be found in many sources; see, for example, [30]. The coordinate radius of the shell in the PN spacetime is just half the distance $A(t)$,

$$R_s(t) = \frac{1}{2}A(t)\,. \tag{5.19}$$

Because the PN and Schwarzschild radii are related by $R = r - M$, one can find that in the

Schwarzschild coordinates, the position of the shell is given by

$$r_s(t) = \frac{1}{2}A(t) + M\,. \tag{5.20}$$

In Schwarzschild coordinates, because $A(t)$ goes to $2M$ at late times, the radius of the shell asymptotes to the horizon. More specifically, let us first define $\delta r_s(t) = r_s(t) - 2M$ and then note that at late times, the trajectory approaches the speed of light as it falls toward the horizon. In terms of the tortoise coordinate, $r_* = r + 2M\log[r/(2M) - 1]$, this occurs when $v = t + r_* = \text{const}$. Writing this with respect to the variable $\delta r_s(t)$, we find

$$-\frac{t}{2M} \sim \frac{\delta r_s(t)}{2M} + \log\left(\frac{\delta r_s(t)}{2M}\right)\,. \tag{5.21}$$

We neglected the constant value of v because doing so has no effect on finding the scaling of $r_s(t)$ at late times t. The equation above has a solution in terms of the Lambert W function, $W(x)$, given by

$$\delta r_s(t) \sim W(e^{-t/(2M)})\,. \tag{5.22}$$

Because we are interested in the behavior at large t, $e^{-t/(2M)}$ is small, and we can use the leading-order term in the Taylor series for the Lambert W function, $W(x) \sim x + O(x^2)$. We find that

$$\delta r_s(t) \sim e^{-t/(2M)}\,. \tag{5.23}$$

Thus, matching the spacetimes at half the PN separation of the binary and having the separation of the binary evolve via a Schwarzschild geodesic in the PN coordinate system makes the shell track the PN reduced-mass motion at early times, but still head to the horizon at late times. We illustrate these different behaviors by plotting the full trajectory of the shell $r_s(t)$, the trajectory of a shell that follows a plunging Newtonian orbit (which we denote by $r_{s,(N)}(t)$ and which represents the behavior of the shell at early times), and $e^{-t/(2M)}$ (the late-time behavior of the shell) in Fig. 5.3. We choose the initial values of the trajectory to conform with those of the numerical simulation with which we compare in Section 5.3.2. The upper and lower insets show how the shell's trajectory converges to the Newtonian behavior at early times and the expected exponential decay at late times.

While choosing the trajectory of the shell might have a slightly ad hoc feel, in future work we will develop a framework that determines the shell motion through a self-consistent radiation-reaction force.

5.2.2.4 Black-Hole Perturbations

One can then take the odd- and even-parity metric perturbations from the second subsection and transform them into two quantities, the Regge-Wheeler and Zerilli functions, respectively, that each

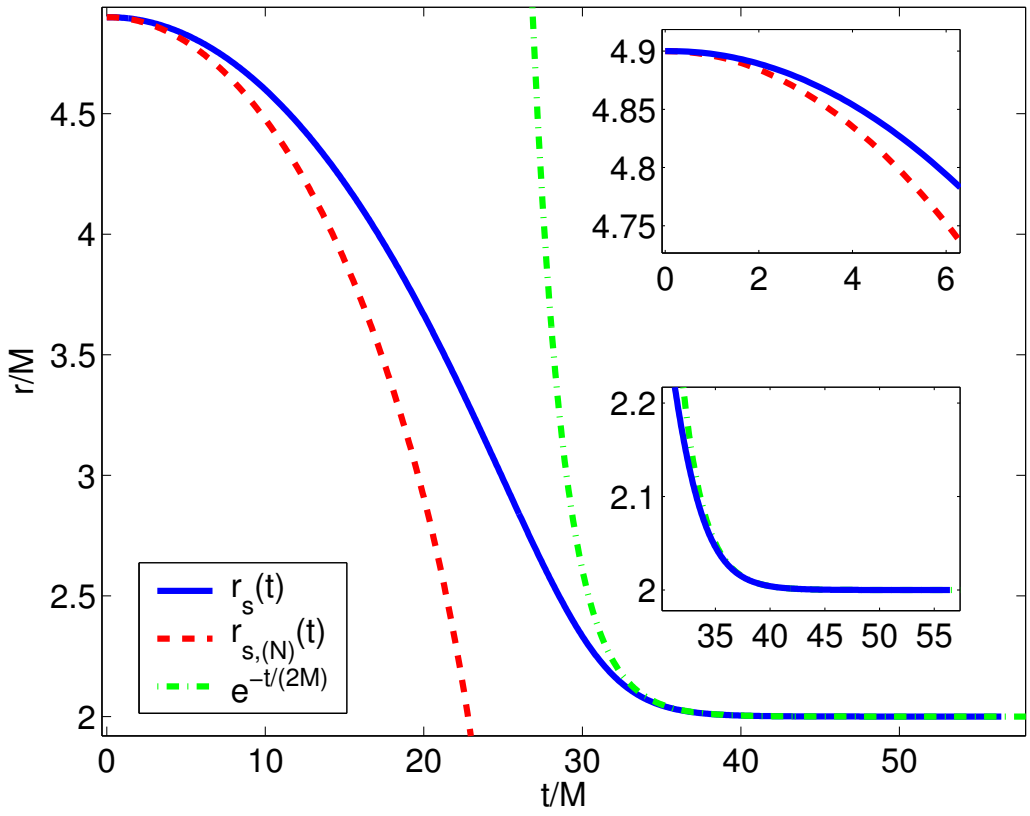

Figure 5.3: The trajectory of the boundary shell as the solid blue (dark) curve labeled by $r_s(t)$. The other two curves show the early- and late-time behavior of the shell. The red (gray) dashed curve labeled by $r_{s,(N)}(t)$ shows the trajectory of a shell that follows the Newtonian equations of motion for a plunge from rest. The green (light gray) dashed and dotted curve (denoted by $e^{-t/(2M)}$) shows the exponential convergence to the horizon at the rate expected in a Schwarzschild spacetime. The upper inset shows how the shell agrees with a Newtonian plunge from rest at early times, and the lower inset shows how the shell converges exponentially to the horizon at the expected rate.

satisfy a simple wave equation. We first treat the even-parity perturbations. Equations (63)–(65) of Ruiz et al. show how to take metric perturbations and transform them into the even-parity, gauge-invariant Zerilli function. Substituting our Eq. (5.15) into those three of Ruiz, we find

$$\Psi^{2,m}_{(\mathrm{e})} = \frac{2r}{3}\left\{U^{2,m}_N + \frac{r-2M}{2r+3M}\left[\left(1-\frac{2M}{r}\right)U^{2,m}_N - r\partial_r U^{2,m}_N\right]\right\}, \tag{5.24}$$

where ∂_r is just the radial derivative with respect to the Schwarzschild radial variable. The odd-parity perturbations come directly from applying our Eq. (5.17) to Eq. (67) of Ruiz et al. This gives that

$$\Psi^{2,m}_{(\mathrm{o})} = 2r\left(\partial_r w^{2,m}_{(\mathrm{o})} - \frac{2}{r}w^{2,m}_{(\mathrm{o})}\right). \tag{5.25}$$

The odd- and even-parity perturbations then evolve according to the Regge-Wheeler and Zerilli equations respectively,

$$[\partial_t^2 - \partial_{r_*}^2 + V^l_{(\mathrm{e,o})}(r)]\Psi^{l,m}_{(\mathrm{e,o})} = 0\,, \tag{5.26}$$

where $r_* = r + 2M\log[r/(2M)-1]$ is the tortoise coordinate. The potentials can be expressed most concisely via the expression

$$V^l_{(\mathrm{e,o})}(r) = \left(1-\frac{2M}{r}\right)\left(\frac{\lambda}{r^2} - \frac{6M}{r^3}U^l_{(\mathrm{e,o})}(r)\right), \tag{5.27}$$

where $\lambda = l(l+1)$ and

$$U^l_{(\mathrm{o})}(r) = 1, \quad U^l_{(\mathrm{e})}(r) = \frac{\Lambda(\Lambda+2)r^2 + 3M(r-M)}{(\Lambda r + 3M)^2}\,. \tag{5.28}$$

Here $\Lambda = (l-1)(l+2)/2 = \lambda/2 - 1$. These expressions follow Eqs. (5.3)–(5.6) of [15].

In our procedure, we find it easiest to evolve the Regge-Wheeler-Zerilli equations using a characteristic method. To do so, we define $u = t - r_*$ and $v = t + r_*$ and see that the evolution equation becomes

$$\frac{\partial^2\Psi^{l,m}_{(\mathrm{e,o})}}{\partial u\partial v} + \frac{V^l_{(\mathrm{e,o})}\Psi^{l,m}_{(\mathrm{e,o})}}{4} = 0\,. \tag{5.29}$$

We will now discuss how we evolve our Regge-Wheeler-Zerilli functions with the aid of Fig. 5.1.

We must provide data in two places, the matching shell (in Fig. 5.1 it is the lower-left curve labeled by AD) and the initial outgoing characteristic (the line labeled by AB on the lower right). Once we do this, however, we can determine the Regge-Wheeler-Zerilli functions within the quadrilateral (with the one curved side) $ABCD$. We already discussed how we determine the shell in Section 5.2.2.3, and the data we provide along that curve are just the Regge-Wheeler, Eq. (5.25), or Zerilli, Eq. (5.24), functions restricted to that curve. The data we must provide along AB are less well determined. If our computational grid extended to past null infinity, then we could impose a no-

ingoing-wave boundary condition. At finite times, we can still impose this boundary condition, but it leads to a small spurious pulse of gravitational radiation at the beginning of our evolution. To limit the effects of this, we keep the shell at rest until the junk radiation dissipates, and then we begin our evolution. At this point, the data along the line AB more closely represent those of a binary about to begin its plunge.

With these data, we can then evolve the Regge-Wheeler-Zerilli equations numerically, using the second-order-accurate, characteristic method described by Gundlach et al. in [31]. The essence of this method is that one can use the data at a point plus those at one step ahead in u and v, respectively, to get the next data point advanced by a step ahead in both u and v. Explicitly, if one defines

$$\begin{aligned} \Psi_N &= \Psi^{l,m}_{(\mathrm{e,o})}(u+\Delta u, v+\Delta v)\,, \qquad & \Psi_W &= \Psi^{l,m}_{(\mathrm{e,o})}(u+\Delta u, v)\,, \\ \Psi_E &= \Psi^{l,m}_{(\mathrm{e,o})}(u, v+\Delta v)\,, \qquad & \Psi_S &= \Psi^{l,m}_{(\mathrm{e,o})}(u, v)\,, \end{aligned} \tag{5.30}$$

then one has that

$$\Psi_N = \Psi_E + \Psi_W - \Psi_S - \frac{\Delta u \Delta v}{8} V^l_{(\mathrm{e,o})}(r_c)(\Psi_E + \Psi_W) + O(\Delta u^2 \Delta v, \Delta u \Delta v^2)\,, \tag{5.31}$$

where r_c is the value of r at the center of the discretized grid. Because our boundary data do not always lie on one of the grid points in the u-v plane, we must interpolate the bottom point $\Psi^{l,m}_{(\mathrm{e,o})}(u, v')$ to fall at the same value of v as the next boundary point at $\Psi^{l,m}_{(\mathrm{e,o})}(u+\Delta u, v)$. As long as we do this interpolation with a polynomial of at least a quadratic degree, it does not seem to influence the second-order convergence of the method. Finally, we can extract the Regge-Wheeler-Zerilli functions from the line BC in Fig. 5.1 as they propagate toward future null infinity.

5.2.2.5 Waveforms and Radiated Energy-Momentum

As we mentioned at the end of the previous section, it is easy to find the Regge-Wheeler-Zerilli functions from the exterior of our computational grid; this is useful, because these functions are directly related to the gravitational waveform h, asymptotically. For radii much larger than the reduced gravitational wavelength, $r \gg \lambda_{\mathrm{GW}}/(2\pi)$, one has that

$$h_+ - i h_\times = \frac{1}{2r} \sum_{l,m} \sqrt{\frac{(l+2)!}{(l-2)!}} \left[\Psi^{l,m}_{(\mathrm{e})} + i\, \Psi^{lm}_{(\mathrm{o})} \right] {}_{-2}Y_{lm}\,, \tag{5.32}$$

where ${}_{-2}Y_{lm}$ is a spin-weighted spherical harmonic. The above comes from Eq. (84) of Ruiz et al., which also contains a discussion about the spin-weighted harmonics in an appendix. One can then substitute this into the usual expressions for the energy and momentum radiated by gravitational

waves,

$$\frac{dE}{dt} = \lim_{r\to\infty}\frac{r^2}{16\pi}\oint |\dot{h}_+ - i\dot{h}_\times|^2 d\Omega\,, \tag{5.33}$$

$$\frac{dP_i}{dt} = \lim_{r\to\infty}\frac{r^2}{16\pi}\oint n_i|\dot{h}_+ - i\dot{h}_\times|^2 d\Omega\,, \tag{5.34}$$

(where n_i is a unit vector, a dot represents a time derivative, and $d\Omega$ is the volume element on a 2-sphere). A lengthy, but straightforward calculation done by Ruiz et al. shows that

$$\frac{dE}{dt} = \frac{1}{64\pi}\sum_{l.m}\frac{(l+2)!}{(l-2)!}\left(|\dot{\Psi}^{l,m}_{(\mathrm{e})}|^2 + |\dot{\Psi}^{l,m}_{(\mathrm{o})}|^2\right) \tag{5.35}$$

(Eq. (91) of Ruiz et al.). For the components of the momentum we are interested in (in the x-$y$plane) combining their Eqs. (86)–(88) and (93) and using their definition $P_+ = P_x + iP_y$ gives

$$\frac{dP_+}{dt} = -\frac{1}{16\pi}\sum_{l.m}\frac{(l+2)!}{(l-2)!}\left[ia_{l,m}\dot{\Psi}^{l,m}_{(\mathrm{e})}\bar{\dot{\Psi}}^{l,m+1}_{(\mathrm{o})} + b_{l+1,m+1}\left(\dot{\Psi}^{l,m}_{(\mathrm{e})}\bar{\dot{\Psi}}^{l+1,m+1}_{(\mathrm{e})} + \dot{\Psi}^{l,m}_{(\mathrm{o})}\bar{\dot{\Psi}}^{l+1,m+1}_{(\mathrm{o})}\right)\right]\,. \tag{5.36}$$

The bar denotes complex conjugation. The coefficients $a_{l,m}$ and $b_{l,m}$ are given by their Eqs. (41) and (42), which we reproduce here

$$a_{l,m} = \frac{\sqrt{(l-m)(l+m+1)}}{l(l+1)} \tag{5.37}$$

$$b_{l,m} = \frac{1}{2l}\sqrt{\frac{(l-2)(l+2)(l+m)(l+m-1)}{(2l-1)(2l+1)}} \tag{5.38}$$

With the framework now in place, we are prepared to make a comparison with numerical relativity.

5.3 Head-on Collision of Spinning Black Holes with Transverse, Antiparallel Spins

In this section, we discuss the specific example of a head-on collision of equal-mass black holes with transverse, antiparallel spins. We will specialize the general framework presented in Section 5.2 to the current configuration in the first subsection and then make the comparison with numerical relativity in the second.

5.3.1 The Hybrid Model for the Head-on Collision

We will mimic the configuration used in the numerical-relativity simulation for ease of comparison. We thus choose our two black holes, labeled by A and B, to have masses $M_A = M_B = M/2$, to start with initial separation $X_A = A(0)/2 = -X_B$ ($A(0) = 7.8M$ in the numerical simulations and $Y_A = Y_B = Z_A = Z_B = 0$) and to have their spins along $\pm Z$ axis, respectively (so that $S^Z_A = 0.5M^2_A$

and $S_B^Z = -0.5M_B^2$ and all other components of the spins are zero). Though they initially fall from rest, as in the numerical simulation, we will denote their speeds by V_A and V_B.

5.3.1.1 Even-Parity Perturbations

As we argued in Section 5.2, the even-parity perturbation will only rely upon the Newtonian potential, which has the familiar form,

$$U_N = \frac{M_A}{R_A} + \frac{M_B}{R_B}\,. \tag{5.39}$$

Here R_A and R_B denote the distance from the centers of black holes A and B in the PN coordinates. We then expand the Newtonian potential, U_N, into multipoles, keeping only the monopole and quadrupole pieces (the dipole piece vanishes),

$$\begin{aligned} U_N &= U_N^{(0)} + U_N^{(2)} \\ &= \frac{M}{R} + \frac{MA(t)^2}{4R^3}\sqrt{\frac{3\pi}{10}}\left[Y_{2,-2} - \sqrt{\frac{2}{3}}Y_{2,0} + Y_{2,2}\right]\,. \end{aligned} \tag{5.40}$$

$Y_{l,m}$ are the usual scalar spherical harmonics. One can then see that the nonzero coefficients of the spherical harmonics are

$$U_N^{2,\pm 2} = \sqrt{\frac{3\pi}{10}}\frac{MA(t)^2}{4R^3} = -\sqrt{\frac{3}{2}}U_N^{2,0}\,. \tag{5.41}$$

After applying the transformation of the PN and Schwarzschild radial coordinates, $R = r - M$, (and similarly $A(t) = a(t) - 2M$) one finds that

$$U_N^{2,\pm 2} = \sqrt{\frac{3\pi}{10}}\frac{M[a(t) - 2M]^2}{4(r-M)^3} = -\sqrt{\frac{3}{2}}U_N^{2,0}\,. \tag{5.42}$$

One can then substitute this into Eq. (5.24) to find the Zerilli function,

$$\Psi_{(\mathrm{e})}^{2,\pm 2} = \sqrt{\frac{3\pi}{10}}\frac{Ma(t)^2}{2r^2}\left(1 - \frac{7M}{6r}\right) = -\sqrt{\frac{3}{2}}\Psi_{(\mathrm{e})}^{2,0}\,. \tag{5.43}$$

We have only kept terms to linear order in M/r in this calculation, because we only use Newtonian physics to calculate the gravitational potential. At the boundary of $r_s(t) = a(t)/2$, the perturbation is constant at leading order, and varying only at higher orders.

$$\Psi_{(\mathrm{e})}^{2,\pm 2}\Big|_{\mathrm{shell}} = \sqrt{\frac{6\pi}{5}}M\left(1 - \frac{7M}{3a(t)}\right)\,, \tag{5.44}$$

$$\Psi_{(\mathrm{e})}^{2,0}\Big|_{\mathrm{shell}} = -\sqrt{\frac{4\pi}{5}}M\left(1 - \frac{7M}{3a(t)}\right)\,. \tag{5.45}$$

5.3.1.2 Odd-Parity Perturbations

The calculation with the gravitomagnetic potential is slightly more difficult, because it involves an additional gauge transformation. The gravitomagnetic potential is given by

$$w_i = \frac{\epsilon_{ijk} S^j N_A^k}{2R_A^2} + \frac{M_A V_A^i}{4R_A} + \frac{\epsilon_{ijk} S^j N_B^k}{2R_B^2} + \frac{M_B V_B^i}{4R_B} \,. \tag{5.46}$$

These results appear, for example, in Eq. (6.1d) of [25]. The new symbols N_A^k and N_B^k represent unit vectors pointing from the centers of the two black holes in the PN coordinates, and V_A^i and V_B^i are the velocities of the two black holes. Expanding the gravitomagnetic potential to leading order in $A(t)$ and simplifying the trigonometric portions of the equations below, we see that

$$w_x = \frac{MVA(t)\sin\theta\cos\varphi}{2R^2} - \frac{3A(t)S\sin^2\theta\sin 2\varphi}{4R^3} \,, \tag{5.47}$$

$$w_y = -\frac{A(t)S(1+3\cos 2\theta - 6\sin^2\theta\cos 2\varphi)}{8R^3} \,, \tag{5.48}$$

$$w_z = 0 \,. \tag{5.49}$$

The variables S and V are just the magnitudes of the spin and velocity of each black hole, respectively. For this equal-mass collision, the spins have the same magnitude, and the velocities of the holes do as well. We must then convert the gravitomagnetic potential into spherical-polar coordinates,

$$w_R = \frac{MVA(t)\sin^2\theta\cos^2\varphi}{2R^2} - \frac{A(t)S\sin\theta\sin\varphi}{2R^3} \,, \tag{5.50}$$

$$w_\theta = \frac{MVA(t)\sin 2\theta\cos^2\varphi}{4R} - \frac{A(t)S\cos\theta\sin\varphi}{2R^2} \,, \tag{5.51}$$

$$w_\varphi = -\frac{MVA(t)\sin^2\theta\sin 2\varphi}{4R} + \frac{A(t)S\cos\varphi(5\sin\theta - 3\sin 3\theta)}{8R^2} \,. \tag{5.52}$$

There is a dipole term in the component w_R of the gravitomagnetic potential, and this term will not evolve according to the Regge-Wheeler-Zerilli equation. One can remove it via the small gauge transformation to the metric,

$$\hat{h}_{\alpha\beta} = h_{\alpha\beta} - \xi_{\alpha|\beta} - \xi_{\beta|\alpha} \,, \tag{5.53}$$

where the bar refers to a covariant derivative with respect to the background metric (in this case flat space). Recall that the metric components, h_{ti}, are related to the gravitomagnetic potential, w_i, by $h_{ti} = -4w_i$. If we make a gauge transformation where the only nonzero component of ξ_μ is

$$\xi_t = \frac{2MA(t)V\sin^2\theta\cos^2\varphi}{R} - \frac{A(t)S\sin\theta\sin\varphi}{R^2} \,, \tag{5.54}$$

this has several important effects. For one, it eliminates $\hat{h}_{tr}$, and it introduces a term,

$$-\xi_{t|t} = -\frac{4M\sin^2\theta\cos^2\varphi}{R}\left(V^2 - \frac{MA(t)}{2R^2}\right), \tag{5.55}$$

into h_{tt}. This term, however, is of 1PN order, and, because we are considering only the leading Newtonian physics, we will drop it. Then, it turns the remaining perturbation into the sum of odd- and even-parity quadrupole perturbations. Letting $b = \theta, \varphi$, one has that

$$\hat{h}_{tb} = -\frac{A(t)S}{R^2}\sqrt{\frac{6\pi}{5}}(X_b^{2,1} - X_b^{2,-1}), -\sqrt{\frac{2\pi}{15}}\frac{4MA(t)V}{R}\left(Y_b^{2,2} - \sqrt{\frac{2}{3}}Y_b^{2,0} + Y_b^{2,-2}\right). \tag{5.56}$$

If one were to include the even-parity, vector-harmonic term in the Zerilli function, one would need to take its time derivative. This means it enters as a next-to-leading-order effect, and we can ignore that term in our leading-order treatment. Thus, the relevant perturbation of the gravitomagnetic potential is

$$w^{2,1}_{(\mathrm{o})} = \sqrt{\frac{6\pi}{5}}\frac{A(t)S}{4R^2} = -w^{2,-1}_{(\mathrm{o})}. \tag{5.57}$$

Finally, we make the transformation to the Schwarzschild radial coordinate, $R = r - M$ (and similarly for $A(t) = a(t) - 2M$), to find that

$$w^{2,1}_{(\mathrm{o})} = \sqrt{\frac{6\pi}{5}}\frac{(a(t) - 2M)S}{4(r-M)^2} = -w^{2,-1}_{(\mathrm{o})}. \tag{5.58}$$

We can then find the Regge-Wheeler function from Eq. (5.25) which is

$$\Psi^{2,1}_{(\mathrm{o})} = -\sqrt{\frac{6\pi}{5}}\frac{2a(t)S}{r^2} = -\Psi^{2,-1}_{(\mathrm{o})}. \tag{5.59}$$

As before, we keep only terms linear in M/r. At the boundary, the odd-parity perturbation is

$$\Psi^{2,1}_{(\mathrm{o})}\Big|_{\mathrm{shell}} = -\frac{8S}{a(t)}\sqrt{\frac{6\pi}{5}} = -\Psi^{2,-1}_{(\mathrm{o})}\Big|_{\mathrm{shell}}. \tag{5.60}$$

5.3.1.3 Energy and Momentum Fluxes

Finally, because we have only quadrupole perturbations, the expressions for the energy and momentum fluxes greatly simplify. The energy flux, for the $l = 2$ modes (taking into account that the $m = \pm 1$ are equal and the $m = \pm 2$ modes are equal, as well) becomes

$$\dot{E} = \frac{3}{8\pi}\left[\frac{8}{3}\left(\dot{\Psi}^{2,2}_{(\mathrm{e})}\right)^2 + 2\left(\dot{\Psi}^{2,1}_{(\mathrm{o})}\right)^2\right], \tag{5.61}$$

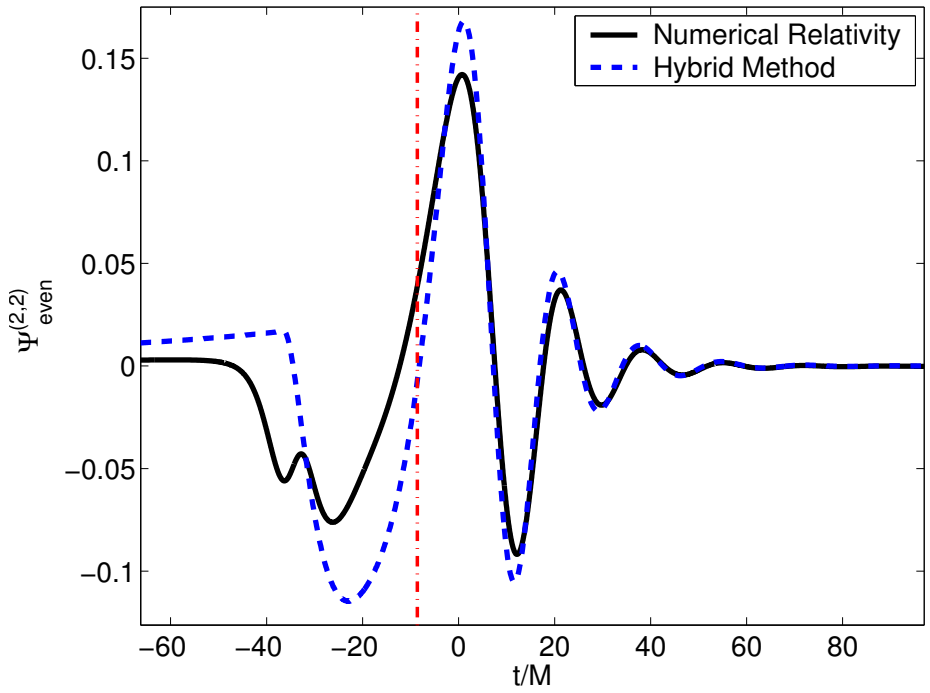

Figure 5.4: The blue (dark gray) dashed curve is $\Psi^{2,2}_{\rm even}$ from our hybrid method, whereas the black solid curve is the same quantity in full numerical relativity. The red (light gray) dashed vertical line corresponds to the retarded time at which the shell in the hybrid method reaches the light ring of the final black hole, $r/M = 3$. We shift the numerical-relativity waveform so that the peaks of the numerical and hybrid $\Psi^{2,2}_{\rm even}$ waveforms align.

and the momentum flux is given by

$$\dot{P}_y = \frac{1}{\pi}\dot{\Psi}^{2,2}_{\rm (e)}\dot{\Psi}^{2,1}_{\rm (o)}\,. \tag{5.62}$$

We have also used the fact that $\Psi^{2,0}_{\rm (e)} = \sqrt{2/3}\Psi^{2,\pm2}_{\rm (e)}$ in this head-on collision.

5.3.2 Comparison with Numerical-Relativity Results

In this section, we compare the results of our head-on collision of spinning black holes (with transverse, anti-parallel spins) with the equivalent results from a numerical-relativity simulation (see the paper by Lovelace et al. [32] for a complete description of the simulation). Although the paper by Lovelace et al. dealt mostly with using the Landau-Lifshitz pseudotensor to define a gauge-dependent 4-momentum and an effective velocity to help develop intuitive understanding of black-hole collisions, they also investigated the gauge-invariant gravitational waveforms and radiated energy-momentum (calculated from the gravitational waves at large radii). We will not attempt to study any of these Landau-Lifshitz quantities in this work, and, instead, we will just look into the gauge-invariant, radiated quantities. Specifically, for our comparison, we focus on the waveforms (the $l = 2$ modes of the gravitational waves) and the radiated energy and momentum.

In Figs. 5.4 and 5.5, we compare, respectively, the even-parity perturbation $\Psi^{(2,2)}_{\rm even}$ and the odd-

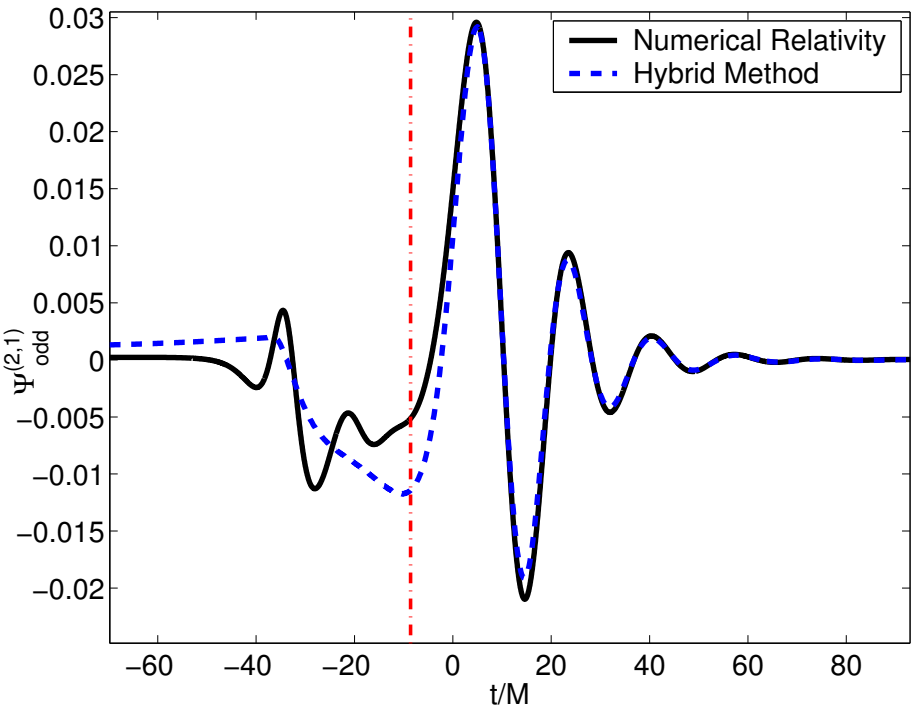

Figure 5.5: The blue (dark gray) dashed curve is $\Psi^{(2,1)}_{\rm odd}$ from our hybrid method, whereas the black solid curve is the same quantity in full numerical relativity. The red (light gray) dashed vertical line corresponds to the retarded time at which the shell in the hybrid method reaches the light ring of the final black hole, $r/M = 3$. We shift the numerical-relativity waveform so that the peaks of the numerical and hybrid $\Psi^{2,2}_{\rm even}$ waveforms align.

parity perturbation $\Psi^{(2,1)}_{\rm odd}$ from our method with the equivalent quantities from the numerical simulation S1 featured in Lovelace et al. (Because the $l = 2$, $m = -2, -1, 0$ components are related by constant multiples to the above perturbations, we do not show them.) In these figures, we also include a vertical, dashed red line that indicates the retarded time at which the shell crossed the light ring of the final black hole $r/M = 3$, in the hybrid method. This is the peak of the effective potential, and because of the low-frequency opacity of this potential, much of the influence of the boundary data is hidden within the potential after this time (and the waveform is primarily composed of the quasinormal modes of the final black hole). Before this time the match is not exact (as a result of junk radiation in the numerical simulation and the difference between the time coordinates), but the Newtonian-order perturbations do quite a good job of exciting quasinormal modes of a reasonable amplitude.

The even- and odd-parity waveforms in the hybrid method are the pieces of $\Psi^{(2,2)}_{\rm even}$ and $\Psi^{(2,1)}_{\rm odd}$ restricted to the outer boundary of the characteristic grid, labeled by *BC* in Fig. 5.1. We found these perturbations through the procedure described in Section 5.2.2, applied to the specific binary parameters described in Section 5.3.1. For the numerical-relativity waveforms, we chose to present them in terms of the even- and odd-parity perturbation functions $\Psi^{(2,2)}_{\rm even}$ and $\Psi^{(2,1)}_{\rm odd}$ as well. To find

these perturbation functions from the numerical simulations, we first integrated the Weyl scalar Ψ_4 with respect to time twice, to calculate the waveforms h_+ and $h_\times$ (because $-\Psi_4 = \ddot{h}_+ - i\ddot{h}_\times$, at large radii, where a dot denotes a time derivative). One can relate them to the gravitational waveforms h_+ and $h_\times$ by Eq. (5.32), at large r. In the case of the $l = 2$ perturbations shown here, $rh_+^{(2,2)} = \sqrt{6}\Psi_{\rm even}^{(2,2)}$ and $rh_\times^{(2,1)} = \sqrt{6}\Psi_{\rm odd}^{(2,1)}$. We compared the h_+ and $h_\times$ found directly from the numerical simulation through extraction of the Regge-Wheeler and Zerilli functions from metric coefficients in the numerical code [33], and the two procedures gave essentially identical results.

In order to make the comparison between our hybrid method and the full numerical-relativity waveforms, we must shift the numerical waveforms by a constant. Specifically, we choose this constant so that the peaks of the exact and approximate waveforms of $\Psi_{\rm even}^{(2,2)}$ match (at a time that we set to be $t = 0$). We add this constant shift in time, because there is no clear relationship between the coordinate time at which the waveform in our code begins and the same coordinate time in the numerical-relativity simulation. Trying to find a relationship between these times is complicated by the fact that the hybrid method evolves on a characteristic grid, whereas the numerical-relativity simulation solves an initial-value problem in a gauge that changes as the black holes move together. Nevertheless, because both the numerical and the hybrid method use asymptotically flat coordinates, at large radii, the time coordinates move at the same rate. This, in turn, means that it is only necessary to shift the time coordinates rather than rescaling them. As an interesting aside, Owen [34] found that this agreement between the time coordinates in the numerical simulation and perturbation theory appears to extend even into the near zone, when he observed that multipole moments of the horizon oscillate at the quasinormal mode frequencies of the black hole. See the end of Section III of that paper for a discussion of why that might be the case.

We also compute the momentum flux, and we show the accumulation of the velocity of the final black hole in Fig. 5.6, for both our method and the full numerical-relativity simulation. For our hybrid method, we use just the $l = 2$ modes of the waveform to compute the momentum flux, $\dot{P}_y$, our Eq. (5.62). We then find the velocity of the final black hole as a function of time by computing

$$v_y(t) = -\frac{1}{M}\int_{t_0}^{t} \dot{P}_y(t')dt' \,, \tag{5.63}$$

where we introduce an extra minus sign to account for the fact that the black-hole's velocity is opposite that of the momentum carried by the gravitational waves. For the numerical waveform, we show the equivalent velocity computed from the full Weyl scalar, Ψ_4. For the numerical simulations, one typically computes

$$\dot{P}_y = \lim_{r\to\infty} \frac{r^2}{16\pi} \oint \sin\theta \sin\phi \left| \int_{-\infty}^{t} \Psi_4 dt' \right|^2 d\Omega, \tag{5.64}$$

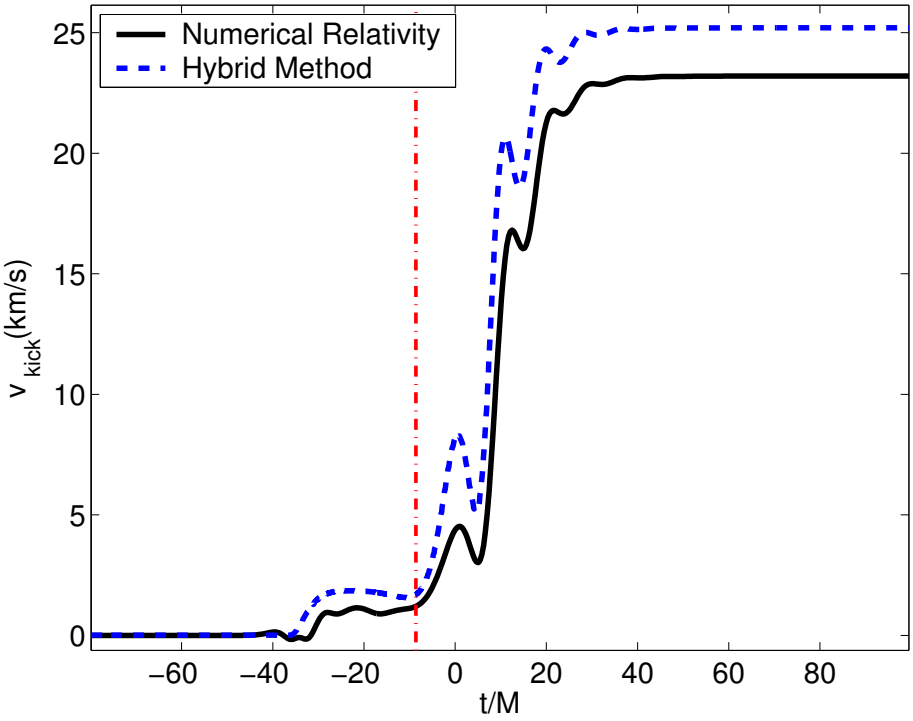

Figure 5.6: The blue (dark gray) dashed curve is the velocity of the final black hole as a function of time (inferred from the gravitational radiation) from our hybrid method, using only the $l = 2$ modes of the wave. The black solid curve is the equivalent quantity in numerical relativity, computed from the full Weyl scalar, ψ_4. The red (light gray) dashed vertical line corresponds to the retarded time at which the shell in the hybrid method reaches the light ring of the final black hole, $r/M = 3$. As before, the numerical-relativity velocity is shifted so that the peaks of the numerical and hybrid $\Psi^{2,2}_{\rm even}$ waveforms align.

where Ψ_4 is the Weyl scalar extrapolated to infinity, and $d\Omega$ is the surface-area element on a unit sphere. This expression appears in a variety of sources (see, for example, Eq. (29) of the paper by Ruiz et al.). We then can compute the velocity of the final black hole in the numerical simulations through Eq. (5.63), as we did for the hybrid method. Again, we perform the same time-shifting procedure as we did with the waveforms. The kick we find is remarkably close; 22 km/s for the numerical simulation and 25 km/s for our hybrid method.

The radiated energy does not agree quite as well, because the even-parity perturbation is somewhat larger than the equivalent numerical quantity (and it is the dominant contribution to the energy flux). Nevertheless, the results agree within a factor of two; the numerical simulation shows that roughly 0.057% of the initial mass is radiated, whereas our hybrid method predicts approximately 0.096% of the initial mass escapes in gravitational waves. This is an improvement over some of the earlier, first-order, close-limit calculations at larger separations (see, for example, Fig. 1 of [35], where more than 1% of the initial mass is radiated for equivalent initial separations of the black holes).

We are not aware of any equivalent calculations of radiated energy for head-on collisions within the EOB formalism. While there have been recent 3PN calculations of the energy flux for a head-on plunge of black holes by Mishra and Iyer [36], in PN-based calculations such as the EOB approach, one must always stop the calculation at some radial separation of the binary. For example, in Fig. 2 of Mishra and Iyer's work, they stop the calculation at a point at which only roughly a tenth of the total energy that will be radiated in the head-on collision has escaped. This poses a small problem for EOB approaches, because as described in the Introduction to this paper (Section 5.1), one must choose a point at which to stop the EOB inspiral-and-plunge waveform and match it to a set of quasinormal modes to obtain a full waveform. For inspiraling black holes, there is a natural point to do this: when the frequency of the inspiral-plunge dynamics approaches the quasinormal mode frequencies of the final black hole that will be formed. For a head-on collision, however, there is no analogous frequency at which one can match. We will, therefore, reserve any comparisons between our method and that of EOB for future work, when we extend our method to inspiraling, black-hole binaries.

5.4 The Three Stages of Black-Hole Mergers

In addition to producing reasonably accurate full waveforms, our approach also provides an interpretation of the infall, merger and ringdown stages of a binary-black-hole merger. As shown in Fig. 5.1, before the shell reaches point e and enters the strong-field region (the red (dark gray) area, in which the $l = 2$, even-parity, effective potential exceeds 1/3 of its peak value), the majority of the retarded waveform propagates along the light cone (the so-called direct part). The direct part overwhelms the waves that scatter off the background curvature, because, far away from the source, the curvature is small. This part of the waveform corresponds to the inspiral or infall phase.

In the strong-field region, however, there is strong curvature (the black-hole effective potential in our model). While some fraction of the waves will pass directly through, as the shell enters this region at point e, waves that scatter off the effective potential (and thereby propagate within the light cone) become more significant. These waves often are called tail waves. Although PN waveforms do include the tail part, the fact that the higher-order PN terms that contain the tail dominate over the lower-order terms [24] does not bode well for the ability of the PN series to easily capture this effect. Nevertheless, we are able to associate this mixture of direct and tail portions in the waveform to the merger. In our model, this stretch of the waveform is related to the retarded times when the shell is passing through the strong-field region of spacetime (points e, f, and g in the diagram).

Finally, after the shell passes through the potential, the details of the perturbation no longer become important, as was found by Price in his stellar collapse model. Because waves do not efficiently propagate through the barrier, the gravitational waveform associated with points g through

D should arise from before and while the shell passes through the effective potential (not after). This last piece is that of ringdown.

There is one subtlety to note about our interpretation of ringdown that might arise if the final black hole is a Kerr black hole. Mino and Brink [37] and Zimmerman and Chen [38] showed that mergers that lead to a Kerr black hole can emit waves at integer multiples of the horizon frequency that decay at a rate proportional to the surface gravity. These modes come from a calculation in the near-horizon limit of a Kerr black hole, and from the vantage point of observers far away, these waves would appear to be coming from the horizon. These modes have a sufficiently high frequency that they could penetrate the effective potential of a Kerr black hole and contribute to the ringdown portion of the gravitational wave. Nevertheless, if we expand our description of the ringdown phase to include these horizon modes, our interpretation holds more or less as described above.

5.5 Conclusion

In this paper, we show, by examining the head-on collisions of spinning black holes, that a combination of PN and BHP theories gives a gravitational waveform that matches well with that of full numerical-relativity simulations. We were able to do this not by applying the approximation methods to distinct times in the evolution of the system, but by choosing regions of space in which the two methods work and finding that the waveform from black-hole-binary collisions can be protected from lack of convergence in these approximations. Specifically, our method lumps all monopole pieces of a PN black-hole-binary spacetime into the Schwarzschild metric and treats the higher multipoles as perturbations of that Schwarzschild that evolve via a wave equation. Moreover, because PN and BHP theories describe the waveform, this suggests that much of the nonlinear dynamics appearing in the gravitational waves of a head-on black-hole-binary merger can be well approximated by linear perturbations of the Schwarzschild solution.

Our approach certainly cannot replace full numerical simulations. For one, we must test its validity for different kinds of coalescence by comparison with fully nonlinear numerical results. Nevertheless, we are hopeful that our method maybe be useful for gaining further understanding of the spacetime of black-hole-binary mergers and for producing templates of gravitational waveforms for data analysis. To move towards these goals, we would need to make several modifications to our method (whose implementation we leave for future work). Most of these changes revolve around finding a way to treat inspirals of black-holes binaries within our method. The most necessary addition would be finding a way to consistently introduce a radiation-reaction force within the formalism. This feature is essential for capturing the correct inspiral and plunge dynamics. Also important for describing realistic physics of the ringdown would be to analyze the problem in a Kerr background. Each of these problems requires significant work, and we leave them for future studies.

Bibliography

[1] F. Pretorius, Phys. Rev. Lett. **95**, 121101 (2005).

[2] M. Campanelli, C. O. Lousto, P. Marronetti, and Y. Zlochower, Phys. Rev. Lett. **96**, 111101 (2006).

[3] J. G. Baker, J. Centrella, D.-I. Choi, M. Koppitz, and J. van Meter, Phys. Rev. Lett. **96**, 111102 (2006).

[4] M. A. Scheel, M. Boyle, T. Chu, L. E. Kidder, K. D. Matthews, and H. P. Pfeiffer, Phys. Rev. D **79**, 024003 (2009).

[5] L. Rezzolla, R. P. Macedo, and J. L. Jaramillo, Phys. Rev. Lett. **104**, 221101 (2010).

[6] R. H. Price and J. Pullin, Phys. Rev. Lett. **72**, 3297 (1994).

[7] G. Khanna, J. Baker, R. J. Gleiser, P. Laguna, C. O. Nicasio, H.-P. Nollert, R. Price, and J. Pullin, Phys. Rev. Lett. **83**, 3581 (1999).

[8] C. W. Misner, Phys. Rev. **118**, 1110 (1960).

[9] R. W. Lindquist, J. Math. Phys. **4**, 938 (1963).

[10] D. R. Brill and R. W. Lindquist, Phys. Rev. **131**, 471 (1963).

[11] J. M. Bowen and J. W. York, Phys. Rev. D **21**, 2047 (1980).

[12] J. Baker, M. Campanelli, and C. O. Lousto, Phys. Rev. D **65**, 044001 (2002).

[13] C. F. Sopuerta, N. Yunes, and P. Laguna, Phys. Rev. D **74**, 124010 (2006).

[14] C. F. Sopuerta, N. Yunes, and P. Laguna, Astrophys. J. **656**, L9 (2007).

[15] A. Le Tiec and L. Blanchet, Classical Quantum Gravity **27**, 045008 (2010).

[16] A. Le Tiec, L. Blanchet, and C. Will, Classical Quantum Gravity **27**, 012001 (2010).

[17] N. K. Johnson-McDaniel, N. Yunes, W. Tichy, B. J. Owen, Phys. Rev. D **80**, 124039 (2009).

[18] A. Buonanno, Y. Pan, H. P. Pfeiffer, M. A. Scheel, L. T. Buchman, and L. E. Kidder, Phys. Rev. D **79**, 124028 (2009).

[19] T. Damour and A. Nagar, Phys. Rev. D **79**, 081503(R) (2009).

[20] A. Buonanno and T. Damour, Phys. Rev. D **62**, 064015 (2000).

[21] R. H. Price, Phys. Rev. D, **5**, 2419 (1972).

[22] L. Blanchet and G. Faye, Phys. Rev. D **63**, 062005 (2001).

[23] A. Garat and R. H. Price, Phys. Rev. D **61**, 044006 (2000).

[24] E. Racine, A. Buonanno, and L. Kidder, Phys. Rev. D **80**, 044010 (2009).

[25] J. D. Kaplan, D. A. Nichols, and K. S. Thorne, Phys. Rev. D **80**, 124014 (2009).

[26] T. Regge and J. A. Wheeler, Phys. Rev. **108**, 1063 (1957).

[27] F. J. Zerilli, Phys. Rev. D **2**, 2141 (1970).

[28] V. Moncrief, Ann. Phys. (N.Y.) **88**, 323 (1974).

[29] M. Ruiz, M. Alcubierre, D. Núñez, and R. Takahashi, Gen. Relativ. Gravit. **40**, 1705 (2008).

[30] H. Stephani. *General Relativity: An Introduction to the Theory of the Gravitational Field*, 2nd ed. (Cambridge University Press, Cambridge, 1990), Sec. 22.2.

[31] C. Gundlach, R. H. Price, and J. Pullin, Phys. Rev. D **49**, 883 (1994).

[32] G. Lovelace, Y. Chen, M. Cohen, J. D. Kaplan, D. Keppel, K. D. Matthews, D. A. Nichols, M. A. Scheel, and U. Sperhake, Phys. Rev. D **82**, 064031 (2010).

[33] O. Rinne, L. T. Buchman, M. A. Scheel, and H. P. Pfeiffer, Classical Quantum Gravity **26**, 075009 (2009).

[34] R. Owen, Phys. Rev. D **80**, 084012 (2009).

[35] R. J. Gleiser, C. O. Nicasio, R. H. Price, and J. Pullin, Phys. Rev. Lett. **77**, 4483 (1996).

[36] C. K. Mishra and B. R. Iyer, Phys. Rev. D **82**, 104005 (2010).

[37] Y. Mino and J. Brink, Phys. Rev. D **78**, 124015 (2008).

[38] A. Zimmerman and Y. Chen, Phys. Rev. D **84**, 084012 (2011).

Chapter 6

A Hybrid Method for Understanding Black-Hole Mergers: II. Inspiralling Mergers

We adapt a method of matching post-Newtonian and black-hole-perturbation theories on a timelike surface (which proved useful for understanding head-on black-hole-binary collisions) to treat equal-mass, inspiralling black-hole binaries. We first introduce a radiation-reaction potential into this method, and we show that it leads to a self-consistent set of equations that describe the simultaneous evolution of the waveform and of the timelike matching surface. This allows us to produce a full inspiral-merger-ringdown waveform of the $l = 2$, $m = \pm 2$ modes of the gravitational waveform of an equal-mass black-hole-binary inspiral. These modes match those of numerical-relativity simulations well in phase, though less well in amplitude for the inspiral. As a second application of this method, we study a merger of black holes with spins antialigned in the orbital plane (the superkick configuration). During the ringdown of the superkick, the phases of the mass- and current-quadrupole radiation become locked together, because they evolve at the same quasinormal-mode frequencies. We argue that this locking begins during the merger, and we show that if the spins of the black holes evolve via geodetic precession in the perturbed black-hole spacetime of our model, then the spins precess at the orbital frequency during the merger. In turn, this gives rise to the correct behavior of the radiation, and produces a kick similar to that observed in numerical simulations.

Originally published as D. A. Nichols and Y. Chen, Phys. Rev. D **85**, 044035 (2012).

6.1 Introduction

Black-hole-binary mergers are both key sources of gravitational waves [1] and two-body systems in general relativity of considerable theoretical interest. It is common to describe the dynamics and

the waveform of a quasicircular black-hole binary as passing through three different stages: inspiral, merger, and ringdown (see, e.g., [2]). For comparable-mass black holes, the three stages correspond to the times one can use different approximation schemes. During the first stage, the inspiral, the two black holes can be modeled by the post-Newtonian (PN) approximation as two point particles (see, e.g., [3] for a review of PN theory). As the speeds of the two holes increase while their separation shrinks, the PN expansion becomes less accurate (particularly as the two objects begin to merge to form a single body). In this stage, the merger, gravity becomes strongly nonlinear (and therefore less accessible to approximation techniques). After the merger, there is the ringdown, during which the spacetime closely resembles a stationary black hole with small perturbations (and one can treat the problem using black-hole perturbation (BHP) theory; see, e.g., [4] for a review of BHP theory).

Because the merger phase of comparable-mass black holes has been so challenging to understand analytically, there have been many attempts to study it with a variety of analytical tools. One approach has been to develop PN and BHP theories to high orders in the different approximations. Since neither approximation can yet describe the complete merger of black-hole binaries, several groups worked on developing methods that aim to get the most out of a given approximation technique. The close-limit approximation (see, e.g., [5, 6, 7, 8] for early work and [9, 10, 11, 12] for more recent work) and the Lazarus project (see, e.g., [13, 14]) both try to push the validity of BHP to early times; the effective-one-body (EOB) approach (see, e.g., [15, 16] for the formative work, and [17, 18, 19, 20] for further developments that allow the method to replicate numerical-relativity waveforms) aims to extend the validity of the PN approximation to later times.

There also have been several methods that do not easily fit into the characterization of extensions of PN or BHP theories. For example, the "particle-membrane" approach of Anninos et al. [21, 22] computes the waveform from head-on collisions by extrapolating results from the point-particle limit to the comparable-mass case (and taking into account changes to the horizons computed within the membrane paradigm [23]). More recently, white-hole fission was used in approximate models of black-hole mergers [24, 25, 26], and quite recently, Jaramillo and collaborators [27, 28, 29, 30] used Robinson-Trautman spacetimes as an approximate analytical model of binary mergers (as part of a larger project correlating geometrical quantities on black-hole horizons with similar quantities at future null infinity).

Analytical approximations are not limited to comparable-mass black-hole binaries, and recently there has been a large body of work on developing techniques to study intermediate- and extreme-mass-ratio inspirals (IMRIs and EMRIs, respectively). Most of these methods aim to produce gravitational waves in ways that are less computationally expensive than computing the exact numerical solution or computing the leading-order gravitational self-force are (see, e.g., [31] for a recent review of the self-force problem). The majority of the approaches rely heavily on BHP techniques combined with some prescription for taking radiative effects into account, though not all approx-

imate methods fall into this classification (Barack and Cutler [32], for example, model EMRIs by instantaneously Newtonian orbits whose orbital parameters vary slowly over the orbital time scale because of higher-order PN effects). A well-known example is that of Hughes [33], Glampedakis [34], Drasco [35], Sundararajan [36], and their collaborators whose semi-analytical approaches are often called Teukolsky-based models. These methods describe the small black hole as moving along a sequence of geodesics whose energy, angular momentum, and Carter constant change from the influence of emitted gravitational waves. They usually involve some additional prescription to treat the transition from the inspiral to the plunge, when the motion is no longer adiabatic. The EOB formalism in the EMRI limit, however, does not require an assumption of adiabatic motion (see, e.g., [37, 38, 39, 40, 41, 42]). By choosing the dynamics of the EMRI to follow the EOB Hamiltonian and a resummed multipolar PN radiation-reaction force [43], these authors can calculate an approximate waveform without any assumption on relative time scales of orbital and radiative effects. One can also make an adiabatic approximation with EOB methods, as Yunes et al. [44, 45] recently did in their calibration of the EOB method to a set of Teukolsky-based waveforms. Lousto and collaborators [46, 47, 48] took a different approach to the EMRI problem in their recent work. They used trajectories from numerical-relativity simulations of IMRIs as a way to calibrate PN expressions for the motion of the small black hole. They then performed approximate calculations of the gravitational waves using the PN trajectories in a black-hole perturbation calculation, and found good agreement with their numerical results.

In a previous article [49] (hereafter referred to as Paper I), we showed that for head-on collisions, one can match PN and BHP theories on a timelike world tube that passes through the centers of the PN theory's point particles. The positions of the point particles as a function of time (and, consequently, the world tube) were chosen before evolving the waveform. Moreover, they were selected in such a way that both PN and BHP theories were sufficiently accurate descriptions of the spacetime on the world tube or the errors in the theories did not enter into the waveform. (A plunging geodesic in the Schwarzschild spacetime worked in Paper I.) This allowed us compute a complete waveform for all three phases of black-hole-binary coalescence and gave us a way to interpret the different portions of the waveform. Moreover, when we compared the waveform from the hybrid method with that of a full numerical simulation of plunging equal-mass black holes with transverse, antialigned spins, we found very good agreement between the two.

There is no reason, *a priori*, why the same procedure of Paper I (namely, specifying the position of the point particles as a function of time and matching the metrics on a surface passing through their positions) should not work for inspiralling black holes as well. The principal difficulty arises from trying to find a way of specifying the positions of the particles for inspiralling black holes (and thus a location at which to match the PN and BHP metrics) that does not introduce errors into any of the three stages of the inspiral, merger, or ringdown portions of the waveform. The most

important development that we introduce in this paper, therefore, is a way of achieving this goal by including a radiation-reaction force into the formalism. In the hybrid method, we compute a radiation-reaction force by using the outgoing waves in the exterior BHP spacetime to modify the PN dynamics in the interior through a radiation-reaction potential [50]. We show, in this formalism, that introducing a radiation-reaction potential is equivalent to solving a self-consistent set of coupled equations that describe the evolution of the point particles' reduced-mass motion and the outgoing gravitational radiation, where the particles generate the metric perturbations of the gravitational waves and the waves carry away energy and angular momentum from the particles (thereby changing their motion).

Our principal goal in the paper is to explore this coupled set of evolution equations and show, numerically, that it gives rise to convergent and reasonable results. We will use these results to make a refinement of our interpretation of the waveform from Paper I, and we will also compare the waveform generated by the hybrid method to that from a numerical-relativity simulation of an equal-mass, nonspinning inspiral of black holes. The two waveforms agree well during the inspiral phase, but less well during merger and ringdown. The discrepancy at late times is well understood: we continue to model the final black hole produced from the merger as nonspinning, although, in fact, numerical simulations have shown the final hole to be spinning relatively rapidly (see, e.g., [51]). Adapting the hybrid approach to treat the final black hole as rotating is beyond the scope of this work, but is something that we will investigate in the future.

As an application of the hybrid method for inspirals, we explore the large kicks produced from black-hole binaries with antialigned spins in the orbital plane (the superkick configuration [52, 53]). As noted by Schnittman et al. [54] and emphasized to us by Thorne [55], the spins must precess at the orbital frequency during the final stage of the merger. While Brügmann et al. [56] were able to replicate this effect using a combination of PN and numerical-relativity results, we will need to take a different approach, by using geodetic precession in the exterior Schwarzschild BHP spacetime, to have the spins lock to the orbital motion at the merger. When we include the geodetic effect, we are able to recover the correct qualitative profile of the kick, although the magnitude does not match precisely.

We organize the paper as follows: We review the results of Paper I in Section 6.2, and we describe the procedure for calculating the radiation-reaction force and the resulting set of evolution equations in Section 6.3. In Section 6.4, we show the convergence of our waveform, we compare with numerical relativity, and we discuss using the hybrid method to interpret the waveform. Next, we discuss the behavior of spinning black holes and describe spin precession as a mechanism for generating large black-hole kicks in Section 6.5. We conclude in Section 6.6. Throughout this paper, we set $G = c = 1$, and we use the Einstein summation convention (unless otherwise noted).

6.2 A Brief Review of Paper I

In this section, we will review the essentials of the formalism from Paper I. In the hybrid method, we divide the spacetime of an equal-mass, black-hole-binary merger into two regions: a PN region within a spherical shell through the centers of the PN theory's point particles, and a perturbed Schwarzschild spacetime outside that shell. Figure 5.2 shows this at a given moment in time (with one spatial dimension suppressed). For the hybrid procedure to work, there must be either a spherical shell on which both BHP and PN theories are simultaneously valid (to a given level of accuracy) or a way to prevent the errors in the approximations from affecting observables, such as the waveform. By finding good agreement between the hybrid waveform and that of numerical relativity in Paper I, we found evidence that matching the theories on a spherical shell that passes through the PN theory's point particles works throughout all three stages of a head-on black-hole-binary merger: infall, merger, and ringdown.

To mesh the two descriptions of spacetime, we match the PN metric to that of the perturbed Schwarzschild black hole, which involves relating the two coordinate systems of PN and BHP theories. In the PN coordinate system, we will use uppercase variables, and we will use a harmonic gauge. For example, we will employ (T, X, Y, Z) when describing the Cartesian coordinates of the background Minkowski space and (T, R, Θ, Φ) when discussing its spherical-polar coordinates. In the perturbed Schwarzschild spacetime, we will use (t, r, θ, φ), primarily, though sometimes we will also use the light-cone coordinates, (u, v, θ, φ), where

$$u = t - r_* \,, \quad v = t + r_* \,, \tag{6.1}$$

and

$$r_* = r + 2M \log\left[\frac{r}{2M} - 1\right] . \tag{6.2}$$

One can match the two coordinate systems, accurate to linear order in M/R by identifying

$$T = t \,, \quad \Theta = \theta \,, \quad \Phi = \varphi \,, \quad R = r - M \,. \tag{6.3}$$

For the equal-mass binaries that we study, we will denote the separation by $A(t) = 2R(t)$ in PN coordinates and $a(t) = 2r(t)$ in Schwarzschild coordinates. Moreover, because we match the two metrics on a shell passing through the centers of the point particles, we will indicate the position of the shell by adding a subscript "s" to the coordinate radius. For example, we will write $R_s(t) = A(t)/2$ or $r_s(t) = a(t)/2$ to denote this. For clarity, we include a table that reviews the essentials of our notation in Table 5.1.

Because we are investigating only the lowest-order effects in our study of radiation reaction and

large black-hole kicks, we shall only need the lowest-order terms in the PN metric that appeared in Paper I to describe the interior of the shell,

$$dS^2 = -(1 - 2M/R - 2U_N^{(l=2)})dt^2 - 8w_b^{(l=2)}dtdx^b + (1 + 2M/R + 2U_N^{(l=2)})(dR^2 + R^2 d^2\Omega)\,. \quad (6.4)$$

In the above equation, M is the total mass of the binary, $d^2\Omega$ is the area element on the unit sphere, $dx^b = d\theta, d\varphi$, and the additional variables $U_N^{(l=2)}$ and $w_b^{(l=2)}$ are the quadrupole parts of the spherical harmonic expansion of the binary's Newtonian potential and gravitomagnetic potential, respectively,

$$U_N^{(l=2)} = \sum_{m=-2}^{2} U_N^{2,m} Y_{2,m}(\theta,\varphi)\,, \quad (6.5)$$

$$w_b^{(l=2)} = \sum_{m=-2}^{2} w_{(\mathrm{o})}^{2,m} X_b^{2,m}(\theta,\varphi)\,. \quad (6.6)$$

We denote the scalar spherical harmonics by $Y_{2,m}(\theta,\varphi)$, and the coefficients $U_N^{2,m}$ and $w_{(\mathrm{o})}^{2,m}$ are functions of R and t. The functions $X_b^{2,m}(\theta,\varphi)$ are odd-parity vector spherical harmonics, whose θ and φ coefficients are given by

$$X_\theta^{l,m} = -(\csc\theta)\partial_\varphi Y^{l,m}(\theta,\varphi)\,, \quad (6.7)$$

$$X_\varphi^{l,m} = (\sin\theta)\partial_\theta Y^{l,m}(\theta,\varphi)\,. \quad (6.8)$$

A more general description is put forth in Paper I, but here we only take the essential components needed for the calculations in the paper.

Outside of the shell, we write down a perturbed Schwarzschild metric,

$$ds^2 = -(1 - 2M/r)dt^2 + (1 - 2M/r)^{-1}(dr^2 + r^2 d^2\Omega) + h_{\mu\nu}dx^\mu dx^\nu, \quad (6.9)$$

where the nonzero components of the perturbed metric $h_{\mu\nu}$ that we shall need in this paper are the

quadrupole pieces, $h_{\mu\nu}^{(l=2)}$, and they take the form,

$$(h_{tt}^{(l=2)})_{(\mathrm{e})} = \sum_{m=-2}^{2} H_{tt}^{2,m} Y^{2,m}(\theta,\varphi)\,, \tag{6.10}$$

$$(h_{rr}^{(l=2)})_{(\mathrm{e})} = \sum_{m=-2}^{2} H_{rr}^{2,m} Y^{2,m}(\theta,\varphi)\,, \tag{6.11}$$

$$(h_{\theta\theta}^{(l=2)})_{(\mathrm{e})} = r^2 \sum_{m=-2}^{2} K^{2,m} Y^{2,m}(\theta,\varphi)\,, \tag{6.12}$$

$$(h_{\varphi\varphi}^{(l=2)})_{(\mathrm{e})} = r^2 \sin^2\theta \sum_{m=-2}^{2} K^{2,m} Y^{2,m}(\theta,\varphi)\,, \tag{6.13}$$

and

$$(h_{t\theta}^{(l=2)})_{(\mathrm{o})} = \sum_{m=-2}^{2} h_{t}^{2,m} X_{\theta}^{2,m}(\theta,\varphi)\,, \tag{6.14}$$

$$(h_{t\varphi}^{(l=2)})_{(\mathrm{o})} = \sum_{m=-2}^{2} h_{t}^{2,m} X_{\varphi}^{2,m}(\theta,\varphi)\,. \tag{6.15}$$

The subscripts (e) and (o) refer to the parity of the perturbations (even and odd, respectively), where we call perturbations that transform as $(-1)^l$ even and as $(-1)^{l+1}$ odd.

The interior PN metric must match the perturbed Schwarzschild metric on a spherical shell between the two regions. To make this identification, we note that because $R = r - M$, then the term

$$\left(1 - \frac{2M}{r}\right)^{-1} = \left(1 + \frac{2M}{R}\right) + O[(M/R)^2]\,. \tag{6.16}$$

We, therefore, identify the monopole piece of the PN metric with the unperturbed Schwarzschild metric. Moreover, at leading order in M/R, we note that the perturbations of the two metrics match exactly,

$$H_{tt}^{2,m} = H_{rr}^{2,m} = K^{2,m} = 2U_N^{2,m}\,, \tag{6.17}$$

$$h_{t}^{2,m} = -4w_{(\mathrm{o})}^{2,m}\,. \tag{6.18}$$

There is then a straightforward procedure that lets one express the metric perturbations in terms of the gauge-invariant perturbation functions of the Schwarzschild spacetime [57] (though in this paper we use the notation of [58]), which are typically called the Zerilli function and the Regge-Wheeler function for the even- and odd-parity perturbations, respectively. We reproduce the expressions

below:

$$\Psi^{2,m}_{(\mathrm{e})} = \frac{2r}{3}\left\{U^{2,m}_N + \frac{r-2M}{2r+3M}\left[\left(1-\frac{2M}{r}\right)U^{2,m}_N - r\partial_r U^{2,m}_N\right]\right\}, \tag{6.19}$$

$$\Psi^{2,m}_{(\mathrm{o})} = 2r\left(\partial_r w^{2,m}_{(\mathrm{o})} - \frac{2}{r}w^{2,m}_{(\mathrm{o})}\right). \tag{6.20}$$

In Paper I, we matched the two metrics on a timelike tube that we specified before evolving the Regge-Wheeler and Zerilli functions. We assumed that this tube would be spherically symmetric, and we found its radius by first assuming the reduced-mass motion of the system followed a radial geodesic of a plunging test mass in the background Schwarzschild spacetime and then setting the radius of the world tube to be half this distance at each time. This allowed us to use the PN data in the form of the Regge-Wheeler and Zerilli functions, Eqs. (6.20), and (6.19), respectively] on this tube to provide a boundary-value problem for the evolution of the Regge-Wheeler [59] or Zerilli [60] equations,

$$\frac{\partial^2\Psi^{l,m}_{(\mathrm{e,o})}}{\partial u\partial v} + \frac{V^l_{(\mathrm{e,o})}\Psi^{l,m}_{(\mathrm{e,o})}}{4} = 0\,. \tag{6.21}$$

The potentials for the Regge-Wheeler (odd-parity) or Zerilli (even-parity) equations are given by

$$V^l_{(\mathrm{e,o})}(r) = \left(1-\frac{2M}{r}\right)\left(\frac{\lambda}{r^2} - \frac{6M}{r^3}U^l_{(\mathrm{e,o})}(r)\right), \tag{6.22}$$

where $\lambda = l(l+1)$ and

$$U^l_{(\mathrm{o})}(r) = 1, \quad U^l_{(\mathrm{e})}(r) = \frac{\Lambda(\Lambda+2)r^2 + 3M(r-M)}{(\Lambda r+3M)^2}, \tag{6.23}$$

where $\Lambda = (l-1)(l+2)/2 = \lambda/2 - 1$. After numerically solving the Regge-Wheeler or Zerilli equations above, we computed the gravitational waveforms and the radiated energy and momentum, all of which we found to be in good agreement with the exact quantities computed from numerical-relativity simulations.

In this paper, while much of the procedure we use for matching the metrics is identical to that set forth above, there are several important differences that we will discuss in Section 6.3. The most important difference between the first paper and the current one arises in how we find the trajectory of the system's reduced mass (and then the timelike tube on which we match the metrics). Before, we chose a region, prior to evolving the Regge-Wheeler and Zerilli equations, that would not introduce spurious effects into the results; here we determine the position of timelike world tube through evolving the position of the reduced mass of the binary subject to a radiation-reaction force. We will discuss the details of this procedure in the next section.

6.3 Radiation-Reaction Potential and Evolution Equations

In this section, we introduce a radiation-reaction potential into the hybrid method, and we show that it leads to a set of evolution equations that simultaneously evolve both the outgoing radiation and dynamics of the reduced mass of the system. This, in turn, allows us to produce a full inspiral-merger-ringdown waveform. We first qualitatively discuss how our method works and how it compares to other analytical methods. We then discuss the hybrid method in further detail, and we close this section by showing, analytically, that the procedure recovers the correct Burke-Thorne radiation-reaction potential [50] in the weak-field limit.

6.3.1 Qualitative Description

It is easiest to discuss our method with the aid of the spacetime diagram in Fig. 6.1. We describe the region within the solid black timelike curve with the near-zone PN metric, and outside this curve, we use a perturbed Schwarzschild region. The black line, which passes through the PN point particles, is where we match the two metrics. We suppress both angular coordinates, so that each point on the curve represents the matching shell that we discuss in Section 6.2. The shaded regions represent the black-hole potential: the yellow (light gray) shade depicts the strong-field portion of the black-hole potential (the strong-field near zone), and the green (gray) shade shows the region where centrifugal potential is significant (the weak-field near zone). There is a wave zone near the horizon (large u), and, consequently, the region where there is a large black-hole potential is confined to a small space in this diagram.

To have Fig. 6.1 be an effective description of the spacetime of a black-hole binary, both PN and BHP theories both must be sufficiently accurate at the PN point particles (the black line where we match the metrics), or the PN approximation could break down if the point particles are well-hidden within the black-hole effective potential. For the errors to stay within the potential, the particles must rapidly fall to the horizon; thus one can see in Fig. 6.1 that the black curve approaches an ingoing null ray asymptotically. (Recall that u and v are the light-cone coordinates of the BHP spacetime.) Following this trajectory, the perturbations induced by the PN spacetime will become strongly redshifted, and they will not escape the black-hole potential (as Price had found in his description of stellar collapse [61]), because the potential reflects low frequency perturbations.

As in Paper I, we will again be able to interpret different portions of the waveform by connecting a region of the waveform with the position of the PN binary's point particles in the near zone (via constant values of the light-cone coordinate, u). In the figure, these are the thick red (gray) dashed lines of constant u. The inspiral part of the waveform, which propagates directly along the light cone, comes from the part of the trajectory within the weak-field near zone. Once the trajectory reaches within the strong-field near zone, the waves scatter off of the potential and propagate within the light cone (often referred to as the PN tail part of the wave) in addition to propagating out

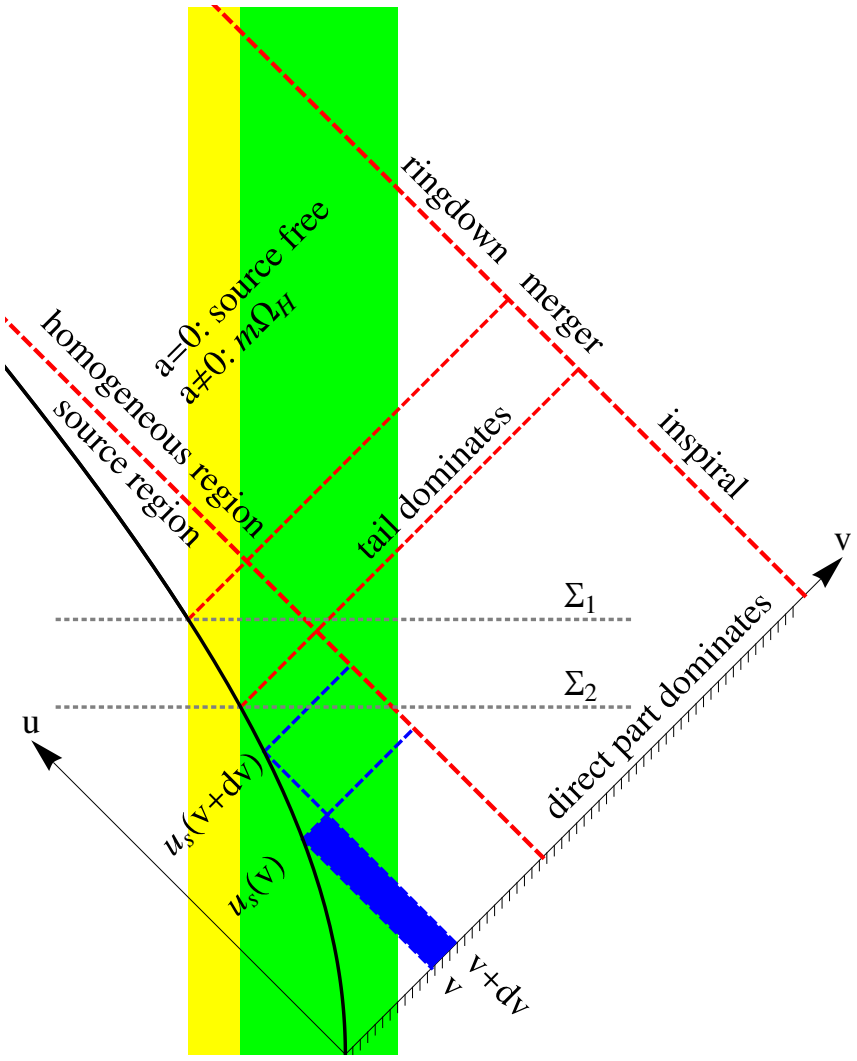

Figure 6.1: A spacetime diagram of our method. The solid black timelike curve depicts the region where we match PN and BHP spacetimes (passing through the centers of the PN theory's point particles). Inside this curve, the spacetime can be reasonably approximated by PN theory, whereas outside, the spacetime is better described by BHP theory. The yellow (light gray) shade shows the strong-field region, whereas the green (gray) shade represents where the black-hole potential is weaker, but the centrifugal barrier of flat space still is important. The dark blue (dark gray) shaded region, surrounded by the blue (dark gray) dashed lines, shows how the value of the perturbations in the exterior (along with the no-ingoing-wave condition) determines the value of the radiation-reaction potential at the next matching point. The horizontal dashed lines represent the region of spacetime where the close-limit approximation or Lazarus approach would begin. The red (gray) dashed lines show how one can connect the near-zone behavior to the wave (through lines of constant u), and thereby tie the motion of the matching region through the black-hole effective potential to portions of the waveform. This gives an interpretation of inspiral, merger, and ringdown phases in terms of the direct and scattered parts of the waves. Further discussion of this figure is given in the text of Section 6.3.

directly. We view this mixed wave as characteristic of the merger phase. Finally, as the trajectory falls within the effective potential, for a Schwarzschild black hole the direct part vanishes and only the scattered waves emerge; this part is the quasinormal ringing of the final black hole and should be associated with the ringdown phase. We distinguish between Schwarzschild and Kerr black holes for the ringdown phase, because Mino and Brink [62] and, subsequently, Zimmerman and Chen [63] found that for Kerr black holes, frame dragging generates a part of the waveform at the horizon frequency (that decays at a rate proportional to the horizon's surface gravity). This piece of the waveform looks like a source, and, thus, only when the final black hole is not spinning do we consider the spacetime to appear to be source free. For this reason (and since the matching surface asymptotes to a line of constant v), we call the values of v greater than this limiting value the homogeneous region, and the values of v less than this the source region.

An important development in this paper is that we no longer prescribe the evolution of the reduced mass of the system (and thereby a matching region) before evolving the Regge-Wheeler or Zerilli equations; rather, we specify a set of evolution equations for the conservative dynamics of the binary, and let the outgoing waves provide back reaction onto the dynamics. This, in turn, leads to a self-consistent system of equations including radiation reaction. More concretely, we continue to match the PN and perturbed Schwarzschild metrics at the centers of the PN theory's point particles. Moreover, we will again let the reduced-mass motion of the binary system follow that of a point particle in a Schwarzschild background; in this paper, however, we will use the fact that there are no ingoing waves to specify a radiation-reaction potential that acts as a dissipative force on the Hamiltonian dynamics of the reduced mass. This follows the spirit of the Burke-Thorne radiation-reaction potential, but the radiation propagates within a BHP spacetime, and, therefore, also takes the effects of the background curvature into account.

Furthermore, adding a radiation-reaction force to the hybrid method leads to a set of equations that simultaneously evolve the Zerilli equation (the waveform) and the reduced-mass motion of the binary. In Fig. 6.1 we represent schematically how this occurs. We start at a given v (a dark blue (dark gray) dashed line given in Fig. 6.1) and assume that there is a no-ingoing-wave boundary condition along the line $u = 0$. In addition, we suppose that we have determined the black-hole-perturbation functions for all smaller values of v, up to the timelike matching surface. By evolving the Zerilli equation, Eq. (6.21), one can find the Zerilli function at $v + dv$ up to the time $u_s(v)$ (within the dark blue (dark gray) shaded region). The no-ingoing-wave condition combined with the boundary condition on the matching surface, however, fixes how the Zerilli function will evolve to larger values of u. When solved simultaneously with the Hamiltonian dynamics describing the binary's motion, this lets one find the position of the reduced mass of the binary at $v + dv$, denoted by $u_s(v + dv)$ in the figure, and the new value of the Zerilli function there. One can evolve the system for all v in such a manner.

Including a radiation-reaction force does not greatly change the hybrid method as reviewed in Section 6.2. The matching procedure works the same; one modification that comes about is that we must include both the Newtonian potential and the radiation-reaction potential in the PN metric (and, therefore, gain an additional term in the Zerilli function). The evolution system is now quite different, because it is a coupled system of Hamiltonian ordinary differential equations and a one-dimensional partial differential equation. We will discuss the system of evolution equations in greater detail after we compare our method with other analytical methods in the next subsection.

6.3.2 Descriptive Comparison with Other Analytical and Semi-Analytical Models

In this section, we will compare the similarities and differences between the hybrid method described above and the most closely related methods mentioned in the Introduction: the close-limit approximation, the Lazarus program, the comparable-mass EOB methods, the Teukolsky-based approach, the EOB description of EMRIs, and the IMRI calculation calibrated to numerical-relativity data. The comparison between the hybrid method and the other methods will be descriptive, but we will compare the waveform from the hybrid method with a numerical-relativity waveform in Section 6.4

To compare with the Lazarus project or the close-limit approximation, we again refer to Fig. 6.1, where we show two spacelike hypersurfaces (the horizontal dashed lines labeled by Σ_1 and Σ_2). In the close-limit and Lazarus methods, initial data is posed on these surfaces at a time near the merger of the black holes. While these approaches have been successful, posing initial data at late times makes it more difficult to smoothly connect the initial inspiral of the binary to the merger and ringdown later. Moreover, because the initial data extends inside the black-hole potential, if it contains high-frequency perturbations, these could escape the potential barrier and enter into the waveform. The hybrid approach escapes this problem by setting boundary data on a timelike world tube rather than on a spacelike hypersurface. This also lets the method connect the inspiral, merger, and ringdown portions of the dynamics and waveform more directly.

The EOB approach, for comparable-mass ratio binaries, only describes times prior to the merger (the hypersurfaces Σ_1 and Σ_2 in Fig. 6.1). To create a full inspiral-merger-ringdown waveform, the EOB method must fit a sequence of quasinormal modes to the end of the inspiral-plunge waveform. This procedure makes a very accurate waveform, but it makes connecting the behavior of the spacetime before and after the merger more difficult. The hybrid method, with its interior PN region that falls toward the horizon at late times, allows one to make a more clear connection between the dynamics of the spacetime during inspiral and merger to that during ringdown. In its current implementation, however, it does not produce a waveform nearly as accurate as that of the EOB.

Although the hybrid method is designed for describing comparable-mass black-hole binaries, it shares a few similarities and has several significant differences from various approximate techniques

used to model EMRIs. It is possible to draw a few general comparisons between the hybrid method and the procedures for studying EMRIs, before moving to more specific comparisons. While the hybrid method evolves perturbations on a black-hole background (as most EMRI methods do), EMRI methods assume a source term as the generator of the perturbations in the background. The hybrid approach, however, does not have a source term; rather, the perturbations of the background come from boundary data that correspond to the multipolar structure of a comparable-mass PN binary. Because the hybrid approach is a boundary-value problem, the details of the implementation will be different from those methods that use a point mass as a source term.

Moving to specific EMRI models, we first compare the hybrid approach with the Teukolsky-based methods of Sundararajan and collaborators [36] (for example). The hybrid approach is similar to that of [36], in that both use time domain codes and are capable of producing smooth inspiral-merger-ringdown waveforms. An important difference is that the hybrid method calculates the waveform simultaneously with the evolution of the matching region, whereas the EMRI method of Sundararajan computes the trajectory before the evolution (using an adiabatic frequency-domain code during inspiral, and a prescription for the plunge and merger) and then finds the waveform from this trajectory. Moreover, we compute the radiation-reaction force in the hybrid method by matching the near-zone PN solution to an outgoing solution in the exterior BHP spacetime, whereas the Teukolsky-based methods include radiative effects by evolving the orbital parameters of geodesics from averaged fluxes at infinity.

The EOB model of Yunes et al. [45], is a calibration of the EOB method to Teukolsky-based waveforms for EMRIs; it, therefore, shares the same similarities and differences as the EOB and the Teukolsky-based methods discussed above. Han and Cao [42] develop an EOB model that uses the a Teukolsky-based energy flux (in the frequency domain) to treat radiative effects. In comparing with the hybrid model, therefore, it also falls somewhere between an EOB model and a Teukolsky-based method. The recent EOB work of Bernuzzi and collaborators [39, 40, 41] shares more similarity with the hybrid method, because they evolve the Regge-Wheeler-Zerilli equations in the time domain. The most notable specific difference (as opposed to the general differences between the hybrid-method and all analytical approaches to EMRIs noted above) is in the radiation-reaction force. The EOB model uses a high-PN-order, resummed energy flux, whereas (as also noted above) the hybrid method determines radiative effects from directly matching a near-zone PN solution to an outgoing BHP solution.

We conclude this section by comparing the hybrid method with the recent analytical work of Lousto et al. [46, 47, 48]. They take two approaches to calculating waveforms for IMRIs perturbatively. In their initial work, they transform the trajectory of the small black hole from their numerical-relativity simulations into the Schwarzschild gauge, and they compute the waveform using this numerical trajectory in a BHP calculation. To be able to study a wider range of mass

ratios, they use PN expressions for the change in frequency and the radial trajectory, but use the numerical-relativity values of the frequency to calibrate the PN functions. The hybrid method differs from this, because it calculates the matching region simultaneously with the waveform, and it does not use numerical-relativity data to calibrate results. Consequently, the hybrid method does not agree as well with exact results as well as the other methods discussed here, but it does present a distinct way of calculating the approximate spacetime and gravitational waveform.

6.3.3 Radiation Reaction and Evolution Equations

In this section, we will discuss the details of radiation reaction in the hybrid method. The end result will be the set of evolution equations described in Eqs. (6.46)–(6.49), and the majority of this section will be devoted to deriving this system of equations.

We begin, as in Paper I, with the PN metric at Newtonian order,

$$dS^2 = -(1-2U_N)dt^2 + (1+2U_N)(dR^2 + R^2 d^2\Omega)\,, \tag{6.24}$$

the same as Eq. (6.4) of Section 6.2, though without the gravitomagnetic terms. Here, however, we write the Newtonian potential (expanded to quadrupole order) as

$$\begin{aligned} U_N &= U_N^{(l=0)} + U_N^{(l=2)} \\ &= \frac{M}{r} + \sum_{m=-2}^{2} \left(\frac{Q_m}{R^3} Y^{2,m} + F_m R^2 Y^{2,m} \right) . \end{aligned} \tag{6.25}$$

The first term is the monopole piece (M is the total mass of the binary) and the first term in the sum is the quadrupole part (and Q_m are the quadrupole moments of the binary). These two terms above are identical to those of Paper I, but the second term in the sum (the polynomial in R with coefficients F_m) is different. One can include the terms proportional to F_m, because like the Newtonian potential, they are solutions to Poisson's equation. These terms diverge at infinity (which restricts their use to the near zone), but they cannot be determined from the near-zone dynamics alone, however. Burke showed [50], using the technique of matched asymptotic expansions, that the terms with coefficients F_m could represent the reaction of the binary in the near-zone to radiation losses to infinity. The portion of the potential corresponding to the moments F_m, therefore, is called the Burke-Thorne radiation-reaction potential.

In the hybrid method, we will find a similar quantity in the interior PN spacetime by matching the PN near-zone solution to a solution in the Schwarzschild exterior with no ingoing waves. Namely, when we assume that there are no ingoing waves from past null infinity in the exterior BHP spacetime, this determines a radiation-reaction potential within the interior PN spacetime. This allows us to incorporate the effects of wave propagation in the background black-hole spacetime into the dynamics

of the binary. While the Schwarzschild background does not capture every detail of the curvature of a binary at small separation, we see that it does capture some of the important qualitative effects.

Proceeding with the calculation, we assume we have an equal-mass, nonspinning binary in the x-y plane, located at

$$\mathbf{X}_A(t) = -\mathbf{X}_B(t) = \frac{1}{2}A(t)(\cos\alpha(t), \sin\alpha(t), 0)\,, \tag{6.26}$$

where A and B are labels for the two members of the binary. Each black hole has mass $M/2$, and a straightforward calculation shows that

$$Q_2(t) = \sqrt{\frac{3\pi}{10}}\frac{MA(t)^2}{4}e^{-2i\alpha(t)}\,, \tag{6.27}$$

$$Q_0(t) = -\frac{MA(t)^2}{4}\sqrt{\frac{\pi}{5}}\,, \tag{6.28}$$

$$Q_{-2}(t) = \overline{Q}_2(t)\,, \tag{6.29}$$

where the overline stands for complex conjugate, and where, by symmetry, the $m = \pm 1$ components must be zero for this equal-mass binary. Throughout this paper, we focus just on the $m = \pm 2$ multipoles, because as one can see from the expressions above, the $m = 0$ moment only evolves because of the radiation-reaction force (for circular orbits), and, therefore, is less significant than the $m = \pm 2$ multipoles, which change on the orbital time scale. Moreover, the $m = -2$ quantity is the complex conjugate of the corresponding $m = 2$ quantity; consequently, when we write $Q(t)$ (or any other variable that might be indexed by m), we refer to the $m = 2$ variable (and similarly, for $\overline{Q}(t)$, we mean the $m = -2$ element). This way, the notation can be simplified by dropping the m label on multipole coefficients. Thus, we can write the quadrupole perturbation as

$$U_N^{2,2} = \overline{U_N^{2,-2}} = \frac{Q(t)}{R^3} + F(t)R^2\,, \tag{6.30}$$

where

$$Q(t) = \sqrt{\frac{3\pi}{10}}\frac{MA(t)^2}{4}e^{-i2\alpha(t)}\,, \tag{6.31}$$

and $F(t)$, an undetermined function of time, is the radiation-reaction potential.

One can substitute Eq. (6.30) into Eq. (6.19) and use the fact that $r = R - M$ to find the Zerilli function. Calculating the Zerilli function introduces many factors of M/R into the final result, but because our calculation is only accurate to Newtonian order, we will keep only the leading-order terms in R and its inverse. We find that

$$\Psi_{(\mathrm{e})} = \frac{2Q(t)}{R^2} + \frac{F(t)R^3}{3}\,. \tag{6.32}$$

We will also shortly need expressions for the derivative of the Zerilli function with respect to the

tortoise coordinate r_*, Eq. (6.2), which we compute here as well. Again, we will keep the leading-order expression in R, but we will also retain the factor of

$$\frac{dr}{dr_*} = \left(1 - \frac{2M}{r}\right) = \frac{(R-M)}{(R+M)}\,, \tag{6.33}$$

because although $\Psi_{(\mathrm{e})}$ may be constant on the horizon, $\partial\Psi_{(\mathrm{e})}/\partial r_*$ should vanish there [61]. The result of this calculation is that

$$\frac{\partial\Psi_{(\mathrm{e})}}{\partial r_*} = \left(\frac{R-M}{R+M}\right)\left(-\frac{4Q(t)}{R^3} + F(t)R^2\right)\,. \tag{6.34}$$

The Zerilli function satisfies the simple wave equation in a potential, Eq. (6.21). As before, the value of the Zerilli function at the matching surface, $R_s(t) = A(t)/2$, provides a boundary condition for the Zerilli equation on the matching surface, but now there is an additional boundary condition on the Zerilli function's derivative with respect to the tortoise coordinate. The two boundary conditions state that

$$\Psi_{(\mathrm{e})}(t) = \frac{8Q(t)}{A(t)^2} + \frac{F(t)A(t)^3}{24}\,, \tag{6.35}$$

$$\frac{\partial\Psi_{(\mathrm{e})}(t)}{\partial r_*} = \left(\frac{A(t)-2M}{A(t)+2M}\right)\left(-\frac{32Q(t)}{A(t)^3} + \frac{F(t)A(t)^2}{4}\right)\,. \tag{6.36}$$

By eliminating the unknown function $F(t)$ from the above equations, one can impose a mixed (Robin) boundary condition at the matching surface between the PN and BHP spacetimes,

$$\frac{\partial\Psi_{(\mathrm{e})}(t)}{\partial r_*} = \left(\frac{A(t)-2M}{A(t)+2M}\right)\left(\frac{6}{A(t)}\Psi_{(\mathrm{e})}(t) - \frac{80Q(t)}{A(t)^3}\right)\,. \tag{6.37}$$

This specifies a boundary condition at a given moment in time, but it does not yet describe how to evolve the matching surface (through evolving the reduced-mass motion of the system) and the value of the Zerilli function on this surface.

One can determine the value of the Zerilli function at later times through the boundary condition above, and the following additional constraint. By integrating the Zerilli equation with respect to u, one finds that

$$\frac{\partial\Psi_{(\mathrm{e})}(t)}{\partial v} = -\frac{1}{4}\int_0^{u_s(t)} V_{(\mathrm{e})}^{(l=2)}(r)\Psi_{(\mathrm{e})}(u',v)du' + \frac{\partial\Psi_{(\mathrm{e})}(0,v)}{\partial v}\,,$$

where we have written r implicitly as a function of u and v, and $u_s(t)$ denotes the value of u at the matching surface for a given time t. Having no ingoing waves forces the second term to be zero, and

$$\frac{\partial\Psi_{(\mathrm{e})}(t)}{\partial v} = -\frac{1}{4}\int_0^{u_s(t)} V_{(\mathrm{e})}^{(l=2)}(r)\Psi_{(\mathrm{e})}(u',v)du'\,. \tag{6.38}$$

Because both $\partial\Psi_{(\mathrm{e})}(t)/\partial v$ and $\partial\Psi_{(\mathrm{e})}(t)/\partial r_*$ are constrained at the point of the matching surface, this determines the evolution of $\Psi_{(\mathrm{e})}(t)$ on the matching surface. It is easiest to express the Zerilli function on the matching surface as a function of time via $\Psi_{(\mathrm{e})}(t, r_*(t))$. Then, taking the total derivative,

$$\frac{d\Psi_{(\mathrm{e})}(t)}{dt} \equiv \dot{\Psi}_{(\mathrm{e})}(t) = \frac{\partial\Psi_{(\mathrm{e})}}{\partial t} + \frac{dr_*}{dt}\frac{\partial\Psi_{(\mathrm{e})}}{\partial r_*}\,, \tag{6.39}$$

using the facts that

$$\frac{\partial\Psi_{(\mathrm{e})}}{\partial t} = 2\frac{\partial\Psi_{(\mathrm{e})}}{\partial v} - \frac{\partial\Psi_{(\mathrm{e})}}{\partial r_*}\,, \tag{6.40}$$

and

$$\frac{dr_*}{dt} = \left(1 - \frac{2M}{r}\right)^{-1}\frac{dr}{dt}\,, \tag{6.41}$$

along with the relationship $a(t) = 2r(t)$, one can write

$$\dot{\Psi}_{(\mathrm{e})}(t) = 2\frac{\partial\Psi_{(\mathrm{e})}(t)}{\partial v} - \left[1 - \frac{1}{2}\left(\frac{A(t)+2M}{A(t)-2M}\right)\dot{A}(t)\right]\frac{\partial\Psi_{(\mathrm{e})}(t)}{\partial r_*}\,. \tag{6.42}$$

In the above equation, $\partial\Psi_{(\mathrm{e})}(t)/\partial v$ is given by the integral of the Zerilli function up to that time, Eq. (6.38), and $\partial\Psi_{(\mathrm{e})}(t)/\partial r_*$ is given by the boundary condition, Eq. (6.37), at that instant. As a result, the only term in Eq. (6.42) that is not yet fixed is the expression for $\dot{A}(t)$.

The term $\dot{A}(t)$ specifies the time evolution of the reduced mass of the binary, which, because it is twice the radius of the matching surface between the Schwarzschild and PN metrics, could conceivably evolve via either the PN equations of motion or those of a particle in the Schwarzschild spacetime. We will choose the latter, for the same reason as described in Paper I: the Schwarzschild Hamiltonian has the advantage that a particle falling toward the horizon approaches it exponentially in time, in the limit that the particle is near the horizon. Because we are using this motion to approximate the region inside of which PN theory holds, we want this space to quickly fall toward the horizon as the theory begins to converge slowly. Moreover, the motion should move smoothly toward the horizon (so as not to introduce high-frequency modes that could escape the black-hole effective potential). The PN equations of motion do not have these desirable features; we consequently favor the point-particle evolution equations in the Schwarzschild spacetime.

We write the evolution equations for the reduced mass of the system in their Hamiltonian form. As in Paper I, we will describe the dynamics of the reduced mass in PN coordinates, because at late times, this causes the point particles in the PN metric to approach the horizon in the external Schwarzschild spacetime as the reduced mass of the system does the same. The equations of motion for the reduced mass, μ, are

$$\dot{A}(t) = \frac{\partial H}{\partial p_A(t)}\,, \quad \dot{\alpha}(t) = \frac{\partial H}{\partial p_\alpha(t)}\,, \quad \dot{p}_A(t) = -\frac{\partial H}{\partial A(t)}\,, \quad \dot{p}_\alpha(t) = \mathcal{F}_\alpha(t)\,,$$

where the Hamiltonian of a point particle in the Schwarzschild spacetime is given by

$$\frac{H(A(t),p_A(t),p_\alpha(t))}{\mu}=\sqrt{\left(1-\frac{2M}{A(t)}\right)\left[1+\left(1-\frac{2M}{A(t)}\right)\frac{p_A(t)^2}{\mu^2}+\frac{p_\alpha(t)^2}{\mu^2 A(t)^2}\right]}\,. \tag{6.43}$$

The radiation-reaction force is given by the derivative of the radiation-reaction potential with respect to φ, and it should be evaluated at the location of the matching region,

$$\frac{\mathcal{F}_\alpha(t)}{\mu}=\frac{1}{\mu}\frac{\partial U_N^{(l=2),F}}{\partial\varphi}=-A^2(t)\sqrt{\frac{15}{2\pi}}\Im[F(t)e^{2i\alpha(t)}]\,, \tag{6.44}$$

where $U_N^{(l=2),F}$ represents the quadrupole part of the radiation-reaction potential. By solving Eq. (6.35) for $F(t)$ in terms of $\Psi_{(\mathrm{e})}(t)$ (and because $Q(t)$, Eq. (6.31), is proportional to a real amplitude times $e^{-2i\alpha(t)}$), one can write

$$\frac{\mathcal{F}_\alpha(t)}{\mu}=-\sqrt{\frac{15}{2\pi}}\frac{24}{A(t)}\Im[\Psi_{(\mathrm{e})}(t)e^{2i\alpha(t)}]\,. \tag{6.45}$$

With the above relationship between the radiation-reaction force and the Zerilli function, there is now a complete set of evolution equations for the reduced-mass motion of the system, the Zerilli function on the matching surface, and the Zerilli function in the exterior spacetime. This system of equations is given by

$$\begin{aligned}
\dot{A}(t) &= \frac{\partial H}{\partial p_A(t)}\,,\quad \dot{\alpha}(t)=\frac{\partial H}{\partial p_\alpha(t)}\,,\quad \dot{p}_A(t)=-\frac{\partial H}{\partial A(t)}\,, && (6.46)\\
\dot{p}_\alpha(t) &= -\mu\sqrt{\frac{15}{2\pi}}\frac{24}{A(t)}\Im[\Psi_{(\mathrm{e})}(t)e^{2i\alpha(t)}]\,, && (6.47)\\
\dot{\Psi}_{(\mathrm{e})}(t) &= -\frac{1}{2}\int_0^{u_s(t)} V_{(\mathrm{e})}^{(l=2)}(r)\Psi_{(\mathrm{e})}(u',v)du' \\
&\quad -\left[\left(\frac{A(t)-2M}{A(t)+2M}\right)-\frac{\dot{A}}{2}\right]\left(\frac{6\Psi_{(\mathrm{e})}(t)}{A(t)}-\frac{80Q(t)}{A(t)^3}\right)\,, && (6.48)\\
\frac{\partial^2\Psi_{(\mathrm{e})}}{\partial u\partial v} &= -\frac{V_{(\mathrm{e})}^{(l=2)}(r)\Psi_{(\mathrm{e})}(u,v)}{4}\,, && (6.49)
\end{aligned}$$

where the Hamiltonian is given by Eq. (6.43), the potential by Eq. (6.22), and the quadrupole by Eq. (6.31). By including a radiation-reaction force, we arrived at a set of evolution equations that simultaneously evolve the reduced-mass motion of the binary and the gravitational waves emitted, taking into account the back action of the emitted radiation on the reduced-mass motion.

6.3.4 Weak-Field Analytical Solution

First, we will confirm that our procedure recovers the correct Burke-Thorne radiation-reaction potential in the weak-field limit. If we have an equal-mass binary in a circular orbit at a large separation,

$r_* \approx r \approx R \gg M$, then the leading-order behavior of the Zerilli equation, Eq. (6.21) is just a wave equation in flat space,

$$\frac{\partial^2 \Psi_{(\mathrm{e})}}{\partial t^2} - \frac{\partial^2 \Psi_{(\mathrm{e})}}{\partial R^2} + \frac{6}{R^2}\Psi_{(\mathrm{e})} = 0\,. \tag{6.50}$$

If one assumes a product solution $\Psi_{(\mathrm{e})} = e^{i\omega t}\psi(R)$, then for the radial motion, one must solve the ordinary differential equation

$$\frac{d^2\psi}{dR^2} + \omega^2\psi = \frac{6}{R^2}\psi\,. \tag{6.51}$$

The solutions for ψ/R are spherical Hankel functions $\psi/R = h_2(\omega A/2) = j_2(\omega A/2) + in_2(\omega A/2)$, assuming there are no ingoing waves. Here ω corresponds to the gravitational-wave frequency. We must match this wave-zone solution to the PN near-zone expression for the Zerilli function given by Eq. (6.35); additionally, we must also match the derivative of the Hankel function with the radial derivative of the PN Zerilli function given in Eq. (6.36).

We will write these conditions in the frequency domain, where

$$B(\omega)Ah_2(\omega A/2) = \frac{8Q(\omega)}{A^2} + \frac{F(\omega)A^3}{24}\,, \tag{6.52}$$

$$B(\omega)Ah_2'(\omega A/2) = -\frac{32Q(\omega)}{A^3} + \frac{F(\omega)A^2}{4}\,, \tag{6.53}$$

and we must solve for the unknown amplitude $B(\omega)$ and the radiation-reaction potential $F(\omega)$ in terms of the quadrupole moment $Q(\omega)$ and the spherical Hankel function $h_2(\omega A/2)$. Since the matching takes place at very large radii, and, by Kepler's law $A\omega \sim A^{-1/2}$ for circular orbits, one can expand the Hankel function in $A\omega/2$. This allows one to solve for F as a series in $1/A$, whose three lowest terms are given by

$$F = \frac{16}{5A^3}\omega^2 Q + \frac{8}{25A}\omega^4 Q + i\frac{2}{15}\omega^5 Q + O(A^{-6})\,. \tag{6.54}$$

The third term is the familiar Burke-Thorne radiation-reaction potential (written in the time domain, this is proportional to five derivatives of the quadrupole moment). The first two terms resemble 1PN and 2PN corrections to the Newtonian potential in the near zone; however, these terms represent the effects of time retardation that are needed to match the near-zone solution to an outgoing wave solution in the wave zone. As a result, our method recovers, asymptotically, the expected result. Consequently, the evolution system, Eqs. (6.46)–(6.49), will also give rise to the correct dynamics in the weak-field limit.

6.4 Numerical Method and Results

We begin this section by describing the numerical method that we use to solve the system of evolution equations, Eqs. (6.46)–(6.49). We then show that the evolution equations give rise to reasonable

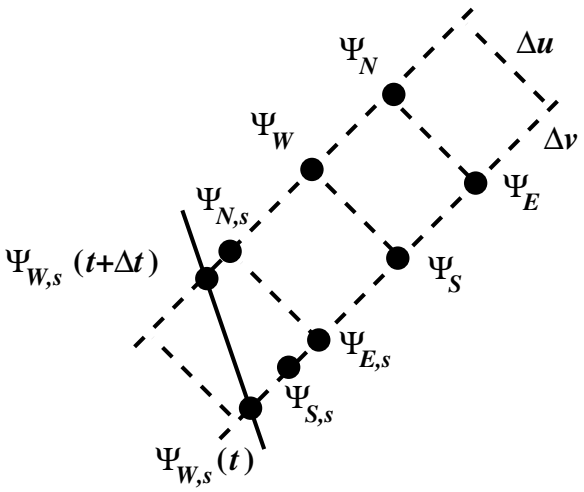

Figure 6.2: A diagram of how we discretize and evolve the Zerilli function. The dots represent the Zerilli function evaluated at the grid points (the points of intersection of the dashed lines), and the solid black line is the matching surface. For all points except those adjacent to the solid line, one can use Eq. (6.56) directly to numerically evolve the Zerilli function. Near the solid line, one can use the same procedure as described in Eq. (6.56), except that one must interpolate the Zerilli function to the point $\Psi_{S,s}$ to use the same procedure. Further detail is given in the text of this section.

and convergent results. With this established, we compare our waveform with one from a numerical-relativity simulation, and we close this section by interpreting the spacetime of the hybrid method.

6.4.1 Numerical Methods and Consistency Checks of the Evolution Equations

Because the set of evolution equations Eqs. (6.46)–(6.49) has a somewhat unusual form, we describe our numerical method in detail, and we present a few basic checks of the waveform and its convergence. To find the field outside the matching surface, we use the same method as that described in Paper I, a second-order accurate, characteristic method. If we define the following points on the discretized grid (see the portion on the right, away from the solid line, in Fig. 6.2):

$$\begin{aligned} \Psi_N &= \Psi^{l,m}_{(\mathrm{e})}(u+\Delta u, v+\Delta v)\,, \qquad & \Psi_W &= \Psi^{l,m}_{(\mathrm{e})}(u+\Delta u, v)\,, \\ \Psi_E &= \Psi^{l,m}_{(\mathrm{e})}(u, v+\Delta v)\,, \qquad & \Psi_S &= \Psi^{l,m}_{(\mathrm{e})}(u, v)\,, \end{aligned} \tag{6.55}$$

then discretizing Eq. (6.49), one can solve for Ψ_N in terms of the other three discretized points and the potential:

$$\Psi_N = \Psi_E + \Psi_W - \Psi_S - \frac{\Delta u \Delta v}{8} V^l_{(\mathrm{e})}(r_c)(\Psi_E + \Psi_W) + O(\Delta u^2 \Delta v, \Delta u \Delta v^2)\,. \tag{6.56}$$

Here r_c is the value of r at the center of the discretized grid, $(u+\Delta u/2, v+\Delta v/2)$.

We must evolve this partial differential equation simultaneously with the five ordinary differential equations describing the Zerilli function on the matching surface and the surface's position, because all these equations are coupled together. We solve the ordinary differential equations using a second-order-accurate, Runge-Kutta method. As in Paper I, the Zerilli function along the matching surface does not always lie on the uniform grid in the u-v plane, and we must be careful when finding the Zerilli function at grid points adjacent to the matching surface. For example, at a given value of u along the discretized grid, it is rare that the Zerilli function on the matching surface, denoted by

$$\Psi_{W,s}(t) = \Psi_{(\mathrm{e})}(u_s(t), v_s(t))\,. \tag{6.57}$$

will actually fall along a grid point (see the left side of Fig. 6.2 near the solid line). Similarly, when evolving the discretized version of Eqs. (6.46)–(6.49), it is again unlikely that the Zerilli function along the matching surface at the next value of u (advanced by one unit of Δu),

$$\Psi_{W,s}(t+\Delta t) = \Psi_{(\mathrm{e})}(u_s(t)+\Delta u, v_s(t+\Delta t))\,, \tag{6.58}$$

will fall at a grid point or even at the same value of v as the previous earlier value of the Zerilli function, $\Psi_{W,s}(t)$.

To be able to use Eq. (6.56) to find the Zerilli function at $u = u_s(t) + \Delta u$ for the next grid point in v (which we denote by $\Psi_{N,s}$), we must interpolate the Zerilli function at fixed $u = u_s(t)$ to the same value of $v = v_s(t)$ as $\Psi_{W,s}(t+\Delta t)$. We will label this point by

$$\Psi_{S,s} = \Psi_{(\mathrm{e})}(u_s(t), v_s(t+\Delta t))\,. \tag{6.59}$$

As in Paper I, this interpolation does not influence the convergence of the algorithm when done with cubic interpolating polynomials. With the value of the Zerilli function at $u = u_s(t)$ and the nearest grid point in v (which we will call $\Psi_{E,s}$), one can then find the point $\Psi_{N,s}$ using Eq. (6.56), where Ψ_E, Ψ_W, and Ψ_S are replaced by $\Psi_{E,s}$, $\Psi_{W,s}(t+\Delta t)$, and $\Psi_{S,s}$, respectively.

As a final note on the numerical methods, we point out that in the evolution equation for the Zerilli function on the matching surface, Eq. (6.42), the term $\partial\Psi_{(\mathrm{e})}(t)/\partial v$ involves an integral of the Zerilli function times the potential, Eq. (6.38). Explicitly evaluating this integral adds to the computational expense significantly. We, therefore, compared the value of $\partial\Psi_{(\mathrm{e})}(t)/\partial v$ obtained through performing the integral with the value found from evaluating $\partial\Psi_{(\mathrm{e})}(t)/\partial v$ numerically using a fourth-order finite-difference approximation of the derivative, calculated from the Zerilli function in the adjacent exterior BHP spacetime. Because the two agreed to within the numerical accuracy of our solution, we used the finite-difference approximation of $\partial\Psi_{(\mathrm{e})}(t)/\partial v$ in our numerical evolutions.

We now examine a few consistency checks of the numerical solutions to the system of evolution

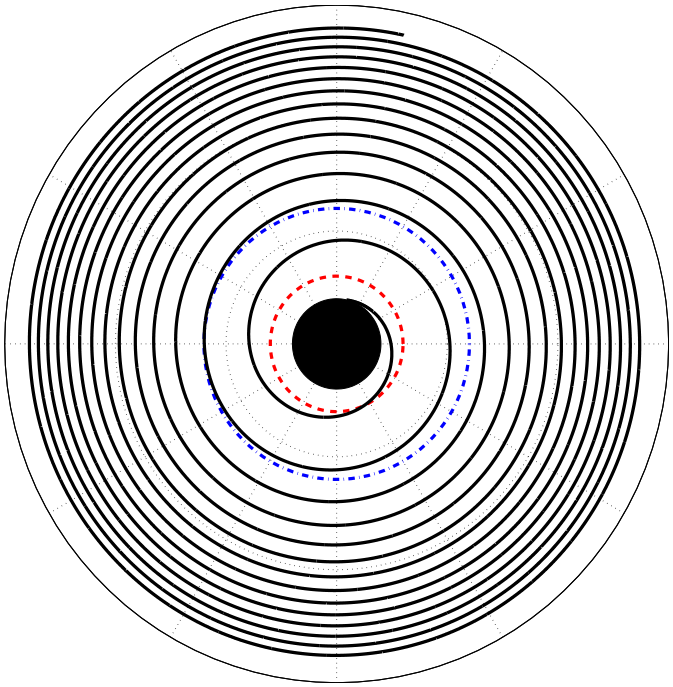

Figure 6.3: In black, the trajectory of the reduced-mass motion of the binary, in the PN coordinate system. The blue (dark) dotted and dashed circle shows the Schwarzschild ISCO, and the red (light) dashed circle depicts the light ring of the Schwarzschild spacetime. The large filled black circle represents the horizon. One can see that the binary plunges soon after it reaches the ISCO of the exterior Schwarzschild spacetime.

equations, Eqs. (6.46)–(6.49). In Fig. 6.3, we show, in black, the trajectory of the reduced mass of the binary in the PN coordinates. On this same figure, we have depicted the Schwarzschild black hole by a filled black circle, the light ring of this black hole by a red (light) dashed circle, and the innermost stable circular orbit (ISCO) by a blue (dark) dashed and dotted circle. One can see that the radiation-reaction force causes the matching region to adiabatically inspiral, until it approaches the ISCO. Once at the ISCO, it begins plunging more rapidly toward the light ring, and then falls past the light ring and asymptotes to the horizon of the final black hole.

The initial conditions of this evolution correspond to a binary with a PN separation of $A(0) = 14$ in a circular orbit, with no ingoing gravitational waves from past-null infinity, and with the radiation-reaction force initially set to zero. We do not let the radiation-reaction force enter into the dynamics (thereby holding the binary at a fixed separation) until we have a stable estimate of the force. At this point, we include the radiation-reaction force (thereby letting the binary begin its inspiral). To minimize eccentricity, we introduce a small change in the radial momentum $p_A(0)$ that corresponds to the radial velocity of a PN binary at that separation. Explicitly, we find this value of $p_A(0)$ by solving

$$\dot{A}(0) = \left.\frac{\partial H}{\partial p_A(t)}\right|_{t=0} = -\frac{16}{5}\frac{M^3}{A(0)^3}\,, \tag{6.60}$$

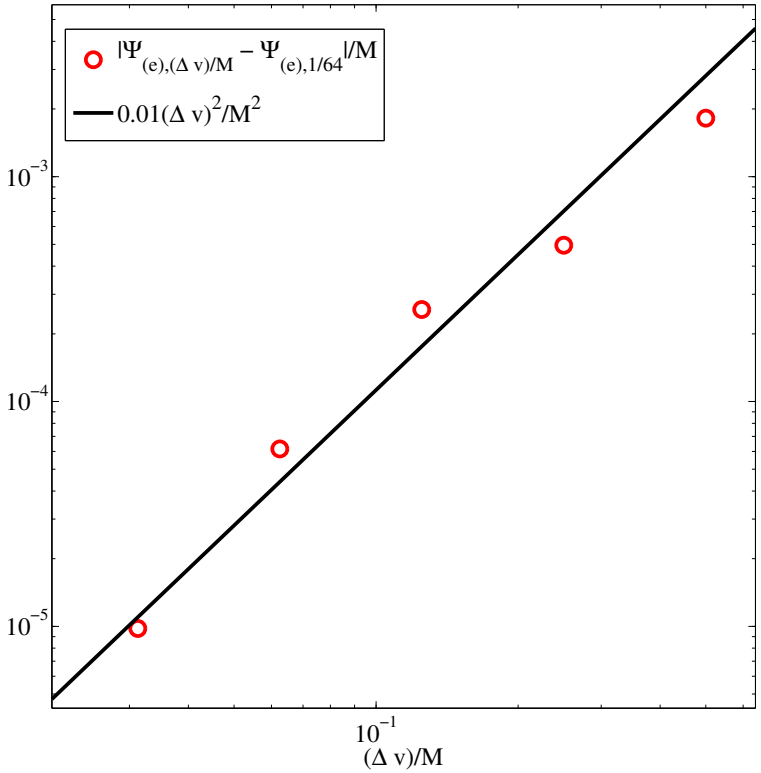

Figure 6.4: The L^2 norm of the Zerilli function at a given resolution, $\Delta v/M$, minus the Zerilli function at the highest resolution, $(\Delta v)/M = 1/64$, which we denote by $|\Psi_{(e),(\Delta v)/M} - \Psi_{(e),1/64}|/M$. We also include a power law proportional to $[(\Delta v)/M]^2$ to indicate the second-order convergence of our result.

(see, e.g. [3]), while assuming that $p_\alpha(0)$ continues to have the value for circular orbits

$$p_\alpha(0) = \frac{MA(0)}{\sqrt{A(0)/M - 3}}\,. \tag{6.61}$$

This is necessary to make the orbit as circular as possible once the binary begins to inspiral. We do not show the initial few orbits before we include the radiation-reaction force, and we denote the zero of our time to be the moment when we let the radiation-reaction force begin acting on the binary.

We also calculate the Zerilli function corresponding to these initial conditions, as a function of increasing numerical resolution. In Fig. 6.4, we show that the Zerilli function at large constant v, does converge in a way that is consistent with the second-order-accurate code we are using. We show the L^2 norm of the difference between the Zerilli function at a given resolution, which we denote $\Psi_{(e),(\Delta v)/M}$ and the highest resolution, $(\Delta v)/M = 1/64$, which we denote by $\Psi_{(e),1/64}$. The L^2 norm, therefore, we write as $|\Psi_{(e),(\Delta v)/M} - \Psi_{(e),1/64}|$, and we normalize this by the number of data points in the evolution, and the mass. We also include a power law, proportional to $[(\Delta v)/M]^2$, which indicates the roughly second-order convergence of the waveform.

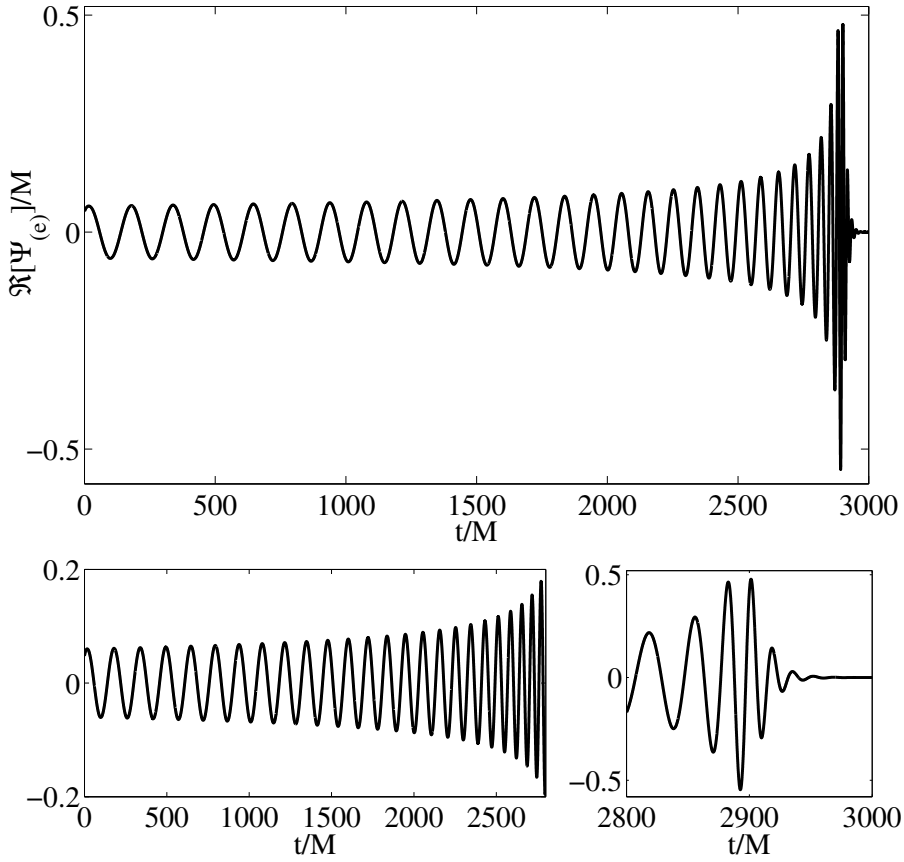

Figure 6.5: The top panel shows the real part of the Zerilli function throughout the entire evolution, extracted at large constant v. The bottom-left panel displays the early part of the same Zerilli function, and the bottom-right zooms in to the merger and ringdown portions of the function. Because only a factor of $\sqrt{6}$ differentiates the Zerilli function from r times the waveform, this can be thought of as the waveform as well.

We then plot the real part of the Zerilli function extracted at large constant v, for the highest resolution $(\Delta v)/M = 1/64$, in Fig. 6.5. The top panel depicts the Zerilli function throughout the full evolution. Because it is difficult to see the slow increase of the amplitude and frequency during early times and the smooth transition from inspiral to merger and ringdown at late times, we highlight the early stages of the inspiral in the lower-left panel, and we depict the merger and ringdown in the lower-right panel. Because $\sqrt{6}\Psi_{(e)} = r(h_+ - ih_\times)$, for the $l = 2$ modes at large r (see Eq. (6.97) below), the Zerilli function is essentially identical to the gravitational waveform. From this one can see the hybrid method produces a smooth inspiral-merger-ringdown waveform. Because the hybrid waveform has the correct qualitative features of a full inspiral-merger-ringdown waveform, it is natural to ask how well it could match a numerical-relativity waveform. We, therefore, turn to this question in the next section.

6.4.2 Comparison with Numerical-Relativity Results

In this section, we will first discuss how well the waveform compares with a similar waveform from numerical-relativity simulations. The first part of the section is devoted to showing how we can make small modifications to the hybrid procedure to make the phase agree well with that of a numerical-relativity waveform during the inspiral (though the comparison of the amplitudes is less favorable). The second part of this section describes why the hybrid method, in its current implementation, does not agree well with numerical-relativity simulations during the merger and ringdown phases. The reason for the discrepancy during the late stages of the waveform is well understood (the background spacetime of the hybrid method is Schwarzschild, whereas the final spacetime of the numerical simulation is Kerr) and could be improved by modifications to the hybrid method.

6.4.2.1 Agreement of the Waveforms During Inspiral

We will briefly describe a small change to the hybrid method that leads to a waveform whose phase agrees well with a numerical-relativity waveform during the inspiral part. We will continue to find the Zerilli function through the procedure described in Section 6.3.3 using the leading-order expression for the Newtonian potential (and thus also the leading-order radiation reaction force). We note, however, that when we took the derivative of the Zerilli function on the matching surface with respect to r_*, Eq. (6.36), we kept the factor of $(1 - 2M/r)$. This is reasonable, physically, because, although the Zerilli function itself may approach a constant on the horizon, its derivative with respect to r_* should vanish. Conversely, if the derivative of the Zerilli function did not vanish, then that could correspond with a perturbation that diverges on the horizon. Nevertheless, because the boundary condition only takes into account the leading Newtonian expressions, the overall factor of $(1 - 2M/r)$ is a higher PN correction, from the point of view of the interior PN spacetime. We, therefore, are justified in dropping this term in our leading Newtonian treatment, and we find the agreement between numerical relativity and the hybrid method is helped by this. It is likely that further adjustments will lead to even better results, though a systematic study of this is beyond the scope of this initial exposition.

The modification above results in only a small change to Eq. (6.36),

$$\frac{\partial \Psi_{(\mathrm{e})}(t)}{\partial r_*} = -\frac{32Q(t)}{A(t)^3} + \frac{F(t)A(t)^2}{4}\,, \tag{6.62}$$

and it also alters the boundary condition, Eq. (6.37) of Section 6.3.3,

$$\frac{\partial \Psi_{(\mathrm{e})}(t)}{\partial r_*} = \frac{6}{A(t)}\Psi_{(\mathrm{e})}(t) - \frac{80Q(t)}{A(t)^3}\,. \tag{6.63}$$

With the exception of these two equations and the fact that we begin the evolution from a larger initial radius, $A(0) = 15.4$, we evolve the new system of equations in exactly the same way as that

described in detail in Section 6.4.1.

For our comparison with a numerical-relativity waveform, we use the $l = 2$, $m = 2$, mode of the waveform from an equal-mass, nonspinning, black-hole binary described in the paper by Buonanno et al. [18]. In this simulation, the black holes undergo 16 orbits before they merge, and the final black hole rings down. We plot the numerical-relativity waveform in black in Fig. 6.6, and we show the equivalent waveform from our approximate method in red (gray). Recall that the $l = 2$ modes of the Zerilli function are related to the waveform by

$$\sqrt{6}\Psi_{(\mathrm{e})} = r(h_+ - ih_\times) \tag{6.64}$$

(see Eq. (6.97) below). Although the amplitudes of the waveforms do not agree exactly, the fact that the phases match so well throughout the entire inspiral is noteworthy. The approximate waveform completes one more orbit than the numerical-relativity one, and the ringdown portions differ as well. This is not too surprising, however, because the final black hole in the numerical-relativity simulation is a Kerr black hole with dimensionless spin $\chi \approx 0.7$ (see, e.g., Scheel et al. [51]), whereas our ringdown takes place around a Schwarzschild (nonspinning) black hole.

6.4.2.2 Differences in the Instantaneous Frequency During Merger and Ringdown

The discrepancy between the two waveforms at late times in Fig. 6.6 is most evident in the instantaneous frequency, often defined as

$$M\omega = i\frac{\dot{\Psi}_{(\mathrm{e})}}{\Psi_{(\mathrm{e})}}\,, \tag{6.65}$$

where $\Psi_{(\mathrm{e})}$ is the Zerilli function measured at large r. We calculate this frequency for both the hybrid and the numerical-relativity waveforms, and we show the real and the imaginary parts (the oscillatory and damping portions, respectively) in Fig. 6.7. The numerical-relativity waveform was offset from zero at late times by a small constant of order 10^{-4}. We subtracted this constant from the waveform to find the instantaneous frequency; otherwise, when the amplitude of the waveform becomes comparable to this constant, there are spurious oscillations in the frequency as it becomes dominated by this constant offset. The hybrid waveform needed no modification.

Solid curves depict the instantaneous frequency of the numerical-relativity waveform in Fig. 6.7; the real (oscillatory) part is the black curve and the imaginary (decaying) part is the red (gray) curve. Similarly, the black dashed curve is the real part of the instantaneous frequency of the hybrid method, and the red (gray) dashed curve is its imaginary part. The hybrid and the numerical-relativity frequencies are in very good agreement for the inspiral up until the late stages highlighted here. The numerical-relativity waveform quickly transitions after the plunge and merger to the least-damped $l = 2$, $m = 2$ quasinormal-mode frequency and decay rate for a Kerr black hole of final dimensionless spin equal to roughly $\chi \approx 0.7$ (see, e.g., [64]). The frequency of the hybrid waveform,

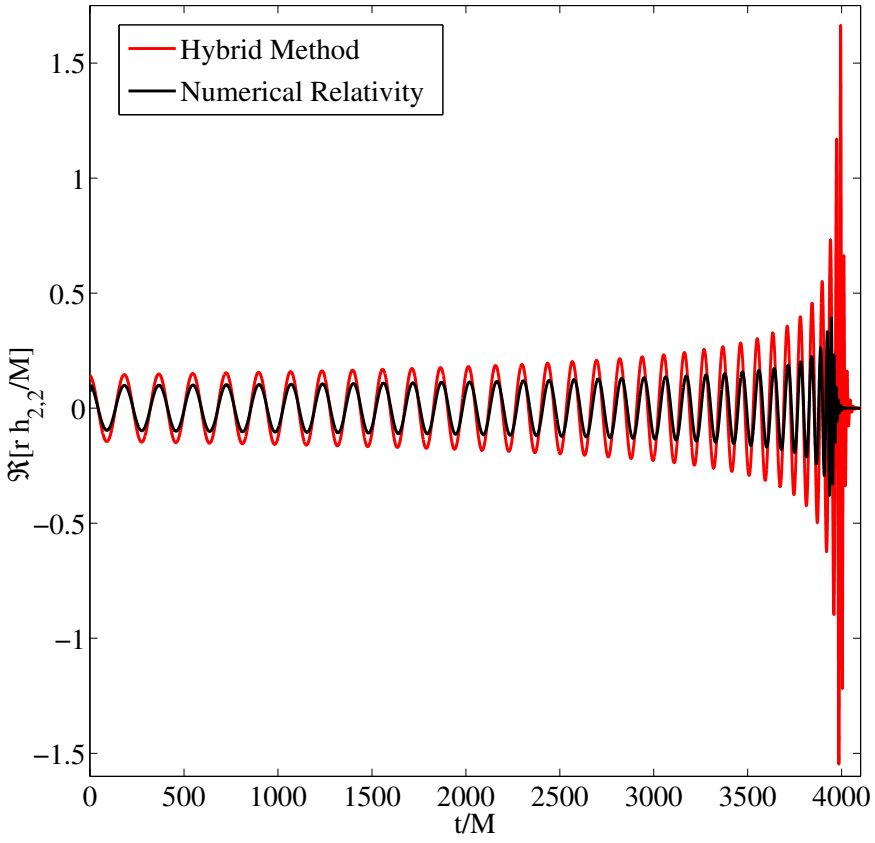

Figure 6.6: In black is the real part of the $l = 2$, $m = 2$ mode of a numerical-relativity waveform, whereas in red (gray) is the equivalent quantity from the approximate method of this paper. The agreement of the waveforms' phases is quite good throughout the entire inspiral, although the amplitudes differ. The approximate and numerical-relativity waveforms differ during ringdown, because the approximate method uses a black-hole with zero spin, whereas the final black hole in the numerical-relativity simulation has considerable spin.

however, undergoes a similar qualitative transition, but it approaches the least-damped $l = 2$, $m = 2$ ringdown frequency of a non-spinning black hole (the background of the hybrid method). The hybrid method, however, oscillates around this value with a frequency that is proportional to twice the frequency of this least-damped, $l = 2$, $m = 2$ quasinormal mode.

The origin of this oscillation is simple and, in fact, was explained by Damour and Nagar [38]. For each l and m, there are quasinormal modes with both positive and negative real parts, which both have a negative decay rate. For a Schwarzschild black hole, the decay rates are the same and the real frequencies are identical, but have the opposite sign. For a Kerr black hole, however, the positive-frequency modes have a lower decay rate than the negative-frequency modes (and the positive frequency is larger in absolute value than the negative frequency is). While a counter-clockwise orbit will tend to excite predominantly the mode with a positive real part, it can also generate the negative real-frequency mode as well. In the hybrid waveform, because the background is Schwarzschild, the positive- and negative-frequency modes decay at the same rate, and they can interfere to make the oscillations at twice the positive real frequency. In the numerical-relativity waveform, however, the difference of the frequencies and decay rates prevents this from happening.

6.4.3 Interpreting the Hybrid Waveform and Spacetime

Because the phase during inspiral agrees so well, and because the transition from inspiral to merger and ringdown is qualitatively similar, this leads one to wonder to what extent the hybrid approach may also be a useful tool for generating gravitational-wave templates for gravitational-wave searches. To capture the correct ringdown behavior, the hybrid method would need to be extended to a Kerr background; however, it is likely that calibrated approaches using the effective-one-body method (see, e.g., [18]) or phenomenological frequency-based templates (see, e.g., [65]) will be more efficient for these purposes. The hybrid approach, as described here, will likely be more helpful as a model of how the near-zone motion of the binary connects to different portions of the gravitational waveform.

As an example of this, we show the real part of the gravitational waveform at large v, the black solid curve, and the corresponding value of the Zerilli function on the matching surface, the red (gray) dashed curve in Fig. 6.8. Interestingly, the Zerilli function on the matching surface and that extracted at large constant v are roughly out-of-phase with one another during the inspiral; namely, along a ray of constant u, the Zerilli function undergoes nearly one half cycle as it propagates out to infinity. This feature is also visible in Fig. 6.9, but it is harder to discern there. This behavior holds through inspiral up to the beginning of the merger. During the merger, however, the two transition away from the out-of-phase relationship, before the Zerilli function on the matching surface becomes a constant during the ringdown (when the reduced mass of the binary falls toward the horizon along a line of constant v).

This change in phasing between the Zerilli function on the matching surface and that at large

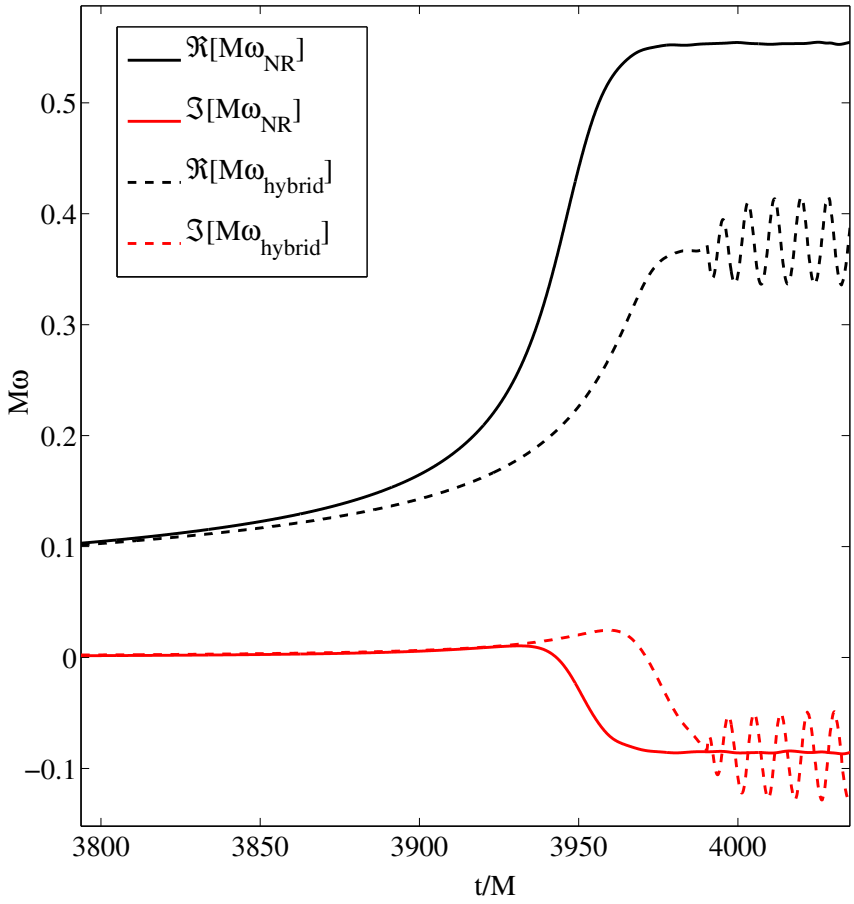

Figure 6.7: The solid curves are the instantaneous frequency, Eq. (6.65), of the numerical-relativity waveform; the black curve is the real, oscillatory part and the red (gray) curve is the imaginary, decaying part. The black, dashed curve and the red (gray) dashed curve are the real and imaginary parts, respectively, of the frequency for the hybrid method. The frequencies agree quite well during the inspiral, but at late times they begin to differ. The qualitative transition from inspiral to merger and ringdown is similar, but the final quasinormal-mode frequencies that the waveforms approach differ, because the numerical-relativity simulation results in a Kerr black hole of dimensionless spin $\chi = 0.7$, whereas the hybrid waveform is generated on a Schwarzschild background. The oscillations in the hybrid waveform arise from the interference of positive- and negative-frequency modes that can arise in a Schwarzschild background, as explained in the text of this section.

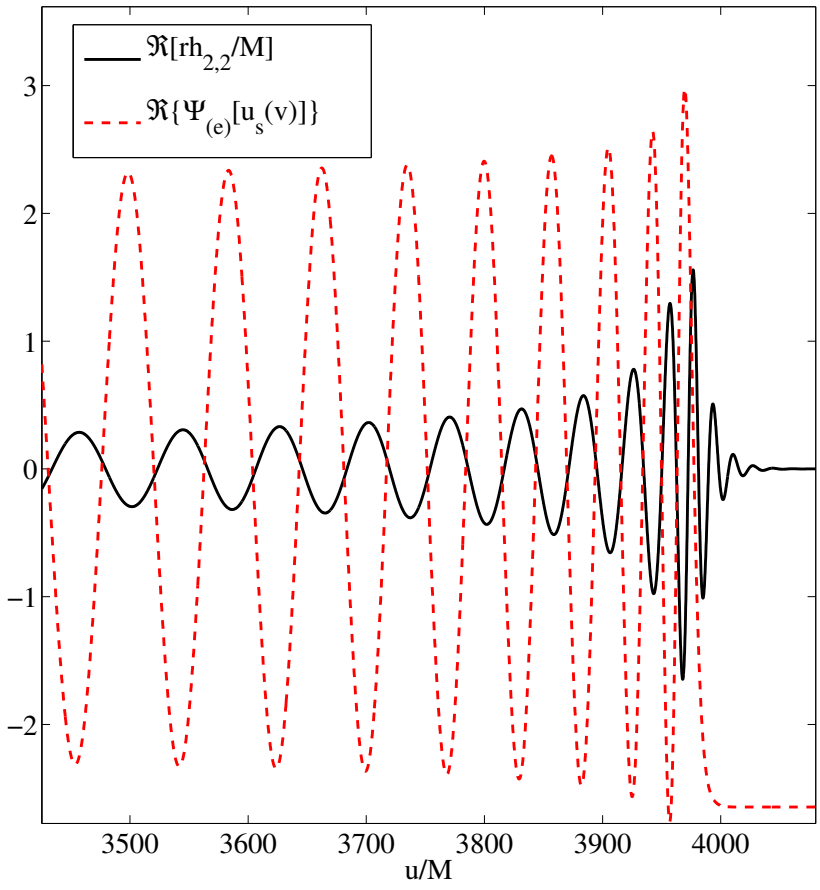

Figure 6.8: The real part of the Zerilli function on the matching surface, the red (gray) dashed curve, and the real part of the gravitational waveform, proportional to the real part of the Zerilli function at large v, (the black solid curve). The two functions are nearly out-of-phase for the inspiral, and the wave propagates more or less directly out. During the merger, they begin to lose this phase relationship, and during ringdown the Zerilli function on the matching surface becomes constant. This implies that the ringdown waveform is due just to the waves scattered from the potential, as also illustrated in Fig. 6.9.

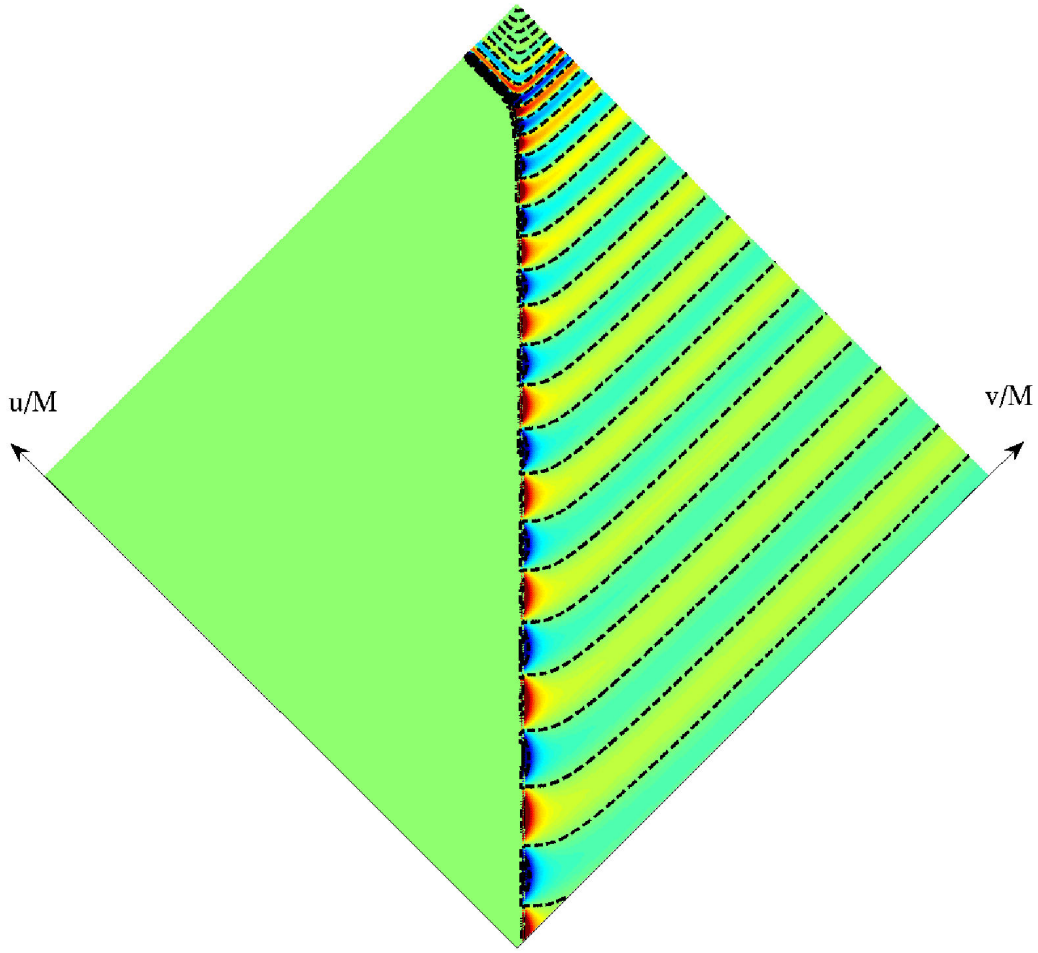

Figure 6.9: A contour-density plot of the real part of the Zerilli function for the evolution discussed in this section. We only show the last few orbits of the inspiral, followed by the merger and ringdown. In this spacetime diagram, time runs up, r_* increases to the right, and the coordinates u and v run at 45 degree angles to the two. The line that starts at nearly constant t and evolves to a line of constant v is the matching surface, and to the left of this line, the solid green (gray) region is the interior PN region (where we do not show any metric perturbations). The exterior is the BHP region, where we show the Zerilli function. During inspiral, the Zerilli function propagates out almost directly, and it oscillates between positive, yellow (light gray) colors and negative, light blue (darker gray). Black, dashed contour curves are used to highlight this oscillation. As the reduced mass of the binary plunges into the potential during merger, the amplitude and frequency of the radiation increases, but it promptly rings down to emit little radiation in the upper green (gray) diamond of the diagram. There are black, dashed contours here as well to indicate that there is still oscillation, even though it is exponentially decaying (and hard to see in the color scale).

v (along a line of constant u) allows one to give an interpretation to the different parts of the waveform. The inspiral occurs when the waveform propagates out directly, but nearly out-of-phase with the matching surface. The merger is the smooth, but brief, transition during which the phase relationship between the matching surface and the waveform evolves, and the ringdown is the last set of waves that are disconnected from the behavior on the surface (they are the scattered waves from the potential barrier).

We also show in Fig. 6.9 a contour-density plot of the real part of the Zerilli function in the u-v plane during the last few orbits of the inspiral, merger, and ringdown (for the evolution discussed in this section). This figure is a spacetime diagram, where time runs up, and the radial coordinate, r_* increases to the right. The matching surface is the dark timelike curve running up that turns to a line of constant v at the end. The region to the left of the surface, the solid green (gray) is the interior PN region, but we do not show the metric perturbation in this region. On its right is the BHP region, where we show the Zerilli function colored so that blue colors (dark gray) are negative and red colors (light gray) are positive. Away from the matching surface, the Zerilli function oscillates between yellow (light gray) and light blue (darker gray) for several orbits before inspiral. Each oscillation is bounded between a black, dashed contour curve. As the reduced mass of the binary plunges toward the horizon, the outgoing waves increase in frequency and amplitude, which is how we describe the transition from the inspiral to the merger phase. The merger phase is short, and the black hole rings down (leading to very little gravitational-wave emission in the top corner of the diagram). As the reduced mass of the system approaches the horizon, there is a small wavepacket of ingoing radiation that accompanies it.

We close this section with one last observation. If we were to plot the equivalent quantities to those in Figs. 6.8 and 6.9 for the evolution in Section 6.3, then one would see that the Zerilli function on the matching surface increases during ringdown instead of approaching a constant. This does not have any effect on the waveform, because it is a low frequency change that occurs within the potential barrier, and is hidden from the region of space outside the potential. In some sense, it is a strong confirmation of Price's idea that the details of the collapse will be hidden within the potential barrier. At the same time, however, this behavior arises from the fact that the derivative of the Zerilli function with respect to r_* vanishes on the matching surface. When this condition was neglected in this section, it led to a more regular behavior there. This suggests that it may be worth while to do a more careful analysis of how the Zerilli function and its derivatives near the horizon should scale in the presence of radiation reaction.

6.5 Spinning Black Holes, Spin Precession, and the Superkick Merger

In this section, we will incorporate the effects of black-hole spins into our method, with the aim of understanding the large kick that arises from the merger of equal-mass black holes with spins antialigned and in the orbital plane (the superkick configuration). To do this, we will first discuss adding odd-parity metric perturbations to the results in the previous section. We will then indicate why spin precession is important in producing large kicks and discuss two ways of implementing spin precession: the PN equations of precession and geodetic precession in the Schwarzschild spacetime. In our method, we will use the geodetic-precession approach, and we will present numerical results for the kick that uses this equation of spin precession.

6.5.1 Odd-Parity Metric Perturbations of Spinning Black Holes

To incorporate the effects of spin into our model, we will add the lowest-order metric perturbations arising from using spinning bodies in the PN metric, as we did in Paper I. This comes from the metric coefficients

$$h_{0i} = -\frac{2\epsilon_{ijk} S_A^j n_A^k}{R_A^2} - \frac{2\epsilon_{ijk} S_B^j n_B^k}{R_B^2} \,. \tag{6.66}$$

Here we use the notation of Paper I, where we label the two bodies by A and B. The new variables S_A^j represent the spin angular momentum of the body, R_A is the distance from body A and n_A^k is a unit vector pointing from body A. The variables for body B are labeled equivalently. Because we will focus on the extreme kick configuration, we will assume that the black holes lie in the x-y plane, at positions $\mathbf{X}_A(t)$ and $\mathbf{X}_B(t)$ (identical to Eq. (6.26) of Section 6.3.3), and that the spins are given by

$$\mathbf{S}_A(t) = -\mathbf{S}_B(t) = S(\cos\beta(t), \sin\beta(t), 0) \,, \tag{6.67}$$

where $S = \chi(M/2)^2$ is the magnitude of the spin, and χ is the dimensionless spin, ranging from zero to one.

Under these assumptions, one can show that the Cartesian components of the metric coefficients above are

$$h_{0X} = -\frac{3SA(t)}{R^3} \sin 2\theta \sin\beta(t) \cos(\alpha(t) - \varphi) \,, \tag{6.68}$$

$$h_{0Y} = \frac{3SA(t)}{R^3} \sin 2\theta \cos\beta(t) \cos(\alpha(t) - \varphi) \,, \tag{6.69}$$

$$h_{0Z} = \frac{2SA(t)}{R^3} \sin[\alpha(t) - \beta(t)] + \frac{6Sa(t)}{R^3} \sin^2\theta \cos(\alpha(t) - \phi) \sin(\beta(t) - \varphi) \,. \tag{6.70}$$

One can then convert the Cartesian components into spherical-polar coordinates to find that

$$h_{0R} = \frac{2SA(t)}{R^3}\sin[\alpha(t)-\beta(t)]\cos\theta\,, \tag{6.71}$$

$$h_{0\theta} = -\frac{2SA(t)}{R^2}\sin[\alpha(t)-\beta(t)]\cos\theta - \frac{6SA(t)}{R^2}\sin\theta\cos(\alpha(t)-\varphi)\sin(\beta(t)-\varphi)\,, \tag{6.72}$$

$$h_{0\varphi} = \frac{6SA(t)}{R^2}\sin^2\theta\cos\theta\cos(\alpha(t)-\varphi)\cos(\beta(t)-\varphi)\,. \tag{6.73}$$

As written above, the metric perturbations do not take the form of an odd-parity vector harmonic, because there is a dipole-like piece in two of the components. This can be eliminated by making a gauge transformation,

$$\xi_0 = -\frac{SA(t)}{R^2}\cos\theta\sin[\alpha(t)-\beta(t)]\,. \tag{6.74}$$

A small gauge transformation produces a change in the metric via

$$\hat{h}_{\mu\nu} = h_{\mu\nu} - \xi_{\mu,\nu} - \xi_{\mu,\nu}\,, \tag{6.75}$$

which in this case sets $\hat{h}_{0R}=0$. The remaining terms in the metric can then be expressed in terms of the odd-parity, vector spherical harmonics,

$$\mathbf{X}^{2,\pm2} = (X^{2,\pm2}_\theta, X^{2,\pm2}_\varphi) \tag{6.76}$$

$$= \frac{1}{2}\sqrt{\frac{15}{2\pi}}\sin\theta e^{\pm i2\varphi}(\mp i, \sin\theta\cos\theta)\,,$$

$$\mathbf{X}^{2,0} = (X^{2,0}_\theta, X^{2,0}_\varphi) = -\frac{3}{2}\sqrt{\frac{5}{\pi}}\sin^2\theta\cos\theta(0,1)\,. \tag{6.77}$$

A short calculation shows that

$$(\hat{h}_{0\theta},\hat{h}_{0\varphi}) = 2\Re\left[\frac{SA(t)}{r^2}\sqrt{\frac{6\pi}{5}}e^{-i[\alpha(t)+\beta(t)]}\mathbf{X}^{2,2}\right] - \frac{8SA(t)}{r^2}\sqrt{\frac{\pi}{5}}\cos[\alpha(t)-\beta(t)]\mathbf{X}^{2,0}\,. \tag{6.78}$$

As with the even-parity, mass-quadrupole perturbations discussed in the previous section, we will only be interested in evolving the $m=2$ perturbation (though in this case it is an odd-parity, current-quadrupole moment). The reason for this is subtle, and will be clarified in the next section. Nevertheless, we will mention here that during the merger and ringdown (when the kick is generated), the spins precess at the orbital frequency, i.e., $\dot{\alpha}(t)=\dot{\beta}(t)$. As a result, the $m=0$ part of the perturbations which depend on $\alpha(t)-\beta(t)$ become constant, and the only changes in the perturbations come from changes in $A(t)$. We mentioned in Section 6.3.3 that we would also neglect the $m=0$ part of the even-parity perturbations, because it also evolved from time variations in $A(t)$, which occur on the time scale of the radiation-reaction force (2.5 PN orders below the leading-order orbital motion). Consequently, because we are interested in the behavior of the binary during the

merger and ringdown, we can neglect the $m = 0$ parts of the odd-parity metric perturbations for this same reason. In addition, because we are treating just the $m = \pm 2$ perturbations (and the $m = -2$ term is the complex conjugate of the $m = 2$ moment), we will again drop the label m on the perturbations.

Thus, the relevant piece of the gravitomagnetic potential for our calculation will be

$$w_{(\mathrm{o})} = -\frac{SA(t)}{4R^2}\sqrt{\frac{6\pi}{5}}e^{-i[\alpha(t)+\beta(t)]}\,, \tag{6.79}$$

and one can then use Eq. (6.20) and the fact that $R = r - M$ to find that the Regge-Wheeler function is (at leading order in r),

$$\Psi_{(\mathrm{o})} = \frac{2SA(t)}{R^2}\sqrt{\frac{6\pi}{5}}e^{-i[\alpha(t)+\beta(t)]}\,. \tag{6.80}$$

This means that on the matching surface,

$$\Psi_{(\mathrm{o})} = \frac{8S}{A(t)}\sqrt{\frac{6\pi}{5}}e^{-i[\alpha(t)+\beta(t)]}\,. \tag{6.81}$$

We can then evolve the Regge-Wheeler equation, Eq. (6.21), (with the odd-parity $l = 2$ potential) using Eq. (6.81) as the boundary condition along the matching surface. We will not take any radiation-reaction effects from the current-quadrupole perturbations into account (since they are 1.5 PN orders below the leading-order Newtonian radiation reaction of Section 6.3.3); as a result, we will evolve the Regge-Wheeler function using the matching surface generated by the even-parity, mass-quadrupole perturbations alone.

6.5.2 Spin Precession

Before we discuss the evolution of the Regge-Wheeler and Zerilli functions, we will mention an effect that is important for our recovering the correct qualitative behavior of the kick in superkick simulations. This effect was observed by Schnittman et al. in [54] and clarified to us by Thorne [55]. In Schnittman et al.'s discussion of the superkick configuration, the authors observe that the spins precess in the orbital plane very rapidly during the merger, approaching the orbital frequency just before the ringdown. We will give a heuristic argument of why this effect should occur before we explore two models that produce spin precession (one based on the PN equations of motion and the other based on geodetic precession in the Schwarzschild spacetime). We will ultimately favor the latter.

6.5.2.1 Motivation for Spin Precession

One can see the need for spin precession from the following simple argument. Just as the even-parity perturbations gave rise to a waveform that increased from twice the orbital frequency to the quasinormal-mode frequency during the merger phase (see Fig. 6.7), so too must the odd-parity

perturbations of the previous section give rise to a part of the waveform that transitions from the orbital frequency to the same quasinormal-mode frequency as the even-parity perturbations. The quasinormal-mode frequencies are the same, because both the Regge-Wheeler and Zerilli functions are generated by $l = 2$, $m = \pm 2$ perturbations. Because the Zerilli function is generated by a boundary condition proportional to $e^{-i2\alpha(t)}$ and the Regge-Wheeler function produced by a boundary condition that changes as $e^{-i[\alpha(t)+\beta(t)]}$, for the two perturbations to evolve in the same way, both $\alpha(t)$, the orbital evolution, and $\beta(t)$, the spin precession, should evolve in identical ways at the end of merger. Stated more physically, at the end of merger, the spins should precess at the orbital frequency.

This rapid precession of the spins was observed by Brügmann et al. [56] in their study of black-hole superkicks. Using a combination of PN spin precession and numerical-relativity data, they were able to match the precession of the spin in their numerical simulations. We will explain in the next section why this worked so well for their simulation, but why it will not work as well in the hybrid method.

6.5.2.2 Post-Newtonian Spin Precession

Brügmann et al. begin from the well-known spin precession for a binary (see, e.g., [66]),

$$\dot{\mathbf{S}}_A(t) = \frac{1}{A(t)^3}\left(2 + \frac{3M_B}{2M_A}\right)[\mathbf{L}_N(t) \times \mathbf{S}_A(t)] \tag{6.82}$$

where we just write the leading-order effect from the Newtonian angular momentum,

$$\mathbf{L}_N(t) = \mu\{[\mathbf{X}_A(t) - \mathbf{X}_B(t)] \times [\dot{\mathbf{X}}_A(t) - \dot{\mathbf{X}}_B(t)]\} \tag{6.83}$$

The vector $\hat{\mathbf{n}}$ is a unit vector from the center of mass. There is an equivalent equation for the precession of $\mathbf{S}_B(t)$, identical to the equation above, under the interchange of A and B. Given the form of the equation above, the magnitude of the spin does not change, and the spin precesses about the Newtonian angular momentum $\mathbf{L}_N(t)$. Moreover, Brügmann et al. found that for the superkick configuration, where the spins lie in the plane, precession of the spins does not produce a large component out of the plane (the z component in this case).

For simplicity, therefore, we will just consider the components of the spin in the orbital plane, which, at leading-order, will precess as a result of coupling to the Newtonian orbital angular momentum. The Newtonian angular momentum is

$$\mathbf{L}_N(t) = \mu A(t)^2 \dot{\alpha}(t)\hat{\mathbf{z}}\,, \tag{6.84}$$

where $\dot{\alpha}(t)$ is the orbital frequency. With the assumption that $S_A^z = S_B^z = 0$, the spins precess via

the equation

$$\dot{\mathbf{S}}_A(t) = \frac{7M\dot{\alpha}(t)}{8A(t)}[\hat{\mathbf{z}} \times \mathbf{S}_A(t)]\,, \tag{6.85}$$

where we have also used the fact that this is an equal-mass binary, ($M_A = M_B = M/2$ and $\mu = M/4$). Taking the time derivative of Eq. (6.67), we obtain the expression for the left-hand side of the equation above,

$$\dot{\mathbf{S}}_A(t) = \dot{\beta}(t)[\hat{\mathbf{z}} \times \mathbf{S}_A(t)]\,. \tag{6.86}$$

Relating the two expressions, we arrive at the equation of spin precession,

$$\dot{\beta}(t) = \frac{7M}{8A(t)}\dot{\alpha}(t)\,. \tag{6.87}$$

For the hybrid method, this expression will not lead to the spin-precession frequency approaching the orbital frequency, because $A(t) \geq 2M$ for the entire evolution (and hence, the spin-precession frequency will not even be half the orbital frequency at its maximum). In the next section, we will put forward an equation of spin precession based on geodetic precession in the external Schwarzschild spacetime, which will have the desired spin-precession behavior.

Before turning to the next section, we address the question of why PN spin precession worked so successfully for Brügmann et al. Their initial data begins in a gauge that is identical to the 2PN ADMTT gauge, and they assume that it continues to stay in that gauge throughout their evolution. As a result, they use the puncture trajectories as the positions of the black holes, and the 2PN ADMTT gauge expressions to relate the momenta of the black holes to their velocities. Although the PN equations of spin precession are written in harmonic gauge, they use the puncture results to calculate these expressions. This is reasonable, because the harmonic and ADMTT gauge positions do not differ much until separations of roughly $A(t) \approx 2M$. Their puncture separations do reach small values of $A(t) < M$ prior to merger, and they continue to use the harmonic-gauge spin-precession formula in this regime (even as the PN approximation starts becoming less accurate). This works remarkably well, nevertheless, and, as one can see from Eq. (6.87), when $A(t) \approx 7M/8$, the spins will precess at the orbital frequency. Thus, the work of Brügmann et al. helps to confirm that the locking of the orbital and spin-precession frequencies is important in the superkick merger, but to replicate this effect in the hybrid method will require a different approach, described below.

6.5.2.3 Geodetic Precession in the Schwarzschild Spacetime

Our approach to spin precession relies on geodetic precession in the Schwarzschild spacetime, which we review below. The problem of geodetic precession of a spin on a circular orbit in the Schwarzschild spacetime is well understood; its derivation appears in the introductory text by Hartle [67], for example. We will reproduce some of the important elements of the derivation here, using our notation, however. One typically starts with the spin 4-vector S^μ (whose spatial components lie in

the orbital plane) that travels along a circular geodesic parametrized by a 4-velocity u^μ. As usual $u^\mu u_\mu = -1$, and one also imposes the spin supplementary condition, $S^\mu u_\mu = 0$. The components of these two vectors are $\vec{S} = (S^t, S^r, 0, S^\varphi)$, and $\vec{u} = u^t(1, 0, 0, \dot{\alpha}(t))$. Because of the spin supplementary condition and the normalization of the four velocity, the components S^t and u^t are not independent variables. Thus, when one writes the equation of geodetic precession of the spin [Eq. (14.6) of Hartle],

$$\frac{dS^\mu}{d\tau} + \Gamma^\mu{}_{\rho\nu} S^\rho u^\nu = 0\,, \tag{6.88}$$

for circular equatorial orbits, it reduces to two coupled equations for the independent variables $S^r(t)$ and $S^\varphi(t)$ (Eqs. (14.3a) and (14.3b) of Hartle),

$$\dot{S}^r(t) - [r_s(t) - 3M]\dot{\alpha}(t) S^\varphi(t) = 0\,, \tag{6.89}$$

$$\dot{S}^\varphi(t) + \frac{\dot{\alpha}(t)}{r_s(t)} S^r(t) = 0\,. \tag{6.90}$$

The dot still refers to derivatives with respect to coordinate time t (not proper time τ). If we assume that $\dot{\alpha}(t)$ does not change much over an orbit (which is true during most of the evolution of the binary, as it only changes from the radiation-reaction force), and we continue to denote the angle of the spin in the orbital plane by $\beta(t)$, then one can write the solution to these equations (Eqs. (14.16a) and (14.16b) of Hartle) as,

$$S^r(t) = S\sqrt{1 - \frac{2M}{r_s(t)}}\cos[\alpha(t) - \beta(t)]\,, \tag{6.91}$$

$$S^\varphi(t) = \frac{S}{r_s(t)}\sqrt{1 - \frac{2M}{r_s(t)}}\frac{\dot{\alpha}(t)}{\dot{\alpha}(t) - \dot{\beta}(t)}\sin[\alpha(t) - \beta(t)]\,, \tag{6.92}$$

where the spin is normalized $S^\mu S_\mu = S^2$, and where (Eq. (14.15) of Hartle)

$$\dot{\alpha}(t) - \dot{\beta}(t) = \sqrt{1 - \frac{3M}{r_s(t)}}\dot{\alpha}(t)\,. \tag{6.93}$$

Because we only describe the spins with leading-order physics, we will only keep the leading-order behavior of the spins. Thus, we will describe the spatial components of the spins by

$$S^r(t) = S\cos[\alpha(t) - \beta(t)]\,, \quad S^\varphi(t) = \frac{S}{r_s(t)}\sin[\alpha(t) - \beta(t)]\,, \tag{6.94}$$

and we will expand the equation for the evolution of $\beta(t)$ in a Taylor series up to linear order in $M/r_s(t)$,

$$\dot{\alpha}(t) - \dot{\beta}(t) = \left(1 - \frac{3M}{2r_s(t)}\right)\dot{\alpha}(t)\,. \tag{6.95}$$

We ultimately arrive at the expression that we will use to describe spin precession in our formalism,

$$\dot{\beta}(t) = \frac{3M}{A(t)}\dot{\alpha}(t)\,, \tag{6.96}$$

because at leading order $A(t) = a(t)$.

Although Eq. (6.96) looks quite similar to the leading-order PN spin precession, Eq. (6.87), the former equation produces a much stronger spin precession than the latter does. Not even the next-order PN spin-precession terms will produce such strong precession (see, e.g., [68]). The equation of spin precession based on geodetic motion takes on more of the strong-gravity character of the Schwarzschild spacetime. It states that when a spinning particle orbits near the light ring, its spin will lock to the its orbital motion. An effect quite similar to this happens during the merger phase in the superkick simulation, as was shown in the work of Brügmann et al., and which we discussed in the previous section. In the next section, we will show how this contributes to the large kick of the superkick simulations.

6.5.3 Numerical Results and Kick

In the first part of this section, we describe how we numerically solve the Regge-Wheeler equation (we continue to solve the Zerilli equation in the same way as described in Section 6.4), and we show a representative waveform obtained from the Regge-Wheeler function. We next describe how we calculate the linear-momentum flux and the kick from the waveforms. Finally, we close this section by studying the dependence of the kick on the initial angle between the spins and the linear momentum of the PN point particles. We recover results that are qualitatively similar to those seen in full numerical-relativity simulations.

6.5.3.1 Numerical Methods and Waveforms

To calculate the Regge-Wheeler function, and thus the radiated energy-momentum in the gravitational waves, we first make the following observation. Because the odd-parity perturbation of the spins of the black holes is a 1.5 PN effect, the corresponding radiation-reaction force will also enter at 1.5 PN beyond the leading-order radiation-reaction force discussed in Section 6.3.3. Consequently, we do not take it into account in the leading-order treatment of the radiation-reaction force. Moreover, we note that the spin-precession angle, $\beta(t)$, does not enter into the evolution equations for the reduced mass or for the Zerilli function. As a result, the evolution of $\beta(t)$ and $\Psi_{(\mathrm{o})}$ can be performed after the evolution of the binary without spin. In fact, the evolution of $\Psi_{(\mathrm{o})}$ is carried out in the same manner as that described in Paper I, because the matching surface is driven by radiation-reaction from the even-parity Zerilli function alone. Were we to include the radiation reaction arising from the spins, however, we would need to evolve the equations for $\beta(t)$ and $\Psi_{(\mathrm{o})}$ simultaneously, and in a manner identical to that described in Section 6.3.3.

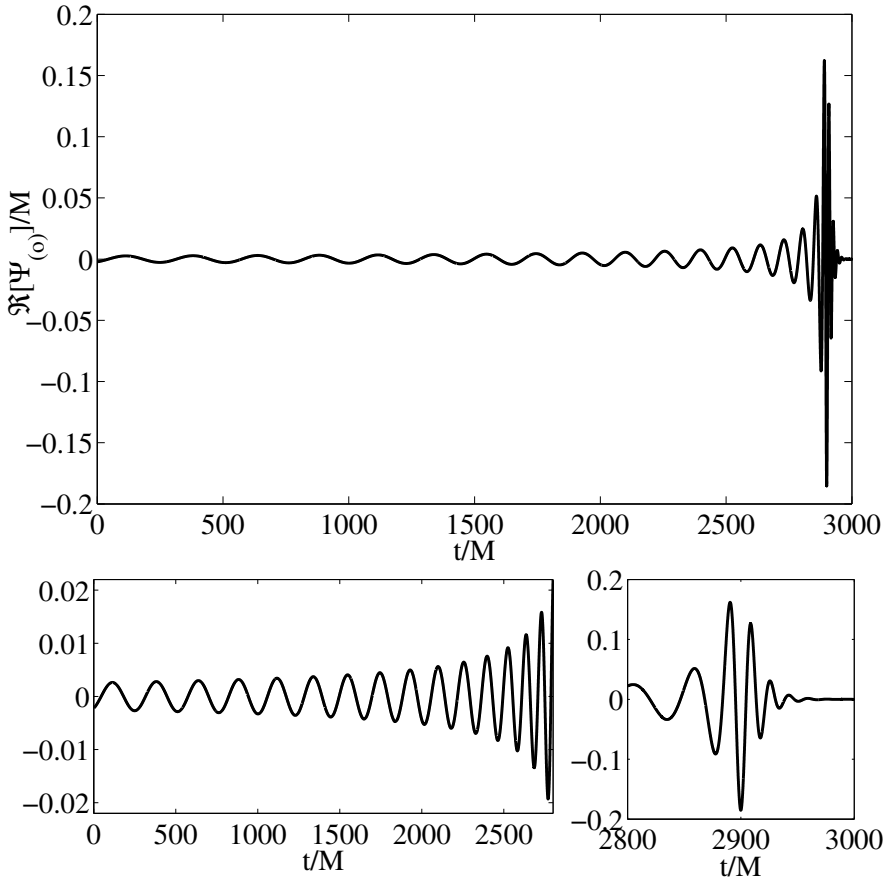

Figure 6.10: The top panel shows the real part of the Regge-Wheeler function throughout the entire evolution. The bottom-left panel just focuses on the early times of inspiral, where the Regge-Wheeler function slowly increases in frequency and amplitude because of the binary's inspiral and the slow spin precession. In the bottom-right panel, one sees that as the spins begin to precess near the orbital frequency, the Regge-Wheeler function dramatically increases in amplitude and frequency.

Our initial conditions are identical to those described in Section 6.4.1, but we will set the dimensionless spin $\chi = 1$, and let $\beta(0)$ vary over several values from 0 to 2π, to study the influence of the initial angle on the kick. We first show the real part of the Regge-Wheeler function extracted at large constant v, in Fig. 6.10. The top panel is the full Regge-Wheeler function, whereas the bottom-left panel features the early part from the inspiral (so that one can see the gradual increase in the amplitude and frequency that comes from the combined effects of the binary inspiral, and the increased rate of spin precession). In the bottom-right panel, we show the merger and ringdown phase, which is obscured in the top panel. As the spins start precessing near the orbital frequency during merger, one can see the rapid growth of the Regge-Wheeler function.

To see how this spin precession leads to a large kick, we plot both the even- and the odd-parity metric perturbations extracted at large constant v in Fig. 6.11. We show the real part of the Zerilli function, $\Psi_{(\mathrm{e})}$, in red (gray) and the imaginary part of the Regge-Wheeler function, $\Psi_{(\mathrm{o})}$, in black,

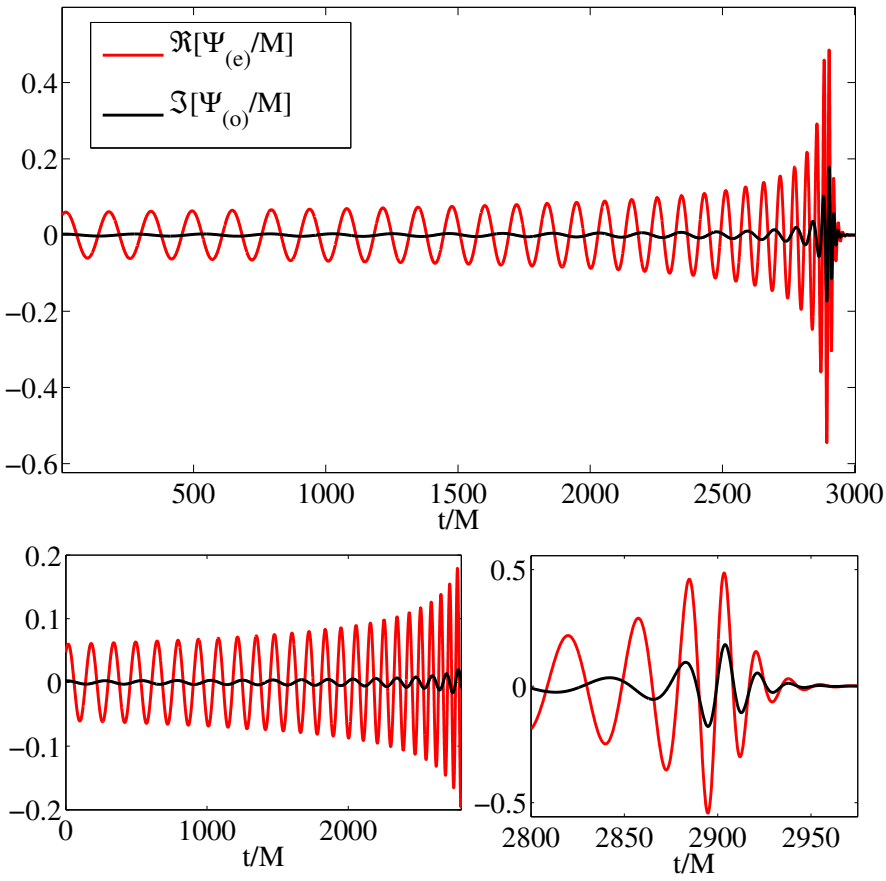

Figure 6.11: The top panel shows the real part of the Zerilli function, the red (gray) curve, and the imaginary part of the Regge-Wheeler function, the black curve, throughout the inspiral, merger, and ringdown. The bottom-left panel shows only the inspiral, where the Regge-Wheeler function is much smaller than the Zerilli function, and oscillates at approximately half the frequency. In the bottom-right panel, during the merger and ringdown, as the spins precess near the orbital frequency, the Regge-Wheeler function increases in amplitude and frequency, and becomes in phase with the Zerilli function. This leads to a large kick.

for the angle $\beta(0)$ that gives the maximum kick. As we show below, in Eq. (6.100), it is the relative phase of the product of these components that is important in producing the kick. During the early part of the evolution, the Regge-Wheeler function is quite small and oscillates with roughly half the period of the Zerilli function. This is difficult to see in the upper panel of the full waveforms in Fig. 6.11, but is more evident in the lower-left panel, showing just the early parts of the evolution. In the last orbit before the merger and ringdown (shown in the lower-right panel), the spins start precessing rapidly, and, in the case that produces the maximum kick, the real part of the even-parity perturbation function, and the imaginary part of the odd-parity function oscillate in phase during the merger and ringdown. (For the case with zero kick, the two functions are now out-of-phase by 90 degrees.)

6.5.3.2 Calculation of the Kick

We now discuss, more concretely, how we calculate the kick from the emitted gravitational waves. At radii much larger than the reduced gravitational wavelength, $r \gg \lambda_{\rm GW}/(2\pi)$, one can relate the gravitational-wave polarizations h_+ and $h_\times$ to the Regge-Wheeler and Zerilli functions via the expression,

$$h_+ - i h_\times = \frac{1}{2r} \sum_{l,m} \sqrt{\frac{(l+2)!}{(l-2)!}} \left[\Psi^{l,m}_{\rm (e)} + i\, \Psi^{lm}_{\rm (o)} \right] {}_{-2}Y_{lm} \,, \tag{6.97}$$

where ${}_{-2}Y_{lm}$ is a spin-weighted spherical harmonic. The linear momentum flux carried by the gravitational waves is typically expressed as

$$\dot{P}_i(t) = \lim_{r\to\infty} \frac{r^2}{16\pi} \oint n_i |\dot{h}_+ - i\dot{h}_\times|^2 d\Omega \,, \tag{6.98}$$

where n_i is a radial unit vector and $d\Omega$ is the area element on a 2-sphere. A somewhat lengthy calculation can then show that the momentum flux in the z direction is given by

$$\dot{P}_z(t) = \frac{1}{16\pi} \sum_{l,m} \frac{(l+2)!}{2(l-2)!} \left[-i c_{l,m} \dot{\Psi}^{l,m}_{\rm (e)} \dot{\bar{\Psi}}^{l,m}_{\rm (o)} + d_{l+1,m} \left(\dot{\Psi}^{l,m}_{\rm (e)} \dot{\bar{\Psi}}^{l+1,m}_{\rm (e)} \dot{\Psi}^{l,m}_{\rm (o)} \dot{\bar{\Psi}}^{l+1,m}_{\rm (o)} \right) \right] \,, \tag{6.99}$$

where $c_{l,m} = 2m/[l(l+1)]$, and $d_{l,m}$ is a constant that also depends upon l and m. The equations above appear in several sources; these agree with those of Ruiz et al. [58] (see their Eqs. (84), (11), (94), and (43), respectively).

In our case, however, we just treat the $l = 2$ and $m = \pm 2$ modes of the Regge-Wheeler and Zerilli functions, and the momentum flux coming from these modes greatly simplifies. Because the $m = \pm 2$ modes are complex conjugates of one another, we find that the momentum flux is

$$\dot{P}_z(t) = \frac{1}{\pi} \Im[\dot{\Psi}_{\rm (e)} \dot{\bar{\Psi}}_{\rm (o)}] \,. \tag{6.100}$$

When we discuss the kick velocity as a function of time, we mean that we take minus the time integral of the momentum flux, normalized by the total mass, i.e.,

$$v_z^{\rm kick}(t) = -\frac{1}{M} \int_{t_0}^{t} \dot{P}_z(t') dt' \,. \tag{6.101}$$

We continue to normalize by the total mass M, because numerical-relativity simulations have shown that it changes only by roughly 4% during a black-hole-binary merger (see, e.g., Campanelli et al. [52]); as a result, normalizing by the total mass M will not be a large source of error.

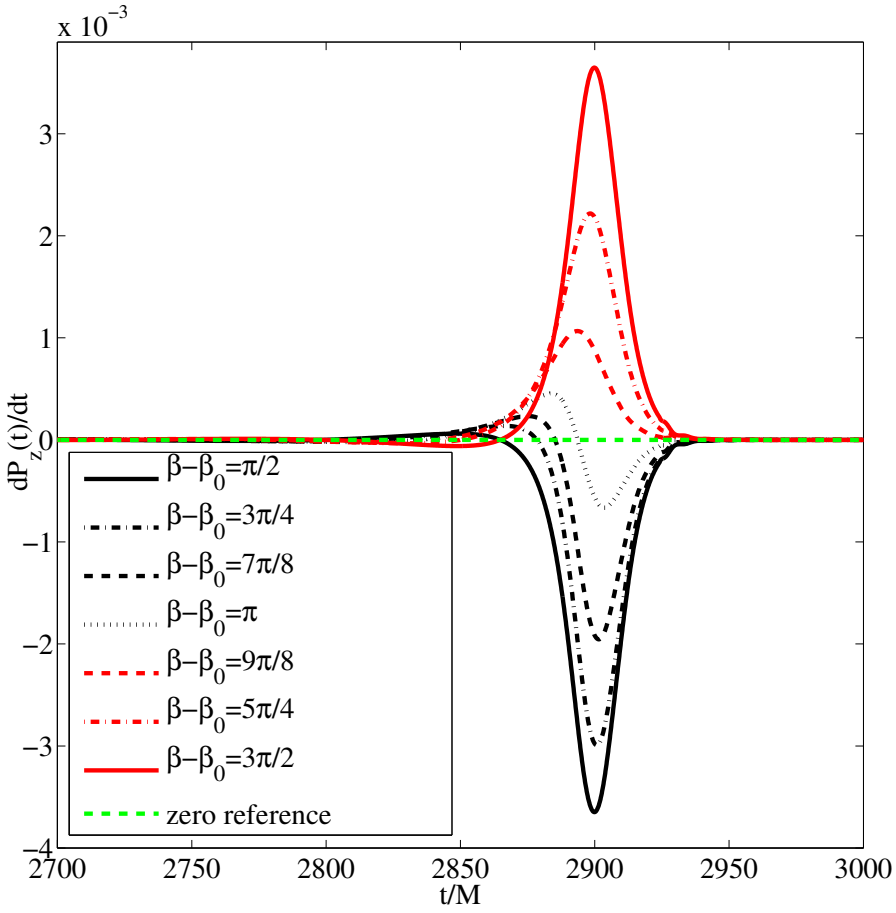

Figure 6.12: The momentum flux, $\dot{P}_z(t)$, as function of time, for several values of $\beta - \beta_0$, where $\beta_0 \approx 215\pi/192$ is the value that gives nearly zero kick. We also include a straight green (light gray) dashed line at zero flux to indicate how the momentum flux varies around this point.

6.5.3.3 Numerical Results for the Momentum Flux and Kick

We now show the results of our numerical solutions for the superkick configuration. We first show in Fig. 6.12 the momentum flux for several different initial angles of the spins, β. In the plots, we subtract the value that gives nearly zero kick, which we denote by $\beta_0 \approx 215\pi/192$. While the shape of the pulse of momentum flux has a similar shape to that seen in numerical-relativity simulations by Brügmann et al. [56], the absolute magnitude is somewhat larger.

The increased overall magnitude of the kick becomes more apparent when we plot $v_{\rm kick}(t)$ in Fig. 6.13, where $v_{\rm kick}(t)$ is defined by Eq. (6.101). As one can see, the largest value of the kick is near 0.08 in dimensionless units, which is roughly a factor of 6 times larger than the estimated maximum from numerical-relativity simulations at lower dimensionless spin parameters. This is largely because the even-parity Zerilli function (proportional to the waveform) is also significantly larger in amplitude

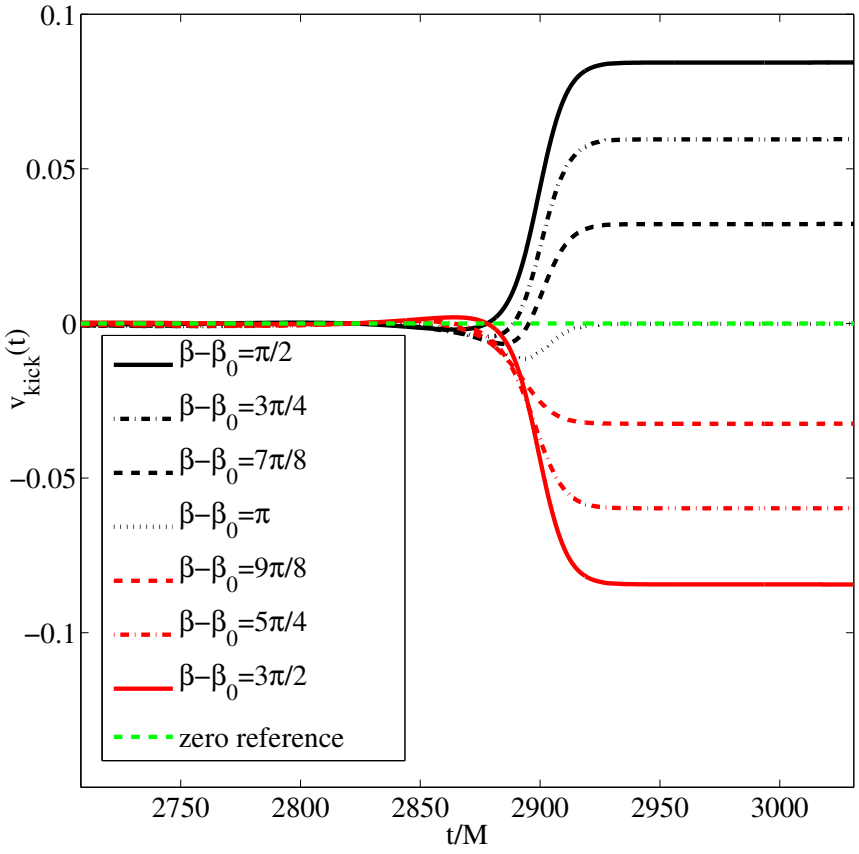

Figure 6.13: The kick as a function of time, for several different initial angles of the spin $\beta - \beta_0$. There is also a straight green (light gray) dashed line at zero velocity to indicate how the kick varies around this point.

than that of numerical-relativity simulations.

Nevertheless, we then show, in this model, that the kick depends sinusoidally upon the initial orientation of the spins, as seen in numerical simulations by Campanelli et al. [52]. We plot the final value of the kick, $v_{\rm kick} \equiv v_z^{\rm kick}(t_f)$, where t_f is the last time in the simulation, as a function of $\beta - \beta_0$ in Fig. 6.14. The sinusoidal dependence in our model is exact up to numerical error. One can see this must be the case from examining the form of our expression for the momentum flux, Eq. (6.100). Because the evolution equations are not influenced by the orientation of the spins, then the Zerilli function will be identical for different initial spin directions. The Regge-Wheeler function, however, will evolve in the same way, but because the value on the matching surface is proportional to $e^{-i\beta(t)}$, Eq. (6.81), the different evolutions will also differ by an overall phase, $e^{i\beta}$, where β is the initial value of the spin. Thus, when one takes the imaginary part of product of the Regge-Wheeler and Zerilli functions to get the momentum flux in Eq. (6.100), one will have sinusoidal dependence.

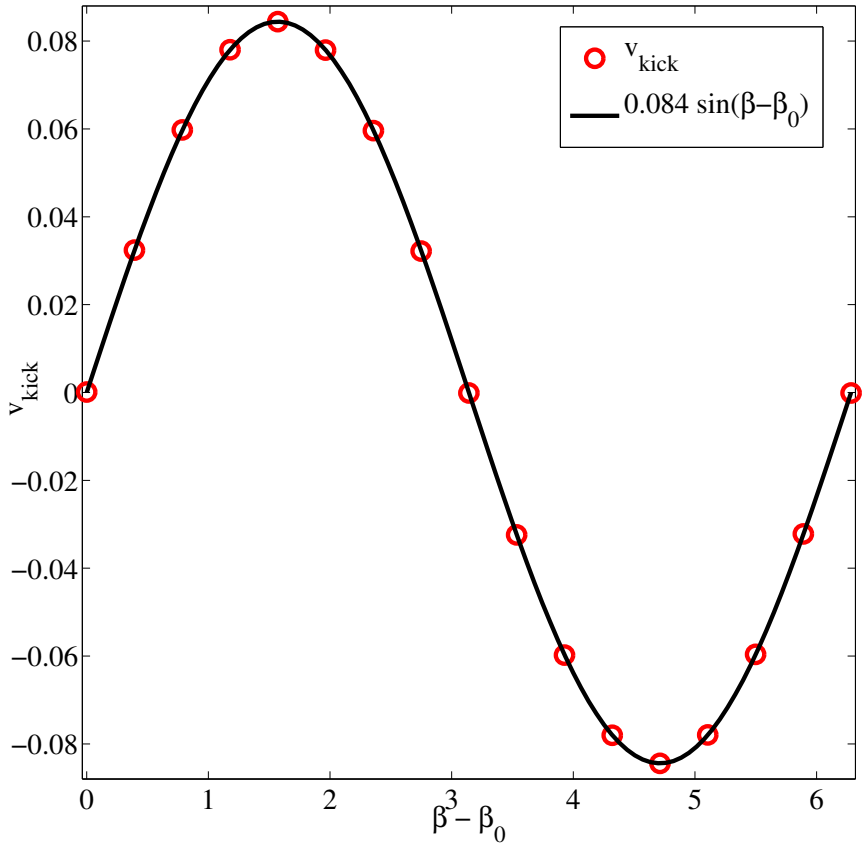

Figure 6.14: The kick calculated for several initial values of β, minus the angle that produces nearly zero kick, $\beta_0 \approx 215\pi/192$. The data points are calculated from the numerical evolutions of this section, while the solid curve is a sinusoidal fit to the data. The hybrid model produces a sinusoidal dependence of the kick on the initial angle $\beta - \beta_0$ very precisely.

(In fact, we could have simply done one evolution and changed the phasing as described above to find the above results; as a test of our method, however, we in fact performed the multiple evolutions to confirm this idea.)

We close this section by making the following observation, which may be known, though we have not seen in numerical-relativity results. Because the dependence on β of the kick is sinusoidal, then for each β, $\beta - \pi$ gives the same kick and momentum flux pattern, $\dot{P}_z(t)$, just opposite in sign. At the same time, though, because of the sinusoidal dependence there are two values that give rise to the same kick in the same direction; however the shape of the momentum flux $\dot{P}_z(t)$ is not the same for these two. One can see this in Fig. 6.12, where the black dotted and dashed curve and minus the red (gray) dotted and dashed curve give rise to the same kick; nevertheless, the pattern of the momentum flux is very different. A careful study of this would reveal more about how the spins

precess and would be of some interest.

6.6 Conclusions

In this paper, we extended a hybrid method for head-on mergers to treat inspiralling black-hole binaries. We introduced a way to include a radiation-reaction force into the hybrid method, and this led to a self-consistent set of equations that evolve the reduced-mass motion of the binary and its gravitational waves. Using just PN and linear BHP theories, we were able to produce a full inspiral-merger-ringdown waveform that agrees well in phase (though less well in amplitude) with those seen in full numerical-relativity simulations. Even though the dynamics during inspiral follow the modified dynamics of a point particle in Schwarzschild rather than the exact dynamics of a black-hole binary, the phasing in the waveform agrees well. Because we assume the background is a Schwarzschild black hole (rather than a Kerr, the true remnant of black-hole binary inspirals), the merger and ringdown parts of the hybrid and numerical-relativity waveforms do not match as well. Nevertheless, the hybrid method does produce a waveform that is quite similar to that of numerical relativity.

We also studied spinning black holes, particularly the superkick configuration (antialigned spins in the orbital plane). We discussed a method to incorporate spin precession, based on the geodetic precession of a spinning point particle in the Schwarzschild spacetime. This caused the spins to lock to the orbital motion during the merger and ringdown, which, in turn, helped to replicate the pattern of the momentum flux and the sinusoidal dependence of the merged black hole's kick velocity seen in numerical simulations. Again, because the amplitude of the emitted gravitational waves does not match that of numerical-relativity simulations, the magnitude of the kick does not completely agree. Nevertheless, because the approximate method was able to capture the pattern of the momentum flux, it gives credence to the idea the locking of the spin-precession frequency to the orbital frequency contributes to large black-hole kicks.

It would be of interest to extend this approach to see if it can recover the results of numerical relativity more precisely. To do this would involve a two-pronged approach: on the one hand, we would need to include higher PN terms in the metric in the interior while using a more accurate Hamiltonian to describe the conservative dynamics of the binary (such as the EOB Hamiltonian); on the other hand, we would need to evolve the perturbations in a Kerr background. It would be simpler to choose the Kerr background to have the spin of the final, merged black hole, but one could also envision evolving perturbations in an adiabatically changing Kerr-like background with a slowly varying mass and angular momentum parameter that change in response to the emitted gravitational waves. It would be of interest to see if such an approach leads to an estimate of the spin of the final black hole similar to that proposed by Buonanno, Kidder, and Lehner [69]. Incorporating the PN corrections and a new Hamiltonian would be the most straightforward improvement, while

those involving the Kerr background are technically more challenging, and computationally more expensive.

Bibliography

[1] A. Abramovici, W. E. Althouse, R. W. P. Driver, Y. Gürsel, S. Kawamura, F. J. Raab, D. Shoemaker, L. Sievers, R. E. Spero, K. S. Thorne, R. E. Vogt, R. Weiss, S. E. Whitcomb, and M. E. Zucker, Science **256**, 325 (1992).

[2] E. E. Flanagan and S. A. Hughes, Phys. Rev. D **57**, 4535 (1998).

[3] L. Blanchet, Living Rev. Relativity **9**, 4 (2006).

[4] M. Sasaki and H. Tagoshi, Living Rev. Relativity **6**, 6 (2003).

[5] R. H. Price and J. Pullin, Phys. Rev. Lett. **72**, 3297 (1994).

[6] R. J. Gleiser, C. O. Nicasio, R. H. Price, and J. Pullin Phys. Rev. Lett. **77**, 4483 (1996).

[7] Z. Andrade and R. H. Price, Phys. Rev. D **56**, 6336 (1997).

[8] G. Khanna, J. Baker, R. J. Gleiser, P. Laguna, C. O. Nicasio, H.-P. Nollert, R. Price, and J. Pullin, Phys. Rev. Lett. **83**, 3581 (1999).

[9] C. F. Sopuerta, N. Yunes, and P. Laguna, Phys. Rev. D **74**, 124010 (2006).

[10] C. F. Sopuerta, N. Yunes, and P. Laguna, Astrophys. J. **656**, L9 (2007).

[11] A. Le Tiec and L. Blanchet, Classical Quantum Gravity **27**, 045008 (2010).

[12] A. Le Tiec, L. Blanchet, and C. Will, Classical Quantum Gravity **27**, 012001 (2010).

[13] J. Baker, M. Campanelli, and C. O. Lousto, Phys. Rev. D **65**, 044001 (2002).

[14] M. Campanelli, B. Kelly, and C. O. Lousto, Phys. Rev. D **73**, 064005 (2006).

[15] A. Buonanno and T. Damour, Phys. Rev. D **59**, 084006 (1999).

[16] A. Buonanno and T. Damour, Phys. Rev. D **62**, 064015 (2000).

[17] T. Damour and A. Nagar, Phys. Rev. D **79**, 081503(R) (2009).

[18] A. Buonanno, Y. Pan, H. P. Pfeiffer, M. A. Scheel, L. T. Buchman, and L. E. Kidder, Phys. Rev. D **79**, 124028 (2009).

[19] Y. Pan, A. Buonanno, L. T. Buchman, T. Chu, L. E. Kidder, H. P. Pfeiffer, and M. A. Scheel, Phys. Rev. D **81**, 084041 (2010).

[20] Y. Pan, A. Buonanno, M. Boyle, L. T. Buchman, L. E. Kidder, H. P. Pfeiffer, and M. A. Scheel, Phys. Rev. D **84**, 124052 (2011).

[21] P. Anninos, D. Hobill, E. Seidel, L. Smarr, and W.-M. Suen, Phys. Rev. D **52**, 2044 (1995).

[22] P. Anninos, R. H. Price, J. Pullin, E. Seidel, and W.-M. Suen, Phys. Rev. D **52**, 4462 (1995).

[23] R. H. Price and K. S. Thorne, Phys. Rev. D **33**, 915 (1986).

[24] M. Campanelli, R. Gómez, S. Husa, J. Winicour, and Y. Zlochower, Phys. Rev. D **63**, 124013 (2001).

[25] S. Husa, Y. Zlochower, R. Gómez, and J. Winicour, Phys. Rev. D **65**, 084034 (2002).

[26] R. Gómez, S. Husa, L. Lehner, and J. Winicour, Phys. Rev. D **66**, 064019 (2002).

[27] L. Rezzolla, R. P. Macedo, and J. L. Jaramillo, Phys. Rev. Lett. **104**, 221101 (2010).

[28] J. L. Jaramillo, R. P. Macedo, P. Moesta, and L. Rezzolla, Phys. Rev. D **85**, 084030 (2012).

[29] J. L. Jaramillo, R. P. Macedo, P. Moesta, and L. Rezzolla, Phys. Rev. D **85**, 084031 (2012).

[30] J. L. Jaramillo, arXiv:1108.2408, (2011).

[31] E. Poisson, A. Pound, and I. Vega, Living Rev. Relativity **14**, 7 (2011).

[32] L. Barack and C. Cutler, Phys. Rev. D **69**, 082005 (2004).

[33] S. A. Hughes, Phys. Rev. D **61**, 084004 (2000).

[34] K. Glampedakis, S. A. Hughes, and D. Kennefick, Phys. Rev. D **66**, 064005 (2002).

[35] S. Drasco and S. A. Hughes, Phys. Rev. D **73**, 024027 (2006).

[36] P. A. Sundararajan, G. Khanna, and S. A. Hughes, Phys. Rev. D **81**, 104009 (2010).

[37] A. Nagar, T. Damour, and A. Tartaglia, Classical Quantum Gravity **24**, S109 (2007).

[38] T. Damour and A. Nagar, Phys. Rev. D **76**, 064028 (2007).

[39] S. Bernuzzi, and A. Nagar, Phys. Rev. D **81**, 084056 (2010).

[40] S. Bernuzzi, A. Nagar, and A. Zenginoglu, Phys. Rev. D **83**, 064010 (2011).

[41] S. Bernuzzi, A. Nagar, and A. Zenginoglu, Phys. Rev. D **84**, 084026 (2011).

[42] W.-B. Han and Z. Cao, Phys. Rev. D **84**, 044014 (2011).

[43] T. Damour, B. R. Iyer, and A. Nagar, Phys. Rev. D **79**, 064004 (2009).

[44] N. Yunes, A. Buonanno, S. A. Hughes, M. Coleman Miller, and Y. Pan, Phys. Rev. Lett. **104**, 091102 (2010).

[45] N. Yunes, A. Buonanno, S. A. Hughes, Y. Pan, E. Barausse, M. C. Miller, and W. Throwe, Phys. Rev. D **83**, 044044 (2011).

[46] C. O. Lousto, H. Nakano, Y. Zlochower, and M. Campanelli, Phys. Rev. Lett. **104**, 211101 (2010).

[47] C. O. Lousto, H. Nakano, Y. Zlochower, and M. Campanelli, Phys. Rev. D **82**, 104057 (2010).

[48] H. Nakano, Y. Zlochower, C. O. Lousto, and M. Campanelli, Phys. Rev. D **84**, 124006 (2011).

[49] D. A. Nichols and Y. Chen, Phys. Rev. D **82**, 104020 (2010).

[50] W. L. Burke, J. Math. Phys. **12**, 401 (1971).

[51] M. A. Scheel, M. Boyle, T. Chu, L. E. Kidder, K. D. Matthews, and H. P. Pfeiffer, Phys. Rev. D **79**, 024003 (2009).

[52] M. Campanelli, C. O. Lousto, Y. Zlochower, and D. Merritt, Phys. Rev. Lett. **98**, 231102 (2007).

[53] J. A. González, M. Hannam, U. Sperhake, B. Brügmann, and S. Husa, Phys. Rev. Lett. **98**, 231101 (2007).

[54] J. D. Schnittman, A. Buonanno, J. R. van Meter, J. G. Baker, W. D. Boggs, J. Centrella, B. J. Kelly, and S. T. McWilliams, Phys. Rev. D **77**, 044031 (2008).

[55] K. S. Thorne, (private communication), 2011.

[56] B. Brügmann, J. A. González, M. Hannam, S. Husa, and U. Sperhake, Phys. Rev. D **77**, 124047 (2008).

[57] V. Moncrief, Ann. Phys. (N.Y.) **88**, 323 (1974).

[58] M. Ruiz, M. Alcubierre, D. Núñez, and R. Takahashi, Gen. Relativ. Gravit. **40** 1705 (2008).

[59] T. Regge and J. A. Wheeler, Phys. Rev. **108**, 1063 (1957).

[60] F. J. Zerilli, Phys. Rev. D **2**, 2141 (1970).

[61] R. H. Price, Phys. Rev. D **5**, 2419 (1972).

[62] Y. Mino and J. Brink, Phys. Rev. D **78**, 124015 (2008).

[63] A. Zimmerman and Y. Chen, Phys. Rev. D **84**, 084012 (2011).

[64] E. W. Leaver, Proc. R. Soc. Lond. A **402**, 285 (1985).

[65] P. Ajith et al., Phys. Rev. D **77**, 104017 (2008).

[66] L. E. Kidder, Phys. Rev. D **52**, 821 (1995).

[67] J. B. Hartle, *Gravity: An Introduction to Einstein's General Relativity* (Reading, MA, Addison-Wesley, 2003), Sec. 14.3.

[68] G. Faye, L. Blanchet, and A. Buonanno, Phys. Rev. D **74**, 104033 (2006).

[69] A. Buonanno, L. E. Kidder, and L. Lehner, Phys. Rev. D **77**, 026004 (2008).

Chapter 7

Degeneracy in the Quasinormal-Mode Spectrum of Kerr Black Holes and Its Geometric Interpretation

There is a well-known, intuitive geometric correspondence between high-frequency quasinormal modes of Schwarzschild black holes and null geodesics that reside on the light-ring (often called spherical photon orbits): the real part of the mode's frequency relates to the photon's orbital frequency, and the imaginary part of the frequency corresponds to the Lyapunov exponent of the orbit. This relation between modal and orbital frequencies also holds for Kerr black holes for equatorial and polar orbits. For slowly rotating Kerr black holes, there is a similar relationship between high-frequency modes and spherical photon orbits: the quasinormal-mode's real frequency relates to a linear combination of a photon orbit's precessional and orbital frequencies, and its imaginary frequency has the same relationship with the Lyapunov exponent. In this paper, we find a similar relationship between the quasinormal-mode frequencies of Kerr black holes of arbitrary (astrophysical) spins and general spherical photon orbits. We do this using several different methods—both geometric-optics and WKB analyses—which give comparable results. We then apply our results to discuss a degeneracy in the quasinormal-mode spectrum of Kerr black holes, and we show that this degeneracy has a simple geometrical interpretation in terms of the related spherical photon orbits. Specifically, we show that for any black-hole spin parameter, a, there are sets of quasinormal modes with the same real part of their frequencies, and their corresponding spherical photon orbits are closed.

Based on a paper in preparation by H. Yang, D. A. Nichols, F. Zhang, A. Zimmerman, and Y. Chen.

7.1 Introduction

Quasinormal modes (QNMs) of black holes are the characteristic modes of linear perturbations of these spacetimes. To represent the natural, resonant modes of black-hole perturbations, they satisfy an outgoing boundary condition at infinity and an ingoing boundary condition at the horizon. These modes oscillate and decay in time; therefore, they are characterized by complex frequencies, $\omega = \omega_{\rm R} - i\omega_{\rm I}$. These frequencies are typically indexed by three numbers, n, l, and m. The overtone number, n, is proportional to the rate of decay of the perturbation, and l and m are multipolar indices related to the angular eigenfunctions of the QNMs.

Since their discovery in numerical calculations of the scattering of gravitational waves around Schwarzschild black holes by Vishveshwara [1], QNMs have been thoroughly studied in a wide range of spacetimes and have found many applications. There are several reviews [2, 3, 4, 5, 6] that summarize the many discoveries about QNMs. The earlier reviews by Kokkotas and Schmidt [2] and Nollert [3] focus on the QNMs of Schwarzschild and Kerr black holes and on compact stars in four (spacetime) dimensions. They describe how QNMs are defined, the many methods used to calculate QNMs—e.g., estimating them from time-domain solutions [7], using shooting methods in frequency-domain calculations [8], approximating them with inverse-potential approaches [9] and WKB methods [10, 11], and numerically solving for them with continued-fraction techniques [12, 13]—and the ways to quantify the excitation of QNMs (see, e.g., [14, 15]). These first two reviews also discuss the prospects for detecting QNMs in gravitational waves using interferometric gravitational-wave detectors (such as LIGO [16] and VIRGO [17]) and for inferring astrophysical information from them (see, e.g., [18, 19] for finding the mass and spin of black holes using QNMs).

The more recent reviews by Ferrari and Gualtieri [4], Berti et al. [5], and Konoplya and Zhidenko [6] discuss similar topics, but they focus on more recent developments in the physics of gravitational waves (such as quantifying the excitation of QNMs in numerical-relativity simulations of comparable-mass, binary-black-hole mergers [20, 21] and ways to test the no-hair theorem with QNMs [23, 24]). In addition, these three reviews discuss the quasinormal modes of higher-dimensional and asymptotically anti-de Sitter black holes (the latter in connection with the anti-de Sitter, conformal-field-theory correspondence [25]). There have also been several other recent applications of QNMs. For example, Zimmerman and Chen [26] (based on work by Mino and Brink [27]) study extensions to the usual spectrum of modes generated in generic ringdowns. Dolan and Ottewill use eikonal methods to approximate the modal wave function, and they use these functions to study the Green's function and to understand wave propagation in the Schwarzschild spacetime [28, 29, 30].

7.1.1 A Geometric Description of Quasinormal Modes

Although the discussion above highlights that QNMs are well-understood—and they can be calculated quite precisely—it remains useful to develop intuitive and analytical descriptions of these

modes. An important calculation in this direction was performed by Ferrari and Mashhoon [9], who show that for a Schwarzschild black hole, the QNM frequency described by a multipolar index l and an overtone index n can be written in the eikonal (also called the geometric-optics) limit, $l \gg 1$, as

$$\omega \approx (l + 1/2)\Omega - i\lambda(n + 1/2)\,. \tag{7.1}$$

The quantities Ω and $\bar{\lambda}$ are the Keplerian frequency of the velocity-of-light circle (often called a spherical photon orbit) and the Lyapunov exponent of the orbit, respectively. The Lyapunov exponent λ characterizes how quickly a congruence of null geodesics on the circular photon orbit increases its cross section under infinitesimal radial perturbations [31, 30]. Equation (7.1) hints at an intriguing physical description of QNMs: for modes whose wavelengths are much shorter than the background curvature, the mode behaves as if it were sourced by a perturbation that rotates on and diffuses away from the light ring on the time scale of the Lyapunov exponent. The reason why the frequency is proportional to l is somewhat subtle, but we can explain it with a simple geometric-optics argument in Section 7.4.

Ferrari and Mashhoon [9] also gave an indication that a similar relationship should hold for rotating black holes when they derived an analogous result to Eq. (7.1) for slowly rotating black holes. They showed for $l \gtrsim m \gg 1$, the real part of the frequency is given by

$$\Omega \approx \omega_{\rm orb} + \frac{m}{l + 1/2}\omega_{\rm prec}\,, \tag{7.2}$$

where $\omega_{\rm orb}$ is now the Keplerian orbital frequency for the circular photon orbit and $\omega_{\rm prec}$ is the Lense-Thiring-precession frequency of the orbit (which arises because of the slow rotation of the black hole). The geometric-optics interpretation of a quasinormal modes has only one additional complication for slowly rotating black holes ($a \ll M$), but again we will explain it with a similar argument in Section 7.4. In fact, our reasoning works independently of the magnitude of the spin of the black hole, and we find that we can write an expression for the real part of the QNM's frequency as a similar superposition of the orbital and precessional frequencies,

$$\omega_{\rm R} = L\omega_{\rm orb} + m\omega_{\rm prec}\,, \tag{7.3}$$

(where we define $L = l + 1/2$). Much of this paper is devoted to deriving and exploring the physical interpretation of an approximate formula of the form of Eq. (7.3). We summarize the methods we use to find this relationship in the next part of the Introduction, below.

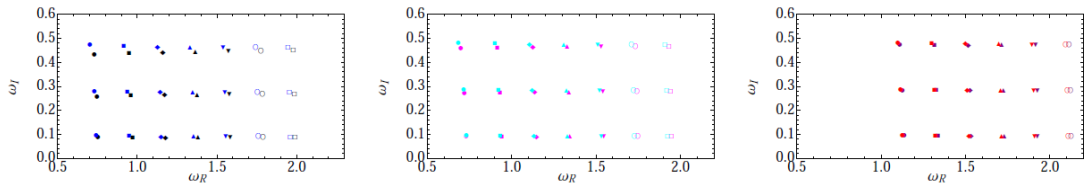

Figure 7.1: Low-overtone and low-multipolar-index QNM spectrum of Kerr black holes of three spins with degenerate modes, computed using Leaver's continued-fraction method [12]. Each panel of the figure corresponds to a fixed spin, and two sets of modes are shown in each panel that have pairs that are nearly degenerate with each other: those with a fixed positive m (for several l and n) and those of a fixed negative m (again for several l and n). In all three panels, we show only the three lowest-overtone frequencies, $n = 0$, 1, and 2 (modes with larger n have larger values of $\omega_{\rm I}$) and several values of l (modes with larger l have larger values of $\omega_{\rm R}$). In the left panel, we plot QNM frequencies for a spin $a/M = 0.69$ and for two sets of modes, $(l, m) = (k, 2)$ (the black symbols) and $(l', m') = (k+1, -2)$ (the blue symbols) for $k = 3, \ldots, 9$; in the middle panel, the spin is $a/M = 0.47$, and we show modes with $(l, m) = (k, 3)$ (magenta symbols) and $(l', m') = (k+1, -3)$ (cyan symbols) for $k = 3, \ldots, 9$; finally, the right panel uses a spin $a/M = 0.35$ and depicts modes with $(l, m) = (k, 4)$ (red symbols) and $(l', m') = (k+1, -4)$ (purple symbols) for $k = 5, \ldots, 10$.

7.1.2 The Methods and Results of This Article

Equation (7.3) implies a geometric-optics interpretation of QNMs of Kerr black holes of arbitrary astrophysical spins that, to the best of our knowledge, is not in the existing literature. To understand why this may be true, we will describe the mechanics of computing QNMs in more detail.

For Schwarzschild and Kerr black holes, QNMs can be found by (i) separating the Teukolsky equation [38] (a linear partial differential equation that describes the evolution of scalar, vector, and gravitational perturbations of Schwarzschild and Kerr black holes) into linear ordinary differential equations and (ii) finding the separation constants describing the QNM's frequency, ω, and the angular separation constant, A_{lm}, by solving the eigenvalue problem subject to appropriate boundary conditions on the ordinary differential equations. For a Schwarzschild black hole, the angular separation constant is fixed by the spin of the perturbing field and the spherical symmetry of the background to be $A_{lm} = l(l+1) - s(s+1)$, and the radial differential equation (called the Teukolsky radial equation) serves as the eigenvalue problem that determines the frequency of the QNM. Because the modal function is subject to an ingoing boundary condition at the horizon and an outgoing boundary condition far from the black hole, the problem can be solved using WKB methods [10, 11]. For a Kerr black hole, one must now solve for the angular separation constant and the frequency of the QNM simultaneously by solving the joint eigenvalue problem of the Teukolsky radial function and the Teukolsky angular function (the solution of the ordinary differential equation describing the polar-angle dependence of the perturbation). Because the radial and angular Teukolsky equations both depend on the frequency and angular separation constant, directly applying WKB methods is not as straightforward.

This is not to say that there has been no work toward finding approximate eigenvalues and developing a geometric-optics interpretation of QNMs of the Kerr spacetime. In addition to Ferrari and Mashhoon's [9] result for slowly rotating black holes, Kokkotas [32] and Iyer and Seidel [33] also used WKB methods to compute the frequency of a QNM. Specifically, they performed an expansion of the separation constants of the angular Teukolsky equation, A_{lm}, for small, dimensionless spin parameters, a/M, and they inserted the expression into the radial Teukolsky equation to solve for the frequency. In a different approach, Dolan developed a matched-expansion formalism for Kerr black-holes of arbitrary spins, that can be applied to compute the frequency of QNMs, but only for modes with $l = |m|$ and $m = 0$ [29].

In this article, we circumvent some of the difficulties in solving the joint eigenvalue problem of the radial and angular Teukolsky equations by applying a change of variables to the angular equation (which turns it into an equation that resembles a bound-state problem in quantum mechanics). When written in this form, we can relate the angular separation constant to the multipolar indices of a QNM through a Bohr-Sommerfeld condition that we call the angular WKB method. When we combine this condition with the WKB method of [11] for the radial equation, we can then solve for the frequency of a QNM and its angular separation constant in the eikonal limit (accurate to terms of order $1/l$). There is not a simple algebraic expression for the frequencies when we use the full Bohr-Sommerfeld condition, however. We can find a simpler expression when we expand the Bohr-Sommerfeld condition (in a Taylor series in terms of the numerically small parameter, $a\omega/l$) to obtain an algebraic expression for the mode's frequency. The frequency calculated through this approximation can be written in the form of Eq. (7.3), and this approximate result agrees well with the frequency computed using the method that includes all powers of $a\omega/l$. We also use a geometric-optics correspondence to relate the conserved quantities of spherical photon orbits to the parameters of a QNM (which, in turn, gives us a second way of computing the frequencies of a QNM).

The expression for the frequency of a QNM, Eq. (7.3), and the geometric-optics correspondence with spherical photon orbits also allows us to develop better intuitive understanding of how the frequency of the QNM behaves as a function of the black-hole's spin parameter a/M. For Schwarzschild black holes, the mode's real frequency is independent of l, because the background is spherically symmetric, and because all spherical photon orbits reside on the same surface (the velocity-of-light circle at $r/M = 3$). Ferrari and Mashhoon's calculation showed that for slowly rotating black holes, the mode's real frequency depends upon the index m, because, for nearly equatorial orbits, the orbits of different inclination angles are influenced by the dragging of inertial frames to slightly different degrees; the orbital frequency of the photon orbit, however, does not differ from its value for a Schwarzschild black hole at leading (zeroth) order in the spin parameter. From our calculations for Kerr black holes of arbitrary spins, we see there are two contributions to the m dependence of a QNM. There still is the frame-dragging effect for slowly rotating black holes, but there is also

the fact that for rapidly rotating black holes, the spherical photon orbits for different inclination angles no longer reside at the same radius. For highly spinning black holes, the orbital frequencies of the spherical photon orbits at various radii can differ significantly, and they form an important contribution to how the QNM's frequency depends upon the index m.

We also use Eq. (7.3) to explain a degeneracy in the QNM spectrum of Kerr black holes of specific spin parameters, in the eikonal limit. This degeneracy extends to small values of l as well (which we show in Fig. 7.1 for three spin parameters), though we are not aware of discussion of this in the existing literature. The degeneracy occurs when the orbital and precession frequencies, $\omega_{\rm orb}$ and $\omega_{\rm prec}$ are rationally related (i.e., $\omega_{\rm orb}/\omega_{\rm prec} = p/q$ for integers p and q) at a specific spin parameter. Then, by substituting this result into Eq. (7.3) one can easily see that modes with multipolar indices l and m become degenerate with those of indices $l' = l + jq$ and $m' = m - jp$ for any non-negative integer j, in the eikonal limit. (Note that in Fig. 7.1, we show an approximate degeneracy for $j = 1$ and for three spin parameters, such that $p/q = 1/4$, $1/6$, and $1/8$, respectively.) For the corresponding geodesics, when their orbital and precession frequencies are rationally related, the photon orbits are closed—a fact that we confirm by numerically comparing the frequencies of closed photon orbits with those of the modes in the eikonal limit. This relationship between closed orbits and degenerate modes evokes the more familiar example of degeneracy in the energy levels of the hydrogen-atom in quantum mechanics and its relationship to the closed classical orbits of the Coulomb potential [34]; as we argue in the concluding remarks, however, it origin is likely quite different.

The remainder of this paper is organized as follows: In Section 7.2, we review wave propagation in the Kerr spacetime in the geometric-optics limit and the Teukolsky formalism for general, small perturbations of Kerr black holes. By relating the two in the eikonal limit, we construct the geometric-optics correspondence that we will use to associate conserved quantities of a geodesic to the frequency and angular separation constant of a solution to the Teukolsky equation. In Section 7.3, we relate the angular separation constant to the QNM frequency and multipolar indices l and m through a Bohr-Sommerfeld quantization condition; when we combine this constraint with the geometric-optics correspondence of Section 7.2 and either the WKB approximation or the assumption of that the geodesics are spherical photon orbits, we have two ways of computing QNM frequencies in the eikonal limit for any spin parameter a and azimuthal index m. We compare our approximate frequencies computed from the different methods with one another and with the exact frequencies computed numerically with Leaver's continued-fraction method [12]. The methods agree to within the errors of the calculation (that scale as $1/l$). In Section 7.4, we discuss our approximate formula for the frequency of the modes, its relation to closed photon orbits, and the relationship between degeneracy in the QNM spectrum and closed photon orbits. Finally, in Section 7.5, we conclude and discuss our results. We use geometrized units in which $G = c = 1$ and the Einstein

Mode Parameters	Geodesic Quantities	Physical Interpretation
$\Re(\omega)$	$\mathcal{E}$	Energy
-$\Im(\omega)$	$\bar{\lambda}$	Lyapunov exponent
m	L_z	Angular momentum about z-axis
$\Re(A_{lm})$	$\mathcal{Q} + L_z^2 \sim L^2$	Total angular momentum ($a = 0$)
$\Im(A_{lm})$	nonzero because $\Im(\omega) \neq 0$	See Section 7.2.2 for further discussion.

Table 7.1: The geometric-optics correspondence between the conserved quantities along geodesics ($\mathcal{E}$, L_z, and $\mathcal{Q}$) and the parameters of a quasinormal mode ($\omega_{\rm R}$, $\omega_{\rm I}$, A_{lm}, l, and m)

summation convention throughout this paper.

7.2 Geometric Optics and Teukolsky's Equations

This section is primarily a review of wave-propagation around Kerr black holes. In the geometric optics limit, perturbations of the Kerr spacetime obey the Hamilton-Jacobi equations for massless particles near rotating black holes. Their orbits are characterized by the three conserved quantities of geodesics in the Kerr spacetime, the specific energy $\mathcal{E}$, the specific angular momentum about the polar axis L_z, and the Carter constant $\mathcal{Q}$. As noted in the Introduction, general perturbations of the Kerr spacetime obey the Teukolsky equation, which, through separation of variables, can be reduced into a joint eigenvalue problem consisting of the radial and angular Teukolsky equations, and the unknown eigenvalues, the complex frequency $\omega = \omega_{\rm R} - i\omega_{\rm I}$ and the separation constant A_{lm}. In the geometric optics limit, where $l \gg 1$, we can relate the conserved quantities $\mathcal{E}$, L_z, and $\mathcal{Q}$ with the eigenvalues ω, and A_{lm} (and the multipolar indices l and m). We call the relationship between geodesic and QNM parameters a geometric-optics correspondence, and it allows us to associate a spherical photon orbit with a QNM. Much of this geometric-optics correspondence was well-understood for Schwarzschild and slowly rotating black holes—$\mathcal{E}$ corresponds to $\omega_{\rm R}$ and m relates to L_z—but we also show that for Kerr black holes that Carter's constant $\mathcal{Q}$ is connected to the sum of the angular separation constant A_{lm} and m^2. In Table 7.1, we summarize the geometric-optics correspondence for the quasinormal modes in the Kerr spacetime that we discuss in detail in the remainder of this section.

7.2.1 Geometric Optics and the Hamilton-Jacobi Equations

In the first portion of this section, we review how localized waves propagate around a Kerr black hole in the geometric-optics limit. An interesting feature of their wave propagation is that in the limit in which the wavelength, λ, is much smaller than the length scale associated with the radius of curvature of the spacetime, R, the wave should obey the covariant wave equation,

$$\nabla^\mu \nabla_\mu u = 0 \tag{7.4}$$

(∇^μ is the covariant-derivative operator of the background Kerr black hole), independent of the spin of the wave. Therefore, the function u can, in principle, be a scalar or tensor of any rank, though we focus scalar functions of a fixed spin weight s. When we draw connections with Teukolsky's equation in the next part, u will represent the Weyl scalars Ψ_0 or Ψ_4 of the Newman-Penrose formalism [35, 36]. A well-known way to simplify Eq. (7.4) is to write the wave function as

$$u(t,\theta,\phi,r) = Ae^{iS(t,\theta,\phi,r)}\,, \tag{7.5}$$

and to expand Eq. (7.4) in a series in the small variable $\lambda/R \ll 1$. In performing this expansion, one finds that terms proportional to $\partial_\mu S$ are larger than those that go as $\partial_\mu\partial_\nu S$ or those that involve the background connection coefficients; consequently at leading order, the wave equation is

$$g^{\mu\nu}\partial_\mu S\partial_\nu S = 0\,. \tag{7.6}$$

Thus, at leading order in $\lambda/R \ll 1$, $S(t,\theta,\phi,r)$ satisfies the Hamilton-Jacobi equation for a massless particle in curved spacetime, and $S(t,\theta,\phi,r)$, therefore, is the Hamilton-Jacobi principal function (see, e.g., [37]). Following an exercise in [37], one can prove that the principal function $S(t,\theta,\phi,r)$ can be separated,

$$S(t,\theta,\phi,r) = S_\theta + L_z\phi + S_r - \mathcal{E}t\,, \tag{7.7}$$

where the functions S_θ and S_r are given by

$$S_r = \int \Delta^{-1}\sqrt{\mathcal{R}}dr\,, \qquad S_\theta = \int \sqrt{\Theta}d\theta\,, \tag{7.8}$$

and where $\mathcal{R}$ and Θ are given by

$$\mathcal{R} = [\mathcal{E}(r^2+a^2) - L_z a]^2 - \Delta[(L_z - a\mathcal{E})^2 + \mathcal{Q}]\,, \tag{7.9}$$

$$\Theta = \mathcal{Q} - \cos^2\theta(L_z^2/\sin^2\theta - a^2\mathcal{E}^2)\,. \tag{7.10}$$

Here $\mathcal{E}$ denotes the particle's specific energy, L_z represents the particle's specific angular momentum along the z axis, and the quantity $\mathcal{Q}$ is used for labeling Carter's constant; we also define $\Delta = r^2 - 2Mr + a^2$.

By substituting the separated principal function into Eq. (7.5), one finds that the wave's complete function is given by

$$u(t,\theta,\phi,r) = Ae^{i(L_z\phi - \mathcal{E}t)}e^{iS_\theta}e^{iS_r}\,. \tag{7.11}$$

Any physical wave packet will contain a narrow range of energies, angular momenta, and Carter's

constants, given by an integral

$$u(t,\theta,\phi,r) = \int A(\mathcal{E},\mathcal{Q},L_z)e^{i(L_z\phi-\mathcal{E}t)}e^{iS_\theta}e^{iS_r}d\mathcal{E}d\mathcal{Q}dL_z\,. \tag{7.12}$$

Because the wavelength is so short, the phase is oscillating extremely quickly, and the integral will be maximized in the vicinity of the coordinate values where the phase is nearly stationary (the extrema of the phase with respect to the conserved quantities). The exercise in [37] shows that this occurs precisely when the localized wave follows the trajectory of a massless particle (a null geodesic)

$$\rho^2\frac{dt}{d\zeta} = \frac{\Sigma^2-2Mar(L_z/\mathcal{E})}{\Delta}\,, \tag{7.13}$$

$$\rho^2\frac{d\phi}{d\zeta} = \frac{2Mar+(\rho^2-2Mr)(L_z/\mathcal{E})(1/\sin^2\theta)}{\Delta}\,, \tag{7.14}$$

$$\rho^2\frac{dr}{d\zeta} = \frac{\sqrt{\mathcal{R}}}{\mathcal{E}}, \qquad \rho^2\frac{d\theta}{d\zeta} = \frac{\sqrt{\Theta}}{\mathcal{E}}\,, \tag{7.15}$$

with the orbital parameters given by $\mathcal{E}$, L_z, and $\mathcal{Q}$ (and where ζ is an affine parameter along null rays and $\Sigma^2 = (r^2+a^2)^2 - a^2\Delta\sin^2\theta$).

Teukolsky's equations represent the propagation of gravitational perturbations on a rotating-black-hole background; therefore, in the eikonal limit the dynamics of a localized, gravitational wave packet should also satisfy the Hamilton-Jacobi equations. To make this correspondence, however, we will need to relate the conserved quantities of the Hamilton-Jacobi function ($\mathcal{E}$, L_z, and $\mathcal{Q}$) to the parameters of the Teukolsky equation (ω, A_{lm}, l, and m) in the eikonal limit. We, therefore, review Teukolsky's equations in the next section, and build the relationship between the two as well.

7.2.2 The Teukolsky Equations

Teukolsky showed in [38] that the master equation for perturbations of the Kerr spacetime can be separated—i.e., one can write the full master function, which for the purposes of comparing to the previous section we will also call $u(t,\theta,\phi,r)$, as

$$u = Ae^{-i\omega t}e^{im\phi}u_\theta u_r\,. \tag{7.16}$$

Here u_θ and u_r are functions of only θ and r, respectively. By comparing Eq. (7.11) and Eq. (7.16), one must have that $L_z = m$ and $\mathcal{E} = \Re(\omega) = \omega_{\rm R}$, so that we can relate the Teukolsky and Hamilton-Jacobi equations. The imaginary part of quasinormal-mode frequency cannot be obtained from comparing the Teukolsky function to the Hamilton-Jacobi function, but it has been argued by, e.g., [39, 29], that the imaginary part of the frequency corresponds to the Lyapunov exponent λ of a bundle of light rays near the spherical photon orbits. To relate Carter's constant, $\mathcal{Q}$, to the other

parameters of a QNM, we will need to look at the angular Teukolsky equation below:

$$\frac{1}{\sin\theta}\frac{d}{d\theta}\left(\sin\theta\frac{du_\theta}{d\theta}\right)+(a^2\omega^2\cos^2\theta-m^2\csc^2\theta+A_{lm})u_\theta \\ -\left(2a\omega s\cos\theta+\frac{2ms\cos\theta}{\sin^2\theta}+s^2\cot^2\theta-s\right)u_\theta \quad = \quad 0\,. \tag{7.17}$$

To bring this into a form that resembles the equation satisfied by the angular Hamilton-Jacobi principal function, we define a variable

$$x=\log\left(2\tan\frac{\theta}{2}\right)\,, \tag{7.18}$$

(with $dx=d\theta/\sin\theta$), whose domain is $-\infty$ to ∞ (rather than 0 to π for θ).

To understand the angular Teukolsky equation in the eikonal limit (large l), we will discuss the scaling of the terms in Eq. (7.17) with l. Specifically, the angular separation constants, A_{lm}, behave at leading order as $l(l+1)$ and the frequency $\omega_{\rm R}$ is proportional to l. Because m can take values between $-l$ and l, we will treat m as if it scales as l. The spin weight of the field, s is always small compared to l in the eikonal limit. As a result, the first set of terms multiplying u_θ in Eq. (7.17) scale as l^2, and the second set of terms on the second line scale as l or s, and are negligible in our leading-order approximation. Expressing the equation in terms of x and taking the leading-order expression in l, the angular Teukolsky equation becomes,

$$\frac{d^2u_\theta}{dx^2}+V^\theta u_\theta=0\,, \tag{7.19}$$

where the potential is defined by

$$V^\theta=a^2\omega^2\cos^2\theta\sin^2\theta-m^2+A_{lm}\sin^2\theta\,. \tag{7.20}$$

The potential V^θ is negative when x goes to $\pm\infty$ (or θ goes to $0,\pi$), and it is subject to the boundary condition $u_\theta\to e^{mx}$ when x goes to $-\infty$ and $u_\theta\to e^{-mx}$ when x goes to ∞; these boundary conditions ensure that the solution remains finite in these limits. The potential also becomes positive for θ around $\pi/2$, which implies that Eq. (7.19) is mathematically equivalent to a one-dimensional, bound-state problem in quantum mechanics. One can then solve this equation approximately using a WKB procedure [11], in which, at leading order, the function u_θ is written as

$$u_\theta=e^{iS_\theta^{(0)}(x)} \tag{7.21}$$

where

$$S_\theta^{(0)}(x)=\int\sqrt{a^2\omega^2\cos^2\theta\sin^2\theta-m^2+A_{lm}\sin^2\theta}dx\,. \tag{7.22}$$

By substituting $dx = d\theta/\sin\theta$ and using elementary trigonometric identities, we find that $S_\theta^{(0)}$ is identical to the Hamilton-Jacobi principal function, S_θ in Eq. (7.8), if we relate Carter's constant and the angular separation constant as shown below:

$$A_{lm} = \mathcal{Q} + m^2 \,. \tag{7.23}$$

To ensure this is a consistent identification, we also compare the radial Teukolsky equation with the radial Hamilton-Jacobi principal function. The Teukolsky radial equation can be written in a compact form, using the tortoise coordinate, defined by $dr_*/dr = (r^2 + a^2)/\Delta$, as was originally shown by Teukolsky [40]. Again, we keep only the leading-order terms in l, in the eikonal limit, in which the radial Teukolsky equation is given by

$$\frac{d^2 u_r}{dr_*^2} + \frac{K^2 - \Delta\lambda_{lm}^0}{(r^2+a^2)^2} u_r = 0 \,, \tag{7.24}$$

where

$$K = -\omega(r^2 + a^2) + am \,, \tag{7.25}$$

$$\lambda_{lm}^0 = A_{lm} + a^2\omega^2 - 2am\omega \,. \tag{7.26}$$

One can again solve for u_r using the WKB approximation at leading order by writing the radial Teukolsky function as

$$u_r = e^{iS_r^{(0)}} \,, \tag{7.27}$$

where the function $S_r^{(0)}$ satisfies

$$S_r^{(0)}(r) = \int \Delta^{-1} \sqrt{K^2 - \Delta\lambda_{lm}^0}\, dr \,. \tag{7.28}$$

When we compare $S_r^{(0)}$ with the radial Hamilton-Jacobi function, S_r of Eq. (7.8) (where Eq. (7.9) lists the explicit form of the function, $\mathcal{R}$), we confirm the relation between Carter's constant and the angular separation constant in Eq. (7.23).

This equation allows us to make a geometric-optics interpretation of the angular eigenvalue, A_{lm}: it is the Carter constant $\mathcal{Q}$ plus L_z^2. For a Schwarzschild black hole ($a/M = 0$), the angular eigenvalue is $A_{lm} = l(l+1) - s(s+1)$, and, consequently, in the eikonal limit, A_{lm} is the total angular momentum; consequently, we can interpret the Carter constant as the square of the planar part of the angular momentum.

For Kerr black holes, the angular separation constant for a QNM contains a small imaginary part, and, consequently, it would be more precise to write the geometric-optics correspondence for

	$M\omega_{\rm R}$	$M\omega_{\rm I}$	$\Re(A_{lm})$	$\Im(A_{lm})$
$l=10, m=10$	3.13816	0.080057	101.411	0.088654
$l=10, m=5$	2.52741	0.083521	101.753	0.12343
$l=10, m=0$	2.09746	0.089044	102.690	0.11126

Table 7.2: Numerical values of A_{lm} and ω for $a/M = 0.8$, computed using Leaver's continued-fraction method. These values allow one to see that numerically $\Im(A_{lm}) \approx a^2\omega_{\rm R}\omega_{\rm I}$.

the real part only (i.e., $\Re(A_{lm}) = \mathcal{Q} + m^2$). This naturally begs the question whether there is a geometric interpretation of its imaginary part, $\Im(A_{lm})$, that cannot be obtained through Hamilton-Jacobi theory (in analogy to ω_I being related the the Lyapunov exponent of a bundle of rays near the spherical photon orbit). Although we do not have a definitive interpretation of $\Im(A_{lm})$, we briefly comment on a few of its features. First, we note (see, e.g., [5]) that a nonvanishing $\Im(A_{lm})$ happens only when $\Im(\omega) \neq 0$; and second, when we compute numerical values of ω and A_{lm} (see those listed in Table 7.2), we find that $\Im(A_{lm})$ is close to the magnitude of $a^2\omega_{\rm R}\omega_{\rm I}$. This may suggest that a nonzero $\Im(A_{lm})$ can be viewed as arising from a combined effect of frame dragging of individual spherical photon orbits and dispersion of a bundle of these neighboring orbits (the time scale of which is set by the Lyapunov exponent).

Despite the ambiguity in the geometric interpretation of the imaginary part of the angular separation constant, the remaining conditions summarized in Table 7.1 are sufficient to allow us to compute the frequency of a QNM and find its corresponding spherical photon orbits in the next section.

7.3 Two Methods to Compute Quasinormal-Mode Frequencies in the Eikonal Limit

In this section, we use the geometric-optics correspondence for large-l QNMs of the previous section to find approximate expressions for $\omega_{\rm R}$, $\omega_{\rm I}$, and A_{lm} and to relate them to the conserved quantities of spherical photon orbits and the orbits themselves. We have two ways of computing the frequencies, which use two different types of approximations that produce comparable results in the eikonal limit. The first method assumes that the conserved quantities of the geodesics are those of spherical photon orbits, and we call this method the geometric correspondence. Assuming a QNM corresponds to a spherical photon orbit is not sufficient to determine the conserved quantities of the orbit that correspond to a given set of QNM indices l and m; one needs one additional condition. A natural condition is a Bohr-Sommerfeld (BS) quantization condition, which we call the angular WKB analysis, and which we describe in detail below. This condition completely determines all three conserved quantities for the spherical photon orbit, and we can then use the geometric-optics correspondence to find the QNM parameters $\omega_{\rm R}$, $\omega_{\rm I}$, and A_{lm}.

Our second method takes a completely different approach. For this approach, we use the leading-order WKB approximation to the radial Teukolsky equation. Once again, to solve for the QNM frequency and angular separation constant, we will need to use the additional angular WKB condition, which relates the angular eigenvalue A_{lm} to a QNM with particular $\omega_{\rm R}$ and multipolar indices l and m. There is no simple analytical expression for the frequency and separation constant from the BS condition (written in all powers of $a\omega/l$), but when we Taylor expand the result to leading (quadratic) order in $a\omega/l$, we find an expression that is nearly as accurate as the full BS condition, but which can be written in an algebraic expression like Eq. (7.3). One can now use the geometric-optics correspondence of the previous section in the other direction to find the three conserved quantities for the spherical photon orbit corresponding to that QNM. We close the section by comparing the results of our methods to each other and to exact, numerical computations of the QNM frequencies performed using Leaver's continued-fraction method. We find the results are consistent to the accuracy of the calculations; in turn, this confirms the different assumptions made in the two methods.

7.3.1 Orbital Equations and the Geometric Correspondence

In the first of our two sets of methods, we will assume that the orbits that correspond to QNMs continue to be spherical photon orbits of Kerr black holes (just as they related to the equivalent spherical photon orbits for Schwarzschild and slowly rotating Kerr black holes). For Kerr black holes, these orbits are parameterized by the two ratios of the conserved geodesic quantities,

$$\mathcal{Q}/\mathcal{E}^2 = -\frac{r^3(r^3-6Mr^2+9M^2r-4a^2M)}{a^2(r-M)^2}\,, \tag{7.29}$$

$$L_z/\mathcal{E} = -\frac{r^3-3Mr^2+a^2r+a^2M}{a(r-M)}\,, \tag{7.30}$$

which are completely determined by the fixed radius, r, of the spherical photon orbit, for a black hole of a fixed mass and spin (see, e.g., [36]). If we were to try to use these two equations to find the conserved geodesic quantities that correspond to a QNM of multipolar indices l and m, then even after using the geometric-optics correspondence $L_z = m$, we have a system of two equations in three unknowns, $\mathcal{Q}$, $\mathcal{E}$, and r. To solve for these three unknowns, we need one additional equation constraining these three variables. We now discuss the method for finding this third equation.

7.3.1.1 The WKB Method and the Angular Teukolsky Equation

The most direct way to obtain this additional constraint among r, $\mathcal{E}$, and $\mathcal{Q}$, is to note that the angular part of the Hamilton-Jacobi principal function, Eq. (7.9) must fit approximately an integral number of half-wavelengths in the region of θ where the integrand in the square root is positive. This condition is equivalent to the well-known Bohr-Sommerfeld quantization condition [32] for the one-dimensional, bound-state problem satisfied by the angular part of the wave equation (or equivalently,

the angular Teukolsky equation).[1] Specifically, when $l \gg 1$, the BS quantization condition requires that an orbit with multipolar indices l and m satisfy

$$\int_{\theta_-}^{\theta_+} \sqrt{\mathcal{Q} - \cos^2\theta (L_z^2/\sin^2\theta - a^2\mathcal{E}^2)}\, d\theta = \left(l - |m| + \frac{1}{2}\right)\pi\,. \tag{7.31}$$

Here θ_+ and θ_- are the two classical turning points in the orbit, and they can be computed by finding the points at which the integrand of Eq. (7.31) vanishes,

$$\mathcal{Q} - \cos^2\theta_\pm (L_z^2/\sin^2\theta_\pm - a^2\mathcal{E}^2) = 0\,. \tag{7.32}$$

By solving Eqs. (7.29)–(7.30) and Eq. (7.31), we can find the orbital parameters $\mathcal{E}$, $\mathcal{Q}$, and r in terms of the multipolar indices l and m. We can then use the geometric-optics correspondence of Table 7.1 to find $\omega_{\rm R}$ and $\Re(A_{lm})$. We did not find a simple analytical expression for these variables, and we present only numerical results in Section 7.3.1.3 and Section 7.4. To help us compute semianalytical expressions for the frequency of a QNM, we will introduce a different condition among the unknown orbital parameters $\mathcal{E}$, $\mathcal{Q}$, and r that can replace the more complicated angular WKB expression, Eq. (7.31).

7.3.1.2 The Taylor-Expanded Bohr-Sommerfeld Condition

The Bohr-Sommerfeld constraint, Eq. (7.31), gives us a way to evaluate $\mathcal{Q}$ in terms of l, m, and $\mathcal{E}$, which is accurate to terms of order $1/l$. Because the BS condition is an integral equation, it is not particularly convenient to solve, and it would be beneficial to have an approximate, but algebraic expression for the frequency of a QNM. With the benefit of hindsight, one can confirm through numerical calculations of exact QNM frequencies performed using Leaver's method that the parameter $a\omega/l$ is numerically a small number for all black hole spins. We can then expand Carter's constant in a series in $a\omega/l$ as

$$\mathcal{Q} = \mathcal{Q}^{(0)} + \mathcal{Q}^{(1)}\,, \tag{7.33}$$

where $\mathcal{Q}^{(0)}$ satisfies the equation

$$\int_{\theta^0_-}^{\theta^0_+} \sqrt{\mathcal{Q}^{(0)} - m^2\cot^2\theta}\, = \pi\left(l - |m| + \frac{1}{2}\right)\,, \tag{7.34}$$

and at leading order, $\theta^0_+, \theta^0_- = \pm \arcsin m/(l + 1/2 - |m|)]$. One can verify that the solution to this equation is the angular eigenvalue of a Schwarzschild black hole minus m^2, $\mathcal{Q}^{(0)} = (l+1/2)^2 - m^2$ (note that we are assuming $l \gg 1$). Now we will compute the lowest-order perturbation in $a\omega/l$,

[1] More details about Bohr-Sommerfeld quantization can be found in [41, 42, 43, 34]. This quantization condition gives the exact result when l approaches infinity in the classical limit.

which turns out to be quadratic in this parameter below:

$$\int_{\theta_-^0}^{\theta_+^0} \frac{\mathcal{Q}^{(1)} + a^2\omega^2\cos^2\theta}{\sqrt{(l+1/2)^2 - m^2/\sin^2\theta}} d\theta = 0\,. \tag{7.35}$$

The integration limits θ_+, θ_- also can be expanded in a series in $a\omega/l$, and the lowest-order terms of this series are given by θ_+^0, θ_-^0. The perturbation in θ_+, θ_- would result in quartic corrections in $a\omega/l$ when we evaluate the integrals of Eqs. (7.35) and (7.34), because the integrand is of order $(a\omega/l)^2$ and the width of the correction in θ_+, θ_- are also of order $(a\omega/l)^2$. As a result, we will not need it here. Evaluating the integral in Eq. (7.35) is straightforward, and we find that Carter's constant at first order can be written as

$$\mathcal{Q} = l(l+1) - m^2 - \frac{a^2\omega^2}{2}\left[1 - \frac{m^2}{l(l+1)}\right]. \tag{7.36}$$

Interestingly, when one uses the geometric-optics correspondence $A_{lm} = \mathcal{Q} + m^2$, the above expression is consistent with the expansion of A_{lm} for small $a\omega$ given in [22], even in the eikonal limit, where $a\omega$ is large. The reason for this fortuitous agreement is that for QNMs of Kerr black hole of any spin, in the eikonal limit, $a\omega/l$ can be verified to be small numerically, and the expansion only involves even powers of this parameter, $(a\omega/l)^2$. Because the coefficients in the expansion of $a\omega$ scale as $1/l^k$ for even powers of $(a\omega)^k$ and $1/l^{k+1}$ for odd powers of $(a\omega)^k$, in the limit of large l, the two series actually are equivalent in this eikonal limit. In principle, one can also expand and solve Eq. (7.9) to higher orders in the parameter $a\omega/l$ and compare with the expansion in $a\omega$ in [22]; we expect that the two series should agree. This would be useful, because it would effectively let one use the small $a\omega$ expansion in the eikonal limit, where the series would, ostensibly, not be valid.

7.3.1.3 The Lyapunov Exponent and the Imaginary Part of the Frequency

The method described in the previous parts allows us to find $\mathcal{E} = \omega_{\rm R}$ and $A_{lm} = m^2 + \mathcal{Q}$ for a QNM of a fixed l and m. The imaginary part of ω, however, is related to the (averaged) Lyapunov exponent through the expression,

$$\omega_{\rm I} = \bar{\lambda}(n + 1/2)\,, \tag{7.37}$$

and it can only be calculated after the spherical photon orbit is found with one of the two methods approximate methods above. To compute the Lyapunov exponent (and then $\omega_{\rm I}$), we use the method noted in [29] for calculating the Lyapunov exponent of polar orbits, and we apply it for modes with arbitrary l and m, in the eikonal limit, as we describe below. The Lyapunov exponent, λ, can be defined by

$$\lambda = \sqrt{\frac{V_r''}{2\dot{t}^2}}\,, \tag{7.38}$$

where, V_r is defined as in [36, 29]:

$$V_r = \rho^{-4}\mathcal{E}^2(r-r_s)^2\left[r^2+2rr_s-\frac{a^2(\mathcal{Q}/\mathcal{E}^2)}{r_s^2}\right]. \tag{7.39}$$

We use r_s to denote the spherical-photon-orbit radius, which can be determined by solving Eqs. (7.29)–(7.30) and Eq. (7.31) or (7.36). For non-equatorial orbits, the averaged Lyapunov exponent is defined by the average

$$\bar{\lambda} = \frac{2}{T}\int_{z^-}^{z^+}\lambda\frac{\dot{t}}{\dot{z}}dz\,, \tag{7.40}$$

where the explicit integral is given by

$$\bar{\lambda} = \frac{2[3r_s^4-a^2(\mathcal{Q}/\mathcal{E}^2)]^{1/2}}{Tr_s}\int_{z^-}^{z^+}\frac{dz}{\sqrt{(\mathcal{Q}/\mathcal{E}^2)(1-z^2)-z^2[L_z^2/\mathcal{E}^2-a^2(1-z^2)]}}\,, \tag{7.41}$$

where $z=\cos\theta$ and T is the period for the given orbit,

$$T = 2\int_{z^-}^{z^+}\frac{\dot{t}}{\dot{z}}dz\,. \tag{7.42}$$

We have now described how to compute both the real part and the imaginary part of the quasinormal-mode's frequency in the eikonal limit, for any multipolar indices l and m. We leave a comparison of numerical results from this approximate methods and from Leaver's continued-fraction method [12] to Section 7.3.3.

7.3.1.4 Numerical Methods for Computing the Frequencies

For all values of m except when $m=0$, we compute the frequency by using the Bohr-Sommerfeld condition to relate Carter's constant to the energy, which, through Eqs. (7.29) and (7.30), determines the radius of the spherical photon orbit. Then, one can directly solve for the energy from Eq. (7.30), using the geometric-optics correspondence that $L_z = m$. This gives the real part of the frequency from the geometric-optics relationship $\mathcal{E}=\omega_R$, and one can then compute the imaginary part from the real part. This procedure does not work when $m=0$, because a polar orbit is completely constrained to be at a specific radius given by a root of the numerator of Eq. (7.30). Consequently, the radius of the photon orbit is already determined, and Eq. (7.29) is already a constraint between Carter's constant and the energy. If one combines this with the Taylor-expanded Bohr-Sommerfeld condition, then the system of equations can be solved for the real part of the frequency,

$$\omega_{\rm R} = \sqrt{\frac{l(l+1)}{a^2/2+F(r)}}\,, \tag{7.43}$$

where we are using $F(r)$ to denote the right-hand side of Eq. (7.29) evaluated at the correct spherical-photon-orbit radius by solving for the correct root of the numerator in Eq. (7.30). This small difference in computing the frequency does not have a large effect on the numerical results, for $m = 0$.

7.3.2 The Radial WKB Method

In the last section, we discussed a method to derive the frequency of a QNM in the eikonal limit, assuming that a QNM corresponded to a spherical photon orbit and using the geometric-optics correspondence in Table 7.1. We presented two variations on this method, which differed only in how they constrained the energy and Carter constant to the multipolar indices l and m of the QNM (to all orders in $a\omega/l$ or to leading order). This gave us two systems of equations, Eqs. (7.29)–(7.30) and either Eq. (7.31) or Eq. (7.36) that we could solve to find r, $\mathcal{E}$, and $\mathcal{Q}$ as a function of l and m (which we could then relate to the frequency and separation constant of the mode). We found the imaginary part of the frequency by solving for the the Lyapunov exponent, Eq. (7.40), after we made the correspondence. Although both approximations can produce numerical solutions for ω for a fixed l and m, neither yielded simple analytical expressions for the modes' frequencies.

In this section, we no longer assume that the corresponding geodesics to a QNM are spherical photon orbits, but we directly evaluate the frequency and separation constant using the radial WKB method with either the full or the Taylor-expanded angular WKB constraints. We can then use the geometric-optics correspondence to confirm that the parameters of the corresponding geodesic are those of a spherical photon orbit (and, in fact, are approximately those found from the two methods of the previous section). When we combine the radial WKB approximation with the Taylor-expanded Bohr-Sommerfeld condition, we obtain a pair of algebraic equations, which can be solved to give the quasinormal mode's frequency in terms of l and m in the eikonal limit. We show that the expression for $\omega_{\rm R}$ has the simple form of Eq. (7.3) in Section 7.4, where we also discuss the degeneracy in the QNM spectrum.

7.3.2.1 A WKB Analysis in Both the Angular and Radial Directions

In this part, we will approximate the joint eigenvalue problem defined by the angular and radial Teukolsky equations, Eqs. (7.19) and (7.24) by using the WKB approximation, in the eikonal limit. The Teukolsky equations for the functions that depend upon θ and r are

$$\frac{d^2u_\theta}{dx^2} + V^\theta(\lambda,\omega,\theta)u_\theta = 0\,, \tag{7.44}$$

$$\frac{d^2u_r}{dr^{*2}} + V^r(\lambda,\omega,r)u_r = 0\,. \tag{7.45}$$

These equations look somewhat similar, but they are subject to different boundary conditions. At the extents of the domain of the angular equation, $x = \pm\infty$, the potential is negative ($V^\theta < 0$)

and at those for the radial equation, $r_* = \pm\infty$, the potential is positive ($V^r > 0$). As a result, the radial Teukolsky equation is analogous to a scattering problem, and the angular Teukolsky equation is similar to a bound-state problem.

In [11], Iyer and Will performed a detailed WKB analysis on an arbitrary potential-barrier scattering problem of the form of the radial equation, and they found an interesting result between the curvature of the potential and the overtone number of the mode:

$$i\frac{V_0^r}{\sqrt{2V_0^{r\prime\prime}}} - \Lambda^r(n_1) - \Omega^r(n_1) = n_1 + \frac{1}{2}\,. \tag{7.46}$$

Here, we let n_1 denote the overtone number, V_0^r be the value of the potential at its maximum, and $V_0^{r\prime\prime}$ stand for the second derivative of the potential with respect to r^*, evaluated at the potential's maximum. The additional terms $\Lambda^r(n_1)$ and $\Omega^r(n_1)$ are two functions of n_1 and of derivatives of V^r (evaluated at the maximum of the potential) that are of a higher order in the WKB expansion than the leading-order analysis of this paper. We will not need these terms in this paper, but interested readers can find the explicit expressions in the first section of [11].

The WKB analysis in [11] cannot be used with the angular Teukolsky equation written in this paper (a bound-state problem), because Eq. (7.46) is derived by expanding the potential around its peak and matching two scattering solutions across this peak. Unlike the radial solution, where the corresponding photon orbit is spherical and stays at the constant value of r at the peak of the potential, for the angular solution, the spherical photon orbits travel over a wide range of θ and are not confined near the minimum of the potential, V^θ, at $\theta_0 = \pi/2$. Consequently, we cannot find an expression analogous to Eq. (7.46), but we can use a Bohr-Sommerfeld quantization condition, Eq. (7.31), for given values of l and m,

$$\int_{\theta_-}^{\theta_+} \sqrt{A_{lm} - \frac{m^2}{\sin^2\theta} + a^2\omega^2\cos^2\theta}\,d\theta = \pi\left(l - |m| + \frac{1}{2}\right)\,, \tag{7.47}$$

to constrain the angular eigenvalue. The limits of the integration are the values of θ where the integrand vanishes,

$$\sin^2\theta_\pm = \frac{1}{2}\left[1 + \frac{A_{lm}}{a^2\omega^2} - \sqrt{\left(1 + \frac{A_{lm}}{a^2\omega^2}\right)^2 - \frac{4m^2}{a^2\omega^2}}\right]\,. \tag{7.48}$$

One can easily verify that Eq. (7.47) holds for a Schwarzschild black hole. Making the substitution $z = \cos\theta$ and directly evaluating the integral when $a = 0$, we find the equation above gives the condition $\pi(\sqrt{A_{lm}} - |m|) \approx \pi(l - |m| + 1/2)$, which is consistent with the angular separation constant for a perturbation of a Schwarzschild black hole, $A_{lm} = l(l+1) - s(s+1)$, in the eikonal limit.

Equations (7.46) and (7.47) define a joint eigenvalue problem for ω and A_{lm} in the lowest order

of the WKB approximation (the accuracy to which we work in this paper). The approach described above could be straightforwardly generalized to arbitrary orders in the WKB approximation if one were to keep the terms in the potentials of Eqs. (7.19) and (7.24) that we dropped in our leading-order calculation; this would let one get more accurate results for QNMs of smaller l.

To compute $\omega = \omega_{\rm R} - i\omega_{\rm I}$, we must solve the radial WKB formula at first order in the expansion. Note that the radial formula has real and imaginary parts, while the angular formula, and its solution for the angular separation constant A_{lm} is real. This occurs because the imaginary part of the radial equation is of next-to-leading order in $l \gg 1$, and we can neglect it when we solve for $\omega_{\rm R}$ at leading order. The maximum of the potential V^r occurs at the real root of

$$r^3\left(1+\frac{2am\omega}{\lambda^0_{lm}}\right) - 3Mr^2 + a^2 r\left(1+\frac{2am\omega - 2m^2}{\lambda^0_{lm}}\right) + a^2 M = 0\,, \tag{7.49}$$

which we denote by r_0, and the WKB analysis further constrains this to be a zero of the potential,

$$V^r_0(\omega_{\rm R}) = 0\,; \tag{7.50}$$

combining these two conditions, we find that

$$\left[\omega_{\rm R}(r_0^2+a^2) - am\right]^2 = \Delta(r_0)(A_{lm} + a^2\omega_{\rm R}^2 - 2am\omega_{\rm R})\,. \tag{7.51}$$

Note that r_0 is a function of $\omega_{\rm R}$ at leading order, and Eqs. (7.47), (7.49), and (7.51) must be solved jointly given some l and m, to find the frequency, $\omega_{\rm R}$. The solution does not have a simple algebraic expression, because it comes from a system of integral equations, but we can find an algebraic expression for the frequency if we expand the Bohr-Sommerfeld condition to quadratic order in the numerically small parameter $a\omega/l$. In the next part of this section, we do precisely this to derive an expression of the form of Eq. (7.3) which, although approximate, agrees well with the full BS condition for Kerr black holes of any spin parameter a.

7.3.2.2 The Radial WKB Method and the Taylor-Expanded Bohr-Sommerfeld Condition

In this section, we will expand the BS condition in a Taylor series in $a\omega/l$; when we solve the eigenvalue problem of the Taylor-expanded BS condition and the radial WKB equation, we derive an approximate algebraic formula for the mode's frequency. We begin by rewriting Eq. (7.36), the expression that relates the angular separation constant to the multipolar indices l and m of the QNM and its frequency (to quadratic order in $a\omega/l$):

$$A_{lm} = l(l+1) - \frac{a^2\omega^2}{2}\left(1 - \frac{m^2}{l(l+1)}\right)\,. \tag{7.52}$$

Although this expression is strictly valid only for the real part, in the eikonal limit, the imaginary part of both the frequency and the angular separation constant are small compared to their real part; consequently, we can use this expression with the radial WKB equations, Eq. (7.24) and Eq. (7.25), and keep only the leading-order result. One can then show that the radial separation constant is given by

$$\lambda^0_{lm} = L^2 + \frac{a^2\omega^2}{2}\left(1 + \frac{m^2}{L^2}\right) - 2am\omega\,, \tag{7.53}$$

where $L = \sqrt{l(l+1)}$. At lowest order in the WKB approximation, the radial Teukolsky equation states that

$$iV_0^r/\sqrt{2V_0^{r\prime\prime}} = n_1 + 1/2\,, \tag{7.54}$$

and, because $\omega_{\rm R}$ is larger than $\omega_{\rm I}$ in the eikonal limit, we can first solve for the real part $\omega_{\rm R}$ by again requiring Eq. (7.50) to hold. When we use the expression for V_0^r in Eq. (7.24), and we note that at lowest order Eq. (7.50) reduces to $K^2 = \Delta\lambda^0_{lm}$, we find that

$$\omega_{\rm R} = \frac{2maMr + \sqrt{4m^2a^2M^2r^2 + (L^2\Delta - m^2a^2)\left[(r^2+a^2)^2 - \frac{a^2}{2}(1+\frac{m^2}{L^2})\right]}}{(r^2+a^2)^2 - \frac{a^2}{2}(1+\frac{m^2}{L^2})}\,. \tag{7.55}$$

This quasinormal-mode frequency must be evaluated at the radius at which the potential, V^r, reaches its maximum (denoted by r_0), which itself depends upon $\omega_{\rm R}$; see Eq. (7.49). We note, therefore, that we have an algebraic system of equations for r_0 and $\omega_{\rm R}$, defined by Eqs. (7.49) and (7.55). To compute the frequencies explicitly, we find it is most convenient to solve the systems of equations numerically (which we do in Section 7.3.3). Note, also, that the frequency can be written in the form

$$\omega_R = Lf\left(\frac{m}{L}\right)\,, \tag{7.56}$$

a fact that we will return to in the next section.

7.3.2.3 Decay Rate from the WKB Approximation

Finally, we describe how to compute the imaginary part of the frequency $\omega_{\rm I}$ in terms of the quantities A_{lm}, r_0, and $\omega_{\rm R}$, for which we have already solved. This can be computed directly from the imaginary part of the radial WKB equation, Eq. (7.46), which gives

$$\omega_{\rm I} = \left(n_1 + \frac{1}{2}\right)\left(\frac{\partial V_0^r}{\partial\omega}\Big|_{\omega_{\rm R}}\right)^{-1}\sqrt{2V_0^{r\prime\prime}(\omega_{\rm R})}\,. \tag{7.57}$$

We now have described how to solve for complex frequency, ω, and the real part of the angular separation constant. We will compare our solutions in the next section.

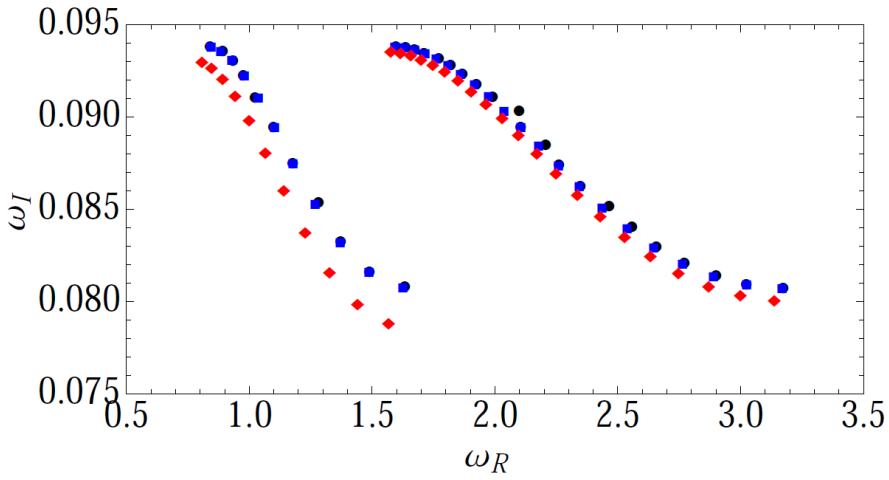

Figure 7.2: Lowest-overtone, quasinormal-mode frequencies from the two methods discussed in Sections 7.3.1 and 7.3.2 using the Taylor-expanded Bohr-Sommerfeld condition, and the frequency computed using Leaver's method. We choose $a/M = 0.8$, we let $l = 5$ or $l = 10$, and we show values of m that range from -l to l for both values of l (m increases from left to right). The group of symbols on the left all correspond to $l = 5$ and those on the right are those for $l = 10$. The black dots are the frequency calculated using the geometric correspondence, and the blue squares are those computed using the radial WKB method. The red diamonds are the exact frequencies found Leaver's continued-fraction method. The relative accuracy (compared to Leaver's method) for $l = 10$ is within 1%. The $l = 10$ calculations are more accurate than those for $l = 5$, which one would expect from approximations in the eikonal limit.

7.3.3 Numerical Results and Comparisons

In this part, we will describe the numerical calculations done with the two methods described in Sections 7.3.1 and 7.3.2. We show the results in Fig. 7.2, in which we plot the lowest-overtone, QNM frequencies for $l = 5$ and $l = 10$ and for all valid values of m from $-l$ to l (m is increasing from left to right in the figure). In the figure, the black circles are the results for the geometric correspondence of Section 7.3.1, while the blue (lighter) diamonds are those for the radial WKB (Section 7.3.2); both methods use the Taylor-expanded BS condition of Eq. (7.36). We do not show the results for the full (non-expanded) BS condition, because they are indistinguishable from the points shown in Fig. 7.2. We also include the numerical mode frequencies generated by Leaver's method [12] for comparison. Interestingly, both methods generate good estimates for the modes' frequencies for $l = 10$, even though l is not very large.

Finally, we show in Fig. 7.3 the frequencies calculated using the radial WKB method with the Taylor-expanded BS condition and those from Leaver's method, as a function of l. Specifically, we compare the $m = 0$ and $m = \pm l$ for $l = 4$ to $l = 15$, and we find that the differences between the radial WKB method of this paper and Leaver's method scale as $1/l$, which is consistent with the errors for our calculation in the eikonal limit. We have also numerically investigated the convergence for other values of l, and this statement seems to be quite general.

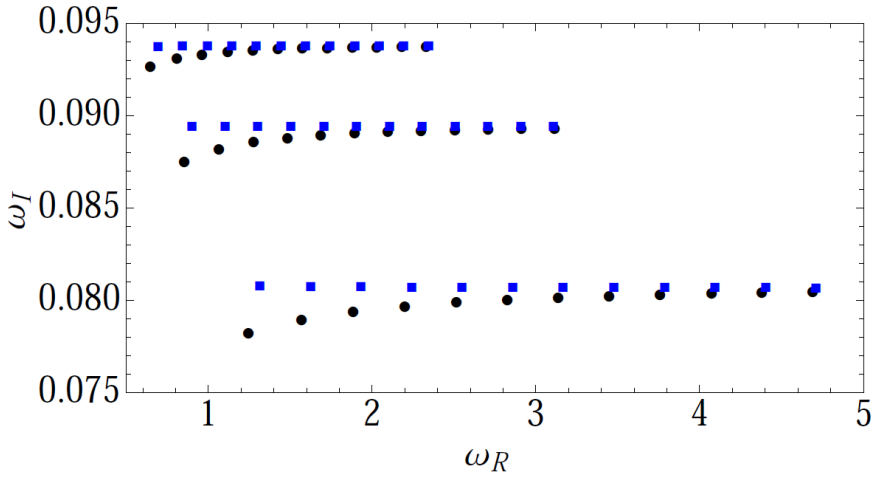

Figure 7.3: A plot comparing the frequencies computed using the radial WKB method and Leaver's method for l from 4 to 15. We focus here on frequencies with $m = \pm l$ and $m = 0$. The black dots are the frequencies calculated numerically using Leaver's method, and the blue squares are the frequencies computed using the radial WKB method of this paper.

7.4 Degenerate Quasinormal Modes and Closed, Spherical Photon Orbits

Our chief purpose in this section is to explore the approximate frequency formula, Eq. (7.55) in greater detail. Specifically, we will show that an equation of the form of Eq. (7.3) can be derived from Eq. (7.55) and that this equation has the same physical interpretation (i.e., the two frequencies are approximately the orbital and precessional frequencies of the corresponding spherical photon orbits). Next, we describe a natural consequence of the frequency formula that was discussed in the introductory section. When the precessional and orbital frequencies are rationally related, then there will be a countable sequence of modes whose frequencies are equivalent (i.e., degenerate); furthermore, the spherical photon orbits corresponding to these modes must be closed.

7.4.1 An Expansion of the Mode's Frequency

Because the expression for $\omega_{\rm R}$ in Eq. (7.55) can be written as $L\, f(m/L)$, we can define two frequencies, Ω_1 and Ω_2, by defining

$$\Omega_1 \equiv \frac{\partial \omega_{\rm R}}{\partial L} = f\left(\frac{m}{L}\right) - \frac{m}{L} f'\left(\frac{m}{L}\right) \tag{7.58}$$

$$\Omega_2 \equiv \frac{\partial \omega_{\rm R}}{\partial m} = f'\left(\frac{m}{L}\right), \tag{7.59}$$

where a prime denotes a derivative with respect to m/L. We cannot find a simple analytical expression for these frequencies, because the function $f\,(m/L)$ contains the radius of the potential barrier's extrema, $r_0(m/L)$, for which we do not have an analytical expression; however it is easy to compute

Ω_1 and Ω_2 numerically. Regardless, a straightforward computation shows that $\omega_{\rm R}$ can be written as a linear combination of the two frequencies Ω_1 and Ω_2:

$$\omega_{\rm R} = L\,\Omega_1 + m\,\Omega_2\,. \tag{7.60}$$

We can understand the physical meaning of Ω_1 and Ω_2 by computing their leading-order expressions in a, so that we can interpret their meaning when $a/M \ll 1$. A short calculation shows that

$$\Omega_1 \approx \frac{1}{\sqrt{27}M} = \sqrt{\frac{M}{r_0^3}}\,, \tag{7.61}$$

$$\Omega_2 \approx \frac{2a}{27M^2} = \frac{2S}{r_0^3}\,, \tag{7.62}$$

where r_0 is the circular photon orbit radius for a Schwarzschild black hole, $r_0/M = 3$ and $S/M = a$. The expression for Ω_1 is the Keplerian frequency of the spherical photon orbit, and $2S/r_0^3$ is the well-known Lense-Thirring precessional frequency; thus, our formula recovers Ferrari and Mashhoon's result [9] in the slow rotation limit.

We briefly note that there are terms linear in a/M in the expansion for Ω_1 (that we neglected at leading order), which come from expanding Eq. (7.58) and from the fact that the corresponding spherical-photon-orbit radii change linearly in a/M (see Fig. 7.4). One can also understand this latter fact, because the prograde and retrograde equatorial, circular orbits have radii, r_1 and r_2, respectively, given by

$$r_1 = 2M\left\{1+\cos\left[\frac{2}{3}\arccos\left(-\frac{|a|}{M}\right)\right]\right\}\,, \tag{7.63}$$

$$r_2 = 2M\left\{1+\cos\left[\frac{2}{3}\arccos\left(\frac{|a|}{M}\right)\right]\right\}\,, \tag{7.64}$$

which when expanded depends linearly on a/M. Thus, we see that the black holes's spin has two effects on the mode's frequency: it changes it from precessional effects and from the change in the orbital frequency of the spherical-photon orbits at different radii.

It seems natural to guess, therefore, that Ω_1 is still the orbital frequency of the corresponding photon orbit and Ω_2 is the precession frequency of that orbit—even for black holes with dimensionless spins close to unity. Being more precise, we will call the orbital frequency, $\omega_{\rm orb}$, the angular frequency corresponding to one period of the motion along the θ direction,

$$\omega_{\rm orb} = \frac{2\pi}{T}\,, \tag{7.65}$$

where T is given in Eq. (7.42). The precession frequency, $\omega_{\rm prec}$, we will define by the change in

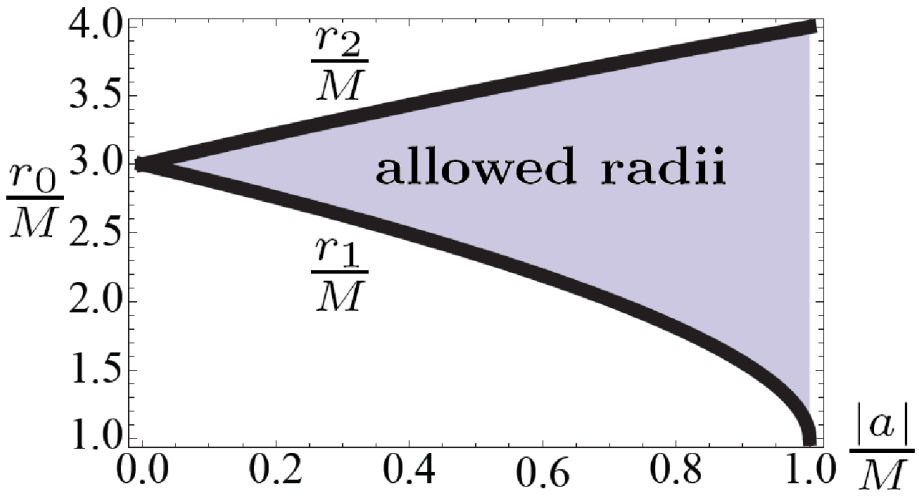

Figure 7.4: The range of spherical-photon-orbit radii as a function of the spin parameter, a/M. The lower curve represents the radii of corotating orbits (the corresponding modes have $m = l$), and the upper curve shows the radii of counterrotating orbits (the corresponding modes have $m = -l$). Between the two lines are the remaining orbits, and the corresponding modes have monotonically decreasing m as one moves to greater radii (for a fixed spin a).

azimuthal angle minus 2π, $\Delta\phi$, divided by the orbital period T, which can be conveniently written as

$$\omega_{\rm prec} = \frac{\Delta\phi}{2\pi}\omega_{\rm orb}\,. \tag{7.66}$$

Interestingly, E. Teo obtained a compact expression for $\Delta\phi$ in [44] in terms of elliptic integrals:

$$\Delta\phi = \frac{4}{\sqrt{z_+ - z_-}}\left[\frac{2Mr - aL_z/\mathcal{E}}{\Delta}K\left(\sqrt{\frac{z_+}{z_+ - z_-}}\right) + \frac{L_z}{\mathcal{E}a}\frac{1}{1-z_+}\Pi\left(-\frac{z_+}{1-z_+}, \sqrt{\frac{z_+}{z_+ - z_-}}\right)\right]. \tag{7.67}$$

Here we call $z = \cos\theta$, and z_+ and z_- are $\cos\theta_+$ and $\cos\theta_-$, where $\theta_\pm$ were written below Eq. (7.31); the functions $K(x)$ and $\Pi(\nu, x)$ are the complete elliptic integrals of the first and third kinds, respectively. Although we cannot definitively show that the frequencies Ω_1 and Ω_2 correspond to orbital and precessional frequencies for black holes of arbitrary spins, we will argue for its plausibility below, and we will show in the next part that for certain arbitrary values and orbits that the correspondence is quite precise.

Thus, we now give a heuristic argument that Ω_1 is the orbital frequency and Ω_2 is the precession frequency using reasoning based on geometric optics. The Hamilton-Jacobi principal function (i.e., the phase of the mode), $L_z\phi(t) - \mathcal{E}t + S_\theta + S_r$, should be stationary; however, after one period of motion in the θ direction, T, Eq. (7.31) requires that phase now be given by

$$m\Delta\phi - (L\Omega_1 + m\Omega_2)T + 2\pi(L - |m|) = 2n\pi\,, \tag{7.68}$$

where n is an integer, and where we have also substituted Eq. (7.60) for $\omega_{\rm R}$. For this to be stationary, the coefficients of the L and m terms must be a multiple of 2π, and one finds that

$$\Omega_1 = \omega_{\rm orb} = \frac{2\pi}{T}\,, \tag{7.69}$$

$$\Omega_2 = \omega_{\rm prec} = \frac{\Delta\phi}{T}\,, \tag{7.70}$$

in the eikonal limit. We, therefore, argue that the real part of the quasinormal-mode frequency given by Eq. (7.60) is equivalent to Eq. (7.3); i.e.,

$$\omega_{\rm R} = L\Omega_1 + m\Omega_2 = L\omega_{\rm orb} + m\omega_{\rm prec}\,. \tag{7.71}$$

We will confirm this heuristic argument in the next part.

7.4.2 Numerical Comparison of Precessional and Orbital Frequencies

To test the idea that the frequencies Ω_1 and Ω_2 correspond to the orbital and precessional frequencies of the unstable photon orbits ($\omega_{\rm orb}$ and $\omega_{\rm prec}$, respectively), we numerically solve the geodesic equation to find $\omega_{\rm orb}$ and $\omega_{\rm prec}$ from the geodesics (the geodesics are plotted in the next section). We solve the second-order geodesic equation,

$$\frac{d^2x^\mu}{d\zeta^2} + \Gamma^\mu{}_{\alpha\beta}\frac{dx^\alpha}{d\zeta}\frac{dx^\beta}{d\zeta} = 0\,, \tag{7.72}$$

(ζ is an affine parameter along the null rays, x^μ are the Boyer-Lindquist coordinates $\{t, r, \theta, \phi\}$, and $\Gamma^\mu{}_{\alpha\beta}$ are Christoffel symbols) rather than the first-order system Eqs. (7.13)–(7.15), because the θ component of the geodesic's tangent vector, $d\theta/d\zeta$, goes to zero at $\theta_\pm$ (the maximum and minimum values of θ for non-polar, non-equatorial orbits). For the first-order system, the numerical solution stalls around these points, but when using the second-order system, however, the differential equations take into account the θ part of the geodesic's curvature, $d^2\theta/d\zeta^2$, and the numerical solution proceeds smoothly.

To find photon orbits for a given value of m/L and a, we use the Taylor-expanded Bohr-Sommerfeld condition, Eq. (7.36), in addition to the conserved quantities of the geodesic, Eqs. (7.29) and (7.30), to compute the radius of the orbit; we can then directly compute the parameters of the spherical photon orbit. Similarly, from this radius, we can use Eqs. (7.58) and (7.59) to find the frequencies Ω_1 and Ω_2. For concrete examples, we choose the spin parameters to be $a/M = 0.502$, 0.612, and 0.768 (the reason for these values will be explained in the next section), for which the unstable photon radii are $r/M = 2.592$, 2.459, and 2.222, respectively. We can then choose the remaining initial values of the coordinates at $\zeta = 0$ to be $t = 0$, $\theta = 0$, and $\phi = \pi/2$ and use Eqs. (7.13)–(7.15) to find the initial tangents to the geodesics (where we must also use Eqs.

a/M	r_0/M	m/L	$M\Omega_1$	$M\Omega_2$	$M\omega_{\rm orb}$	$M\omega_{\rm prec}$
0.502	2.592	0.5	0.19358	0.04849	0.19354	0.04837
0.612	2.459	0.5	0.19390	0.06520	0.19379	0.06465
0.768	2.222	0.5	0.19355	0.09974	0.19330	0.09666

Table 7.3: For photon orbits at $r/M = 2.221$, 2.459, and 2.592 with $m/L = 0.5$ and for black holes with spins $a/M = 0.767$, 0.611, 0.502, respectively, we show that the expansion of the real part of the quasinormal-mode frequencies, $\omega_{\rm R} = L\Omega_1 + m\Omega_2$, do lend themselves to the interpretation that Ω_1 is the θ-orbital frequency, $\omega_{\rm orb}$, and Ω_2 is the precessional frequency, $\omega_{\rm prec}$. The frequencies agree to within one percent.

(7.29) and (7.30) to find the values of $\mathcal{Q}/\mathcal{E}^2$ and $L_z/\mathcal{E}$).

Because the null geodesics are unstable spherical orbits, even though the initial conditions specify solutions that should reside exactly on this sphere, numerical error causes the solutions to eventually move away from the photon spheres. When the time scale of this error is larger than the period T, we can compute the periods accurately despite this potential issue. We also compare these periods with the periods found by holding the radii at precisely the photon spheres (to avoid the issue of numerical error discussed above). The two methods agree well. We compute the orbital frequencies as the inverse of the Boyer-Lindquist time, t, it takes for the geodesics to pass through the equatorial plane in the direction of decreasing θ. We similarly keep track of the angles in ϕ that the geodesics traverse during this time.

We summarize the results of these calculations in Table 7.3. We find that for the spins shown here, the values of Ω_1 agree with the orbital frequencies of the geodesics, $\omega_{\rm orb}$, to within fractions of a percent. The agreement of values of Ω_2 to the precession frequencies $\omega_{\rm prec}$ are comparable. Consequently, we have further evidence that Eq. (7.71) holds true.

7.4.3 Degeneracy in the Spectrum of Kerr Black Holes

With the decomposition of the real part of the quasinormal-mode frequency in Eq. (7.71), we are able to connect the θ-orbital frequencies and the ϕ-precession frequencies of unstable photon orbits to the corresponding decomposition of the quasinormal-mode frequencies. This relationship is particularly interesting when, for specific values of m/L and spin parameters, a, the frequencies have a ratio $\omega_{\rm orb}/\omega_{\rm prec} = p/q$ for integers p and q. In terms of the unstable null geodesics, the orbits must close, because after every p cycles of latitudinal motion the particle also completes exactly q cycles of azimuthal motion. In terms of the algebraic expression for the modes, Eq. (7.3), the real part of the mode frequency for a given l and m becomes degenerate with the real part of a mode frequency with $l' = l + kq$ and $m' = m - kp$ for any non-negative integer k. Thus, one can relate degeneracies in the spectrum of quasinormal modes of a Kerr black hole with closed photon orbits.

First we discuss how, given a quasinormal mode with multipolar indices, l and m, and a rational number, p/q, we can find the black-hole spin parameter, a, at which the ratio of the orbital and

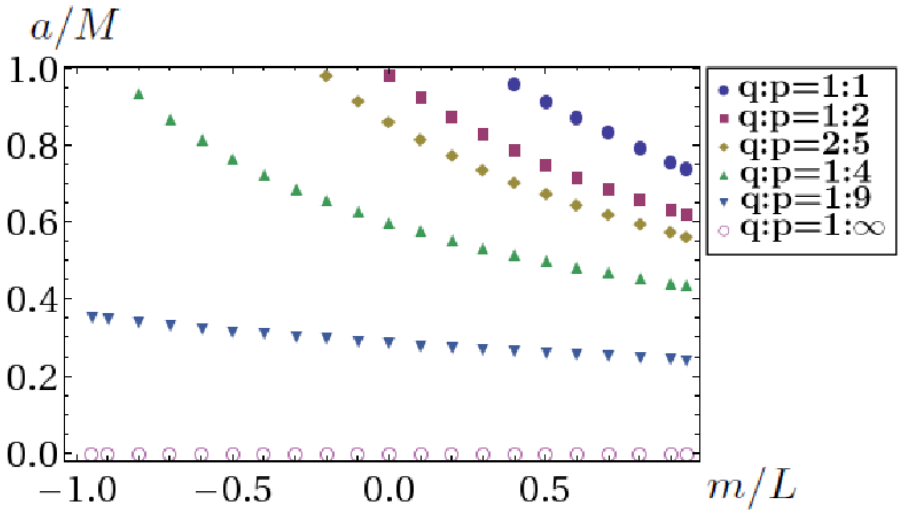

Figure 7.5: A diagram showing the spin parameters, a, and the ratios of the multipolar indices, m/L, at which the orbital and precessional frequencies have a ratio of p/q. Although we only show the points at which we performed our numerical calculations, in the eikonal limit, each set of points for a given ratio of p/q approaches a continuous curve.

precessional frequencies of the quasinormal mode are p/q. We do this by solving the relationship

$$q\Omega_1\left(a, \frac{m}{L}, r_0\right) = p\Omega_2\left(a, \frac{m}{L}, r_0\right) \tag{7.73}$$

(i.e., the statement that $\Delta\phi = 2q\pi/p$) for a, once we constrain the radius of the spherical photon orbit, r_0, to correspond to that of a mode with with multipolar indices l and m. Thus, we use the Taylor-expanded Bohr-Sommerfeld condition, Eq. (7.36), and the conserved quantities of the geodesic, Eqs. (7.29) and (7.30) to calculate the radius of the orbit as a function of the unknown parameter a. We can solve this system of equations numerically, which we do for a range of multipolar indices m and l (in the eikonal limit, where m/L approaches a continuum rather than discrete values), and for several values of p/q. We plot the results of this calculation in what we call the mode-degeneracy diagram in Fig. 7.5.

To understand the physical content of Fig. 7.5, it is helpful to describe the physics in terms of the corresponding closed spherical photon orbits and to keep in mind the position of the radius of the photon orbit in Fig. 7.4. When the black hole is not spinning, $a = 0$, there should be no precession, and the ratio of the precessional to orbital frequencies is $q/p = 0$; moreover, orbits with any value of m/L are closed, because they all form great circles of different inclinations on the light ring $r/M = 3$. For a fixed non-zero ratio of q/p, orbits with negative m/L (retrograde orbits) are closed at larger spins than prograde orbits (positive m/L). This, too, is reasonable, because the radius of the orbit is monotonically decreasing from negative to positive m/L, and, based on the intuition from the small spin limit in Eq. (7.62), the ratio of the orbital to precessional frequencies

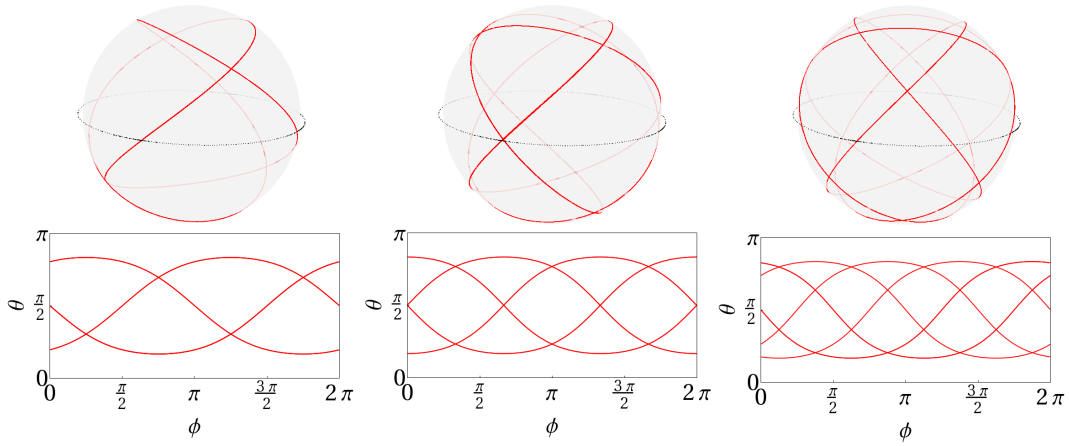

Figure 7.6: For black holes with spins $a/M = 0.768$, 0.612, and 0.502, we show an unstable null geodesic with $\omega_{\rm orb} = 2\omega_{\rm prec}$ on the left, $\omega_{\rm orb} = 3\omega_{\rm prec}$ in the center, and $\omega_{\rm orb} = 4\omega_{\rm prec}$ on the right, respectively. These orbits correspond with quasinormal modes in the eikonal limit with $m/L = 0.5$. The top figures show the photon orbit (the red, solid curve) on its photon sphere (represented by a transparent sphere). The dashed black line is the equatorial $\theta = \pi/2$ plane, which was inserted for reference. The bottom figures are the same photon orbits, but plotted in the ϕ-θ plane, instead.

is an increasing function of radius and inversely proportional to spin; hence, to have the same ratio for decreasing m/L, one must have an increasing black-hole spin. Thus, it is reasonable that the curves of fixed p/q form monotonically decreasing curves when plotted in the (m/L)-a plane.

We close this section by showing closed photon orbits with $m/L = 0.5$ for black holes of spins $a/M = 0.768$, 0.612, and 0.502 in Fig. 7.6 (going from left to right). The top panels show the trajectories of the geodesics on their photon spheres (with the equatorial plane highlighted by a dashed circle), and the bottom panels depict the same trajectories in the ϕ-θ plane. We calculate these geodesics as described in Section 7.4.1. The spins predicted from Fig. 7.5, $a/M = 0.758$, 0.609, and 0.501, agree with the spins that give closed orbits quoted above to about one percent.

7.5 Conclusions and Discussion

This paper describes the correspondence between the motion of massless scalar particles in the Kerr spacetime and the quasinormal modes of this black hole in the eikonal limit ($l \gg 1$). The massless, scalar particles obey the Hamilton-Jacobi equations, which, are very similar to the Teukolsky equations when $l \gg 1$. By identifying terms in the Hamilton-Jacobi equations and Teukolsky equations, we can relate the conserved quantities of the Hamilton-Jacobi equations to the eigenvalues of the separated Teukolsky equations in a geometric-optics correspondence. Specifically, we found that the real part of the angular eigenvalue is related to the sum of Carter's constant and the square of the angular momentum along the symmetry axis, and we confirmed that the energy corresponds to the real part of the mode's frequency and the Lyapunov exponent of the orbit relates to the imaginary-part of the frequency. We found that the imaginary part of the angular eigenvalue is very small and

non-zero because the imaginary part of the frequency is nonzero; the geometric interpretation of the imaginary part of the angular constant remains an open question, however.

Combining the geometric-optics correspondence and a WKB analysis, we developed several ways to calculate the quasinormal mode's frequency in the eikonal limit. We obtained a semianalytical formula for the frequency, which is a good approximation as long as $l \gg 1$, but for any Kerr spin parameter, a. With this formula, we showed that the modes' frequencies in the eikonal limit are a linear combination of the orbital and precession frequencies of the corresponding spherical photon orbits. We found that when the orbital and precessional frequencies are rationally related—i.e., when the spherical photon orbits are closed—then the corresponding quasinormal mode frequencies are also degenerate.

We hope that the approximate expressions for the quasinormal modes' frequencies in this paper will prove helpful for understanding wave propagation in the Kerr spacetime. The is not unreasonable to suppose, because Dolan, Ottewill, and Wardell have shown in [30, 28, 45] that to analytically calculate the Green's function in the Schwarzschild spacetime, one needs to know analytical expressions for the frequency of the quasinormal modes (specifically, this comes from the fact that the frequencies of the quasinormal mode enter as poles of the Green's function in the frequency domain). We, therefore, think that our approximate formulas could assist with the calculation of the Green's function in the Kerr spacetime, in future work.

Finally, we close this paper by discussing the relationship between degenerate modes and closed orbits in greater detail. This relationship brings to mind the more well-known relationship between closed classical orbits of a particle in a Coulomb potential and the degenerate quantum energy levels of the hydrogen atom. In a more mathematical language, the degeneracy could be understood from the fact that the hydrogen atom has an $O(4)$ symmetry group, because there is an additional vector (the quantum analog of the classical Laplace-Runge-Lenz vector) that commutes with the Hamiltonian (see, e.g., the review [46] or more recent work in [47]). Aside from the obvious differences between the classical perturbations of the Kerr spacetime and the quantum mechanics of the hydrogen atom—the quasinormal modes are decaying oscillations in time, but the energy levels of a hydrogen atom are time-independent eigenstates—there are some intriguing similarities: both have nontrivial symmetries corresponding to conserved quantities for test-particle orbits (from a Noetherian perspective, the $O(4)$ symmetry gives rise to a conserved Laplace-Runge-Lenz vector for the hydrogen atom, and a Killing tensor generates Carter's constant for the Kerr spacetime), both involve second-order eigenvalue problems, and both have degeneracies in their spectra.

Nevertheless, there is a somewhat different fundamental character about the degeneracy in the quasinormal-mode spectrum of black holes and that of the hydrogen atom. In the absence of fine structure, the energy levels of hydrogen depend upon only a single quantum number n, which is one greater than the number of nodes in the wavefunction, and each level has a degeneracy of

$(l+1)^2$. The fact that it is enhanced over the $(2l+1)$-fold degeneracy that one would expect of a spherically symmetric system with a multipolar index l is precisely related to the existence of the additional quantity that commutes with the Hamiltonian (i.e., the Laplace-Runge-Lenz vector in the classical problem). For a Schwarzschild black hole, there is an exact $(2l+1)$-fold degeneracy in the quasinormal-mode spectrum for all l (from the spherical symmetry of the background); there are no additional symmetries that enhance the degeneracy, however. For a Kerr black hole, one would naively expect that there is no degeneracy (because the spacetime is axisymmetric), but we showed that in the eikonal limit, $l \gg 1$, for a Kerr black hole of a given spin, there are a countable number of distinct sequences of modes that are degenerate (each sequence corresponding to when the orbital and precessional frequencies form a different ratio). Because the degeneracy is only precise in the eikonal limit, it seems less likely that it is related to a symmetry of the Kerr spacetime (e.g., the Killing tensor and Carter's constant), and more likely related to the properties of the spherical photon orbits in Kerr (i.e., there are a continuum of photon orbits with precessional and orbital frequencies that take on a real-valued, compact range of frequencies; there will be a dense subset of frequencies where the orbital and precessional frequencies are rationally related and the orbits are closed). While the outlook for finding whether there exists a deeper connection between the QNM degeneracy and the closed orbits of Kerr black holes looks somewhat pessimistic, this, nevertheless, remains an open question.

Bibliography

[1] C. V. Vishveshwara, Nature **227**, 936 (1970).

[2] K. D. Kokkotas and B. Schmidt, Living Rev. Relativity **2**, 2 (1999).

[3] H.-P. Nollert, Classical Quantum Gravity **16**, R159, (1999).

[4] V. Ferrari and L. Gualtieri, Gen. Relativ. Gravit. **40**, 945 (2008).

[5] E. Berti, V. Cardoso, A. O. Starinets, Classical Quantum Gravity **26**, 163001 (2009).

[6] R. A. Konoplya and A. Zhidenko, Rev. Mod. Phys. **83**, 793 (2011).

[7] M. Davis, R. Ruffini, W. H. Press, and R. H. Price, Phys. Rev. Lett. **27**, 1466 (1971).

[8] S. Chandrasekhar and S. Detweiler, Proc. R. Soc. Lond. A **344**, 441 (1975).

[9] V. Ferrari and B. Mashhoon, Phys. Rev. D **30**, 295 (1984).

[10] B. F. Schutz and C. M. Will, Astrophys. J. **291**, L33 (1985).

[11] S. Iyer and C. M. Will, Phys. Rev. D **35**, 3621 (1987).

[12] E. W. Leaver, Proc. R. Soc. Lond. A **402**, 285 (1985).

[13] H.-P. Nollert, Phys. Rev. D **47**, 5253 (1993).

[14] E. W. Leaver, Phys. Rev. D **34**, 384 (1986).

[15] Y. Sun and R. H. Price, Phys. Rev. D **38** 1040 (1988).

[16] http://www.ligo.caltech.edu/

[17] http://www.ego-gw.it/public/virgo/virgo.aspx

[18] F. Echeverria, Phys. Rev. D **40**, 3194 (1989).

[19] E. E. Flanagan and S. A. Hughes, Phys. Rev. D **57**, 4566 (1998).

[20] A. Buonanno, G. B. Cook, and F. Pretorius, Phys. Rev. D **75**, 124018 (2007).

[21] E. Berti, V. Cardoso, J. A. Gonzalez, U. Sperhake, M. Hannam, S. Husa, and B. Brügmann, Phys. Rev. D **76**, 064034 (2007).

[22] E. Berti, V. Cardoso, and M. Casals, Phys. Rev. D **73**,024013, (2006).

[23] O. Dreyer, B. Kelly, B. Krishnan, L. S. Finn, D. Garrison, and R. Lopez-Aleman, Classical Quantum Gravity **21**, 787 (2004).

[24] E. Berti, V. Cardoso, and C. M. Will, Phys. Rev. D **73**, 064030 (2006).

[25] J. M. Maldacena, Adv. Theor. Math. Phys. **2**, 231 (1998).

[26] A. Zimmerman and Y. Chen, Phys. Rev. D **84**, 084012 (2011).

[27] Y. Mino and J. Brink, Phys. Rev. D **78**, 124015 (2008).

[28] S. R. Dolan and A. C. Ottewill, Classical Quantum Gravity **26**, 225003 (2009).

[29] S. R. Dolan, Phys. Rev. D **82**, 104003 (2010).

[30] S. R. Dolan and A. C. Ottewill, Phys. Rev. D **84**, 104002 (2011).

[31] V. Cardoso, A. S. Miransa, E. Berti, H. Witek, and V. T. Zanchin, Phys. Rev. D **79**, 064016 (2009).

[32] K. D. Kokkotas, Classical Quantum Gravity **8**, 2217 (1991).

[33] E. Seidel and S. Iyer, Phys. Rev. D **41**, 374 (1990).

[34] R. Shankar *Principals of Quantum Mechanics*, (Plenum Press, New York, 1980).

[35] E. Newman and R. Penrose, J. Math. Phys. **3**, 566 (1962).

[36] S. Chandrasekhar, *The Mathematical Theory of Black Holes* (Oxford University Press, Oxford, 1983).

[37] C. W. Misner, K. S. Thorne and J. A. Wheeler *Gravitation*, (W. H. Freeman, New York, 1973).

[38] S. A. Teukolsky, Phys. Rev. Lett. **29**, 1114 (1972).

[39] B. Mashhoon, Phys. Rev. D **31**, 290 (1985).

[40] S. A. Teukolsky, Astrophys. J. **185**, 635 (1973).

[41] C. M. Bender and S. A. Orszag, *Advanced Mathematical Methods for Scientists and Engineers* (McGraw Hill, New York, 1978).

[42] J. L. Dunheim, Phys. Rev. **41**, 713 (1932).

[43] J. W. Guinn, C. M. Will, Y. Kojima, and B. F. Schutz, Classical Quantum Gravity **7**, L47 (1990).

[44] E. Teo, Gen. Relativ. and Gravit. **35**, 1909 (2003).

[45] B. Wardell, arXiv:0812.3853, (2008).

[46] M. Bander and C. Itzykson, Rev. Mod. Phys. **38**, 330 (1966).

[47] Z.-B. Wu and J.-Y. Zeng, Phys. Rev. A **62**, 032509 (2000).

Part III

Visualizing Spacetime Curvature with Frame-Drag Vortexes and Tidal Tendexes

Chapter 8

Frame-Dragging Vortexes and Tidal Tendexes Attached to Colliding Black Holes: Visualizing the Curvature of Spacetime

When one splits spacetime into space plus time, the spacetime curvature (Weyl tensor) gets split into an "electric" part $\mathcal{E}_{jk}$ that describes tidal gravity and a "magnetic" part $\mathcal{B}_{jk}$ that describes differential dragging of inertial frames. We introduce tools for visualizing $\mathcal{B}_{jk}$ (frame-drag vortex lines, their vorticity, and vortexes) and $\mathcal{E}_{jk}$ (tidal tendex lines, their tendicity, and tendexes), and also visualizations of a black-hole horizon's (scalar) vorticity and tendicity. We use these tools to elucidate the nonlinear dynamics of curved spacetime in merging black-hole binaries.

Originally published as R. Owen, J. Brink, Y. Chen, J. D. Kaplan, G. Lovelace, K. D. Matthews, D. A. Nichols, M. A. Scheel, F. Zhang, A. Zimmerman, and K. S. Thorne, Phys. Rev. Lett. **106**, 151101 (2011).

8.1 Introduction

When one foliates spacetime with spacelike hypersurfaces, the Weyl curvature tensor $C_{\alpha\beta\gamma\delta}$ (same as the Riemann tensor in vacuum) splits into "electric" and "magnetic" parts $\mathcal{E}_{jk} = C_{\hat{0}j\hat{0}k}$ and $\mathcal{B}_{jk} = \frac{1}{2}\epsilon_{jpq}C^{pq}{}_{k\hat{0}}$ (see e.g., [1] and references therein); both $\mathcal{E}_{jk}$ and $\mathcal{B}_{jk}$ are spatial, symmetric, and trace-free. Here the indices are in the reference frame of "orthogonal observers" who move orthogonal to the space slices; $\hat{0}$ is their time component, ϵ_{jpq} is their spatial Levi-Civita tensor, and throughout we use units with $c = G = 1$.

Because two orthogonal observers separated by a tiny spatial vector $\boldsymbol{\xi}$ experience a relative tidal acceleration $\Delta a_j = -\mathcal{E}_{jk}\xi^k$, $\mathcal{E}_{jk}$ is called the *tidal field*. And because a gyroscope at the tip of $\boldsymbol{\xi}$

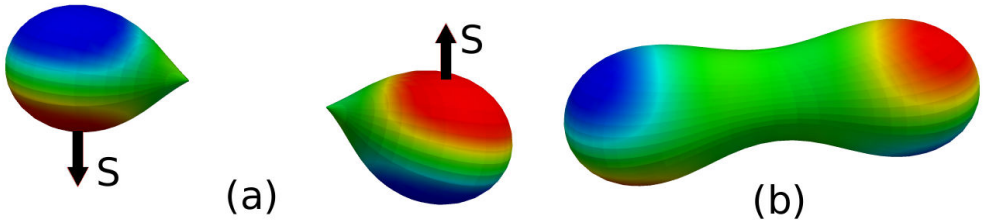

Figure 8.1: Vortexes (with positive vorticity blue, negative vorticity red) on the 2D event horizons of spinning, colliding black holes, just before and just after merger. (A description of the simulation can be found in [4].)

precesses due to frame dragging with an angular velocity $\Delta\Omega_j = \mathcal{B}_{jk}\xi^k$ relative to inertial frames at the tail of $\boldsymbol{\xi}$, we call $\mathcal{B}_{jk}$ the *frame-drag field.*

8.2 Vortexes and Tendexes in Black-Hole Horizons

For a binary black hole, our space slices intersect the 3-dimensional (3D) event horizon in a 2D horizon with inward unit normal $\mathbf{N}$; $\mathcal{B}_{NN}$, therefore, is the rate the frame-drag angular velocity around $\mathbf{N}$ increases as one moves inward through the horizon. Because of the connection between rotation and vorticity, we call $\mathcal{B}_{NN}$ the horizon's *frame-drag vorticity*, or simply its *vorticity.* Because $\mathcal{B}_{NN}$ is boost-invariant along $\mathbf{N}$ [2], the horizon's vorticity is independent of how fast the orthogonal observers fall through the horizon, and is even unchanged if the observers hover immediately above the horizon (the FIDOs of the "black-hole membrane paradigm" [3]).

Figure 8.1 shows snapshots of the horizon for two identical black holes with transverse, oppositely directed spins $\mathbf{S}$, colliding head on. Before the collision, each horizon has a negative-vorticity region (red) centered on $\mathbf{S}$, and a positive-vorticity region (blue) on the other side. We call these regions of concentrated vorticity *horizon vortexes.* Our numerical simulation [4] shows the four vortexes being transferred to the merged horizon (Fig. 8.1b), then retaining their identities, but sloshing between positive and negative vorticity and gradually dying, as the hole settles into its final Schwarzschild state; see the movie in [5].

Because $\mathcal{E}_{NN}$ measures the strength of the tidal-stretching acceleration felt by orthogonal observers as they fall through (or hover above) the horizon, we call it the horizon's *tendicity* (a word coined by David Nichols from the Latin *tendere*, "to stretch"). On the two ends of the merged horizon in Fig. 8.1b there are regions of strongly enhanced tendicity, called *tendexes*; see Fig. 8.5 below.

An orthogonal observer falling through the horizon carries an orthonormal tetrad consisting of her 4-velocity $\mathbf{U}$, the horizon's inward normal $\mathbf{N}$, and transverse vectors $\mathbf{e_2}$ and $\mathbf{e_3}$. In the null tetrad $\mathbf{l} = (\mathbf{U}-\mathbf{N})/\sqrt{2}$ (tangent to horizon generators), $\mathbf{n} = (\mathbf{U}+\mathbf{N})/\sqrt{2}$, $\mathbf{m} = (\mathbf{e_2}+i\mathbf{e_3})/\sqrt{2}$, and $\mathbf{m}^*$, the Newman-Penrose Weyl scalar Ψ_2 [6] is $\Psi_2 = (\mathcal{E}_{NN} + i\mathcal{B}_{NN})/2$. Here we use sign conventions of [7],

appropriate for our (-+++) signature. Penrose and Rindler [8] define a complex scalar curvature $\mathcal{K} = \mathcal{R}/4 + i\mathcal{X}/4$ of the 2D horizon, with $\mathcal{R}$ its intrinsic (Ricci) scalar curvature (which characterizes the horizon's shape) and $\mathcal{X}$ proportional to the 2D curl of its Hájíček field [9] (the space-time part of the 3D horizon's extrinsic curvature). Penrose and Rindler show that $\mathcal{K} = -\Psi_2 + \mu\rho - \lambda\sigma$, where ρ, σ, μ, and λ are spin coefficients related to the expansion and shear of the null vectors $\mathbf{l}$ and $\mathbf{n}$, respectively. In the limit of a shear- and expansion-free horizon (e.g., a quiescent black hole; Fig. 8.2a, b, and c), $\mu\rho - \lambda\sigma$ vanishes, and $\mathcal{K} = -\Psi_2$ (and, therefore, $\mathcal{R} = -2\mathcal{E}_{NN}$ and $\mathcal{X} = -2\mathcal{B}_{NN}$).

As the dimensionless spin parameter a/M of a quiescent (Kerr) black hole is increased, the scalar curvature $\mathcal{R} = -2\mathcal{E}_{NN}$ at its poles decreases, becoming negative for $a/M > \sqrt{3}/2$; see the blue spots on the poles in Fig. 8.2b compared to solid red for the nonrotating hole in Fig. 8.2a. In our binary-black-hole simulations, the contributions of the spin coefficients to $\mathcal{K}$ on the apparent horizons are small (L^2-norm $\lesssim 1\%$); therefore, we find that $\mathcal{R} \simeq -2\mathcal{E}_{NN}$ and $\mathcal{X} \simeq -2\mathcal{B}_{NN}$, except for a time interval $\sim 5M_{\rm tot}$ near merger. Here $M_{\rm tot}$ is the binary's total mass. On the event horizon, the duration of spin-coefficient contributions $> 1\%$ is somewhat longer, but we do not yet have a good measure of it.

Because $\mathcal{X}$ is the 2D curl of a 2D vector, its integral over the 2D horizon vanishes. Therefore, positive-vorticity regions must be balanced by negative-vorticity regions; it seems impossible to have a horizon with just one vortex. By contrast, the Gauss-Bonnet theorem says the integral of $\mathcal{R}$ over the 2D horizon is 8π (assuming S_2 topology), which implies the horizon tendicity $\mathcal{E}_{NN}$ is predominantly negative (because $\mathcal{E}_{NN} \simeq -\mathcal{R}/2$ and $\mathcal{R}$ is predominantly positive). Many black holes have negative horizon tendicity everywhere (an exception is Fig. 8.2b); consequently, their horizon tendexes must be distinguished by deviations of $\mathcal{E}_{NN}$ from a horizon-averaged value.

8.3 Three-Dimensional Vortex and Tendex Lines

The frame-drag field $\mathcal{B}_{jk}$ is symmetric and trace free and, therefore, is fully characterized by its three orthonormal eigenvectors $\mathbf{e}_{\tilde{j}}$ and their eigenvalues $\mathcal{B}_{\tilde{1}\tilde{1}}$, $\mathcal{B}_{\tilde{2}\tilde{2}}$, and $\mathcal{B}_{\tilde{3}\tilde{3}}$. We call the integral curves along $\mathbf{e}_{\tilde{j}}$ *vortex lines*, and their eigenvalue $\mathcal{B}_{\tilde{j}\tilde{j}}$ those lines' *vorticity*; we call a concentration of vortex lines with large vorticity a *vortex*. For the tidal field $\mathcal{E}_{jk}$ the analogous quantities are *tendex lines*, *tendicity* and *tendexes*. For a nonrotating (Schwarzschild) black hole, we show a few tendex lines in Fig. 8.2a; and for a rapidly-spinning black hole (Kerr metric with $a/M = 0.95$) we show tendex lines in Fig. 8.2b and vortex lines in Fig. 8.2c.

If a person's body (with length ℓ) is oriented along a positive-tendicity tendex line (blue in Fig. 8.2a), she feels a head-to-foot compressional acceleration $\Delta a = |\text{tendicity}|\ell$; for negative tendicity (red) it is a stretch. If her body is oriented along a positive-vorticity vortex line (blue in Fig. 8.2c), her head sees a gyroscope at her feet precess clockwise with angular speed $\Delta\Omega = |\text{vorticity}|\ell$, and her feet see a gyroscope at her head also precess clockwise at the same rate. For negative vorticity

(red), the precessions are counterclockwise.

For a nonrotating black hole, the stretching tendex lines are radial, and the squeezing ones lie on spheres (Fig. 8.2a). When the hole is spun up to $a/M = 0.95$ (Fig. 8.2b), its toroidal tendex lines acquire a spiral, and its poloidal tendex lines, when emerging from one polar region, return to the other polar region. For any spinning Kerr hole (e.g., Fig. 8.2c), the vortex lines from each polar region reach around the hole and return to the same region. The red vortex lines from the red north polar region constitute a *counterclockwise vortex*; the blue ones from the south polar region constitute a *clockwise vortex*.

As a dynamical example, consider a Schwarzschild black hole's fundamental odd-parity $l = m = 2$ quasinormal mode of pulsation, which is governed by Regge-Wheeler perturbation theory [11] and has angular eigenfrequency $2M\omega = (0.74734 - 0.17792i)$, with M being the hole's mass. From the perturbation equations, we have deduced the mode's horizon vorticity: $\mathcal{B}_{NN} = \Re\{9\sin^2\theta/(2i\omega M^3)\exp[2i\phi - i\omega(\tilde{t} + 2M)]\}$. (Here $\tilde{t}$ is the ingoing Eddington-Finkelstein time coordinate, and the mode's Regge-Wheeler radial eigenfunction $Q(r)$ is normalized to unity near the horizon.) At time $\tilde{t} = 0$, this $\mathcal{B}_{NN}$ exhibits four horizon vortexes (red and blue in Fig. 8.2d), centered on the equator at $(\theta, \phi) = (\pi/2, 1.159 + k\pi/2)$ $(k = 0, 1, 2, 3)$, and with central vorticities $\mathcal{B}_{NN} = -(-1)^k 39.22/(2M)^2$. From analytic formulas for $\mathcal{B}_{jk}$ and a numerical $Q(r)$, we have deduced the equatorial-plane red vortex lines and vorticities shown in Fig. 8.2d. As time $\tilde{t}$ passes, the vortexes rotate counterclockwise, so they resemble water splayed out from a turning sprinkler. The transition from near zone to wave zone is at $r/M \sim 4$ (near the outermost part of the second contour line). As one moves into the wave zone, each of the red vortexes is smoothly transformed into a gravitational-wave trough and the 3D vortexes that emerge from the blue horizon vortexes (concentrated in the dark region of this figure) are transformed into gravitational-wave crests.

8.4 Vortex and Tendex Evolutions in Binary Black Holes (BBHs)

We have explored the evolution of frame-drag vortexes and tidal tendexes in numerical simulations of three BBHs that differ greatly from one another.

Our first simulation (documented in [4] with movies in [5]) is the head-on, transverse-spin merger depicted in Fig. 8.1 above, with spin magnitudes $a/M = 0.5$. As the holes approach each other then merge, their 3D vortex lines, which originally link a horizon vortex to itself on a single hole (Fig. 8.2c), reconnect so that on the merged hole, they link one horizon vortex to the other of the same polarity (Fig. 8.3a). After merger, the near-zone 3D vortexes slosh (their vorticity oscillates between positive and negative), generating vortex loops (Fig. 8.3b) that travel outward as gravitational waves.

Our second simulation (documented in [12] with movies in [13]) is the inspiral and merger of two

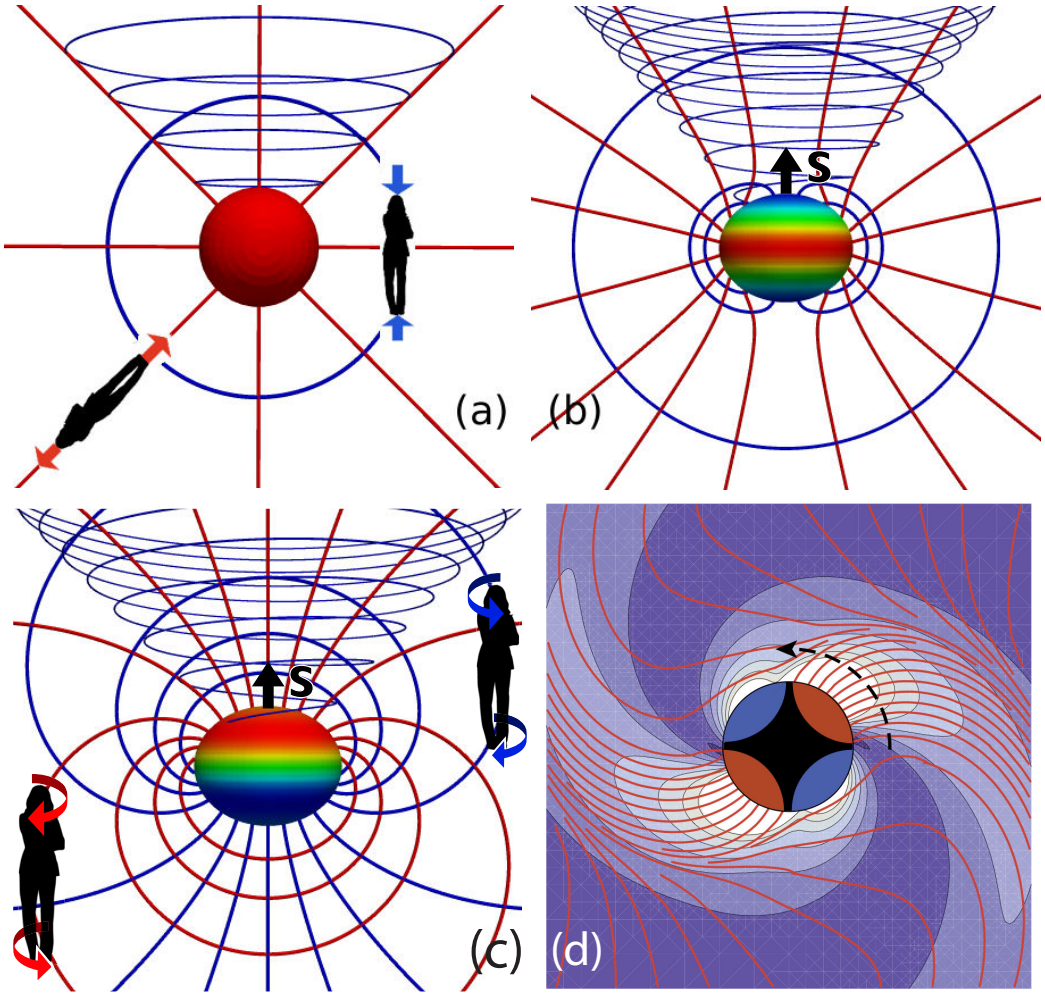

Figure 8.2: Four different black holes, with horizons colored by their tendicity (upper two panels) or vorticity (lower two panels), ranging from most negative (red) to most positive (blue), and with a Kerr-Schild, horizon-penetrating foliation (Exercise 33.8 of Ref. [10]). (a) A nonrotating black hole and its tendex lines; negative-tendicity lines are red and positive blue. (b) A rapidly rotating (Kerr) black hole, with spin $a/M = 0.95$, and its tendex lines. (c) The same Kerr black hole and its vortex lines. (d) Equatorial plane of a nonrotating black hole that is oscillating in an odd-parity $l = m = 2$ quasinormal mode, with negative-vorticity vortex lines emerging from red horizon vortexes. The lines' vorticities are indicated by contours and colors; the contour lines, in units $(2M)^{-2}$ and going outward from the hole, are -10, -8, -6, -4, -2.

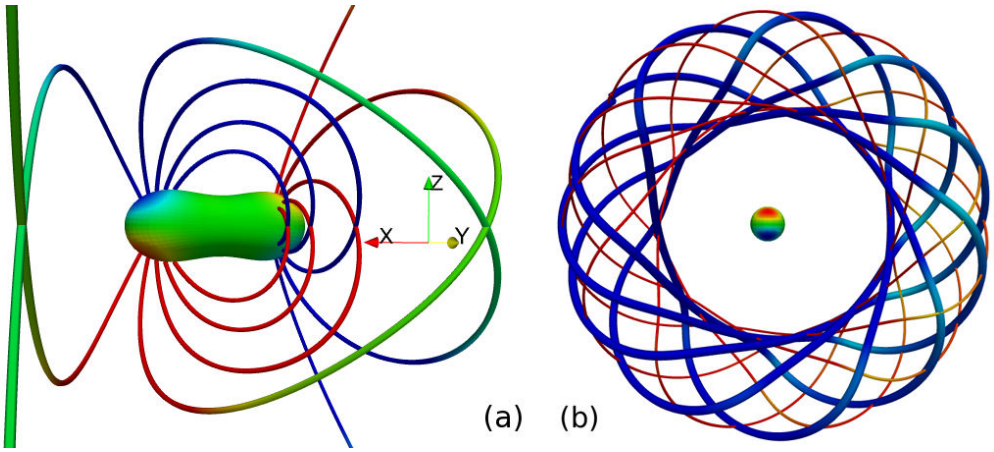

Figure 8.3: Head-on, transverse-spin simulation: (a) Shortly after merger, vortex lines link horizon vortexes of same polarity (red to red; blue to blue). Lines are color coded by vorticity with a different scale from that used to color the horizon. (b) Sloshing of near-zone vortexes modify vortex loops traveling outward as gravitational waves; thick and thin lines are orthogonal vortex lines.

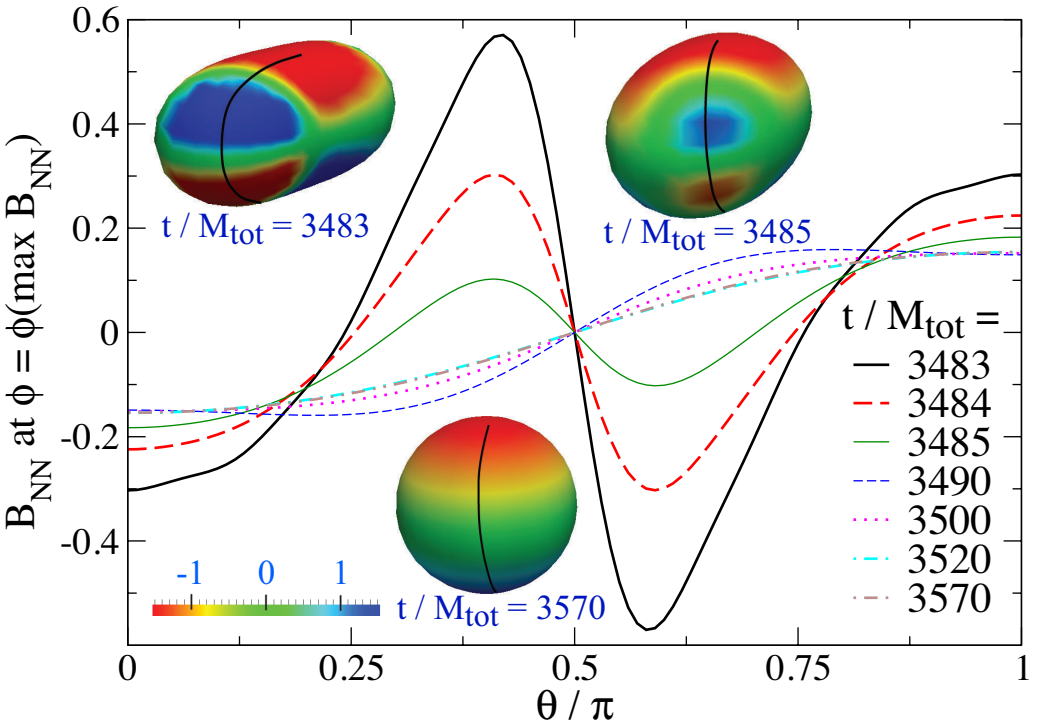

Figure 8.4: Insets: snapshots of the common apparent horizon for the $a/M = 0.95$ anti-aligned simulation, color coded by the horizon vorticity B_{NN}. Graphs: B_{NN} as a function of polar angle θ at the azimuthal angle ϕ that bisects the four vortexes (along the black curves in snapshots)

identical, fast-spinning holes ($a/M = 0.95$) with spins anti-aligned to the orbital angular momentum. Figure 8.4 shows the evolution of the vorticity $\mathcal{B}_{NN}$ on the common apparent horizon beginning just after merger (at time $t/M_{\rm tot} = 3483$), as seen in a frame that co-rotates with the small horizon vortexes. In that frame, the small vortexes (which arise from the initial holes' spins) appear to diffuse into the two large central vortexes (which arise from the initial holes' orbital angular momentum), annihilating some of their vorticity. (This is similar to the diffusion and annihilation of magnetic field lines with opposite polarity threading a horizon [3].) Making this heuristic description quantitative, or disproving it, is an important challenge.

Our third simulation (with movies in [14]) is a variant of the "extreme-kick" merger studied by Campanelli et al. [15] and others [16, 17]: two identical holes, merging from an initially circular orbit, with oppositely directed spins $a/M = 0.5$ lying in the orbital (x, y) plane. In this case, the vortexes and tendexes in the merged hole's (x, y) plane rotate as shown in Fig. 8.2d. We have tuned the initial conditions to make the final hole's kick (nearly) maximal, in the $+z$ direction. The following considerations explain the origin of this maximized kick: In a plane gravitational wave, all the vortex and tendex lines with nonzero eigenvalues lie in the wave fronts and make angles of 45 degrees to each other (bottom inset of Fig. 8.5.) For vectors $\boldsymbol{E}$ (parallel to solid, positive-tendicity tendex line) and $\boldsymbol{B}$ (parallel to dashed, positive-vorticity vortex line), $\boldsymbol{E} \times \boldsymbol{B}$ is in the wave's propagation direction.

Now, during and after merger, the black hole's near-zone rotating tendex lines (top left inset in Fig. 8.5) acquire accompanying vortex lines as they travel outward into the wave zone and become gravitational waves; and the rotating near-zone vortex lines acquire accompanying tendex lines. Because of the evolution-equation duality between $\mathcal{E}_{ij}$ and $\mathcal{B}_{ij}$, the details of this wave formation are essentially the same for the rotating tendex and vortex lines. Now, in the near zone, the vectors $\boldsymbol{E}$ and $\boldsymbol{B}$ along the tendex and vortex lines (Fig. 8.5) make the same angle with respect to each other as in a gravitational wave (45 degrees) and have $\boldsymbol{E} \times \boldsymbol{B}$ in the $-z$ direction. This means that the gravitational waves produced by the rotating near-zone tendex lines and those produced by the rotating near-zone vortex lines will superpose constructively in the $-z$ direction and destructively in the $+z$ direction, leading to a maximized gravitational-wave momentum flow in the $-z$ direction and maximized black-hole kick in the $+z$ direction. An extension of this reasoning shows that the black-hole kick velocity is sinusoidal in twice the angle between the merged hole's near-zone rotating vortexes and tendexes, in accord with simulations.

8.5 Conclusions

In our BBH simulations, the nonlinear dynamics of curved spacetime appears to be dominated by (i) the transfer of spin-induced frame-drag vortexes from the initial holes to the final merged hole, (ii) the creation of two large vortexes on the merged hole associated with the orbital angular momentum,

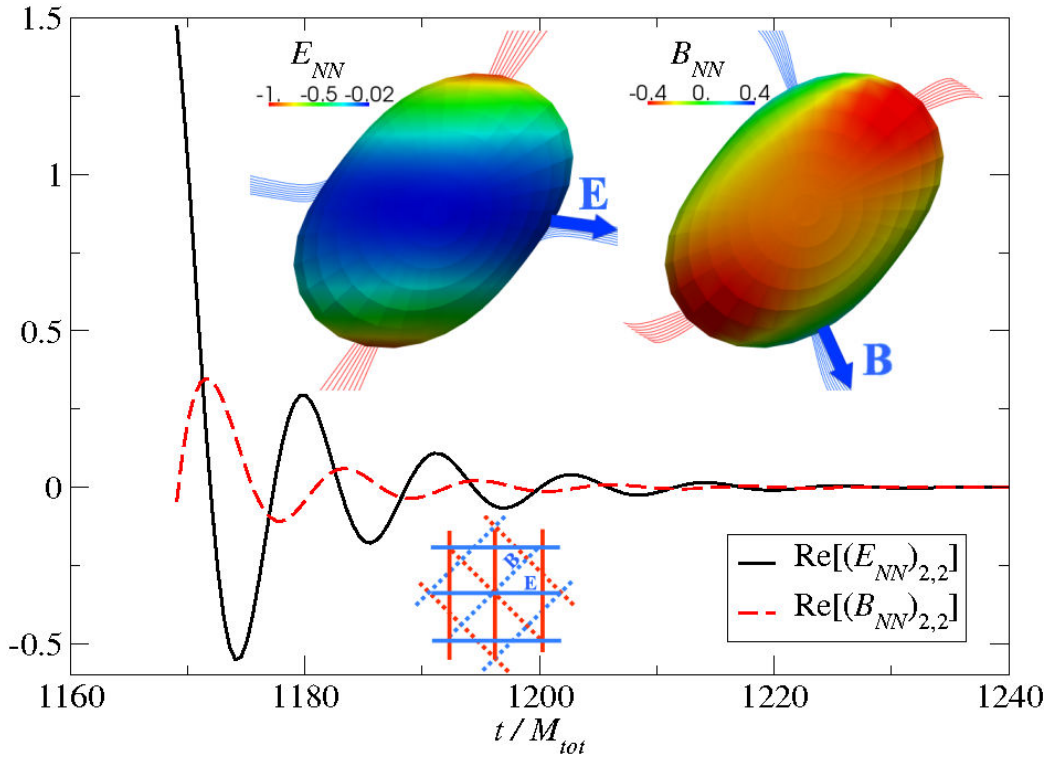

Figure 8.5: Bottom inset: tendex and vortex lines for a plane gravitational wave; $\boldsymbol{E} \times \boldsymbol{B}$ is in the propagation direction. Upper two insets: for the "extreme-kick simulation", as seen looking down the merged hole's rotation axis ($-z$ direction), the apparent horizon is color coded by the horizon tendicity (left inset) and vorticity (right inset), and with 3D vortex lines and tendex lines emerging from the horizon. The tendexes with the most positive tendicity (colored blue and labeled by $\boldsymbol{E}$) lead the positive-vorticity vortexes (also blue but labeled by$\boldsymbol{B}$) by about 45° as they rotate counterclockwise. This 45° lead is verified in the oscillating curves, which show the rotating $\mathcal{B}_{NN}$ and $\mathcal{E}_{NN}$ projected onto a nonrotating $\ell = 2$, $m = 2$ spherical harmonic.

(iii) the subsequent sloshing, diffusion, and/or rotational motion of the spin-induced vortexes, (iv) the formation of strong negative $\mathcal{E}_{NN}$ poloidal tendexes on the merged horizon at the locations of the original two holes, associated with the horizon's elongation, and a positive $\mathcal{E}_{NN}$ tendex at the neck where merger occurs, and (v) the oscillation, diffusion, and (or) circulatory motion of these tendexes.

We *conjecture* that there is no other important dynamics in the merger and ringdown of BBHs. If so, there are important consequences: (i) This could account for the surprising simplicity of the BBH gravitational waveforms predicted by simulations. (ii) A systematic study of frame-drag vortexes and tidal tendexes in BBH simulations may produce improved understanding of BBHs, including their waveforms and kicks. The new waveform insights may lead to improved functional forms for waveforms that are tuned via simulations to serve as templates in LIGO/VIRGO data analysis. (iii) Approximation techniques that aim to smoothly cover the full spacetime of BBH mergers (e.g., the combined post-Newtonian and black-hole-perturbation theory method [18]) might be made to capture accurately the structure and dynamics of frame-drag vortexes and tidal tendexes. If so, these approximations may become powerful and accurate tools for generating BBH waveforms.

Bibliography

[1] R. Maartens and B. A. Bassett, Classical Quantum Gravity **15**, 705 (1998).

[2] R. H. Price and K. S. Thorne, Phys. Rev. D **33**, 330915 (1986).

[3] K. S. Thorne, R. H. Price, and D. A. MacDonald, *Black Holes: The Membrane Paradigm* (Yale University Press, New Haven and London, 1986).

[4] G. Lovelace, Y. Chen, M. Cohen, J. D. Kaplan, D. Keppel, K. D. Matthews, D. A. Nichols, M. A. Scheel, and U. Sperhake, Phys. Rev. D **82**, 064031 (2010).

[5] `http://www.black-holes.org/headon05aa.html`.

[6] E. Newman and R. Penrose, J. Math. Phys. **3**, 566 (1962).

[7] V. P. Frolov and I. D. Novikov, *Black Hole Physics: Basic Concepts and New Developments* (Kluwer Academic Publishers, Drodrecht, Netherlands, 1998).

[8] R. Penrose and W. Rindler, *Spinors and Space-time, Volume 1* (Cambridge University Press, Cambridge, 1992).

[9] T. Damour, in *Proceedings of the Second Marcel Grossman Meeting on General Relativity*, edited by R. Ruffini (North-Holland Publishing Company, Amsterdam, 1982), pp. 587–606.

[10] C. W. Misner, K. S. Thorne, and J. A. Wheeler, *Gravitation* (W. H. Freeman, New York, 1973).

[11] S. Chandrasekhar and S. Detweiler, Proc. R. Soc. A **344**, 441 (1975).

[12] G. Lovelace, M. Scheel, and B. Szilagyi, Phys.Rev. **D83**, 024010 (2011).

[13] `http://www.black-holes.org/inspiral95aa.html`.

[14] `http://www.black-holes.org/extreme-kick.html`.

[15] M. Campanelli, C. O. Lousto, Y. Zlochower, and D. Merritt, Phys. Rev. Lett. **98**, 231102 (2007).

[16] J. A. Gonzalez, M. D. Hannam, U. Sperhake, B. Brügmann, and S. Husa, Phys. Rev. Lett. **98**, 231101 (2007).

[17] C. O. Lousto and Y. Zlochower, Phys. Rev. D. **83**, 024003 (2011).

[18] D. A. Nichols and Y. Chen, Phys. Rev. D **82**, 104020 (2010).

Chapter 9

Classifying the Isolated Zeros of Asymptotic Gravitational Radiation with Tendex and Vortex Lines

A new method to visualize the curvature of spacetime was recently proposed. This method finds the eigenvectors of the electric and magnetic components of the Weyl tensor and, in analogy to the field lines of electromagnetism, uses the eigenvectors' integral curves to illustrate the spacetime curvature. Here we use this approach, along with well-known topological properties of fields on closed surfaces, to show that an arbitrary, radiating, asymptotically flat spacetime must have points near null infinity where the gravitational radiation vanishes. At the zeros of the gravitational radiation, the field of integral curves develops singular features analogous to the critical points of a vector field. We can, therefore, apply the topological classification of singular points of unoriented lines as a method to describe the radiation field. We provide examples of the structure of these points using linearized gravity and discuss an application to the extreme-kick black-hole-binary merger.

Originally published as A. Zimmerman, D. A. Nichols, and F. Zhang, Phys. Rev. D **84**, 044037 (2011).

9.1 Introduction

A recent study [1] proposed a method for visualizing spacetime curvature that is well-suited for studying spacetimes evolved from initial data using numerical-relativity codes. The method first projects the Riemann curvature tensor $R_{\mu\nu\sigma\rho}$ into a spatial slice, thereby splitting it into two symmetric, trace-free spatial tensors, $\boldsymbol{\mathcal{E}}$ and $\boldsymbol{\mathcal{B}}$ (see, e.g., [2] and the references therein). These tensors

are the spacetime-curvature analogs of the electric and magnetic fields in Maxwell's theory. The electric tensor $\boldsymbol{\mathcal{E}}$ is familiar; it is the tidal field in the Newtonian limit. The frame-drag field $\boldsymbol{\mathcal{B}}$ (the magnetic curvature tensor) describes the differential precession of nearby inertial gyroscopes. The eigenvectors of the tidal field provide the preferred directions of strain at a point in spacetime, and its eigenvalues give the magnitude of the strain along those axes. Similarly, the eigenvectors of the frame-drag field give preferred directions of differential precession of gyroscopes, and their eigenvalues give the magnitude of this precession [1, 3, 4].

The study [1] then proposed using the integral curves of these eigenvectors as a way to visualize the curvature of spacetime. Three orthogonal curves associated with $\boldsymbol{\mathcal{E}}$, called tendex lines, pass through each point in spacetime. Along each tendex line there is a corresponding eigenvalue, which is called the tendicity of the line. For the tensor $\boldsymbol{\mathcal{B}}$, there is a second set of three orthogonal curves, the vortex lines, and their corresponding eigenvalues, the vorticities. These six curves are analogous to the field lines of electromagnetism, and the six eigenvalues to the electric and magnetic field strengths. The tendex and vortex lines, with their corresponding vorticities and tendicities, represent very different physical phenomena from field lines of electromagnetism; they allow one to visualize the aspects of spacetime curvature associated with tidal stretching and differential frame-dragging. In addition, each set of curves satisfies the constraint that its eigenvalues sum to zero at every point, because $\boldsymbol{\mathcal{E}}$ and $\boldsymbol{\mathcal{B}}$ are trace-free.

Wherever the eigenvector fields are well-behaved, the tendex and vortex lines form extended, continuous fields of lines in a spatial slice. At points where two (or more) eigenvectors have the same eigenvalue, the eigenvectors are said to be degenerate. Any linear combination of the degenerate eigenvectors at these points is still an eigenvector with the same eigenvalue; therefore, the span of these eigenvectors forms a degenerate subspace. Singular features can appear at points of degeneracy, where many lines intersect, terminate, or turn discontinuously. The topology of unoriented fields of lines and their singular points has been studied both in the context of general relativity and elsewhere. For example, Delmarcelle and Hesselink [5] investigated the theory of these systems and applied them to real, symmetric two-dimensional tensors. In the context of relativity, Penrose and Rindler [6] examined the topology of unoriented lines, or ridge systems, to characterize the principal null directions about single points in spacetime. Finally, Penrose [7] also used ridge systems to analyze human handprint and fingerprint patterns.

In this paper, we focus on the vortex and tendex lines and their singular points far from an isolated, radiating source. In Section 9.2, we show that two of the vortex and tendex lines lie on a sphere (the third, therefore, is normal to the sphere), and that the vortex and tendex lines have the same eigenvalues. Moreover, the two eigenvalues on the sphere have opposite sign, and the eigenvalue normal to the sphere has zero eigenvalue. This implies that the only singular points in the lines occur where all eigenvalues vanish (i.e., when the curvature is exactly zero at the point,

and all three eigenvectors are degenerate).

In Section 9.3 we employ a version of the Poincaré-Hopf theorem for fields of integral curves to argue that there must be singular points where the curvature vanishes. Penrose, in a 1965 paper [8], made a similar observation. There, he notes in passing that gravitational radiation must vanish for topological reasons, although he does not discuss the point any further. Here we show that the topological classification of singular points of ridge systems can be applied to the tendex and vortex lines of gravitational radiation (which serves as a topological classification of the zeros of the radiation field).

In Section 9.4, we visualize the tendex and vortex lines of radiating systems in linearized gravity. We begin with radiation from a rotating mass-quadrupole moment, the dominant mode in most astrophysical gravitational radiation. We then move to an idealized model of the "extreme-kick" configuration (an equal-mass binary-black-hole merger with spins antialigned in the orbital plane [9]). As we vary the magnitude of the spins in the extreme-kick configuration, we can relate the positions of the singular points of the tendex and vortex patterns to the degree of beaming of gravitational waves. We also visualize the radiation fields of individual higher-order multipole moments, which serve, primarily, as examples of patterns with a large number of singularities. Astrophysically, these higher multipoles would always be accompanied by a dominant quadrupole moment; we also, therefore, look at a superposition of multipoles. Because the tendex lines depend nonlinearly upon the multipoles, it is not apparent, *a priori*, how greatly small higher multipoles will change the leading-order quadrupole pattern. Nevertheless, we see that for an equal-mass black-hole binary, higher multipoles make only small changes to the tendex-line patterns. Finally, we discuss our results in Section 9.5.

Throughout this paper we use Greek letters for spacetime coordinates in a coordinate basis and Latin letters from the beginning of the alphabet for spatial indices in an orthonormal basis. We use a spacetime signature $(-+++)$ and a corresponding normalization condition for our tetrad. We will use geometric units, in which $G = c = 1$.

We will also specialize to vacuum spacetimes, where the Riemann tensor is equal to the Weyl tensor $C_{\mu\nu\rho\sigma}$. To specify our slicing and to compute $\boldsymbol{\mathcal{E}}$ and $\boldsymbol{\mathcal{B}}$, we use a hypersurface-orthogonal, timelike unit vector, $\boldsymbol{e}_0$, which we choose to be part of an orthonormal tetrad, $(\boldsymbol{e}_0, \boldsymbol{e}_1, \boldsymbol{e}_2, \boldsymbol{e}_3)$. We then perform a $3+1$ split of the Weyl tensor by projecting it and its Hodge dual ${}^*C_{\mu\nu\rho\sigma} = \frac{1}{2}\epsilon_{\mu\nu}{}^{\alpha\beta}C_{\alpha\beta\sigma\rho}$ into this basis,

$$\mathcal{E}_{ab} = C_{a\mu b\nu} e_0{}^{\mu} e_0{}^{\nu} , \tag{9.1}$$

$$\mathcal{B}_{ab} = -{}^*C_{a\mu b\nu} e_0{}^{\mu} e_0{}^{\nu} . \tag{9.2}$$

Here our convention for the alternating tensor is that $\epsilon_{0123} = +1$ in an orthonormal basis. Note

that, while the sign convention on $\boldsymbol{\mathcal{B}}$ is not standard (see e.g., [10]), it has the advantage that $\boldsymbol{\mathcal{E}}$ and $\boldsymbol{\mathcal{B}}$ obey constraints and evolution equations under the $3+1$ split of spacetime that are directly analogous to Maxwell's equations of electromagnetism [2, 4]. After the projection, we will solve the eigenvalue problem for the tensors $\boldsymbol{\mathcal{E}}$ and $\boldsymbol{\mathcal{B}}$ in the orthonormal basis,

$$\mathcal{E}_{ab} v^b = \lambda v_a \,, \tag{9.3}$$

and we will then find their streamlines in a coordinate basis via the differential equation relating a curve to its tangent vector,

$$\frac{dx^\mu}{ds} = v^a e_a{}^\mu \,. \tag{9.4}$$

Here s is a parameter along the streamlines.

9.2 Gravitational Waves Near Null Infinity

Consider a vacuum, asymptotically flat spacetime that contains gravitational radiation from an isolated source. We are specifically interested in the transverse modes of radiation on a large sphere, S, near future null infinity. To describe these gravitational waves, we use an orthonormal tetrad $(\boldsymbol{e}_0, \boldsymbol{e}_1, \boldsymbol{e}_2, \boldsymbol{e}_3)$, with $\boldsymbol{e}_0$ timelike and $\boldsymbol{e}_2, \boldsymbol{e}_3$ tangent to the sphere, and we associate with this tetrad a corresponding complex null tetrad,

$$\begin{aligned} \boldsymbol{l} &= \frac{1}{\sqrt{2}}(\boldsymbol{e}_0 + \boldsymbol{e}_1) \,, & \boldsymbol{n} &= \frac{1}{\sqrt{2}}(\boldsymbol{e}_0 - \boldsymbol{e}_1) \,, \\ \boldsymbol{m} &= \frac{1}{\sqrt{2}}(\boldsymbol{e}_2 + i\boldsymbol{e}_3) \,, & \bar{\boldsymbol{m}} &= \frac{1}{\sqrt{2}}(\boldsymbol{e}_2 - i\boldsymbol{e}_3) \,. \end{aligned} \tag{9.5}$$

Here, $\boldsymbol{l}$ is tangent to outgoing null rays that pass through S and intersect a sphere at null infinity. We enforce that the null tetrad is parallelly propagated along these rays, and that it is normalized such that $l_\mu n^\mu = -m_\mu \bar{m}^\mu = -1$ (all other inner products of the null tetrad vanish). With these rays, we can associate Bondi-type coordinates (see, e.g., [11, 12]) on a sphere at future null infinity with those on S. The timelike vector $\boldsymbol{e}_0$ specifies our spatial slicing in this asymptotic region. When the orthonormal and null tetrads are chosen as in Eq. (9.5), $\boldsymbol{\mathcal{E}}$ and $\boldsymbol{\mathcal{B}}$ are related to the complex Weyl scalars [13]. With the Newman-Penrose conventions appropriate to our metric signature (see, e.g., [10]), and our conventions in Eqs. (9.1) and (9.2), one can show that when written in a matrix form,

$$\mathcal{E}_{ab} + i\mathcal{B}_{ab} = \begin{pmatrix} 2\Psi_2 & \Psi_3 - \Psi_1 & i(\Psi_1 + \Psi_3) \\ * & \frac{1}{2}(\Psi_0 + \Psi_4) - \Psi_2 & \frac{i}{2}(\Psi_4 - \Psi_0) \\ * & * & -\frac{1}{2}(\Psi_0 + \Psi_4) - \Psi_2 \end{pmatrix} , \tag{9.6}$$

where $*$ indicates that the entries can be inferred from the symmetry of $\boldsymbol{\mathcal{E}}$ and $\boldsymbol{\mathcal{B}}$.

In an asymptotically flat spacetime, the peeling theorem [13] ensures that $\Psi_4 \sim r^{-1}$ (with r

an affine parameter along the rays), and that the remaining Weyl scalars fall off with progressively higher powers of r, $\Psi_3 \sim r^{-2}, \Psi_2 \sim r^{-3}, \Psi_1 \sim r^{-4}$, and $\Psi_0 \sim r^{-5}$. Asymptotically, only Ψ_4 contributes to $\boldsymbol{\mathcal{E}}$ and $\boldsymbol{\mathcal{B}}$, and

$$\mathcal{E}_{ab} + i\mathcal{B}_{ab} = \frac{1}{2}\begin{pmatrix} 0 & 0 & 0 \\ 0 & \Psi_4 & i\Psi_4 \\ 0 & i\Psi_4 & -\Psi_4 \end{pmatrix} . \tag{9.7}$$

We see immediately that one eigenvector of both $\boldsymbol{\mathcal{E}}$ and $\boldsymbol{\mathcal{B}}$ is the "radial" basis vector $\boldsymbol{e}_1$, with vanishing eigenvalue. The remaining 2×2 block is transverse and traceless, and the eigenvectors in this subspace have a simple analytical solution. The eigenvalues are $\lambda_\pm = \pm|\Psi_4|/2$ for both tensors, and the eigenvectors of $\boldsymbol{\mathcal{E}}$ have the explicit form

$$\begin{aligned} \boldsymbol{v}_\pm &= \frac{-\mathcal{E}_{23}\boldsymbol{e}_2 + (\mathcal{E}_{22} - \lambda_\pm)\boldsymbol{e}_3}{\sqrt{\mathcal{E}_{23}^2 + (\mathcal{E}_{22} - \lambda_\pm)^2}} \\ &= \frac{\mathrm{Im}\Psi_4 \boldsymbol{e}_2 + (\mathrm{Re}\Psi_4 \mp |\Psi_4|)\boldsymbol{e}_3}{\sqrt{(\mathrm{Im}\Psi_4)^2 + (\mathrm{Re}\Psi_4 \mp |\Psi_4|)^2}} , \end{aligned} \tag{9.8}$$

though the expression gives degenerate eigenvectors when $\mathcal{E}_{23} = -\mathrm{Im}\Psi_4 = 0$ (i.e., when $\boldsymbol{e}_2$ and $\boldsymbol{e}_3$ are the eigenvectors).

The eigenvectors of $\boldsymbol{\mathcal{B}}$ are locally rotated by $\pm\pi/4$ radians with respect to those of $\boldsymbol{\mathcal{E}}$ [4]. As a result, although the global geometric pattern of vortex and tendex lines may differ, their local pattern and their topological properties on S will be identical. Moreover, when the eigenvalues of $\boldsymbol{\mathcal{E}}$ (the tendicity of the corresponding tendex line) vanish, so must those of $\boldsymbol{\mathcal{B}}$ (the vorticity of the vortex lines). In arguing that the radiation must vanish, we can, therefore, focus on the tendex lines on S without loss of generality. Physically, however, both the vortex and the tendex lines are of interest. Similarly, because the two sets of tendex lines on S have equal and opposite eigenvalue and are orthogonal, we need only consider the properties of a single field of unoriented lines on S in order to describe the topological properties of all four tendex and vortex lines on the sphere. Note that, thus far, we leave the coordinates (x^2, x^3) on S unspecified. We will assume that these coordinates are everywhere nonsingular, for instance by being constructed from two smooth, overlapping charts on S.

9.3 The Topology of Tendex Patterns Near Null Infinity

Before investigating the properties of the tendex lines on S, we first recall a few related properties of vector fields on a 2-sphere. A well-known result regarding vector fields on a sphere is the "hairy-ball" theorem. This result states, colloquially, that if a sphere is covered with hairs at each point, the hair cannot be combed down everywhere without producing cowlicks or bald spots. The hairy-ball theorem is a specific illustration of the Poincaré-Hopf theorem, applied to a 2-sphere. On a

2-sphere, this theorem states that the sum of the indices of the zeros of a vector field must equal the Euler characteristic, χ, of the sphere, specifically $\chi = 2$. The index of a zero of a vector field (also called a singular point) can be found intuitively by drawing a small circle around the point and traveling once around the circle counterclockwise. The number of times the local vector field rotates counterclockwise through an angle of 2π during this transit is the index. More precisely, we can form a map from the points near a zero of the vector field to the unit circle. To do this consider a closed, oriented curve in a neighborhood of the zero, and map each point on the curve to the unit circle by associating the direction of the vector field at that point with a particular point on the unit circle. The index is the degree of the map (the number of times the map covers the circle in a positive sense). Around the zero of a vector field, the index is a positive or negative integer, because the field must return to its original configuration as one completes a transit along the closed curve surrounding the field's zero point.

The concept of an index and the formal statement of the Poincaré-Hopf theorem generalizes naturally to ridge systems (fields of unoriented lines, such as the tendex lines on S). For ridge systems on the sphere, the index of a singular point can be a half-integer [5], because, intuitively, fields of lines do not have an orientation (i.e., as one traverses counterclockwise about a small circle around a singular point, the local pattern of lines can rotate through an angle of only $\pm\pi$ during the transit and still maintain a consistent pattern). We illustrate the two fundamental types of singularities in Fig. 9.1, which, following [6], we call loops for index $i = 1/2$ and triradii for $i = -1/2$. One can argue that the Poincaré-Hopf Theorem holds for ridge systems, by noting that we can create a singular point with integer index by bringing two half-index singularities together (see Fig. 9.2 for a schematic of the creation of a singularity of index $i = 1$ from two loop singularities). Ridge patterns near singularities with integer index $i = \pm 1$ can be assigned orientations consistently; they must, therefore, have the same topological properties as streamlines of vector fields (which, in turn, have the same properties as the underlying vector fields themselves). By arguing that one can always deform a ridge system so that its singular points have integer index, one can see that the sum of the indices of a ridge system on a sphere must equal the Euler characteristic of the surface, $\chi = 2$ (see [5] and the references therein for a more formal statement and proof of this theorem). In Fig. 9.3 we show several other ridge singularities with integer index for completeness. In the top row, we show three patterns with index $i = 1$, and in the bottom left, we sketch a saddle-like singularity with index $i = -1$. All of these patterns can be consistently assigned an orientation and, thus, have the same topological properties as vector-field singularities.

Having arrived at the result that the tendex lines on S must have singular points in a general, asymptotically flat, vacuum spacetime, we now recall the fact that the singular points appear where there is a degenerate eigenvalue of the tidal tensor. From the result of Section 9.2, the only degeneracies occur where the curvature vanishes completely, and it follows, therefore, that there must

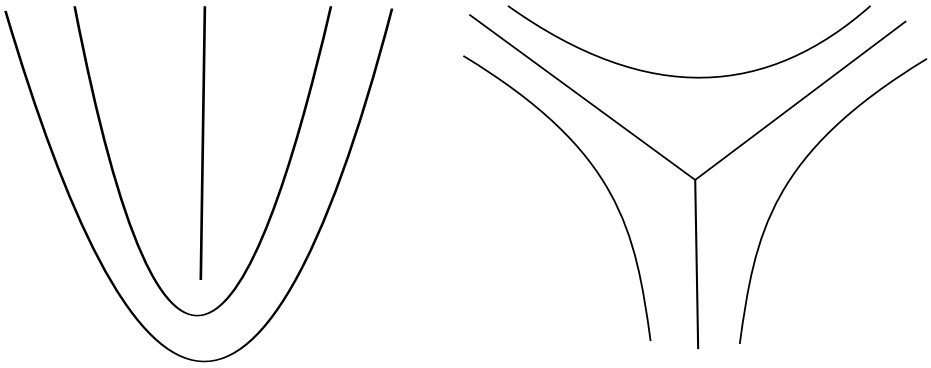

Figure 9.1: Illustrations of the two types of half-index singularities for ridge systems on a two-dimensional space. On the left is a loop singularity with index $i = 1/2$, and on the right is a triradius with $i = -1/2$.

be points of vanishing curvature on S. In general, we would expect the radiation to vanish at a minimum of four points, as Penrose [8] had previously noted. In this case, there would be four loop singularities with index $i = 1/2$, whose index sums to $\chi = 2$. As we highlight in Section 9.4, where we show several examples of multipolar radiation in linearized theory, the number of singular points, the types of singularities, and the pattern of the tendex lines contain additional information.

Additional symmetry, however, can modify the structure of the singular points, as we see in the simple example of an axisymmetric, head-on collision of two nonspinning black holes. Axisymmetry guarantees that the Weyl scalar Ψ_4 is purely real when we construct our tetrad, Eq. (9.5), by choosing $\mathbf{e}_2$ and $\mathbf{e}_3$ to be the orthonormal basis vectors of spherical polar coordinates on S, $\boldsymbol{e}_\theta$ and $\boldsymbol{e}_\phi$ [14]. Using the relation $\Psi_4 = -\ddot{h}_+ + i\ddot{h}_\times$, we see that the waves are purely + polarized. By substituting this relationship into Eq. (9.7), we also see that $\boldsymbol{e}_\theta$ and $\boldsymbol{e}_\phi$ are the eigenvectors whose integral curves are the tendex lines. The tendex lines, therefore, are the lines of constant latitude and longitude, and the singular points reside on the northern and southern poles of S. Their index must be $i = 1$, and the local pattern at the singularity will resemble the pattern at the top left of Fig. 9.3, for one set of lines, and the image on the top right of Fig. 9.3, for the other set (see also [4]). In this special situation, axisymmetry demands that there be two singular points on the axis, rather than four (or more). Moreover, these singular points are each generated from the coincidence of two loop singularities, with one singular point at each end of the axis of symmetry. Similarly, if Ψ_4 were purely imaginary, then the radiation would only contain the $\times$ polarization. The rotations of the unit spherical vectors by and angle of $\pi/4$ would then be the eigenvectors of the tidal field, and the two singularities at the poles would resemble that illustrated at the top middle of Fig. 9.3.

It is even conceivable that four loops could merge into one singular point. This singularity would have the dipole-like pattern illustrated at the bottom right of Fig. 9.3, and it would have index $i = 2$. Though this situation seems very special, we show in the next section how a finely tuned linear combination of mass and current multipoles can give rise to this pattern. Because there is

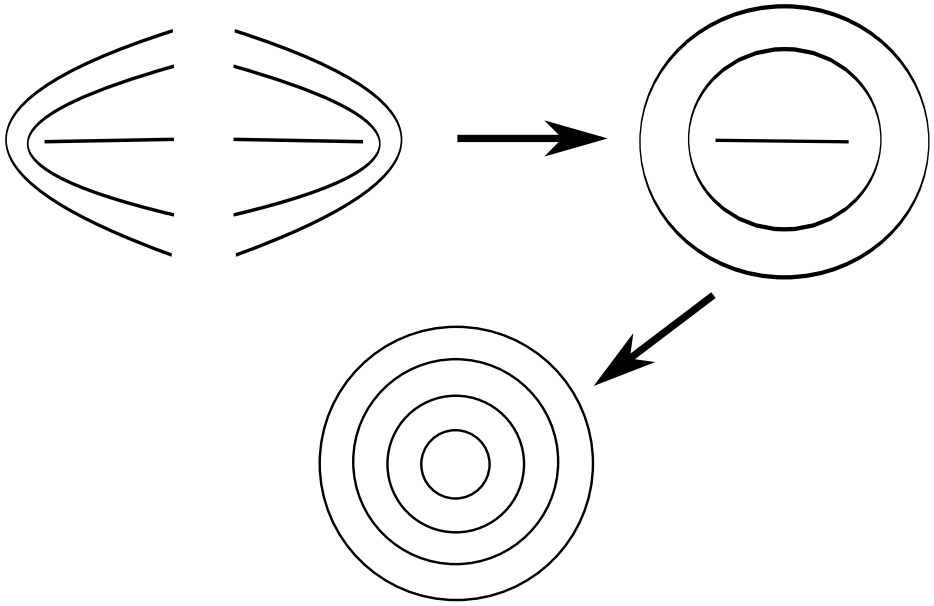

Figure 9.2: An illustration of the formation of a singularity with index $i = 1$ from two loop singularities with index $i = 1/2$. The local structure of the two loops is shown in the top left, and the arrow represents, schematically, how they might join together into the extended pattern at the top right. Finally, the two loop singularities can be brought together until they coincide (which we represent by an arrow pointing to the image at the bottom). This resulting local pattern can be assigned an orientation and is equivalent to the singular point of a vector field.

only one zero, the radiation is beamed in the direction opposite the zero, resulting in a net flux of momentum opposite the lone singular point.

Before concluding this section, we address two possible concerns. The scalar $\Psi_4 = C_{\mu\nu\rho\sigma} n^\mu \bar{m}^\nu n^\rho \bar{m}^\sigma$ depends both on the curvature and on the chosen tetrad. We first emphasize that the singular points we have discussed have nothing to do with tetrad considerations, in particular with the behavior of the vectors tangent to the sphere, $\boldsymbol{m}$, and $\bar{\boldsymbol{m}}$. Though these vectors will also become singular at points on the sphere, we are free to use a different tetrad on S in these regions, just as we can cover the sphere everywhere with smooth coordinates using overlapping charts. Secondly, the vanishing of radiation does not occur because the null vector $\boldsymbol{n}$ coincides with a principal null direction of the spacetime. We note that, if Ψ_4 vanishes at a point on S, then a change of basis cannot make Ψ_4 (or any of the other curvature scalars) nonvanishing. For example, a rotation about $\boldsymbol{l}$ by a complex parameter a induces a transformation on the other basis vectors,

$$\begin{aligned} \boldsymbol{l}' &= \boldsymbol{l}\,, \\ \boldsymbol{m}' &= \boldsymbol{m} + a\boldsymbol{l}\,, \\ \bar{\boldsymbol{m}}' &= \bar{\boldsymbol{m}} + \bar{a}\boldsymbol{l}\,, \\ \boldsymbol{n}' &= \boldsymbol{n} + a\bar{\boldsymbol{m}} + \bar{a}\boldsymbol{m} + a\bar{a}\boldsymbol{l}\,. \end{aligned} \tag{9.9}$$

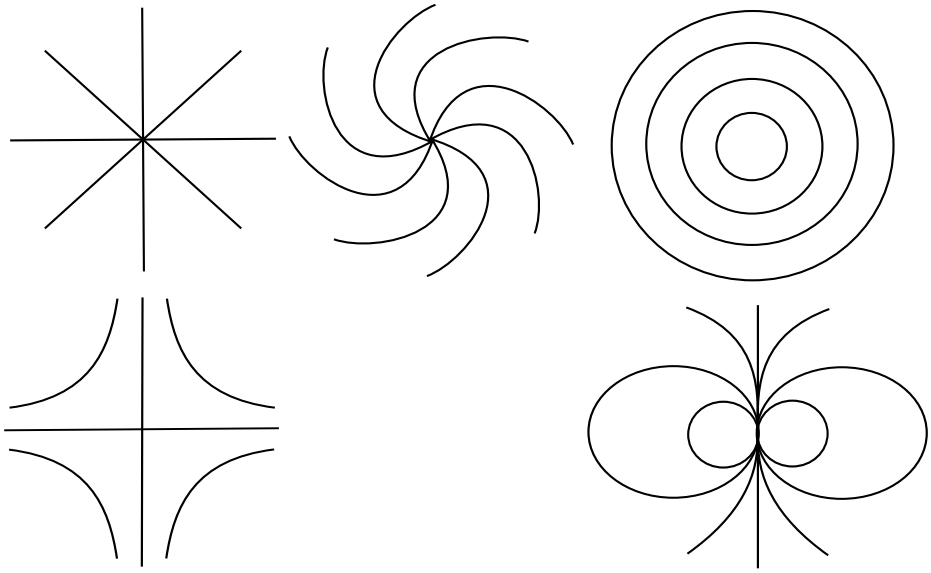

Figure 9.3: Top row: Diagrams of three orientable ridge patterns, which can be made from a combination of two loops, all with index $i = 1$. Bottom row: On the left is an orientable ridge pattern with index $i = -1$ (which is identical to a saddle point of a vector field). It can be constructed by joining two triradius singularities. The figure on the right shows a dipole-like pattern with index $i = 2$, which can come from the coincidence of four loops.

Under this rotation, Ψ_4 transforms as

$$\Psi_4' = \Psi_4 + 4\bar{a}\Psi_3 + 6\bar{a}^2\Psi_2 + 4\bar{a}^3\Psi_1 + \bar{a}^4\Psi_0\,, \tag{9.10}$$

which vanishes when the Weyl scalars are zero in the original basis. The remaining scalars transform analogously, and the other independent tetrad transformations are also homogeneous in the Weyl scalars (see, e.g., [10]).

9.4 Examples from Linearized Gravity

We now give several examples of the tendex and vortex lines on S from weak-field, multipolar sources. We first investigate quadrupolar radiation, produced by a time-varying quadrupole moment. For many astrophysical sources, such as the inspiral of comparable-mass compact objects, the gravitational radiation is predominantly quadrupolar. As a result, our calculations will capture features of the radiation coming from these astrophysical systems. We will then study a combination of rotating mass- and current-quadrupole moments that are locked in phase. The locking of these moments was observed by Schnittman et al. [15] in their analysis of black-hole kicks using a multipolar decomposition of the gravitational waveform (including that of the superkick merger). We conclude this section by discussing isolated higher multipoles. Although it is unlikely that astrophysical sources will contain only higher multipoles, it is still of interest to understand the tendex lines of these mul-

tipoles. More importantly, while the tidal tensor is a linear combination of multipoles, the tendex lines will depend nonlinearly on the different moments. Actual astrophysical sources will contain a superposition of multipoles, and it is important to see how superpositions of multipoles change the leading-order quadrupole pattern.

We perform our calculations in linearized theory about flat space, and we use spherical polar coordinates and their corresponding unit vectors for our basis. One can compute from the multipolar metric in [16] that for a symmetric, trace-free (STF) quadrupole moment $\mathcal{I}_{ab}$, the leading-order contributions to $\boldsymbol{\mathcal{E}}$ and $\boldsymbol{\mathcal{B}}$ on S are

$$\mathcal{E}^{(\ell=2)}_{ab} = -\frac{1}{2r}\left[{}^{(4)}\mathcal{I}_{ab}(t-r) + \epsilon_{ac}{}^{(4)}\mathcal{I}_{cd}(t-r)\epsilon_{db}\right]^{\rm TT}, \tag{9.11}$$

$$\mathcal{B}^{(\ell=2)}_{ab} = -\frac{1}{r}\left[\epsilon_{c(a}{}^{(4)}\mathcal{I}_{b)c}(t-r)\right]^{\rm TT}. \tag{9.12}$$

Here, the superscript ${}^{(4)}$ indicates four time derivatives, TT means to take the transverse-traceless projection of the expression, and ϵ_{ac} is the antisymmetric tensor on a sphere. In this expression, and in what follows, the Latin indices run only over the basis vectors $\boldsymbol{e}_\theta$ and $\boldsymbol{e}_\phi$, and repeated Latin indices are summed over even when they are both lowered.

9.4.1 Rotating Mass Quadrupole

As our first example, we calculate the STF quadrupole moment of two equal point masses (with mass $M/2$) separated by a distance, a, in the equatorial plane, and rotating at an orbital frequency Ω. We find that

$$\begin{aligned}
{}^{(4)}\mathcal{I}_{\theta\theta}(t-r) &= Ma^2\Omega^4(1+\cos^2\theta)\cos\{2[\phi-\Omega(t-r)]\}\,,\\
{}^{(4)}\mathcal{I}_{\theta\phi}(t-r) &= -2Ma^2\Omega^4\cos\theta\sin\{2[\phi-\Omega(t-r)]\}\,,\\
{}^{(4)}\mathcal{I}_{\phi\phi}(t-r) &= -{}^{(4)}\mathcal{I}_{\theta\theta}(t-r)\,.
\end{aligned} \tag{9.13}$$

By substituting these expressions into Eqs. (9.11) and (9.8), we find the eigenvectors of the tidal field. We can then calculate the tendex lines on the sphere by solving Eq. (9.4) with a convenient normalization of the parameter along the curves,

$$\frac{d\theta}{ds} = \frac{1}{r}{}^{(4)}\mathcal{I}_{\theta\phi}\,, \tag{9.14}$$

$$\frac{d\phi}{ds} = \frac{1}{r\sin\theta}(-{}^{(4)}\mathcal{I}_{\theta\theta}-\lambda_+)\,. \tag{9.15}$$

Here, λ_+ is the positive eigenvalue. The differential equation for the vortex lines, found from the corresponding frame-drag field of Eq. (9.12), has the same form as those of the tendex lines above; however, one must replace ${}^{(4)}\mathcal{I}_{\theta\phi}$ in the first equation by ${}^{(4)}\mathcal{I}_{\theta\theta}$ and ${}^{(4)}\mathcal{I}_{\theta\theta}$ by $-{}^{(4)}\mathcal{I}_{\theta\phi}$ in the second

equation.

We show the tendex and vortex lines corresponding to the positive eigenvalues in Figs. 9.4 and 9.5, respectively, at a retarded time $t - r = 0$. We also plot the magnitude of the eigenvalue on the sphere, using a color scheme in which purple (darker) regions at the poles correspond to large eigenvalues and yellow (lighter) colors near the equator are closer to zero. Both the tendex and vortex lines have four equally spaced loop singularities on the equator at the points where the field is zero (the two on the back side of the sphere are not shown). Because the vortex and tendex lines must cross each other at an angle of $\pi/4$, the global geometric patterns are quite different.

We note here that these two figures also provide a visualization for the transverse-traceless, "pure-spin" tensor spherical harmonics [16]. For example, we can see that the mass-quadrupole tendex lines are the integral curves of the eigenvectors of the real part of the $\ell = 2,\ m = 2$ electric-type transverse-traceless tensor harmonic. First, the tendex lines correspond to the electric-type harmonic, because the tidal tensor is even under parity. Second, the radiation pattern will not contain an $\ell = 2,\ m = 0$ harmonic, because the overall magnitude of the quadrupole moment of the source is not changing in time; also, the $\ell = 2,\ m = \pm 1$ harmonics are absent, because the source is an equal-mass binary and is symmetric under a rotation of π radians. Finally, the $\ell = 2,\ m = -2$ moment is equal in magnitude to the $m = 2$ harmonic, because the tidal tensor is real. By similar considerations, we can identify the vortex lines of the mass quadrupole as a visualization of the real parts of the $\ell = 2,\ m = 2$ magnetic-type tensor harmonics.

In addition, the eigenvalue (the identical color patterns of Figs. 9.4 and 9.5) is given by the magnitude of the sum of spin-weighted spherical harmonics,

$$\lambda_+ \propto \left| {}_{-2}Y_{22} + {}_{-2}Y_{2-2} \right| . \tag{9.16}$$

One can see this most easily by using the symmetries described above, the expression for the eigenvalue $\lambda_+ = |\Psi_4|/2$, and the spin-weighted spherical harmonic decomposition of Ψ_4. It is also possible to verify this expression using the tensor harmonics above and the standard relations between tensor spherical harmonics and spin-weighted spherical harmonics (see, e.g., [16]). Radiation from numerical spacetimes is usually decomposed into spin-weighted spherical harmonics, and, as a result, the pattern of the eigenvalue is familiar. The tendex lines, however, also show the polarization pattern of the waves on S (a feature that numerical simulations rarely explicitly highlight). Figure 9.4 (and the accompanying negative-tendicity lines not shown) gives the directions of preferred strain on S, and, hence, the wave's polarization that can be inferred from gravitational-wave-interferometer networks such as LIGO/VIRGO. Thus, visualizations such as Fig. 9.4 give complete information about the gravitational waves passing through S.

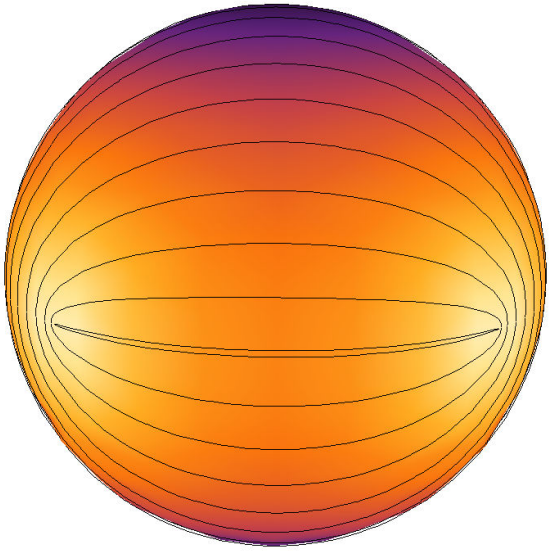

Figure 9.4: The positive tendex lines on S generated by a rotating quadrupole moment in linearized gravity. The sphere is colored by the magnitude of the eigenvalue; purple (darker) areas at the poles corresponding to a large eigenvalue, and yellow (lighter) areas near the equator indicate a value closer to zero. Four loop singularities appear equally spaced on the equator at the points of vanishing tendicity.

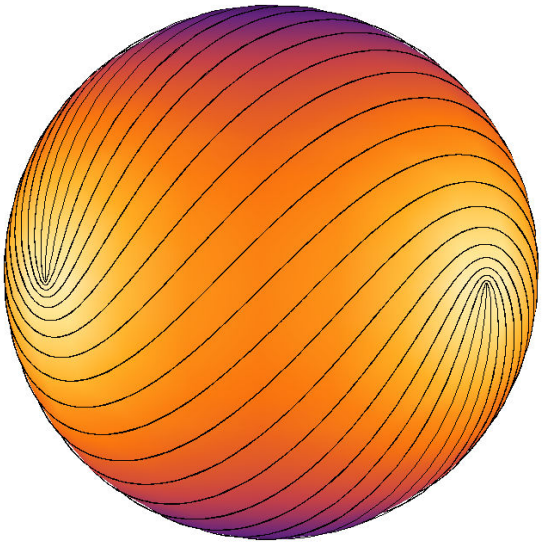

Figure 9.5: As in Fig. 9.4, we show the positive vortex lines and their magnitude of the eigenvalue on S (using the same coloring as in that figure). The loop singularities lie at the same locations as they do for the tendex lines, but they are locally rotated by $\pi/4$ radians.

9.4.2 Rotating Mass and Current Quadrupoles in Phase

As our second example, we will consider a source that also has a time-varying current-quadrupole moment, $\mathcal{S}_{ab}$. In linearized theory, one can show that the tidal tensor and frame-drag field of a current quadrupole are related simply to those of a mass quadrupole. In fact, $\mathcal{B}_{ab}$ of the current quadrupole has exactly the same form as $\mathcal{E}_{ab}$ of a mass quadrupole, Eq. (9.11), when one replaces ${}^{(4)}\mathcal{I}_{ab}$ by $(4/3){}^{(4)}\mathcal{S}_{ab}$. Similarly, $\mathcal{E}_{ab}$ of the current quadrupole is identical to $\mathcal{B}_{ab}$ of a mass quadrupole, Eq. (9.12), when ${}^{(4)}\mathcal{I}_{ab}$ is replaced by $-(4/3){}^{(4)}\mathcal{S}_{ab}$.

We impose that the source's mass- and current-quadrupole moments rotate in phase, with frequency Ω, and with the current quadrupole lagging in phase by $\pi/2$ radians. This arrangement of multipoles models the lowest multipoles during the merger and ringdown of the extreme-kick configuration (a collision of equal-mass black holes in a quasicircular orbit that have spins of equal magnitude lying in the orbital plane, but pointing in opposite directions), when the mass- and current-quadrupole moments rotate in phase [15]. The relative amplitude of the mass- and current-multipoles depends upon, among other variables, the amplitude of the black-holes' spin. We, therefore, include a free parameter C in the strength of the current quadrupole which represents the effect of changing the spin. An order-of-magnitude estimate based on two fast-spinning holes orbiting near the end of their inspiral indicates that their amplitudes could be nearly equal, $C = O(1)$. To determine the exact relative amplitude of the mass- and current-quadrupole moments of the radiation would require comparison with numerical-relativity results.

We calculate the current-quadrupole moment by scaling the mass quadrupole by the appropriate factor of C and letting the term $2[\phi-\Omega(t-r)]$ in the equations for $\mathcal{I}_{ab}(t-r)$ become $2[\phi-\Omega(t-r)]-\pi/2$ in the corresponding expressions for $\mathcal{S}_{ab}(t-r)$. In linearized theory, the tidal tensor and frame-drag fields of the different multipoles add directly. As a result, the equations for the tendex lines have the same form as Eqs. (9.14) and (9.15), but one must now replace the mass quadrupole ${}^{(4)}\mathcal{I}_{\theta\phi}$ by ${}^{(4)}\mathcal{I}_{\theta\phi} - (4/3){}^{(4)}\mathcal{S}_{\theta\theta}$ in the first expression and ${}^{(4)}\mathcal{I}_{\theta\theta}$ by ${}^{(4)}\mathcal{I}_{\theta\theta} + (4/3){}^{(4)}\mathcal{S}_{\theta\phi}$ in the second.

First, we allow the current quadrupole to be half as large as the mass quadrupole, $C = 1/2$. We show the positive tendex lines and positive eigenvalue in Fig. 9.6. Because of the relative phase and amplitude of the two moments, the tensors add constructively in the northern hemisphere and destructively in the southern hemisphere on S. This is evident in the eigenvalue on the sphere in Fig. 9.6, which, one can argue, is now given by an unequal superposition of

$$\lambda_+ \propto \left|{}_{-2}Y_{22} + b\,{}_{-2}Y_{2-2}\right|, \tag{9.17}$$

with $b < 1$. As in previous figures, dark colors (black and purple) represent where the eigenvalue is large, and light colors (white and yellow) show where it is nearly zero. Although the singular points are still equally spaced on a line of constant latitude, they no longer reside on the equator; they now

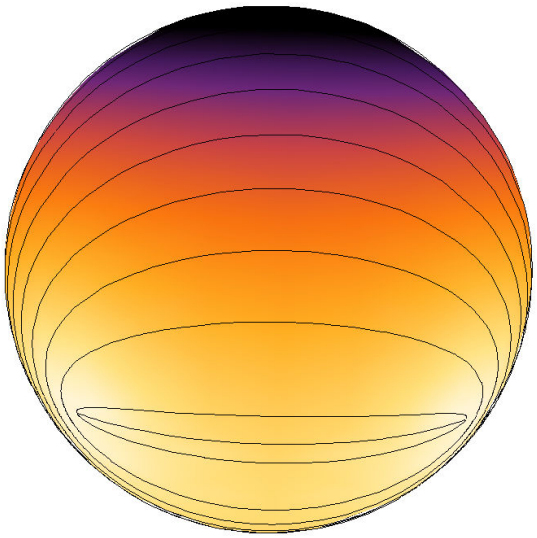

Figure 9.6: The positive tendex lines on S generated by the superposition of rotating mass- and current-quadrupole moments, $\pi/2$ radians out of phase, in linearized gravity. The sphere is colored by the tendicity as in Fig. 9.4. Interference between the moments leads to beaming of the radiation toward the northern pole. Similarly, the singular points of the tendex lines now fall on a line of constant latitude in the southern hemisphere.

fall in the southern hemisphere. This is a direct consequence of the beaming of radiation toward the northern pole.

The case shown above has strong beaming, but it is possible to make the beaming more pronounced. To get the greatest interference of the multipoles, the mass and current quadrupoles must have equal amplitude in the tidal field. Because the tidal field of the current quadrupole is 4/3 as large as the tidal field of the mass quadrupole, setting $C = 3/4$ gives the strongest constructive interference in the tidal fields. In this case, the eigenvalue vanishes at just one point, the southern pole, and the eigenvalue can be shown to be proportional to just a single spin-weighted spherical harmonic,

$$\lambda_+ \propto |{}_{-2}Y_{22}| \,. \tag{9.18}$$

As a result, the four equally spaced singular points of the tendex lines must coincide at one singular point whose index must be $i = 2$. This is precisely the dipole-like pattern depicted in Fig. 9.3. We show the tendex lines around the south pole in Fig. 9.7. The vortex lines are identical to the tendex lines, but they are globally rotated by $\pi/4$ radians in this specific case.

We see that the beaming can be maximized by carefully tuning the phase and amplitude of the mass- and current-quadrupole moments. Interestingly, the maximally beamed configuration corresponds with the coincidence of all singular points at the south pole in the radiation zone. Whether this degree of beaming could occur from astrophysical sources is an open question.

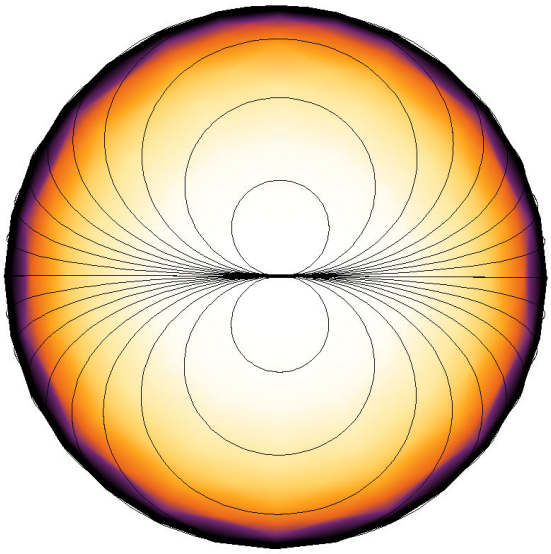

Figure 9.7: Southern polar region of the tendex-line pattern of a gravitational wave generated by rotating mass- and current-quadrupole moments. The amplitude and phase of the moments are chosen so that the radiation vanishes only at the southern pole. The purple (darker) areas indicate a positive eigenvalue, while yellow (lighter) areas are values closer to zero. The singularity at the pole has index $i = 2$.

9.4.3 Higher Multipoles of Rotating Point Masses

We also investigate the effect of including higher multipoles on the tendex lines on S. For the orbiting, nonspinning, point masses of the first example, the next two lowest multipoles arise from the current octopole (the $\ell = 3$ STF moment [16]) and the mass hexadecapole (the $\ell = 4$ STF moment). From the multipolar metric in [16], one can show that the tidal field for these two moments are

$$\mathcal{E}^{\ell=3}_{ab} = -\frac{1}{2r}\left[\epsilon_{c(a}{}^{(5)}\mathcal{S}_{b)cr}(t-r)\right]^{\rm TT}, \tag{9.19}$$

$$\mathcal{E}^{\ell=4}_{ab} = -\frac{1}{24r}\left[{}^{(6)}\mathcal{I}_{abrr}(t-r) + \epsilon_{ac}\epsilon_{db}{}^{(4)}\mathcal{I}_{cdrr}(t-r)\right]^{\rm TT}, \tag{9.20}$$

where the index r indicates contraction with the radial basis vector $\boldsymbol{e}_r$, and repeated r indices are not being summed over. The STF current-octopole moment, can be expressed compactly as $\mathcal{S}_{ijk} = (L^i_N x^j_A x^k_A)^{\rm STF}$, where L^i_N is the Newtonian angular momentum and x^j_A is the position of one of the point masses. The superscript STF indicates that all indices should be symmetrized, and all traces removed. In Cartesian coordinates, the vectors have the simple forms $\mathbf{L}_N = (0, 0, Mav/4)$ and $\mathbf{x}_A = (a/2)(\cos[\Omega t], \sin[\Omega t], 0)$, where Ω is the Keplerian frequency and v is the relative velocity. Similarly, one can write the STF mass-hexadecapole moment as $\mathcal{I}_{ijkl} = M(x^i_A x^j_A x^k_A x^l_A)^{\rm STF}$, for the same vector x^j_A as above. Because these tensors have many components, we shall only list those that are relevant for finding the tendex lines. We will also define $\alpha = \phi - \Omega(t-r)$ for convenience.

For the current octopole the relevant components are

$$
\begin{aligned}
{}^{(5)}\mathcal{S}_{\theta\theta r}(t-r) &= -\frac{Ma^3 v\Omega^5}{24}(5\cos\theta + 3\cos 3\theta)\sin 2\alpha\,, \\
{}^{(5)}\mathcal{S}_{\theta\phi r}(t-r) &= -\frac{Ma^3 v\Omega^5}{3}\cos 2\theta\cos 2\alpha\,, \\
{}^{(5)}\mathcal{S}_{\phi\phi r}(t-r) &= -{}^{(5)}\mathcal{S}_{\theta\theta r}(t-r)\,,
\end{aligned}
\tag{9.21}
$$

and for the mass hexadecapole, they are

$$
{}^{(6)}\mathcal{I}_{\theta\theta rr}(t-r) = \frac{Ma^4\Omega^6}{8}[(\cos^2\theta + \cos 4\theta)\cos 2\alpha - 128\sin^2\theta(1+\cos^2\theta)\cos 4\alpha]\,,
$$

$$
{}^{(6)}\mathcal{I}_{\theta\phi rr}(t-r) = -\frac{Ma^4\Omega^6}{4}[\cos 3\theta\sin 2\alpha - 128\sin^2\theta\cos\theta\sin 4\alpha]\,, \tag{9.22}
$$

$$
{}^{(6)}\mathcal{I}_{\phi\phi rr}(t-r) = -{}^{(6)}\mathcal{I}_{\theta\theta rr}(t-r)\,. \tag{9.23}
$$

The tendex lines of the current octopole can be found by solving the system of differential equations in Eqs. (9.14) and (9.15) by substituting ${}^{(4)}\mathcal{I}_{\theta\phi}$ by ${}^{(5)}\mathcal{S}_{\theta\theta r}/2$ and ${}^{(4)}\mathcal{I}_{\theta\theta}$ by $-{}^{(5)}\mathcal{S}_{\theta\phi r}/2$ Similarly, for the mass hexadecapole, one must make the substitutions of ${}^{(4)}\mathcal{I}_{\theta\phi}$ by ${}^{(6)}\mathcal{I}_{\theta\phi rr}/12$ and ${}^{(4)}\mathcal{I}_{\theta\theta}$ by ${}^{(6)}\mathcal{I}_{\theta\theta rr}/12$ in the same equations.

In Fig. 9.8 we show the tendex lines for the current octopole, and in Fig. 9.9 we show the lines for the mass hexadecapole. Together with the mass quadrupole, Fig. 9.4, these are the three lowest multipole moments for the equal-mass circular binary. For the current octopole, there are eight triradius singular points and 12 loop singularities (and thus the net index is two). Four of the loop singularities remain equally spaced on the equator, at the same position of those of the quadrupole, but the remaining singularities appear at different points on S. The mass hexadecapole has eight loop singularities equally spaced on the equator, and there are integer-index, saddle-point-like singularities at each pole.

Gravitational radiation from astrophysical sources will likely not be dominated by these higher multipoles. Nevertheless, these figures are of interest as examples of tendex lines with many singular points and as visualizations of tensor harmonics. By analyzing the symmetries in a way analogous to that discussed in Section 9.4.1, we can identify the current-octopole tendex lines with the integral curves of $\ell = 3,\ m = 2$ magnetic-type harmonics, and we can associate the mass-hexadecapole lines with those of the $\ell = 4,\ m = 4$ electric-type harmonics. In the case of the mass hexadecapole, the $m = 2$ moment is not ruled out by symmetry, but it is suppressed relative to the $m = 4$ moment. This occurs because the $m = 4$ moment oscillates at twice the frequency of the $m = 2$ moment, and the tidal tensor for this higher-order moment is given by taking six time derivatives of the STF moment, Eq. (9.23). This enhances the $m = 4$ radiation by a factor of 2^6 over the $m = 2$ contribution. Similarly, we can relate the eigenvalue to the magnitude of the corresponding

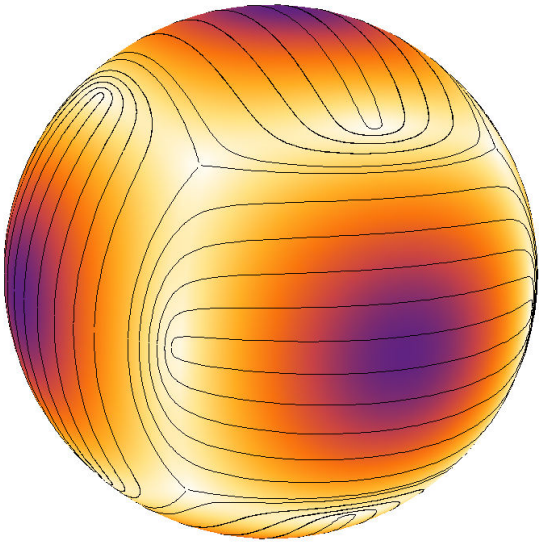

Figure 9.8: The tendex lines of a current-octopole moment of an equal-mass, circular binary of point masses. The colors on the sphere represent the tendicity, with the same scale described in Fig. 9.4. The current octopole also has four loop singularities on the equator (at the same position of those of the rotating quadrupole), but it has eight additional loops and eight triradius singularities away from the equator. Only half of the singular points are visible on the sphere; the other half appear on the back side.

sum of $s = -2$ spin-weighted spherical harmonics, and the tendex-line patterns to the polarization directions that could be inferred from networks of gravitational-wave interferometers.

Finally, we show the tendex lines generated from the linear combination of the three lowest multipole moments in Fig. 9.10. Any astrophysical source will contain several multipoles, with the quadrupole being the largest. The tendex lines depend nonlinearly on the multipoles, and it is important, therefore, to see to what extent higher multipoles change the overall pattern. We find the total tidal tensor by linearly combining the tidal tensor of each individual moment, and we then find the eigenvectors and tendex lines of the total tidal tensor. The pattern formed from the combination of multipoles depends upon the parameters of the binary; in making this figure we assumed (in units in which $M = 1$) a separation of $a = 15$, an orbital frequency $\Omega = a^{-3/2}$, and a velocity $v = a\Omega = a^{-1/2}$. When these higher moments are combined with the mass quadrupole, the tendex-line structure resembles that of the mass quadrupole. The pattern is deformed slightly, however, by the presence of the higher multipoles. The loop singularities on the equator are no longer evenly spaced; rather, the pair illustrated (and the corresponding pair which is not visible) are pushed slightly closer together.

9.5 Conclusions

Tendex and vortex lines provide a new tool with which to visualize and study the curvature of spacetime. They allow for the visualization of the Riemann tensor, through its decomposition into

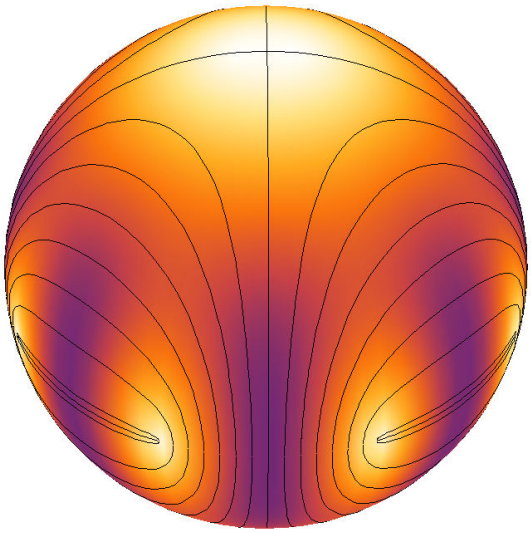

Figure 9.9: The tendex lines on S of the mass hexadecapole of an equal-mass, circular binary of point masses, with the sphere colored by the tendicity as in Fig. 9.4. The hexadecapole has eight loop singularities equally spaced on the equator and two saddle-point-like singularities (from the coincidence of two triradius singularities at a point) at the poles. Again, only half are visible in the figure. Four of the singular points on the equator coincide with those of the quadrupole, but the remaining four appear at different locations.

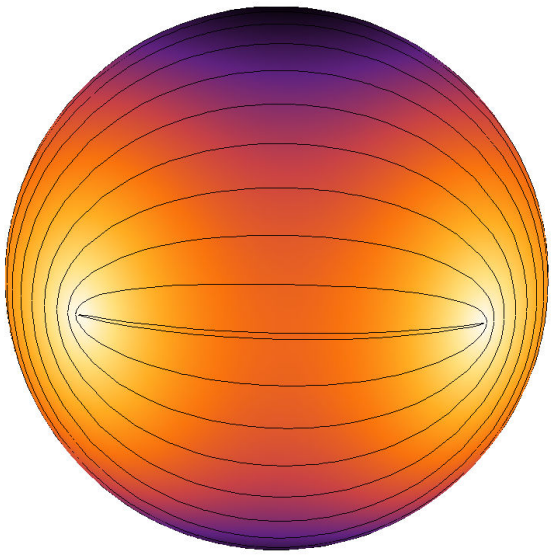

Figure 9.10: The tendex lines of a superposition of mass-quadrupole, current-octopole, and mass-hexadecapole moments of an equal-mass circular binary. It assumes a total mass $M = 1$, a separation $a = 15$, an orbital frequency $\Omega = a^{-3/2}$, and a velocity $v = a\Omega = a^{-1/2}$. The sphere is colored by the tendicity in an identical way to that of Fig. 9.4. When the tidal tensors of the three multipoles are combined, the net pattern is dominated by the quadrupole and contains only the four loops. The loop singularities are no longer equally spaced on the equator; the two pairs are pushed closer together because of the influence of the higher multipoles.

two simpler, trace-free and symmetric spatial tensors. These tensors, $\boldsymbol{\mathcal{E}}$ and $\boldsymbol{\mathcal{B}}$, can be completely characterized by their eigenvectors and corresponding eigenvalues. The integral curves of these eigenvector fields are easily visualized, and their meaning is well understood; physically, the lines can be interpreted in terms of local tidal strains and differential frame dragging. Here, the simple nature of these lines allows us to apply well-known topological theorems to study the radiation passing through a sphere near null infinity.

Tendex-line patterns must develop singularities (and thus have vanishing tendicity) on a closed surface. When we applied this fact to the tendex lines of gravitational radiation near null infinity from arbitrary physical systems, we could easily show that the gravitational radiation must vanish in isolated directions. Although this result is somewhat obvious in retrospect and has been noted before [8], the result does not appear to be well-known. We also began exploring the manner in which these singular points can provide a sort of fingerprint for radiating spacetimes. The essential elements of this fingerprint consist of the zeros of the curvature on the sphere, together with the index and the tendex-line pattern around these zeros. We studied these patterns for a few specific examples, such as the four equally spaced loops of a rotating mass quadrupole. A more interesting case is that of a radiating spacetime composed of locked, rotating mass and current quadrupoles, which can be thought of as a simplified model of the late stages of the extreme-kick black-hole-binary merger. Here, the shifted positions of the singular points of the tendex pattern provide a direct illustration of gravitational beaming for this system. By seeking the most extreme topological arrangement of singular points, we also described a maximally beaming configuration of this system.

The radiation generated by higher-order STF multipole moments gives more complex examples of tendex and vortex patterns, with many singular points of varied types. Additionally, we argued that their tendex and vortex patterns provide a visualization of the tensor spherical harmonics on the sphere; the eigenvalue illustrates the magnitude of these harmonics, and the lines show the tensor's polarization in an intuitive manner. The sum of the three multipoles illustrated in Fig. 9.10 shows how including higher-order multipoles slightly deforms the pattern of quadrupole radiation to make a more accurate total radiation pattern of the equal-mass binary. Similar illustrations of complete radiation patterns could be readily produced from numerical spacetimes, when Ψ_4 is extracted asymptotically using a tetrad with appropriate peeling properties. Such visualizations, and their evolution in time, could provide a useful method for visualizing the gravitational emission from these systems.

This study of the tendex and vortex lines (and their singular points) of asymptotic radiation fields is one of several [4] exploring and developing this new perspective on spacetime visualization. Naturally, it would be of interest to extend the two-dimensional case here to a larger study of the singular points in the full, three-dimensional tendex and vortex fields. Methods to find and visualize the singular points (and singular lines) of 3D tensors have been discussed preliminarily in

[17], though there is still room for further work. We suspect that singular points will be important in visualizing and studying the properties of numerical spacetimes with these methods. Further, we expect that there is still much to be learned from the study of the vortexes and tendexes of dynamical spacetimes.

Bibliography

[1] R. Owen et al., Phys. Rev. Lett. **106**, 151101 (2011).

[2] R. Maartens and B. A. Bassett, Classical Quantum Gravity **15**, 705 (1998).

[3] F. B. Estabrook and H. D. Wahlquist, J. Math. Phys. **5**, 1629 (1964).

[4] D. A. Nichols, R. Owen, F. Zhang, A. Zimmerman, J. Brink, Y. Chen, J. D. Kaplan, G. Lovelace, K. D. Matthews, M. A. Scheel, et al., Phys. Rev. D **84**, 124014 (2011).

[5] T. Delmarcelle and L. Hesselink, in *Proceedings of the Conference on Visualization 1994* (IEEE Computer Society Press, Los Alamitos, CA, 1994), pp. 140–147.

[6] R. Penrose and W. Rindler, *Spinors and Space-time. Volume 2: Spinor and Twistor Methods in Space-time Geometry* (Cambridge University Press, Cambridge, 1986).

[7] R. Penrose, Ann. Human Genet., Lond. **42**, 435 (1979).

[8] R. Penrose, Proc. Roy. Soc. A **284**, 159 (1965).

[9] M. Campanelli, C. O. Lousto, Y. Zlochower, and D. Merritt, Phys. Rev. Lett. **98**, 231102 (2007).

[10] H. Stephani, D. Kramer, M. MacCallum, C. Hoenselaers, and E. Herlt, *Exact Solutions of Einstein's Field Equations* (Cambridge University Press, Cambridge, 2003).

[11] H. Bondi, M. G. J. van der Burg, and A. W. K. Metzner, Proc. R. Soc. A **269**, 21 (1962).

[12] L. A. Tamburino and J. H. Winicour, Phys. Rev. **150**, 1039 (1966).

[13] E. Newman and R. Penrose, J. Math. Phys. **3**, 566 (1962).

[14] D. R. Fiske, J. G. Baker, J. R. van Meter, D.-I. Choi, and J. M. Centrella, Phys. Rev. D **71**, 104036 (2005).

[15] J. D. Schnittman, A. Buonanno, J. R. van Meter, J. G. Baker, W. D. Boggs, J. Centrella, B. J. Kelly, and S. T. McWilliams, Phys. Rev. D **77**, 044031 (2008).

[16] K. S. Thorne, Rev. of Mod. Phys. **52**, 299 (1980).

[17] J. Weickert and H. Hagen, eds., *Visualization and Processing of Tensor Fields* (Springer Verlag, Berlin, 2006).

Chapter 10

Visualizing Spacetime Curvature via Frame-Drag Vortexes and Tidal Tendexes: I. General Theory and Weak-Gravity Applications

When one splits spacetime into space plus time, the Weyl curvature tensor (vacuum Riemann tensor) gets split into two spatial, symmetric, and trace-free (STF) tensors: (i) the Weyl tensor's so-called "electric" part or *tidal field* $\mathcal{E}_{jk}$, which raises tides on the Earth's oceans and drives geodesic deviation (the relative acceleration of two freely falling test particles separated by a spatial vector ξ^k is $\Delta a_j = -\mathcal{E}_{jk}\xi^k$); and (ii) the Weyl tensor's so-called "magnetic" part or (as we call it) *frame-drag field* $\mathcal{B}_{jk}$, which drives differential frame dragging (the precessional angular velocity of a gyroscope at the tip of ξ^k, as measured using a local inertial frame at the tail of ξ^k, is $\Delta\Omega_j = \mathcal{B}_{jk}\xi^k$).

Being STF, $\mathcal{E}_{jk}$ and $\mathcal{B}_{jk}$ each have three orthogonal eigenvector fields which can be depicted by their integral curves. We call the integral curves of $\mathcal{E}_{jk}$'s eigenvectors *tidal tendex lines* or simply *tendex lines*, we call each tendex line's eigenvalue its *tendicity*, and we give the name *tendex* to a collection of tendex lines with large tendicity. The analogous quantities for $\mathcal{B}_{jk}$ are *frame-drag vortex lines* or simply *vortex lines*, their *vorticities*, and *vortexes*.

These concepts are powerful tools for visualizing spacetime curvature. We build up physical intuition into them by applying them to a variety of weak-gravity phenomena: a spinning, gravitating point particle, two such particles side-by-side, a plane gravitational wave, a point particle with a dynamical current-quadrupole moment or dynamical mass-quadrupole moment, and a slow-motion binary system made of nonspinning point particles. We show that a rotating current quadrupole has four rotating vor-

texes that sweep outward and backward like water streams from a rotating sprinkler. As they sweep, the vortexes acquire accompanying tendexes and thereby become outgoing current-quadrupole gravitational waves. We show similarly that a rotating mass quadrupole has four rotating, outward-and-backward sweeping tendexes that acquire accompanying vortexes as they sweep, and become outgoing mass-quadrupole gravitational waves. We show, further, that an oscillating current quadrupole ejects sequences of vortex loops that acquire accompanying tendex loops as they travel, and become current-quadrupole gravitational waves; and similarly for an oscillating mass quadrupole. And we show how a binary's tendex lines transition, as one moves radially, from those of two static point particles in the deep near zone, to those of a single spherical body in the outer part of the near zone and inner part of the wave zone (where the binary's mass monopole moment dominates), to those of a rotating quadrupole in the far wave zone (where the quadrupolar gravitational waves dominate).

In Paper II we will use these vortex and tendex concepts to gain insight into the quasi-normal modes of black holes, and in subsequent papers, by combining these concepts with numerical simulations, we will explore the nonlinear dynamics of curved spacetime around colliding black holes. We have published a brief overview of these applications in *Physical Review Letters* [1]. We expect these vortex and tendex concepts to become powerful tools for general-relativity research in a variety of topics.

Originally published as D. A. Nichols, R. Owen, F. Zhang, A. Zimmerman, J. Brink, Y. Chen, J. D. Kaplan, G. Lovelace, K. D. Matthews, M. A. Scheel, and K. S. Thorne, Phys. Rev. D **84** 124014 (2011).

10.1 Motivation and Overview

In the 1950s, John Archibald Wheeler coined the phrase *geometrodynamics* to epitomize his intuition that curved spacetime must have a rich range of nonlinear dynamical behaviors—behaviors that are important in our Universe and are worthy of probing deeply by both theoretical and observational means (see [2] and earlier papers by Wheeler reprinted therein and also [3]). It was obvious to Wheeler that analytical tools by themselves would not be sufficient to reveal the richness of geometrodynamics; he, therefore, encouraged his colleagues and students to begin developing numerical tools [4, 5, 6], and he encouraged Joseph Weber to develop technology for gravitational-wave observations [7].

Today, a half century later, numerical relativity has finally reached sufficient maturity (for a review, see [8] and the references therein) that, hand in hand with analytical relativity, it can be used to explore nonlinear geometrodynamics in generic situations; and gravitational-wave detectors

are sufficiently mature [9, 10, 11, 12, 13] that they may soon observe nonlinear geometrodynamics in black-hole collisions.

Unfortunately, there is a serious obstacle to extracting geometrodynamical insights from numerical-relativity simulations: a paucity of good tools for visualizing the dynamics of curved spacetime. We are reasonably sure that buried in the billions of numbers produced by numerical-relativity simulations there are major discoveries to be made, but extracting those discoveries is exceedingly difficult and perhaps impossible with the tools we have had thus far.

Until now, curved spacetime has been visualized primarily via (isometric) embedding diagrams (Section 23.8 of [14]): choosing spacelike two-dimensional surfaces in spacetime, and embedding them in flat 3-dimensional Euclidean space or 2+1-dimensional Minkowski spacetime in a manner that preserves the surfaces' intrinsic geometry. (For some examples of embedding diagrams applied to black-hole spacetimes, see, e.g., [15, 16, 17]). Unfortunately, such embedding diagrams are of very limited value. They capture only two dimensions of spacetime, and the 2-surfaces of greatest interest often cannot be embedded globally in flat Euclidean 3-space or flat Minkowski 2+1-dimensional spacetime [15, 18, 19, 20]. Mixed Euclidean/Minkowski embeddings are often required (e.g., Fig. 4 of [15]), and such embeddings have not proved to be easily comprehended. Moreover, although it is always possible to perform a local embedding in a flat 3-space (in the vicinity of any point on the two-surface), when one tries to extend the embedding to cover the entire two-surface, one often encounters discontinuities analogous to shocks in fluid mechanics [18, 20].

A systematic approach to understanding the connection between nonlinear near-field dynamics in general relativity and emitted gravitational waves is being developed by Rezzolla, Jaramillo, Macedo, and Moesta [21, 22, 23, 24]. This approach focuses on correlations between data on a surface at large radius (ideally null infinity) and data on world tubes in the source region (such as black-hole horizons). The purpose is to use such correlations to infer the dynamics of a black hole (e.g., the kick) directly from data on its horizon. While we find this approach exciting and attractive, in our own work we seek a more direct set of tools: tools that can probe the dynamics of spacetime curvature that cause such correlations in the first place, and that can be more readily and intuitively applied to a wider range of other geometrodynamic phenomena. It is our hope that eventually our tools and those of Rezzolla et al. [21, 22, 23] will provide complementary pictures for understanding spacetime dynamics, and particularly black-hole kicks.

We have introduced our new set of tools in a recent paper in *Physical Review Letters* [1]. They are tools for visualizing spacetime curvature, called *tidal tendex lines, tendicities, and tendexes*; and *frame-drag vortex lines, vorticities and vortexes*. These tools capture the full details of the Weyl curvature tensor (vacuum Riemann tensor), which embodies spacetime curvature. They do so in three-dimensional, dynamically evolving pictures, of which snapshots can be printed in a paper such

as this one, and movies can be made available online.[1] Specifically, as of this writing two movies can be seen at [26, 27]; one shows the vortex lines from a rotating current quadrupole, the other, vortex lines from two particles that collide head-on with transverse, antiparallel spins.

We have found these tools to be an extremely powerful way to visualize the output of numerical simulations. We have also used them to obtain deep new insights into old analytical spacetimes. We have applied them, thus far, to pedagogical linear-gravity problems (this paper and [28]), to stationary and perturbed black holes (Paper II in this series), and to simulations of the inspiral and mergers of spinning black holes ([1] and Paper III). We plan to apply them in the future in a variety of other geometrodynamical venues, such as black holes ripping apart neutron stars and curved spacetime near various types of singularities.

This is the first of a series of papers in which we will (i) present these tools, (ii) show how to use them, (iii) build up physical intuition into them, and (iv) employ them to extract geometrodynamical insights from numerical-relativity simulations.

Specifically, in this paper (Paper I), we introduce these vortex and tendex tools, and we then apply them to weak-gravity situations (linearized general relativity) with special focus on the roles of vortexes and tendexes in gravitational-wave generation. In a closely related paper [28], three of us have applied these tools to visualize asymptotic gravitational radiation and explore the topology of its vortex and tendex lines, and also to explore a linearized-gravity model of an extreme-kick merger. In Paper II we shall apply our new tools to quiescent black holes and quasinormal modes of black holes, with special focus once again on the roles of vortexes and tendexes in generating gravitational waves. In Paper III and subsequent papers we shall apply our tools to numerical simulations of binary black holes, focusing on nonlinear geometrodynamics in the holes' near zone and how the near-zone vortexes and tendexes generate gravitational waves.

The remainder of this paper is organized as follows: In Section 10.2.1 we review the well-known split of the Weyl curvature tensor into its electric and magnetic parts, $\mathcal{E}_{ij}$ and $\mathcal{B}_{ij}$, and in Section 10.2.2 we review the Maxwell-like evolution equations for $\mathcal{E}_{ij}$ and $\mathcal{B}_{ij}$ and discuss the mathematical duality between these fields. Then, in Section 10.3, we review the well-known physical interpretation of $\mathcal{E}_{ij}$ as the *tidal field* that drives geodesic deviation and the not so well-known interpretation of $\mathcal{B}_{ij}$ [29, 30] as the *frame-drag* field that drives differential frame dragging, and we derive the equation of differential frame dragging.

In Section 10.4 we introduce our new set of tools for visualizing spacetime curvature. Specifically, in Section 10.4.1 we introduce tendex lines and their tendicities, and we quantify them by their stretching or compressional force on a person; and we also introduce vortex lines and their vorticities

[1] Just as there is no unique method to evolve field lines in electromagnetism, so too is there no unique way to match tendex or vortex lines at one time with others at a later time. Nevertheless, animations of field lines are useful for pedagogical purposes and for building intuition [25]. While some of the authors and colleagues are investigating how to evolve tendex and vortex lines in generic situations, the animations of the lines posted online all have special symmetries that provide a natural way to connect lines at one time with lines at the next.

and quantify them by their twisting (precessional) force on gyroscopes attached to the head and feet of a person. Then in Section 10.4.2 we introduce *vortexes* and *tendexes* (bundles of vortex and tendex lines that have large vorticity and tendicity) and give examples. In the remainder of this paper we illustrate these new concepts by applying them to some well-known, weak-gravity, analytic examples of spacetime curvature. In Section 10.5 we focus on the spacetime curvature of stationary systems, and in Section 10.6 we focus on dynamical systems and develop physical pictures of how they generate gravitational waves.

More specifically, in Section 10.5.1, we compute $\mathcal{E}_{ij}$ and $\mathcal{B}_{ij}$ for a static, gravitating, spinning point particle; we explain the relationship of $\mathcal{B}_{ij}$ to the particle's dipolar "gravitomagnetic field," we draw the particle's tendex lines and vortex lines, and we identify two vortexes that emerge from the particle, a counterclockwise vortex in its northern polar region and a clockwise vortex in its southern polar region. In Section 10.5.2, we draw the vortex lines for two spinning point particles that sit side-by-side with their spins in opposite directions, and we identify their four vortexes. Far from these particles, they look like a single point particle with a current-quadrupole moment. In Section 10.5.3, we draw the vortex lines for such a current-quadrupole particle and identify their vortexes. Then, in Section 10.5.4, we show that the tendex lines of a mass-quadrupole particle have precisely the same form as the vortex lines of the current-quadrupole particle, and we identify the mass quadrupole's four tendexes.

Turning to dynamical situations, in Section 10.6.1 we compute $\mathcal{E}_{ij}$ and $\mathcal{B}_{ij}$ for a plane gravitational wave, we express them in terms of the Weyl scalar Ψ_4, and we draw their vortex and tendex lines. In Section 10.6.2 we explore the quadrupolar ($l = 2$, $m = 0$) angular pattern of gravitational waves from the head-on collision of two black holes, and we draw their vortex lines and tendex lines, intensity-coded by vorticity and tendicity, on a sphere in the wave zone. In Section 10.6.3 we compute $\mathcal{E}_{ij}$ and $\mathcal{B}_{ij}$ for a general, time-varying current-quadrupolar particle, and then in Sections 10.6.4 and 10.6.5 we specialize to a rotating current quadrupole and an oscillating current quadrupole, and draw their vortex and tendex lines. Our drawings and the mathematics reveal that the particle's outgoing gravitational waves are generated by its near-zone vortexes. The rotating current quadrupole has four vortexes that spiral outward and backward like four water streams from a rotating sprinkler. As it bends backward, each vortex acquires an accompanying tendex, and the vortexes and tendexes together become a gravitational-wave crest or gravitational-wave trough. The oscillating current quadrupole, by contrast, ejects vortex loops that travel outward, acquiring accompanying tendex loops with strong tendicity on the transverse segment of each loop and weak on the radial segment—thereby becoming outgoing gravitational waves.

In Section 10.6.6, we show that a time-varying mass quadrupole produces the same phenomena as a time-varying current quadrupole, but with vortexes and tendexes interchanged. In Section 10.6.7, we study the vortexes and tendexes of a slow-motion binary made of nonspinning point

particles. In the near zone, the tendex lines transition, as one moves radially outward, from those of two individual particles (radial and circular lines centered on each particle) toward those of a single spherical body (radial and circular lines centered on the binary and produced by the binary's mass monopole moment). In the transition zone and inner wave zone, the mass monopole continues to dominate. Then at radii $r \sim a^2/M$ (where a is the particles' separation and M is the binary's mass), the radiative quadrupole moment begins to take over and the tendex lines gradually transition into the outward-and-backward spiraling lines of a rotating quadrupole. We make some concluding remarks in Section 10.7.

Throughout this paper we use geometrized units with $c = G = 1$, and we use the sign conventions of MTW [14] for the metric signature, the Weyl curvature, and the Levi-Civita tensor. We use Greek letters for spacetime indices (0–3) and Latin letters for spatial indices (1–3), and we use arrows over 4-vectors and bold-face font for spatial 3-vectors and for tensors. We place a caret over indices that refer to components in an orthonormal basis.

10.2 The Tidal Field $\mathcal{E}_{ij}$ and the Frame-Drag Field $\mathcal{B}_{ij}$

10.2.1 3+1 Split of the Weyl Curvature Tensor into $\mathcal{E}_{ij}$ and $\mathcal{B}_{ij}$

For a given spacetime, the Weyl curvature tensor can be calculated from the Riemann tensor by subtracting Riemann's trace from itself; i.e., by subtracting from Riemann the following combinations of the Ricci curvature tensor $R^\mu{}_\nu$, and Ricci curvature scalar R (Eq. (13.50) of MTW [14]):

$$C^{\mu\nu}{}_{\rho\sigma} = R^{\mu\nu}{}_{\rho\sigma} - 2\delta^{[\mu}{}_{[\rho}R^{\nu]}{}_{\sigma]} + \frac{1}{3}\delta^{[\mu}{}_{[\rho}\delta^{\nu]}{}_{\sigma]}R\,. \tag{10.1}$$

Here $\delta^\mu{}_\rho$ is the Kronecker delta, and the square brackets represent antisymmetrization. Note that in vacuum, $C^{\mu\nu}{}_{\rho\sigma} = R^{\mu\nu}{}_{\rho\sigma}$, and thus, in vacuum, the Weyl tensor contains all information about the spacetime curvature.

Let us pick a foliation of spacetime into a family of spacelike hypersurfaces. We shall denote by u^μ the 4-velocity of observers who move orthogonal to the foliation's space slices, and by $\gamma_{\mu\nu} = g_{\mu\nu} + u_\mu u_\nu$ the induced spatial three-metric on these slices, so that $\gamma_\alpha{}^\mu$ is the projection operator onto the slices. As is well known (e.g., [31]), using this projection operator, one can split the Weyl tensor covariantly into two irreducible parts, which are symmetric, trace-free (STF) tensors that lie in the foliation's hypersurfaces (i.e., that are orthogonal to u^μ). These pieces are

$$\mathcal{E}_{\alpha\beta} = \gamma_\alpha{}^\rho\gamma_\beta{}^\sigma C_{\rho\mu\sigma\nu}u^\mu u^\nu\ , \quad \text{i.e.,} \quad \mathcal{E}_{ij} = C_{i\hat{0}j\hat{0}}\ , \tag{10.2a}$$

an even-parity field called the "electric" part of $C^{\mu\nu}{}_{\rho\sigma}$, and

$$\mathcal{B}_{\alpha\beta} = -\gamma_\alpha{}^\rho \gamma_\beta{}^\sigma {}^*C_{\rho\mu\sigma\nu} u^\mu u^\nu \ , \quad \text{i.e.,} \quad \mathcal{B}_{ij} = \frac{1}{2}\epsilon_{ipq} C^{pq}{}_{j\hat{0}}, \tag{10.2b}$$

an odd-parity field known as the "magnetic" part of $C^{\mu\nu}{}_{\rho\sigma}$. Here the symbol * represents the (left) Hodge dual, ${}^*C_{\rho\mu\sigma\nu} = \frac{1}{2}\epsilon_{\rho\mu\eta\lambda} C^{\eta\lambda}{}_{\sigma\nu}$, and for each field the second expression is written in 3+1 notation: the Latin (spatial) indices are components in the foliation's hypersurface, and the $\hat{0}$ is a component on the foliation's unit, time basis vector, $\vec{e}_{\hat{0}} \equiv \vec{u}$. Our normalization for the Levi-Civita tensor is that of MTW: in a right-handed orthonormal frame, $\epsilon_{\hat{0}\hat{1}\hat{2}\hat{3}} = +1$, and the spatial Levi-Civita tensor is defined by $\epsilon_{ipq} = \epsilon_{\hat{0}ipq}$, with $\epsilon_{\hat{1}\hat{2}\hat{3}} = 1$ in a right-handed orthonormal basis. Note that Eqs. (10.2) are a direct and intentional analogy to the decomposition of the Maxwell tensor of electromagnetism $F_{\mu\nu}$ into the familiar electric and magnetic fields E_i and B_i [31]:

$$E_i = F_{i\hat{0}} \ , \quad B_i = -\,{}^*F_{i\hat{0}} = \frac{1}{2}\epsilon_{ipq} F^{pq}. \tag{10.3}$$

Note that our sign conventions differ from [31], where $\epsilon_{\hat{0}\hat{1}\hat{2}\hat{3}} = -1$; therefore, our Eq. (10.2b) has an additional minus sign in order to maintain a strict analogy with the magnetic field B_i of electromagnetism. This results in a $\mathcal{B}_{ij}$ defined with a different sign convention from that in [32, 33] (for example).

10.2.2 Evolution of $\mathcal{E}_{ij}$ and $\mathcal{B}_{ij}$

The propagation equations for the Weyl tensor and its gravito-electromagnetic representation are the Bianchi identities. We shall write them down and discuss them in three contexts: a general foliation and coordinate system, the local-Lorentz frame of a freely falling observer, and the weak-gravity, nearly Minkowski spacetimes of the current paper (Paper I in this series).

10.2.2.1 General Foliation and Coordinate System in the Language of Numerical Relativity

Because this paper is a foundation for using $\mathcal{E}_{ij}$ and $\mathcal{B}_{ij}$ to interpret the results of numerical-relativity simulations, we shall write their evolution equations (the Bianchi identities) in a general coordinate system of the type used in numerical relativity, and we shall discuss these equations' mathematical structure in the language of numerical relativity.

We denote by t a time coordinate that is constant on the foliation's hypersurfaces, and by α and $\vec{\beta}$ the foliation's lapse and shift functions; one can then write the orthogonal observers' 4-velocity as $\vec{u} = \alpha^{-1}(\vec{\partial}_t - \vec{\beta})$. The 3+1 split divides the Bianchi identities into evolution equations that govern the time evolution of the spatial fields, and constraint equations that are obeyed by the fields on

each time slice. The evolution equations are [34, 35]

$$\partial_t \mathcal{E}_{ij} = \mathcal{L}_\beta \mathcal{E}_{ij} + \alpha[D_k \mathcal{B}_{l(i}\epsilon_{j)}{}^{kl} - 3\mathcal{E}^k{}_{(i}K_{j)k} + K^k{}_k \mathcal{E}_{ij} - \epsilon_i{}^{kl}\mathcal{E}_{km}K_{ln}\epsilon_j{}^{mn} + 2a_k \mathcal{B}_{l(i}\epsilon_{j)}{}^{kl}], \quad (10.4)$$

$$\partial_t \mathcal{B}_{ij} = \mathcal{L}_\beta \mathcal{B}_{ij} + \alpha[-D_k \mathcal{E}_{l(i}\epsilon_{j)}{}^{kl} - 3\mathcal{B}^k{}_{(i}K_{j)k} + K^k{}_k \mathcal{B}_{ij} - \epsilon_i{}^{kl}\mathcal{B}_{km}K_{ln}\epsilon_j{}^{mn} - 2a_k \mathcal{E}_{l(i}\epsilon_{j)}{}^{kl}]\,. \quad (10.5)$$

Here the extrinsic curvature, Lie derivative on a second rank tensor, and acceleration of the slicing are, respectively, defined by

$$K_{ij} = -\frac{1}{2\alpha}(\partial_t \gamma_{ij} - D_i\beta_j - D_j\beta_i)\,, \quad (10.6)$$

$$\mathcal{L}_\beta \mathcal{E}_{ij} = \beta^k D_k \mathcal{E}_{ij} + \mathcal{E}_{ik}D_j\beta^k + \mathcal{E}_{kj}D_i\beta^k\,, \quad (10.7)$$

$$a_k = D_k \ln\alpha\,. \quad (10.8)$$

The derivative D_i is the covariant derivative associated with the induced metric γ_{ij} on the slices. The evolution system, Eqs. (10.4) and (10.5) is closed by an additional evolution equation for the 3-metric, which is Eq. (10.6), and evolution equations for the extrinsic curvature and the 3-dimensional connection coefficients, Γ^k_{ij}, which are

$$\partial_t K_{ij} = \mathcal{L}_\beta K_{ij} - \alpha[\partial_k\Gamma^k_{ij} - \Gamma^k_{lj}\Gamma^l_{ki} + \partial_i\partial_j q + \partial_i \ln\alpha\,\partial_j \ln\alpha - \Gamma^k_{ij}\partial_k q - 2\mathcal{E}_{ij} + K^k{}_k K_{ij}]\,, \quad (10.9)$$

$$\partial_t \Gamma^k_{ij} = \mathcal{L}_\beta \Gamma^k_{ij} - \alpha D^k K_{ij} + K_{ij}D^k\alpha - 2K^k{}_{(i}D_{j)}\alpha + 2\alpha\epsilon^{kl}{}_{(i}\mathcal{B}_{j)l}\,, \quad (10.10)$$

where we have defined

$$q = \ln(\alpha\gamma^{-1/2})\,, \quad (10.11)$$

$$\mathcal{L}_\beta \Gamma^k_{ij} = \beta^l\partial_l\Gamma^k_{ij} + 2\Gamma^k_{l(j}\partial_{i)}\beta^l - \Gamma^l_{ij}\partial_l\beta^k + \partial_i\partial_j\beta^k\,. \quad (10.12)$$

The above equations are symmetric hyperbolic if q and β^i are specified functions of time and space.

The constraint equations on each slice are the definitions of $\mathcal{E}_{ij}$ and $\mathcal{B}_{ij}$,

$$\mathcal{E}_{ij} = {}^{(3)}R_{ij} + K^k{}_k K_{ij} - K^k{}_i K_{jk}\,, \quad (10.13)$$

$$\mathcal{B}_{ij} = \epsilon_j{}^{lk} D_k K_{li}\,, \quad (10.14)$$

from which the Einstein constraints follow from the condition that $\mathcal{E}_{ij}$ and $\mathcal{B}_{ij}$ are symmetric and trace-free, and the definition of Γ^k_{ij},

$$\Gamma^k_{ij} = \frac{1}{2}\gamma^{k\ell}\left(\partial_i\gamma_{j\ell} + \partial_j\gamma_{i\ell} - \partial_\ell\gamma_{ij}\right)\,. \quad (10.15)$$

The Bianchi identities imply derivative constraints on $\mathcal{E}_{ij}$ and $\mathcal{B}_{ij}$:

$$D^i\mathcal{E}_{ij} = \mathcal{B}_{ik}K^i{}_l\epsilon^{kl}{}_j\,, \tag{10.16}$$

$$D^i\mathcal{B}_{ij} = -\mathcal{E}_{ik}K^i{}_l\epsilon^{kl}{}_j\,. \tag{10.17}$$

These last equations are automatically satisfied if Eqs. (10.13) and (10.14) are satisfied. Equations (10.16) and (10.17) are nonlinear, but otherwise they have the same structure as the constraints in simple electromagnetism.

Note also that the equations governing $\boldsymbol{\mathcal{E}}$ and $\boldsymbol{\mathcal{B}}$, Eqs. (10.4)–(10.5) and (10.16)–(10.17) share another similarity with the field equations of electromagnetism: namely, just as the Maxwell equations are invariant under the duality transformation

$$\boldsymbol{E} \to \boldsymbol{B}\,, \quad \boldsymbol{B} \to -\boldsymbol{E}\,, \tag{10.18}$$

i.e., under a rotation in the complexified notation

$$\boldsymbol{E} - i\boldsymbol{B} \to e^{i\pi/2}(\boldsymbol{E} - i\boldsymbol{B})\,, \tag{10.19}$$

so the exact Maxwell-like Bianchi identities (10.4) are also invariant under the same duality transformation

$$\boldsymbol{\mathcal{E}} \to \boldsymbol{\mathcal{B}}\,, \quad \boldsymbol{\mathcal{B}} \to -\boldsymbol{\mathcal{E}}\,. \tag{10.20}$$

This duality in the structure of Eqs. (10.4)–(10.5) and also (10.16)–(10.17) does not in general enable one to construct one metric solution of Einstein's equations from another, known solution. However, as we shall see, we can utilize this duality in weakly gravitating systems to find the $\boldsymbol{\mathcal{E}}$ and $\boldsymbol{\mathcal{B}}$ generated by one set of source moments, given the expressions for $\boldsymbol{\mathcal{E}}$ and $\boldsymbol{\mathcal{B}}$ for a dual set of moments.

10.2.2.2 Local-Lorentz Frame of a Freely Falling Observer

When one introduces the local-Lorentz frame of a freely falling observer in curved spacetime, one necessarily specializes one's foliation: (i) The local-Lorentz foliation's space slices are flat at first order in the distance from the observer's world line, so its extrinsic curvature K_{ij} vanishes along the observer's world line. (ii) Because the observer is freely falling, her acceleration a_k vanishes, which means that successive hypersurfaces in the foliation are parallel to each other along the observer's world line.

These specializations, plus the vanishing shift $\beta_i = 0$ and unit lapse function $\alpha = 1$ of a local-Lorentz frame, bring the constraint and evolution equations, Eqs. (10.16)–(10.17) and (10.4)–(10.5),

into the following Maxwell-like form:

$$\begin{aligned} \boldsymbol{\nabla}\cdot\boldsymbol{\mathcal{E}} &= 0\,, \quad \boldsymbol{\nabla}\cdot\boldsymbol{\mathcal{B}} = 0\,, \\ \frac{\partial\boldsymbol{\mathcal{E}}}{\partial t} - (\boldsymbol{\nabla}\times\boldsymbol{\mathcal{B}})^S &= 0\,, \quad \frac{\partial\boldsymbol{\mathcal{B}}}{\partial t} + (\boldsymbol{\nabla}\times\boldsymbol{\mathcal{E}})^S = 0\,. \end{aligned} \tag{10.21}$$

Here the superscript S means "take the symmetric part" and the remaining notation is the same as in the flat-spacetime Maxwell equations (including changing from $\mathbf{D}$ to $\boldsymbol{\nabla}$ for the spatial gradient).

10.2.2.3 Weak-Gravity, Nearly Minkowski Spacetimes

In this paper's applications (Sections 10.5 and 10.6), we shall specialize to spacetimes and coordinate systems that are weakly perturbed from Minkowski, and we shall linearize in the perturbations. In this case, the Bianchi identities, Eqs. (10.4) and (10.5), take on precisely the same Maxwell-like form as in a local-Lorentz frame in strongly curved spacetime, Eqs. (10.21). To see that this is so, note that β_k, K_{jk}, a_k, $\mathcal{E}_{jk}$, and $\mathcal{B}_{jk}$ are all first-order perturbations and that α is one plus a first-order perturbation; the, linearize Eqs. (10.4) and (10.5) in these first-order quantities.

When the weak-gravity spacetime is also characterized by slow motion, so that its source regions are small compared to the wavelengths of its gravitational waves, the evolution equations control how the near-zone $\mathcal{E}_{jk}$ and $\mathcal{B}_{jk}$ get transformed into gravitational-wave fields. For insight into this, we specialize to harmonic gauge, in which the trace-reversed metric perturbation $\bar{h}_{\mu\nu}$ is divergence-free, $\partial^\mu\bar{h}_{\mu\nu} = 0$.

Then, in the near zone, $\mathcal{E}_{jk}$ and $\mathcal{B}_{jk}$ (which by Eqs. (10.21) are divergence-free and curl-free, respectively) are expressible in terms of the metric perturbation itself as

$$\mathcal{E}_{ij} = -\frac{1}{2}\partial_i\partial_j h_{00}\,, \quad \mathcal{B}_{ij} = \frac{1}{2}\epsilon_i{}^{pq}\partial_q\partial_j h_{p0}\,. \tag{10.22}$$

Because h_{00}, at leading order in $r/\lambda\!\!\!^{-}$ (ratio of radius to reduced wavelength), contains only mass multipole moments (Eq. (8.13a) of [36]), so also $\mathcal{E}_{jk}$ contains only mass-multipole moments. And because h_{p0} at leading order in $r/\lambda\!\!\!^{-}$ contains only current-multipole moments, so also $\mathcal{B}_{jk}$ contains only current-multipole moments.

In the wave zone, by contrast, Eqs. (10.21) show that the locally planar waves are sustained by mutual induction between $\boldsymbol{\mathcal{E}}$ and $\boldsymbol{\mathcal{B}}$, just like for electromagnetic waves, which means that these two wave-zone fields must contain the same information. This is confirmed by the wave-zone expressions for $\mathcal{E}_{jk}$ and $\mathcal{B}_{jk}$ in terms of the metric perturbation,

$$\mathcal{E}_{ij} = -\frac{1}{2}\partial_0^2 h_{ij}\,, \quad \mathcal{B}_{ij} = -\frac{1}{2}\epsilon_i{}^{pq}n_p\partial_0^2 h_{qj}\,. \tag{10.23}$$

Both fields are expressed in terms of the same quantity, h_{ij}. In addition, in the wave zone, $\boldsymbol{\mathcal{E}}$ and

$\boldsymbol{\mathcal{B}}$ are related to each other through a local rotation of $\pi/4$ radians of their polarization tensors (see Section 10.6.1 below). Correspondingly, we will see in Section 10.6 that, if a time-varying mass moment produces + polarized radiation in the wave zone, then the current moment that is dual to it produces $\times$ polarized radiation of the same magnitude.

In the transition zone, the inductive coupling between $\boldsymbol{\mathcal{E}}$ and $\boldsymbol{\mathcal{B}}$, embodied in Eqs. (10.4) and (10.5), enables these equations to act like a blender, mixing up the multipolar information that in the near zone is stored separately in these two fields. After an infinite amount of inductive blending, we arrive at future null infinity, $\mathcal{I}^+$, where the mixing has been so thorough that $\boldsymbol{\mathcal{E}}$ and $\boldsymbol{\mathcal{B}}$ contain precisely the same information, though it is distributed differently among their tensor components, Eqs. (10.23).

The details of this transition-zone mixing, as embodied in Eqs. (10.21), are in some sense the essence of gravitational-wave generation. We shall explore those details visually in Section 10.6 by tracking the tendex and vortex lines (introduced in Section 10.4) that extend from the near zone, through the transition zone, and into the wave zone.

Finally, note that the duality of $\boldsymbol{\mathcal{E}}$ and $\boldsymbol{\mathcal{B}}$ becomes especially convenient for slow-motion systems, where we can relate $\boldsymbol{\mathcal{E}}$ and $\boldsymbol{\mathcal{B}}$ to source multipole moments that appear in the weak-field near zone. In particular, to obtain the $\boldsymbol{\mathcal{E}}$ and $\boldsymbol{\mathcal{B}}$ generated by a specific current moment $\boldsymbol{\mathcal{S}}_\ell$, we can simply apply the duality transformation in Eq. (10.20) to the $\boldsymbol{\mathcal{E}}$ and $\boldsymbol{\mathcal{B}}$ for its dual moment, which is the mass moment $\boldsymbol{\mathcal{I}}_\ell$, but with one caveat: the differing normalizations used for mass moments and current moments [36] enforce the duality relation

$$\boldsymbol{\mathcal{I}}_\ell \to \frac{2\ell}{\ell+1}\boldsymbol{\mathcal{S}}_\ell\ , \qquad \boldsymbol{\mathcal{S}}_\ell \to -\frac{\ell+1}{2\ell}\boldsymbol{\mathcal{I}}_\ell\ , \tag{10.24}$$

when making this duality transformation; note that both transformations, Eqs. (10.20) and (10.24), must be made at once to arrive at the correct expressions; see Section 10.6.

10.3 Physical Interpretations of $\mathcal{E}_{ij}$ and $\mathcal{B}_{ij}$

It is rather well-known that in vacuum[2] the electric part of the Weyl tensor, $\mathcal{E}_{ij}$, describes tidal gravitational accelerations: the relative acceleration of two freely falling particles with separation vector ξ^k is $\Delta a^i = -\mathcal{E}^i{}_j\xi^j$. For this reason $\mathcal{E}_{ij}$ is often called the *tidal field*, a name that we shall adopt.

Not so well-known is the role of the magnetic part of the Weyl tensor, $\mathcal{B}_{jk}$, as governing differential frame dragging (i.e., the differential precession of inertial reference frames): in vacuum[2] a gyroscope

[2] In a non-vacuum region of spacetime, the local stress-energy tensor also contributes to tidal accelerations via its algebraic relation to the Ricci tensor, which, in turn, contributes to the Riemann tensor. In this case, $\mathcal{E}_{ij}$ describes that portion of the tidal acceleration due to the "free gravitational field" (i.e., the portion that is sourced away from the location where the tidal acceleration is measured); a similar caveat holds for $\mathcal{B}_{jk}$ and differential frame dragging. In this paper, we shall ignore this subtle point and focus on tidal forces and differential frame dragging in vacuum.

at the tip of the separation vector ξ^k, as observed in the local-Lorentz frame of an observer at the tail of ξ^k, precesses with angular velocity $\Delta\Omega^j = \mathcal{B}^j{}_k\xi^k$. For this reason, we call $\mathcal{B}_{jk}$ the *frame-drag field*.

We deduced this frame-drag role of $\mathcal{B}_{jk}$ during our research and then searched in vain for any reference to it in the literature, while writing our paper published in *Physical Review Letters* on vortexes and tendexes [1]. More recently, we have learned that this role of $\mathcal{B}_{jk}$ was known to Frank Estabrook and Hugo Wahlquist [29] 46 years ago and was rediscovered two years ago by Christoph Schmidt [30] (who states it without proof). For completeness, in this section we shall give a precise statement and proof of the frame-drag role of $\mathcal{B}_{jk}$, and a corresponding precise statement of the tidal-acceleration role of $\mathcal{E}_{jk}$.

10.3.1 Physical Setup

Consider an event $\mathcal{P}$ in spacetime and an observer labeled A whose world line passes through $\mathcal{P}$ and has 4-velocity $\vec{u}$ there; see Fig. 10.1. Introduce an infinitesimally short 4-vector $\vec{\xi}$ at $\mathcal{P}$, that is orthogonal to $\vec{u}$ and, thus, is seen as spatial by observer A. Denote by $\mathcal{P}'$ the event at the tip of $\vec{\xi}$. Introduce a second observer B, whose world line passes through $\mathcal{P}'$ and is parallel there to the world line of observer A, such that if we denote B's 4-velocity by the same symbol $\vec{u}$ as that of A and imagine a vector field $\vec{u}$ that varies smoothly between the two world lines, then $\nabla_{\vec{\xi}}\vec{u} = 0$ at $\mathcal{P}$. Let $\vec{\xi}$ be transported by observer A in such a way that it continues to reach from world line A to world line B. Then the vectors $\vec{u}$ and $\vec{\xi}$ satisfy the following three relations at $\mathcal{P}$:

$$\vec{\xi}\cdot\vec{u} = 0\ , \quad [\vec{u},\vec{\xi}] = 0, \quad \nabla_{\vec{\xi}}\vec{u} = 0\ . \tag{10.25}$$

The first says that the separation vector is purely spatial at $\mathcal{P}$ in the reference frame of observer A; the second says that $\vec{\xi}$ continues to reach between world lines A and B, so the quadrilateral formed by $\vec{u}$ and $\vec{\xi}$ in Fig. 10.1 is closed; the third says that the two observers' world lines are parallel to each other at $\mathcal{P}$—i.e., these observers regard themselves as at rest with respect to each other.

10.3.2 Interpretation of $\mathcal{E}_{ij}$ as the Tidal Field

Let the two observers A and B fall freely, i.e., move on geodesics. Then for this physical setup, the equation of geodesic deviation states that (see, e.g., Eq. (11.10) of MTW [14])

$$\nabla_{\vec{u}}\nabla_{\vec{u}}\vec{\xi} = -\mathsf{R}(\_\,,\vec{u},\vec{\xi},\vec{u})\ , \tag{10.26}$$

where R is the Riemann tensor. In physical language, the left side is the acceleration $\Delta\vec{a}$ of observer B at $\mathcal{P}'$, as measured in the local-Lorentz frame of observer A at $\mathcal{P}$. This relative acceleration is purely spatial as seen by observer A, and the right side of Eq. (10.26) tells us that in spatial,

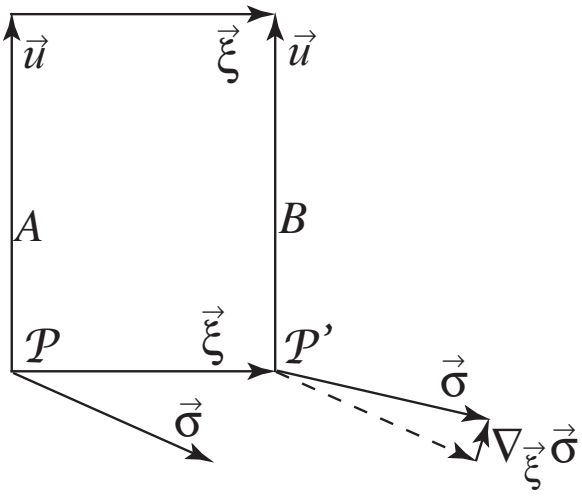

Figure 10.1: Spacetime diagram used for computing the precession of a gyroscope at one location $\mathcal{P}'$, relative to gyroscopic standards at a nearby location $\mathcal{P}$. The points and vectors are explained in the text.

3-dimensional vector and tensor notation (and in vacuum so $R_{\alpha\beta\gamma\delta} = C_{\alpha\beta\gamma\delta}$), it is given by

$$\Delta a^j = -R^j{}_{\hat{0}k\hat{0}}\xi^k = -\mathcal{E}^j{}_k\xi^k \; ; \quad \text{i.e.,} \quad \Delta \boldsymbol{a} = -\boldsymbol{\mathcal{E}}(\_\,, \boldsymbol{\xi}) \; . \tag{10.27}$$

Since (as is well-known) this relative acceleration produces the Earth's tides when $\mathcal{E}_{jk}$ is caused by the moon and sun, $\mathcal{E}_{jk}$ is called the *tidal field*, and Eq. (10.27) is known as *the tidal-acceleration equation*.

10.3.3 Interpretation of $\mathcal{B}_{ij}$ as the Frame-Drag Field

Next let the two observers A and B in Fig. 10.1 be accelerated if they wish (with the same 4-acceleration $\vec{a}$ up to differences proportional to $\vec{\xi}$), and give each of them a spatial unit vector $\vec{\sigma}$ that is tied to an inertial-guidance gyroscope, so that the following relations are satisfied:

$$\vec{\sigma}\cdot\vec{u} = 0 \; , \quad \vec{\sigma}\cdot\vec{\sigma} = 1 \; , \quad \nabla_{\vec{u}}\vec{\sigma} = (\vec{a}\cdot\vec{\sigma})\vec{u} \; , \quad \vec{a} \equiv \nabla_{\vec{u}}\vec{u} \; . \tag{10.28}$$

The first of these says that $\vec{\sigma}$ is purely spatial as seen in the observer's reference frame, the second says that $\vec{\sigma}$ has unit length, and the third is the Fermi-Walker transport law for an inertial-guidance gyroscope.

The local-frame-dragging-induced rate of change of $\vec{\sigma}$ at $\mathcal{P}'$, as measured using inertial-direction standards at $\mathcal{P}$, is $\nabla_{\vec{u}}\nabla_{\vec{\xi}}\vec{\sigma}$. We can write this as

$$\begin{aligned} \nabla_{\vec{u}}\nabla_{\vec{\xi}}\vec{\sigma} &= \nabla_{\vec{\xi}}\nabla_{\vec{u}}\vec{\sigma} + [\nabla_{\vec{u}}, \nabla_{\vec{\xi}}]\vec{\sigma} \\ &= \nabla_{\vec{\xi}}\nabla_{\vec{u}}\vec{\sigma} + \mathsf{R}(\_\,, \vec{\sigma}, \vec{u}, \vec{\xi}) \; , \end{aligned} \tag{10.29}$$

where R is the Riemann tensor, and we have used the fact that $[\vec{u},\vec{\xi}]=0$; see Eqs. (11.8) and (11.9) of MTW [14].

Evaluating the first term, $\nabla_{\vec{\xi}}\nabla_{\vec{u}}\vec{\sigma}$, using the Fermi-Walker transport law, the third of Eqs. (10.28), and the fact that the observers are momentarily at rest with respect to each other (the third of Eqs. (10.25) as well), we bring Eq. (10.29) into the form

$$\nabla_{\vec{u}}\nabla_{\vec{\xi}}\vec{\sigma} = \mathsf{R}(\_,\vec{\sigma},\vec{u},\vec{\xi}) + \vec{u}\nabla_{\vec{\xi}}(\vec{a}\cdot\vec{\sigma}) \ . \tag{10.30}$$

We are only interested in the spatial part of this rate of change, and, therefore, we can ignore the second term on the right side of the equation. We switch to the 3-dimensional viewpoint of the observer at $\mathcal{P}$ (where our calculation is being done) and we denote the spatial part of $\nabla_{\vec{u}}\nabla_{\vec{\xi}}\vec{\sigma}$ by $\dot{\boldsymbol{\sigma}}$:

$$\dot{\boldsymbol{\sigma}} \equiv \left[\nabla_{\vec{u}}\nabla_{\vec{\xi}}\vec{\sigma}\right]_{\text{project orthogonal to } \vec{u}} \ . \tag{10.31}$$

Equation (10.30) tells us that this rate of change is not only orthogonal to $\vec{u}$ (spatial) but also orthogonal to $\boldsymbol{\sigma}$; it, therefore, can be written as a rotation

$$\dot{\boldsymbol{\sigma}} = \Delta\boldsymbol{\Omega}\times\boldsymbol{\sigma} \tag{10.32}$$

Here $\Delta\boldsymbol{\Omega}$ *is the frame-dragging angular velocity at* $\mathcal{P}'$ *as measured using inertial standards at* $\mathcal{P}$. We can solve for this angular velocity $\Delta\boldsymbol{\Omega}$ by crossing $\boldsymbol{\sigma}$ into Eq. (10.32) and using $\boldsymbol{\sigma}\cdot\boldsymbol{\sigma}=1$:

$$\Delta\boldsymbol{\Omega} = \boldsymbol{\sigma}\times\dot{\boldsymbol{\sigma}} \ . \tag{10.33}$$

Inserting Eq. (10.30) for $\dot{\boldsymbol{\sigma}}$ and switching to index notation, we obtain

$$\Delta\Omega_i = \epsilon_{ijk}\sigma^j R^k{}_{p\hat{0}q}\sigma^p\xi^q \ . \tag{10.34}$$

Rewriting the Riemann tensor component in terms of the magnetic part of the Weyl tensor (in vacuum), $R^k{}_{p\hat{0}q} = -\epsilon^k{}_{ps}\mathcal{B}^s{}_q$, performing some tensor manipulations, and noticing that because $\Delta\boldsymbol{\Omega}$ is crossed into $\boldsymbol{\sigma}$ when computing the precession any piece of $\Delta\boldsymbol{\Omega}$ along $\boldsymbol{\sigma}$ is irrelevant, we obtain

$$\Delta\Omega_i = \mathcal{B}_{ij}\xi^j \ , \quad \text{i.e. } \Delta\boldsymbol{\Omega} = \boldsymbol{\mathcal{B}}(\_,\boldsymbol{\xi}) \ . \tag{10.35}$$

In words, the equation gives the following physical interpretation: in vacuum, the frame-dragging angular velocity at $\mathcal{P}'$, as measured using inertial directions at the adjacent event $\mathcal{P}$, is obtained by inserting the vector $\boldsymbol{\xi}$ (which reaches from $\mathcal{P}$ to $\mathcal{P}'$) into one slot of the gravitomagnetic part of the Weyl tensor. Because of the role of $\mathcal{B}_{ij}$ in this equation of differential frame dragging, we call $\mathcal{B}_{ij}$

the *frame-drag field*.

10.4 Our New Tools: Tendex and Vortex Lines, Their Tendicities and Vorticities, Tendexes and Vortexes

10.4.1 Tendex Lines and Their Tendicities; Vortex Lines and Their Vorticities

As symmetric, trace-free tensors, the tidal field $\boldsymbol{\mathcal{E}}$ and frame-drag field $\boldsymbol{\mathcal{B}}$ can each be characterized completely by its three principal axes (eigendirections) and its three associated eigenvalues. If $\boldsymbol{p}$ is a (smoothly changing) unit eigenvector of the tidal field $\boldsymbol{\mathcal{E}}$ (or of the frame-drag field $\boldsymbol{\mathcal{B}}$), then the integral curves of $\boldsymbol{p}$ can be regarded as field lines associated with $\boldsymbol{\mathcal{E}}$ (or $\boldsymbol{\mathcal{B}}$). For $\boldsymbol{\mathcal{E}}$ we call these integral curves *tidal tendex lines*, or simply *tendex lines*[3], because $\boldsymbol{\mathcal{E}}$ tidally stretches objects it encounters, and *tendere* means "to stretch" in Latin. For $\boldsymbol{\mathcal{B}}$ we call the integral curves *frame-drag vortex lines*, or simply *vortex lines*, because $\boldsymbol{\mathcal{B}}$ rotates gyroscopes, and *vertere* means "to rotate" in Latin. At each point $\mathcal{P}$ in space, there are three orthogonal eigendirections of $\boldsymbol{\mathcal{E}}$ (and three of $\boldsymbol{\mathcal{B}}$); therefore, through each point there pass three orthogonal tendex lines and three orthogonal vortex lines.

Outside a spherically symmetric gravitating body with mass M, such as the Earth or even a Schwarzschild black hole, the tidal field, in a spherical-polar orthonormal basis, has components

$$\mathcal{E}_{\hat{r}\hat{r}} = -\frac{2M}{r^3}\ , \quad \mathcal{E}_{\hat{\theta}\hat{\theta}} = \mathcal{E}_{\hat{\phi}\hat{\phi}} = +\frac{M}{r^3} \tag{10.36}$$

(e.g., Section 1.6 and Eq. (31.4) of [14]). The tidal-acceleration equation $\Delta a^j = -\mathcal{E}^j{}_k \xi^k$ tells us that this tidal field stretches objects radially and squeezes them equally strongly in all tangential directions (see the people in Fig. 10.2). Correspondingly, one eigenvector of $\boldsymbol{\mathcal{E}}$ is radial, and the other two are tangential with degenerate eigenvalues. This means that one set of tendex lines is radial (the red tendex lines in Fig. 10.2), and any curve lying on a sphere around the body is a tendex line. If we break the tangential degeneracy by picking our tangential unit eigenvectors to be the basis vectors $\boldsymbol{e}_{\hat{\theta}}$ and $\boldsymbol{e}_{\hat{\phi}}$ of a spherical-polar-coordinate system, then the tangential tendex lines are those vectors' integral curves—the blue curves in Fig. 10.2.

When the spherical body is weakly gravitating and is set rotating slowly, then it acquires a nonzero frame-drag field given by Eqs. (10.47) below. The corresponding vortex lines are shown in Fig. 10.3. (See Section 10.5.1 below for details.)

To any tendex (or vortex) line, with unit eigenvector $\boldsymbol{p}$, there is associated an eigenvalue, $\mathcal{E}_{pp} = \mathcal{E}_{jk}p^j p^k$, which is called the line's *tendicity* (or $\mathcal{B}_{pp} = \mathcal{B}_{jk}p^j p^k$, which is called the line's *vorticity*).

[3]The word tendex was coined by David Nichols.

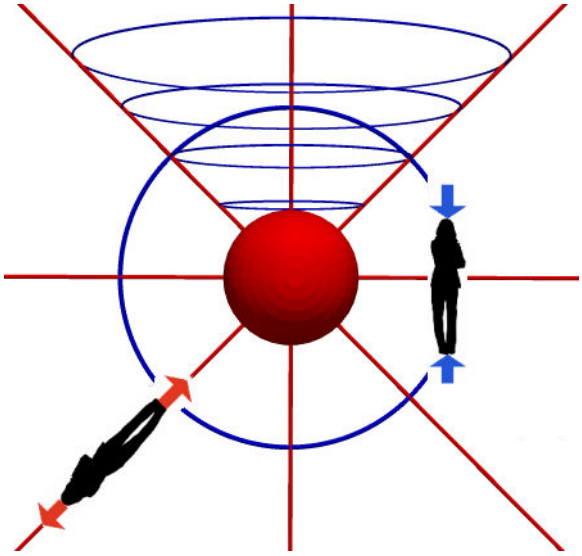

Figure 10.2: Tendex lines outside a spherically symmetric, gravitating body. The lines are colored by the sign of their tendicity: red lines have negative tendicity (they stretch a person oriented along them); blue lines have positive tendicity (they squeeze).

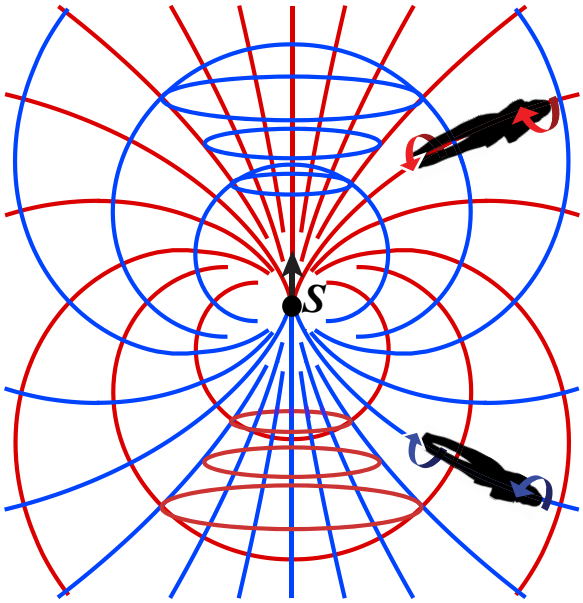

Figure 10.3: Vortex lines outside a slowly spinning, spherically symmetric, gravitating body with spin angular momentum $\boldsymbol{S}$. The lines are colored by the sign of their vorticity: red lines have negative vorticity (they produce a counterclockwise differential precession of gyroscopes); blue lines have positive vorticity (clockwise differential precession).

The physical meaning of this tendicity (or vorticity) can be read from the tidal-acceleration equation, Eq. (10.27), or the equation of differential frame dragging, Eq. (10.35). Specifically, if a person's body (with length ℓ) is oriented along a tidal tendex line (Fig. 10.2), she feels a head-to-foot stretching acceleration given by $\Delta a = -\mathcal{E}_{pp}\ell$. If the line's tendicity $\mathcal{E}_{pp}$ is negative (red tendex line), her body gets stretched; if the tendicity is positive (blue tendex line), she gets compressed.

If her body is oriented along a vortex line (Fig. 10.3), then a gyroscope at her feet precesses around the vortex line with an angular speed, relative to inertial frames at her head, given by $\Delta\Omega = \mathcal{B}_{pp}\ell$. If the line's vorticity is negative (red vortex lines in Fig. 10.3), then the gyroscope at her feet precesses counterclockwise relative to inertial frames at her head, and (because $\mathcal{B}_{pp}$ is unchanged when one reverses the direction $\boldsymbol{p}$), a gyroscope at her head precesses counterclockwise relative to inertial frames at her feet. Correspondingly, we call the (red) vortex line a *counterclockwise vortex line*. If the line's vorticity is positive (blue vortex lines in Fig. 10.3), the precessions are clockwise and the vortex line is said to be clockwise.

For any spacetime, the tendex lines color coded by their tendicities (e.g., Fig. 10.2) and the vortex lines color coded by their vorticities (e.g., Fig. 10.3) depict visually all details of the Weyl curvature tensor.

Because $\boldsymbol{\mathcal{E}}$ and $\boldsymbol{\mathcal{B}}$ are trace-free, at any point in space the sum of the three tendex lines' tendicities vanishes, and the sum of the three vorticities vanishes. Because $\boldsymbol{\mathcal{E}}$ and $\boldsymbol{\mathcal{B}}$ are also symmetric, each is characterized by five numbers at any point in space. The direction of one tendex line fixes two numbers and its tendicity fixes a third, leaving only two numbers to be specified. The direction of a second tendex line, in the plane orthogonal to the first, fixes a fourth number and the second line's tendicity fixes the fifth and final number—leaving the last line's direction and tendicity fully determined. Similarly, this is the case for vortex lines and their vorticities.

10.4.2 Vortexes and Tendexes

We give the name *frame-drag vortex*, or simply *vortex*, to a bundle of vortex lines with large vorticity. In Fig. 10.3, the red vortex lines near the northern polar axis, which are enclosed by blue circles, constitute a negative-vorticity (counterclockwise) vortex; the blue vortex lines near the southern polar axis, which are enclosed by red circles, constitute a positive-vorticity (clockwise) vortex. These two vortexes emerge from the northern and southern poles of the spinning point particle. Similarly, we give the name *tidal tendex*, or simply *tendex*, to a strong concentration of tendex lines. We shall meet our first example at the end of Section 10.5.4 below.

10.5 Weak-Gravity, Stationary Systems

10.5.1 One Stationary, Weakly Gravitating, Spinning Body

When gravity is weak and slowly changing (e.g., outside a slowly precessing, spinning, weakly gravitating body such as the Earth), one can write the spacetime metric in the form

$$ds^2 = -\alpha^2 dt^2 + \delta_{jk}(dx^j + \beta^j dt)(dx^k + \beta^k dt) \tag{10.37a}$$

(e.g., Section 23.9.3 of [37]; or Chapter 10 of MTW [14] with the spatial coordinates changed slightly). Here

$$\alpha^2 = \left(1 - \frac{2M}{r}\right) , \quad \boldsymbol{\beta} = -\frac{2\boldsymbol{S}}{r^2} \times \boldsymbol{n} , \tag{10.37b}$$

are the squared lapse function and the shift function, M is the body's mass, $\boldsymbol{S}$ is its spin angular momentum, and

$$r = \sqrt{x^2 + y^2 + z^2} , \quad \boldsymbol{n} = \boldsymbol{e}_{\hat{r}} \tag{10.37c}$$

are radius and the unit radial vector, with $\{x^1, x^2, x^3\} = \{x, y, z\}$. In spherical polar coordinates (associated with the Cartesian coordinates $\{x, y, z\}$ in the usual way), the metric, Eq. (10.37a), becomes

$$\begin{aligned} ds^2 &= -\alpha^2 dt^2 + dr^2 + r^2 d\theta^2 + r^2 \sin^2\theta (d\phi - \omega dt)^2 , \\ \omega &= 2S/r^3 . \end{aligned} \tag{10.37d}$$

It is conventional to rewrite general relativity, in this weak-field, slow-motion situation, as a field theory in flat spacetime. In this language, the geodesic equation for a test particle takes the form

$$\frac{d^2\boldsymbol{x}}{dt^2} = \boldsymbol{g} + \boldsymbol{v} \times \boldsymbol{H} , \tag{10.38}$$

which resembles the Lorentz force law in electromagnetic theory; see, e.g., [38] and references therein, especially [39]. Here $\boldsymbol{v} = d\boldsymbol{x}/dt$ is the particle's velocity and

$$\begin{aligned} \boldsymbol{g} &= -\frac{1}{2}\boldsymbol{\nabla}\alpha^2 = -\frac{M}{r^2}\boldsymbol{n} , \\ \boldsymbol{H} &= \boldsymbol{\nabla} \times \boldsymbol{\beta} = 2\left[\frac{\boldsymbol{S} - 3(\boldsymbol{S}\cdot\boldsymbol{n})\boldsymbol{n}}{r^3}\right] \end{aligned} \tag{10.39}$$

are the body's *gravitoelectric field* (same as Newtonian gravitational acceleration) and its *gravitomagnetic field*. Note that these fields have the same monopole and dipole structures as the electric and magnetic fields of a spinning, charged particle.

In this paper, we shall adopt an alternative to this "gravito-electromagnetic" viewpoint. For the gravitational influence of the mass M, we shall return to the Newtonian viewpoint of a gravitational acceleration $\boldsymbol{g}$ and its gradient, the tidal gravitational field (the electric part of the Weyl tensor)

$$\boldsymbol{\mathcal{E}} = -\boldsymbol{\nabla}\boldsymbol{g} \ , \quad \text{i.e.,} \quad \mathcal{E}_{ij} = -g_{i,j} = \Phi_{,ij} = \frac{1}{2}\alpha^2{}_{,ij} \ . \tag{10.40}$$

Here the comma denotes a partial derivative (actually, the gradient in our Cartesian coordinate system) and Φ is the Newtonian gravitational potential, which is related to the lapse function by $\alpha^2 = 1 + 2\Phi$ in the Newtonian limit. The components of this tidal field in the spherical coordinates' orthonormal basis $\boldsymbol{e}_{\hat{r}} = \partial/\partial r$, $\boldsymbol{e}_{\hat{\theta}} = (1/r)\partial/\partial\theta$, $\boldsymbol{e}_{\hat{\phi}} = (1/r\sin\theta)\partial/\partial\phi$ are easily seen to be

$$\mathcal{E}_{\hat{r}\hat{r}} = -\frac{2M}{r^3} \ , \quad \mathcal{E}_{\hat{\theta}\hat{\theta}} = \mathcal{E}_{\hat{\phi}\hat{\phi}} = +\frac{M}{r^3} \ , \tag{10.41}$$

(Eqs. (10.36) above), which are symmetric and trace-free as expected. The field lines associated with this tidal field are easily seen to be those depicted in Fig. 10.2 above.

For the effects of the spin angular momentum, we shall think of the spinning body as "dragging space into motion" with a velocity and angular velocity (relative to our Cartesian coordinates) given by

$$\frac{d\boldsymbol{x}_{\rm space}}{dt} \equiv \boldsymbol{v}_{\rm space} = -\boldsymbol{\beta} = \frac{2\boldsymbol{S}}{r^2} \times \boldsymbol{n}; \ , \quad \frac{d\phi_{\rm space}}{dt} = \omega = \frac{2S}{r^3} \ ; \tag{10.42}$$

see the $\delta_{jk}(dx^j + \beta^j dt)(dx^k + \beta^k dt)$ term in the metric of Eq. (10.37a) and the $(d\phi - \omega dt)^2$ term in the metric of Eq. (10.37d). Just as the vorticity $\boldsymbol{\nabla} \times \boldsymbol{v}$ of a nonrelativistic fluid with velocity field $\boldsymbol{v}(\boldsymbol{x})$ is twice the angular velocity $\boldsymbol{\Omega}$ of rotation of a fluid element relative to an inertial reference frame, so the vorticity associated with the "space motion," $\boldsymbol{\nabla} \times \boldsymbol{v}_{\rm space}$, turns out to be twice the vectorial angular velocity of an inertial-guidance gyroscope relative to inertial reference frames far from the body ("at infinity")—or equivalently, relative to our spatial Cartesian coordinates $\{x, y, z\}$, which are locked to inertial frames at infinity. In formulas, let $\boldsymbol{\sigma}$ be a unit vector along the spin angular momentum vector of an inertial-guidance gyroscope. Viewed as a vector in our Cartesian basis, it precesses

$$\frac{d\boldsymbol{\sigma}}{dt} = \boldsymbol{\Omega}_{\rm fd} \times \boldsymbol{\sigma} \ , \tag{10.43}$$

with a frame-dragging vectorial angular velocity equal to half the vorticity of space viewed as a fluid:

$$\begin{aligned} \boldsymbol{\Omega}_{\rm fd} &= \frac{1}{2}\boldsymbol{\nabla} \times \boldsymbol{v}_{\rm space} = -\frac{1}{2}\boldsymbol{\nabla} \times \boldsymbol{\beta} = -\frac{1}{2}\boldsymbol{H} \\ &= -\left[\frac{\boldsymbol{S} - 3(\boldsymbol{S}\cdot\boldsymbol{n})\boldsymbol{n}}{r^3}\right]; \end{aligned} \tag{10.44}$$

see, e.g., Eq. (25.14) of [37], or Eq. (40.37) of [14]. This dipolar frame-dragging angular velocity is

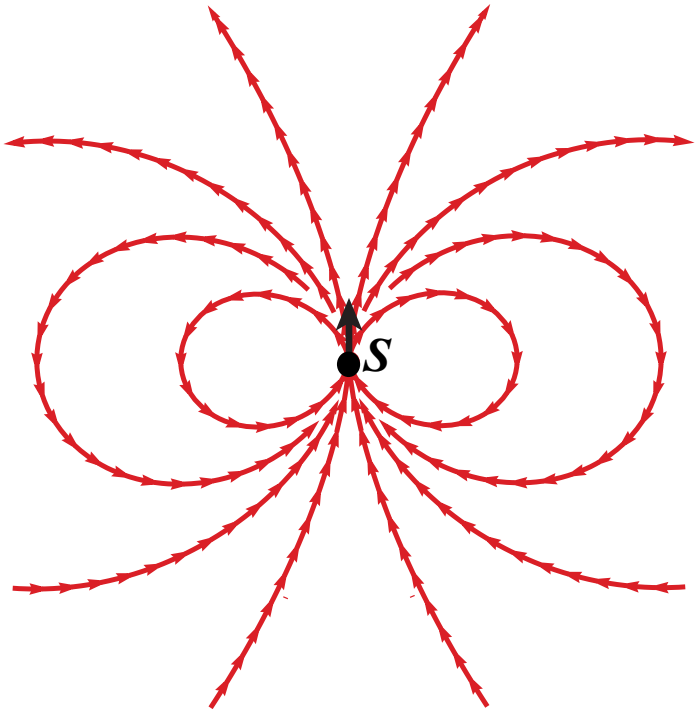

Figure 10.4: For a weakly gravitating, slowly rotating body with spin angular momentum $\boldsymbol{S}$, the dipolar frame-dragging angular velocity relative to inertial frames at infinity, $\boldsymbol{\Omega}_{\rm fd}$. The arrows are all drawn with the same length rather than proportional to the magnitude of $\boldsymbol{\Omega}_{\rm fd}$.

shown in Fig. 10.4.

For dynamical black holes and other strong-gravity, dynamical situations, it is not possible to measure gyroscopic precession with respect to inertial frames at infinity, because there is no unambiguous way to compare vectors at widely separated events.[4] On the other hand, we can, in general, measure the precession of inertial-guidance gyroscopes at one event, with respect to inertial frames at a neighboring event—i.e., we can measure differential frame dragging as embodied in the frame-drag field (magnetic part of the Weyl tensor) $\mathcal{B}_{ij}$. In our weak-gravity, slow-motion situation, this frame-drag field is equal to the gradient of $\boldsymbol{\Omega}_{\rm fd}$ (Eq. (5.45b) of [42]):

$$\boldsymbol{\mathcal{B}} = \boldsymbol{\nabla}\boldsymbol{\Omega}_{\rm fd} \ , \quad \text{i.e.,} \quad \mathcal{B}_{jk} = \Omega_{{\rm fd}\,j,k} \ . \tag{10.45}$$

For our weakly gravitating, spinning body, $\boldsymbol{\Omega}_{\rm fd}$ has the dipolar form, Eq. (10.44), and, therefore, the frame-drag field is

$$\mathcal{B}_{jk} = \frac{3}{r^4}\left[2S_{(j}n_{k)} + (\boldsymbol{S}\cdot\boldsymbol{n})(\delta_{jk} - 5n_jn_k)\right] \ . \tag{10.46}$$

[4]There is an exception: one can introduce additional geometric structure, e.g., an auxiliary flat spacetime, that provides a way of carrying a reference frame inward from infinity to all other locations and thereby compare vectors at different events. Some of us have used this approach to localize linear momentum in the gravitational field around black holes [40, 41]. However, the auxiliary structure has great arbitrariness, and for the vortex and tendex concepts of this paper there is no need for such auxiliary structure, and we eschew it.

Here the parentheses on the subscripts indicate symmetrization. In spherical polar coordinates, the components of this frame-drag field are

$$\begin{aligned} \mathcal{B}_{\hat{r}\hat{r}} &= -2\mathcal{B}_{\hat{\theta}\hat{\theta}} = -2\mathcal{B}_{\hat{\phi}\hat{\phi}} = -\frac{6S\cos\theta}{r^4} \,, \\ \mathcal{B}_{\hat{r}\hat{\theta}} &= \mathcal{B}_{\hat{\theta}\hat{r}} = -\frac{3S\sin\theta}{r^4} \,. \end{aligned} \tag{10.47}$$

For this (and any other axially symmetric) frame-drag field, one of the three sets of vortex lines is along the ϕ direction (i.e., the $\boldsymbol{S}\times\boldsymbol{x}$ direction)—i.e., it is axial—and the other two are poloidal. By computing the eigenvectors of the tensor in Eq. (10.46) and then drawing the curves to which they are tangent, one can show that the body's vortex lines have the forms shown in Fig. 10.3.

Notice that the poloidal, negative-vorticity vortex lines (the poloidal red curves in Fig. 10.3) all emerge from the northern polar region of the spinning body, encircle the body, and return back to the northern polar region. One can understand why these lines have negative rather than positive vorticity by choosing the eigendirection $\boldsymbol{p}$ at the body's northern pole to point away from the body. Then, the body drags inertial frames in a right-handed manner (counterclockwise as seen looking down on the northern pole), and the frame dragging is stronger at the tail of $\boldsymbol{p}$ (nearer the body) than at the tip. Because the the frame-dragging angular velocity decreases from tail to tip, this means it is more left-handed (clockwise) at the tip than the tail (i.e., it has negative vorticity). The poloidal, positive-vorticity vortex lines (the poloidal blue curves in Fig. 10.3) all emerge from the body's southern polar region, swing around the body, and return to the southern polar region. The azimuthal vortex lines have negative vorticity above the hole's equatorial plane (blue azimuthal circles) and positive vorticity below the hole's equatorial plane (red azimuthal circles).

10.5.2 Two Stationary, Weakly Gravitating, Spinning Point Particles with Opposite Spins

Consider, next, two weakly gravitating, spinning point particles with opposite spins, sitting side-by-side. Place the particles (named A and B) on the x axis, at locations $\{x_A, y_A, z_A\} = \{+a, 0, 0\}$, $\{x_B, y_B, z_B\} = \{-a, 0, 0\}$ and give them vectorial spins $\boldsymbol{S}_A = S\boldsymbol{e}_z$, $\boldsymbol{S}_B = -S\boldsymbol{e}_z$. Then the frame-drag angular velocity relative to inertial frames at infinity is

$$\boldsymbol{\Omega}_{\rm fd} = -\frac{\boldsymbol{S}_A - 3(\boldsymbol{S}_A\cdot\boldsymbol{n}_A)\boldsymbol{n}_A}{{r_A}^3} - \frac{\boldsymbol{S}_B - 3(\boldsymbol{S}_B\cdot\boldsymbol{n}_B)\boldsymbol{n}_A}{{r_B}^3} \,, \tag{10.48}$$

where $r_A = |\boldsymbol{x}-\boldsymbol{x}_A|$ and $r_B = |\boldsymbol{x}-\boldsymbol{x}_B|$ are the distances to the particles and $\boldsymbol{n}_A = (\boldsymbol{x}-\boldsymbol{x}_A)/r_A$ and $\boldsymbol{n}_B = (\boldsymbol{x}-\boldsymbol{x}_B)/r_B$ are unit vectors pointing from the particles' locations to the field point; see Eq. (10.44). This vector field is plotted in Fig. 10.5a. It has just the form one might expect from the one-spin field of Fig. 10.4.

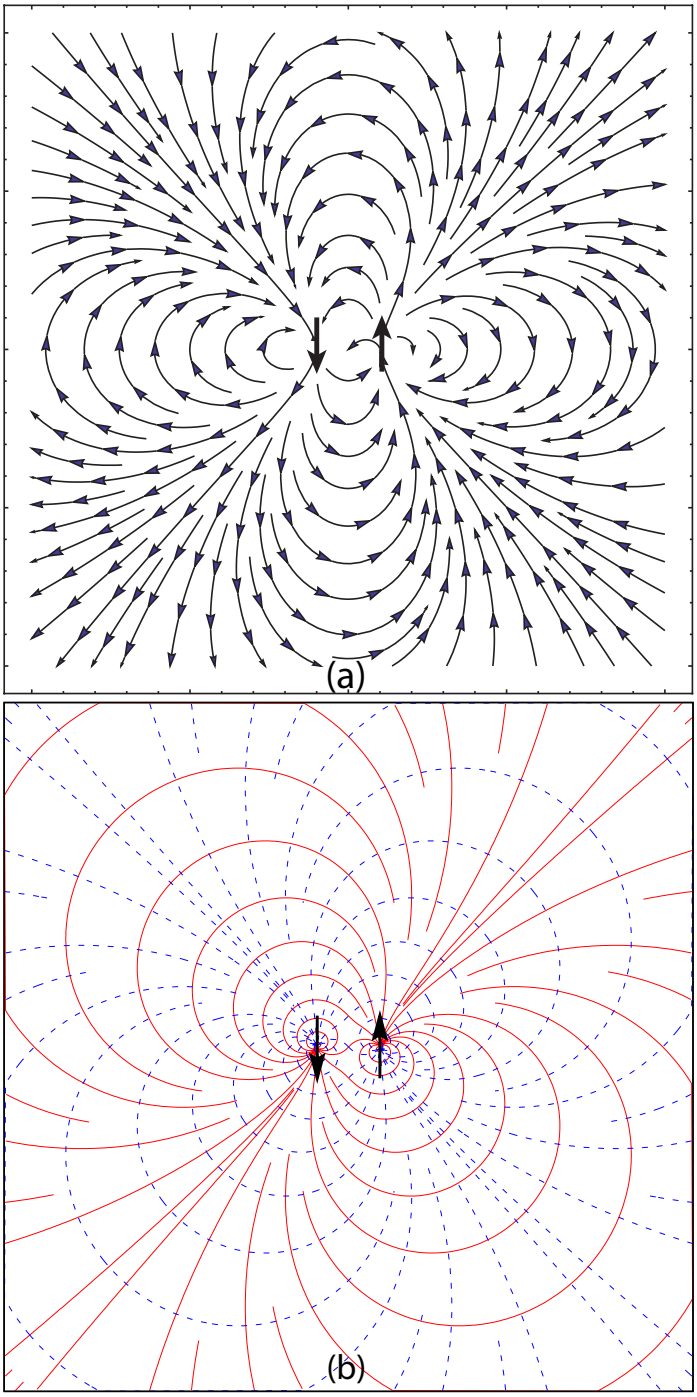

Figure 10.5: For two stationary point particles sitting side-by-side with their spins in opposite directions (thick black arrows), two types of streamlines in the plane of reflection symmetry formed by the particles' spins and their separation vector. (a) The frame-dragging angular velocity $\boldsymbol{\Omega}_{\rm fd}$ and its streamlines, with the arrows all drawn at the same length rather than proportional to the magnitude of $\boldsymbol{\Omega}_{\rm fd}$. (b) The two sets of vortex lines of the frame-drag field $\boldsymbol{\mathcal{B}}$. The negative-vorticity vortex lines are solid and colored red, and the positive-vorticity ones are dashed and blue. In this figure, as in preceding figures, the colors are not weighted by the lines' vorticities, but only by the signs of the vorticities.

For these two spinning particles, the frame-drag field, which is given by the gradient of Eq. (10.48), is

$$\mathcal{B}_{jk} = \frac{3}{{r_A}^4}\left[2S_A^{(j}n_A^{k)} + (\boldsymbol{S}_A\cdot\boldsymbol{n}_A)(\delta^{jk} - 5n_A^j n_A^k)\right] + \frac{3}{{r_B}^4}\left[2S_B^{(j}n_B^{k)} + (\boldsymbol{S}_B\cdot\boldsymbol{n}_B)(\delta^{jk} - 5n_B^j n_B^k)\right] \tag{10.49}$$

(Eq. (10.46) repeated once for each particle), where we have moved the vector and tensor indices up for simplicity of notation. (In our Cartesian basis, there is no difference between up and down indices.)

The best two-dimensional surface on which to visualize vortex lines of this $\boldsymbol{\mathcal{B}}$ is the x-z plane (the plane formed by the particles' spins and their separation vector). The system is reflection symmetric through this plane. On this plane, one of the principal directions of $\boldsymbol{\mathcal{B}}$ is orthogonal to it (in the y direction); the other two lie in the plane and are tangent to the in-plane vortex lines. By computing the eigendirections of $\boldsymbol{\mathcal{B}}$ in Eq. (10.49), mapping out their tangent vortex lines, and checking the sign of $\mathcal{B}_{pp}$ along their tangent directions $\boldsymbol{p}$, we obtain Fig. 10.5.

Note that, as for a single spinning particle (Fig. 10.3), so also here for two spins, the negative-vorticity vortex lines (solid red curves) emerge from the tips of the spins and the positive-vorticity vortex lines (dashed blue curves) emerge from their tails. For a single spin, the negative-vorticity vortex lines emerge from the tip, travel around the body, and return to the same tip. Here, the lines close to each spinning body leave and enter the same body's tip, but the majority emerge from one body's tip, travel around that body and enter the other body's tip. Similarly the positive-vorticity vortex lines (dashed and blue) emerge from one body's tail, travel around that body, and enter the other body's tail (aside from the lines near each body that exit and return to the same body's tail). The collection of solid red vortex lines near each arrow tip in Fig. 10.5b constitutes a negative-vorticity frame-drag vortex, and the collection of dashed blue vortex lines near each arrow tail is a positive-vorticity vortex.

10.5.3 The Two Spinning Particles Viewed from Far Away: Stationary, Quadrupolar Frame-Drag Field

When viewed from afar, the two spinning bodies produce a current-quadrupole gravitational field with quadrupole moment (e.g., Eq. (5.28b) of [36])

$$\begin{aligned}\mathcal{S}_{pq} &= \left(\int j_p x_q d^3x\right)^{\rm STF} = [S_p a_q + (-S_p)(-a_q)]^{\rm STF} \\ &= S_p a_q + S_q a_p - \frac{2}{3}(\boldsymbol{S}\cdot\boldsymbol{a})\delta_{pq}\,.\end{aligned} \tag{10.50}$$

Here $j_p = S_p\delta(\boldsymbol{x}-\boldsymbol{a}) - S_p\delta(\boldsymbol{x}+\boldsymbol{a})$ is the angular-momentum density. Because the only nonzero components of $\boldsymbol{S}$ and $\boldsymbol{a}$ are $S_z = S$ and $a_x = a$, the only nonzero components of the current-

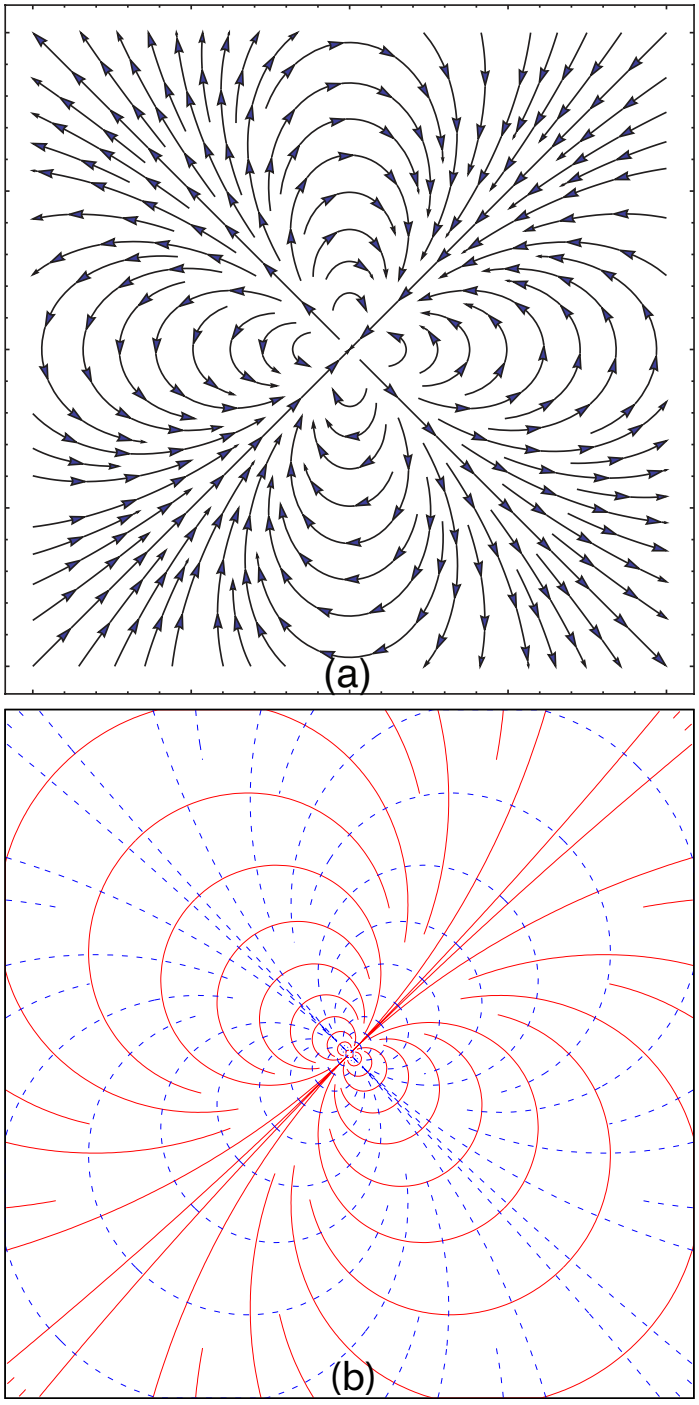

Figure 10.6: Current-quadrupolar streamlines associated with the two stationary spinning particles of Fig. 10.5, for which the current-quadrupole moment has nonzero components $\mathcal{S}_{xz} = \mathcal{S}_{zx} = Sa$. (a) The frame-dragging angular velocity $\mathbf{\Omega}_{\rm fd}$ and its streamlines, and (b) the two sets of vortex lines, in the x-z plane. Figure (b) also describes the tendex lines for a static mass-quadrupolar particle whose only nonzero quadrupole-moment components are $\mathcal{I}_{xz} = \mathcal{I}_{zx}$.

quadrupole moment are

$$\mathcal{S}_{xz} = \mathcal{S}_{zx} = Sa \ . \tag{10.51}$$

The frame-drag-induced velocity of space (negative of the shift function) for this current quadrupole, and the frame-drag angular velocity and frame-drag tensor field are

$$\begin{aligned} \boldsymbol{v}_{\rm space} &= -\boldsymbol{\beta} = \frac{4\boldsymbol{n}\times\boldsymbol{\mathcal{S}}\cdot\boldsymbol{n}}{r^3} \ , \\ \boldsymbol{\Omega}_{\rm fd} &= \frac{1}{2}\boldsymbol{\nabla}\times\boldsymbol{v}_{\rm space} \ , \quad \boldsymbol{\mathcal{B}} = \boldsymbol{\nabla}\boldsymbol{\Omega}_{\rm fd} \end{aligned} \tag{10.52}$$

(e.g., Eq. (10.6b) of [36]; also Eqs. (10.44) and (10.45) above). Inserting Eq. (10.51) for the quadrupole moment into Eqs. (10.52), and plotting $\boldsymbol{\Omega}_{\rm fd}$ and the vortex lines of $\boldsymbol{\mathcal{B}}$ in the x-z plane, we obtain the graphs shown in Fig. 10.6.

Notice that the current-quadrupolar frame-drag angular velocity in Fig. 10.6a is, indeed, the same as that for two oppositely directed spins (Fig. 10.5a) in the limit that the spins' separation goes to zero—i.e., as seen from afar—and the current-quadrupolar vortex lines of the frame-drag tensor field (Fig. 10.6b) is the vanishing-separation limit of that for the two oppositely directed spins (Fig. 10.5b).

Here, as for finitely separated spinning particles, there are two red frame-drag vortexes, one emerging from the origin in the upper-right direction, the other in the lower-left direction; and similarly, there are two blue frame-drag vortexes, one emerging in the upper-left direction and the other in the lower-right direction.

10.5.4 Static, Quadrupolar Tidal Field and Its Tendex Lines and Tendexes

For an idealized static particle with time-independent mass-quadrupole moment $\mathcal{I}_{pq}$ and all other moments (including the mass) vanishing, the squared lapse function is $\alpha^2 = 1 + 2\Phi = 1 - (\mathcal{I}_{pq}/r)_{,pq}$ [36], where Φ is the Newtonian gravitational potential. Therefore, the particle's tidal field $\mathcal{E}_{jk} = \Phi_{,jk}$ is given by

$$\mathcal{E}_{jk} = -\frac{1}{2}\left(\frac{\mathcal{I}_{pq}}{r}\right)_{,pqjk} \ . \tag{10.53}$$

For comparison, for a particle with time-independent current-quadrupole moment $\mathcal{S}_{pq}$, the shift function is $\beta_j = (-4/3)\epsilon_{jpq}(\mathcal{S}_{pk}/r)_{,kq}$, which implies that the frame-drag field is

$$\mathcal{B}_{jk} = -\frac{2}{3}\left(\frac{\mathcal{S}_{pq}}{r}\right)_{,pqjk} \ . \tag{10.54}$$

Notice that, once the differing normalization conventions in Eq. (10.24) are accounted for, Eqs. (10.53) and (10.54) are the same, as required by the duality relations, Eqs. (10.20) and (10.24).

This means that, for a static current quadrupole whose only nonzero components are $\mathcal{I}_{xz} = \mathcal{I}_{zx}$, the tendex lines will have precisely the same forms as the vortex lines of the static current quadrupole in Eq. (10.51); i.e., they will have the forms shown in Fig. 10.6b. In this case, there are two negative-tendicity (solid red) tidal tendexes, one emerging from the origin in the upper-right direction, and the other in the lower-left direction; and there are two positive-tendicity (dashed blue) tidal tendexes, one emerging in the upper-left direction and the other in the lower-right direction.

10.6 Gravitational Waves and Their Generation

We turn now to dynamical situations, which we describe using linearized gravity. We first discuss the tendexes and vortexes of planar gravitational waves. We then examine wave generation by time-varying multipolar fields, and the accompanying tendex and vortex structures of these systems.

10.6.1 Planar Gravitational Waves

In this section, we will describe the features of $\boldsymbol{\mathcal{E}}$ and $\boldsymbol{\mathcal{B}}$ for locally planar gravitational waves, and we will connect our results to those of linearized-gravity theory and the Newman-Penrose (NP) formalism. In Appendix 10.A, we review the Newman-Penrose formalism and its connection to the spatial tensors $\boldsymbol{\mathcal{E}}$ and $\boldsymbol{\mathcal{B}}$.

Consider gravitational-wave propagation in an asymptotically flat spacetime, in a transverse-traceless (TT) gauge. Near future null infinity, $\mathcal{I}^+$, we can linearize around a Minkowski background to find the following expressions for $\boldsymbol{\mathcal{E}}$ and $\boldsymbol{\mathcal{B}}$:

$$\mathcal{E}_{ij} = -\frac{1}{2}\partial_0^2 h_{ij}\,, \quad \mathcal{B}_{ij} = -\frac{1}{2}\epsilon_i{}^{pq} n_p \partial_0^2 h_{qj}\,. \tag{10.55}$$

It is convenient to expand these expressions in terms of the two gravitational-wave polarization tensors, e^+_{ij} and $e^\times_{ij}$, as

$$\mathcal{E}_{ij} = -\frac{1}{2}(\ddot{h}_+ e^+_{ij} + \ddot{h}_\times e^\times_{ij})\,, \tag{10.56}$$

$$\mathcal{B}_{ij} = -\frac{1}{2}(\ddot{h}_+ e^\times_{ij} - \ddot{h}_\times e^+_{ij})\,, \tag{10.57}$$

where e^+_{ij} and $e^\times_{ij}$ are symmetric, trace-free, and orthogonal to the waves' propagation direction. Letting the unit-norm vector $\mathbf{e}_{\hat{1}}$ denote the direction of propagation of the gravitational wave, then one can expand the polarization tensors in terms of the remaining two vectors of an orthonormal triad, $\mathbf{e}_{\hat{2}}$ and $\mathbf{e}_{\hat{3}}$, as

$$\boldsymbol{e}_+ = \boldsymbol{e}_{\hat{2}} \otimes \boldsymbol{e}_{\hat{2}} - \boldsymbol{e}_{\hat{3}} \otimes \boldsymbol{e}_{\hat{3}}\,, \tag{10.58}$$

$$\boldsymbol{e}_\times = \boldsymbol{e}_{\hat{2}} \otimes \boldsymbol{e}_{\hat{3}} + \boldsymbol{e}_{\hat{3}} \otimes \boldsymbol{e}_{\hat{2}}\,. \tag{10.59}$$

For a + polarized wave, Eq. (10.56) states that

$$\boldsymbol{\mathcal{E}} = -\frac{1}{2}\ddot{h}_+ \boldsymbol{e}^+ = \frac{1}{2}[(-\ddot{h}_+)\boldsymbol{e}_{\hat{2}} \otimes \boldsymbol{e}_{\hat{2}} + \ddot{h}_+ \boldsymbol{e}_{\hat{3}} \otimes \boldsymbol{e}_{\hat{3}}]\,, \tag{10.60}$$

and we conclude that $\mp\ddot{h}_+/2$ are the two eigenvalues of $\boldsymbol{\mathcal{E}}$ (the two tendicities), and $\boldsymbol{e}_{\hat{2}}$ and $\boldsymbol{e}_{\hat{3}}$ are the two corresponding eigenvectors. Now, define a second basis locally rotated at each point by an angle $\pi/4 = 45^{\rm o}$,

$$\begin{pmatrix} \tilde{\boldsymbol{e}}_{\hat{2}} \\ \tilde{\boldsymbol{e}}_{\hat{3}} \end{pmatrix} = \begin{pmatrix} \cos\frac{\pi}{4} & \sin\frac{\pi}{4} \\ -\sin\frac{\pi}{4} & \cos\frac{\pi}{4} \end{pmatrix} \begin{pmatrix} \boldsymbol{e}_{\hat{2}} \\ \boldsymbol{e}_{\hat{3}} \end{pmatrix}\,. \tag{10.61}$$

Then, a simple calculation shows that

$$\boldsymbol{e}_\times = \tilde{\boldsymbol{e}}_{\hat{2}} \otimes \tilde{\boldsymbol{e}}_{\hat{2}} - \tilde{\boldsymbol{e}}_{\hat{3}} \otimes \tilde{\boldsymbol{e}}_{\hat{3}}\,, \tag{10.62}$$

and one can immediately see that $\boldsymbol{\mathcal{B}}$ is diagonal in this new basis

$$\boldsymbol{\mathcal{B}} = -\frac{1}{2}\ddot{h}_+ \boldsymbol{e}^\times = -\frac{1}{2}[\ddot{h}_+ \tilde{\boldsymbol{e}}_{\hat{2}} \otimes \tilde{\boldsymbol{e}}_{\hat{2}} - \ddot{h}_+ \tilde{\boldsymbol{e}}_{\hat{3}} \otimes \tilde{\boldsymbol{e}}_{\hat{2}}]\,. \tag{10.63}$$

The eigenvalues of $\boldsymbol{\mathcal{B}}$ (the vorticities), like those of $\boldsymbol{\mathcal{E}}$ (the tendicities), are $\mp\ddot{h}_+/2$, but $\boldsymbol{\mathcal{B}}$'s eigenvectors, $\tilde{\boldsymbol{e}}_{\hat{2}}$ and $\tilde{\boldsymbol{e}}_{\hat{3}}$, are locally rotated by $\pi/4$ radians compared to those of $\boldsymbol{\mathcal{E}}$ (and the vortex lines of h_+ must be locally rotated by $\pi/4$ with respect to the tendex lines as well).

This relationship between the tendex and vortex lines is most transparent for a planar gravitational wave. In Fig. 10.7, we show the tendex and vortex lines of a gravitational wave propagating out of the page (i.e., $\mathbf{e}_{\hat{1}} = \mathbf{e}_{\hat{z}}$ is the propagation direction). Because the eigenvectors of $\boldsymbol{\mathcal{E}}$ are $\mathbf{e}_{\hat{2}} = \mathbf{e}_{\hat{x}}$ and $\mathbf{e}_{\hat{3}} = \mathbf{e}_{\hat{y}}$, the tendex lines are the lines of constant x and y, illustrated by red (solid) lines and blue (dashed) lines, respectively, on the left of Fig. 10.7. Similarly, the vortex lines are lines of constant $x \pm y$, again drawn as blue (dashed) lines and red (solid) lines, respectively. The tendicity (vorticity) has constant magnitude along the lines, but the two sets of tendex (vortex) lines have opposite sign; consequently, the tidal (frame-drag) field produces a stretching (counterclockwise differential precession) along the solid red direction and a squeezing (clockwise differential precession) of the same magnitude along the dashed blue direction.

More generally, gravitational waves will contain both + and × polarizations, and to study their vortex and tendex lines, it will be useful to express the electric and magnetic tensors in the spatial

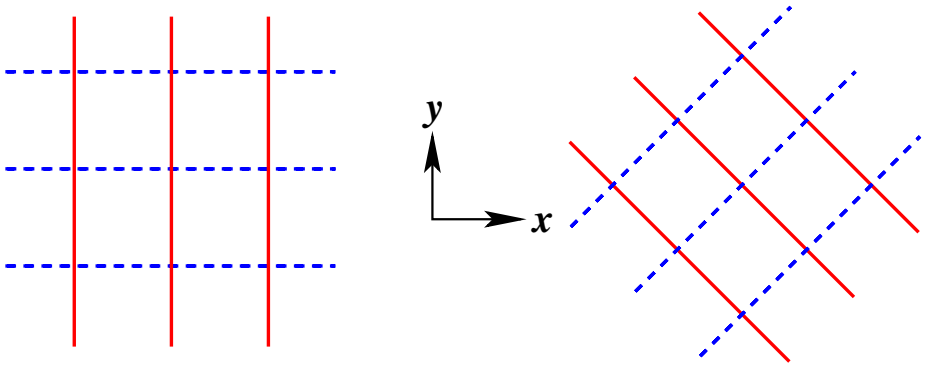

Figure 10.7: The tendex lines (left) and vortex lines (right) of a planar gravitational wave propagating in the z direction (out of the picture). The tendex lines are lines of constant x and y, and the vortex lines are rotated by $\pi/4$ radians (lines of constant $x \pm y$). The blue (dashed) curves correspond to positive tendicity and vorticity (squeezing and clockwise differential precessing, respectively) and the red (solid) curves denote negative tendicity and vorticity (stretching and counterclockwise precessing). The tendicity (vorticity) is constant along a tendex line (vortex line), and the tendicity (vorticity) of a red line is equal in magnitude but opposite in sign to that of a blue (dashed) line.

orthonormal basis $(\boldsymbol{e}_{\hat{1}}, \boldsymbol{e}_{\hat{2}}, \boldsymbol{e}_{\hat{3}})$. They can be written conveniently as matrices:

$$\mathcal{E}_{\hat{a}\hat{b}} = \frac{1}{2}\begin{pmatrix} 0 & 0 & 0 \\ 0 & -\ddot{h}_+ & -\ddot{h}_\times \\ 0 & -\ddot{h}_\times & \ddot{h}_+ \end{pmatrix}, \tag{10.64a}$$

$$\mathcal{B}_{\hat{a}\hat{b}} = \frac{1}{2}\begin{pmatrix} 0 & 0 & 0 \\ 0 & \ddot{h}_\times & -\ddot{h}_+ \\ 0 & -\ddot{h}_+ & -\ddot{h}_\times \end{pmatrix}. \tag{10.64b}$$

It is useful to introduce an associated Newman-Penrose null tetrad consisting of two real null vectors, $\vec{l}$ (along the waves' propagation direction) and $\vec{n}$, and a conjugate pair of complex null vectors $\vec{m}$ and $\vec{m}^*$ given by

$$\vec{l} = \frac{1}{\sqrt{2}}(\vec{e}_{\hat{0}} + \vec{e}_{\hat{1}})\,, \qquad \vec{n} = \frac{1}{\sqrt{2}}(\vec{e}_{\hat{0}} - \vec{e}_{\hat{1}})\,,$$
$$\vec{m} = \frac{1}{\sqrt{2}}(\vec{e}_{\hat{2}} + i\vec{e}_{\hat{3}})\,, \qquad \vec{m}^* = \frac{1}{\sqrt{2}}(\vec{e}_{\hat{2}} - i\vec{e}_{\hat{3}}) \tag{10.65}$$

(Eqs. (10.80) of Appendix 10.A). For plane waves on a Minkowski background, the NP curvature scalar that characterizes the radiation is

$$\Psi_4 = C_{\mu\nu\rho\sigma} n^\mu m^{*\nu} n^\rho m^{*\sigma} = -\ddot{h}_+ + i\ddot{h}_\times\,; \tag{10.66}$$

we can compactly rewrite Eqs. (10.64), therefore, as

$$\mathcal{E}_{\hat{a}\hat{b}} + i\mathcal{B}_{\hat{a}\hat{b}} = \frac{1}{2}\begin{pmatrix} 0 & 0 & 0 \\ 0 & \Psi_4 & i\Psi_4 \\ 0 & i\Psi_4 & -\Psi_4 \end{pmatrix} . \tag{10.67}$$

This expression holds for any gravitational wave propagating in the $\vec{e}_{\hat{1}}$ direction.

For any outgoing gravitational wave in an asymptotically flat space, as one approaches asymptotic null infinity the general expression for $\mathcal{E}_{\hat{a}\hat{b}} + i\mathcal{B}_{\hat{a}\hat{b}}$ (Eq. (10.82) of Appendix 10.A) reduces to Eq. (10.67), because all the curvature scalars except Ψ_4 vanish near future null infinity (because of the peeling property of the Weyl scalars). Further discussion of the tidal and frame-drag fields of radiation near null infinity and their tendex and vortex lines is given in [28].

It is helpful to draw some simple analogies between gravitational and electromagnetic plane waves. For a generic mixture of + and × polarizations, the magnitudes of the nonvanishing eigenvalues of both $\boldsymbol{\mathcal{E}}$ and $\boldsymbol{\mathcal{B}}$ are simply

$$\frac{1}{2}\sqrt{\ddot{h}_+^2 + \ddot{h}_\times^2} = \frac{1}{2}|\Psi_4| . \tag{10.68}$$

This mirrors plane waves in electromagnetism, where $|\vec{E}| = |\vec{B}|$ is equal to the sum in quadrature of the magnitudes of the two polarizations. The absence of longitudinal components in an electromagnetic plane wave corresponds to the vanishing of the eigenvalues for the eigenvectors of $\boldsymbol{\mathcal{E}}$ and $\boldsymbol{\mathcal{B}}$ along the propagation direction. Finally, the orthogonality of the vectorial electromagnetic field strengths $\vec{E}\perp\vec{B}$ is analogous to the relative angle of $\pi/4$ between the two grids formed by the two vortex lines and the two tendex lines in Fig. 10.7), respectively.

10.6.2 Gravitational Waves from a Head-on Collision of Two Black Holes

As an application of our results for gravitational waves, we calculate the tendex and vortex lines at large radii for gravitational waves emitted by the head-on collision of two equal-mass nonspinning black holes. If the holes move along the z axis, we use as our spatial triad the unit vectors of spherical polar coordinates $[(\mathbf{e}_{\hat{1}}, \mathbf{e}_{\hat{2}}, \mathbf{e}_{\hat{3}}) = (\mathbf{e}_{\hat{r}}, \mathbf{e}_{\hat{\theta}}, \mathbf{e}_{\hat{\phi}}) = (\partial_r, r^{-1}\partial_\theta, (r\sin\theta)^{-1}\partial_\phi)]$, and we choose our null tetrad as shown in Eq. (10.65), then we can apply the results described by Fiske et al. [43]: namely, that $\Re[\Psi_4]$ is axisymmetric (and, when decomposed into spin-weighted spherical harmonics, is dominated by ${}_{-2}Y_{2,0}(\theta,\phi)$, an $l = 2$, $m = 0$ harmonic) and that $\Im[\Psi_4] = 0$. Then the electric and

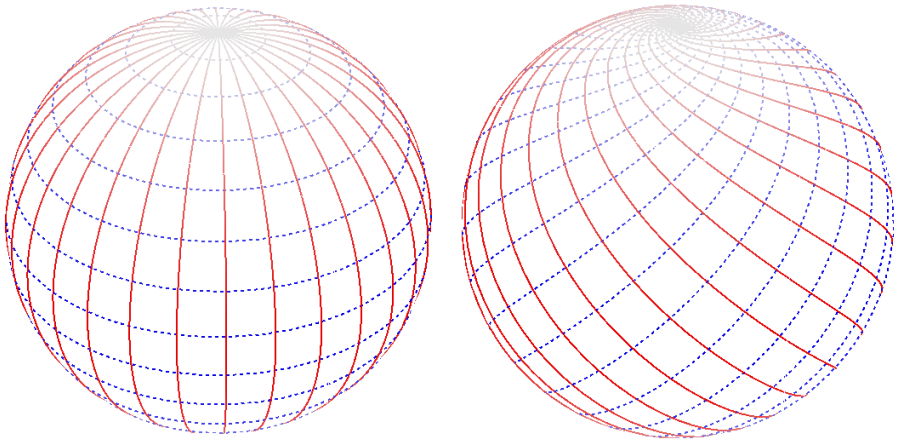

Figure 10.8: Tendex lines (left) and vortex lines (right) for the gravitational waves that would arise from the merger of equal-mass black holes falling together along the z axis. The positive tendicity and vorticity lines are shown in blue (dashed) and the negative lines are depicted in red (solid). Each line's intensity is proportional to its tendicity (or vorticity), which varies over the sphere as the dominant spin-weighted spherical harmonic, ${}_{-2}Y_{2,0}(\theta,\phi) \propto \sin^2\theta$. Dark red and blue near the equator correspond to large-magnitude tendicity and vorticity, and light, nearly white, colors at the poles indicate that the tendicity and vorticity are small there.

magnetic parts of the Weyl tensor are given by

$$\mathcal{E}_{\hat{a}\hat{b}} = \frac{1}{2}\begin{pmatrix} 0 & 0 & 0 \\ 0 & \Re(\Psi_4) & 0 \\ 0 & 0 & -\Re(\Psi_4) \end{pmatrix}, \tag{10.69}$$

$$\mathcal{B}_{\hat{a}\hat{b}} = \frac{1}{2}\begin{pmatrix} 0 & 0 & 0 \\ 0 & 0 & \Re(\Psi_4) \\ 0 & \Re(\Psi_4) & 0 \end{pmatrix}, \tag{10.70}$$

and the eigenvalues of both $\boldsymbol{\mathcal{E}}$ and $\boldsymbol{\mathcal{B}}$ are $\pm\Re(\Psi_4)/2$. The eigenvectors of $\boldsymbol{\mathcal{E}}$ are the unit vectors $\mathbf{e}_{\hat{\theta}}$ and $\mathbf{e}_{\hat{\phi}}$, and those of $\boldsymbol{\mathcal{B}}$ are $\mathbf{e}_{\hat{\theta}} \pm \mathbf{e}_{\hat{\phi}}$. Thus, the radiation is purely + polarized in this basis. The tendex lines are the lines of constant θ and ϕ on a sphere, and the vortex lines are rotated relative to the tendex lines by an angle of $\pi/4 = 45°$.

We show these lines in Fig. 10.8: the tendex lines on the left, and the vortex lines on the right. As in Fig. 10.7, the red (solid) lines correspond to negative tendicity and vorticity, and the blue (dashed) lines denote positive values. The intensity of each line is proportional to the magnitude of its tendicity (or vorticity), which varies over the sphere as ${}_{-2}Y_{2,0}(\theta,\phi) \propto \sin^2\theta$ (the dominant spherical harmonic). Correspondingly, the dark blue and red regions near the equator represent strong tendicity and vorticity, whereas the light, off-white colors near the poles indicate that the tendicity and vorticity are small there.

We remark in passing that the duality of $\boldsymbol{\mathcal{E}}$ and $\boldsymbol{\mathcal{B}}$ implies that, if there were a source of gravitational waves which had a purely imaginary Ψ_4 that was equal to $i\Re[\Psi_4]$ for our colliding black holes,

then those waves' vortex lines would be the same as the tendex lines of Fig. 10.8, and the tendex lines would be the same as the vortex lines of the same figure (but with the sign of the lines' vorticity flipped). One can see this because (i) Eq. (10.66) shows we would have a pure $\times$ polarized wave, and (ii) when we apply the rotation of the basis in Eq. (10.61) to Eq. (10.67) under the condition that $\Re(\Psi_4) = 0$, we get once again the matrices (10.69), but with $(\tilde{\boldsymbol{e}}_{\hat{2}}, \tilde{\boldsymbol{e}}_{\hat{3}})$ as basis vectors and with all instances of $\Re(\Psi_4)$ replaced by $\Im(\Psi_4)$. This duality does not address, however, how to construct a source with a purely imaginary Ψ_4.

10.6.3 Wave Generation by a Time-Varying Current Quadrupole

A dynamical current-quadrupole moment $\mathcal{S}_{pq}(t)$ generates a metric perturbation described by the $\mathcal{S}_{pq}(t-r)/r$ terms in Eqs. (8.13) of [36]. It is straightforward to show that the corresponding frame-drag field is

$$\mathcal{B}_{ij} = \frac{2}{3}\left[-\left(\frac{\mathcal{S}_{pq}}{r}\right)_{,pqij} + \epsilon_{ipq}\left(\frac{{}^{(2)}\mathcal{S}_{pm}}{r}\right)_{,qn}\epsilon_{jmn} + 2\left(\frac{{}^{(2)}\mathcal{S}_{p(i}}{r}\right)_{,j)p} - \left(\frac{{}^{(4)}\mathcal{S}_{ij}}{r}\right)\right] . \tag{10.71}$$

Here $\mathcal{S}_{pq}$ is to be regarded as a function of retarded time, $t-r$, and the prefixes ${}^{(2)}$ and ${}^{(4)}$ mean two and four time derivatives, respectively. This equation shows explicitly how $\mathcal{B}_{ij}$ in the near zone transitions into $\mathcal{B}_{ij}$ in the wave zone—or equivalently, how rotating (or otherwise time-changing) frame-drag vortexes in the near zone generate gravitational waves.

This transition from the near zone to the far zone can also be described by the linear approximation to the Maxwell-like equations for the frame-drag field, $\boldsymbol{\mathcal{B}}$, and the tidal field, $\boldsymbol{\mathcal{E}}$, Eqs. (10.21). These equations govern the manner by which the current-quadrupole, near-zone frame-drag field, Eq. (10.54), acquires an accompanying tidal field as it reaches outward into and through the transition zone, to the wave zone. That accompanying tidal field is most easily deduced from the $\mathcal{S}_{pq}(t-r)/r$ terms in the metric perturbation, Eqs. (8.13) of [36]. The result is

$$\mathcal{E}_{ij} = \frac{4}{3}\epsilon_{pq(i}\left[-\left(\frac{{}^{(1)}\mathcal{S}_{pk}}{r}\right)_{,j)kq} + \left(\frac{{}^{(3)}\mathcal{S}_{j)p}}{r}\right)_{,q}\right] . \tag{10.72}$$

In the near zone, the current quadrupole's tidal field (in Eq. (10.72), the first term) behaves differently from its frame-drag field (in Eq. (10.71), the first term): it has one additional time derivative and one fewer spatial derivative. As a result, the tidal field is smaller than the frame-drag field in the near zone by a factor of $r/\lambda\!\!\!^{-}$, where $\lambda\!\!\!^{-}$ is the reduced wavelength of the emitted gravitational waves. As one moves outward through the near zone to the transition zone, where $r \sim \lambda\!\!\!^{-}$, the tidal field increases in magnitude to become roughly the same strength as the frame-drag field. The frame-drag and tidal fields behave this way, because it is the near-zone vortexes that generate the gravitational waves, as discussed above.

In the wave zone, the general current-quadrupole (outgoing-wave) frame-drag field, Eq. (10.71), reduces to

$$\mathcal{B}_{\hat{a}\hat{b}} = \frac{4}{3r}\left[{}^{(4)}S_{\hat{a}\hat{b}}(t-r)\right]^{\rm TT} \ . \tag{10.73}$$

Here the indices are confined to transverse directions (the surface of a sphere of constant r) in the orthonormal basis $\boldsymbol{e}_{\hat{\theta}}$, $\boldsymbol{e}_{\hat{\phi}}$, and "TT" means to take the transverse, traceless part. From the third of the Maxwell-like equations in Eq. (10.21), or equally well from the general current-quadrupole tidal field, Eq. (10.72), we infer the wave-zone tidal field:

$$\mathcal{E}_{\hat{a}\hat{b}} = \frac{4}{3r}\left[\epsilon_{\hat{c}(\hat{a}}\,{}^{(4)}\mathcal{S}_{\hat{b})\hat{c}}(t-r)\right]^{\rm TT} \ , \tag{10.74}$$

where $\epsilon_{\hat{c}\hat{d}}$ is the 2-dimensional Levi-Civita tensor on the sphere. Because $\mathcal{E}_{\hat{a}\hat{b}} = \mathcal{R}_{\hat{a}\hat{0}\hat{b}\hat{0}} = -\frac{1}{2}{}^{(2)}h^{\rm TT}_{\hat{a}\hat{b}}$, where $h^{\rm TT}_{\hat{a}\hat{b}}$ is the transverse, traceless gravitational-wave field, our wave-zone tidal distortion, Eq. (10.74), agrees with the standard result for the wave-zone current-quadrupole gravitational-wave field (Eq. (4.8) of [36]).

10.6.4 Rotating Current Quadrupole

In this section, we will discuss the vortex and tendex lines of a rotating current quadrupole. A large rotating-current-quadrupole moment arises during the merger and ringdown of the extreme-kick configuration of a binary black hole (a quasicircular binary made of identical black holes, whose spins are antialigned and lie in the orbital plane). During the merger, the four vortexes associated with the initial holes' spins get deposited onto the merged horizon's equator, and they then rotate around the final Kerr hole's spin axis at the same rate as their separation vector rotates, generating a large, rotating-current-quadrupole moment (Paper III in this series).

As a simple linearized-gravity model of this late time behavior, imagine that at an initial time $t = 0$, the two vortex-generating spins, of magnitude S, are separated by a distance a along the x axis and are pointing in the $\pm y$ direction—i.e., they have the same configuration as the static current quadrupole discussed in Section 10.5.3 above. Then at $t = 0$, the spins' current-quadrupole moment has as its nonzero components $\mathcal{S}_{xy} = \mathcal{S}_{yx} = Sa$ (Eq. (10.51) with the spin axes changed from z to y). As time passes, the spins' separation vector and the spins' directions rotate at the same angular velocity ω so that the configuration rotates rigidly. Then it is not hard to show that the current-quadrupole moment evolves as

$$\begin{aligned} \mathcal{S}_{xy} &= \mathcal{S}_{yx} = Sa\cos(2\omega t)\,, \\ \mathcal{S}_{xx} &= -\mathcal{S}_{yy} = -Sa\sin(2\omega t)\,. \end{aligned} \tag{10.75}$$

It is straightforward to calculate the frame-drag field produced by this quadrupole moment using

Eq. (10.71), and to then compute the vortex lines and their vorticities. The explicit expressions for these lines are somewhat lengthy, and not particularly instructive, but the shapes of the vortex lines and the values of their vorticities are quite interesting.

10.6.4.1 Vortex and Tendex Lines in the Plane of Reflection Symmetry

There are two sets of vortex lines that lie in the x-y plane (the plane of reflection symmetry) and one set that passes orthogonally through this plane. We show the in-plane vortex lines in Figs. 10.9 and 10.10. The two figures depict the negative-vorticity vortex lines by red (solid) curves and the positive-vorticity lines by blue (dashed) curves. The darkness of the lines is proportional to the vorticity; dark red (blue) indicates strong negative (positive) vorticity, and light red (blue) indicates weaker vorticity. To remove the effects of the radial dependence in the coloring, we have scaled the vorticity by $(kr)^5/[1+(kr)^4]$, where $k = 1/\lambda\!\!\!^{-} = 2\omega$ is the wave number of the radiation. Figure 10.9 shows the region of the near zone that is difficult to see in Fig. 10.10, an equivalent figure that spans a larger region of the x-y plane. As one can see from the figures, the two sets of lines have the same pattern, but are rotated with respect to each other by $\pi/2 = 90°$.

In the near zone (inner region of Fig. 10.9), the vortex-line pattern is the same as for the static current quadrupole of Fig. 10.6b. At the transition to the wave zone, the vortex lines fail to curve back into the central region and instead bend outward, joining a wave-zone spiral pattern. That spiral pattern consists of four vortexes (regions of concentrated vorticity) that spiral outward and backward as the quadrupole rotates. These four regions of alternating positive and negative vorticity are bounded by tight clusters of vortex lines, just outside of which the sign of the dominant vorticity changes. This same rotating vortex structure occurs in the case of an $l = 2$, $m = 2$, odd-parity (current-quadrupolar) perturbation of a Schwarzschild black hole (Paper II in this series). There the horizon vorticity takes the place of the current quadrupole in the near zone.

In Fig. 10.11 we indicate the structure of the tendex lines on the equatorial plane. Because the symmetry properties of the system imply different constraints on the tendex field than on the vortex field, some explanation is needed. The plane in which this and the previous two figures are drawn is a plane of reflection symmetry for the problem. However, because the source is a pure current quadrupole, it must be antisymmetric under reflection across this plane (as such a reflection is a parity inversion). The vorticity, which itself has an odd-parity relationship with its source, is symmetric under this reflection, constraining the vortex lines to be either tangent or orthogonal to the plane, as noted above. The tendicity is antisymmetric under this reflection; therefore, one family of lines can be tangent to the plane, so long as it has zero tendicity, and two other families of lines must cross the plane at equal and opposite inclinations, with equal and opposite tendicities, such that they are exchanged under the reflection. The diagram in Fig. 10.11 shows the single family of tendex lines tangent to the symmetry plane. As these curves have exactly zero tendicity, they

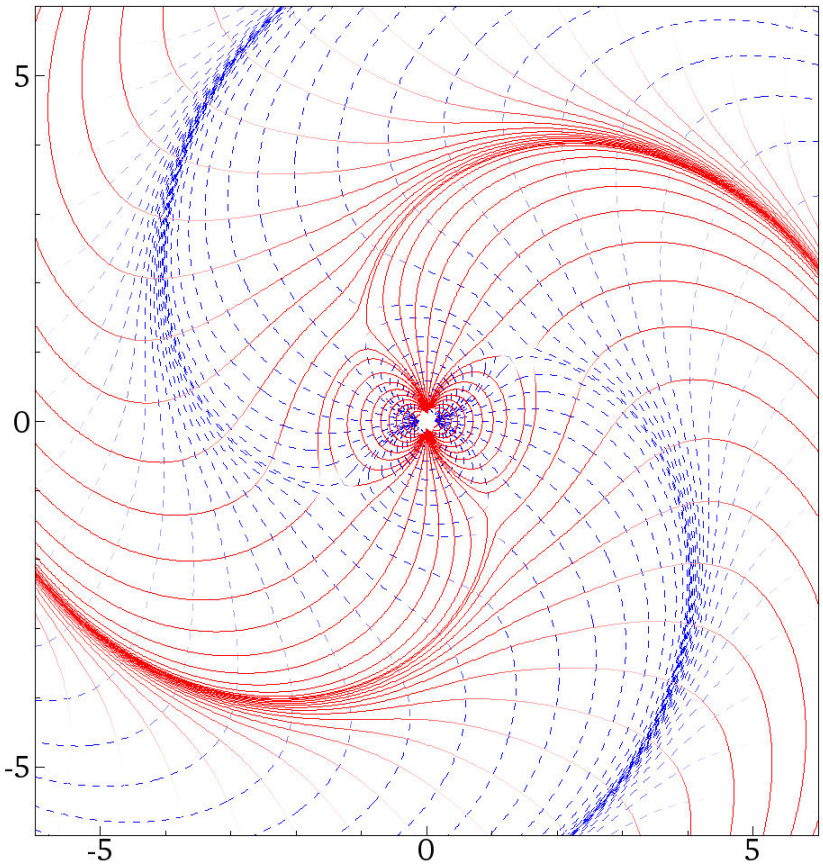

Figure 10.9: For a rotating current quadrupole in linearized theory, two families of vortex lines in the plane of reflection symmetry (the x-y plane). The red (solid) curves are lines with negative vorticity, and the blue (dashed) curves are lines of positive vorticity. The color intensity of the curves represents the strength of the vorticity, but rescaled by $(kr)^5/[1+(kr)^4]$ (with k the wave number) to remove the vorticity's radial decay. We see the quadrupolar near-zone pattern and the transition into the induction zone. In the induction zone, the pattern carries four "triradius" singular points [44] in each family of curves; they are necessary for the transition from the static quadrupole pattern to the spiraling radiation pattern. This same figure also describes the tendex lines of a rotating mass quadrupole (see the end of Section 10.6.6).

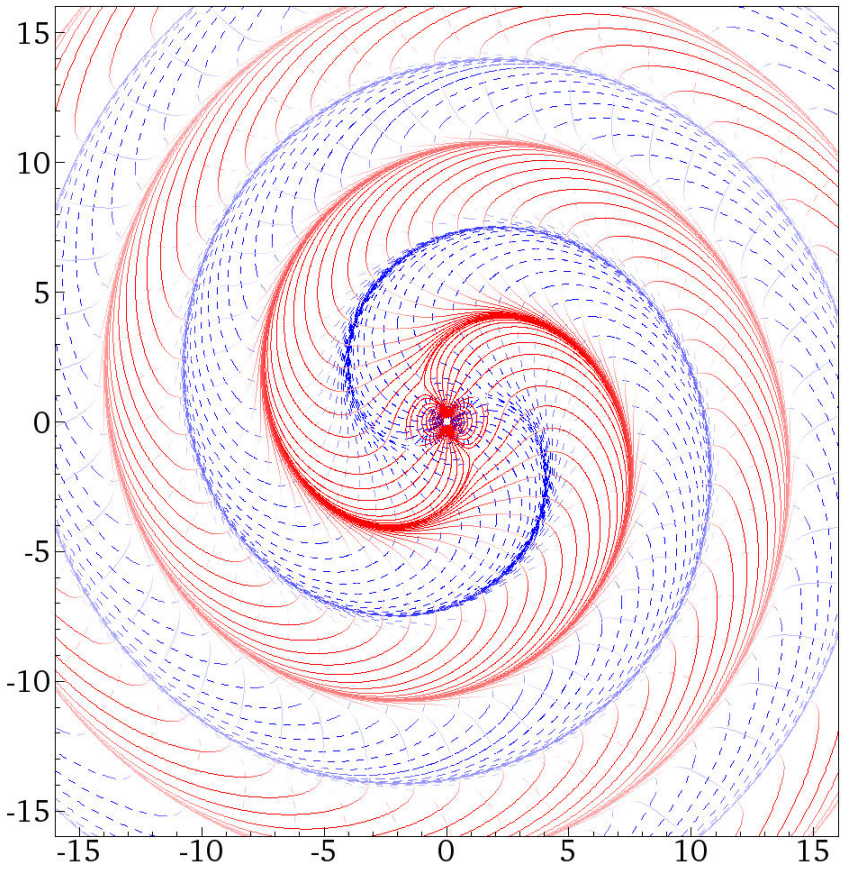

Figure 10.10: Same as Fig. 10.9 but zoomed out to show the wave zone. In the wave zone, the lines generically collect into spirals, which form the boundaries of vortexes (regions of concentrated vorticity).

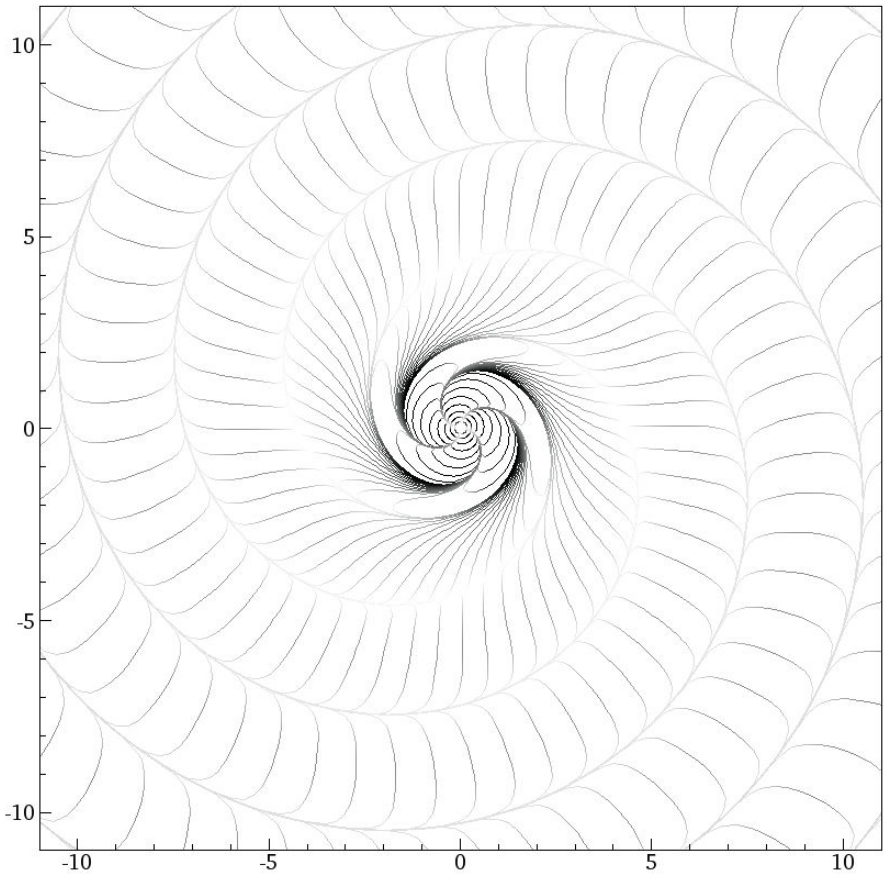

Figure 10.11: Tendex lines in the equatorial plane for a rotating current quadrupole in linearized theory. The curves shown are lines of identically zero tendicity (required by symmetry of the current quadrupole). The lines are shaded by the absolute value of the tendicity of the other two tendex lines that cross the lines shown, but are not tangent to the plane, and have equal and opposite tendicities.

are physically relevant only in that they denote the orientation of the other two families of tendex lines, which are not tangent to the plane, but whose projection onto the plane must be orthogonal to the curves shown (because all three curves are mutually orthogonal). The shading of the lines in Fig. 10.11 does not represent the tendicity of the lines drawn (which is identically zero), but rather of the other two tendex lines, which intersect the lines drawn with mutually equal and opposite tendicity. Again, this shading is rescaled by $(kr)^5/[1+(kr)^4]$. Though it is not apparent to the eye, the strength of the tendicity grows only as r^4 near the singular point (origin), rather than r^5 as for the vorticity. As argued early in Section 10.6.3, this can be interpreted intuitively as meaning that the vorticity is sourced directly from the current quadrupole, while the tendicity is sourced by induction from the time-varying vortex field.

For a rotating mass quadrupole (e.g., the quadrupole moment of an equal-mass binary), the tendex lines in the plane of reflection symmetry will have precisely the same form as the rotating-current-quadrupole vortex lines of Figs. 10.9 and 10.10; see Section 10.6.6.

10.6.4.2 Vortex Lines Outside the Plane of Reflection Symmetry: Transition from the Near Zone to the Wave Zone

Outside the plane of reflection symmetry and in the wave zone, the extrema of the vorticity show a spiraling pattern that is the same at all polar angles. More specifically, at all polar angles θ, the magnitude of the vorticity, as a function of azimuthal angle ϕ, has four maxima, and the locations of those maxima are the same as in the equator ($\theta = \pi/2$). As in the equator, the maxima at fixed time t spiral around at an angular rate $d\phi_{\rm max}/dr = -\omega$ as one moves outward in radius, and as in the equator, vortex lines collect near these spiraling maxima, and those lines too undergo spiraling behavior.

Figure 10.12 shows the development of this spiraling structure as one moves outward from the near zone (innermost inset) into the wave zone (outer region of figure). This figure focuses on the family of vortex lines that pass orthogonally through the x-y plane of reflection symmetry. After entering the wave zone, the lines with non-negligible vorticity (the blue and red lines) collect into a somewhat complicated spiral pattern, tangling among themselves a bit as they spiral. The gray lines with very low vorticity, by contrast, point radially outward. An animation of this rotating system can be seen at [26].

It should be noted Fig. 10.12, and the animation at [26], represent somewhat incomplete descriptions of the structure of these field lines. The red and blue helical spirals shown in Fig. 10.12 do not cross one another. However, at any point in space, there must be three mutually orthogonal vortex lines, with vorticities summing to zero. Because at all points in the wave zone there is a field line of nearly zero vorticity directed in a nearly radial direction, through any point along these spirals of positive or negative vorticity, field lines of opposite vorticity must lie orthogonal to the spiral and to

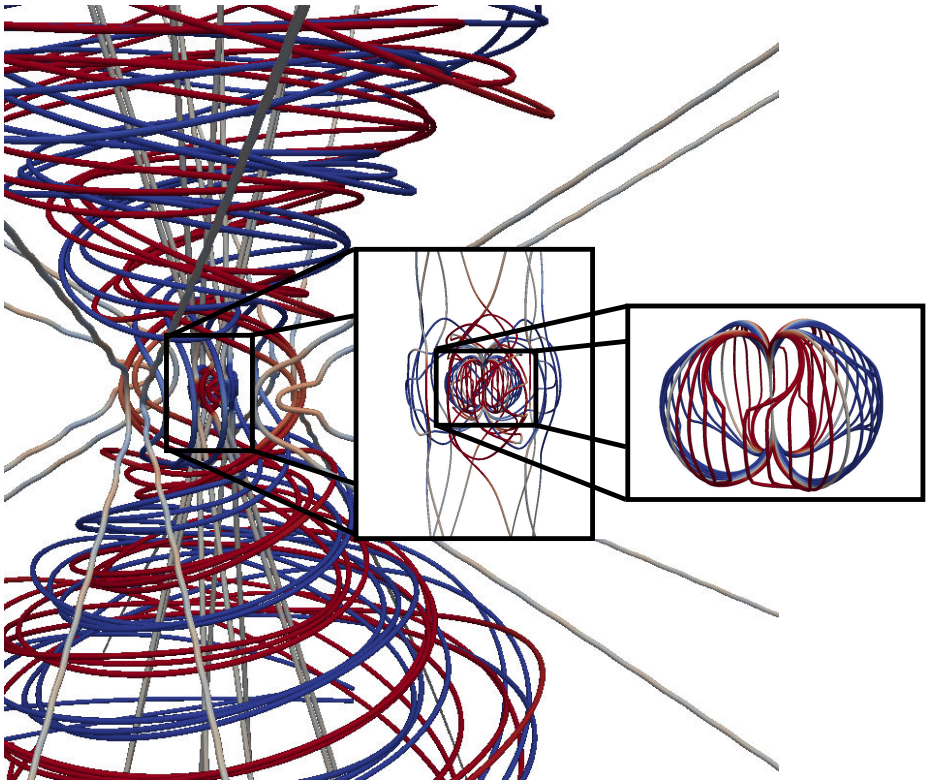

Figure 10.12: For the same rotating current quadrupole as in Figs. 10.9 and 10.10, the family of vortex lines that pass orthogonally through the x-y plane of reflection symmetry, color coded as in Fig. 10.9. In the wave zone, lines with approximately zero vorticity extend away from the source nearly radially, while lines with significant vorticity are dragged into tangled spirals by the rotation of the source. The left inset shows the transition between the near and wave zones. Here, lines with nearly zero vorticity escape to infinity, as in the wave zone, but those with significant vorticity are drawn toward the source. The right inset delves down into the near zone, where the lines are approximately those of a stationary current quadrupole. This same figure also describes the tendex lines of a rotating mass quadrupole (see the end of Section 10.6.6).

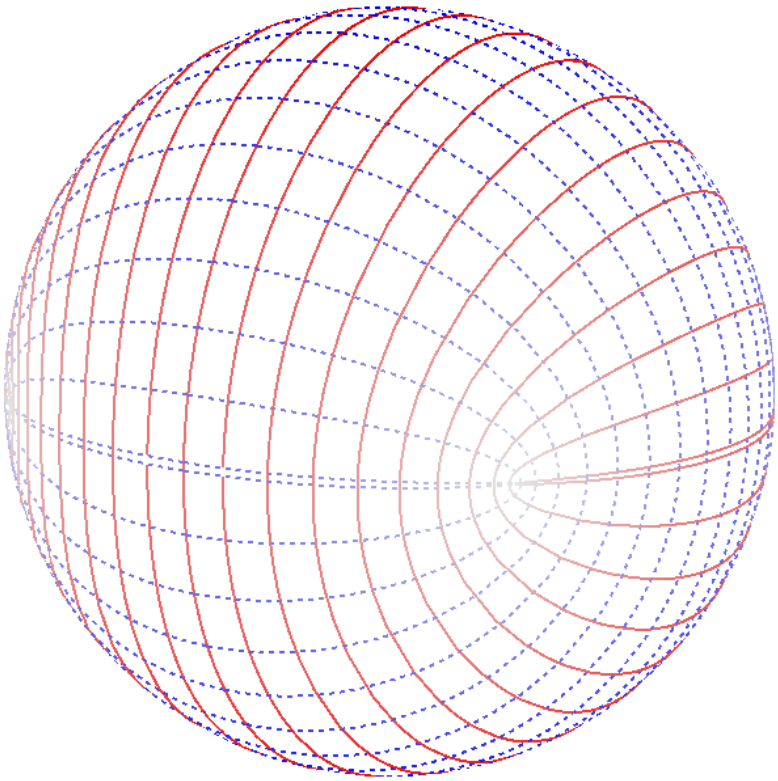

Figure 10.13: Vortex lines of a time-varying current quadrupole at very large r. The lines are colored by the vorticity scaled by r, to remove the $1/r$ falloff, but the color coding is the same as in previous figures. At very large distances from the source, the lines are transverse and live on a sphere. The third set of vortex lines not shown are radial and has vanishing vorticity.

the approximately radial lines. As shown in the following subsection, these lines form closed loops in the far-field region.

10.6.4.3 Vortex Lines in the Far Wave Zone

In the far wave zone (strictly speaking at future null infinity), the frame-drag field becomes transverse and traceless, and takes the simple form in Eq. (10.73). Of its three sets of vortex lines, one is radial (with vanishing vorticity) and the other two are tangent to a sphere of constant radius r (with vorticity of equal and opposite sign). The two sets of vortex lines on the sphere have an interesting angular pattern that is shown in Fig. 10.13. The vortex line that lies in the equator alternates between positive and negative vorticity, going to zero at four points (one of which is shown at the front of the sphere). This line is just the limit of the spirals where vortex lines collect in Fig. 10.10 at very large r. (Further discussion of the vortex and tendex lines of radiation at large r is given in [28], where the dual figure to Fig. 10.13, the tendex lines of a rotating mass quadrupole, is discussed in detail.)

How the vortex lines transition to the transverse pattern of Fig. 10.13 at very large r, from the

spiraling pattern of Fig. 10.12 in the inner wave zone, is of considerable interest. We can explore this by examining the frame-drag field at sufficiently large radii that the $1/r$ piece dominates over all other components, and that the $1/r^2$ part of the frame-drag field may be thought of as a perturbation to the leading-order $1/r$ part. In this region, the vortex lines show two kinds of qualitative behavior. Some of the vortex lines continue to form spirals that meander out and do not close, as in Fig. 10.12. There also are lines that form closed loops similar to the leading-order vortex lines of Fig. 10.13. We show both of these types of lines in Fig. 10.14. The red, solid, spiraling lines continue to collect on the maximum-vorticity spirals in the far wave zone. These lines begin to resemble the transverse lines of Fig. 10.13 more than the spiraling lines in the near wave zone of Fig. 10.12 do, because they rise and fall in polar angle as they wind around the maximum-vorticity spiral. It is only in the limit of infinite radius that these spirals close to form loops. The blue, dashed, closed lines, on the other hand, resemble the closed lines at infinity in Fig. 10.13 much more closely. The lines at finite r do have some subtle differences between the corresponding lines at infinity: At finite radii, each individual line passes from one maximum-vorticity spiral to the other; in doing so the line must slightly increase in radius and rotate in azimuthal angle. At the large radii shown in Fig. 10.14, this effect is very subtle. We finally note that there are also spiraling, positive-vorticity lines and closed, negative-vorticity lines that we do not show to avoid visual clutter.

10.6.5 Oscillating Current Quadrupole

The vortex lines of an oscillating current quadrupole (this section) have a very different structure from those of the rotating current quadrupole (last section). This should not be surprising, because the two quadrupoles arise from very different physical scenarios (e.g., for the oscillating quadrupole, the ringdown following a head-on collision of black holes with antialigned spins, and for the rotating quadrupole, the ringdown following the inspiral and merger of an extreme-kick black-hole binary). See Papers II and III of this series.

In linearized theory, one can envision an oscillating current quadrupole as produced by two particles, separated by a distance a along the x axis, whose spins, antialigned and pointing in the $\pm y$ direction, oscillate in magnitude as $S\cos\omega t$. The resulting quadrupole moment is similar to that in Eq. (10.50)

$$\mathcal{S}_{xy} = \mathcal{S}_{yx} = Sa\cos\omega t\,. \tag{10.76}$$

The frame-drag and tidal fields, and then the vortex and tendex lines, for this current quadrupole can be computed from Eqs. (10.71) and (10.72).

As for the rotating quadrupole, the x-y plane of reflection symmetry contains two families of vortex lines, and a third family passes orthogonally through that plane. The in-plane vortex lines are depicted in Figs. 10.15 and 10.16 using the same color conventions as for the rotating quadrupole (Figs. 10.9 and 10.10). Figure 10.15 shows the region of the near zone that is difficult to see in Fig.

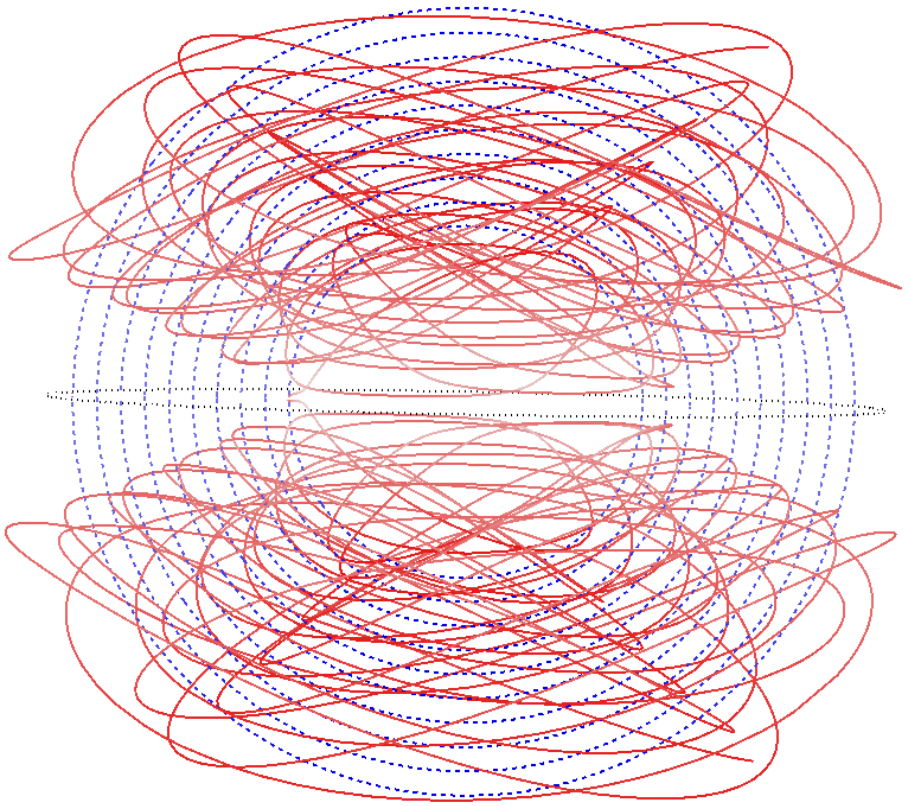

Figure 10.14: Vortex lines of a rotating current quadrupole at sufficiently large r that the $1/r^2$ part of the frame-drag field may be thought of as a perturbation to the transverse vortex lines of Fig. 10.13. The lines are colored by the vorticity, as in that figure. We also show a black dotted circle in the equatorial plane to identify this plane. The red solid lines shown here continue to collect on the maximum-vorticity spiral, but they oscillate much more in polar angle than do the similar lines shown in the near wave zone in Fig. 10.12. The blue dashed lines shown here form closed loops that pass from one positive-vorticity spiral to the next. This family of lines more closely resembles the transverse lines of Fig. 10.13, though in the limit of infinite radius, the spiraling lines will also close to form transverse lines on the sphere. There are also spiraling positive-vorticity (blue) lines and closed-loop, negative-vorticity (red) lines, but to keep the figure from appearing muddled, we do not show them.

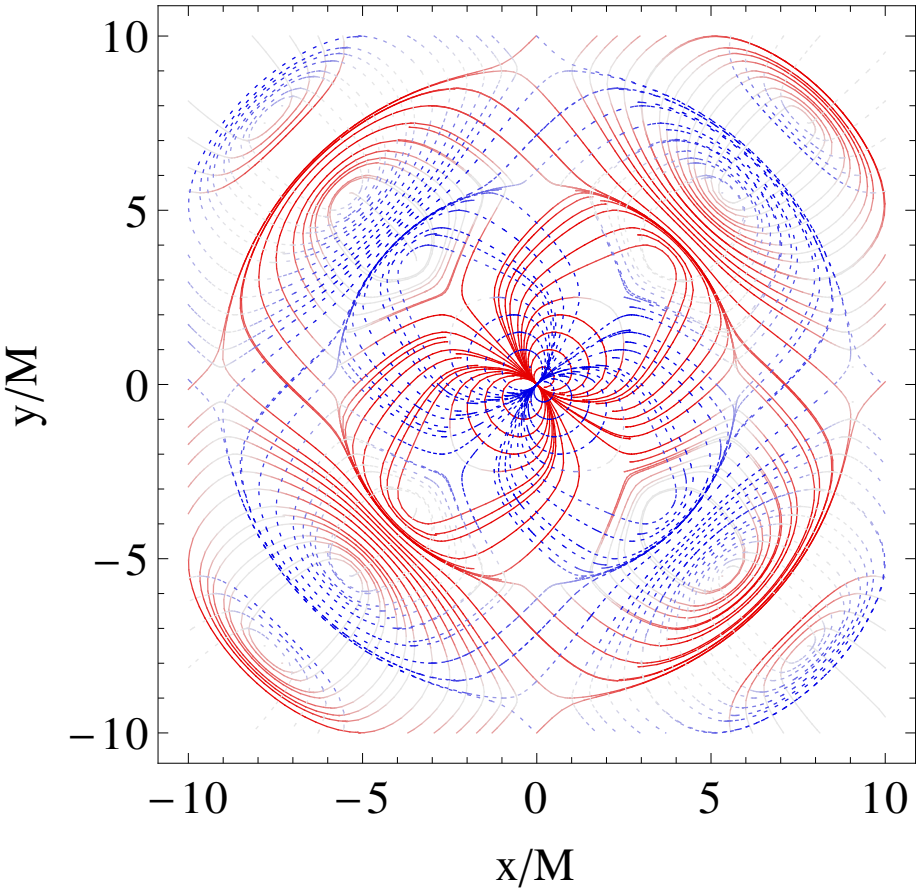

Figure 10.15: For an oscillating current quadrupole in linearized theory, two families of vortex lines in the plane of reflection symmetry (the x-y plane). The color coding is the same as for the rotating current quadrupole, Fig. 10.9. The vortex lines begin, near the origin, like the static quadrupole pattern of Fig. 10.6. The effects of time retardation cause the pattern to stretch, making larger rectangular loops in the transition zone. As time passes and the quadrupole oscillates, these loops detach from the origin and propagate out into the wave zone. This same figure also describes the tendex lines of an oscillating mass quadrupole (see the end of Section 10.6.6).

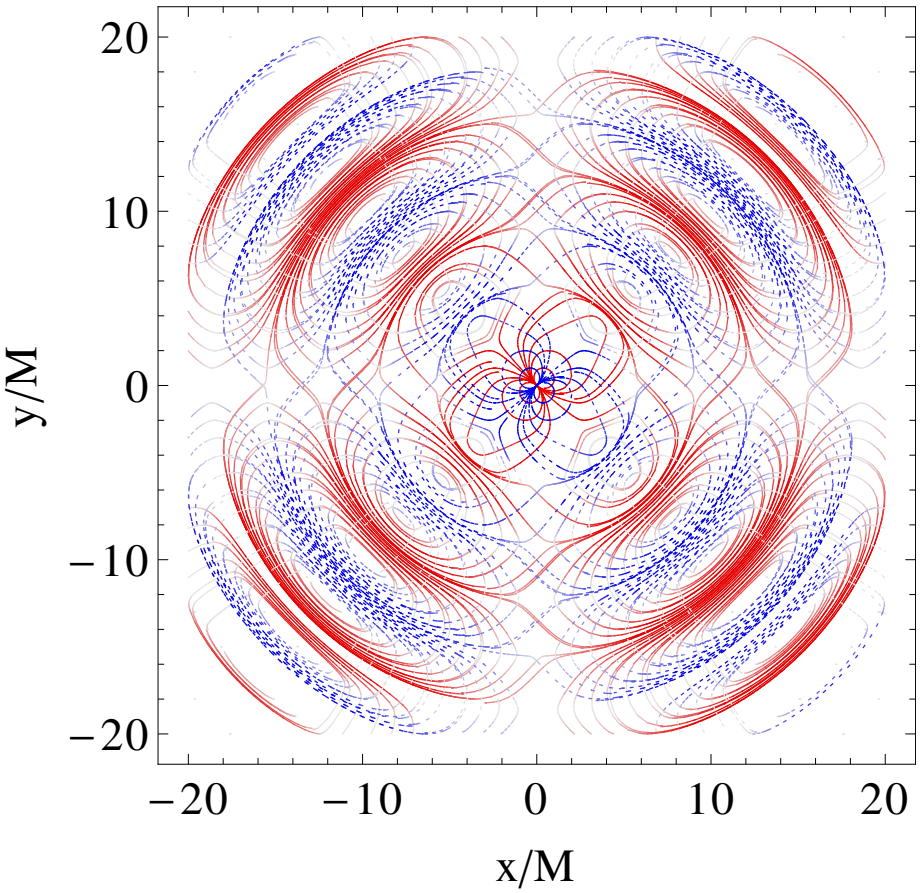

Figure 10.16: Same as Fig. 10.15, but zoomed out to show the wave zone. Farther from the source, the loops take on a more regular alternating pattern of gravitational waves. The coloring shows that the vorticity is strongest at the fronts and backs of the loops, where the vortex lines are transverse to the direction of propagation. In the regions of the closed loops that extend radially, the field is weak (as one would expect for a transverse gravitational wave).

10.16, an equivalent figure that spans a larger region of the x-y plane. As one can see from the figures, the two families of vortex lines, solid red (negative vorticity) and dashed blue (positive vorticity) have the same pattern, but are rotated by $\pi/2 = 90°$.

The way in which the gravitational waves are generated differs greatly from the rotating current quadrupole of the previous section. In the near zone, the two sets of vortex lines form a static quadrupole pattern (identical to the near-zone rotating quadrupole of Fig. 10.9, but rotated by $\pi/4$ radians because of the orientation of the spins). In the transition zone, the vortex lines form distorted loops that head away from the origin, along the lines $y = \pm x$, in an alternating fashion. As they extend into the wave zone, the lines form two qualitatively different kinds of loops. The majority of the loops reside only in one of the four quadrants of the equatorial plane, but there are also loops that pass through all four quadrants, staying near the regions of maximum vorticity, where lines collect at the gravitational-wave crests. For both types of loops, they maintain the same wavelength,

but the wave front becomes wider at larger radii, as they become gravitational waves. The portion of a loop transverse to the radial direction (the direction of propagation) has strong vorticity, as one would expect for a gravitational wave; in the radial portion of the loop, the vorticity is weak. Each cycle of the oscillating quadrupole casts off another set of vortex loops as the near-zone region passes through zero vorticity, and the loops travel outward towards infinity. This illustrates clearly the way in which the near-zone vortex pattern generates gravitational waves in the far zone through its dynamics.

As with the rotating current quadrupole, one can envision the equatorial vortex line of Fig. 10.13 as the limit of the wave fronts of the planar vortex lines in Fig. 10.16 at large distances. It is again of interest to understand how the vortex lines outside the equatorial plane become the remaining vortex lines in Fig. 10.13. To do so, we will make reference to Fig. 10.17, which shows the vortex lines at a distance sufficiently large that the $1/r^2$ portions of the frame-drag field can be thought of as a small perturbation to the transverse vortex lines of Fig. 10.13. We show only the three-dimensional analog of the lines that pass through all four quadrants in the equatorial plane, and do not show the lines that remain in just one octant (analogous to the loops that remain in one quadrant in the equatorial plane) to keep the figure as simple as possible.

Near the poles, these vortex lines have nearly the same structure as the purely transverse lines of Fig. 10.13; it is only near the equator that the lines begin to differ. As the lines approach the equator, they also increase in radius, because of the $1/r^2$ parts of the frame-drag field. In doing so, they pass from one gravitational-wave crest to the next, and the lines sharply turn during their passage between successive crests. The portion of the line on this next crest runs nearly parallel to the equator, until it begins moving slightly inward (again because of the $1/r^2$ parts of the frame-drag field). As it then sharply turns again, it returns to the original crest and begins heading back toward the poles. This sharp turning happens on both sides of the sphere, which causes the lines to form the closed loops that reside in either the northern or the southern hemisphere in Fig. 10.17. Only in the limit that r goes to infinity do the radial perturbations vanish, and the loops in the northern and southern hemisphere connect to form the transverse pattern in Fig. 10.13.

10.6.6 Wave Generation by a Time-Varying Mass Quadrupole

A time-varying mass-quadrupole moment $\mathcal{I}_{pq}(t)$ gives rise to metric perturbations of flat space given by the terms proportional to $\mathcal{I}_{pq}(t-r)/r$ and its derivatives in Eqs. (8.13) of [36]. It is straightforward to calculate that the frame-drag field for these metric perturbations is

$$\mathcal{B}_{ij} = \epsilon_{pq(i} \left[\left(\frac{{}^{(1)}\mathcal{I}_{pk}}{r} \right)_{,j)kq} - \left(\frac{{}^{(3)}\mathcal{I}_{j)p}}{r} \right)_{,q} \right] . \tag{10.77}$$

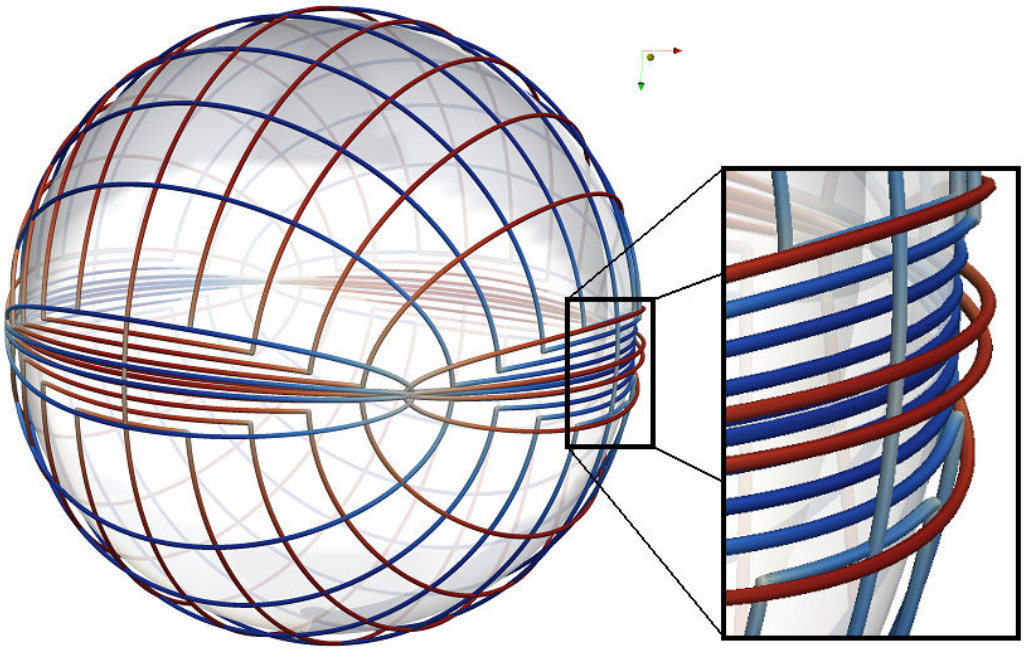

Figure 10.17: Vortex lines of an oscillating current quadrupole at sufficiently large r that the $1/r^2$ part of the frame-drag field may be thought of as a perturbation to the transverse vortex lines of Fig. 10.13. The lines are colored in the same way as in that figure, and the pattern of the lines around the poles is nearly identical to the transverse lines of Fig. 10.13. Near the equator, the $1/r^2$ perturbation causes the lines to bend and form closed loops that reside in either the northern or the southern hemisphere. The blue horizontal lines in the blow-up inset should be compared with dense blue (dashed) bundles in Fig. 10.16, and red lines with the red bundles immediately outside of the blue ones.

Notice that this mass-quadrupolar frame-drag field is the same as the current-quadrupolar tidal field in Eq. (10.72), with the current-quadrupole moment $\mathcal{S}_{pq}$ replaced by $-\frac{3}{4}\mathcal{I}_{pq}$; see the duality relations in Eqs. (10.20) and (10.24). Correspondingly, the vortex lines of this mass quadrupole will be the same as the tendex lines of the equivalent current quadrupole.

The mass quadrupole's tidal field can be deduced from its frame-drag field in Eq. (10.77) by using the third of the Maxwell-like equations in Eq. (10.21). The result is

$$\mathcal{E}_{ij} = \frac{1}{2}\left[-\left(\frac{\mathcal{I}_{pq}}{r}\right)_{,pqij} + \epsilon_{ipq}\left(\frac{{}^{(2)}\mathcal{I}_{pm}}{r}\right)_{,qn}\epsilon_{jmn} + 2\left(\frac{{}^{(2)}\mathcal{I}_{p(i}}{r}\right)_{,j)p} - \left(\frac{{}^{(4)}\mathcal{I}_{ij}}{r}\right)\right] . \tag{10.78}$$

Alternatively, this mass-quadrupolar tidal field can be deduced from the current-quadrupolar frame-drag field in Eq. (10.71) by using the duality relation $\mathcal{S}_{pq} \to +\frac{3}{4}\mathcal{I}_{pq}$ of Eqs. (10.20) and (10.24). As a result, the tendex lines of this mass quadrupole will be the same as the vortex lines of the current quadrupole, Figs. 10.9–10.10 and 10.12–10.16, with the red (solid) lines describing tidal stretching, and the blue (dashed) lines, tidal squeezing.

10.6.7 Slow-Motion Binary System Made of Identical, Nonspinning Point Particles

As a final example of a weakly gravitating system, we investigate the tendex lines of a Newtonian, equal-mass binary made of nonspinning point particles in a circular orbit. We assume a separation, a, between particles that is large compared to their mass, M, so that the orbital velocity $v = \frac{1}{2}\sqrt{M/a}$ is small compared to the speed of light (a slow-motion binary).

Close to the binary, where retardation effects are negligible, the tidal field is given by the Newtonian expression $\mathcal{E}_{jk} = \Phi_{,jk}$, Eq. (10.40), with Φ the binary's Newtonian gravitational potential

$$\Phi = -\frac{M_A}{|\boldsymbol{x} - \boldsymbol{x}_A|} - \frac{M_B}{|\boldsymbol{x} - \boldsymbol{x}_B|} . \tag{10.79}$$

Here $M_A = M_B = M/2$ are the particles' masses, with M the total mass, and $\boldsymbol{x}_A$ and $\boldsymbol{x}_B$ are the locations of particles, which we take to be on the x axis, separated by the distance, a.

In Fig. 10.18, we show the near-zone tendex lines associated with this potential's tidal field, color coded in the usual way (see the figure's caption). Close to each particle, the tendex lines resemble those of a static, spherically symmetric object. Moving farther from the particle, one can see the effects of the particle's companion, bending and compressing the lines. At radii $r \gtrsim a$, the Newtonian potential and tidal field can be expanded in multipole moments with the monopole and quadrupole dominating. At $r \gg a$, the monopole dominates and the tendex lines become those of a single spherical body.

The binary's orbital angular velocity is $\omega = \sqrt{M/a^3}$ (Kepler's formula), and the binary emits

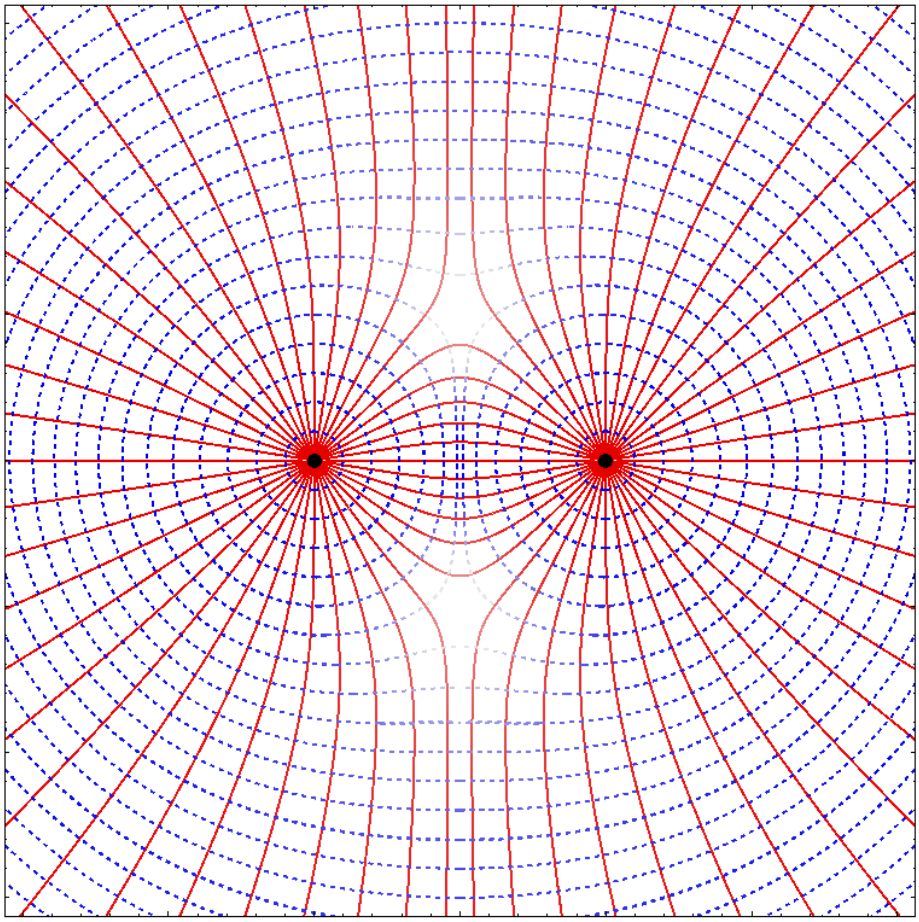

Figure 10.18: For a weak-gravity binary made of identical nonspinning point particles, in the near zone where retardation is negligible, two families of tendex lines lying in a plane that passes through the two particles (e.g., the orbital plane). The red (solid) curves are lines with negative tendicity, and the blue (dashed) curves have positive tendicity. The color intensity of the curves represents the magnitude of the tendicity, rescaled by $r_A^3 r_B^3/[M^3(r_A^3+r_B^3)]$, where r_A and r_B are the distances from the particles, to remove the tendicity's radial die out. Near each particle, the tendex lines resemble those of an isolated spherical body; as one moves closer to the particle's companion, the lines bend in response to its presence. At radii large compared to the particles' separation a, the binary's monopole moment comes to dominate, and the tendex lines nearly resemble those of a single isolated spherical body.

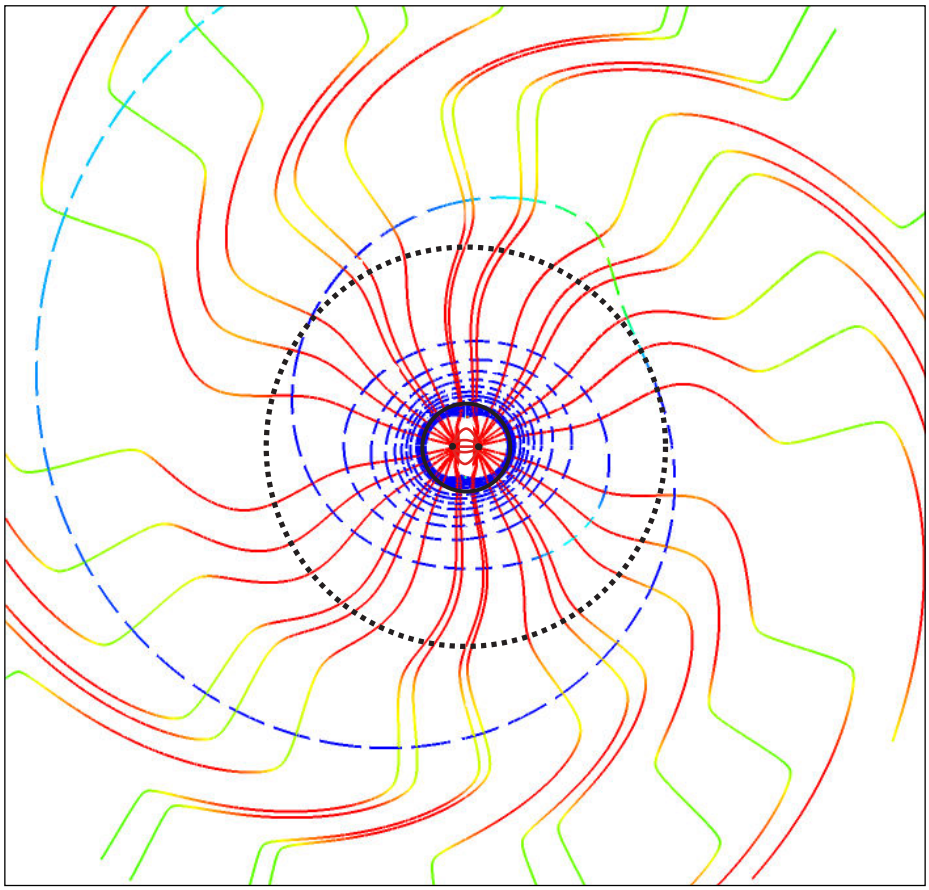

Figure 10.19: Tendex lines in the orbital plane of the same binary as Fig. 10.18, with separation $a/M = 20$ (where M is the total mass), focusing on the transition and wave zones around $r \gtrsim \lambda\!\!\!^{-} = 2.24a$. The solid black circle has radius $\lambda\!\!\!^{-}$. The colors are fixed by the tendicity weighted by ωr, so as to scale out the $1/r$ falloff in the wave zone (with dark blue strongly positive, dark red strongly negative, and light green near zero). Inside the dotted black curve ($r = \frac{1}{2}a^2/M = 10a$), the binary's (nonradiative) monopole moment dominates, $\mathcal{E} \simeq M/r^3$, and the red (stretching) tendex lines are nearly radial. Outside the dotted black curve, the (radiative) quadrupole moment dominates, $\mathcal{E} \simeq 4M^3/a^4 r$, and the tendex lines are strong (significant tendicity) only where they are approximately transverse to the radial direction.

gravitational waves with angular frequency 2ω, reduced wavelength $\lambda\!\!\!^{-} = 1/(2\omega) = \frac{1}{2}\sqrt{a^3/M}$, and wavelength $\lambda = 2\pi\lambda\!\!\!^{-}$. As a concrete example, we choose the particles' separation to be $a/M = 20$; then $\lambda\!\!\!^{-} = \sqrt{5}a \simeq 2.24a$, and $\lambda = 2\pi\sqrt{5}a \simeq 14a$.

Figure 10.19 shows tendex lines in this binary's orbital plane, focusing on the transition and wave zones $r \gtrsim \lambda\!\!\!^{-} = 2.24a$ (outside the solid black circle). The shapes and colors of the tendex lines in this figure can be understood in terms of the binary's multipole moments: In the transition zone and wave zone, $r \gtrsim \lambda\!\!\!^{-}$, the tidal field is the sum of a nonradiative monopolar piece with magnitude $\mathcal{E}_M \simeq M/r^3$, and a quadrupolar piece with magnitude $(1/r)\partial^4\mathcal{I}/\partial t^4 \simeq (2\omega)^4(\frac{1}{4}Ma^2)/r \simeq 4M^3/a^4 r$; higher order moments are negligible. The two moments contribute about equally at radius $r = \frac{1}{2}a^2/M = 10a$ (dotted black circle in the figure). The (nonradiative) monopole moment, with its red radial and blue

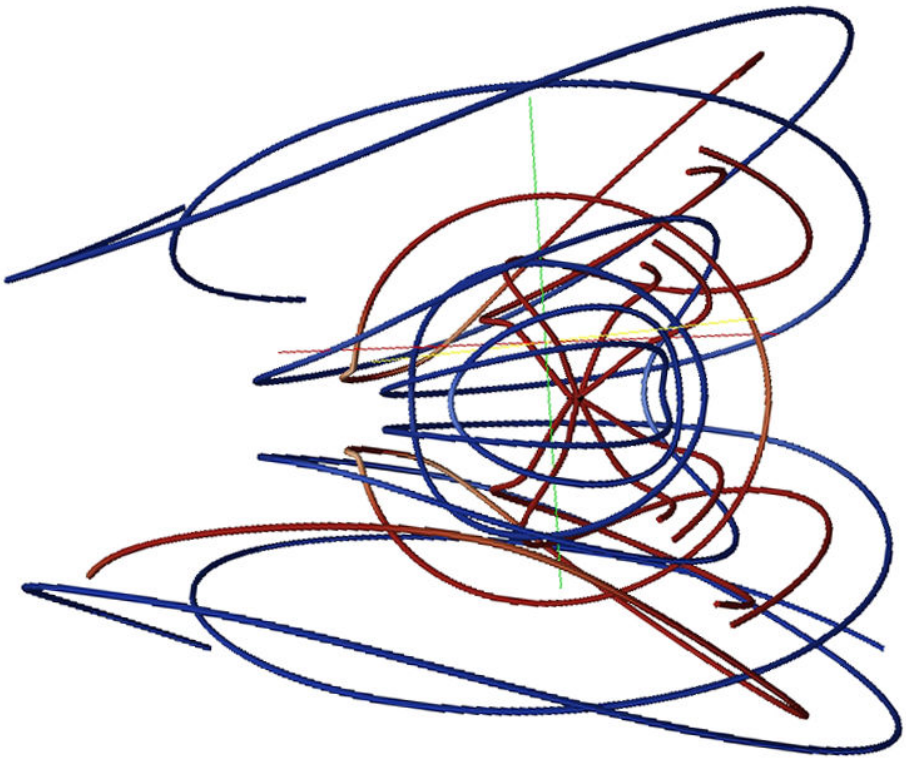

Figure 10.20: Tendex lines outside the (central, horizontal) orbital plane, for the same binary and parameters as Fig. 10.19. In the inner region, the binary's monopole moment dominates, $\mathcal{E} \simeq M/r^3$, and the red (stretching) tendex lines are nearly radial and the blue (squeezing) tendex lines are nearly circular. At larger radii, the (radiative) quadrupole moment begins to be significant and then dominate, and the tendex lines begin to spiral outward, as for the rotating quadrupole of Fig. 10.12.

circular tendex lines, dominates inside this circle. The (radiative) quadrupole moment dominates outside the circle, where the tendicity is significant (strong red and blue) only when the tendex lines are transverse; strong red alternates, radially, with strong blue as the waves propagate radially. Ultimately, at very large radii (far outside the domain of Fig. 10.19), the quadrupole moment will totally dominate, and the tendex-line pattern will become that of a rotating quadrupole, depicted in Fig. 10.10.

Figure 10.20 shows the tendex lines for this same binary, with the same parameters, in three dimensions, i.e., above and below the equatorial plane. In the inner region, the monopole moment dominates where the red (stretching) tendex lines are nearly radial, and the blue (squeezing) tendex lines are nearly circular, centered on the binary. As one moves outward, the radiative quadrupole moment begins to distort these radial and circular tendex lines, and then at large radii, the now-dominant quadrupole moment drives them into the same spiraling pattern as we have seen in Fig. 10.12 for the tendex lines of a rotating, pure mass quadrupole.

10.7 Conclusions

In this paper, we have focused on the electric and magnetic parts of the Weyl curvature tensor, $\mathcal{E}_{ij}$ and $\mathcal{B}_{ij}$, and have given them the names *tidal field* and *frame-drag field*, based on their roles in producing tidal gravitational accelerations and differential frame dragging. Being parts of the Riemann tensor, these fields are well defined (though slicing dependent) in strong-gravity situations such as the near zone of colliding black holes. For this reason, and because they embody the full vacuum Riemann tensor and are easily visualized, $\mathcal{E}_{ij}$ and $\mathcal{B}_{ij}$ are powerful tools for exploring the nonlinear dynamics of spacetime curvature (geometrodynamics).

As tools for visualizing $\mathcal{E}_{ij}$ and $\mathcal{B}_{ij}$, we have introduced tendex and vortex lines (the integral curves of the eigenvectors of $\mathcal{E}_{ij}$ and $\mathcal{B}_{ij}$), along with their tendicities and vorticities (the eigenvectors' eigenvalues). The tendex and vortex lines are gravitational analogs of electric and magnetic field lines. Moreover, just as the electromagnetic field tensor is fully determined by its electric and magnetic field lines, together with their field-line densities (which encode the lengths of the electric and magnetic vectors), so the vacuum Riemann curvature tensor is fully determined by its tendex and vortex lines, together with their colors (which encode the tendicities and vorticities as in Fig. 10.19).

In terms of their transformation properties, the ($\mathcal{E}_{ij}$, $\mathcal{B}_{ij}$) pair is strictly analogous to the pair of electric and magnetic 3-vector fields; they are components of a 4-tensor, divided into two groups in a slicing-dependent manner. We are confident that this mild and transparent form of frame dependence will not prevent our tendex and vortex concepts from becoming useful tools for studying geometrodynamics, any more than the frame dependence of electric and magnetic fields and field lines have been impeded these fields from being useful tools for studying electromagnetism in flat or curved spacetime.

Using various examples from linearized gravity, for which analytical formulas are available, we have plotted color-coded tendex and vortex lines, and thereby we have gained insight into the behaviors of the tidal and frame-drag fields. This intuition from weak-gravity examples will be of great value when studying strongly gravitating systems in asymptotically flat spacetimes, e.g., binary black holes. This is because, in the weak-gravity region of spacetime outside such strong-gravity systems, linearized gravity is a good approximation. More specifically, for stationary, strongly gravitating systems (e.g., stationary black holes and neutron stars), the tendex and vortex lines in their asymptotic, weak-gravity regions will be well approximated by our linearized-theory results in Section 10.5 (and, perhaps in some cases, extensions to higher multipoles).

For oscillatory, strongly gravitating systems (e.g., binary black holes and oscillating neutron stars), the wave zones' tendex and vortex lines will be well approximated by those of our examples in Section 10.6, and their extensions. Whether the system has strong gravity or weak gravity, its

wave-zone field lines are controlled by radiative multipole moments that are tied to the system's near-zone dynamics. As one moves inward through the weak-gravity wave zone into the near zone and the region of strong gravity, the details of the field lines and the system's dynamics may be quite different for strong-gravity systems than for our weak-gravity examples. Nevertheless it seems likely that in all cases, the gravitational waves will be generated by dynamical motions of near-zone tendexes and vortexes (regions of strong tendicity and vorticity). By exploring that near-zone tendex/vortex dynamics, we can gain deep physical insight into nonlinear spacetime curvature. This will be a central theme of Papers II and III in this series.

Whatever may be a source's strong-field dynamics, it will be useful to focus on the imprints that the strong-field dynamics leaves on the tendex and vortex structures in the strong-to-weak-gravity transition region. Those transition-region, tendex-vortex imprints will govern spacetime curvature throughout the asymptotic, weak-gravity region, and in particular will govern the radiative multipole moments that control the emitted gravitational waves. Moreover, the imprinted structures in the strong-to-weak-gravity-transition region may turn out to have some sort of effective dynamics that can be captured by simple analytical models and can become a powerful tool for generating approximate gravitational waveforms, e.g., for use in gravitational-wave data analysis.

10.A Appendix: The Newman-Penrose Formalism

In this appendix, we give the connection between the electric and magnetic parts of the Weyl tensor $\boldsymbol{\mathcal{E}}$ and $\boldsymbol{\mathcal{B}}$, and the five Newman-Penrose (NP) curvature scalars [45]. The NP formalism [45] is especially useful for expressing the gravitational-wave content of a dynamical spacetime at asymptotic null infinity. The NP formalism is used in numerical simulations to extract the gravitational waves at large radii, at which the waves are propagating on a nearly flat background. It is also a crucial foundation for the study of black-hole perturbations and for the Petrov classification of vacuum spacetimes, both of which we will eventually analyze using our vortex and tendex tools. Because we use the opposite metric signature to that of the original Newman-Penrose paper [45] and the widely used Penrose-Rindler book [32], our sign conventions for the NP quantities and for Eqs. (10.82) and (10.87) below differ from theirs. Ours are the same as in [33].

To begin, we define an orthonormal tetrad, $\vec{e}_{\hat{\alpha}} = (\vec{e}_{\hat{0}}, \vec{e}_{\hat{1}}, \vec{e}_{\hat{2}}, \vec{e}_{\hat{3}})$, with a time basis vector $\vec{e}_{\hat{0}} = \vec{u}$ orthogonal to our chosen foliation's spacelike hypersurfaces, and with the spatial basis vectors $\vec{e}_{\hat{1}}, \vec{e}_{\hat{2}}, \vec{e}_{\hat{3}}$ lying in those hypersurfaces. We use this tetrad to build a complex null tetrad that is used in the NP formalism:

$$\vec{l} = \frac{1}{\sqrt{2}}(\vec{e}_{\hat{0}} + \vec{e}_{\hat{1}})\,, \qquad \vec{n} = \frac{1}{\sqrt{2}}(\vec{e}_{\hat{0}} - \vec{e}_{\hat{1}})\,,$$
$$\vec{m} = \frac{1}{\sqrt{2}}(\vec{e}_{\hat{2}} + i\vec{e}_{\hat{3}})\,, \qquad \vec{m}^* = \frac{1}{\sqrt{2}}(\vec{e}_{\hat{2}} - i\vec{e}_{\hat{3}})\,. \tag{10.80}$$

By projecting the Weyl tensor onto this null basis, we construct the complex Weyl scalars,

$$\Psi_0 = C_{\mu\nu\rho\sigma} l^\mu m^\nu l^\rho m^\sigma \,, \tag{10.81a}$$

$$\Psi_1 = C_{\mu\nu\rho\sigma} l^\mu n^\nu l^\rho m^\sigma \,, \tag{10.81b}$$

$$\Psi_2 = C_{\mu\nu\rho\sigma} l^\mu m^\nu m^{*\rho} n^\sigma \,, \tag{10.81c}$$

$$\Psi_3 = C_{\mu\nu\rho\sigma} l^\mu n^\nu m^{*\rho} n^\sigma \,, \tag{10.81d}$$

$$\Psi_4 = C_{\mu\nu\rho\sigma} n^\mu m^{*\nu} n^\rho m^{*\sigma} \,. \tag{10.81e}$$

Using the null tetrad in Eq. (10.80) built from the orthonormal tetrad, we can express the spatial, tetrad components of the electric and magnetic parts of the Weyl tensor (written as a matrix) in terms of the Weyl scalars as follows:

$$\mathcal{E}_{\hat{a}\hat{b}} + i\mathcal{B}_{\hat{a}\hat{b}} = \begin{bmatrix} 2\Psi_2 & -(\Psi_1 - \Psi_3) & i(\Psi_1 + \Psi_3) \\ * & \frac{1}{2}(\Psi_0 + \Psi_4) - \Psi_2 & -\frac{i}{2}(\Psi_0 - \Psi_4) \\ * & * & -\frac{1}{2}(\Psi_0 + \Psi_4) - \Psi_2 \end{bmatrix}, \tag{10.82}$$

(see Eq (3.65) of [33], where the differences are due to our differing conventions for both $\boldsymbol{\mathcal{B}}$ and our null tetrad). In Eq. (10.82), the rows and columns are ordered by $\hat{1}, \hat{2}, \hat{3}$ and the entries indicated by $*$ can be inferred from the symmetry of the matrix.

The entries in Eq. (10.82) can be derived in a straightforward manner from the definitions of $\boldsymbol{\mathcal{E}}$ and $\boldsymbol{\mathcal{B}}$, Eqs. (10.2a) and (10.2b), and the definitions of the Weyl scalars, Eqs. (10.81a)–(10.81e). For example, we have

$$\begin{aligned} \mathcal{E}_{\hat{1}\hat{1}} &= R_{\hat{1}\hat{0}\hat{1}\hat{0}} = \frac{1}{2}(R_{\hat{r}l\hat{r}l} + 2R_{\hat{r}l\hat{r}n} + R_{\hat{r}n\hat{r}n}) \\ &= \frac{1}{4}(R_{nlnl} - 2R_{nlln} + R_{lnln}) = R_{lnln} \,, \end{aligned} \tag{10.83}$$

where we have used the symmetry properties of the Riemann tensor to eliminate and combine many terms. This result is not obviously equal to any of the Weyl scalars, but note that

$$\begin{aligned} R_{lnln} &= -R^n{}_{nln} = R^n{}_{nnl} = -(R^l{}_{nll} + R^m{}_{nml} + R^{m^*}{}_{nm^*l}) \\ &= -R_{m^*nml} - R_{mnm^*l} = R_{lmm^*n} + R_{lm^*mn} \\ &= \Psi_2 + \Psi_2^* \,, \end{aligned} \tag{10.84}$$

where we have used the fact that in the null tetrad basis $\{\vec{l}, \vec{n}, \vec{m}, \vec{m}^*\}$, indices are raised and lowered

with a metric given by

$$g_{\alpha\beta} = g^{\alpha\beta} = \begin{pmatrix} 0 & -1 & 0 & 0 \\ -1 & 0 & 0 & 0 \\ 0 & 0 & 0 & 1 \\ 0 & 0 & 1 & 0 \end{pmatrix}, \tag{10.85}$$

and the fact that the Ricci tensor vanishes in vacuum spacetimes. Similar calculations show that

$$\begin{aligned} B_{\hat{1}\hat{1}} &= \frac{1}{2}\epsilon_{\hat{1}}{}^{\hat{p}\hat{q}} R_{\hat{p}\hat{q}\hat{1}\hat{0}} = R_{\hat{2}\hat{3}\hat{1}\hat{0}} = -iR_{m^*mln} \\ &= i(R_{lmnm^*} + R_{lm^*mn}) = i(-\Psi_2 + \Psi_2^*)\,, \end{aligned} \tag{10.86}$$

from which we conclude that $\mathcal{E}_{\hat{1}\hat{1}} + i\mathcal{B}_{\hat{1}\hat{1}} = 2\Psi_2$. Similar computations can be used to fill out the remaining components in the matrix in Eq. (10.82).

In future papers, we will discuss quantities that we call the horizon tendicity and horizon vorticity in more detail. These are the values of $\boldsymbol{\mathcal{E}}$ and $\boldsymbol{\mathcal{B}}$ at the horizon for the component that is projected along the normal to the 2-dimensional event horizon of a black hole, for both indices of the tidal and frame-drag fields. When we denote the inward normal to the horizon by $\boldsymbol{N}$, and we choose the vector $\boldsymbol{e}_{\hat{1}}$ such that it coincides with $-\boldsymbol{N}$ at the horizon, then we immediately have the useful result that

$$\Psi_2 = \frac{1}{2}(\mathcal{E}_{NN} + i\mathcal{B}_{NN}) = \frac{1}{2}(\mathcal{E}_{ij} + i\mathcal{B}_{ij})N^i N^j\,. \tag{10.87}$$

We will use this results when we apply our vortex and tendex tools to analytical and numerical black-hole spacetimes (Papers II and III in this series).

Bibliography

[1] R. Owen, J. Brink, Y. Chen, J. D. Kaplan, G. Lovelace, K. D. Matthews, D. A. Nichols, M. A. Scheel, F. Zhang, A. Zimmerman, et al., Phys. Rev. Lett. **106**, 151101 (2011).

[2] J. A. Wheeler, *Geometrodynamics* (Academic Press, New York, 1963).

[3] J.A. Wheeler, in *Relativity, Groups and Topology (Les Houches Summer School, 1963)*, edited by B. DeWitt and C. DeWitt (Gordon and Breach, New York, 1964), pp. 325–520.

[4] C. W. Misner, Phys. Rev. **118**, 1110 (1960).

[5] D. R. Brill and R. W. Lindquist, Phys. Rev. **131**, 471 (1963).

[6] S. Hahn and R. Lindquist, Ann. Phys. (NY) **29**, 304 (1964).

[7] J. Weber, Phys. Rev. **117**, 306 (1960).

[8] J. Centrella, J. G. Baker, B. J. Kelly, and J. R. van Meter, Rev. Mod. Phys. **82**, 3069 (2010).

[9] B. C. Barish and R. Weiss, Phys. Today **52**, 44 (1999).

[10] D. Sigg and the LIGO Scientific Collaboration, Classical Quantum Gravity **25**, 114041 (2008).

[11] F. Acernese, M. Alshourbagy, P. Amico, F. Antonucci, S. Aoudia, et al., Classical Quantum Gravity **25**, 184001 (2008).

[12] K. Kuroda and the LCGT Collaboration, Classical Quantum Gravity **27**, 084004 (2010).

[13] G. M. Harry (for the LIGO Scientific Collaboration), Classical Quantum Gravity **27**, 084006 (2010).

[14] C. W. Misner, K. S. Thorne, and J. A. Wheeler, *Gravitation* (W. H. Freeman, New York, 1973).

[15] L. Smarr, Phys. Rev. D **7**, 289 (1973).

[16] D. Marolf, Gen. Relativ. Gravit. **31**, 919 (1999).

[17] U. Jacob and T. Piran, Classical Quantum Gravity **23**, 4035 (2006).

[18] J. D. Romano and R. H. Price, Classical Quantum Gravity **12**, 875 (1995).

[19] M. Bondarescu, M. Alcubierre, and E. Seidel, Classical Quantum Gravity **19**, 375 (2002).

[20] H. Chan, Classical Quantum Gravity **23**, 225 (2006).

[21] L. Rezzolla, R. P. Macedo, and J. L. Jaramillo, Phys. Rev. Lett. **104**, 221101 (2010).

[22] J. L. Jaramillo, R. P. Macedo, P. Moesta, and L. Rezzolla, Phys. Rev. D **85**, 084030 (2012).

[23] J. L. Jaramillo, R. P. Macedo, P. Moesta, and L. Rezzolla, Phys. Rev. D **85**, 084031 (2012).

[24] J. L. Jaramillo (2011), `arxiv:1108.2408`.

[25] J. W. Belcher and S. Olbert, Am. J. Phys. **71**, 220 (2003).

[26] `http://www.black-holes.org/curQuadVortex.html`.

[27] `http://www.black-holes.org/antiAliPoints.html`.

[28] A. Zimmerman, D. A. Nichols, and F. Zhang, Phys. Rev. D **84**, 044037 (2011).

[29] F. B. Estabrook and H. D. Wahlquist, J. Math. Phys. **5**, 1629 (1964).

[30] C. Schmid, Phys. Rev. D **79**, 064007 (2009).

[31] R. Maartens and B. A. Bassett, Classical Quantum Gravity **15**, 705 (1998).

[32] R. Penrose and W. Rindler, *Spinors and Space-time, Volume 1* (Cambridge University Press, Cambridge, 1992).

[33] H. Stephani, D. Kramer, M. MacCallum, C. Hoenselaers, and E. Herlt, *Exact Solutions of Einstein's Field Equations* (Cambridge University Press, Cambridge, UK, 2003).

[34] H. Friedrich, Classical Quantum Gravity **13**, 1451 (1996).

[35] A. Anderson, Y. Choquet-Bruhat, and J. W. York, Jr., Topol. Meth. Nonlin. Anal. **10**, 353 (1997).

[36] K. S. Thorne, Rev. Mod. Phys. **52**, 299 (1980).

[37] R. D. Blandford and K. S. Thorne, *Applications of Classical Physics* (California Institute of Technology, 2008).

[38] J. D. Kaplan, D. A. Nichols, and K. S. Thorne, Phys. Rev. D **80**, 124014 (2009).

[39] R. L. Forward, Proc. IRE **49**, 892 (1961).

[40] D. Keppel, D. A. Nichols, Y. Chen, and K. S. Thorne, Phys. Rev. D **80**, 124015 (2009).

[41] G. Lovelace, Y. Chen, M. Cohen, J. D. Kaplan, D. Keppel, K. D. Matthews, D. A. Nichols, M. A. Scheel, and U. Sperhake, Phys. Rev. D **82**, 064031 (2010).

[42] K. S. Thorne, R. H. Price, and D. A. MacDonald, *Black Holes: The Membrane Paradigm* (Yale University Press, New Haven and London, 1986).

[43] D. R. Fiske, J. G. Baker, J. R. van Meter, D.-I. Choi, and J. M. Centrella, Phys. Rev. D **71**, 104036 (2005).

[44] R. Penrose, Ann. Human Genet., Lond. **42**, 435 (1979).

[45] E. Newman and R. Penrose, J. Math. Phys. **3**, 566 (1962).

Chapter 11

Visualizing Spacetime Curvature via Frame-Drag Vortexes and Tidal Tendexes: II. Stationary and Perturbed Black Holes

In a recent series of papers, we introduced a method of visualizing all ten degrees of freedom of the Weyl tensor using tools that we called tidal tendexes and frame-drag vortexes. The visualizations begin from a time-space split of the Weyl tensor into two symmetric trace-free tensors, the tidal field (the tensor's electric part), $\mathcal{E}_{ij}$, and the frame-drag field (the tensor's magnetic part), $\mathcal{B}_{ij}$. The tensors can always be diagonalized, and their eigenvalues (the tendicity and vorticity, respectively) as well as the integral curves of their eigenvectors (the tendex and vortex lines, respectively) are simple functions that, together, capture all the independent components of the Weyl tensor. These quantities also have simple physical interpretations: the tendex lines show the preferred directions of tidal forces and the tendicity indicates the forces' strengths; similarly, the vortex lines show the preferred directions of differential precession of gyroscopes and the vorticities indicate the rates of the precession. In addition, the tendexes and vortexes (regions of large tendicity and vorticity in magnitude) are important structures that guide the visualization and interpretation of a spacetime's dynamics.

In this paper, we analyze the tendexes and vortexes of stationary and perturbed black holes, as a test-bed for understanding these tools in spacetime regions of strong curvature and strong, but linearly dynamical, curvature; we aim to build intuition from these results that we will then apply to the strong, dynamical, and nonlinear spacetime curvature of black-hole binary simulations, in future papers. In particular, we find that for a Schwarzschild black hole, the tendexes are uniform and spherically symmetric and the vortexes vanish. For a stationary Kerr black hole, however, there is a positive and a

negative vortex that extends out from the horizon of each hole, respectively, and that is concentrated about the axis of rotation. The tendexes of a Kerr black hole look similar to a Schwarzschild black hole far away, but for a rapidly spinning hole, near the horizon, there are two positive tendexes near the poles, and a band-shaped negative tendex around the equator. For $l = 2$, $m = 2$, odd-parity perturbations of Schwarzschild and Kerr black holes, there are two positive and two negative equatorial vortexes that stretch out from the horizon and which, at larger radii, collect into the polar vortexes of gravitational waves. The vortexes induce accompanying perturbative tendexes that extend from near the equatorial plane (close to the horizon) to the poles (at larger radii). For electric-parity perturbations, the perturbative tendexes play the role of the magnetic-parity vortexes, and the vortexes are quite similar to the magnetic-parity tendexes.

In regions of strong curvature the choice of slicing and spatial gauge can have a significant effect on the mathematical expressions for the metric and curvature; we, therefore, investigate the effects of these changes on the vortexes and tendexes of a spacetime. For stationary black holes, we look at the effect of changes in the time and spatial coordinates, separately. We find that for several well-known coordinate choices, neither has a large influence on the vortexes and tendexes at large radii. Furthermore, when we restrict to time coordinates that smoothly pass through the horizon, the qualitative behavior of the vortexes and tendexes are, in essence, identical. For perturbed black holes, we investigate the effect of changes of coordinates by comparing perturbations of Schwarzschild black holes in two well-known gauges: Regge-Wheeler gauge and ingoing-radiation gauge. We find that the vortexes are very similar, qualitatively. We, therefore, are cautiously optimistic that vortexes and tendexes will be a helpful and reasonably gauge-invariant method of gaining insight from strong, nonlinear, and dynamical spacetime curvature around black-hole binaries.

Based on a paper in preparation by D. A. Nichols, R. Owen, F. Zhang, A. Zimmerman, J. Brink, Y. Chen, J. D. Kaplan, G. Lovelace, K. D. Matthews, M. A. Scheel, and K. S. Thorne.

11.1 Motivation and Overview

Numerical simulations of compact-binary mergers and stellar collapse have provided a rich set of solutions of Einstein's field equations in the highly nonlinear and dynamical regime [1]. These computations offer accurate gravitational waveforms, which are key to the success of gravitational-wave detection programs (see, e.g., [2]). Another, less well-defined opportunity provided by such simulations would be to further appreciate how spacetime evolves dynamically in such dramatic

scenarios of high curvature. A way to test our understanding is to try to build physically-motivated semianalytical models that approximately describe such spacetimes. These models may eventually help the gravitational-wave-detection effort in building high-precision wave templates that are much faster to compute than those generated by numerical-relativity simulations; they may also guide us towards appreciating the physical meaning of various components of the outgoing gravitational waves, and the dependence of the waveform on the parameters of the system.

Powerful visualization techniques are required in order to glimpse into the strong-field region of a numerical-relativity spacetime. In the past, several ways have been used to visualize the entire numerical spacetime. The Newman-Penrose scalar, Ψ_4, [3] has been used, but it is of a limited usefulness, because it only has a straightforward meaning in the wave zone for outgoing radiation, and it is only a small part of the full spacetime curvature. The lapse and shift are a second set of quantities used to visualize the spacetime curvature particularly in numerical-relativity simulations. These quantities do label where the black holes are and how deep the gravitational potential is, but they are also highly coordinate dependent. Isometric embedding in three-dimensional Euclidean space (see, e.g., [4]) have been used for horizons; they do not cover the entire spacetime, however, and for spinning Kerr black hole with $a/M > \sqrt{3}/2$ [5], the event horizon cannot be embedded anymore.

Recently, in [6, 7], we proposed visualizing curved spacetimes using the eigenvectors and eigenvalues of the tidal and frame-drag tensors—two three-dimensional tensor fields, $\mathcal{E}_{ij}$ and $\mathcal{B}_{ij}$, defined on the spatial (three-dimensional) slice in a space-time (3+1) decomposition of a spacetime—which together describe the ten independent components of the Weyl curvature tensor, $C_{\alpha\beta\gamma\delta}$. The tidal and frame-drag fields, therefore, completely determine the curvature of the vacuum region of a spacetime. The way $\boldsymbol{C}$ splits into $\boldsymbol{\mathcal{E}}$ and $\boldsymbol{\mathcal{B}}$ depends only on the local direction of time used for the 3+1 split, analogous to the way the Maxwell field-strength tensor splits into electric and magnetic fields. In fact, visualizing curvature using the eigendirections of $\mathcal{E}_{ij}$ and $\mathcal{B}_{ij}$ is much like visualizing an electromagnetic field using electric and magnetic field lines. For the vortex and tendex quantities, however, the most interesting physics is contained within the tendexes (regions of large tendicity in magnitude) and vortexes (regions or large vorticity), rather than along individual field lines.

Our strategy is to first visualize "analytically understood" spacetimes using our tools, in order gain intuition into the relation between the visual picture and the analytics, and then to visualize numerical-relativity spacetimes (looking for features we have already found and retrieve their analytical origin). In [7] (henceforth Paper I), using examples of nearly flat spacetimes, we have shown that integral curves of the eigenvectors, tendex lines (for the tidal tensor) and vortex lines (for the frame-drag tensor), can already illustrate very well the spacetime around oscillating multipole sources, and we have been able to connect features of the field lines to physical understanding: in the near zone, the field lines are attached to the source; in the transition zone, retardation effects

cause the field lines to change character in understandable ways; and in the wave zone, the field lines approach those of freely propagating plane waves. In a supplementary study [8], tendex and vortex lines of asymptotically flat spacetimes at future null infinity (a 2-sphere) have been classified according to their topological features.

In this paper, henceforth Paper II, we will visualize static and perturbed black-hole spacetimes. We are motivated by the fact that black holes are important components of the numerical-relativity simulations that we would like to learn about; the tools available to us are from black-hole-perturbation theory. We are especially interested in the tendexes and vortexes of black holes undergoing quasinormal-mode oscillations, because these modes will mirror the appearance of numerical-relativity simulations of black-hole mergers at late times, where the nonlinear dynamics has given way to the simple evolution of weak perturbations of the final black hole. We will visualize numerical spacetimes in a forthcoming paper, henceforth Paper III, in which we will apply the understandings gained in Papers I and II. The remainder of this paper is organized as follows:

In Section 11.2, we briefly review the detailed conventions we use for tidal field, $\mathcal{E}_{ij}$, and it tendexes, and the frame-drag field, B_{ij}, and its vortexes (which are contained in [6, 7]). Next, in Section 11.3, we discuss the tendexes and vortexes on black-hole horizons, and we relate them to other well-known horizon quantities. Section 11.4 shows the tendex lines of a static Schwarzschild black hole, and Section 11.5 shows the vortexes and tendexes of a slowly rotating black hole. We compute the tendexes and vortexes of a (rapidly rotating) Kerr black hole, in Section 11.6, which we show in several different time slicings and coordinate systems. In the time slices that smoothly pass through the horizon, the qualitative features of the vortex and tendex quantities do not strongly depend, qualitatively speaking, on the specific time slicing or the spatial coordinates.

In Section 11.7, we show the vortex lines of a perturbed Schwarzschild black hole, for odd-parity $l = 2$ quasinormal-mode perturbations (in this part we use Regge-Wheeler gauge [9, 10]). We find that for a mode with $m = 2$, the vortexes in the equatorial plane emerge normal to the horizon and collect into spirals that asymptotically become the gravitational waves. For a superposition of $m = \pm 2$ modes, the vortexes in the equatorial plane still emerge normal to the horizon, but they form oscillating bands that are the gravitational waves at large radii.

Section 11.8 is devoted to computing the three-dimensional perturbative tendexes and vortexes of even-parity $l = 2$, $m = 2$ perturbations of both Schwarzschild and Kerr black holes in an ingoing-radiation gauge (see, [11, 12, 13, 14] for the formative work on this gauge and [15, 16, 17, 18, 19, 20] for more recent work). In the three-dimensional plots, we see that there are two positive and negative perturbative tendexes that emerge from the horizon near the equator, and, at larger radii, they collect into the tendexes of gravitational waves near the poles. They induce vortexes near the equator in the near zone, that also coalesce around the poles at larger radii. The dynamics of wave generation is not largely different for Schwarzschild or Kerr black holes. We compare the vortex lines

of a quasinormal-mode perturbation to a Kerr black hole (in an ingoing-radiation gauge) to those of a weakly perturbed Kerr black hole formed after the merger of two rapidly spinning black holes in a numerical-relativity simulation by Lovelace and collaborators [21], at the end of this section; we find remarkably good agreement between the two. Finally, in Section 11.9 we summarize our results and discuss directions for future research.

Many details about our calculations and some of our results are included in several appendices. Appendix 11.A gives explicit expressions the tidal and frame-drag fields, and their tendex and vortex lines. It also contains figures of vortex and tendex lines using a time coordinate that does not smoothly pass through the horizon and a discussion of these figures. Appendix 11.B is a review of the Regge-Wheeler-Zerilli formalism for black-hole perturbations, and it contains some computations of the frame-drag field for quasinormal-mode perturbations of these black holes. In Appendix 11.C, we review elements of Teukolsky's formalism for computing perturbations to the Weyl scalars [22], which are needed to compute the perturbed metric in an ingoing-radiation gauge. In Appendix 11.D, we review the procedure for calculating metric perturbations in the ingoing-radiation gauge for general perturbations, and we also specialize the procedure to compute the metric corresponding to modes of definite parities. Appendix 11.E presents analytical expressions for definite-parity metric perturbations of Schwarzschild black holes, and it contains analytical expressions for the tidal and frame-drag fields. In Appendix 11.F, we show that the frame-drag fields in Regge-Wheeler and the ingoing-radiation gauges are, in fact, equal; the tidal fields are not, however. Next, Appendix 11.G describes the numerical and analytical methods we use to compute the vortex and tendex lines in greater detail.

The final two appendices present a few additional results. Appendix 11.H shows odd-parity $l = 2$, $m = 2$ perturbations of Schwarzschild black holes in an ingoing-radiation gauge. First, it shows that there is a near duality between electric- and magnetic-parity perturbations of Schwarzschild black holes (i.e., the vortexes of a magnetic-parity perturbation are almost identical to the tendexes of an electric-parity perturbation, and vice versa). Second, because the equatorial vortexes are so similar to those of a Regge-Wheeler-gauge perturbation of the Schwarzschild spacetime, we have an additional piece of evidence that the vortexes and tendexes may not be too strongly gauge dependent (in time slices that smoothly pass through the event horizon). The appendix also shows odd-parity $l = 2$, $m = 2$ perturbations of a Kerr black hole, and there is a similar (though weaker) duality with the electric-parity perturbations of a Kerr black hole. Appendix 11.I shows three-dimensional vortex and tendex lines of the background plus the perturbative fields, which we suspect will be useful for comparisons with numerical-relativity simulations in the future.

Throughout this paper we use geometrized units, in which $G = c = 1$. Greek indices will be used for 4D spacetime quantities, and will run from 0 to 3, while Latin indices are reserved for spatial quantities (which run from 1 to 3); indices with carets above them will indicate a projection onto an

orthonormal basis, and capital Latin indices from the start of the alphabet are reserved for angular quantities defined on spheres of some constant radius (that run over angular coordinates θ, ϕ or the last two spatial indices, 2 to 3). We use a signature $(-+++)$ for the spacetime metric, and our Newman-Penrose quantities are defined appropriately for this signature, as in [23].

11.2 Tendex and Vortex Lines

In this section, we review the $3+1$ split of the Weyl curvature tensor and the definitions of the vortex and tendex quantities (see Paper I for a more detailed overview). The split of spacetime begins with a unit timelike vector field $\vec{u}$ that is orthogonal to a spacelike hypersurface of a constant time function, t; this vector field is the four-velocity of a family of observers who observe these time slices as moments of simultaneity. We treat only vacuum spacetimes in this paper, where the Riemann tensor, $R_{\mu\nu\rho\sigma}$, is the same as the Weyl tensor, $C_{\mu\nu\rho\sigma}$. The Weyl tensor has ten independent degrees of freedom, and in a 3+1 split, they are represented by two symmetric, trace-free spatial tensors $\mathcal{E}_{ij}$ and $\mathcal{B}_{ij}$, which we call the tidal and frame-drag fields, respectively, and which are defined below:

$$\mathcal{E}_{\alpha\beta} = \gamma_\alpha{}^\rho \gamma_\beta{}^\sigma C_{\rho\mu\sigma\nu} u^\mu u^\nu \,, \qquad \text{i.e.,} \qquad \mathcal{E}_{ij} = C_{i\hat{0}j\hat{0}} \,, \tag{11.1}$$

$$\mathcal{B}_{\alpha\beta} = -\gamma_\alpha{}^\rho \gamma_\beta{}^\sigma {}^*C_{\rho\mu\sigma\nu} u^\mu u^\nu \,, \qquad \text{i.e.,} \qquad \mathcal{B}_{ij} = \frac{1}{2}\epsilon_{ipq} C^{pq}{}_{j\hat{0}} \,. \tag{11.2}$$

The quantity ${}^*C_{\mu\nu\rho\sigma}$ is the Hodge dual of the Weyl tensor, and $\gamma_\alpha{}^\mu$ is the projection operator into a spatial slice (which is equivalent to raising one index of the spatial metric). We use the conventions for the antisymmetric tensors which, when expressed in an orthonormal basis, require that $\epsilon_{\hat{0}\hat{1}\hat{2}\hat{3}} = +1$ and $\epsilon_{\hat{1}\hat{2}\hat{3}} = +1$.

Because $\mathcal{E}_{ij}$ and $\mathcal{B}_{ij}$ are symmetric, trace-free tensors, they can always be diagonalized by finding their three eigenvalues and eigenvectors (shown below for the tidal field):

$$\mathcal{E}^i{}_j v^j = \lambda v^i \,. \tag{11.3}$$

We call the streamlines of these eigenvector fields *tendex lines* for the tidal field and *vortex lines* for the frame-drag field, and the eigenvalue along these lines the *tendicity* and *vorticity*, respectively. A region of large tendicity (in magnitude) we will call a *tendex*, and that of large vorticity we will call a *vortex*.

Vortex and tendex lines (and their corresponding vorticity and tendicity) also have a simple physical interpretation. In Paper I, we rederived the facts that the tidal field describes the local tidal forces between nearby points in the spacetime and the frame-drag field determines the relative precession of nearby gyroscopes. Specifically, in the local Lorentz frame of two freely falling observers,

separated by a spatial vector ξ^j, the differential acceleration experienced by the observers is

$$\Delta a^i = -\mathcal{E}^i{}_j \xi^j \,, \tag{11.4}$$

and, if these same observers carry inertial guidance gyroscopes, each will measure the gyroscope of the other to precess (relative to her own) with the same vectorial angular velocity,

$$\Delta \Omega^i = \mathcal{B}^i{}_j \xi^j \,. \tag{11.5}$$

The physical interpretation of the tendex and vortex lines (and their corresponding tendicities and vorticities) is now clear: if two observers have a small separation along a tendex line, they experience an acceleration along that line with a magnitude given by the tendicity of that line (pushed together if positive and pulled apart if negative); similarly, two observers separated along a vortex line will have their gyroscopes differentially precess with a magnitude given by the vorticity along the line (clockwise if positive and counterclockwise if negative).

11.3 Black-Hole Horizons; The Horizon Tendicity $\mathcal{E}_{NN}$ and Vorticity $\mathcal{B}_{NN}$

In many problems of physical interest, such as black hole perturbations and numerical-relativity simulations using excision (as in the `SpEC` code [24]), the interior of a black hole is not included in the domain of the solution. This does not effect the evolution of the exterior of the spacetime, because the event horizon prevents information from the black hole's interior from escaping to the outside world. We, however, are interested in structures defined on spacelike surfaces that pass through the horizon, and we would like to have an indicator on the horizon of the spacetime dynamics surrounding the horizon. To do this, we define quasilocal quantities (see, e.g., [25]), which we call the horizon tendicity and vorticity.

We define the horizon tendicity and vorticity as follows: For a hypersurface-normal observer with 4-velocity $\vec{u}$, passing through a world tube such as an event horizon or a dynamical horizon, the world tube has an inward pointing normal, $\vec{N}$, orthogonal to $\vec{u}$, and two orthonormal vectors tangent to its surface, $\vec{e}_2$ and $\vec{e}_3$. It is useful to choose these four vectors to make an orthonormal tetrad. The horizon tendicity is defined as $\mathcal{E}_{NN} = \mathcal{E}_{ij} N^i N^j$ and the horizon vorticity is $\mathcal{B}_{NN} = \mathcal{B}_{ij} N^i N^j$. Physically, they represent the amplitude of the differential acceleration and precession of gyroscopes, respectively, measured by an observers separated along the normal of the horizon.

The horizon tendicity and vorticity have several interesting connections with other geometric quantities of 2-surfaces; in particular, they are well adapted to Newman-Penrose (NP) formalism [3]. Rather than using tetrad of time- and space-like vectors ($\vec{u}$, $\vec{N}$, $\vec{e}_2$ and $\vec{e}_3$), the NP approach

uses a null tetrad, with two null vectors $\vec{l}$ and $\vec{n}$, together with a complex spatial vector $\vec{m}$ and its complex conjugate $\vec{m}^*$. It is convenient to adapt this tetrad to the 2-surface so that it is given by

$$\vec{l} = \frac{1}{\sqrt{2}}(\vec{u} - \vec{N}) \,, \quad \vec{n} = \frac{1}{\sqrt{2}}(\vec{u} + \vec{N}) \,, \quad \vec{m} = \frac{1}{\sqrt{2}}(\vec{e}_2 + i\vec{e}_3) \,. \tag{11.6}$$

On an event horizon, $\vec{l}$ is tangent to the generators of the horizon and $\vec{n}$ is the ingoing null normal. It is not difficult to show that in this tetrad the complex Weyl scalar Ψ_2 is given by

$$\Psi_2 = C_{lmm^*n} = (\mathcal{E}_{NN} + i\mathcal{B}_{NN})/2 \,, \tag{11.7}$$

where C_{lmm^*n} is the Weyl tensor contracted into the four different null vectors of the tetrad in the order of the indices.

Penrose and Rindler [26] relate the NP quantities to the curvature scalars of a spacelike 2-surface in spacetime; in turn, we can then connect their results to the horizon tendicity and vorticity. More specifically, Penrose and Rindler define a complex curvature of a two-surface by

$$\mathcal{K} = \frac{1}{4}\left(\mathcal{R} + i\mathcal{X}\right) \,. \tag{11.8}$$

Here $\mathcal{R}$ is the intrinsic Ricci curvature scalar of a the 2D horizon and $\mathcal{X}$ is a scalar extrinsic curvature (a curvature of the bundle of vector spaces normal to the two-surface in spacetime). This extrinsic curvature $\mathcal{X}$ is related to the Hájíček field [27] $\Omega_A = n^\mu \nabla_A l_\mu$ (where ∇_A denotes the covariant derivative projected into the 2D horizon) by $\mathcal{X} = \epsilon^{AB}\nabla_A \Omega_B$, where ϵ^{AB} is the antisymmetric tensor of the 2D horizon. In the language of differential forms, $\mathcal{X}$ is the dual of the exterior derivative of the Hájíček 1-form.

Penrose and Rindler [26] show that

$$\mathcal{K} = -\Psi_2 + \mu\rho - \lambda\sigma \,, \tag{11.9}$$

where ρ, σ, μ, and λ are spin coefficients related to the expansion and shear of the null vectors $\vec{l}$ and $\vec{n}$, respectively; this implies that the horizon tendicity and vorticity are given by

$$\mathcal{E}_{NN} = -\mathcal{R}/2 + 2\Re[\mu\rho - \lambda\sigma] \,, \tag{11.10}$$

$$\mathcal{B}_{NN} = -\mathcal{X}/2 + 2\Im[\mu\rho - \lambda\sigma] \,. \tag{11.11}$$

For a stationary black hole, ρ and σ vanish, $\mathcal{E}_{NN} = -\mathcal{R}/2$ and $\mathcal{B}_{NN} = -\mathcal{X}/2$, and the two-dimensional horizon of a stationary black hole must have a spherical topology. By the Gauss-Bonnet theorem (which requires that the integral of the scalar curvature $\mathcal{R}$ over such surfaces is 8π) the

integral of the horizon tendicity $\mathcal{E}_{NN}$ over the horizon is -4π; similarly, Stokes' theorem (the integral of an exact form vanishes on a surface without a boundary) requires that the integral of the horizon vorticity vanishes; i.e., they satisfy

$$\oint \mathcal{E}_{NN} dA = -4\pi \,, \quad \oint B_{NN} dA = 0 \tag{11.12}$$

for the horizon of a stationary black hole.

For weakly perturbed Schwarzschild black holes, one can choose a tetrad, the Hartle-Hawking tetrad [28], in which $-\Psi_2$ is the same as the complex curvature of the horizon to linear order in perturbation theory. For a weakly perturbed Kerr black hole, Hartle showed that $-\Psi_2$ is the same as the complex curvature at zeroth order, and, in the Hartle-Hawking tetrad,

$$\mathcal{K}^{(1)} = -\Psi_2^{(1)} - \lambda^{(0)}\sigma^{(1)} \,, \tag{11.13}$$

on the horizon [29]. Here, and throughout this paper, the superscripts, (i), indicate orders in the perturbation; similarly we will sometimes use subscripts, (i).

We briefly digress to note that in the calculations performed in this paper, even though we do not generically work in the Hartle-Hawking tetrad, Eqs. (11.12) still seem to hold even for perturbed black holes to a very good approximation. Intuitively, this is likely the case, because we focus on perturbations of definite parities, and we do not see asymmetries that would lead this equality to no longer hold. Interestingly, in preliminary numerical-relativity simulations, we do not see very large deviations from the relationships given in Eqs. (11.12) either; whether this is an indication of a deeper relationship is still an open question.

The horizon tendicity and vorticity are only markers of the surrounding spacetime dynamics, and they do not directly affect the spacetime outside, because the event horizon is defined by the condition that its generators do not escape from the surface and reach future null infinity. In 1974, Hartle [29] captured this effect clearly, when he showed that perturbations to the complex horizon curvature of a Kerr black hole are driven by ingoing gravitational radiation (represented by the Weyl scalar Ψ_0). This point is emphasized in a recent series of papers by Jaramillo, Macedo, Moesta, and Rezzola [30, 31], in which correlations between quantities on the horizon and infinity reveal properties of the spacetime dynamics between the two.

It is worth noting a few other examples in the literature where the complex-curvature quantities have been used. The most common use of horizon vorticity (in a disguised form) is to compute the spin angular momentum associated with a quasilocal black-hole horizon. Following [32, 33, 34], it has become common to compute black-hole angular momenta using the following integral over the

horizon:

$$J = -\frac{1}{8\pi} \oint K_{ij} N^i \varphi^j dA, \tag{11.14}$$

where K_{ij} is the extrinsic curvature of the spatial slice embedded in spacetime, $\vec{N}$ is the inward-pointing unit normal vector to the horizon in the spatial slice, and $\vec{\varphi}$ is a rotation-generating vector field tangent to the two-dimensional horizon surface. If $\vec{\varphi}$ is a Killing vector, then one can show that J is conserved. In Ref. [35], this was applied to binary-black-hole simulations with $\vec{\varphi}$ given by a certain kind of approximate Killing vector that can be computed on a deformed two-surface. In [36], and independently in [37, 38], this idea was refined. The quantity J can be shown to be boost-invariant (independent of boosts of the spatial slice in the direction of $\vec{N}$) if $\vec{\varphi}$ is divergence-free. Hence, in [36, 37, 38], $\vec{\varphi}$ is restricted to have the form $\varphi^A = \epsilon^{AB} \nabla_B \zeta$, where ζ is some scalar quantity on the two-surface (eventually fixed by a minimization problem for other components of the Killing equation). Once this substitution has been made, an integration by parts allows J to be written as

$$J = \frac{1}{8\pi} \oint \mathcal{X} \zeta dA. \tag{11.15}$$

The quantity ζ is fixed by a certain eigenvalue problem on the horizon's two-dimensional surface. On a round 2-sphere, the operator in this eigenvalue problem reduces to the conventional Laplacian, and ζ can be shown to reduce to an $\ell = 1$ spherical harmonic. Therefore, the quasilocal black hole spin defined in [36, 37, 38] can be thought of as the dipole part of the horizon vorticity.

In [39], it was shown that higher spherical-harmonic components of these horizon quantities provide natural definitions of source multipoles on axisymmetric isolated horizons. In [40] and [41], this formalism was extended to less symmetric cases (so that it could be used within numerical-relativity simulations) introducing as little gauge ambiguity as possible; similar applications of this formalism can be found in [42, 43].

11.4 Schwarzschild Black Hole

In this section, we examine the vortex and tendex lines of a nonrotating black hole with mass M, Even for a spherically symmetric black hole, our choice of time slicing will affect the appearance of these lines. As in the numerical-relativity simulations that are the focus of Paper III, so also here, we shall use a slicing that penetrates smoothly through the black hole's horizon. The slices of constant Schwarzschild time, t, for the hole's Schwarzschild metric

$$ds^2 = -\left(1 - \frac{2M}{r}\right) dt^2 + \left(1 - \frac{2M}{r}\right)^{-1} dr^2 + r^2 d\theta^2 + r^2 \sin^2\theta d\phi^2 \tag{11.16}$$

do not penetrate the horizon smoothly; rather, they become singular as they approach the horizon. The simplest horizon-penetrating slices are those of constant ingoing Eddington-Finkelstein (EF)

time

$$\tilde{t} = t + 2M \log|r/2M - 1| \,. \tag{11.17}$$

The Schwarzschild metric (11.16), rewritten using EF coordinates $\{\tilde{t}, r, \theta, \phi\}$, takes the form

$$ds^2 = -\left(1 - \frac{2M}{r}\right) d\tilde{t}^2 + \frac{4M}{r} d\tilde{t} dr + \left(1 + \frac{2M}{r}\right) dr^2 + r^2 d\theta^2 + r^2 \sin^2\theta d\phi^2 \,. \tag{11.18}$$

The observers who measure the tidal and frame-drag fields that lie in a slice of constant $\tilde{t}$ have 4-velocities $\vec{u} = -\alpha_{\rm EF} \vec{\nabla}\tilde{t}$, where $\alpha_{\rm EF} = 1/\sqrt{1 + 2M/r}$ is the normalizing lapse function. These observers can be regarded as carrying the following orthonormal tetrad for use in their measurements:

$$\vec{u} = \frac{1}{\sqrt{1+2M/r}} \left[\left(1 + \frac{2M}{r}\right) \partial_{\tilde{t}} - \frac{2M}{r} \partial_r\right] , \quad \vec{e}_{\hat{r}} = \frac{1}{\sqrt{1+2M/r}} \partial_r \,, \quad \vec{e}_{\hat{\theta}} = \frac{1}{r} \partial_\theta \,, \quad \vec{e}_{\hat{\phi}} = \frac{1}{r\sin\theta} \partial_\phi \,. \tag{11.19}$$

The nonzero components of the tidal field that they measure using this tetrad are

$$\mathcal{E}_{\hat{r}\hat{r}} = -\frac{2M}{r^3} \,, \quad \mathcal{E}_{\hat{\theta}\hat{\theta}} = \mathcal{E}_{\hat{\phi}\hat{\phi}} = \frac{M}{r^3} \,, \tag{11.20}$$

and the frame-drag field $\mathcal{B}_{\hat{a}\hat{b}}$ vanishes.

Note that the black hole's tidal field Eq. (11.20) has the same form as the Newtonian tidal tensor outside of a spherical source. Because this tidal field is diagonal, we conclude that the spatial triad in Eq. (11.20) are the tendex directions and the diagonal components of the tidal field are the corresponding tendicities, as we show below:

$$\vec{V}_r = \vec{e}_{\hat{r}} \leftrightarrow \lambda_r = -\frac{2M}{r^3} \,, \quad \vec{V}_\theta = \vec{e}_{\hat{\theta}} \leftrightarrow \lambda_\theta = \frac{M}{r^3} \,, \quad \vec{V}_\phi = \vec{e}_{\hat{\phi}} \leftrightarrow \lambda_\phi = \frac{M}{r^3} \,. \tag{11.21}$$

Because the two transverse eigenvalues λ_θ and λ_ϕ are degenerate, any vector in the transverse vector space spanned by $\vec{e}_{\hat{\theta}}$ and $\vec{e}_{\hat{\phi}}$ is a solution to the eigenvalue problem, and correspondingly, any curve that lies in a sphere of constant r can be regarded as a tendex line. However (as we shall see in the next section), when the black hole is given an arbitrarily small rotation about its polar axis $\theta = 0$, the degeneracy is broken, the nondegenerate transverse eigenvectors become nearly $\vec{e}_{\hat{\theta}}$ and $\vec{e}_{\hat{\phi}}$, and the transverse tendex lines become circles of constant latitude and longitude.

In Fig. 11.1, we plot a few of these transverse tendex lines (giving them a blue color corresponding to positive tendicity, $\lambda_\theta > 0$ and $\lambda_\phi > 0$), and also a few of the radial tendex lines (colored red for negative tendicity, $\lambda_r < 0$). Also shown are two human observers, one is oriented along a blue tendex line and, therefore, is being squeezed by the tidal field; the other is oriented along a red tendex line and is, therefore, being stretched.

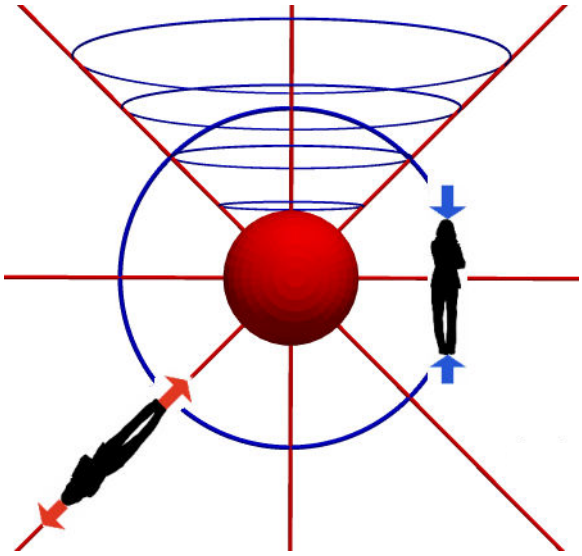

Figure 11.1: Tendex lines for a nonrotating (Schwarzschild) black hole. These lines are identical to those generated by a spherically symmetric mass distribution in the Newtonian limit. Also shown are observers who experience the tidal stretches and compressions associated with the tendex lines.

11.5 Slowly Rotating Black Hole

11.5.1 Slicing and Coordinates

When the black hole is given a slow rotation with angular momentum per unit mass a, its metric, Eq. (11.16), in Schwarzschild coordinates acquires an off-diagonal $g_{t\phi}$ term:

$$ds^2 = -\left(1-\frac{2M}{r}\right)dt^2 + \left(1-\frac{2M}{r}\right)^{-1}dr^2 + r^2 d\theta^2 + r^2\sin^2\theta d\phi^2 - \frac{4aM}{r}\sin^2\theta dt d\phi \qquad (11.22)$$

(the Kerr metric in Boyer-Lindquist coordinates, Eq. (11.31) below, linearized in a). The slices of constant EF time $\tilde{t} = t + 2M\log|r/2M-1|$ are still smoothly horizon penetrating, but the dragging of inertial frames (the off-diagonal $g_{t\phi}$ term in the metric) causes the Schwarzschild ϕ coordinate to become singular at the horizon. To fix this, we must unwrap ϕ, e.g., by switching to the coordinate

$$\tilde{\phi} = \phi + (a/2M)\log|1-2M/r|\ , \qquad (11.23)$$

thereby bringing the slowly rotating Kerr metric, Eq. (11.22), into the form

$$\begin{aligned} ds^2 &= -\left(1-\frac{2M}{r}\right)d\tilde{t}^2 + \frac{4M}{r}d\tilde{t}dr + \left(1+\frac{2M}{r}\right)dr^2 + r^2 d\theta^2 + r^2\sin^2\theta d\tilde{\phi}^2 \\ &\quad -\frac{4aM}{r}\sin^2\theta d\tilde{t}d\tilde{\phi} - 2a\sqrt{1+\frac{2M}{r}}\sin^2\theta dr d\tilde{\phi} \end{aligned} \qquad (11.24)$$

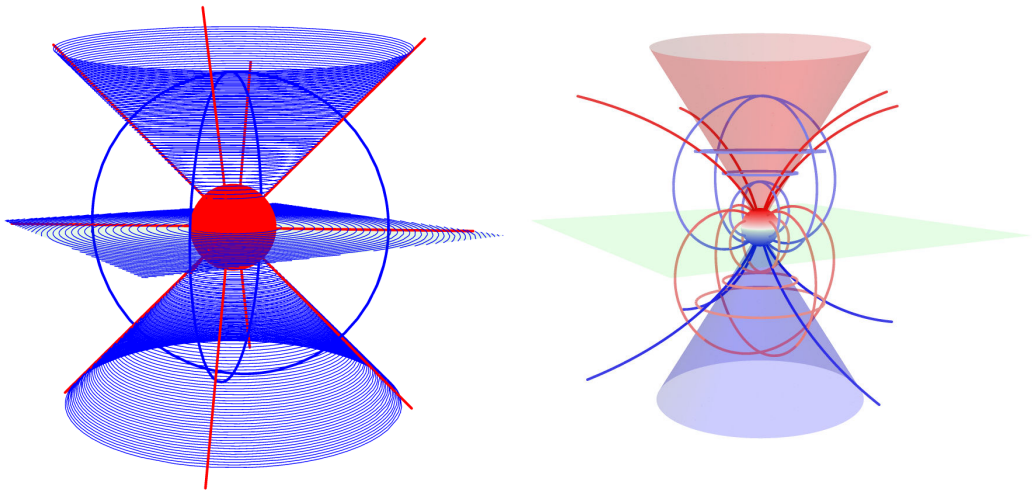

Figure 11.2: Left are tendex lines and right are vortex lines for a slowly rotating black hole. For the visualization here, we choose $a/M = 0.1$. The horizon is color coded by its tendicity $\mathcal{E}_{NN}$ (left) and vorticity $\mathcal{B}_{NN}$ (right), and the field lines are color coded by the sign of their tendicity or vorticity. The semi-transparent cone-like surfaces emerging from the horizon's north and south polar regions are the edges of the hole's frame-drag vortexes (defined as the regions where the emerging vortex lines have vorticity greater that 0.9 of the maximum vorticity at the poles).

(Eq. (11.53) below, linearized in a), which is well-behaved at and through the horizon. The observers who move orthogonally to the slices of constant $\tilde{t}$ have four-velocity $\vec{u}$ and an orthonormal basis the same as for a nonrotating black hole, Eq. (11.19), except that $\vec{e}_{\hat{r}}$ is changed to

$$\vec{e}_{\hat{r}} = \frac{1}{\sqrt{1+2M/r}}\left[\partial_r + \frac{a}{r^2}(1+2M/r)\partial_{\tilde{\phi}}\right] \tag{11.25}$$

(Eq. (11.54) below, linearized in a).

11.5.2 Frame-Drag Field and Deformed Tendex Lines

The slow rotation gives rise to a frame-drag field

$$\mathcal{B}_{\tilde{r}\tilde{r}} = \frac{-6aM\cos\theta}{r^4}\,, \quad \mathcal{B}_{\tilde{r}\tilde{\theta}} = \mathcal{B}_{\tilde{\theta}\tilde{r}} = \frac{-3aM\sin\theta}{r^4\sqrt{1+2M/r}}\,, \quad \mathcal{B}_{\tilde{\theta}\tilde{\theta}} = \mathcal{B}_{\tilde{\phi}\tilde{\phi}} = \frac{3aM\cos\theta}{r^4} \tag{11.26}$$

that lives in the slices of constant EF time $\tilde{t}$. This field's vortex lines, shown in the right panel of Fig. 11.2, are poloidal and closely resemble those of a spinning point mass in the linearized approximation to general relativity (Fig. 3 of Paper I [7]). At radii $r \gg M$, the field asymptotes to that of a linearized current dipole.

The rotating hole's horizon vorticity is $\mathcal{B}_{NN} = \mathcal{B}_{\hat{r}\hat{r}} = -6(aM/r^4)\cos\theta$, which is negative in the northern polar regions and positive in the southern polar regions. Correspondingly, there is a

counterclockwise frame-drag vortex sticking out of the hole's northern pole, and a clockwise one sticking out if its southern pole. We arbitrarily identify the edge of each vortex, at radius r, as the location where the vorticities of the vortex lines, that emerge from the hole at the base of the vortex, fall (as a function of θ at fixed r) to 90 percent of the on-pole vorticity. The vortex edges are shown, in Fig. 11.2, as semi-transparent surfaces.

The hole's (small) spin not only generates a frame-drag field $\mathcal{B}_{ij}$; it also modifies, slightly, the hole's tidal field $\mathcal{E}_{ij}$ and its tendex lines. However, the spin does not change the field's tendicities, which (to first order in a/M) remain $\lambda^{\mathcal{E}}_r = -2M/r^3$, $\lambda^{\mathcal{E}}_\theta = \lambda^{\mathcal{E}}_\phi = M/r^3$, as in Eq. (11.21). The modified unit tangent vectors to the tendex lines are

$$\vec{V}^{\mathcal{E}}_r = \vec{e}_{\hat{r}} - \frac{2Ma\sin\theta}{r^2\sqrt{1+\frac{2M}{r}}}\vec{e}_{\hat{\phi}}\ , \quad \vec{V}^{\mathcal{E}}_{\hat{\phi}} = \vec{e}_{\hat{\phi}} + \frac{2Ma\sin\theta}{r^2\sqrt{1+\frac{2M}{r}}}\vec{e}_{\hat{r}}\ , \quad \vec{V}^{\mathcal{E}}_{\hat{\theta}} = \vec{e}_{\hat{\theta}}\ . \tag{11.27}$$

Correspondingly, there is a slight (though hardly noticeable) bending of the radial tendex lines near the black hole, and, more importantly, the azimuthal tendex lines (the ones tangent to $\vec{V}^{\mathcal{E}}_{\hat{\phi}}$) no longer close. Instead, the azimuthal tendex lines spiral outward along cones of fixed θ, as shown in the left panel of Fig. 11.2.

11.5.3 Robustness of the Frame-Drag Field and Tendex-Line Spiral

The two new features induced by the hole's small spin (the frame-drag field, and the spiraling of the azimuthal tendex lines) are, in fact, robust under changes of slicing. We elucidate the robustness of the frame-drag field and its vortex lines and vorticities through the following argument:

Suppose that we change the time function $\tilde{t}$, which defines our time slices, by a small fractional amount of order a/M; i.e., we introduce a new time function

$$t' = \tilde{t} + \xi(r,\theta)\ , \tag{11.28}$$

where $\tilde{t}$ is EF time and ξ has been chosen axisymmetric and time-independent, so it respects the symmetries of the black hole's spacetime. Then observers who move orthogonal to slices of constant t' will be seen by the EF observers (who move orthogonal to slices of constant $\tilde{t}$) to have small spatial-velocities that are poloidal, $\mathbf{v} = v^{\hat{r}}\mathbf{e}_{\hat{r}} + v^{\hat{\theta}}\mathbf{e}_{\hat{\theta}}$. The Lorentz transformation from the EF reference frame to the primed reference frame at some event in spacetime induces a change of the frame-drag field given by

$$\delta\mathcal{B} = -2(\mathbf{v}\times\mathcal{E})^S\ , \tag{11.29}$$

where the S means symmetrize. Inserting the EF tidal field in Eq. (11.20) and the poloidal compo-

nents of $\mathbf{v}$, we obtain as the only nonzero components of $\delta\mathcal{B}$

$$\delta\mathcal{B}_{\hat{r}\hat{\phi}\hat{\theta}} = \delta\mathcal{B}_{\hat{\phi}\hat{r}\hat{\theta}} = -(3M/r^3)v^{\hat{\theta}} \,. \tag{11.30}$$

This axisymmetric, slicing-induced change of the frame-drag field causes the vortex lines, which are originally purely poloidal, to acquire a small toroidal component (breaking the field's symmetry). Correspondingly, no small, axisymmetric change of slicing can alter the frame-drag field of a slowly rotating black hole in such a way as to preserve the poloidal nature of its vortex lines. In this sense, the frame-drag field is robust under slicing changes.

11.6 Rapidly Rotating (Kerr) Black Hole

We shall now explore a rapidly rotating black hole described by the exact Kerr metric.

11.6.1 Kerr Black Holes in Boyer-Lindquist Coordinates

The Kerr metric is usually written in Boyer-Lindquist (BL) coordinates $\{t, r, \theta, \phi\}$, where it takes the form

$$ds^2 = -\left(1 - \frac{2Mr}{\Sigma}\right) dt^2 + \frac{\Sigma}{\Delta} dr^2 + \Sigma d\theta^2 + \frac{\sin^2\theta}{\Sigma} A d\phi^2 - \frac{4Mar\sin^2\theta}{\Sigma} dt d\phi \,, \tag{11.31}$$

where

$$\Sigma = r^2 + a^2\cos^2\theta \,, \quad \Delta = r^2 - 2Mr + a^2 \,, \quad A = (r^2 + a^2)^2 - a^2\Delta\sin^2\theta \,. \tag{11.32}$$

Because the slices of constant t are singular at the horizon and, therefore, not of much interest to us, we relegate to Appendix 11.A.1 the details of their tidal and frame-drag fields, and their vortex and tendex lines.

11.6.2 Horizon-Penetrating Slices

In our study of Kerr black holes, we shall employ two different slicings that penetrate the horizon smoothly: surfaces of constant Kerr-Schild time coordinate $\tilde{t}$, and surfaces of constant Cook-Scheel time coordinate $\bar{t}$. By comparing these two slicings' tendex lines with each other, and also their vortex lines with each other, we shall gain insight into the lines' slicing-dependence.

The Kerr-Schild time coordinate (see, e.g., [44] also sometimes called ingoing-Kerr time) is defined by

$$\tilde{t} = t + r_* - r \,, \quad \text{where} \quad \frac{dr_*}{dr} = \frac{r^2 + a^2}{\Delta} \,. \tag{11.33}$$

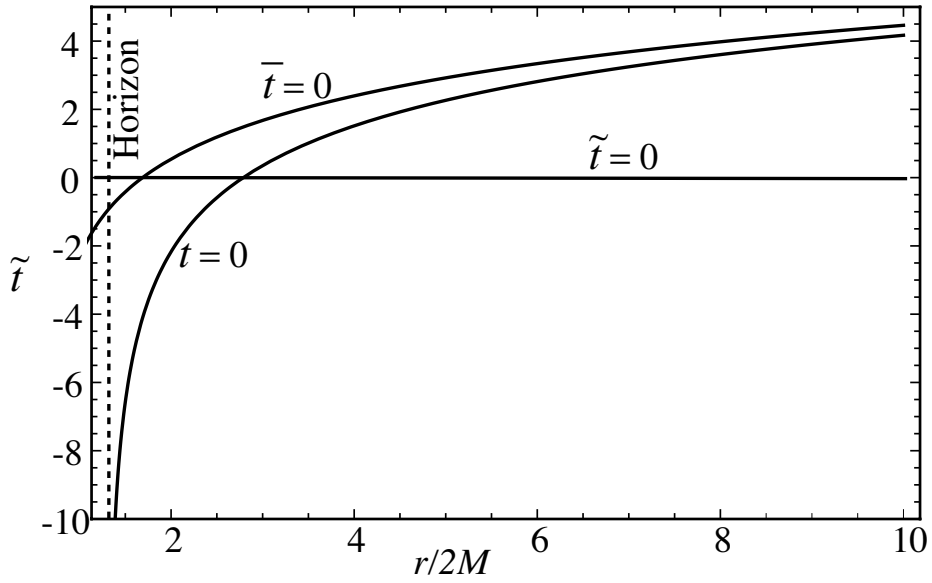

Figure 11.3: Slices of constant Boyer-Lindquist time t, Kerr-Schild time $\tilde{t}$, and Cook-Scheel time $\bar{t}$, drawn in a Kerr-Schild spacetime diagram. The dashed vertical line is the event horizon, r_+, and the black hole has spin $a/M = 0.95$.

The Cook-Scheel [45] time coordinate is

$$\bar{t} = t + \frac{r_+^2 + a^2}{r_+ - r_-} \log \left| \frac{r - r_+}{r - r_-} \right| , \tag{11.34}$$

where r_+ is the value of the Boyer-Lindquist radial coordinate r at the event horizon, and r_- is its value at the (inner) Cauchy horizon:

$$r_\pm = M \pm \sqrt{M^2 - a^2} . \tag{11.35}$$

Figure 11.3 shows the relationship between these slicings. In this figure, horizontal lines are surfaces of constant Kerr-Schild time $\tilde{t}$. Because t, $\bar{t}$, and $\tilde{t}$ differ solely by functions of r, the surfaces of constant Cook-Scheel time $\bar{t}$ are all parallel to the $\bar{t} = 0$ surface shown in the figure, and the surfaces of constant Boyer-Lindquist time t are all parallel to the $t = 0$ surface. The Kerr-Schild and Cook-Scheel surfaces penetrate the horizon smoothly; by contrast, the Boyer-Lindquist surfaces all asymptote to the horizon in the deep physical past, never crossing it (i.e., they become physically singular at the horizon).

11.6.3 Horizon-Penetrating Coordinate Systems

Not only is the Boyer-Lindquist time coordinate t singular at the event horizon; the Boyer-Lindquist azimuthal angular coordinate ϕ is singular as well. It winds around an infinite number of times as it asymptotes to the horizon. We shall use two different ways to unwind it, associated with

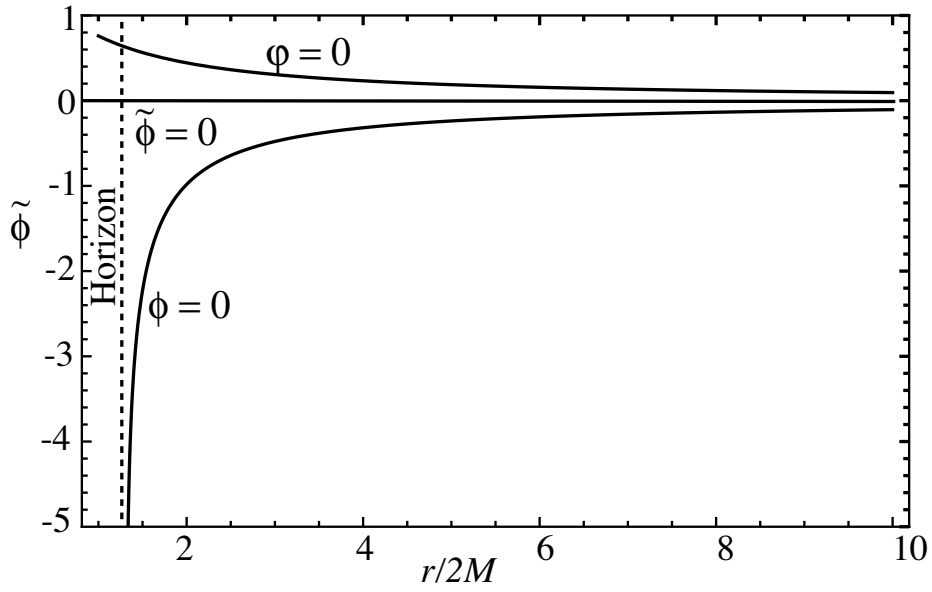

Figure 11.4: Curves of constant Boyer-Lindquist angle ϕ, Kerr-Schild angle φ, and ingoing-Kerr angle $\tilde{\phi}$ (same as Cook-Scheel angle $\bar{\phi}$). The dashed vertical line gain represents the event horizon, r_+, and the black hole again has spin $a/M = 0.95$.

two different horizon-penetrating angular coordinates: the Cook-Scheel (also called ingoing-Kerr) coordinate

$$\tilde{\phi} = \phi + \frac{a}{r_+ - r_-} \log \left| \frac{r - r_+}{r - r_-} \right| = \phi + \int_r^\infty \frac{a}{\Delta} dr \ , \tag{11.36}$$

and the Kerr-Schild coordinate

$$\varphi = \bar{\phi} - \tan^{-1}(a/r) \ . \tag{11.37}$$

Figure 11.4 shows the relationship of these three angular coordinates. Notice that (i) all three angular coordinates become asymptotically the same as $r \to \infty$; (ii) the two horizon-penetrating coordinates, Cook-Scheel $\tilde{\phi}$ and Kerr-Schild φ, differ by less than a radian as one moves inward to the horizon; and (iii) the Boyer-Lindquist coordinate ϕ plunges to $-\infty$ (relative to horizon-penetrating coordinates) as one approaches the horizon, which means it wraps around the horizon an infinite number of times.

In the literature on Kerr black holes, there are several sets of spacetime coordinates that are built from the coordinates r and θ, in addition to one of the three time coordinates t, $\tilde{t}$, and $\bar{t}$ and one of the angular coordinates ϕ, $\tilde{\phi}$, and φ. We review these coordinates below.

The most common choice are the Boyer-Lindquist coordinates, $\{t, r, \theta, \phi\}$, but these coordinates are singular at the horizon. Of horizon-penetrating coordinates, a well-known example are ingoing-Kerr coordinates, $\{\tilde{t}, r, \theta, \tilde{\phi}\}$, or a variant in which $\tilde{t}$ is replaced by a null coordinate (one whose gradient is null), $v = \tilde{t} + r$. There are also two types of quasi-Cartesian coordinates that are commonly used, both of which are regular at the horizon. We discuss these coordinates next.

The first are Kerr-Schild coordinates, $\{\tilde{t}, x, y, z\}$, and their cylindrical variant, $\{\tilde{t}, \varpi, z, \varphi\}$. Here

$$x + iy = (r + ia)e^{i\tilde{\phi}} \sin\theta \ , \quad z = r\cos\theta \ , \tag{11.38}$$

and

$$\varpi = \sqrt{x^2 + y^2} = \sqrt{r^2 + a^2} \ , \quad \varphi = \arctan(y/x) = \tilde{\phi} + \arctan(r/a) \ . \tag{11.39}$$

The Kerr-Schild spatial coordinates $\{x, y, z\}$ resemble the coordinates typically used in numerical-relativity simulations of binary black holes at late times, when the merged hole is settling down into its final, Kerr state. These coordinate systems resemble each other in the senses that (i) both are quasi-Cartesian, and (ii) for a fast-spinning hole, the event horizon in both cases, when plotted in the coordinates being used, looks moderately oblate. For this reason, in our study of Kerr black holes, we shall focus our greatest attention on Kerr-Schild coordinates. The Kerr metric, written in Kerr-Schild coordinates, has the form

$$ds^2 = \left(\eta_{\mu\nu} + \frac{2Mr^3}{r^4 + a^2z^2}k_\mu k_\nu\right) dx^\mu dx^\nu \ , \quad k_\mu = \left(1, \frac{rx + ay}{r^2 + a^2}, \frac{ry - ax}{r^2 + a^2}, \frac{z}{r}\right) \ , \tag{11.40}$$

where r is the Boyer-Lindquist radial coordinate, and is the larger root of

$$x^2 + y^2 + z^2 = r^2 + a^2\left(1 - \frac{z^2}{r^2}\right) \ . \tag{11.41}$$

The other set of coordinates are Cook-Scheel harmonic coordinates [45], $\{\bar{t}, \bar{r}, \theta, \tilde{\phi}\}$, where

$$\bar{r} = \sqrt{\frac{(r - M)^4 + a^2(r - M)^2}{a^2\cos^2\theta + (r - M)^2}} \ , \tag{11.42}$$

and the quasi-Cartesian coordinates constructed from them, $\{\bar{t}, \bar{x}, \bar{y}, \bar{z}\}$, where

$$\bar{x} + i\bar{y} = (r - M + ia)e^{i\tilde{\phi}} \sin\theta \ , \quad \bar{z} = (r - M)\cos\theta \ . \tag{11.43}$$

These coordinates are harmonic in the sense that the scalar wave operator acting on the quasi-Cartesian coordinates vanishes, $\Box x^\mu = \partial_\nu\left(\sqrt{-g}g^{\nu\rho}\partial_\rho x^\mu\right) = 0$. In these coordinates, the event horizon of a spinning black hole is more oblate than in Kerr-Schild coordinates—much more oblate for large a/M. The Kerr ring singularity, inside the inner Cauchy horizon, is located at $\bar{r} = a$.

11.6.4 Computation of Tendex and Vortex Quantities

Below we shall show images of tendex and vortex lines, color coded with their tendicities and vorticities, for our two horizon-penetrating slicings and using the three sets of spatial coordinates that are regular at the horizon. In all cases, we have computed the field lines and their eigenvalues

numerically, beginning with analytical formulae for the tidal and frame-drag fields in ingoing-Kerr spacetime coordinates, which we give in Appendix 11.A.2. Specifically, whenever the slicing is Kerr-Schild, from our analytic formulas for $\mathcal{E}_{ij}$ and $\mathcal{B}_{ij}$, we compute analytic formulas for the eigenvectors and eigenvalues in ingoing-Kerr spatial coordinates (Appendix 11.A.2), from the eigenvectors we compute tendex and vortex lines numerically in ingoing-Kerr spatial coordinates, and we then transform the lines to whatever other spatial coordinate system we may be using. When the slicing is Cook-Scheel (or anything else), we express the ingoing-Kerr Riemann tensor in terms of our analytic expressions for $\mathcal{E}_{ij}$ and $\mathcal{B}_{ij}$, then transform that Riemann tensor to the new slicing and coordinate system, then read off the new tidal and frame-drag fields, then numerically compute from them the new eigenvectors and eigenvalues, and then from the eigenvectors compute numerically the tendex and vortex lines.

11.6.5 Kerr-Schild Slicing: Tendex and Vortex Lines in Various Spatial Coordinate Systems

Once the slicing is chosen, the tidal and frame-drag fields, and also the tendex and vortex lines and their tendicities and vorticities, are all fixed as geometric, coordinate-independent entities that live in a slice. If we could draw an embedding diagram showing the three-dimensional slice isometrically embedded in a higher-dimensional flat space, then we could visualize the tendex and vortex lines without the aid of a coordinate system. There is no simple way to draw embedding diagrams in such high-dimensional spaces, however, and we are forced to draw the tendex and vortex lines in some coordinate system for the slice, in a manner that makes the coordinate system look like it is one for flat space.

Such a coordinate-diagram plot of the lines makes them look coordinate dependent—i.e., their shapes depend on the coordinate system used. Nevertheless, we expect that the qualitative and semi-quantitative features of the lines will be the same in all reasonable coordinate systems.

Figure 11.5 is an important example. It shows the tendex lines (left column of plots) and vortex lines (right column of plots) for a fast-spinning Kerr black hole, with $a/M = 0.95$. In all cases the slicing is Kerr-Schild; i.e., the lines lie in a slice of constant $\tilde{t}$. The three rows of figures are drawn in three different spatial coordinate systems: Kerr-Schild, ingoing-Kerr, and Cook-Scheel. We describe the important features of this figure in the next five paragraphs below.

As expected, the qualitative and semi-quantitative features of the tendex and vortex lines are independent of the spatial coordinates, as expected. The only noticeable differences from one coordinate system to another are a flattening of the strong-gravity region near the hole as one goes from ingoing-Kerr coordinates (upper row of panels) to Kerr-Schild coordinates (center row of panels) and then a further flattening for Cook-Scheel coordinates (bottom row of panels).

The azimuthal (toroidal) tendex and vortex lines (those that point predominantly in the $\vec{e}_{\tilde{\phi}}$

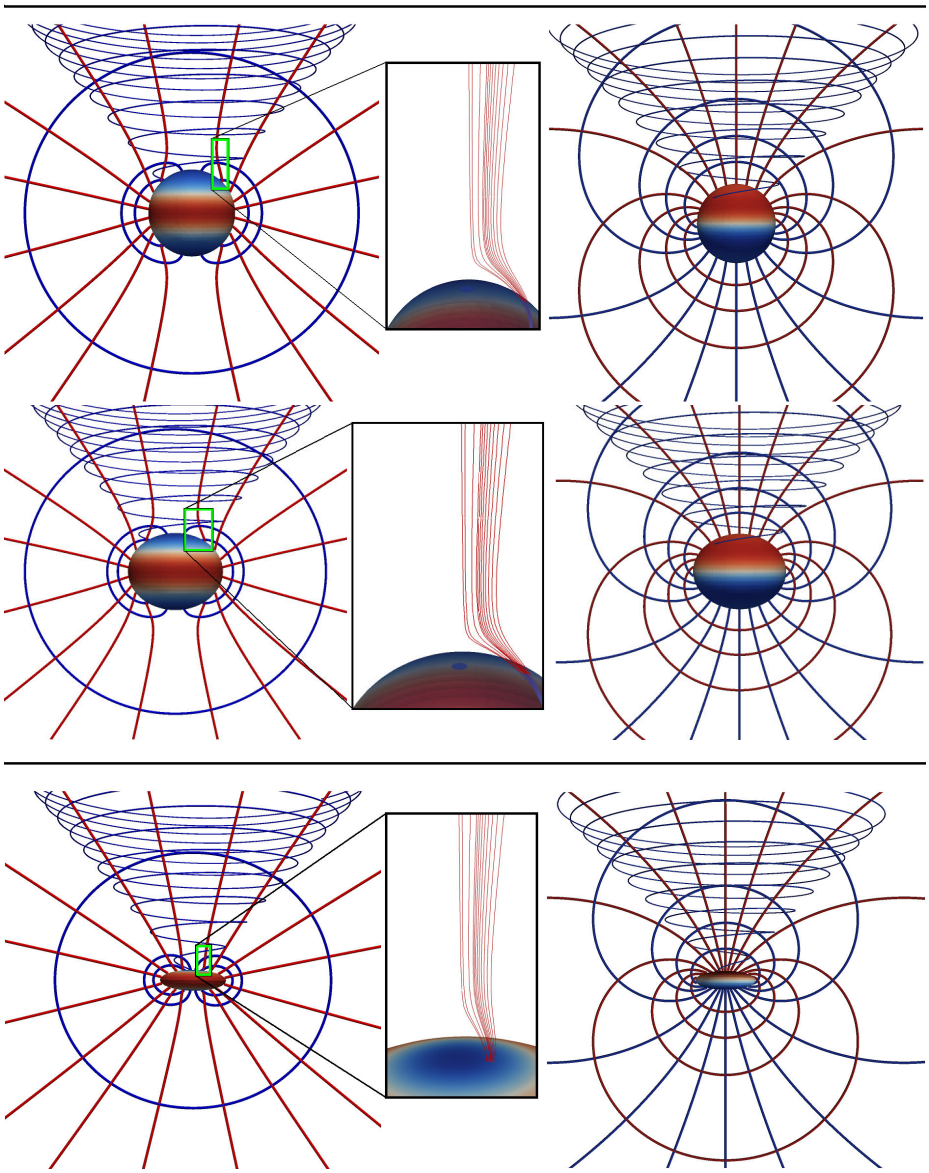

Figure 11.5: Tendex lines and vortex lines for a Kerr black hole with $a/M = 0.95$ in Kerr-Schild slicing, drawn in three different spatial coordinate systems. The left and center columns of drawings show tendex lines; the right column of drawings show vortex lines. The three rows, from top downward, use ingoing-Kerr spatial coordinates $\{r, \theta, \tilde{\phi}\}$, Kerr-Schild spatial coordinates $\{r, \theta, \varphi\}$, and Cook-Scheel spatial coordinates $\{\bar{r}, \theta, \tilde{\phi}\}$. In all cases, the lines with positive tendicity or vorticity are colored blue; those with negative tendicity or vorticity are colored red, and the horizon is shown with its horizon tendicity (left column of drawings) and horizon vorticity (right column) color coded from dark blue for strongly positive to dark red for strongly negative.

direction) spiral outward from the horizon along cones of constant θ, as for the tendex lines of a slowly spinning black hole; see the form of $\vec{V}_{\hat{\phi}}$ in Eqs. (11.61). As we shall discuss in Appendix 11.A.3, this is an unavoidable, slicing-independent consequence of the black hole's spin. All the poloidal tendex and vortex lines have small azimuthal ($\tilde{\phi}$) components, which do not show up in this figure; see the $\partial_{\hat{\phi}}$ components of the eigenvectors $\vec{V}^{\mathcal{E}}_r$, $\vec{V}^{\mathcal{E}}_\theta$, $\vec{V}^{\mathcal{B}}_-$ and $\vec{V}^{\mathcal{B}}_+$ in Eqs. (11.61) and (11.62).

For this rapidly spinning black hole, the horizon tendicity (in the left column of images) is positive (blue) in the northern and southern polar regions, and negative (red) in the equatorial region, by contrast with a slowly spinning hole, where the horizon tendicity is everywhere negative (Fig. 11.2). Correspondingly, a radially oriented person falling into a polar region of a fast-spinning hole gets squeezed from head to foot, rather than stretched, as conventional wisdom might suggest. The relationship $\mathcal{E}_{NN} = -\mathcal{R}/2$ between the horizon's tendicity and its scalar curvature tells us that this peculiar polar feature results from the well-known fact that, when the spin exceeds $a/M = \sqrt{3}/2 = 0.8660$, the scalar curvature goes negative near the poles, at angles θ satisfying $2(a/M)^2\cos^2\theta > 1 + \sqrt{1-(a/M)^2}$. This negative scalar curvature is also responsible for the impossibility to embed the horizon's 2-geometry in a 3-dimensional Euclidean space [5].

Again, in the left column of images, the blue (positive tendicity) tendex lines that emerge from the northern polar region sweep around the hole, just above the horizon, and descend into the southern polar region. In order to stay orthogonal to these blue (squeezing) tendex lines, the red (stretching) lines descending from radial infinity get deflected away from the horizon's polar region until they reach a location with negative tendicity (positive scalar curvature), where they can attach to the horizon; see the central panels, which are enlargements of the northern polar region for the left panels.

The vortex-line structure (the right column of images) for this fast-spinning black hole is very similar to that for the slow-spinning hole of Fig. 11.2, and similar to that for a spinning point mass in the linear approximation to general relativity (see Fig. 3 of Paper I [7]). The principal, obvious change is that the azimuthal vortex lines are not closed; instead, they spiral away from the black hole, like the azimuthal tendex lines. Most importantly, as for a slow-spinning black hole, there are two vortexes (regions of strong vorticity): as a counterclockwise vortex emerging from the north polar region and a clockwise vortex emerging from the south polar region. As we shall see in Paper III, when certain configurations of two spinning black holes collide and merge, these vortexes sweep around, emitting gravitational waves.

11.6.6 Slicing-Dependence of Tendex and Vortex Lines

To explore how a Kerr black hole's vortex and tendex lines depend on the choice of slicing, we focus on a black hole with $a/M = 0.875$, viewed in a slice of constant Kerr-Schild time, $\tilde{t}$ =constant, and in a slice of constant Cook-Scheel harmonic time, $\bar{t}$ =constant (Fig. 11.6). In the two slices, we use

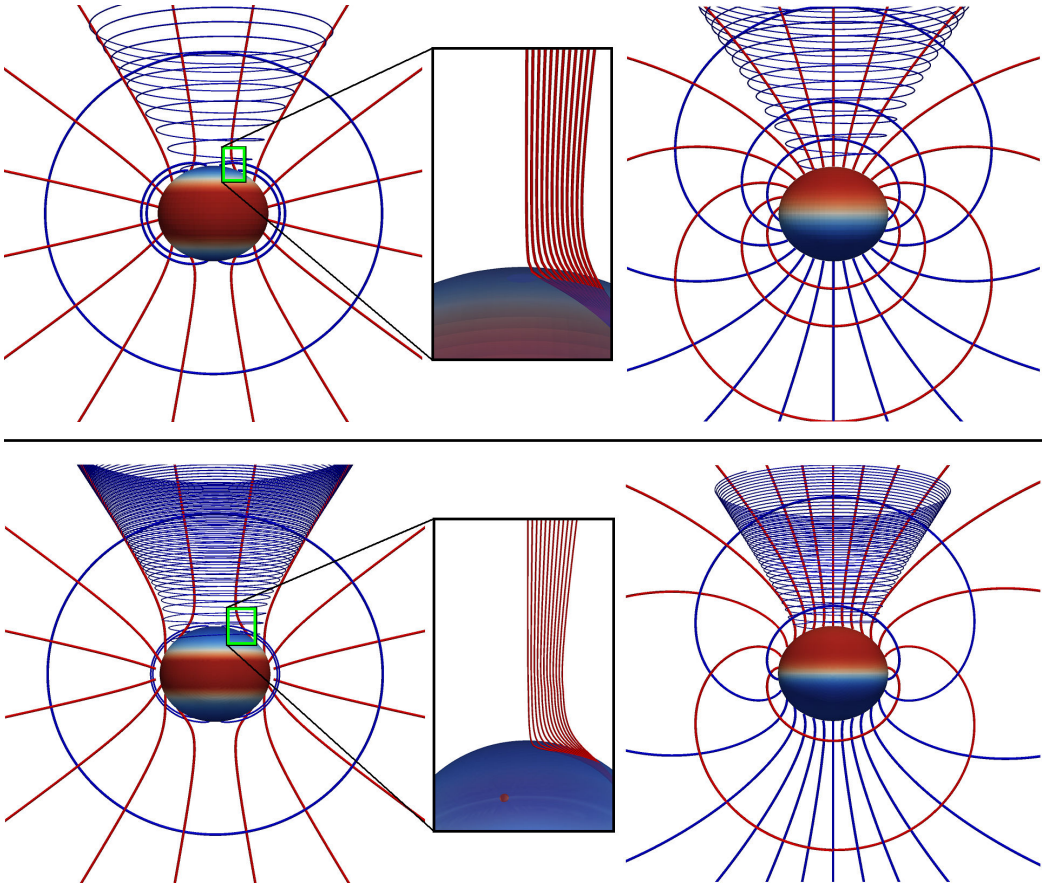

Figure 11.6: Tendex lines and vortex lines for a Kerr black hole with $a/M = 0.875$ in Kerr-Schild coordinates, for two different slicings: Kerr-Schild $\tilde{t}$ =constant, and Cook-Scheel $\bar{t}$ =constant. The left and center columns of drawings show tendex lines; the right column of drawings show vortex lines. The top row of drawings is for Kerr-Schild slicing; the bottom row is for Cook-Scheel slicing. Because the slicings are different, it is not possible to focus on the same sets of field lines in the Kerr-Schild (upper panels) and Cook-Scheel (lower panels). However, we have attempted to identify similar field lines by ensuring they pass through the same Kerr-Schild spatial coordinate locations on selected surfaces.

the same spatial coordinates (Kerr-Schild). We choose $a/M = 0.875$, rather than the 0.95 that we used for exploring slicing dependence, because our numerical techniques had difficulty dealing with higher spins in the Cook-Scheel case.

The most striking aspect of Fig. 11.6 is the close similarity of the tendex lines (left column of drawings) in the two slicings (upper and lower drawings), and also the close similarity of the vortex lines (right column of drawings) in the two slicings (upper and lower). There appears to be very little slicing dependence when we restrict ourselves to horizon-penetrating slicings.

By contrast, if we switch from a horizon-penetrating to a horizon-avoiding slice, there are big changes in the field lines near the black hole: compare the top row of Fig. 11.5 ($a/M = 0.95$ for a Kerr-Schild, horizon-penetrating slice) with Fig. 11.17 (the same hole, $a/M = 0.95$, for a Boyer-Lindquist, horizon-avoiding slice). The most striking differences are (i) the radial tendex lines'

horizon avoidance for horizon-avoiding slices, contrasted with their plunging through the horizon for horizon-penetrating slices, and (ii) the closed-circle azimuthal tendex and vortex lines for Boyer-Lindquist horizon-avoiding slices, contrasted with the outward-spiraling azimuthal lines for horizon-penetrating slices. In Appendix 11.A.3, we argue that this outward spiral is common to all horizon-penetrating slices.

Based on our comparison of Kerr-Schild and Cook-Scheel slicings (Fig. 11.6), and our analysis of the ubiquity of azimuthal spiraling lines in horizon-penetrating slices (Appendix 11.A.3), we conjecture that horizon-penetrating slicings of any black-hole spacetime will all lead to the same qualitative and semi-quantitative structure for tendex and vortex lines. This conjecture is of key importance for our use of tendex and vortex lines to extract intuition into the dynamical processes observed in numerical-relativity simulations.

More specifically, numerical-relativity spacetimes have dynamically chosen slicings, and the primary commonality from simulation to simulation is that the time slicing must be horizon penetrating, to prevent coordinate singularities from arising on the numerical grid near the horizon. Our conjecture implies that, regardless of the precise slicing used in a simulation, we expect the tendex and vortex lines to faithfully reveal the underlying physical processes. We will build more support for this conjecture in Section 11.8.3, by comparing the final stages of a numerical black-hole merger with a perturbed Kerr black hole, using very different slicing prescriptions.

We conclude this section with a digression from its slicing-dependence focus. When we compare the $a/M = 0.875$ black hole of Fig. 11.6 with the $a/M = 0.95$ hole of Fig. 11.5, the most striking difference is in the tendex lines very near the horizon. The value $a/M = 0.875$ is only slightly above the critical spin $a/M = \sqrt{3}/2 = 0.8660$ at which the horizon's poles acquire negative scalar curvature. Correspondingly, for $a/M = 0.875$, the blue tendex lines that connect the two poles emerge from a smaller region at the poles than for $a/M = 0.95$, and they hug the horizon more tightly as they travel from one pole to the other; and the red, radial tendex lines near the poles suffer much smaller deflections than for $a/M = 0.95$ as they descend into the horizon (see the insets).

11.7 Vortexes of a Perturbed Schwarzschild Black Hole in Regge-Wheeler Gauge

In this section and the next, we explore the tendexes and vortexes of linearized, quadrupolar metric perturbations of black holes. Here, we focus on the simplest example, the vortex lines of a perturbed Schwarzschild black hole in Regge-Wheeler gauge (see, e.g., [9, 46, 47, 48, 49, 50]) in a slice of constant Eddington-Finkelstein time. One can directly see the vortexes of the perturbations in this slicing, because the background frame-drag field vanishes (this will not be the case for the tendexes of a perturbed Schwarzschild black hole, or for both the tendexes and vortexes for Kerr black holes).

Specifically, we will visualize the vortexes of quasinormal-mode oscillations of Schwarzschild black holes. The quasinormal modes of a Schwarzschild black hole are characterized by their complex eigenfrequencies ω_{nlm}, where n is an overtone number, and l and m are the multipolar indices of spherical harmonics (the value of the frequency is independent of m). We will only visualize the least-damped modes $n = 0$ and quadrupolar perturbations (focusing particularly on $m = 2$ and a superposition of $m = \pm 2$ modes). The frequency of this mode, to five digits of accuracy is $M\omega = 0.37367 - i0.08896$, which we obtained through [51] (in connection with the review [52]).

We will relegate the details of our calculations involving Regge-Wheeler gauge to Appendix 11.B, where we also review the Regge-Wheeler formalism. We also discuss more explicit details about how we perform the calculation in Appendix 11.G. We briefly digress to describe the language we use to describe the parity of the perturbations, because there are several different conventions. The Zerilli perturbations transform as $(-1)^l$ under parity, and are often called either electric or even parity; Regge-Wheeler perturbations transform as $(-1)^{l+1}$, and are described as magnetic or odd parity. We will use the electric-magnetic convention for our perturbations here (which also relates nicely to the properties of the corresponding tidal and frame-drag fields), and we will reserve even and odd for quantities that either change sign or not, respectively, under a parity transformation. For example, the vortexes of a magnetic-parity, $l = 2$ perturbations are even under parity, and the tendexes are odd.

We find several important results in this section. First, we show that the horizon vorticity is nonzero for a magnetic-parity perturbation, whereas the perturbative horizon tendicity vanishes. In addition, we see that an $l = 2$, $m = 2$ perturbation has two positive and two negative vortexes in the equatorial plane that collect into spirals that will become the gravitational waves. Finally, we find that a superposition of $l = 2$, $m = \pm 2$ perturbations have two positive and negative vortexes that pass out from the horizon and form oscillating regions further from the black hole.

11.7.1 Horizon Vorticity

We first discuss the horizon vorticity of a perturbed black hole, $\mathcal{B}_{NN} = \mathcal{B}_{\hat{r}\hat{r}}$, at the horizon ($r/M = 2$). Because $\mathcal{B}_{NN}$ is boost invariant, it is also equal to the radial-radial component of $\boldsymbol{\mathcal{B}}$ as seen by Schwarzschild observers who hover immediately above the horizon, $\mathcal{B}_{\tilde{r}\tilde{r}}$, which is even easier to compute than the equivalent quantity in the perturbed EF basis. A straightforward computation in Schwarzschild coordinates yields for the magnetic-parity perturbations,

$$\mathcal{B}_{\tilde{r}\tilde{r}} = \frac{l(l+1)[l(l+1)-2]}{2\omega r^3} iQe^{-i\omega t}Y^{lm} \ , \tag{11.44}$$

where Q is the Regge-Wheeler function (see Eq. (11.71) below), and the functions Y^{lm} are scalar spherical harmonics. Near the horizon, the Regge-Wheeler function Q has the asymptotic behavior

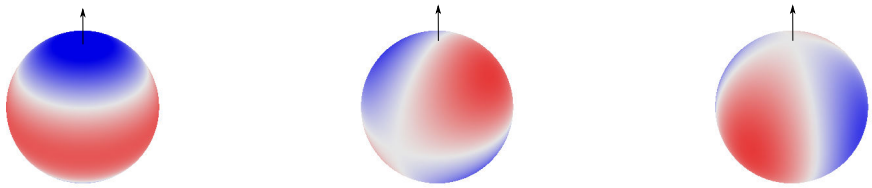

Figure 11.7: The horizon vorticities, $\mathcal{B}_{NN}$, of quadrupolar, $l = 2$, magnetic-parity perturbations for $m = 0$, 1, and 2, on the left, in the middle, and on the right, respectively. In all three figures, blue (darker shading) indicates posivite vorticity, and red (lighter shading) indicates negative vorticity, while white regions have nearly zero vorticity. The arrow points along the polar axis (the axis of rotation symmetry for $m = 0$ modes).

$Q \sim e^{-i\omega r_*}$, which implies that

$$Qe^{-i\omega t} \sim \exp[-i\omega(r_* + t)] \sim \exp[-i\omega(r + \tilde{t})] \tag{11.45}$$

(namely, that the Regge-Wheeler function is finite at the horizon in a slice of constant EF time). Correspondingly, the horizon vorticity is

$$\mathcal{B}_{NN} = \frac{l(l+1)[l(l+1)-2]}{16\omega M^3} ie^{-i\omega(2M+\tilde{t})} Y^{lm}(\theta, \phi) \ . \tag{11.46}$$

(We also note that the electric-parity modes have vanishing horizon vorticity.) At a fixed time, therefore, the horizon vorticity is proportional to the real part of the scalar spherical harmonics Y^{lm}. We plot the horizon vorticity in Fig. 11.7 for quadrupolar perturbations $l = 2$, for $m = 0$, 1, and 2.

As we noted in Section 11.3, the horizon vorticity reflects the normal parts of the vortexes that pass through the horizon. We, therefore, can use it to interpret the behavior of the vortexes near the horizon. For the $m = 0$ quadrupolar perturbation in the left panel of Fig. 11.7, the northern and southern polar regions have positive vorticity and the equatorial region has negative vorticity. Outside the horizon, one would expect that the positive vortexes emerge in a band shape from the equator, and the negative vortexes head out from the poles. The perturbation would also oscillate sinusoidally in time with a frequency given by the real part of ω, the vortexes would change signs after each half period, and the perturbation's amplitude will also decay at a rate proportional to ω's imaginary part.

For the $m = 1$ perturbations, there are two vortexes in the northern hemisphere, one positive and one negative, and similarly two in the southern hemisphere. These vortexes rotate around the polar axis with a frequency, $\Re[\omega]$, as they decay in time. For equal superpositions of $m = 1$ and $m = -1$ modes, the vortexes oscillate like the $m = 0$ mode does. Finally, for the $m = 2$ perturbations,

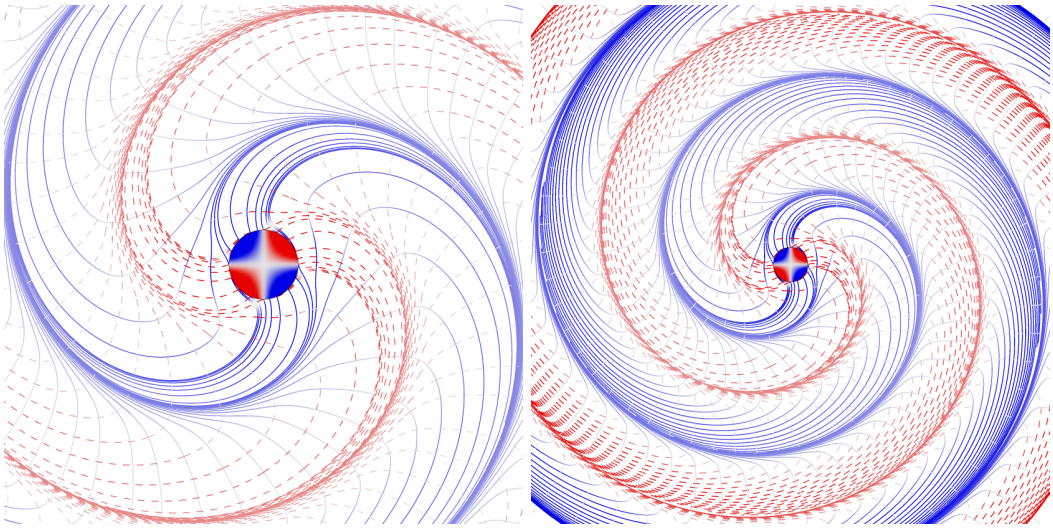

Figure 11.8: Positive and negative vortex lines, colored by their vorticities, in the equatorial plane, for the fundamental $l = 2$, $m = 2$ mode. The blue, solid lines are the positive-vorticity vortex lines, and the red, dashed lines are the negative-vorticity vortex lines. The strength of the lines' vorticities are indicated by shading intensity; lighter lines have smaller vorticity in magnitude. The panel on the left is a zoom-in of the panel on the right.

there are four vortexes of alternating sign, but they are centered around the equator. They will also rotate, but with an angular velocity of $\Re[\omega/2]$. Again, an equal superposition of $m = 2$ and $m = -2$ modes oscillates and decays in time.

11.7.2 Magnetic-Parity Equatorial Vortex Lines

We discuss the computation of the frame-drag field in Appendix 11.B, and we give an analytic expression there in terms of the Regge-Wheeler function Q. Here, we focus on the vortexes in the plane of reflection symmetry of a fundamental quadrupolar mode with $l = 2$ and $m = 2$ and the superposition of two modes, $l = 2$, $m = \pm 2$. Two of the vortex lines for these perturbations lie exactly in the plane of reflection symmetry, and the third line is everywhere orthogonal to this plane.

11.7.2.1 Magnetic-Parity $l = 2$, $m = 2$ Mode: Rotating Vortexes

In Fig. 11.8 we show the positive (clockwise) and negative (counterclockwise) vortex lines in the equatorial plane (the plane of reflection symmetry). We color the lines by their vorticity (blue, solid lines for positive vorticity, red, dashed lines for negative vorticity), and we shade the lines by the magnitude of their vorticity, where darker shading on the lines indicates a larger magnitude of vorticity, and lighter shading indicates smaller magnitude. Note that the negative vortex lines form the same pattern as the positive, after a rotation of $\pi/2$ radians about the origin.

The positive vortex lines emerge from the blue, clockwise horizon vortexes and spiral outward; the negative vortex lines similarly extend from the regions of negative horizon vorticity. The lines

collect into four spirals that extend outward to become part of the gravitational waves. In doing so, they must also acquire accompanying perturbative tendex lines, analogously to how a rotating current-quadrupolar source in linearized gravity generated gravitational waves (see Paper I, Section VI D, Fig. 9).

We estimate that the near zone begins transitioning into the wave zone very close to the horizon, at $r/M \simeq 1/\Re[M\omega] \simeq 2.7$. The size of the transition zone is also small (we estimate its range to be $r/M \simeq \pi/\Re[M\omega] \simeq 8$, extending to near the outer edge of Fig. 11.8, which is at $r/M \simeq 15$ for the left panel). At around this radius, the wave zone begins. Here, as for the rotating current-quadrupolar source in linearized theory, we interpret the near-zone vortexes, attached to the horizon, as generating the gravitational waves through their rotation.

11.7.2.2 Superposed Magnetic-Parity $l = 2$, $m = \pm 2$ Modes: Ejected Vortex Tubes

Next, we illustrate the vortex lines for a superposition of two quadrupolar modes ($l = 2$ and $m = \pm 2$), in Fig. 11.9. Unlike the $m = 2$ perturbation, both sets of vortex lines can have both negative and positive signs of vorticity, although one set is predominantly positive, and the other is mostly negative (as usual, red is negative and blue is positive in the figure). The lines with mostly positive vorticities are drawn with solid lines, while mostly-negative-vorticity lines are dashed. The lines are shaded to show the strength of the vorticity in the same way: darker lines indicate a larger magnitude of vorticity, and lighter is a smaller magnitude. The two families of lines are identical, after rotating one by 90° about the polar axis and reversing the sign.

The dynamics of the black hole's vortexes are closer to those of the oscillating current-quadrupole in linearized gravity (Paper I, Section VI E, Fig. 15): each time the horizon vorticity $\mathcal{B}_{NN}$ vanishes, the black hole ejects two bundles of vortex lines, which propagate outward, acquiring an accompanying bundle of tendex lines as they become the gravitational waves. The horizon vorticity reflects the vortexes near the horizon; hence, it is only when the horizon vorticity vanishes that the near-zone vortexes are mostly transverse around the horizon. When the vorticity is large, there are radial portions of the vortexes pushing these transverse vortexes to larger radii, to become the outgoing gravitational radiation.

11.8 Tendexes and Vortexes of Perturbed Schwarzschild and Kerr Black Holes in an Ingoing-Radiation Gauge

Unlike the Regge-Wheeler [9] or Zerilli [48] formalism for Schwarzschild black holes, there is no procedure for computing separable metric perturbations of Kerr black holes. Nevertheless, there is a way to use Teukolsky's separable wave equation for perturbations of the Weyl scalars Ψ_0 and Ψ_4 [53] to compute the perturbed metric of a Kerr black hole. The procedure arose from work by Chrzanowski [11], Kegeles and Cohen [12], Stewart [13], and Wald [14]. Collectively, they showed

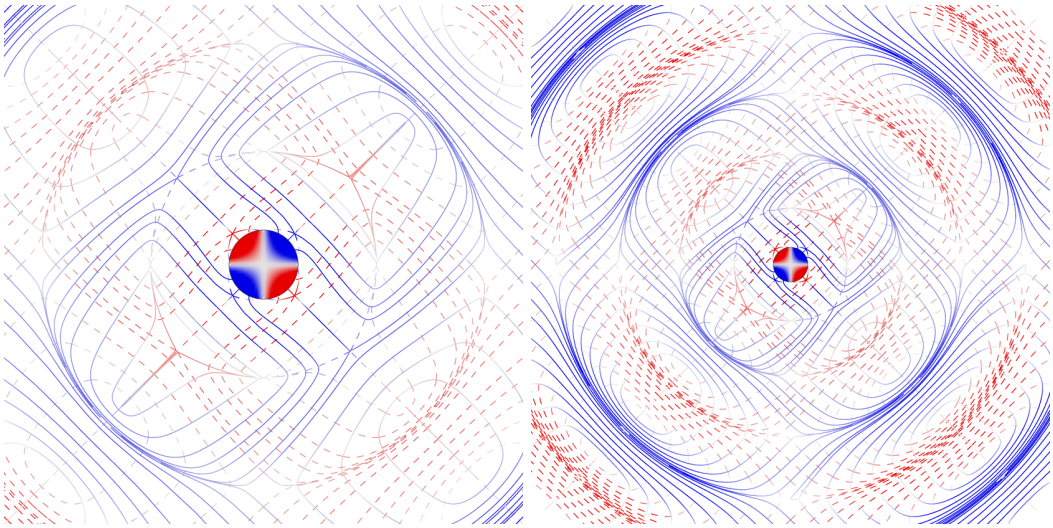

Figure 11.9: The two sets of vortex lines in the equatorial plane, shaded by their vorticities, for a superposition of the fundamental $l = 2$, $m = \pm 2$ modes. The vortex lines are colored and shaded in the same way as in Fig. 11.8. Both sets of vortex lines have lines with positive and negative vorticity; the solid lines correspond to the set that has predominantly positive vorticity, while the dashed lines have predominantly negative vorticity. The left panel is a zoom-in of the right panel.

that one can use a mathematical construction known as a Hertz potential, which is related to perturbations of the Weyl scalars, to construct the metric perturbations of algebraically special spacetimes. When specialized to Schwarzschild and Kerr black holes, the procedure allows one to compute metric perturbations in two gauges, known as ingoing- and outgoing-radiation gauges (IRG and ORG, respectively).

The IRG metric perturbation is regular on the future horizon of a perturbed Schwarzschild or Kerr black hole; consequently, we will perform all our calculations in this gauge. As in previous sections, we will also choose our time slicing to be regular on the horizon. For perturbations of Schwarzschild black holes, we will use values of constant Eddington-Finkelstein time, and for Kerr black holes, we choose constant values of Kerr-Schild time.

We relegate the details describing how to compute the metric perturbations, the tidal and frame-drag fields, and the tendexes and vortexes to several appendices. Because the procedure relies upon the formalism of curvature perturbations, we review this topic in Appendix 11.C. In Appendix 11.D, we describe the formalism for computing the metric perturbation of Chrzanowski, Cohen, and Kegeles (often called the CCK procedure). Immediately following, in Appendix 11.E, we specialize the CCK procedure to the Schwarzschild spacetime and confirm analytical results for the metric originally found by Chrzanowski [11]. We then present analytical expressions for the tidal and frame-drag fields corresponding to this metric perturbation. In Appendix 11.F, we show that the frame-drag field in the ingoing-radiation gauge is the same as that in Regge-Wheeler gauge (but the tidal fields differ). Finally, in Appendix 11.G, we explain in detail our numerical procedure for

computing the tendex and vortex quantities of this section.

In the two parts of this section, we visualize how the vortexes and tendexes qualitatively generate gravitational waves for $l = 2$, $m = 2$ quasinormal-mode perturbations of Schwarzschild and Kerr black holes of electric (even) parity, respectively. Because a Schwarzschild black hole has a non-perturbative tidal field, and a Kerr black hole has both non-perturbative tidal and frame-drag fields, the quasinormal-mode perturbations, which carry the gravitational waves, are largely hidden by the background fields.[1] As a result, in this section, we will focus only on how the perturbative tendexes and vortexes in the near zone extend away from the horizon and become gravitational waves, as we describe below.

The tendexes of an electric-parity perturbation in the near zone are tied to regions of large horizon tendicity, which is predominantly centered around the plane of reflection symmetry. The vortexes, in the near zone, reside close to the equatorial plane, but they are not tied to the horizon; rather they are induced by the motion of the near-zone tendexes. Both the tendexes and vortexes move out of the equatorial plane at larger radii, and at even larger distances from the horizon, they collect into two identical conical regions as they become gravitational waves.

Finally, we recall that in Paper I, there was a duality in linearized gravity about flat space between the tidal field of a mass-multipolar perturbation and the frame-drag field of a current-multipolar perturbation (and similarly between the frame-drag field and tidal field of the respective perturbations). Naturally, one might wonder if there is a similar duality between electric- and magnetic-parity perturbations of Schwarzschild or Kerr black holes (of the same multipolar indices l and m). We show explicit analytical expressions for Schwarzschild black holes, and we find that there is a near duality (see Appendix 11.E). We do not present any analytical results for Kerr black holes, but we show the magnetic-parity tendexes and vortexes of both Schwarzschild and Kerr black holes in Appendix 11.H. By comparing the figures there with those in this section, one can see that there is a near duality for the perturbative fields of Schwarzschild black holes, which becomes less strong for Kerr holes with large spin parameters.

11.8.1 Tendexes and Vortexes of Perturbations to a Schwarzschild Black Hole

We begin this section by plotting the horizon tendicity and vorticity in Fig. 11.10. The perturbative tendicity, at a fixed moment in time, is proportional to the scalar spherical harmonic $Y_{2,2}(\theta, \phi)$, whereas the horizon vorticity vanishes exactly. This is a first indication that the tendexes will play the dominant role in generating gravitational waves for an electric-parity perturbation.

Next, we show the perturbative tendicity and tendex lines in the plane of reflection symmetry ($\theta = \pi/2$) in Fig. 11.11. The plane is colored by the tendicity, and to remove the radial fall-off in the

[1] See Appendix 11.I for examples of tendex and vortex lines with the background fields included.

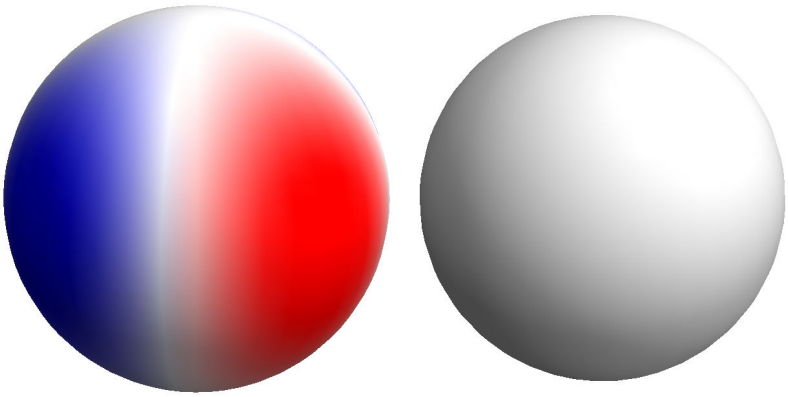

Figure 11.10: Perturbative horizon tendicity (left) and vorticity (right) of an electric-parity $l = 2$, $m = 2$ quasinormal-mode perturbation of a Schwarzschild black hole. The tendicity is proportional to a scalar spherical harmonic, $Y_{2,2}(\theta, \phi)$, and the vorticity vanishes.

tendicity (to better highlight the angular dependence of the tendicity), we compute the maximum tendicity at each radius, and we normalize the tendicity at each radius by this maximum. The solid, black lines are the tendex lines in the plane of reflection symmetry corresponding to the tendicity shown, and the dashed, black lines are the orthogonal set of tendex lines from the other tendicity not shown (but that is identical to that shown, when one rotates it by 90° and changes its sign). The region in the center of the figure encircled by a white line is the event horizon colored by the horizon tendicity.

The figure clearly shows there are two tendexes that emerge from the horizon tendexes and spiral out from the horizons. A concentration of tendex lines emerges from these tendexes, but they ultimately collect on the outer edge of the tendexes as they wind out. Why they do this becomes more clear from the tendexes outside of the plane of reflection symmetry, in the left-panel of Fig. 11.12. The inner sphere in the left panel is the horizon colored by its tendicity. The large shaded volumes represent the regions of large and small tendicity in the spacetime. Specifically, the blue region shows where the tendicity is at least 85% of the maximum value at that radius, and the off-white regions show where it is at most 35% of the maximum value at that radius. The black lines are tendex lines corresponding to the tendicity shown. The right panel shows the vortexes and vortex lines, which are drawn in the same way as the left panel, except the blue (dark) region indicates where the vorticity is 90% of the radial maximum.

The tendexes and vortexes of Fig. 11.12 illustrate how gravitational waves are generated around a Schwarzschild black hole. The tendicity and vorticity at large radii correspond to those of the positive eigenvalues of a gravitational wave, which have the largest value at the poles and four zeros on the equator (see, e.g., [8]). The other tendicities and vorticities not shown are those that asymptotically become radial and have vanishing strength, and those that correspond to the negative eigenvalue of the gravitational waves at large radii, which are identical to those shown, but are rotated by 90°. At

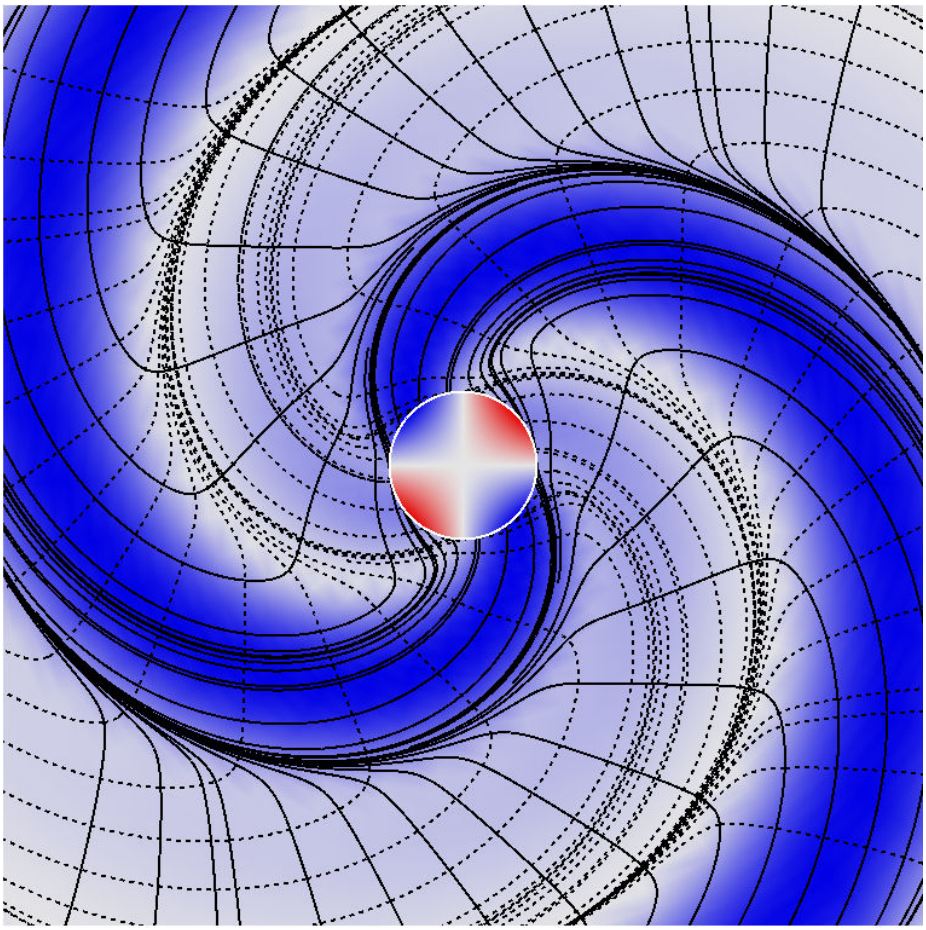

Figure 11.11: Tendex lines and tendicity in the plane of reflection symmetry for an electric-parity, $l = 2$, $m = 2$ quasinormal-mode perturbation of a Schwarzschild black hole. The tendicity is normalized by the maximum value at a given radius to remove the radial fall off. The solid, black lines are the tendex lines corresponding the tendicity shown and the dashed, black lines are the orthogonal set. The horizon, enclosed by a white circle, is colored by the horizon tendicity as in previous figures.

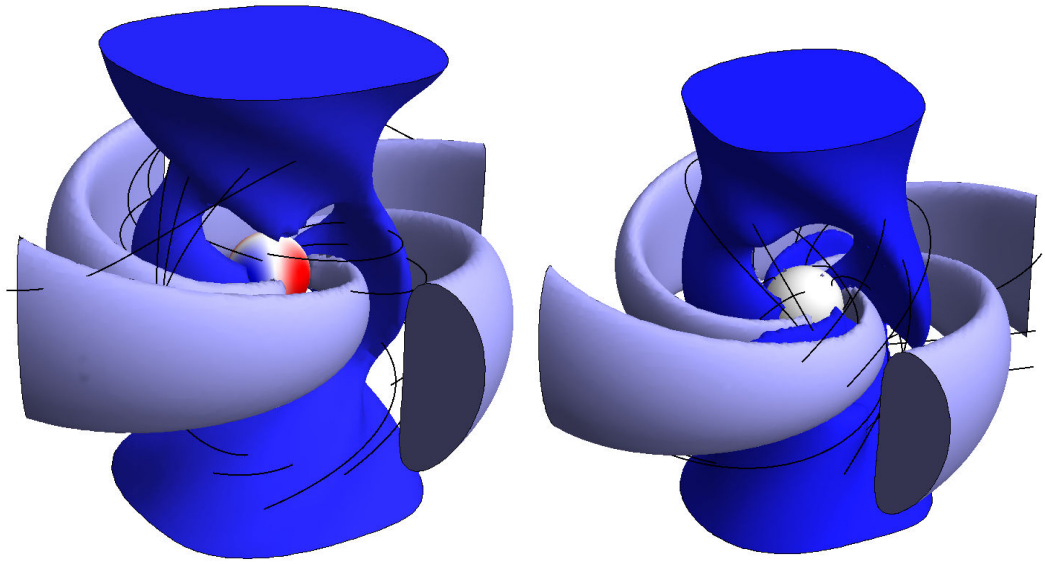

Figure 11.12: *Left*: Three-dimensional tendex lines and tendexes of the same perturbation as that shown in Fig. 11.11. The black solid lines are the tendex lines, and the inner sphere is the horizon, colored by its tendicity. The blue region represents where the tendicity is at least 85% of the maximum value at that radius; the four nearly white regions show where the tendicity is at most 35% of the maximum value at that radius. *Right*: Three-dimensional vortex lines and vortexes. The horizon is left uncolored, because the horizon vorticity vanishes for this perturbation. The regions are similar to the tendexes, but the blue (dark) region indicates where the vorticity is 90% of the maximum value at that radius.

the largest radii in Fig. 11.12, the tendexes and vortexes are not significantly different from those of gravitational waves; they are largest near the poles, and the zeros are concentrated near the equator. Closer to the event horizon, however, the vortexes and tendexes transition toward the equatorial plane as well, and the tendexes and vortexes now begin to differ qualitatively. This transition occurs at radii close to where the tendex lines in the plane of reflection symmetry move out of the tendexes. The three-dimensional tendexes then form two symmetric tubes about the equatorial plane that connect with the horizon tendexes, whereas the vortexes are two wedges above the equatorial plane and two below the equatorial plane (this is required by the parity of the metric perturbation).

Unlike at large radii, there is not as simple a physical interpretation of the near-zone tendexes and vortexes. Close to the horizon, the tidal and frame-drag fields contain radial, longitudinal, and transverse pieces that become mixed together when one finds the tendexes and vortexes from these fields. Nevertheless, very close to the horizon, the tendexes appear to be predominantly radial, and the vortexes are more transverse (this is closely connected to the fact that the horizon tendicity is non-zero, but the horizon vorticity vanishes exactly). We, therefore, describe the tendexes that stick radially out from the horizon as generating the gravitational waves as they rotate by inducing near-zone vortexes. Then, these near-zone structures around the equatorial plane extend to the poles and become the outgoing gravitational waves.

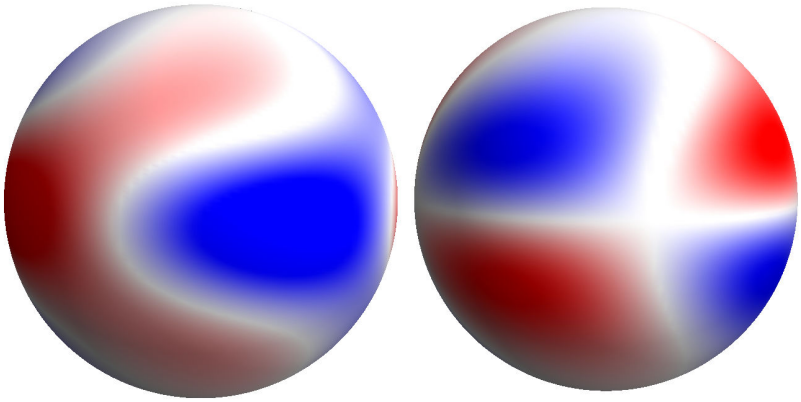

Figure 11.13: Perturbative horizon tendicity (left) and vorticity (right) of an electric-parity $l = 2$, $m = 2$ perturbation of a Kerr black hole of spin $a/M = 0.945$. The perturbative tendicity is concentrated more closely around the plane of reflection symmetry and varies with polar angle θ; the perturbative vorticity is dominated by an $l = 3$, $m = 2$ spherical harmonic, and it also shows similar variation with the polar angle θ.

11.8.2 Tendexes and Vortexes of Perturbations to a Kerr Black Hole

To visualize the influence of the black-hole's spin on the perturbative tendexes and vortexes, we will show results for an electric-parity $l = 2$, $m = 2$ quasinormal-mode perturbation of a Kerr black hole with spin $a/M = 0.945$, computed in an ingoing-radiation gauge. All the figures produced in this section are chosen assuming a foliation of spacetime into slices of constant Kerr-Schild time, and they are plotted in ingoing-Kerr coordinates.

We begin again by showing the perturbative horizon tendicity (left) and vorticity (right) in Fig. 11.13. Comparing with Fig. 11.10 of the horizon quantities for a similar perturbation of a Schwarzschild black hole, two large differences stand out. The tendicity of the Kerr horizon is concentrated closer to the plane of reflection symmetry, and it is dragged more strongly at the equator than at the poles, which gives it the appearance of being twisted. The difference between the perturbative vorticity of a Schwarzschild and a Kerr black hole is even more pronounced, because the Kerr black hole's vorticity no longer vanishes. If one were to decompose the horizon vorticity into spherical harmonics, the perturbative vorticity is predominantly an $l = 3$, $m = 2$ scalar spherical harmonic; like the horizon tendicity, the vorticity also is differentially dragged at different polar angles, θ. Because the vorticity has a higher l than the tendicity, it will again be the tendexes that play the primary role in the generation of gravitational waves.

We next show the tendexes and tendex lines in the plane of reflection symmetry, in Fig. 11.14. The figure is the analogous figure to Fig. 11.11 for a Schwarzschild black hole, and comparing the two will allow one to develop intuition about the effects of the background black hole's spin on the dynamics of the perturbative tendexes. For this reason, we color the horizon tendicity and the spacetime vorticity in the same way as in Fig. 11.11, and we plot tendex lines similarly.

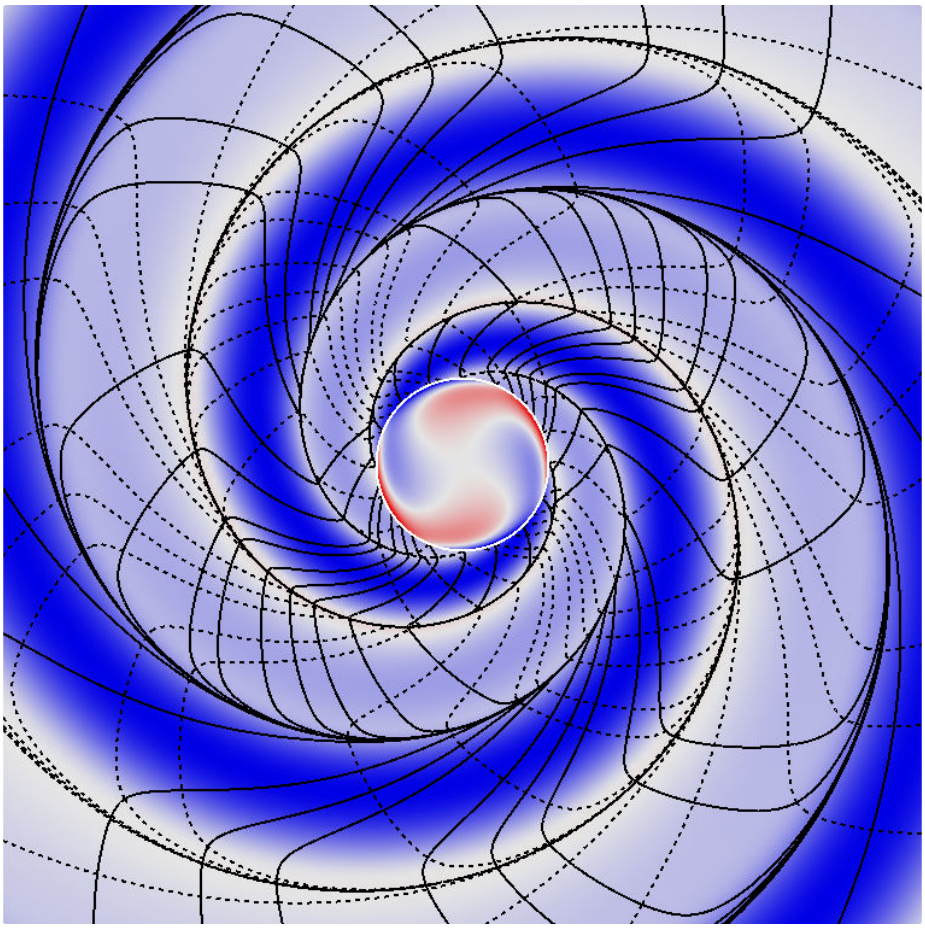

Figure 11.14: Perturbative tendex lines and tendicity in the plane of reflection symmetry for the same perturbation as in Fig. 11.13. The horizon tendicity is shown in the center of the diagram, surrounded by a white circle. The coloring of the perturbative tendicity and the plotting of the lines is the same as that in Fig. 11.11.

There are several interesting similarities and differences between Figs. 11.11 and 11.14, that can be attributed, in part, to the spin of the background black hole. The two tendexes both emerge from regions of large horizon tendicity and they spiral out; the tendexes of the perturbed Kerr black hole look as if they are dragged by the spin of the black hole, which make them appear narrower and more twisted. The distance between successive spirals is a shorter coordinate length, because the Kerr black hole has a higher frequency of oscillation. The solid tendex lines (corresponding to the tendicity shown) also emerge from regions of large horizon tendicity, but unlike the perturbation of the Schwarzschild black hole, the lines loop back and connect to the horizon. This leads us to suspect that the tendexes, rather than the tendex lines, will be the more invariant markers of the structures that generate gravitational waves.

In Fig. 11.15, we show the tendexes (left) and vortexes (right) outside of the plane of reflection symmetry. We color the horizon in the same way and the regions of large tendicity and vorticity in the same way as in Fig. 11.12, and we show a few similar vortex lines. The regions of small vorticity have different values (at most 17.5% of the radial maximum for the tendicity and 20% for the vorticity), so that they hide less of the horizon. We again show the quantities associated with the tendicity and vorticity that correspond to the positive tendicity and vorticity of a gravitational wave, asymptotically; we do not show the negative tendicity or vorticity quantities that are rotated by 90° with respect to the positive one, or the final set which is asymptotically radial and has vanishing tendicity or vorticity.

Comparing Fig. 11.15 with the equivalent figure for a non-rotating black hole (Fig. 11.12), one can again notice several similarities and differences between perturbations of rotating and non-rotating black holes. All the qualitative features of the tendexes and vortexes are the same: both have four regions of small tendicity or vorticity that extend out from the horizon around the equatorial plane; two tendexes extend out from regions of large horizon tendicity and extend symmetrically into the volumes around the poles, where, asymptotically, the gravitational waves are strongest; and there are four wedge-shaped vortexes near the horizon that also extend toward the poles and that will eventually become the vortexes of gravitational waves. The detailed differences are similar to those mentioned in the discussion surrounding Fig. 11.14. The tendexes and vortexes are significantly narrower and they appear to be dragged by the spin of the black hole. In addition, the individual tendex and vortex lines of Fig. 11.15 are qualitatively different from those of Fig. 11.12. The tendex lines for the perturbation of a rotating hole again loop around and connect back to the horizon; the vortex lines no longer cross the equatorial plane, but they stay either above or below it, close to the black hole.

For the Schwarzschild-black-hole perturbation, we interpreted the generation of gravitational waves as near-zone tendexes as inducing near-zone vortexes that propagate out and become the gravitational waves. We reached this conclusion because the horizon tendicity is non-vanishing,

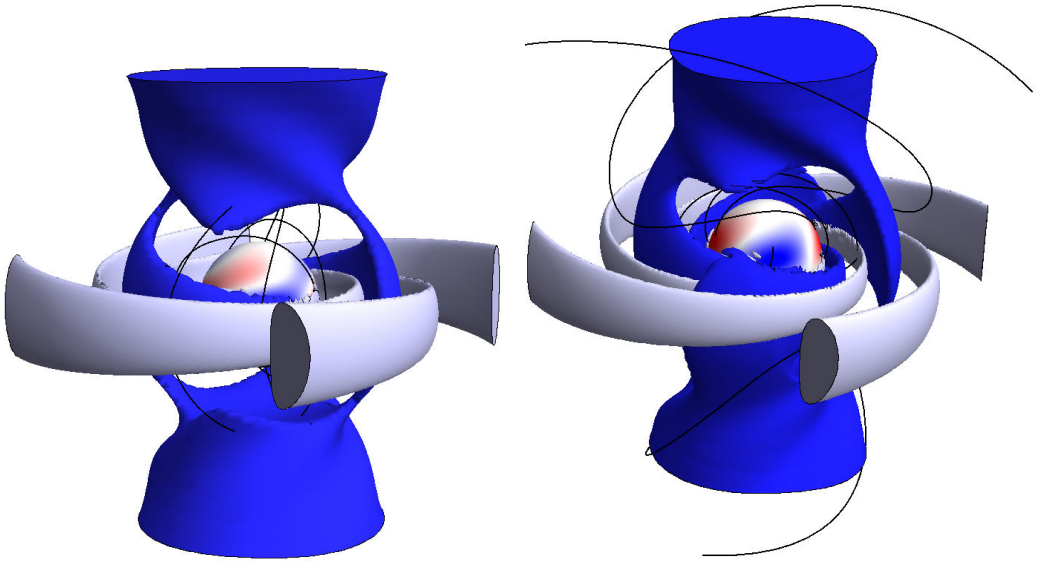

Figure 11.15: *Left*: Three-dimensional perturbative tendexes and tendex lines of the same perturbation as in Fig. 11.14. The horizon, the colored volumes, and the lines are drawn in the same way as in the left panel of Fig. 11.12, but the off-white regions show where the tendicity is at most 17.5% of the maximum value at that radius. *Right*: Three-dimensional perturbative vortexes and vortex lines of this perturbation. The quantities shown are depicted in the same way as those in the right panel of Fig. 11.12, but the off-white regions again correspond to at most a smaller fraction (20%) of the radial maximum.

while the horizon vorticity is zero, and, this made the tendexes more radial whereas the vortexes were more transverse. For the Kerr-black-hole perturbation, however, the spin of the black hole drags both the tendexes and vortexes (making them appear more transverse) and the horizon vorticity is no longer vanishes, but its pattern is dominated by a higher multipole index l. Thus, for Kerr black holes, we can say that it is primarily the near-zone tendexes that induce near-zone vortexes, which become gravitational waves, but there are also small corrections to this picture from higher-order near-zone vortexes inducing tendexes, which make small contributions to the gravitational waves. Roughly speaking, though, the picture that near-zone tendexes induce near-zone vortexes that become gravitational waves holds empirically.

11.8.3 Comparing Vortex Lines of a Perturbed-Kerr Black Hole and a Binary-Black-Hole-Merger Remnant

As a conclusion to this section and a prelude to future work, in Fig. 11.16 we compare the vortex lines found using our analytic methods to those found in a numerical ringdown of a fast-spinning Kerr black hole. Here we compare an electric-parity, $l = 2$, $m = 2$ quasinormal-mode perturbation of a Kerr black hole with dimensionless spin, $a/M = 0.945$, that was computed using the CCK procedure to a perturbed black hole of the same spin formed in a numerical simulation of the merger of two black holes with spins of magnitude $a/M = 0.97$ [21]. For the analytical calculation, we

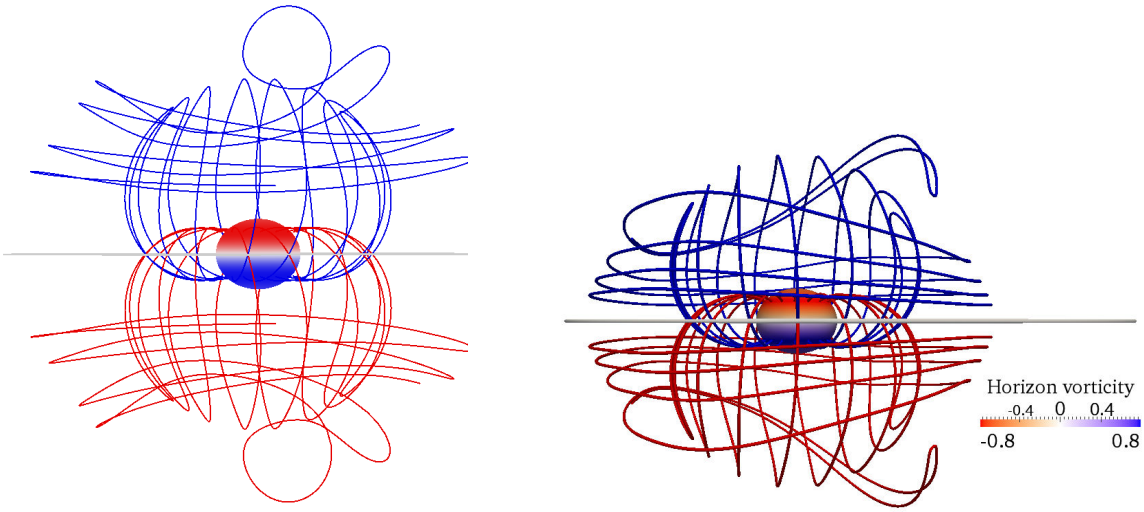

Figure 11.16: *Left:* Vortex lines of a Kerr black hole perturbed by an electric-parity $l = 2$, $m = 2$ quasinormal-mode, computed in an ingoing-radiation gauge. The dimensionless spin magnitude is $a/M = 0.945$, as in previous figures. *Right:* Vortex lines from a perturbed black hole with spin magnitude $a/M = 0.945$ obtained from a numerical simulation of two merging black holes with equal masses and equal, aligned spins of magnitude 0.97 [21].

continue to use Kerr-Schild slicing, but we now use Kerr-Schild spatial coordinates as well, which make the horizon and the lines appear oblately deformed. The vortex lines and horizon vorticity in the numerical simulation were computed at a suitably late time (so that the common horizon is essentially a single, perturbed black hole) using the methods summarized in [6]. Although the vortex lines from these similar physical situations were computed using very different methods and gauge conditions, the results are remarkably similar (see Fig. 11.16).

11.9 Conclusion

This paper took an important first step toward visualizing and understanding the nonlinear dynamics of curved spacetime. Specifically, we used vortex and tendex lines to show the statics and dynamics of the curvature of stationary and linearly perturbed rotating and nonrotating black holes. We aim to build from the results described above to understand the spacetime curvature around numerical-relativity simulations of black-hole binaries.

An important indicator of the spacetime dynamics is the horizon vorticity and tendicity. They are related to the complex scalar curvature of the horizon, and they are connected to several other well-studied quantities used in analytical and numerical relativity. Because they are quantities on the horizon (a surface detached from the spacetime outside), the horizon vorticity and tendicity serve as indicators of the nearby spacetime curvature, rather than a source of dynamics. One can use them, however, to understand the behavior of the vortexes and tendexes that stick out away from the horizon.

For stationary black holes, we found that the tendexes and vortexes of a Schwarzschild black hole are quite simple: the vortexes vanish, and the tendexes are spherically symmetric. A stationary Kerr black hole, however, has more interesting vortexes and tendexes. There are two vortexes around the poles that stick out from regions of large horizon vorticity; two positive tendexes emerge from the poles, and one large axisymmetric tendex near the equator. We studied these quantities and the tendex and vortex lines in several time slicings and in several spatial coordinates. As long as we used a time coordinate that passed smoothly through the horizon (the type of time coordinate used by numerical-relativity simulations) the tendex and vortex lines (and their tendicities and vorticities) were qualitatively the same, throughout the entire spatial region.

Turning to perturbations of black holes, we found interesting similarities between quadrupolar magnetic-parity perturbations of Schwarzschild black holes and perturbations sourced by current quadrupoles in linearized gravity (about flat space from Paper I). Rotating quadrupoles and $l = 2$, $m = 2$ perturbations of the Schwarzschild spacetime both had two pairs of positive and negative equatorial vortexes that spiraled away from the near zone and became gravitational waves. For the black hole, the horizon vorticity reflected the near zone structures that generate the waves, as opposed to the current-quadrupole moment in linearized theory, whose dynamics directly source gravitational waves. (There was a similar parallel between an oscillating current quadrupole, and a superposition of $l = 2$, $m = \pm 2$ quasinormal-mode perturbations of a Schwarzschild black hole.) We performed the calculation of the $l = 2$, $m = 2$ perturbation in both Regge-Wheeler and ingoing-radiation gauges, and we found the results were remarkably similar between the two, because the frame-drag fields are equal in the two gauges (see Appendix 11.F). This was yet another indication that vortexes and tendexes can be robust across different gauges and slicings.

We also studied electric-parity perturbations of Schwarzschild and Kerr black holes to understand how the perturbations varied with spins. We found that the qualitative features of the generation of gravitational waves did not depend strongly on the spin of the black hole, although there were some indications that the perturbation was being dragged for rapidly rotating Kerr black holes. The dynamics of the wave generation was remarkably similar to the dual description of a rotating current quadrupole in linearized theory, a rotating mass-quadrupole moment. When we visualized $l = 2$, $m = 2$, perturbations of Schwarzschild and Kerr black holes, we saw that equatorial tendexes that connect to the horizon tendexes quickly transition into the polar tendexes of gravitational waves in roughly one reduced wavelength of the gravitational waves. In addition, the tendexes induced vortexes in the process of becoming the outgoing radiation.

From the $l = 2$, $m = 2$, electric-parity perturbation of the Kerr spacetime, we were able to compute its vortex lines and compare it to those from the end stages of a black-hole-binary merger, when the black hole has nearly reached its stationary state. The comparison between the two was remarkably strong. Because the coordinates of the numerical-relativity simulation of the merger

could, in principal, be quite different from those of the perturbation-theory calculation, this was yet another indication for the robustness of tendexes and vortexes, under changes of coordinates that ensure the time coordinate smoothly passes through the horizon. With these initial positive results, we are optimistic about the prospects of using these tools to understand the nonlinear and dynamical spacetime curvature around the time of merger in a black-hole binary.

11.A Appendix: Analytical Expressions for the Vortex and Tendex Quantities of Kerr Black Holes

This appendix presents results for the eigenvectors and eigenvalues of the frame-drag and tidal fields in Boyer-Lindquist slicing and coordinates, and in ingoing Kerr coordinates (with Kerr-Schild slicing).

11.A.1 Kerr Black Hole in Boyer-Lindquist Slicing and Coordinates

For a rapidly rotating Kerr black hole in Boyer-Lindquist (BL) coordinates, $\{t, r, \theta, \phi\}$, the metric is given by Eq. (11.31) above. An observer, who moves orthogonally to the slices of constant BL time t, has a 4-velocity $\vec{u}$ and orthonormal tetrad given by

$$\vec{u} = \sqrt{\frac{A}{\Sigma\Delta}}\left(\partial_t - \frac{2Mar}{A}\partial_\phi\right), \quad \vec{e}_{\hat{r}} = \sqrt{\frac{\Delta}{\Sigma}}\partial_r, \quad \vec{e}_{\hat{\theta}} = \frac{1}{\sqrt{\Sigma}}\partial_\theta, \quad \vec{e}_{\hat{\phi}} = \sqrt{\frac{\Sigma}{A}}\frac{1}{\sin\theta}\partial_\phi. \tag{11.47}$$

In this orthonormal basis, the tidal and frame-drag fields are given by

$$\mathcal{E}_{\hat{a}\hat{b}} = \begin{pmatrix} -Q_e\frac{2+\xi}{1-\xi} & \mu Q_m & 0 \\ * & Q_e\frac{1+2\xi}{1-\xi} & 0 \\ * & * & Q_e \end{pmatrix}, \tag{11.48}$$

$$\mathcal{B}_{\hat{a}\hat{b}} = \begin{pmatrix} -Q_m\frac{2+\xi}{1-\xi} & -\mu Q_e & 0 \\ * & Q_m\frac{1+2\xi}{1-\xi} & 0 \\ * & * & Q_m \end{pmatrix}, \tag{11.49}$$

with entries denoted by $*$ fixed by the symmetry of the tensors, and where

$$Q_e = \frac{Mr(r^2 - 3a^2\cos^2\theta)}{\Sigma^3}, \tag{11.50}$$

$$Q_m = \frac{Ma\cos\theta(3r^2 - a^2\cos^2\theta)}{\Sigma^3}, \tag{11.51}$$

and

$$\xi = \frac{\Delta a^2\sin^2\theta}{(r^2+a^2)^2}, \quad \mu = \frac{3a\sqrt{\Delta}(r^2+a^2)\sin\theta}{A}. \tag{11.52}$$

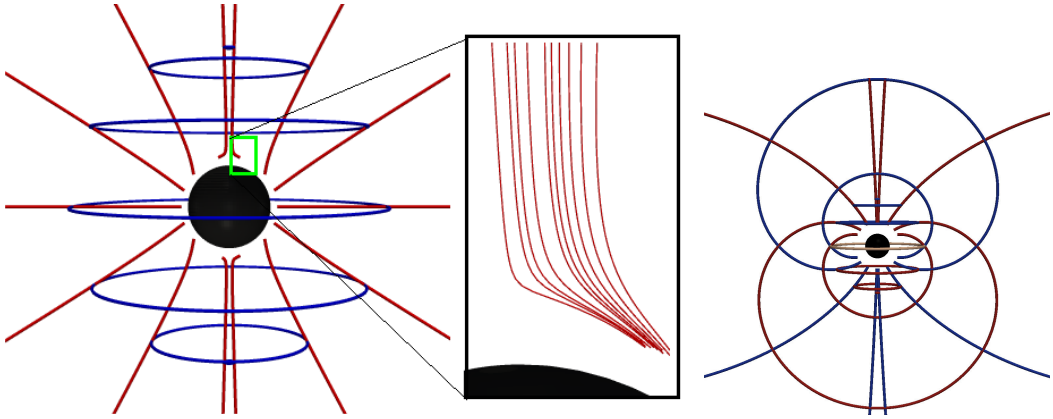

Figure 11.17: *Left*: Tendex lines for a Kerr black hole with $a/M = 0.95$ on a slice of constant Boyer-Lindquist time t, plotted in spatial Boyer-Lindquist coordinates. The lines with positive tendicity are colored blue and negative tendicity are colored red. The inset in the middle shows the lines near the horizon. *Right*: Vortex lines for this same black hole, slicing, and coordinates, with lines of positive vorticity colored blue and negative vorticity colored red. The vortex lines are remarkably similar to those of a spinning point particle in linearized theory.

The functions Q_e and Q_m are related to the real and imaginary parts of the complex Weyl scalar Ψ_2 calculated using the Kinnersley null tetrad (see Eq. (11.64) in Appendix 11.A.3), by $\Psi_2 = -Q_e + iQ_m$. Note that there is a duality between the electric and magnetic curvature tensors: namely letting $Q_e \to Q_m$ and $Q_m \to -Q_e$, turns the tidal field become the frame-drag field, $\mathcal{E}_{\hat{a}\hat{b}} \to \mathcal{B}_{\hat{a}\hat{b}}$.

Because $\mathcal{E}_{\hat{a}\hat{b}}$ and $\mathcal{B}_{\hat{a}\hat{b}}$ are block diagonal, one can immediately see that one of the eigenvectors for both tensors will be $\vec{e}_\phi$; therefore, the corresponding tendex and vortex lines are azimuthal closed circles. The other two sets of lines for each tensor are poloidal; i.e., they lie in slices of constant ϕ. Because they are two-dimensional, they can be computed analytically, but their explicit expressions do not give great insight, and we do not show them here.

The tendex and vortex lines in Fig. 11.17 are those of a Kerr black hole with spin $a/M = 0.95$. The lines with positive eigenvalues (tendicity or vorticity) are colored blue, and those with negative eigenvalues are colored red. Far from the black hole, the tendex lines resemble those of a Schwarzschild black hole, and the vortex lines resemble those of a slowly spinning Kerr black hole (the same as those of spinning point particle in linearized gravity about flat space). Near the horizon, however, the behavior is quite different: the nearly radial tendex lines in the inset of Fig. 11.17 bend sharply as they near the horizon, eventually becoming tangential to the horizon and piling up there. This must happen, because the observers associated with BL coordinates do not pass through the horizon. In a time coordinate that smoothly passes through the horizon, such as Kerr-Schild time, the tendex and vortex lines thread through the horizon.

11.A.2 Kerr Black Hole in Kerr-Schild Slicing and Ingoing-Kerr Coordinates

In ingoing-Kerr coordinates $\{\tilde{t}, r, \theta, \tilde{\phi}\}$ (see Eqs. (11.33) and (11.36) above), the Kerr metric takes the form (see, e.g., [44])

$$\begin{aligned} ds^2 &= -\left(1-\frac{2Mr}{\Sigma}\right)d\tilde{t}^2 + \frac{4Mr}{\Sigma}dr d\tilde{t} - \frac{4Mar\sin^2\theta}{\Sigma}d\tilde{t}d\tilde{\phi} + H^2 dr^2 + \Sigma d\theta^2 \\ &\quad -2aH\sin^2\theta dr d\tilde{\phi} + \frac{A\sin^2\theta}{\Sigma}d\tilde{\phi}^2\,, \end{aligned} \tag{11.53}$$

where $H^2 = 1+\frac{2Mr}{\Sigma}$, and where Σ and A are defined in Eq. (11.31). The 4-velocities of ingoing-Kerr observers, who move orthogonally to slices of constant $\tilde{t}$, and the orthonormal tetrads they carry, are given by

$$\vec{u} = H\partial_{\tilde{t}} - \frac{2Mr}{H\Sigma}\partial_r\,, \quad \vec{e}_{\hat{r}} = \frac{\sqrt{A}}{H\Sigma}\partial_r + \frac{aH}{\sqrt{A}}\partial_{\tilde{\phi}}\,, \quad \vec{e}_{\hat{\theta}} = \frac{1}{\sqrt{\Sigma}}\partial_\theta\,, \quad \vec{e}_{\hat{\phi}} = \sqrt{\frac{\Sigma}{A}}\frac{1}{\sin\theta}\partial_{\tilde{\phi}}\,. \tag{11.54}$$

The components of the tidal field in this orthonormal basis are

$$\mathcal{E}_{\hat{a}\hat{b}} = \begin{pmatrix} -Q_e\frac{2+\xi}{1-\xi} & Q_m\frac{3a(r^2+a^2)\sin\theta}{H\sqrt{A\Sigma}} & Q_e\frac{6aMr(r^2+a^2)\sin\theta}{HA\sqrt{\Sigma}} \\ * & Q_e\left(1+\frac{3a^2\sin^2\theta}{H^2\Sigma}\right) & -Q_m\frac{6a^2Mr\sin^2\theta}{H^2\Sigma\sqrt{A}} \\ * & * & Q_e\frac{2+\xi}{1-\xi} - Q_e\left(1+\frac{3a^2\sin^2\theta}{H^2\Sigma}\right) \end{pmatrix}, \tag{11.55}$$

where Q_e, Q_m, and ξ are defined in Eqs. (11.50) and (11.51). Just as in Boyer-Lindquist slicing and coordinates (Appendix 11.A.1), so also here, the components, $\mathcal{B}_{\hat{a}\hat{b}}$, of the frame-drag field can be deduced from $\mathcal{E}_{\hat{a}\hat{b}}$ by the duality relation

$$\mathcal{B}_{\hat{a}\hat{b}} = \mathcal{E}_{\hat{a}\hat{b}}|_{Q_e\to Q_m,\, Q_m\to -Q_e}\,. \tag{11.56}$$

The eigenvalues of the tidal field (11.55), i.e., the tendicities, are

$$\lambda^{\mathcal{E}}_r = -\frac{3\zeta}{2H^2\Sigma} - \frac{Q_e}{2}\,, \quad \lambda^{\mathcal{E}}_\theta = \frac{3\zeta}{2H^2\Sigma} - \frac{Q_e}{2}\,, \quad \lambda^{\mathcal{E}}_\phi = Q_e\,, \tag{11.57}$$

where we defined

$$\zeta^2 = Q_e^2(H^2\Sigma)^2 + \frac{(2Ma\sin\theta)^2 F}{\Sigma^3}\,, \quad F = r^2 + 2Mr + a^2\,, \tag{11.58}$$

and their corresponding eigenvectors are

$$\vec{V}^{\mathcal{E}}_r = \frac{1}{v_r}\left(H\sqrt{\Sigma}(r^2+a^2)\vec{e}_{\hat{r}} + \frac{\sqrt{A}}{2Q_m a\sin\theta}\left[Q_e(F+a^2\sin^2\theta)-\zeta\right]\vec{e}_{\hat{\theta}} - 2Mar\sin\theta\vec{e}_{\hat{\phi}}\right), \quad (11.59)$$

$$\vec{V}^{\mathcal{E}}_\theta = \frac{1}{v_\theta}\left(H\sqrt{\Sigma}(r^2+a^2)\vec{e}_{\hat{r}} + \frac{\sqrt{A}}{2Q_m a\sin\theta}\left[Q_e(F+a^2\sin^2\theta)+\zeta\right]\vec{e}_{\hat{\theta}} - 2Mar\sin\theta\vec{e}_{\hat{\phi}}\right), \quad (11.60)$$

$$\vec{V}^{\mathcal{E}}_{\tilde{\phi}} = \frac{1}{v_{\tilde{\phi}}}\left(2Mar\sin\theta\vec{e}_{\hat{r}} + H\sqrt{\Sigma}(r^2+a^2)\vec{e}_{\hat{\phi}}\right). \quad (11.61)$$

Here the quantities v_r, v_θ, and $v_{\tilde{\phi}}$ are the norms of the vectors in large parentheses; they give the eigenvectors $\vec{V}^{\mathcal{E}}$ unit norms. The labels $(r,\,\theta,\,\phi)$ for the eigenvectors and eigenvalues are such that as $a \to 0$, they limit to the corresponding Schwarzschild quantities in Eddington-Finkelstein slicing.

As for Boyer-Lindquist slicing, so also here, the eigenvectors and eigenvalues (vorticities) for $\mathcal{B}_{\hat{a}\hat{b}}$ can be derived from those for $\mathcal{E}_{\hat{a}\hat{b}}$ using the Kerr duality relations:

$$\{\vec{V}^{\mathcal{B}}_-, \vec{V}^{\mathcal{B}}_+, \vec{V}^{\mathcal{B}}_{\tilde{\phi}}\} = \{\vec{V}^{\mathcal{E}}_r, \vec{V}^{\mathcal{E}}_\theta, \vec{V}^{\mathcal{E}}_{\tilde{\phi}}\}|_{Q_e\to Q_m,\, Q_m\to -Q_e} \quad (11.62)$$

$$\{\lambda^{\mathcal{B}}_-, \lambda^{\mathcal{B}}_+, \lambda^{\mathcal{B}}_{\tilde{\phi}}\} = \{\lambda^{\mathcal{E}}_r, \lambda^{\mathcal{E}}_\theta, \lambda^{\mathcal{E}}_{\tilde{\phi}}\}|_{Q_e\to Q_m\,,Q_m\to -Q_e}\,. \quad (11.63)$$

This is not surprising, because the frame-drag field can be deduced from the tidal field using the same transformations. As in the case of Boyer-Lindquist slicing, so also for Kerr-Schild slicing, the transverse (nonradial) eigenvectors are degenerate on the polar axis. This can be seen, for example, from the form of $\mathcal{E}_{\hat{a}\hat{b}}$ in Eq. (11.55), or from the corresponding eigenvalues in Eqs. (11.57): as $\sin\theta \to 0$, the matrix becomes diagonal with two equal eigenvalues, λ_θ and λ_ϕ. This is an inevitable consequence of axisymmetry.

11.A.3 Ubiquity of Spiraling Axial Vortex and Tendex Lines for Kerr Black Holes in Horizon-Penetrating Slices

In Figures 11.17, 11.5, and 11.6, we saw that the azimuthal tendex and vortex lines of a Kerr black hole in horizon-avoiding Boyer-Lindquist slices are closed circles, while those in horizon-penetrating Kerr-Schild and Cook-Scheel slices are outward spirals. In this section, we argue that outward spirals are ubiquitous for (i.e., common to all) horizon-penetrating slices.

We begin by considering the Kinnersley tetrad (KT), a null tetrad which is integral to the theory of black hole perturbations. The tetrad is given by

$$\begin{aligned} l^\mu &= \frac{1}{\Delta}(r^2+a^2, \Delta, 0, a)\,, \\ n^\mu &= \frac{1}{2\Sigma}(r^2+a^2, -\Delta, 0, a)\,, \\ m^\mu &= \frac{1}{\sqrt{2}(r+ia\cos\theta)}(ia\sin\theta, 0, 1, i\csc\theta)\,, \end{aligned} \quad (11.64)$$

where Δ and Σ are defined in Eq. (11.31), and the vector index runs over the Boyer-Lindquist coordinates (t, r, θ, ϕ). We can associate a slicing and an orthonormal tetrad with this null tetrad through Eq. (11.6). Because the Kerr (and by extension Schwarzschild) spacetime is Type D, and the KT is the principal null tetrad of this spacetime, only the Weyl scalar Ψ_2 is non-vanishing in this spacetime. It can be shown (see, e.g., Appendix A of [7]) that $\mathcal{E}_{\hat{a}\hat{b}}$ (and $\mathcal{B}_{\hat{a}\hat{b}}$) are diagonal and their eigenvalues are analogous to those of a non-rotating black hole in Schwarzschild coordinates,

$$\mathcal{E}_{\hat{a}\hat{b}} = \text{diag}[-2\Re(\Psi_2), \Re(\Psi_2), \Re(\Psi_2)]\,, \tag{11.65}$$

$$\mathcal{B}_{\hat{a}\hat{b}} = \text{diag}[-2\Im(\Psi_2), \Im(\Psi_2), \Im\Psi_2]\,. \tag{11.66}$$

In particular, the two transverse eigenvalues are degenerate. The time-like vector field associated with the Kinnersley tetrad, however, has a nonzero twist; i.e., it is not hypersurface orthogonal and does not serve as a normal to any slicing. Because the spin parameter, a, appears in the ∂_ϕ direction of the slicing vector associated with the KT, this produces a twist, which makes the slicing differ from BL slicing. We describe what happens to the simple tidal and frame-drag tensors in the KT-based orthonormal tetrad, when we transform into a slicing that is, first, hypersurface-orthogonal and, second, horizon-penetrating.

When we transform the tetrad associated with the KT into the hypersurface-orthogonal BL coordinate tetrad, there is a coupling between r and θ components in the tetrad vectors and in the tidal and frame-drag tensors that breaks the degeneracy of the transverse directions. The tensors $\mathcal{E}_{\hat{a}\hat{b}}$ and $\mathcal{B}_{\hat{a}\hat{b}}$ pick up off-diagonal components, as a result. This transformation does not influence the azimuthal direction, and the fields in BL slicing still have purely axial tendex and vortex lines (closed circles). Transforming into a horizon-penetrating slicing, such as the Kerr-Schild time, the transformation mixes the t and r components of the orthonormal basis vectors, which, because the metric has a nonzero shift, $g_{t\phi}$, will introduce off-diagonal terms with r and ϕ indices into $\mathcal{E}_{\hat{a}\hat{b}}$ and $\mathcal{B}_{\hat{a}\hat{b}}$. In turn, this causes the axial lines to form the open spirals in Figs. 11.5 and 11.6.

11.B Appendix: Quasinormal Modes of Schwarzschild Black Holes in Regge-Wheeler Gauge

In this section, we review the Regge-Wheeler formalism for perturbations of Schwarzschild black holes, and we present analytical expressions for the frame-drag field used in the calculations in Section 11.7. We focus on the least-damped quasinormal mode, and discuss magnetic-parity and electric-parity quadrupolar perturbations. These calculations are also helpful for comparing with the results of Appendix 11.E to understand the differences between the gauges.

11.B.1 Regge-Wheeler-Zerilli Formalism

Here we review the equations governing magnetic-parity quasinormal modes for a nonrotating black hole in the Regge-Wheeler gauge [9].[2] We write the metric in Schwarzschild coordinates with a small perturbation $h_{\mu\nu}$,

$$ds^2 = -\alpha^2 dt^2 + \frac{dr^2}{\alpha^2} + r^2(d\theta^2 + \sin^2\theta d\phi^2) + h_{\mu\nu}dx^\mu dx^\nu \ , \tag{11.67}$$

where $\alpha^2 = 1 - 2M/r$. The metric perturbations can further be divided into two sets of modes of definite parities. We first treat the magnetic-parity perturbations of the black hole, whose components change sign as $(-1)^{l+1}$ under a parity operation. In the Regge-Wheeler gauge, the only nonzero components of the metric perturbation are

$$h_{tA} = h_0(r)e^{-i\omega t}X_A^{lm}(\theta,\phi) \ , \quad h_{rA} = h_1(r)e^{-i\omega t}X_A^{lm}(\theta,\phi) \ . \tag{11.68}$$

Here ω is the mode's complex quasinormal-mode eigenfrequency, and X_a^{lm} is a magnetic-parity vector spherical harmonic on the unit two-sphere,

$$X_\theta^{lm} = -\csc\theta\, Y^{lm}{}_{,\phi} \ , \qquad X_\phi^{lm} = \sin\theta\, Y^{lm}{}_{,\theta} \ , \tag{11.69}$$

and $Y^{lm}(\theta,\phi)$ is a scalar spherical harmonic. Regge and Wheeler [9, 47] showed that the radial parts of the metric perturbation, $h_0(r)$ and $h_1(r)$ can be expressed in terms of a single scalar radial function $Q(r)$ as

$$h_0 = -\frac{\alpha^2}{i\omega}(rQ)_{,r} \ , \quad h_1 = \frac{rQ}{\alpha^2} \ . \tag{11.70}$$

The radial function $Q(r)$ satisfies the equation

$$Q_{,r_*r_*} + \omega^2 Q = \mathcal{V}_Q(r)Q \ , \ \ \mathcal{V}_Q(r) = \alpha^2\left(\frac{l(l+1)}{r^2} - \frac{6M}{r^3}\right) \ , \tag{11.71}$$

where r_* is the tortoise coordinate

$$dr_* = \frac{dr}{\alpha^2} \ , \quad r_* = r + 2M\log[r/(2M) - 1] \ , \tag{11.72}$$

which goes to $+\infty$ far from the hole and $-\infty$ at the hole's horizon. To find quasinormal-mode solutions, this equation must be solved subject to the boundary conditions of outgoing waves at infinity, $Q \sim e^{i\omega r_*}$ as $r_* \to +\infty$, and ingoing waves at the horizon, $Q \sim e^{-i\omega r_*}$ as $r_* \to -\infty$.

The electric-parity modes, meanwhile, change sign as $(-1)^l$ under a parity operation, and their

[2] There are many errors in the original paper of Regge and Wheeler [9], some of which were corrected by Edelstein and Vishveshwara [47]. We use the corrected equations without further comment.

metric perturbations can be written in Regge-Wheeler gauge as [48]

$$h_{tt} = \alpha^2 H_0(r) e^{-i\omega t} Y^{lm} , \qquad h_{rr} = \frac{H_0(r)}{\alpha^2} e^{-i\omega t} Y^{lm} ,$$
$$h_{tr} = H_1(r) e^{-i\omega t} Y^{lm} , \qquad h_{AB} = r^2 \Omega_{AB} K(r) e^{-i\omega t} Y^{lm} . \tag{11.73}$$

Here Ω_{AB} denotes the metric on the unit 2-sphere. We can write the metric perturbation functions in terms of the Zerilli function $Z(r)$ as[3]

$$\begin{aligned} K &= \left[\frac{\lambda(\lambda+1)r^2 + 3\lambda M r + 6M^2}{r^2(\lambda r + 3M)}\right] Z + \alpha Z_{,r} , \\ H_1 &= -i\omega \left[\frac{\lambda r^2 - 3\lambda M r - 3M^2}{(r-2M)(\lambda r + 3M)}\right] Z - i\omega r Z_{,r} , \\ H_0 &= \left[\frac{\lambda r(r-2M) - \omega^2 r^4 + M(r-3M)}{(r-2M)(\lambda r + 3M)}\right] K + \left[\frac{(\lambda+1)M - \omega^2 r^3}{i\omega r(\lambda r + 3M)}\right] H_1 . \end{aligned} \tag{11.74}$$

Here we have used Zerilli's notation

$$\lambda = \frac{1}{2}(l-1)(l+2) . \tag{11.75}$$

The Zerilli function satisfies the equation

$$Z_{,r_* r_*} + \omega^2 Z = \mathcal{V}_z(r) Z , \tag{11.76}$$

where

$$\mathcal{V}_z(r) = \alpha^2 \left[\frac{2\lambda^2(\lambda+1)r^3 + 6\lambda^2 M r^2 + 18\lambda M^2 r + 18M^3}{r^3(\lambda r + 3M)^2}\right] . \tag{11.77}$$

When we compute the frame-drag field of these perturbations, we will use slices of constant Eddington-Finkelstein time, $\tilde{t} = t + 2M \log(r/2M - 1)$, and the EF tetrad in Schwarzschild coordinates, Eq. (11.19). As discussed in Section 11.G, the time slicing vector of this tetrad has been corrected so that we continue to slice the perturbed spacetime into slices of constant EF time, $\tilde{t}$; see Eq. (11.145). With the corrected slicing vector, basis, we can calculate the frame-drag field $\mathcal{B}_{\hat{a}\hat{b}}$, which we do for an $l = 2$, $m = 2$ mode in the next part.

11.B.2 The Fundamental, Magnetic-Parity, $l = 2$, $m = 2$ Quasinormal Mode of a Schwarzschild Black Hole

In this part, we describe how we calculate the frame-drag field for a magnetic-parity $l = 2$, $m = 2$ quasinormal-mode perturbation, and then its vortex lines and vorticities. We compute the perturbed Riemann tensor, perturbed basis, and frame-drag field in Schwarzschild coordinates, and we express

[3] In H_1 we have corrected a term in the numerator of the fraction: the last term, $-3M^2$, was incorrectly written as $-3M$ by Zerilli—an error that should be obvious on dimensional grounds.

the metric functions in terms of Q and use the Regge-Wheeler equation, Eq. (11.71), in order to simplify $\mathcal{B}_{\hat{a}\hat{b}}$ further. As discussed more fully in Section 11.8.1, the resulting frame-drag field can be expressed in terms of electric-parity scalar, vector, and tensor harmonics. It can be written most concisely as

$$\mathcal{B}_{\hat{r}\hat{r}} = B_{1(\mathrm{m})} e^{-i\omega t} Y^{22} \ , \quad \mathcal{B}_{\hat{r}\hat{A}} = B_{2(\mathrm{m})} e^{-i\omega t} Y^{22}_{\hat{A}} \ , \quad \mathcal{B}_{\hat{A}\hat{B}} = \left(-\frac{1}{2} B_{1(\mathrm{m})} \delta_{\hat{A}\hat{B}} Y^{22} + B_{3(\mathrm{m})} Y^{22}_{\hat{A}\hat{B}} \right) e^{-i\omega t} \ , \tag{11.78}$$

where the radial functions are defined by

$$B_{1(\mathrm{m})} = -\frac{12Q}{i\omega r^3} \ , \quad B_{2(\mathrm{m})} = -\frac{4iM\omega Q + 2\alpha^2 r Q'}{i\omega r^3 \alpha^2 \sqrt{1+2M/r}} \ , \tag{11.79}$$

and by

$$\begin{aligned} B_{3(\mathrm{m})} \quad = \quad & -\frac{1}{i\omega r^5 \alpha^4 (r+2M)} \left\{ \left[3\alpha^2 (r-M)(r^2+4M^2) + 4iM\omega r^2 (r-3M) - r^3\omega^2 (r^2+4M^2) \right] Q \right. \\ & \left. + r\alpha^2 \left[(r-3M)(r^2+4M^2) + 4iM\omega r^3 \right] Q' \right\} \ , \end{aligned} \tag{11.80}$$

where a prime denotes a derivative with respect to r, Y^{lm}_{A} and Y^{lm}_{AB} are given by Eq. (11.114), and $\delta_{\hat{A}\hat{B}}$ is the Kronecker delta function.

We solved the Regge-Wheeler equation, Eq. (11.71), numerically for the lowest-damped, quadrupolar quasinormal mode. When the numerical solution is inserted into the above expressions for $\mathcal{B}_{\hat{a}\hat{b}}$, numerical errors cause problems with delicate cancellations in the transverse-transverse and transverse-radial components near the horizon. To deal with this, we have derived the following asymptotic formula for $Q(r)$ near the horizon, $r_*/M \ll -1$:

$$Q = Y^{-2i\omega} \left[1 + \frac{3Y}{(1-4i\omega)e} + \frac{9i\omega Y^2}{(1-4i\omega)(1-2i\omega)e^2} - \frac{3i(1+12i\omega+40\omega^2)Y^3}{2(1-4i\omega)(1-2i\omega)(3-4i\omega)e^3} + O(Y^4) \right] \tag{11.81}$$

where $Y = e^{r_*/2M}$. Inserting this into Eq. (11.78), we find that all components of $\mathcal{B}_{\hat{a}\hat{b}}$ are finite at the horizon.

Using Eq. (11.78) for the frame-drag field, our analytic formula, Eq. (11.81) for $Q(r)$ near the horizon, and our numerical solution for $Q(r)$ at larger radii, we compute the vortex lines and their vorticities for the fundamental $l = 2$, $m = 2$ quasinormal mode. We illustrate them in Fig. 11.8.

11.B.3 The Fundamental, Electric-Parity, $l = 2$, $m = 2$ Quasinormal Mode of a Schwarzschild Black Hole

We now discuss an electric-parity, fundamental $l = 2$, $m = 2$ perturbation of the Schwarzschild spacetime. As with the magnetic-parity perturbation, we compute the Riemann tensor using the perturbative metric components, Eq. (11.73), we express the tensor in terms of the Zerilli function

Z using Eq. (11.75) (to relate the metric functions to Z), and we use the Zerilli differential equation, Eq. (11.76) to make additional simplifications. Finally, we use the tetrad in Eqs. (11.145) and (11.146) to ensure that we are using EF slicing. The resulting frame-drag field can be expressed in terms of the magnetic-parity vector and tensor spherical harmonics, as noted in Section 11.8.1. we specialize to $l = 2$, $m = 2$ for the frame-drag field below,

$$\mathcal{B}_{\hat{r}\hat{r}} = 0\,, \quad \mathcal{B}_{\hat{r}\hat{A}} = B_{1(\mathrm{e})} e^{-i\omega t} X^{22}_{\hat{A}}\,, \quad \mathcal{B}_{\hat{A}\hat{\theta}} = B_{2(\mathrm{e})} e^{-i\omega t} X^{22}_{\hat{A}\hat{B}}\,, \tag{11.82}$$

where we have defined

$$B_{1(\mathrm{e})} = \frac{\left[6M^2\alpha^2 - i\omega r^2(2r+3M)\right] Z - 2Mr\alpha^2(2r+3M)Z'}{2r^4\alpha^2(r+2M)}\,, \tag{11.83}$$

$$B_{2(\mathrm{e})} = \frac{1}{2r^4\alpha^4(2r+3M)(r+2M)} \left\{ r\alpha^2 \left[4M\beta_2 - i\omega r^2(2r+3M)(r^2+4M^2)\right] Z' \right.$$
$$\left. \left[12M\alpha^2(1+4r\beta_1) - i\omega(r^2+4M^2)\beta_2 + 4M\omega^2 r^3(2r+3M)\right] Z \right\}\,, \tag{11.84}$$

where a prime denotes a derivative with respect to r, and X^{lm}_A and X^{lm}_{AB} are given by Eq. (11.129). We have defined the functions

$$\beta_1 = \frac{r^2 + Mr + M^2}{2r+3M}\,, \quad \beta_2 = (2r^2 - 6Mr - 3M^2)\,, \tag{11.85}$$

to simplify the expressions above. We note that the horizon vorticity, $\mathcal{B}_{NN}$, vanishes for an electric-parity perturbation. From this frame-drag field, we can compute its eigenvectors and eigenvalues for the perturbed spacetime, and from them compute the vortex lines.

Once again we expand Z in terms of $Y = e^{r_*/2M}$ up to $O(Y^3)$ near the horizon, in order to ensure our numerical solution of the Zerilli equation satisfies the correct, ingoing boundary conditions. Because the Zerilli potential, $\mathcal{V}_z$, is more complicated than the Regge-Wheeler potential, $\mathcal{V}_Q$, the coefficients of the expansion of Z in powers of Y are sufficiently long that we do not write them here; they can be computed using algebraic software such as Mathematica, however.

11.C Appendix: Teukolsky's Equation and Black-Hole Perturbations in the Newman-Penrose Formalism

The results in this appendix appear in many places in the literature (see, for example, Teukolsky's paper [22]), but we summarize them here for completeness. Teukolsky's equation relies upon the Newman-Penrose formalism using Kinnersley's tetrad, Eq. (11.64), (note that when a is taken to zero, we recover the Kinnersley tetrad for a Schwarzschild black hole). It also requires the spin coefficients, certain contractions of covariant derivatives of the tetrad above given by Eq. (4.1a) of [3] (though with the opposite sign because of differing metric-signature conventions). The nonzero

spin coefficients in this tetrad are

$$\begin{aligned}\rho &= -\frac{1}{r-ia\cos\theta}\,, \quad \pi = \frac{ia}{\sqrt{2}}\rho^2\sin\theta\,, \quad \beta = -\frac{1}{2\sqrt{2}}\rho^*\cot\theta\,, \quad \alpha = \pi - \beta^*\,,\\ \mu &= \frac{\rho^*\Delta}{2\Sigma}\,, \quad \gamma = \mu + \frac{r-M}{2\Sigma}\,, \quad \tau = -\frac{ia}{\sqrt{2}\Sigma}\sin\theta\,. \end{aligned} \tag{11.86}$$

The Weyl scalar Ψ_4 is defined as $\Psi_4 = C_{\mu\nu\rho\sigma}n^\mu m^{*\nu}n^\rho m^{*\sigma}$, and it vanishes in the background when using the Kinnersley tetrad; hence it is gauge-invariant at leading-order in perturbation theory [22]. Its perturbative part satisfies a decoupled, linear second-order partial-differential equation, Teukolsky's equation (see Teukolsky [22] for the explicit expression). When we define the quantity $\psi_{-2} \equiv \rho^{-4}\Psi_4$, we find that Teukolsky's equation for ψ_{-2} is separable and satisfies an equation similar to that of the Weyl scalar Ψ_0. Namely, assuming a solution $\psi_{-2}^{lm\omega} = {}_{-2}R_{lm\omega}(r){}_{-2}S_{lm\omega}(\theta)e^{i(m\phi-\omega t)}$, the radial function ${}_{-2}R_{lm\omega}$ satisfies an ordinary differential equation (in vacuum),

$$\Delta^{-s}\frac{d}{dr}\left(\Delta^{s+1}\frac{d\,{}_sR_{lm\omega}}{dr}\right) + \left(\frac{K^2 - 2is(r-M)K}{\Delta} + 4is\omega r + 2am\omega - a^2\omega^2 - {}_sA_{lm}\right){}_sR_{lm\omega} = 0\,, \tag{11.87}$$

where $K = (r^2+a^2)\omega - am$, ${}_sA_{lm}$ is a separation constant that is a function of $a\omega$ (i.e., ${}_sA_{lm}(a\omega) = {}_sA_{lm}$), and s is the spin-weight of the field ($s = -2$ for a perturbation of Ψ_4). The radial function satisfies the symmetries ${}_sR_{lm\omega} = (-1)^m{}_sR_{l-m-\omega^*}$. Similarly, the angular function, ${}_{-2}S_{lm\omega}(\theta)$, (called the spin-weighted spheroidal harmonics) satisfies an ordinary differential equation (in vacuum),

$$\begin{aligned}\csc\theta\frac{d}{d\theta}\left(\sin\theta\frac{d\,{}_sS_{lm\omega}}{d\theta}\right) + (a^2\omega^2\cos^2\theta - m^2\csc^2\theta - 2a\omega s\cos\theta \\ -2ms\cot\theta\csc\theta - s^2\cot^2\theta + s + {}_sA_{lm}){}_sS_{lm\omega} &= 0\,. \end{aligned} \tag{11.88}$$

The angular functions satisfy the symmetries ${}_sS_{lm\omega}(\pi-\theta) = (-1)^{(m+l)}{}_{-s}S_{lm\omega}(\theta)$ and ${}_sS^*_{lm\omega}(\theta) = (-1)^{m+s}{}_{-s}S_{l-m-\omega^*}(\theta)$, where we are using a phase convention such that the angular functions agree with the usual convention for spin-weighted spherical harmonics in the limit that spin parameter, a, goes to zero.

We also use the angular separation constants of Chandrasekhar [44], denoted $\not{\lambda}$ (we generally follow his convention of suppressing the indices s, l, m on these quantities). They are related to the angular separation constants used above by ${}_s\not{\lambda}_{lm} = {}_sA_{lm} + s + |s| - 2am\omega + a^2\omega^2$. The separation constants, $\not{\lambda}$, are the same for both positive and negative spin weights, $\pm s$, unlike the constants ${}_sA_{lm}$.

11.D Appendix: The Chrzanowski-Cohen-Kegeles Procedure and the Ingoing-Radiation-Gauge Metric

In this appendix, we will review the formalism used for computing the ingoing-radiation-gauge (IRG) metric, using what is known as the Chrzanowski-Cohen-Kegeles (CCK) procedure. We will also connect the CCK procedure to Chrzanowski's original calculation of definite-parity harmonics, which we find useful for our calculations.

Although Chrzanowski conjectured that "the conceptual benefits of having found the perturbed Kerr metric potentials surpass the usefulness of these potentials for doing future computations" [11], the procedure he helped to formulate has found several applications in the past few years. Lousto and Whiting [15] revisited Chrzanowski's construction and found explicit expressions for computing the Hertz potential corresponding to specific perturbations of the Weyl curvature scalars, Ψ_0 and Ψ_4, in the Schwarzschild spacetime. Ori then derived a similar result for Kerr black holes, using a frequency-domain calculation [16]. Yunes and Gonzalez were the first to explicitly compute the metric of a perturbed Kerr black hole from the Hertz potential [17], and Keidl, Friedman, and Wiseman were the first to use the procedure to calculate the metric perturbation from a static point particle in the Schwarzschild spacetime [18]. More recently, Keidl, Shah, and their collaborators [19] articulated a formalism for computing the gravitational self-force of a point particle in the Schwarzschild or Kerr spacetimes using the metric constructed from a Hertz potential. They were then able to compute the conservative piece of the self-force from this metric perturbation in the Schwarzschild spacetime [20]. In the first article [19], they gave a concise summary of constructing metric perturbations from a Hertz potential, and they called this process the Chrzanowski-Cohen-Kegeles (CCK) procedure or formalism (names we will also adopt).

In the first part of this section, we will review the CCK formalism in a similar way to how Keidl summarized it in [19]. While the metric we ultimately compute, in this paper, is nearly identical to that described by Chrzanowski [11], we find it helpful to put Chrzanowski's original calculation into the context of the more recent work on the CCK procedure. Furthermore, we review the CCK procedure here, rather than simply referring the interested reader to [19], because there are several differences between our calculation and that set forth in [19]: we use a metric of the opposite signature, we calculate the metric corresponding to quasinormal modes with complex frequencies, we construct the metric in a different radiation gauge, and (like Chrzanowski's original calculation) we are interested in metric perturbations of definite parities. Because the CCK formalism relies heavily upon the Newman-Penrose formalism and Teukolsky's equation for perturbations of Weyl curvature scalars, we review these in Appendix 11.C. In the second part of this section, we will describe how to use the CCK procedure to compute definite-parity metric perturbations corresponding to quasinormal modes.

11.D.1 The CCK Procedure

The purpose of the CCK procedure is to construct a metric perturbation, $h_{\mu\nu}$, from a given solution to Teukolsky's equation, either Ψ_0 or $\rho^{-4}\Psi_4$ (see Appendix 11.C for a summary of the Teukolsky formalism). For ease of notation, we will denote the quantities that satisfy Teukolsky's equation by $\psi_2 \equiv \Psi_0$ and $\psi_{-2} \equiv \rho^{-4}\Psi_4$ below. The CCK procedure can construct a metric in either ingoing-radiation gauge (IRG),

$$h_{\mu\nu}l^\nu = 0\,, \quad h_{\mu\nu}g^{\mu\nu}_{(0)} = 0\,, \tag{11.89}$$

or outgoing-radiation gauge

$$h_{\mu\nu}n^\nu = 0\,, \quad h_{\mu\nu}g^{\mu\nu}_{(0)} = 0\,, \tag{11.90}$$

for Schwarzschild and Kerr black holes. Here l^ν and n^ν are two vectors of a Newman-Penrose null tetrad (for our calculations, we will use the Kinnersley tetrad, Eq. (11.64) above), and $g^{\mu\nu}_{(0)}$ is the background Schwarzschild or Kerr metric. Because our goal is to compute vacuum perturbations of Kerr that are regular on the future event horizon, we will construct the metric perturbation in IRG, and we will be able to compute it by algebraically inverting a differential relationship between the harmonics of the Hertz potential and those of ψ_{-2}.

The Hertz potential is tensor with the same symmetries as the Riemann tensor whose double coordinate divergence is a harmonic-coordinate metric. Stewart [13] showed that in Type D spacetimes, there is sufficient gauge freedom that one can represent the independent degrees of freedom of the perturbative part of the Hertz potential as a single complex scalar; furthermore, if one applies a coordinate transformation from harmonic gauge into IRG, the Hertz potential, which we will denote by Ψ_H, is a solution of the vacuum Teukolsky equation for scalars of spin weight $s = -2$ (the same as ψ_{-2}). One can then construct a metric perturbation from the Hertz potential by applying several differential operators to Ψ_H,

$$\begin{aligned} h_{\mu\nu} \;=\; & \big\{ l_{(\mu}m_{\nu)} \left[(\boldsymbol{D} + \rho^* - \rho + \epsilon^* + 3\epsilon)(\boldsymbol{\delta} + 4\beta + 3\tau) + (\boldsymbol{\delta} + 3\beta - \alpha^* - \pi^* - \tau)(\boldsymbol{D} + 3\rho + 4\epsilon) \right] \\ & - l_\mu l_\nu (\boldsymbol{\delta} + \alpha^* + 3\beta - \tau)(\boldsymbol{\delta} + 4\beta + 3\tau) - m_\mu m_\nu (\boldsymbol{D} - \rho + 3\epsilon - \epsilon^*)(\boldsymbol{D} + 3\rho + 4\epsilon) \big\} \Psi_H + \text{c.c.} \end{aligned} \tag{11.91}$$

The differential operators are defined by $\boldsymbol{D} = l^\mu\nabla_\mu$ and $\boldsymbol{\delta} = m^\mu\nabla_\mu$, and for the calculations involving Schwarzschild and Kerr black holes in this paper, we will use the Kinnersley tetrad and its spin coefficients (see Appendix 11.C). The last term in Eq. (11.91), c.c., means to take the complex conjugate of the expression before it on the right-hand side, so that the metric perturbation is real.

When computing perturbations of black holes, it is helpful to be able to relate a given Hertz potential Ψ_H to a specific perturbation of the Weyl scalar Ψ_4. One can do this by computing the

components of the perturbative Riemann tensor from the metric perturbations, Eq. (11.91), that correspond to the Weyl scalar

$$\Psi_4 = C_{\alpha\beta\mu\nu} n^\alpha m^{*\beta} n^\mu m^{*\nu} \,. \tag{11.92}$$

The result can be expressed compactly as

$$\psi_{-2} = \frac{1}{8}\left(\mathcal{L}^{\dagger 4}\Psi_H^* - 12M\partial_t \Psi_H\right) \,; \tag{11.93}$$

see, e.g., the paper by Keidl [19]. We have used the shorthand that $\mathcal{L}^{\dagger 4} = \mathcal{L}^\dagger_{-1}\mathcal{L}^\dagger_0\mathcal{L}^\dagger_1\mathcal{L}^\dagger_2$ where

$$\mathcal{L}^\dagger_s = -\left(\partial_\theta + s\cot\theta - i\csc\theta\partial_\phi\right) + ia\sin\theta\partial_t \,. \tag{11.94}$$

In general, solving for the Hertz potential, Ψ_H, that corresponds to a perturbed Weyl scalar Ψ_4 involves inverting the fourth-order partial differential equations, Eq. (11.93); however, when Ψ_H and ψ_{-2} are expanded in harmonics in the frequency domain, it is possible to perform the inversion algebraically.

One can expand ψ_{-2} in harmonics as

$$\psi_{-2} = \sum_{lm\omega} \psi_{-2}^{(lm\omega)} = \sum_{lm\omega} {}_{-2}R_{lm\omega}(r)\, {}_{-2}S_{lm\omega}(\theta) e^{i(m\phi-\omega t)} \,, \tag{11.95}$$

where the ordinary differential equations satisfied by ${}_{-2}R_{lm\omega}(r)$ and ${}_{-2}S_{lm\omega}(\theta)$ (the radial and angular Teukolsky equations, respectively) are given in Appendix 11.C. In the IRG, the Hertz potential is a solution to the Teukolsky equation with spin $s = -2$; consequently, we can also expand Ψ_H in the same harmonics

$$\Psi_H = \sum_{lm\omega} \Psi_H^{(lm\omega)} = \sum_{lm\omega} {}_{-2}X_{lm\omega}(r)\, {}_{-2}S_{lm\omega}(\theta) e^{i(m\phi-\omega t)} \,. \tag{11.96}$$

The radial function of the Hertz potential's harmonics ${}_{-2}X_{lm\omega}(r)$ also satisfies the vacuum Teukolsky radial equation, but because it is not the same radial function as in the harmonics of ψ_{-2}, we denote it with a different function. One can relate the radial functions of the harmonics of Ψ_H and ψ_{-2} by substituting Eqs. (11.95) and (11.96) into Eq. (11.93) and using the Teukolsky-Starobinsky identity

$$\mathcal{L}^{\dagger 4}\, {}_2S_{lm\omega} = D_{-2}S_{lm\omega} \tag{11.97}$$

(note that our $\mathcal{L}^\dagger_s$ is equivalent to $-\mathcal{L}_s$ in the commonly used book by Chandrasekhar [44]), and the identity

$${}_{-2}S^*_{lm\omega} = (-1)^m\, {}_2S_{l-m-\omega^*} \,. \tag{11.98}$$

Then, one can equate the full radial function for a given angular and time harmonic of the Hertz potential to the radial functions ${}_{-2}R_{lm\omega}$ of ψ_{-2}. Inverting this relationship, one can find the individual radial harmonics of the Hertz potential,

$$ {}_{-2}X_{lm\omega} = 8\frac{(-1)^m D^* \, {}_{-2}R^*_{l-m-\omega^*} - 12iM\omega \, {}_{-2}R_{lm\omega}}{D^{*2} + 144M^2\omega^2}\,, \tag{11.99} $$

The constant $D^* \equiv D^*_{lm\omega} = D_{l-m-\omega^*}$ is defined by

$$ D^2 = \lambda\!\!\!^{-2}(\lambda\!\!\!^{-}+2)^2 - 8\lambda\!\!\!^{-}(5\lambda\!\!\!^{-}+6)(a^2\omega^2 - am\omega) + 96\lambda\!\!\!^{-}a^2\omega^2 + 144(a^2\omega^2 - am\omega)^2\,, \tag{11.100} $$

where $\lambda\!\!\!^{-}$ is the separation constant used by Chandrasekhar [44] (a choice of the separation constant that gives the same constant for both the angular and the radial equations). Although the Teukolsky-Starobinsky identities are usually derived assuming real frequencies, they have been shown to hold for complex frequencies as well (for a recent derivation, see [54]).

The general description of the CCK formalism is now complete; for a vacuum perturbation of Ψ_4, we can now find the Hertz potential, Ψ_H, that corresponds to this perturbation by expanding the potential in harmonics, relating their radial functions through Eq. (11.99) and computing their metric perturbations from Eq. (11.91). In the next section, we will describe how we specialize the CCK formalism above to compute the metric perturbations corresponding to a single even- or odd-parity quasinormal mode, and how we compute the vortex and tendex lines corresponding to these metric perturbations.

11.D.2 Definite-Parity Harmonics and Chrzanowski's Calculation

Before we connect the CCK procedure above with Chrzanowski's original calculation of metric perturbations of definite parities, we will briefly discuss the terminology we use to describe black-hole perturbations of definite parities. First, it is reasonable to discuss the parity of the perturbation, because the background Schwarzschild and Kerr spacetimes have definite parities: the former is invariant under a parity transformation,

$$ \theta \to \pi - \theta \quad \text{and} \quad \phi \to \phi + \pi\,, \tag{11.101} $$

because the spacetime is spherically symmetric; the latter is invariant under parity, because it is reflection symmetric about the equatorial plane ($\theta = \pi/2$) and it is rotationally invariant about the polar axis ($\theta = 0, \pi$). Consequently, we will call a metric perturbation that transforms as

$$ h_{\mu\nu}dx^\mu dx^\nu \to h_{\mu\nu}dx^\mu dx^\nu \tag{11.102} $$

under a parity transformation as even, and we will call a perturbation that transforms as

$$h_{\mu\nu}dx^\mu dx^\nu \rightarrow -h_{\mu\nu}dx^\mu dx^\nu \tag{11.103}$$

under parity as odd. For a Schwarzschild black hole, it is common to call any metric perturbations constructed from scalar, vector, and tensor electric-parity spherical harmonics of any l as even, despite the fact that the electric-parity harmonics transform as $(-1)^l$ (and are even only for even l); similarly, those perturbations made from vector and tensor magnetic-parity spherical harmonics are often called odd, although they are only odd under parity for even l (the magnetic-parity harmonics transform as $(-1)^{l+1}$ under parity). As a result, we will describe the two types of Schwarzschild metric perturbations as being either of electric or magnetic parities, and we will use the words "even" and "odd" only to refer to the parity of a specific harmonic of order l, in the sense of Eqs. (11.102) and (11.103).

This electric and magnetic naming convention fits the perturbation to the Weyl tensor of a Schwarzschild black hole well, because an electric-parity perturbation will generate a perturbative correction to the horizon tendicity and not the horizon vorticity, and a magnetic-parity perturbation will produce a perturbation to the horizon vorticity and not the tendicity. Although the structure of the perturbed metric is somewhat more complicated in Kerr, describing the metric perturbations as of either electric or magnetic parity again is natural. An electric-parity perturbation of order l produces a perturbation to the horizon tendicity that appears like a spherical harmonic of order l, whereas the perturbation to the horizon vorticity looks like a spherical harmonic of order $l+1$; similarly, a magnetic-parity perturbation of order l induces a change in the horizon vorticity of the same order l and in the horizon tendicity of order $l+1$.

We find that if the perturbations have a electric or magnetic parity, then the Hertz potential must itself transform as $\Psi_H \rightarrow \pm(-1)^l\Psi_H^*$ under parity (the plus and minus correspond to electric- and magnetic-parity perturbations, respectively), and its radial harmonics must satisfy ${}_{-2}X^*_{l-m-\omega^*} = \pm(-1)^m {}_{-2}X_{lm\omega}$. In turn, this implies that the radial harmonics of ψ_{-2} must satisfy the same relationship ${}_{-2}R^*_{l-m-\omega^*} = \pm(-1)^m {}_{-2}R_{lm\omega}$. The electric- and magnetic-parity perturbations correspond to the appropriate real and imaginary parts of the metric perturbation in Eq. (11.91).

To see why the radial functions of ψ_{-2} must satisfy the relationship above, we discuss the parity of the terms that appear in Eq. (11.91). The Newman-Penrose tetrad and spin coefficients of the background spacetime transform in several different ways under parity: $\vec{l}$, $\vec{n}$, are even under parity, and $\vec{m}$ does not have a definite parity, $\vec{m} \rightarrow -\vec{m}^*$. Similarly, the differential operator $\boldsymbol{D} = l^\mu\nabla_\mu$ is even under parity, and $\boldsymbol{\delta} = m^\mu\nabla_\mu$ again does not have a definite parity, $\boldsymbol{\delta} \rightarrow -\boldsymbol{\delta}^*$. Three of the nonzero spin coefficients map to their complex conjugates under parity ($\rho \rightarrow \rho^*$, $\mu \rightarrow \mu^*$, and

$\gamma \to \gamma^*$), and the remaining four spin coefficients become minus their complex conjugates under parity ($\alpha \to -\alpha^*$, $\beta \to -\beta^*$, $\pi \to -\pi^*$, and $\tau \to -\tau^*$). These relationships hold true for both Schwarzschild and Kerr, although in the former case, the spin coefficients are real and, therefore, have definite parity.

When applying a parity transformation to the perturbative metric tensor, $h_{\mu\nu}dx^\mu dx^\nu$, where $h_{\mu\nu}$ is given by Eq. (11.91), we can show that the tensor differential operator in Eq. (11.91) becomes its complex conjugate by using the parity transformations for the spin coefficients, NP tetrad, and differential operators above. As a result, the metric perturbation will have either electric or magnetic parity when the Hertz potential transforms as

$$\Psi_H \to \pm(-1)^l \Psi_H^* \tag{11.104}$$

under parity. The plus sign corresponds to an electric-parity perturbation, and the minus sign describes a magnetic-parity perturbation. The condition this implies on the harmonics is also quite simple, which one can determine by applying a parity transformation to the Hertz potential expanded in harmonics, Eq. (11.96), and equating it to its complex conjugate. Then using the properties of the Teukolsky angular functions

$$ {}_sS_{lm\omega}(\pi - \theta) = (-1)^{m+l} {}_{-s}S_{lm\omega}(\theta) \tag{11.105}$$

$$ {}_sS^*_{lm\omega}(\theta) = (-1)^{m+s} {}_{-s}S_{l-m-\omega^*}(\theta) \tag{11.106}$$

(see Appendix 11.C) and equating the radial function of each time and angular harmonic, one obtains the following condition on its radial functions,

$$ {}_{-2}X^*_{l-m-\omega^*} = \pm(-1)^m {}_{-2}X_{lm\omega}\,. \tag{11.107}$$

Similarly by substituting Eq. (11.99) into the expression above, one finds an analogous relationship for the radial function of the Weyl scalar ψ_{-2},

$$ {}_{-2}R^*_{l-m-\omega^*} = \pm(-1)^m {}_{-2}R_{lm\omega}\,. \tag{11.108}$$

For these definite-parity perturbations, the relationship between the radial functions of the Hertz potential and ψ_{-2}, Eq. (11.99) also simplifies,

$$ {}_{-2}X_{lm\omega} = \pm 8(D^* \pm 12iM\omega)^{-1} {}_{-2}R_{lm\omega}\,; \tag{11.109}$$

namely, for definite-parity perturbations, the radial functions of ψ_{-2} and Ψ_H differ by only a complex

constant.

Because the background spacetime is even under parity transformations, the background metric and curvature will have even parity. The tidal field takes on the same parity as the Weyl tensor, and the frame-drag field has the opposite parity; consequently, for the unperturbed black holes the tidal field (and its tendex lines) will have even parity, and the frame-drag field (and its vortex lines) will have odd parity. Moreover, because the background has even parity, this implies that perturbative Weyl tensor computed from the electric- or magnetic-parity metric perturbations will also take on the same parity as the metric perturbation. Similarly, the perturbative tidal field and tendex lines will have the same parity as the metric perturbation, and the equivalent frame-drag field and vortex lines will have the opposite.

In our calculations of the least-damped $l = 2$, $m = 2$ quasinormal modes of Schwarzschild and Kerr black holes, we will always compute a metric perturbation that corresponds to Hertz potential of the form

$$\Psi_H = {}_{-2}R_{lm\omega}e^{i(m\phi-\omega t)}{}_{-2}S_{lm\omega} \pm (-1)^m {}_{-2}R^*_{lm\omega 2}e^{-i(m\phi-\omega^* t)}{}_{-2}S_{l-m-\omega^*} \,. \tag{11.110}$$

From Eq. (11.109), the corresponding perturbation of ψ_{-2} is

$$\begin{aligned} \psi_{-2} &= \pm\frac{1}{8}(D^* \pm 12iM\omega){}_{-2}R_{lm\omega}e^{i(m\phi-\omega t)}{}_{-2}S_{lm\omega} \\ &\quad +\frac{1}{8}(-1)^m(D \mp 12iM\omega^*){}_{-2}R^*_{lm\omega}e^{-i(m\phi-\omega^* t)}{}_{-2}S_{l-m-\omega^*} \,. \end{aligned} \tag{11.111}$$

We choose the coefficients of the modes of ψ_{-2} so as to make the Hertz potential (and, therefore, the metric) as simple as possible. Furthermore, this choice gives the same definite-parity metric as that of Chrzanowski (when one takes the real part of his expressions).

11.E Appendix: Definite-Parity Metric Perturbations in an Ingoing-Radiation Gauge for Schwarzschild Black Holes

In this appendix, we will calculate the metric perturbations corresponding to electric (even) and magnetic (odd) parity quasinormal-mode perturbations of Schwarzschild in IRG. Because Chrzanowski performed this calculation in Table III of [11], and our results agree with his, we do not go into great detail describing the calculation; instead, we aim show the results here so as to be able to compare with the Regge-Wheeler-Zerilli (RWZ) gauge calculations in Appendix 11.B. We will focus, in addition, on the tidal and frame-drag fields corresponding to these metric perturbations.

11.E.1 Electric-Parity Metric Perturbations

We begin this part by comparing the metric produced by the CCK procedure to that of the RWZ formalism. We will write the RWZ metric using the gauge-invariant and covariant notation described by Martel and Poisson [50]. Martel and Poisson write the electric-type perturbations as

$$p_{ab} = \sum_{lm} h_{ab}^{lm} Y^{lm}\,, \quad p_{aB} = \sum_{lm} j_{a}^{lm} Y_{B}^{lm}\,, \quad p_{AB} = r^2 \sum_{lm} \left(K^{lm} \Omega_{AB} Y^{lm} + G^{lm} Y_{AB}^{lm} \right)\,, \tag{11.112}$$

where the lower-case indices run over the radial and time coordinates (e.g., $a, b = t, r$), and upper-case indices run over the angular coordinates, $A, B = \theta, \phi$. The angular functions Y^{lm} are scalar spherical harmonics, Y_B^{lm} are the electric-type Regge-Wheeler harmonics, and Y_{AB}^{lm} are trace-free electric tensor harmonics; the term Ω_{AB} is the metric on a 2-sphere. The vector and tensor harmonics are defined by

$$Y_A^{lm} = D_A Y^{lm}\,, \quad Y_{AB}^{lm} = \left[D_A D_B + \frac{1}{2} l(l+1) \Omega_{AB} \right] Y^{lm}\,, \tag{11.113}$$

where D_A is the covariant derivative on a 2-sphere.

Because the Schwarzschild spacetime is spherically symmetric, one can see, intuitively, that the CCK metric, Eq. (11.91), corresponding to an electric-parity quasinormal-mode perturbation (Eq. (11.110) taking the plus sign) will have a relatively simple form. The angular operators acting on the Hertz potential in Eq. (11.91) become the spin-weight raising and lowering operators, and the angular functions become the spin-weighted spherical harmonics; furthermore, when the spin-weighted harmonics are combined with the appropriate factors of $\vec{m}$ and $\vec{m}^*$ the angular functions become proportional to the scalar, vector, and tensor harmonics described above. When performing the calculation, one will need to use the following identities, which can be found, for example, by adapting the results in the review by Thorne [55] to the notation used here,

$$Y_A^{lm} = \sqrt{\frac{l(l+1)}{2}} ({}_{-1}Y_{lm} m_A - {}_{1}Y_{lm} m_A^*)\,, \quad Y_{AB}^{lm} = \frac{\sqrt{D}}{2} ({}_{-2}Y_{lm} m_A m_B + {}_{2}Y_{lm} m_A^* m_B^*)\,. \tag{11.114}$$

The Teukolsky-Starobinsky constant for spin-weighted spherical harmonics is $D = (l+2)!/(l-2)!$. One can then find that the scalar metric coefficients are given by

$$p_{tt} = -\alpha^2 f p_{tr} = \alpha^4 p_{rr} = -\frac{2\sqrt{D}}{r^2} \Re[{}_{-2}R_{lm} e^{-i\omega t} Y^{lm}]\,, \tag{11.115}$$

where $\alpha^2 = (1 - 2M/r)$. Similarly, one can compute the electric-parity vector-harmonic metric perturbations, and one can find that

$$p_{tA} = -\alpha^2 p_{rA} = \frac{\sqrt{D}}{2l(l+1) r^2 \alpha^2} \Re \left\{ \left[\frac{d}{dr_*} {}_{-2}R_{lm} \left(-i\omega + \frac{2\alpha^2}{r} \right) {}_{-2}R_{lm} \right] Y_A^{lm} e^{-i\omega t} \right\}\,. \tag{11.116}$$

Finally, one can show that the electric-parity tensor-harmonic metric perturbation is given by

$$p_{AB} = \frac{2}{\sqrt{D}\alpha^4}\Re\left\{\left[(i\omega r^2 - M)\frac{d}{dr_*}{}_{-2}R_{lm} - [2\alpha^2 - i\omega(-3r+7M) - r^2\omega^2]_{-2}R_{lm}\right] Y^{lm}_{AB} e^{-i\omega t}\right\}. \tag{11.117}$$

In the equation above, we used the radial Teukolsky equation to eliminate the second-derivative term for the radial function.

There are a few noteworthy differences between the IRG electric-parity perturbations, and the electric-parity RWZ-gauge metric. The CCK metric has a strictly angular part of the perturbation which is proportional to the transverse, trace-free harmonics, and the trace portion of the angular part vanishes; conversely, the angular part of the RWZ metric perturbation has a trace, but no transverse trace-free perturbation. The p_{tr} part of the metric perturbation also has a simpler relationship to the p_{tt} and p_{rr} components in the IRG metric than in the RWZ metric; one reason for this is that the IRG metric has electric-parity vector perturbations, whereas the RWZ metric sets these to zero. Finally, the IRG gauge metric is finite on the future event horizon for ingoing radiation. One can see this by noting that both ${}_{-2}R_{lm}$ and $d_{-2}R_{lm}/dr_*$ scale as $\alpha^4 e^{-i\omega r_*}$ near the horizon, which will cancel any negative powers of α^2 in the expressions for the metric coefficients. The same is not as manifest for the RWZ perturbations (see Appendix 11.B for more details on the RWZ formalism).

We next calculate the electric and magnetic tensors from the IRG metric following the procedure described in Section 11.G. Because the background is spherically symmetric and the perturbation has electric parity, the components of the tidal field are proportional to electric-parity spherical harmonics of a single l, and the components of the frame-drag field are proportional to magnetic-parity harmonics of the same l. Namely, one can write the tidal field as

$$\mathcal{E}^{(1)}_{\hat{r}\hat{r}} = 2\Re[E_{1(\mathrm{e})}(r)Y^{lm}e^{-i\omega t}], \quad \mathcal{E}^{(1)}_{\hat{r}\hat{A}} = 2\Re[E_{2(\mathrm{e})}(r)Y^{lm}_{\hat{A}}e^{-i\omega t}], \tag{11.118}$$

$$\mathcal{E}^{(1)}_{\hat{A}\hat{B}} = 2\Re\left[\left(-\frac{1}{2}E_{1(\mathrm{e})}(r)\delta_{\hat{A}\hat{B}}Y^{lm} + E_{3(\mathrm{e})}(r)Y^{lm}_{\hat{A}\hat{B}}\right)e^{-i\omega t}\right]. \tag{11.119}$$

The symbol $\delta_{\hat{A}\hat{B}}$ is the Kronecker delta function, and the trace-free property of $\mathcal{E}$ requires that the radial function in front of the Kronecker delta must be minus one-half that of $\mathcal{E}^{(1)}_{\hat{r}\hat{r}}$; namely, it must be $-(1/2)E_{1(\mathrm{e})}(r)$. Although the triad components of the tidal and frame-drag fields correspond to the perturbed triad of Eq. (11.146), the functional form of the spherical harmonics with hatted indices is identical to the projections of the spherical harmonics into the background angular components of the triad (i.e., the unit vectors on a sphere of radius r).

The radial dependence of the three complex radial functions above is not particularly simple, but they can be summarized in a few lines, which we do below for an $l = 2$, $m = 2$ mode. This allows

us to compare with the RWZ results in Appendix 11.B.

$$
\begin{aligned}
E_{1(\mathrm{e})}(r) &= -\frac{2\sqrt{6}}{r^6\alpha^4}\Big\{[-5r^2+16Mr-12M^2-i\omega r^2(4r-9M)+r^4\omega^2]_{-2}R_{lm} \\
&\quad +r^2(r-3M+i\omega r^2)\frac{d}{dr_*}{}_{-2}R_{lm}\Big\} \qquad (11.120)\\
E_{2(\mathrm{e})}(r) &= \frac{1}{r^6\sqrt{6r(r+2M)}\alpha^4}\Big\{r^3[-6r+3M\alpha^2-2i\omega r(r-3M)+2r^3\omega^2]\frac{d}{dr_*}{}_{-2}R_{lm} \\
&\quad +[6(-r^3+7Mr^2-4M^2r+4M^3)-i\omega r^2(16r^2-35Mr+30M^2) \\
&\quad +2\omega^2r^4(4r-9M)+2ir^6\omega^3]_{-2}R_{lm}\Big\}, \qquad (11.121)\\
E_{3(\mathrm{e})}(r) &= \frac{1}{r^5(r+2M)\alpha^4\sqrt{6}}\Big\{r^2\omega(-2r^2+3Mr+3M^2+r^4\omega^2)\frac{d}{dr_*}{}_{-2}R_{lm} \\
&\quad +[6(r^2+4M^2)+i\omega(4r^3-11Mr^2+12M^2r+12M^3) \\
&\quad -\omega^2r^2(4r^2-4MR-9M^2)-3i\omega^3r^5\alpha^2+r^6\omega^4]_{-2}R_{lm}\Big\}, \qquad (11.122)
\end{aligned}
$$

To remove higher-order radial derivatives from the above equation, we used the radial Teukolsky equation. As with the metric, one can see that the tidal field is well-behaved on the horizon, because, as noted above, ${}_{-2}R_{lm}$ and $d{}_{-2}R_{lm}/dr_*$ scale as $\alpha^4 e^{-i\omega r_*}$ near the horizon; consequently, they will cancel the corresponding powers of α^2 in the denominator.

Next, we will present similar expressions for the frame-drag field. It can be written as

$$
\mathcal{B}^{(1)}_{\hat{r}\hat{r}}=0\,,\quad \mathcal{B}^{(1)}_{\hat{r}\hat{A}}=2\Re[B_{1(\mathrm{e})}(r)X^{lm}_{\hat{A}}e^{-i\omega t}]\,,\quad \mathcal{B}^{(1)}_{\hat{A}\hat{B}}=2\Re[B_{2(\mathrm{e})}(r)X^{lm}_{\hat{A}\hat{B}}e^{-i\omega t}]\,, \qquad (11.123)
$$

where we define the magnetic-parity harmonics in Eqs. (11.127) and (11.128). Because $\mathcal{B}_{\hat{r}\hat{r}}$ vanishes everywhere, the horizon vorticity for an electric-parity mode will be zero. The complex radial functions, for an $l=2$, $m=2$ mode are given by

$$
\begin{aligned}
B_{1(\mathrm{e})}(r) &= \frac{\sqrt{2}}{r^5\sqrt{3r(r+2M)}\alpha^4}\Big\{r^2[9M-i\omega r(r-3M)+r^3\omega^2]\frac{d}{dr_*}{}_{-2}R_{lm} \qquad (11.124)\\
&\quad +[-24Mr\alpha^2+i\omega r(12M^2-25Mr+5r^2)+\omega^2r^3(4r-9M)-ir^5\omega^3]_{-2}R_{lm}\Big\}, \\
B_{2(\mathrm{e})}(r) &= \frac{1}{r^4(r+2M)\alpha^4\sqrt{6}}\Big\{i\omega r(-2r^2+3Mr+3M^2+r^4\omega^2)\frac{d}{dr_*}{}_{-2}R_{lm} \qquad (11.125)\\
&\quad +[-24M+2i\omega r(2r-7M)+\omega^2r(-4r^2+4Mr+9M^2)-3i\omega^3r^4\alpha^2+r^5\omega^4]_{-2}R_{lm}\Big\}.
\end{aligned}
$$

One can now see that the frame-drag field is also regular on the horizon.

11.E.2 Magnetic-Parity Metric Perturbations

To begin this part, we will also draw connections between the IRG metric from the CCK procedure and the RWZ metric. The magnetic-type perturbations, in Martel and Poisson's notation, are given

by

$$p_{ab} = 0\,, \quad p_{aB} = \sum_{lm} h_a^{lm} X_B^{lm}\,, \quad p_{AB} = r^2 \sum_{lm} h_2^{lm} X_{AB}^{lm}\,, \tag{11.126}$$

where the magnetic-parity harmonics are defined by

$$X_A^{lm} = -\epsilon_A{}^B D_B Y^{lm}\,, \tag{11.127}$$

$$X_{AB}^{lm} = -\frac{1}{2}(\epsilon_A{}^C D_B + \epsilon_B{}^C D_A) D_C Y^{lm}\,, \tag{11.128}$$

and ϵ_{AB} is the Levi-Civita tensor on a unit 2-sphere. As in the previous part, we can compute the CCK metric, Eq. (11.91), which is relatively simple for a Schwarzschild black hole. The reason for the simplification is the same, but we will need the following two identities that relate the spin-weighted spherical harmonics to magnetic-parity vector and tensor harmonics

$$X_A^{lm} = -i\sqrt{\frac{l(l+1)}{2}}({}_{-1}Y_{lm} m_A - {}_1Y_{lm} m_A^*)\,, \quad X_{AB}^{lm} = -i\frac{\sqrt{D}}{2}({}_{-2}Y_{lm} m_A m_B + {}_2Y_{lm} m_A^* m_B^*)\,. \tag{11.129}$$

These relationships can also be found in [55]. The magnetic-parity vector-harmonic metric perturbations have the same radial and time dependence as the electric-parity perturbations, which one can see by comparing Eq. (11.116) with the expression below:

$$-p_{tA} = \alpha^2 p_{rA} = \frac{\sqrt{D}}{2l(l+1)r^2\alpha^2} \Im\left\{\left[\frac{d}{dr_*}{}_{-2}R_{lm}\left(-i\omega + \frac{2\alpha^2}{r}\right){}_{-2}R_{lm}\right] X_A^{lm} e^{-i\omega t}\right\}\,. \tag{11.130}$$

Unlike the electric-parity perturbation, the harmonic now has magnetic-parity, and the physical metric perturbation corresponds to minus the imaginary part. There is a similar relationship between the magnetic-parity tensor-harmonic metric perturbations and the equivalent electric-parity expression, which can be found from examining Eq. (11.117) and the expression below:

$$p_{AB} = -\frac{2}{\sqrt{D}\alpha^4} \Im\left\{\left[(i\omega r^2 - M)\frac{d}{dr_*}{}_{-2}R_{lm} - [2\alpha^2 - i\omega(-3r + 7M) - r^2\omega^2]{}_{-2}R_{lm}\right] X_{AB}^{lm} e^{-i\omega t}\right\}\,. \tag{11.131}$$

Because the magnetic-parity metric perturbations have the same radial dependence as the electric-parity metric, they will be well-behaved on the future event horizon as well.

We will compute the tidal field of the perturbation in the same way that we computed the electric-parity perturbation. Because the perturbation has magnetic-parity, now the tidal field will now have magnetic parity, and it can be expanded in terms of magnetic-parity harmonics as

$$\mathcal{E}^{(1)}_{\hat{r}\hat{r}} = 0\,, \quad \mathcal{E}^{(1)}_{\hat{r}\hat{A}} = 2\Re[E_{1(\mathrm{m})}(r) X^{lm}_{\hat{A}} e^{-i\omega t}]\,, \quad \mathcal{E}^{(1)}_{\hat{A}\hat{B}} = 2\Re[E_{2(\mathrm{m})}(r) X^{lm}_{\hat{A}\hat{B}} e^{-i\omega t}]\,, \tag{11.132}$$

where, for an $l = 2$, $m = 2$ mode, the complex radial functions can be written as

$$E_{1(\mathrm{m})}(r) = -iB_{1(\mathrm{e})}(r) + i\frac{M\sqrt{3(r+2M)}}{r^5\alpha^4\sqrt{2r}}\left[-(\alpha^2+i\omega r){}_{-2}R_{lm} + r\frac{d}{dr_*}{}_{-2}R_{lm}\right], \quad (11.133)$$

$$E_{2(\mathrm{m})}(r) = -iB_{2(\mathrm{e})}(r) - \frac{\sqrt{3}(r+2M)}{r^5\alpha^4\sqrt{2}}(M\omega){}_{-2}R_{lm}\,. \quad (11.134)$$

Interestingly, there is a near duality between the tidal field of an magnetic-parity perturbation and the frame-drag field of an electric-parity perturbation. A similar relationship exists between the frame-drag field of a magnetic-parity perturbation and the tidal field of an electric-parity perturbation. The frame-drag field of the magnetic perturbation can be expanded in terms of electric-parity harmonics as

$$\mathcal{B}^{(1)}_{\hat{r}\hat{r}} = 2\Re[B_{1(\mathrm{m})}(r)Y^{lm}e^{-i\omega t}], \quad \mathcal{B}^{(1)}_{\hat{r}\hat{A}} = 2\Re[B_{2(\mathrm{m})}(r)Y^{lm}_{\hat{A}}e^{-i\omega t}], \quad (11.135)$$

$$\mathcal{B}^{(1)}_{\hat{A}\hat{B}} = 2\Re\left[\left(-\frac{1}{2}B_{1(\mathrm{m})}(r)\delta_{\hat{A}\hat{B}}Y^{lm} + B_{3(\mathrm{m})}(r)Y^{lm}_{\hat{A}\hat{B}}\right)e^{-i\omega t}\right], \quad (11.136)$$

where again the trace-free property of $\mathcal{B}_{\hat{a}\hat{b}}$ requires that the radial function of the strictly angular part of the frame-drag field proportional to the identity be minus one half the radial function of the strictly radial component. The expression for the radial functions is given by

$$B_{1(\mathrm{m})}(r) = iE_{1(\mathrm{e})}(r) \quad (11.137)$$

$$B_{2(\mathrm{m})}(r) = iE_{2(\mathrm{e})}(r) - i\frac{M\sqrt{3(r+2M)}}{r^5\alpha^4\sqrt{2r}}\left[-(\alpha^2+i\omega r){}_{-2}R_{lm} + r\frac{d}{dr_*}{}_{-2}R_{lm}\right], \quad (11.138)$$

$$B_{3(\mathrm{m})}(r) = iE_{3(\mathrm{e})}(r) - \frac{\sqrt{3}(r+2M)}{r^5\alpha^4\sqrt{2}}(M\omega){}_{-2}R_{lm}\,. \quad (11.139)$$

One can see from the above expression that there is the same near-duality of the frame-drag field of a magnetic-parity perturbation and the tidal field of an electric-parity perturbation. There is an exact duality of the radial-radial components, which, in turn, implies that the horizon vorticity of a magnetic-parity perturbation is the same as the horizon tendicity of an electric-parity perturbation.

11.F Appendix: Equality of Frame-Drag Fields in Regge-Wheeler and Ingoing-Radiation Gauges

In this appendix, we show that the frame-drag field for an $l = 2$, $m = 2$, magnetic-parity, quasinormal-mode perturbation of a Schwarzschild black hole is the same in Regge-Wheeler and ingoing-radiation gauges; the tidal fields, however, have small perturbative differences.

The calculation that shows this is straightforward. Use the relationship between the Regge-Wheeler function and the radial function of the radial Teukolsky equation (see, e.g., Eq. (319) of

Chapter 4 of [44][4]) to show that for an $l = 2$, $m = 2$, mode

$$\begin{aligned} Q &= -\frac{2i\omega}{r^3\alpha^4}\Big\{[-5r^2 + 16Mr - 12M^2 - i\omega r^2(4r - 9M) + r^4\omega^2]_{-2}R_{lm} \\ &\quad + r^2(r - 3M + i\omega r^2)\frac{d}{dr_*}{}_{-2}R_{lm}\Big\} . \end{aligned} \tag{11.140}$$

Substituting this expression into Eqs. (11.78)–(11.80), one finds that it is identical to the frame-drag field of Eqs. (11.135)–(11.139); i.e., one has that

$$\boldsymbol{\mathcal{B}}_{\rm IRG} = \boldsymbol{\mathcal{B}}_{\rm RW} . \tag{11.141}$$

Although we do not give an explicit expression for the perturbative tidal field of the Regge-Wheeler-gauge metric perturbation in this paper, a quick calculation shows that the tidal fields differ. We briefly discuss why this might be the case, below.

Regge-Wheeler and ingoing-radiation gauges are related by a coordinate transformation of the form

$$x^\mu_{\rm RW} = x^\mu_{\rm IRG} + \xi^\mu . \tag{11.142}$$

For the magnetic-parity perturbations, the transformation vector has the form

$$\vec{\xi}_{\rm mag} = \Im[f(r)e^{-i\omega t}(0, 0, \mathbf{X}_{l,m}(\theta, \phi))] , \tag{11.143}$$

where $\mathbf{X}_{l,m}(\theta, \phi)$ is a magnetic-parity, vector spherical harmonic, and where $f(r)$ is minus one-half times the radial function that appears in the expression for p_{AB} in Eq. (11.131). One can see that the time and radial coordinates, t and r, are identical in the two gauges, therefore. Because we use a slice of constant Eddington-Finkelstein time (a function of only t and r) to set the slicings for both gauges, the slicing, and the one-form associated with this slicing are the same in both coordinates. Note that this does not mean that the vector associated with the observers' four-velocities that are normal to the slice will have the same coordinate components; see Eq. (11.145).

Because there is no background frame-drag field (i.e., it is a strictly perturbative quantity), and because the slicings are the same, it is not surprising that the frame-drag fields are identical in these two gauges. The perturbative differences in the coordinates produce changes in the frame-drag field that are of second-order in the perturbative expansion, as would second-order differences in the slicing.

The tidal field, however, has a background piece, and the first-order differences in the coordinates will produce first-order differences in the tidal fields. There are additional differences between the

[4]Note that the magnetic-parity function used by Chandrasekhar, $Z^{(-)}$, is related to the Regge-Wheeler function by $Q = i\omega Z^{(-)}$, and his radial function for the Teukolsky equation, Y_{-2} is related to that of this paper by ${}_{-2}R_{lm} = r^3 Y_{-2}$.

tidal fields, however, beyond these simple distinctions. The extrinsic curvature of the slices will differ in the two gauges, and because these terms couple to the background tidal field in the Maxwell-like evolution equations for the tidal field (see Eq. (2.4) of Paper I), this requires that the perturbative tidal field must differ in the two gauges.

11.G Appendix: Analytical and Numerical Methods for Computing Tendex and Vortex Quantities

In this section, we discuss the details of how we compute the vortex and tendex lines. The procedure for calculating tendex and vortex lines is identical for Schwarzschild and Kerr black holes; however, because the analytical expressions for the Newman-Penrose quantities, the Teukolsky angular function, and the metric derived from these mathematical objects is significantly simpler for Schwarzschild black holes, the amount of work we can perform analytically differs for rotating and non-rotating black holes. Even for Schwarzschild black holes, however, we will not be able to compute all aspects of the metric perturbation analytically. We calculate the least-damped $l = 2$, $m = 2$ quasinormal mode frequencies for both Schwarzschild and Kerr black holes using the Mathematica notebook associated with [52], an implementation of Leaver's method [56]. Similarly, we compute the radial Teukolsky functions ${}_{-2}R_{lm\omega}$ corresponding to a quasinormal-mode solution for both Schwarzschild and Kerr black holes numerically. We compute it in two ways, which give comparable results: we solve the boundary-value problem for a quasinormal mode solution to the radial Teukolsky equation, Eq. (11.87), using a shooting method, and we compare the result with a series solution given by Leaver [56] (as is also done in the notebook of [52]). For Kerr black holes, the numerical solution requires the angular eigenvalue, ${}_sA_{lm}$ associated with the quasinormal mode frequency, which we again compute from the implementation of Leaver's method in [52].

The most significant difference between the calculations of quasinormal modes of Schwarzschild and Kerr black holes arises from differences in the Teukolsky angular function, and the angular operators used in computing the metric of Eq. (11.91). First, the spin-weighted spheroidal harmonics in the expression for the Hertz potential, Eq. (11.110), reduce to spin-weighted spherical harmonics for Schwarzschild black holes. Second, the angular operators in Eq. (11.91) reduce to spin-weight lowering operators, in the non-spinning limit. As a result, the metric perturbation can be expressed, analytically, in terms of electric- or magnetic-parity scalar, vector, and tensor spherical harmonics of a single l, for Schwarzschild black holes. For perturbations of Kerr black holes, there are not these additional simplifications. First, we must calculate the spin-weighted spheroidal harmonics numerically, which we do using a series solution put forward by Leaver [56] (the same method as that implemented in [52]). Second, the angular operators are no longer the spin-weight lowering operators. The metric perturbation computed from these functions, therefore, is not nearly as simple

as that of the Schwarzschild limit. In fact, for our calculations with spinning black holes, we find it easier to work with a numerical fit to the analytical expression for the metric.

Once we calculate the metric perturbation, we construct the perturbation to the Weyl tensor in the same way for both rotating and non-rotating black holes; namely, we compute the perturbative connection coefficients and take the appropriate combination of them and their derivatives to find the first-order perturbation to the vacuum curvature tensor. We can then calculate the tetrad components of the tidal field, $\mathcal{E}_{\hat{a}\hat{b}}$, and frame drag-field, $\mathcal{B}_{\hat{a}\hat{b}}$, through Eqs. (11.1) and (11.2), respectively. The orthonormal tetrad into which we decompose our tidal and frame-drag fields deserves a brief discussion.

For computing and visualizing the vortex and tendex lines, it is convenient to specify a slicing that is a simple analytical function of the perturbative Schwarzschild or Kerr coordinates; as a result, we continue to foliate the spacetime by surfaces of constant $\tilde{t}$ (Eddington-Finkelstein time for Schwarzschild and Kerr-Schild time for Kerr). The components of the normal one-form to the slicing will still be proportional to the gradient of the appropriate time coordinate (i.e., $u_\mu \propto \nabla_\mu \tilde{t}$). We now aim to construct a vector, $\vec{u}$, and a triad in the spatial slice, $\vec{e}_{\hat{a}}$ such that together, $\vec{u}$ and $\vec{e}_{\hat{a}}$ form an orthonormal tetrad with respect to the background metric plus the perturbed metric, $g_{\mu\nu} + h_{\mu\nu}$. We will write this full orthonormal tetrad, schematically, as

$$\vec{u} = \vec{u}^{\,(0)} + \vec{u}^{\,(1)}\,, \quad \vec{e}_{\hat{a}} = \vec{e}^{\,(0)}_{\hat{a}} + \vec{e}^{\,(1)}_{\hat{a}}\,, \tag{11.144}$$

where the zeroth-order (unperturbed) tetrad is given by Eq. (11.19) for Schwarzschild and Eq. (11.54) for Kerr. It is then convenient to expand the perturbative piece of the tetrad in terms of the unperturbed tetrad. A quick calculation shows that

$$u^\mu_{(1)} = -\frac{1}{2} h_{\hat{0}\hat{0}} u^\mu_{(0)} - h^{\mu\nu} u^{(0)}_\nu\,, \tag{11.145}$$

$$\vec{e}^{\,(1)}_{\hat{a}} = -\frac{1}{2} h_{\hat{a}\hat{b}} \vec{e}^{\,\hat{b}}_{(0)}\,, \tag{11.146}$$

where $h_{\hat{0}\hat{0}} = h_{\mu\nu} u^\mu_{(0)} u^\nu_{(0)}$ and $h_{\hat{a}\hat{b}} = h_{\mu\nu} e^{(0)\mu}_{\hat{a}} e^{(0)\nu}_{\hat{b}}$ are the projections of the covariant components of the perturbed metric into the unperturbed tetrad. Consequently, our tidal and frame-drag fields will contain both background and perturbative pieces; namely

$$\mathcal{E}_{\hat{a}\hat{b}} = \mathcal{E}^{(0)}_{\hat{a}\hat{b}} + \mathcal{E}^{(1)}_{\hat{a}\hat{b}}\,, \quad \mathcal{B}_{\hat{a}\hat{b}} = \mathcal{B}^{(0)}_{\hat{a}\hat{b}} + \mathcal{B}^{(1)}_{\hat{a}\hat{b}}\,, \tag{11.147}$$

and the perturbative pieces, $\mathcal{E}^{(1)}_{\hat{a}\hat{b}}$ and $\mathcal{B}^{(1)}_{\hat{a}\hat{b}}$ will contain terms from both the perturbative Weyl tensor contracted appropriately into the unperturbed tetrad, and the same contractions of the background Weyl tensor into the perturbed tetrad.

One can then solve the eigenvalue problem, Eq. (11.3), to find the eigenvectors and the tendicity

and vorticity of the tidal and frame-drag fields, respectively. Because we computed the tidal and frame-drag fields through first order in perturbation theory, it would seem natural to calculate their eigenvectors (as well as the vorticity and the tendicity) through first order in perturbation theory, too. There is good reason, however, to calculate the exact eigenvectors and the exact vorticity and tendicity instead of the perturbative values. Computing perturbative eigenvectors uses two different procedures depending upon whether the unperturbed eigenvalues are equal or not (they are formally identical to non-degenerate and degenerate time-independent perturbation theory in quantum mechanics): in non-degenerate regions, one takes appropriate linear combinations of the background eigenvectors; in degenerate regions, one computes the exact eigenvectors of the perturbative tidal and frame-drag fields in the subspace spanned by the eigenvectors corresponding to the degenerate eigenvalues. One must use a different procedure in degenerate regions, because when the magnitude of the perturbative eigenvalues becomes comparable to the difference of the nearly degenerate eigenvalues, the scale of the first-order correction no longer becomes perturbative in the degenerate subspace.

The Kerr spacetime, for example, has large spatial regions near the axis of rotation where the unperturbed tendicity and vorticity corresponding to the angular tendex and vortex directions are nearly degenerate, and regions near the plane of reflection symmetry where they are not. Were we to use perturbation theory, then we would need to find an *ad hoc* prescription for deciding when to consider a perturbation degenerate and for connecting different degenerate and non-degenerate methods in different spatial regions as smoothly as possible. The simpler and more transparent approach, therefore, is to compute the exact eigenvectors everywhere. While the nonlinear process of computing eigenvectors and eigenvalues introduces terms that are formally of higher order than the accuracy of the calculation of the tidal and frame-drag fields, in our numerical calculations, we keep the magnitude of the perturbation sufficiently small that these higher-order terms are very small numerically.

From the exact eigenvectors of the tidal and frame-drag fields, we can compute the vortex and tendex lines through the differential equation

$$\frac{dx^\mu}{ds} = v^{\hat{a}} e^\mu_{\hat{a}} \,. \tag{11.148}$$

In the above equation, x^μ are Schwarzschild or Boyer-Lindquist coordinates, s is an affine parameter along the vortex and tendex lines, $v^{\hat{a}}$ are the exact eigenvectors found from solving Eq. (11.3), and $e^\mu_{\hat{a}}$ are the spatial triad (background plus the perturbative corrections). In the next two appendices, we will show a few additional results for the tendex and vortex quantities from explicit calculations using the CCK procedure for Schwarzschild and Kerr black holes. We will focus on quasinormal modes of magnetic parity, first; then, to help with future comparisons with numerical-relativity simulations,

we will compute the vortexes and tendexes of $l = 2$, $m = 2$, quasinormal-mode perturbations of both parities for Schwarzschild and Kerr black holes, when we include the background tidal and frame-drag fields in addition to the perturbative fields.

11.H Appendix: Magnetic-Parity, $l = 2$, $m = 2$, Quasinormal-Mode Perturbations of Schwarzschild and Kerr Black Holes in an Ingoing-Radiation Gauge

To understand the extent to which there is a duality between electric- and magnetic-parity perturbations, we plot the vortexes and tendexes of magnetic-parity perturbations in this appendix. The analytical expressions for Schwarzschild-black-hole perturbation in Appendix 11.E showed that there is a near duality, and it is of interest to see visually what these small differences do to the tendexes and vortexes. For Kerr black holes, we neither found nor presented explicit analytical expressions like those in Appendix 11.E for the tidal and frame-drag fields of Schwarzschild black holes. As a result, the exploration of duality for Kerr black holes is more qualitative. This comparison will give some insight into how the background tidal and frame-drag fields affect the generation of gravitational waves, because in their absence there is an exact duality.

11.H.1 Perturbations of Schwarzschild Black Holes

Unlike the sections on electric-parity modes, it is not necessary to begin by showing the horizon vorticity and tendicity, because, from the computations in Appendix 11.E, the horizon vorticity of a magnetic-parity mode is exactly the horizon tendicity of an electric-parity mode (and vice versa). Therefore, Fig. 11.10 describes the horizon quantities, with vorticity and tendicity reversed.

We, therefore, begin by showing the vortex lines and the vorticity in the plane of reflection symmetry in Fig. 11.18. We plot the vortex quantities there identically to the tendex quantities in Fig. 11.11. The two figures are nearly identical, but by carefully scrutinizing both figures, one can observe small differences in curvature of the vortex lines in the regions of small vorticity. Nevertheless, the essential qualitative features are the same: there are two vortexes that emerge from the horizon vortexes and spiral out, and the vortex lines emerge from the horizon and collect into spirals that reside on the outer edge of the vortexes.

In three dimensions, the magnetic-parity vortexes and tendexes are nearly dual to their electric-parity counterparts in Fig. 11.12, but the small differences are somewhat more pronounced. The magnetic-parity quantities are shown in Fig. 11.19, with the vortexes on the left and the tendexes on the right. The manner in which the vortex and tendex results are depicted is identical to that of the nearly dual quantities in Fig. 11.12, except now the blue (dark) volume showing the vortexes represents the region where the vorticity is at least 80% of the maximum vorticity, and the equivalent

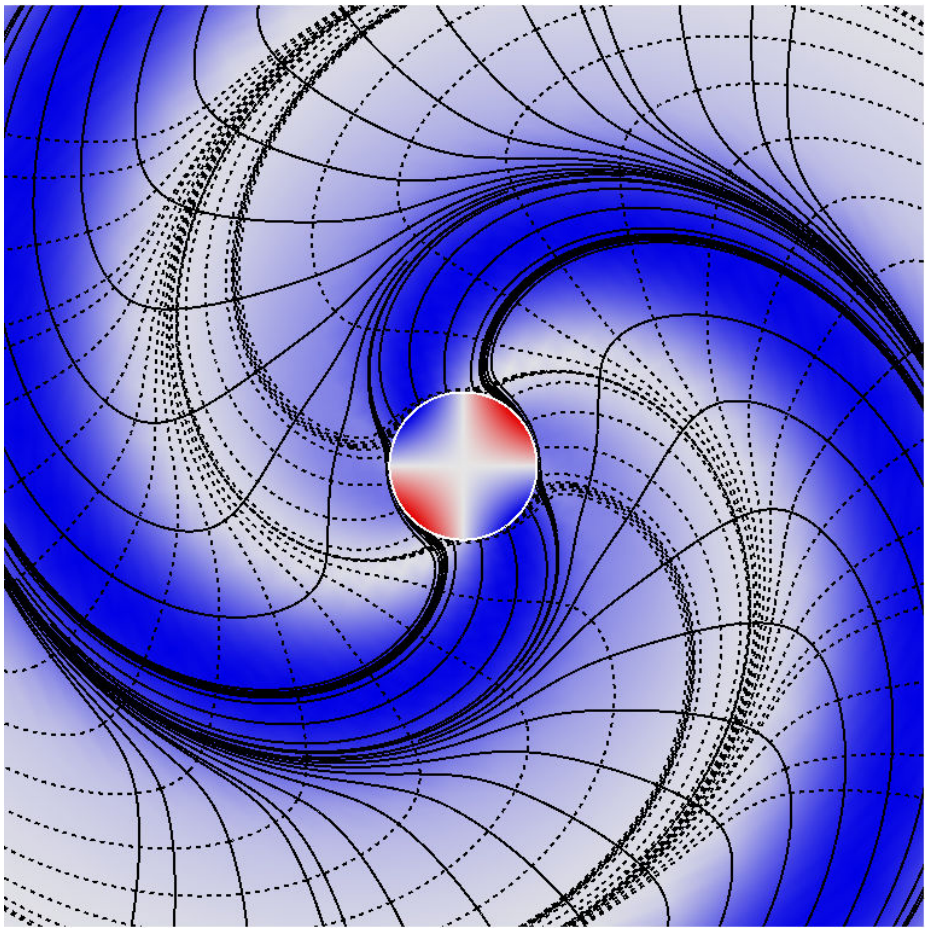

Figure 11.18: The vorticity and vortex lines in the plane of reflection symmetry for a magnetic-parity perturbation (the approximate dual of Fig. 11.11). The coloring of the vorticity and the plotting of the lines is equivalent to that in Fig. 11.11 for the tendicity and tendex lines.

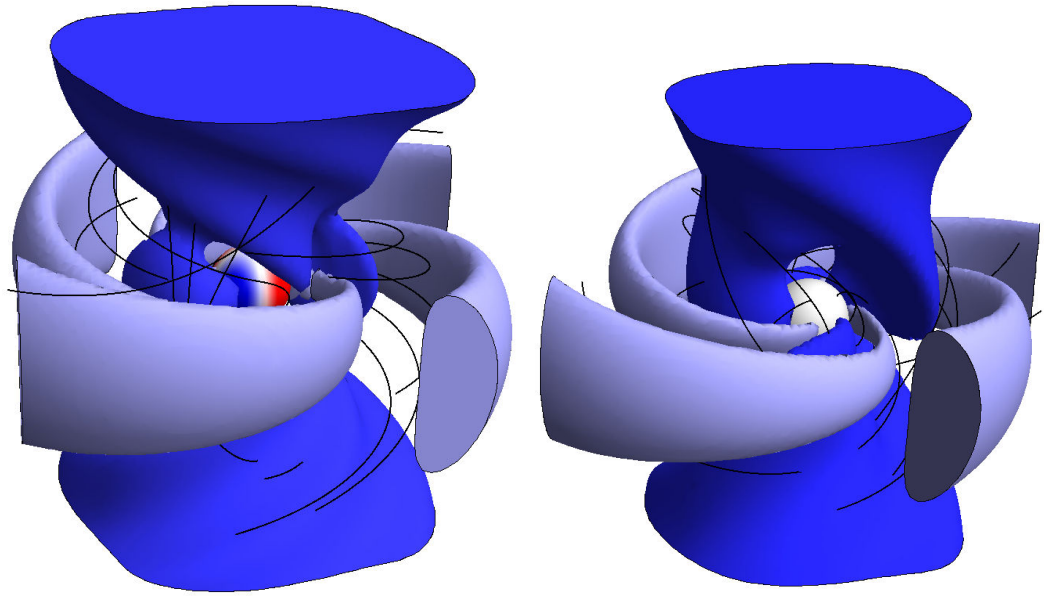

Figure 11.19: *Left*: Three-dimensional vortex lines and vortexes of the same perturbation as that shown in Fig. 11.18 (and the approximate dual to Fig. 11.12). The vortex quantities are plotted in the same way as the tendex quantities in the left panel of Fig. 11.12, except the blue (dark) volume corresponds to where vorticity is at least 80% of the radial maximum. *Right*: Three-dimensional perturbative tendexes and tendex lines for the perturbation. Similarly, the tendex results shown are identical to the dual vortex images in the right panel of Fig. 11.12, except the blue (dark) volume corresponds to where tendicity is at least 85% of the radial maximum.

one for the perturbative tendexes is 85% of the radial maximum. Both the lines and the eigenvalues are nearly dual; one can only see a few small differences in the precise shape of the vortexes and tendexes. As a result, the way we will describe the generation of gravitational waves will be dual to that of the electric-parity mode: there are two positive near-zone vortexes that induce near-zone perturbative tendexes around the equatorial plane; as they extend out in radius, they collect around the poles and will, asymptotically, become the gravitational radiation.

11.H.2 Perturbations of Kerr Black Holes

One can now ask whether the horizon vorticity and tendicity of a magnetic-parity $l = 2$, $m = 2$ perturbation of a Kerr black hole with spin $a/M = 0.945$ will be the dual to the comparable electric-parity perturbation shown in Fig. 11.13. Although we do not explicitly perform this calculation in this paper, we can make this comparison by investigating the differences between the horizon quantities of the electric-parity perturbation in Fig. 11.13, and those of the magnetic-parity perturbation in Fig. 11.20, shown here. We show the horizon vorticity on the left, and the tendicity on the right, in Fig. 11.20. By comparing the two figures, one can see that the duality appears to be exact. It will be of interest to confirm this with future calculations.

Next, we will show the vortexes and vortex lines in the plane of reflection symmetry in Fig.

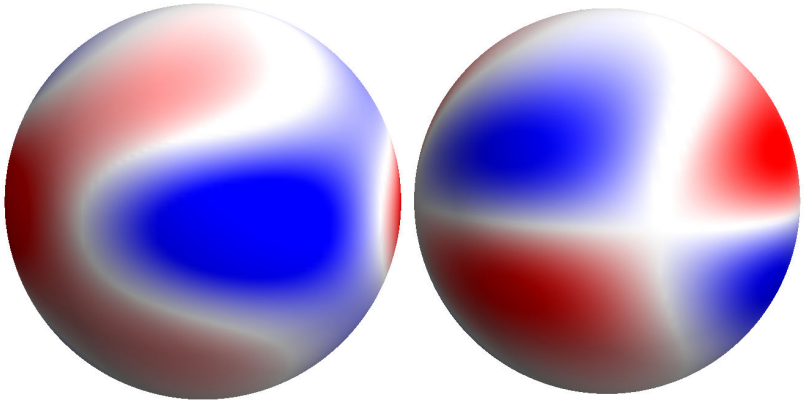

Figure 11.20: Perturbative horizon vorticity (left) and tendicity (right) of a magnetic-parity, $l = 2$, $m = 2$ quasinormal-mode perturbation of a Kerr black hole of spin $a/M = 0.945$. The horizon vorticity and tendicity appears dual to that of the equivalent electric-parity perturbation in Fig. 11.13.

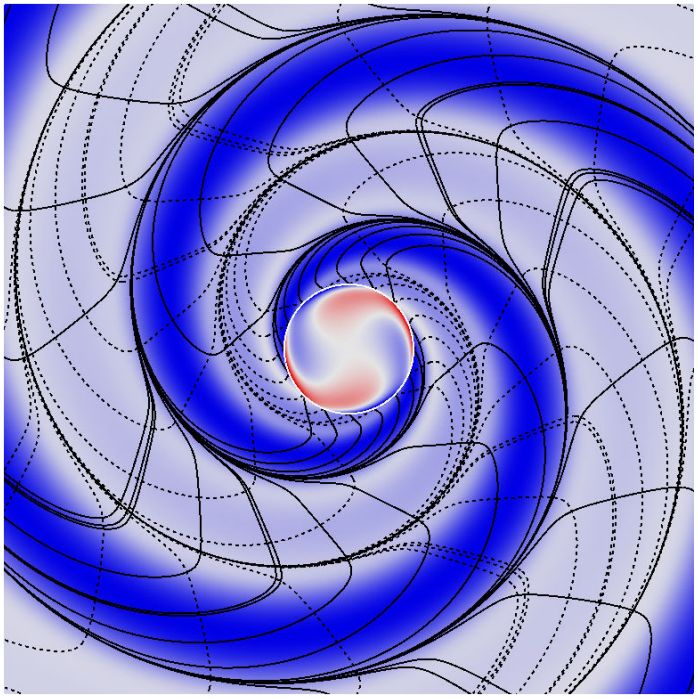

Figure 11.21: Perturbative vortex lines and vorticity in the plane of reflection symmetry for a magnetic-parity, $l = 2$, $m = 2$ quasinormal-mode perturbation of a Kerr black hole of spin $a/M = 0.945$. The coloring of the perturbative vorticity and the plotting of the lines is identical to that in Fig. 11.18.

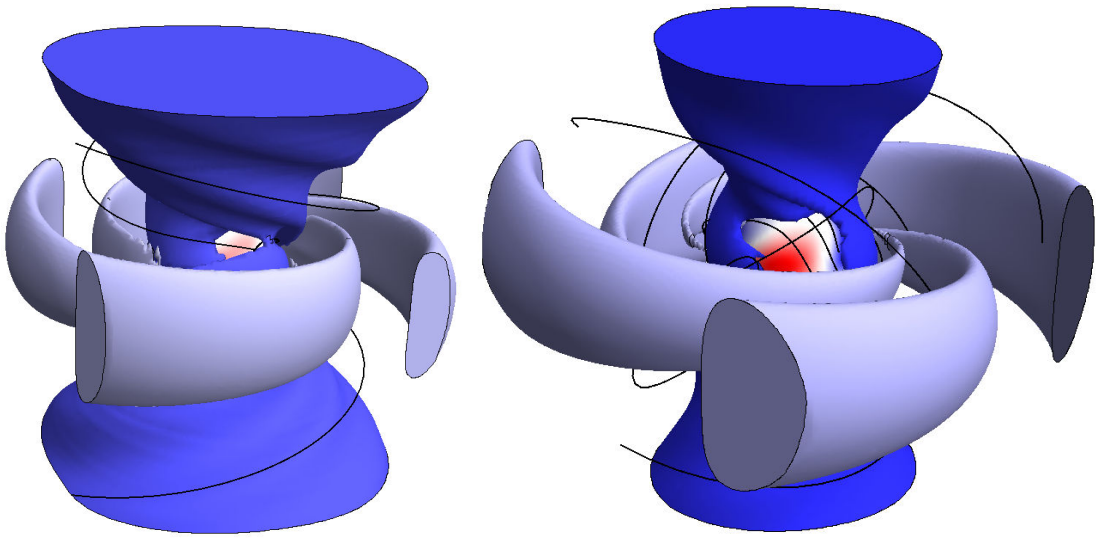

Figure 11.22: *Left*: Three-dimensional perturbative vortexes and vortex lines of the same perturbation as in Fig. 11.21. The horizon, the colored volumes, and the lines are depicted in the same way as the tendex quantities in Fig. 11.15, except the off-white regions show where the perturbative tendicity is at most 25% of the maximum value at each radius, and the blue (dark) regions show where it is at least 67.5% of the radial maximum. *Right*: Three-dimensional perturbative tendexes and tendex lines of this perturbation. The blue volume represents where the perturbative tendicity is at least 82.5% of the maximum value at that radius, and the off-white volume shows where it is at most 30% of this maximum value.

11.21. We color the vortex quantities in this figure similarly to the tendex quantities in Fig. 11.14, so that we can explore the duality. By comparing Figs. 11.21 and 11.14, we see that there is a strong duality between the perturbative vorticity and tendicity of these opposite-parity modes; the major difference is in the perturbative vortex and tendex lines. The vortex lines head out from the regions of large perturbative horizon vorticity, and they collect on the outside of the vortexes as they spiral out. In fact, the vortex lines look much more like a frame-dragged version of the magnetic-parity vortex lines of a perturbation of Schwarzschild (Fig. 11.18).

Finally, we look at the three-dimensional vortexes and tendexes in Fig. 11.22. The coloring of the perturbative vortex results are equivalent to those of the opposite-parity results in Fig. 11.15 except for the exact percentages of the volumes shown. For the blue (dark) vortexes correspond to regions of at least 67.5% of the radial maximum, and accompanying off-white regions are where it is at most 25% of that maximum. Similarly, for the tendexes, the off-white regions are now at most 30% of their radial maximum and the (dark) blue regions are at least 82.5% of the maximum. As one can see by comparing the Figs. 11.22 and 11.15, the duality looks to be much weaker for highly spinning black holes. The vortex lines for the magnetic-parity perturbation do not connect back to the horizon (as the electric-parity tendex lines did), and the perturbation's tendex lines do cross the equatorial plane. In addition, even the shapes of the tendexes and vortexes are somewhat different for the opposite-parity modes.

Focusing only on the general, qualitative features of the magnetic-parity vortexes and tendexes, one sees that wave generation does occur in the dual way to the electric-parity mode of a perturbed Kerr black hole. There are two equatorial perturbative vortexes that connect to the horizon vortexes that primarily induce the near-zone perturbative tendexes. These vortexes and tendexes transition out of the equatorial plane towards the poles to become the gravitational waves far from the black hole. In this sense, there is a consistent description of wave generation by magnetic-parity modes of black holes of any spins.

11.I Appendix: Vortex and Tendex Lines of $l = 2$, $m = 2$ Perturbations of Schwarzschild and Kerr Black Holes with the Background Frame-Drag and Tidal Fields

In this appendix, we show the tendex lines of the perturbed Schwarzschild black holes of Section 11.8.1, when we also include the background tidal field of an unperturbed Schwarzschild black holes. Similarly, we will also describe the tendex and vortex lines of the perturbed Kerr black holes of Section 11.8.2 when we do not subtract away the background tidal and frame-drag fields of the unperturbed Kerr black hole. We find these images useful for comparing with the results of numerical-relativity simulations, for which it is more difficult to separate the background spacetime from its perturbations.

11.I.1 Tendex Lines of Electric- and Magnetic-Parity Quasinormal-Mode Perturbations of Schwarzschild Black Holes

Following the procedure in Appendix 11.G, we can compute the tendex and vortex lines of electric- and magnetic-parity $l = 2$, $m = 2$, quasinormal-mode perturbations of Schwarzschild black holes, for the complete (background plus perturbation) tidal field. The results are shown in Fig. 11.23, where the electric-parity perturbation is on the left and the magnetic-parity perturbation is on the right.

In both panels of Fig. 11.23, we scale the tendex lines by r^3, so that we can remove the radial fall-off in the tendicity. We make the perturbation sufficiently small that one cannot see the effect of the perturbation in either the horizon tendicity, or the red (light) radial tendex lines; consequently, it is the tendex lines in the angular directions that carry the information about the quasinormal-mode perturbation. In Section 11.4, we noted that because an unperturbed Schwarzschild black hole is spherically symmetric, the tendicity on a sphere of constant radius is constant, and, therefore, any direction tangent to the sphere is a valid tendex line. For a weakly perturbed Schwarzschild black hole, although the perturbation may be small, the perturbation restricted to a sphere of constant r completely determines the variation in the tendicity, and, furthermore, it will determine the pattern

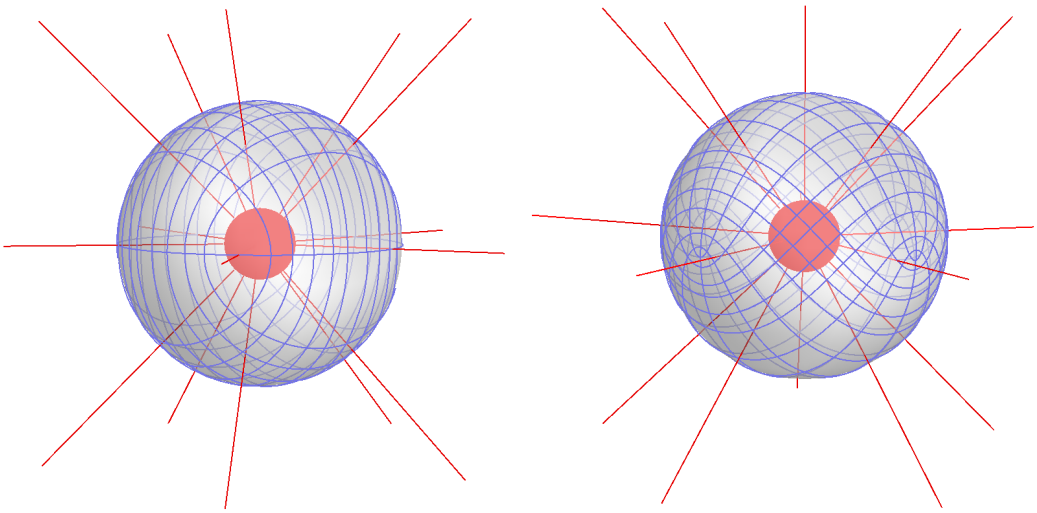

Figure 11.23: *Left*: Tendex lines of an electric-parity, $l = 2$, $m = 2$ quasinormal-mode perturbation of a Schwarzschild black hole. The lines are colored by tendicity scaled by r^3, but the coloring is otherwise the same as in previous figures. The transparent sphere is used to clarify the perspective of the tendex lines and to highlight the fact that the angular tendex lines lie nearly on a sphere. *Right*: Tendex lines of a magnetic-parity, $l = 2$, $m = 2$ quasinormal-mode perturbation of a Schwarzschild black hole. The figure is otherwise the same as that on the left.

of the tendex lines. This is analogous to degenerate perturbation theory in quantum mechanics, in which the eigenstates of the perturbing Hamiltonian restricted to the subspace spanned by the degenerate eigenstates are treated as the unperturbed states within the degenerate subspace.

One can now use these facts about degeneracy to understand the pattern of the tendex lines in the angular direction. The tidal field in the strictly angular directions, Eq. (11.119) will determine the structure of the tendex lines on the sphere. The angular dependence is determined by the transverse-traceless, electric-parity tensor harmonic (for the left panel), because the trace term in Eq. (11.119) is proportional to the identity and will not lift the degeneracy of the tendex lines. One would expect, therefore, that the tendex lines in the angular direction would resemble those of transverse-traceless, $l = 2$, $m = 2$, gravitational waves generated by a time-dependent mass quadrupole. These were shown in [8, 7], and the pattern of the lines is nearly identical. We also include a transparent sphere to emphasize the fact that the lines stay nearly on a sphere; this sphere also helps to add depth to the figure. The tendicity along the lines is quite different from those of a gravitational wave, because for the perturbed Schwarzschild black hole, the tendicity is primarily determined by the constant unperturbed value on the sphere. Nevertheless, the tendex lines on the sphere show a striking similarity to those of gravitational waves at infinity.

For the magnetic-parity perturbation (on the right), the pattern is now set by an $l = 2$, $m = 2$, magnetic-parity tensor harmonic; consequently, one would expect that the lines would resemble those of transverse-traceless gravitational waves at infinity, produced by a time-dependent, current-

quadrupole source. Those lines were shown in [8], and they appear identical. Once more, though, the value of the tendicity along the lines is set by the background Schwarzschild black hole for the lines in Fig. 11.23, and, therefore, the tendicity of these lines differs from those studied in [8].

11.I.2 Tendex and Vortex Lines of Quasinormal-Mode Perturbations of Electric and Magnetic Parities of Kerr Black Holes

Using the procedure in Section 11.G, we compute here the tendex and vortex lines of an electric- and magnetic-parity, $l = 2$, $m = 2$, quasinormal-mode perturbation of a rapidly rotating Kerr black hole of dimensionless spin, $a/M = 0.945$, for the full tidal and frame-drag fields (the background and the perturbative pieces, combined). Because the images here will be useful for comparing to the results of numerical-relativity simulations, we choose our slicing and our spatial coordinates to be similar to those of the simulations. We again choose a horizon-penetrating slicing (values of constant Kerr-Schild time), and oblately deformed spatial coordinates (Kerr-Schild coordinates). We summarize our result in the four panels of Fig. 11.24, and we explain these panels below.

As in the previous part of this section, we must choose a magnitude for the perturbations. We choose it to be sufficiently small that we do not see its effects in the radial tendex lines; consequently, the information about the perturbation will be carried in the predominantly angular tendex lines. We also impose an additional constraint on the magnitude of the perturbation. Near the event horizon, the tendicity of the two non-radial tendex lines are distinct near the equatorial plane (they are always nearly equal at the poles); at larger values of r, the tendicities becomes nearly equal even in the equatorial plane. For our perturbations, we will choose the perturbation to be smaller than the difference of the angular tendicities in the equatorial plane, where we begin the lines. With this choice, the angular tendex lines will retain some features of the unperturbed lines before they become more distorted by the perturbation in the regions near the poles.

Our prescription for choosing the magnitude of the perturbation helps to explain the tendex and vortex lines depicted in Fig. 11.24. For both the tendex and vortex lines, when the lines are near the equatorial plane ($\theta = \pi/2$) they resemble the unperturbed lines, but as they head toward the poles, they begin to become perturbed. The reason for this is similar to that described in the section on Schwarzschild black holes above: when the perturbation is small compared to the difference in the eigenvalues, the perturbations have little effect on the tendex or vortex lines; when the perturbation is large compared to the difference of the eigenvalues, then the perturbation restricted to the degenerate subspace completely determines the pattern of the lines.

In the vicinity of the poles, the degenerate subspace is a plane parallel to the equatorial plane, and the perturbative tendex lines must form a regular grid around these points. When one combines this observation with the parity of the perturbation, one can then argue why the lines at the opposite poles must be either parallel or orthogonal. Thus, these few simple constraints combine to explain

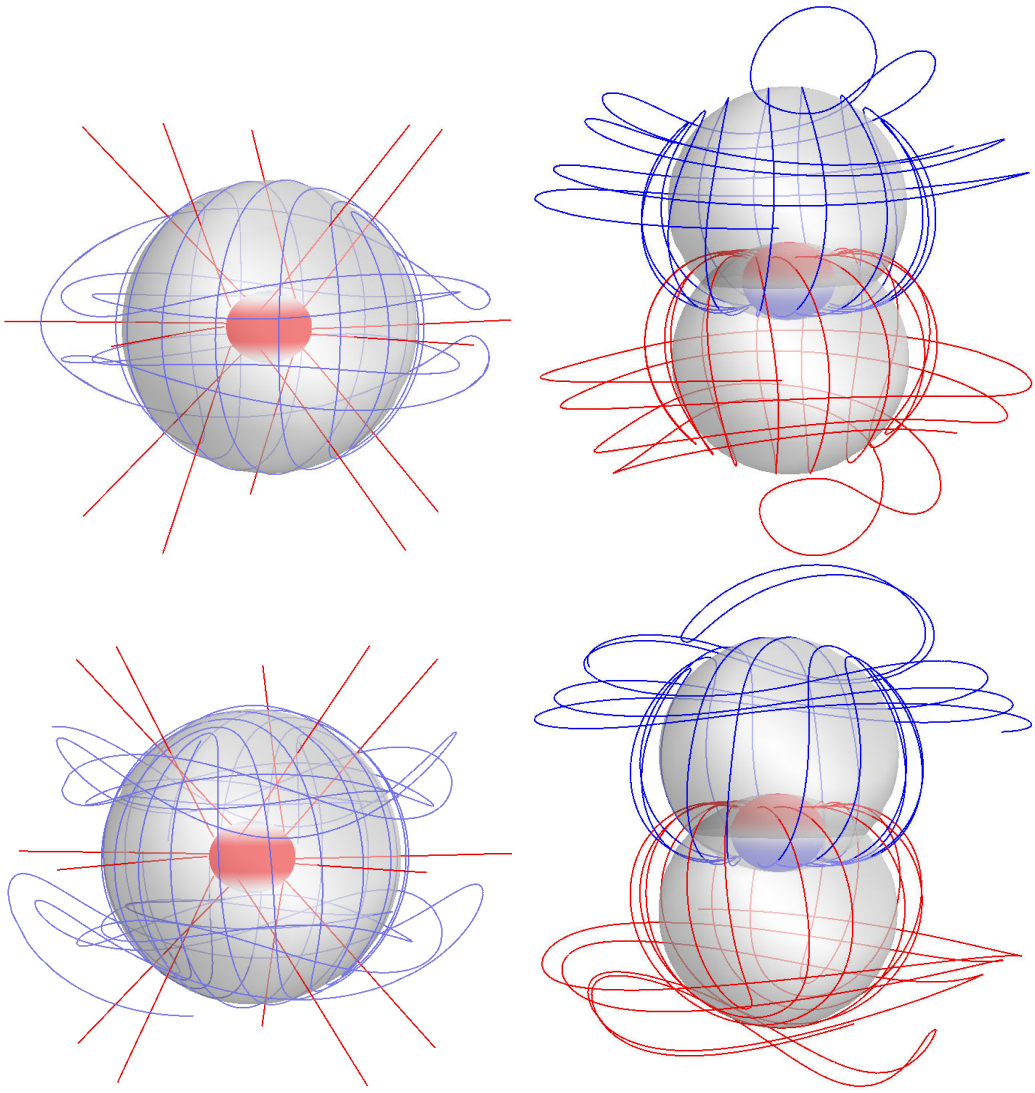

Figure 11.24: *Top left*: Tendex lines of an electric-parity, $l = 2$, $m = 2$, quasinormal-mode perturbation of a rapidly rotating Kerr black hole of dimensionless spin $a/M = 0.945$, plotted in Kerr-Schild coordinates. The lines are colored by tendicity scaled by r^3, and the transparent sphere is used (here and in the other panels) to improve the perspective of the three-dimensional lines. *Top right*: Vortex lines of the same perturbation as the top-left panel. The lines are colored by vorticity scaled by r^4, but are otherwise colored in the same way as previous figures. *Bottom left*: Tendex lines of a magnetic-parity, $l = 2$, $m = 2$, quasinormal-mode perturbation of a Kerr black hole of dimensionless spin $a/M = 0.945$. The coloring of the lines is the same as in the top-left panel. *Bottom right*: Vortex lines of the same quasinormal-mode perturbation of a Kerr black hole as in the bottom-left panel; the coloring of the lines is the same as in the top-right panel.

the relatively simple pattern of the vortex and tendex lines of the perturbation plus the background frame-drag and tidal fields.

Bibliography

[1] J. Centrella, J. G. Baker, B. J. Kelly, and J. R. van Meter, Rev. Mod. Phys. **82**, 3069 (2010).

[2] P. Jaranowski and A. Krlak, Living Rev. Relativity **15**, 4 (2012).

[3] E. Newman and R. Penrose, J. Math. Phys. **3**, 566 (1962).

[4] C. W. Misner, K. S. Thorne, and J. A. Wheeler, *Gravitation* (Freeman, New York, 1973).

[5] L. Smarr, Phys. Rev. D **7**, 289 (1973).

[6] R. Owen, J. Brink, Y. Chen, J. D. Kaplan, G. Lovelace, K. D. Matthews, D. A. Nichols, M. A. Scheel, F. Zhang, A. Zimmerman, et al., Phys. Rev. Lett. **106**, 151101 (2011).

[7] D. A. Nichols, R. Owen, F. Zhang, A. Zimmerman, J. Brink, Y. Chen, J. Kaplan, G. Lovelace, K. D. Matthews, M. A. Scheel, et al. (2011).

[8] A. Zimmerman, D. A. Nichols, and F. Zhang, Phys. Rev. D **84**, 044037 (2011).

[9] T. Regge and J. A. Wheeler, Phys. Rev. **108**, 1063 (1957).

[10] F. J. Zerilli, Phys. Rev. Lett. **24**, 737 (1970).

[11] P. L. Chrzanowski, Phys. Rev. D **11**, 2042 (1975).

[12] L. S. Kegeles and J. M. Cohen, Phys. Rev. D **19**, 1641 (1979).

[13] J. M. Stewart, Proc. R. Soc. Lond. A **367**, 527 (1979).

[14] R. M. Wald, Phys. Rev. Lett. **41**, 203 (1978).

[15] C. O. Lousto and B. F. Whiting, Phys. Rev. D **66**, 024026 (2002).

[16] A. Ori, Phys. Rev. D **67**, 124010 (2003).

[17] N. Yunes and J. Gonzalez, Phys. Rev. D **73**, 024010 (2006).

[18] T. S. Keidl, J. L. Friedman, and A. G. Wiseman, Phys. Rev. D **75**, 124009 (2007).

[19] T. S. Keidl, A. G. Shah, J. L. Friedman, D.-H. Kim, and L. R. Price, Phys. Rev. D **82**, 124012 (2010).

[20] A. G. Shah, T. S. Keidl, J. L. Friedman, D.-H. Kim, and L. R. Price, Phys. Rev. D **83**, 064018 (2011).

[21] G. Lovelace, M. Boyle, M. A. Scheel, and B. Szilágyi, Classical Quantum Gravity **29**, 045003 (2012).

[22] S. Teukolsky, Astrophys. J. **185**, 635 (1973).

[23] H. Stephani, D. Kramer, M. MacCallum, C. Hoenselaers, and E. Herlt, *Exact Solutions of Einstein's Field Equations* (Cambridge University Press, Cambridge, UK, 2003).

[24] `http://www.black-holes.org/SpEC.html`.

[25] L. B. Szabados, Living Rev. Relativity **12**, 4 (2009).

[26] R. Penrose and W. Rindler, *Spinors and Space-time, Volume 1* (Cambridge University Press, Cambridge, 1992).

[27] T. Damour, in *Proceedings of the Second Marcel Grossman Meeting on General Relativity*, edited by R. Ruffini (North-Holland Publishing Company, Amsterdam, 1982), pp. 587–606.

[28] S. W. Hawking and J. B. Hartle, Commun. Math. Phys. **27**, 283 (1972).

[29] J. Hartle, Phys. Rev. D **9**, 2749 (1974).

[30] J. L. Jaramillo, R. P. Macedo, P. Moesta, and L. Rezzolla, Phys. Rev. D **85**, 084030 (2012).

[31] J. L. Jaramillo, R. P. Macedo, P. Moesta, and L. Rezzolla, Phys. Rev. D **85**, 084031 (2012).

[32] J. D. Brown and J. W. York, Phys. Rev. D **47**, 1407 (1993).

[33] A. Ashtekar, C. Beetle, and J. Lewandowski, Phys. Rev. D **64**, 044016 (2001).

[34] A. Ashtekar and B. Krishnan, Phys. Rev. D **68**, 104030 (2003).

[35] O. Dreyer, B. Krishnan, D. Shoemaker, and E. Schnetter, Phys. Rev. D **67**, 024018 (2003).

[36] G. B. Cook and B. F. Whiting, Phys. Rev. D **76**, 041501(R) (2007).

[37] R. Owen, Ph.D. thesis, California Institute of Technology (2007).

[38] G. Lovelace, R. Owen, H. P. Pfeiffer, and T. Chu, Phys. Rev. D **78**, 084017 (2008).

[39] A. Ashtekar, J. Engle, T. Pawlowski, and C. V. D. Broeck, Classical Quantum Gravity **21**, 2549 (2004).

[40] E. Schnetter, B. Krishnan, and F. Beyer, Phys. Rev. D **74**, 024028 (2006).

[41] R. Owen, Phys. Rev. D **80**, 084012 (2009).

[42] N. Vasset, J. Novak, and J. L. Jaramillo, Phys. Rev. D **79**, 124010 (2009).

[43] M. Jasiulek, Classical Quantum Gravity **26**, 254008 (2009).

[44] S. Chandrasekhar, *The Mathematical Theory of Black Holes* (Oxford University Press, Oxford, 1983).

[45] G. B. Cook and M. A. Scheel, Phys. Rev. D **56**, 4775 (1997).

[46] C. V. Vishveshwara, Nature **227**, 936 (1970).

[47] L. A. Edelstein and C. V. Vishveshwara, Phys. Rev. D **1**, 3514 (1970).

[48] F. J. Zerilli, Phys. Rev. D **2**, 2141 (1970).

[49] V. Moncrief, Annals of Physics **88** (1974).

[50] K. Martel and E. Poisson, Phys. Rev. D **71**, 104003 (2005).

[51] `http://www.phy.olemiss.edu/~berti/qnms.html`.

[52] E. Berti, V. Cardoso, and A. O. Starinets, Classical Quantum Gravity **26**, 163001 (2009).

[53] S. Teukolsky, Phys. Rev. Lett. **29**, 1114 (1972).

[54] P. P. Fiziev, Phys. Rev. D **80**, 124001 (2009).

[55] K. S. Thorne, Rev. Mod. Phys. **52**, 299 (1980).

[56] E. W. Leaver, Proc. R. Soc. Lond. A **402**, 285 (1985).

Epilogue

This thesis had the ultimate goal of gaining greater insight into the dynamics of and the gravitational waveform from black-hole binaries. Chapter 1 described the challenges associated with this problem, and it described three types of methods that could help produce a better understanding of these binaries. Part I (Chapters 2–4) described a way of quantifying the linear momentum of black holes and the momentum in the gravitational field, and used this approach to study how black holes radiate gravitational waves asymmetrically and recoil from the emission. Part II (Chapters 5–7) used analytical approximations to make simpler modes of black-hole waveforms. The first two chapters of this part introduced a new way of combining well-known approximation techniques to make gravitational waveforms that cover all three stages of the binary's dynamics: the inspiral, the merger, and the ringdown. The third chapter in this part related the ringdown of a binary to properties of geodesics near the black hole's horizon. Finally, Part III (Chapters 8–11) introduced a new way of visualizing spacetime curvature and developed intuition into these new tools by applying them to well-known analytical spacetimes; then it began exploring nonlinear numerical simulations.

These three different methods together helped to explain the simplicity of the dynamics and waveform from full numerical simulations of black-hole binaries. Part I showed that some of the most nonlinear dynamics occur very close to the time of merger and very near the black holes; furthermore, much of the nonlinearity is engulfed by the formation of a larger final black hole after the two merge. This point was affirmed by the hybrid model in the first two chapters of Part II. There, the nonlinear part of the spacetime was neglected and replaced by an analytical approximation to the exact dynamics; nevertheless, the waveform produced by this model agreed very well with exact results. In Part III, the simplicity of the spacetime curvature near the black holes was visualized clearly. By comparing visualizations of exact numerical spacetimes with those of simpler analytical models of black holes, we found remarkable similarity between the two, and we developed better intuition about the dynamics of spacetime curvature during these dramatic astrophysical events.

The simple behavior of the binary's dynamics and waveforms suggests that there should be an effective description of the problem in terms of simpler variables than those of the full, nonlinear, Einstein field equations. The methods and tools of this thesis were three proposals for these simpler

effective descriptions. Because they are still under active research, it is not clear which of these models will ultimately become the most useful for understanding black-hole binaries; nevertheless, we are optimistic that these methods, and their variations, will continue to extract geometrodynamical insights into the physics of black holes in the future.